Arthritis & Rheumatology

An Official Journal of the American College of Rheumatology
www.arthritisrheum.org and wileyonlinelibrary.com

GENERAL INFORMATION

TO SUBSCRIBE

Institutions and Non-Members

Email: wileyonlinelibrary.com
Phone: (201) 748-6645
Write: Wiley Periodicals LLC
Attn: Journals Admin Dept UK
111 River Street
Hoboken, NJ 07030

Volumes 74, 2022:
Institutional Print Only: **Arthritis & Rheumatology and Arthritis Care & Research:** $2,603 in US, Canada, and Mexico; $2,603 outside North America
Institutional Online Only: $2,495 in US, Canada, Mexico, and outside North America
Institutional Print and Online Only: $2,802 in US, Canada, and Mexico; $2,802 outside North America

For submission instructions, subscription, and all other information visit: wileyonlinelibrary.com.

Arthritis & Rheumatology accepts articles for Open Access publication. Please visit https://authorservices.wiley.com/author-resources/Journal-Authors/open-access/hybrid-open-access.html for further information about OnlineOpen.

Wiley's Corporate Citizenship initiative seeks to address the environmental, social, economic, and ethical challenges faced in our business and which are important to our diverse stakeholder groups. Since launching the initiative, we have focused on sharing our content with those in need, enhancing community philanthropy, reducing our carbon impact, creating global guidelines and best practices for paper use, establishing a vendor code of ethics, and engaging our colleagues and other stakeholders in our efforts.
Follow our progress at www.wiley.com/go/citizenship.

Access to this journal is available free online within institutions in the developing world through the HINARI initiative with the WHO. For information, visit www.healthinternetwork.org.

Disclaimer

The Publisher, the American College of Rheumatology, and Editors cannot be held responsible for errors or any consequences arising from the use of information contained in this journal; the views and opinions expressed do not necessarily reflect those of the Publisher, the American College of Rheumatology and Editors, neither does the publication of advertisements constitute any endorsement by the Publisher, the American College of Rheumatology and Editors of the products advertised.

Members:

American College of Rheumatology/Association of Rheumatology Professionals

For membership rates, journal subscription information, and change of address, please write:
American College of Rheumatology
2200 Lake Boulevard
Atlanta, GA 30319-5312
(404) 633-3777

ADVERTISING SALES AND COMMERCIAL REPRINTS

Sales: Kathleen Malseed, National Account Manager
E-mail: kmalseed@pminy.com
Phone: (215) 852-9824
Pharmaceutical Media, Inc.
30 East 33rd Street, New York, NY 10016

Production: Patti McCormack
E-mail: pmccormack@pminy.com
Phone: (212) 904-0376
Pharmaceutical Media, Inc.
30 East 33rd Street, New York, NY 10016

Publisher: Arthritis & Rheumatology is published by Wiley Periodicals LLC, 101 Station Landing, Suite 300, Medford, MA 02155
Production Editor: Ramona Talantor, artprod@wiley.com

ARTHRITIS & RHEUMATOLOGY (Print ISSN 2326-5191; Online ISSN 2326-5205 at Wiley Online Library, wileyonlinelibrary.com) is published monthly on behalf of the American College of Rheumatology by Wiley Periodicals LLC, a Wiley Company, 111 River Street, Hoboken, NJ 07030-5774. Periodicals postage paid at Hoboken, NJ and additional offices. POSTMASTER: Send all address changes to Arthritis & Rheumatology, Wiley Periodicals LLC, c/o The Sheridan Press, PO Box 465, Hanover, PA 17331. **Send subscription inquiries care of** Wiley Periodicals LLC, Attn: Journals Admin Dept UK, 111 River Street, Hoboken, NJ 07030, (201) 748-6645 (nonmember subscribers only; American College of Rheumatology/Association of Rheumatology Health Professionals members should contact the American College of Rheumatology). **Subscription Price:** (Volumes 74, 2022: Arthritis & Rheumatology and Arthritis Care & Research) Print only: $2,603.00 in U.S., Canada and Mexico, $2,603.00 rest of world. For all other prices please consult the journal's website at wileyonlinelibrary.com. All subscriptions containing a print element, shipped outside U.S., will be sent by air. Payment must be made in U.S. dollars drawn on U.S. bank. Prices are exclusive of tax. Asia-Pacific GST, Canadian GST and European VAT will be applied at the appropriate rates. For more information on current tax rates, please go to www.wileyonlinelibrary.com/tax-vat. The price includes online access to the current and all online backfiles to January 1st 2018, where available. For other pricing options including access information and terms and conditions, please visit https://onlinelibrary.wiley.com/library-info/products/price-lists. Terms of use can be found here: https://onlinelibrary.wiley.com/terms-and-conditions. **Delivery Terms and Legal Title:** Where the subscription price includes print issues and delivery is to the recipient's address, delivery terms are Delivered at Place (DAP); the recipient is responsible for paying any import duty or taxes. Title to all issues transfers Free of Board (FOB) our shipping point, freight prepaid. We will endeavor to fulfill claims for missing or damaged copies within six months of publication, within our reasonable discretion and subject to availability. **Change of Address:** Please forward to the subscriptions address listed above 6 weeks prior to move; enclose present mailing label with change of address. **Claims** for undelivered copies will be accepted only after the following issue has been received. Please enclose a copy of the mailing label or cite your subscriber reference number in order to expedite handling. Missing copies will be supplied when losses have been sustained intransit and where reserve stock permits. Send claims care of Wiley Periodicals LLC, Attn: Journals Admin Dept UK, 111 River Street, Hoboken, NJ 07030. If claims are not resolved satisfactorily, please write to Subscription Distribution c/o Wiley Periodicals LLC, 111 River Street, Hoboken, NJ 07030. **Cancellations:** Subscription cancellations will not be accepted after the first issue has been mailed. **Journal Customer Services:** For ordering information, claims and any enquiry concerning your journal subscription please go to https://wolsupport.wiley.com/s/contactsupport?tabset-a7d10=2 or contact your nearest office. **Americas:** Email: cs-journals@wiley.com; Tel: +1 877 762 2974. **Europe, Middle East and Africa:** Email: cs-journals@wiley.com; Tel: +44 (0) 1865 778315; 0800 1800 536 (Germany). **Asia Pacific:** Email: cs-journals@wiley.com; Tel: +65 6511 8000. **Japan:** For Japanese speaking support, Email: cs-japan@wiley.com. **Visit our Online Customer Help** at https://wolsupport.wiley.com/s/contactsupport?tabset-a7d10=2. **Back Issues:** Single issues from current and prior year volumes are available at the current single issue price from csjournals@wiley.com. Earlier issues may be obtained from Periodicals Service Company, 351 Fairview Avenue-Ste 300, Hudson, NY 12534, USA. Tel: + 1 518 822-9300, Fax: +1 518 822-9305, Email: psc@periodicals.com. Printed in the USA by The Sheridan Group.

Arthritis & Rheumatology

An Official Journal of the American College of Rheumatology
www.arthritisrheum.org and wileyonlinelibrary.com

Cover design: Todd Machen

♾This journal is printed on acid-free paper.

Arthritis & Rheumatology

An Official Journal of the American College of Rheumatology
www.arthritisrheum.org and wileyonlinelibrary.com

VOLUME 74 • June 2022 • NO. 6

Cover image: The figure on the cover (from Tong et al, pages 1001–1012) shows human endometrial stromal cells undergoing decidualization in response to estradiol, medroxyprogesterone, and cyclic AMP in the presence of antiphospholipid antibodies. After 96 hours, F-actin staining (red) demonstrates that the cells are becoming more cuboidal morphologically, characteristic of decidualization. Nuclei are counterstained with DAPI (blue).

In this Issue

Highlights from this issue of *A&R* | By Lara C. Pullen, PhD

Rheumatoid Factor and Anti–Modified Protein Antibody Reactivities Converge on IgG Epitopes

In this issue, Mergaert et al (p. 984) describe the repertoire of epitopes bound by anti–modified protein antibodies (AMPAs) and demonstrate that this repertoire includes modified IgG epitopes. The newly discovered IgG epitopes are bound by AMPAs in addition to rheumatoid factors (RFs). The findings expand on and partially merge the known reactivities of RFs and AMPAs and position IgG as a common antigen that connects the otherwise divergent reactivities of RFs and AMPAs.

p. 984

In their study, the investigators evaluated IgG binding to all possible linear epitopes on the constant region of IgG heavy chain. They found that seropositive RA sera showed high IgG binding to multiple citrulline- and homocitrulline-containing IgG-derived peptides, and they characterized the variability among epitopes as well as variability in IgG binding among subjects and monoclonal AMPAs. When the researchers examined sera from patients with non-RA disease, however, they found consistent IgG binding to only 1 linear IgG epitope: a hinge region epitope bound in anti-SSA+ Sjögren's syndrome. The team discovered that the monoclonal AMPAs bound citrulline- and homocitrulline-containing IgG peptides and modified IgG Fc. In their discussion, the authors suggest that AMPAs with limited multireactivity may develop first, and are then followed by anti–modified IgG antibodies and later RF, possibly via epitope spreading.

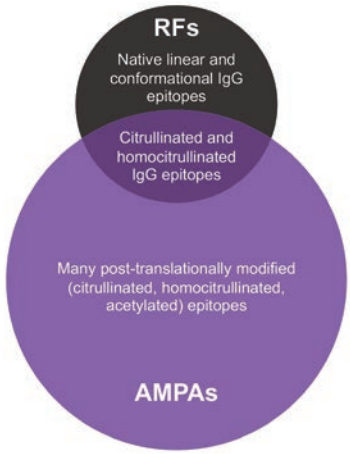

Figure 1. The reactivities of RFs and AMPAs converge on IgG epitopes. The Venn diagram illustrates RF and AMPA reactivities.

Antiphospholipid Antibodies Increase Cell Decidualization, Senescence, and Inflammation

The presence of antiphospholipid antibodies (aPLs) is one of the single biggest maternal risk factors for recurrent miscarriage. Because appropriately controlled decidualization and function of endometrial stromal cells (EnSCs) are key for successful implantation, placentation, and the establishment of a healthy pregnancy, scientists wonder whether these processes may be impaired in obstetric antiphospholipid syndrome (APS). In this issue, Tong et al (p. 1001) report findings that shed new light on the pathogenesis of pregnancy complications in women with aPLs.

p. 1001

For their experiments, the investigators used the aPL IIC5, describing it in their article as a well-characterized mouse IgG1 anti-human β2-glycoprotein I monoclonal antibody. They found that aPLs increased decidualization and senescence and induced inflammation in human EnSC cells, findings that they were able to replicate in primary human EnSCs. The researchers described the aPL-induced response in primary human EnSCs as reminiscent of an inflammatory senescence-associated secretory phenotype.

The team then turned to a mouse model of decidualization and APS to validate their in vitro findings and demonstrated that aPLs increased decidualization and induction of uterine inflammation and senescence. The researchers next sought to determine which receptor on human EnSCs was activated by aPLs to mediate the process; they found that aPL-induced up-regulation of EnSC decidualization and inflammation occurred, in part, through Toll-like receptor 4 and, in part, through p38 MAPK, a signaling pathway reported to be increased in trophoblasts exposed to aPLs. In contrast, the decidualization and senescence responses were reactive oxygen species-dependent.

Finally, the team investigated whether the standard therapeutics for women with obstetric APS, low molecular weight heparin (LMWH), could protect against the effect of aPLs on EnSC function. They found that LMWH reduced the ability of aPLs to increase EnSC decidualization and inflammation. The authors conclude that their findings underscore the benefit of heparin in the prevention of pregnancy loss in this high-risk population.

Necroptosis Contributes to Myofiber Death in Idiopathic Inflammatory Myopathies

Idiopathic inflammatory myopathies (IIMs) include several distinct entities: dermatomyositis (DM), amyopathic DM (ADM), and immune-mediated necrotizing myopathy (IMNM). Not only do DM and IMNM show different clinical manifestations and pathologic features, but animal studies indicate that DM and IMNM have differing pathogeneses. While muscle damage is a prominent feature of all IIMs, the underlying mechanism behind this damage has not been fully clarified. Some researchers have suggested, however, that necroptosis (programmed necrosis that has been associated with many types of diseases affecting the tissue) may be behind the damage.

p. 1048

Initiators of necroptosis include death receptors, pathogen-recognition receptors, and the nucleic-acid–sensing protein ZBP1.

In this issue, Peng et al (p. 1048) report the results of the first attempt to investigate the dysregulation of necroptosis in IIMs. Their data demonstrate that overactivated necroptosis contributes to muscle damage in IIM (both DM and IMNM). The team analyzed muscle biopsy samples from 26 patients with confirmed IIM and identified elevated expression of receptor-interacting protein 3 and mixed-lineage kinase domain–like proteins. The researchers also found elevated expression of high mobility group box chromosomal protein 1, a protein released extracellularly during necroptotic cell death in the muscle tissue of patients with IIM. Taken together, their results indicate that the muscle tissues of IIM patients not only had significant features of myofiber necrosis but also had high levels of expression of key molecules that participate in the necroptosis machinery.

The investigators then performed in vitro cell culture experiments in which they used tumor necrosis factor to induce necroptosis in C2C12 myoblasts in the presence of the pan-caspase inhibitor Z-VAD. They found that when they inhibited necroptosis, they were able to prevent necroptosis-induced cell death of C2C12 cells. The authors suggest that necroptosis inhibitors could represent a new therapeutic target in the treatment of IIMs.

Journal Club

A monthly feature designed to facilitate discussion on research methods in rheumatology.

Nintedanib in Patients with Autoimmune Disease–Related Progressive Fibrosing ILDs: Subgroup Analysis of the INBUILD Trial

Matteson et al, *Arthritis Rheumatol* 2022;74:1039–1047

Interstitial lung disease (ILD) is a common manifestation of systemic autoimmune diseases. Progression of ILD is associated with a poor prognosis. Nintedanib is a tyrosine kinase inhibitor that has been shown to slow the decline in forced vital capacity (FVC) in patients with idiopathic pulmonary fibrosis (IPF), other fibrosing ILDs with a progressive phenotype, and fibrosing ILD associated with systemic sclerosis (SSc). The INBUILD trial investigated the efficacy and safety of nintedanib compared to placebo in 663 patients with progressive fibrosing ILDs other than IPF. To be eligible to enter the INBUILD trial, patients needed to have >10% extent of fibrosing ILD on a high-resolution computed tomography (HRCT) scan and to have shown progression of their ILD, based on a worsening of FVC, symptoms, or fibrotic abnormalities on HRCT, within the previous 2 years, despite management deemed appropriate in clinical practice.

This study presents data from the 170 patients with autoimmune disease–related ILDs who participated in the INBUILD trial. Results are presented for this subgroup on the annual rate of decline in FVC in ml/year over 52 weeks (i.e., the primary end point in the overall trial population and in patients with a usual interstitial pneumonia–like fibrotic pattern on HRCT), as well as on the proportions of patients with acute exacerbation of ILD or death, an absolute decline in FVC percent predicted of ≥10% or death, and death over the whole trial (i.e., after a mean exposure to trial medication of ~16 months). For the annual rate of decline in FVC, a *P* value for interaction was calculated as an indicator of the potential heterogeneity in the effect of nintedanib versus placebo across subgroups based on diagnosis (rheumatoid arthritis, SSc, mixed connective tissue disease, other autoimmune diseases). The safety and tolerability of nintedanib was assessed by examining the proportions of patients with adverse events and with adverse events leading to discontinuation of the trial drug, irrespective of causality.

Questions

1. **How easy would it be to use the inclusion criteria from this trial to identify patients with progressive ILD in clinical practice?**
2. **What do these results tell us about the effects of nintedanib in patients with autoimmune disease–related ILDs in general and in those with specific diseases?**
3. **How compelling are the findings on end points that were underpowered, such as the risk of acute exacerbations and death?**
4. **What evidence is there to support the use of other drugs in patients with ILD associated with autoimmune diseases other than SSc?**

In this Issue

Highlights from this issue of *A&R* | By Lara C. Pullen, PhD

Rheumatoid Factor and Anti–Modified Protein Antibody Reactivities Converge on IgG Epitopes

In this issue, Mergaert et al (p. 984) describe the repertoire of epitopes bound by anti–modified protein antibodies (AMPAs) and demonstrate that this repertoire includes modified IgG epitopes. The newly discovered IgG epitopes are bound by AMPAs in addition to rheumatoid factors (RFs). The findings expand on and partially merge the known reactivities of RFs and AMPAs and position IgG as a common antigen that connects the otherwise divergent reactivities of RFs and AMPAs.

p. 984

In their study, the investigators evaluated IgG binding to all possible linear epitopes on the constant region of IgG heavy chain. They found that seropositive RA sera showed high IgG binding to multiple citrulline- and homocitrulline-containing IgG-derived peptides, and they characterized the variability among epitopes as well as variability in IgG binding among subjects and monoclonal AMPAs. When the researchers examined sera from patients with non-RA disease, however, they found consistent IgG binding to only 1 linear IgG epitope: a hinge region epitope bound in anti-SSA+ Sjögren's syndrome. The team discovered that the monoclonal AMPAs bound citrulline- and homocitrulline-containing IgG peptides and modified IgG Fc. In their discussion, the authors suggest that AMPAs with limited multireactivity may develop first, and are then followed by anti–modified IgG antibodies and later RF, possibly via epitope spreading.

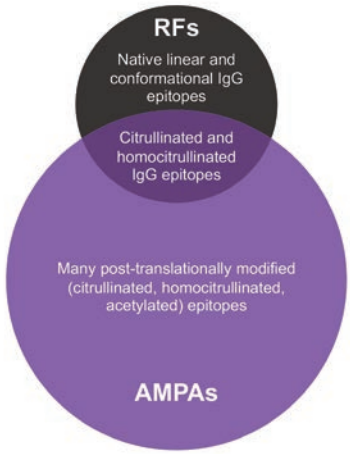

Figure 1. The reactivities of RFs and AMPAs converge on IgG epitopes. The Venn diagram illustrates RF and AMPA reactivities.

Antiphospholipid Antibodies Increase Cell Decidualization, Senescence, and Inflammation

The presence of antiphospholipid antibodies (aPLs) is one of the single biggest maternal risk factors for recurrent miscarriage. Because appropriately controlled decidualization and function of endometrial stromal cells (EnSCs) are key for successful implantation, placentation, and the establishment of a healthy pregnancy, scientists wonder whether these processes may be impaired in obstetric antiphospholipid syndrome (APS). In this issue, Tong et al (p. 1001) report findings that shed new light on the pathogenesis of pregnancy complications in women with aPLs.

p. 1001

For their experiments, the investigators used the aPL IIC5, describing it in their article as a well-characterized mouse IgG1 anti-human β2-glycoprotein I monoclonal antibody. They found that aPLs increased decidualization and senescence and induced inflammation in human EnSC cells, findings that they were able to replicate in primary human EnSCs. The researchers described the aPL-induced response in primary human EnSCs as reminiscent of an inflammatory senescence-associated secretory phenotype.

The team then turned to a mouse model of decidualization and APS to validate their in vitro findings and demonstrated that aPLs increased decidualization and induction of uterine inflammation and senescence. The researchers next sought to determine which receptor on human EnSCs was activated by aPLs to mediate the process; they found that aPL-induced up-regulation of EnSC decidualization and inflammation occurred, in part, through Toll-like receptor 4 and, in part, through p38 MAPK, a signaling pathway reported to be increased in trophoblasts exposed to aPLs. In contrast, the decidualization and senescence responses were reactive oxygen species-dependent.

Finally, the team investigated whether the standard therapeutics for women with obstetric APS, low molecular weight heparin (LMWH), could protect against the effect of aPLs on EnSC function. They found that LMWH reduced the ability of aPLs to increase EnSC decidualization and inflammation. The authors conclude that their findings underscore the benefit of heparin in the prevention of pregnancy loss in this high-risk population.

Necroptosis Contributes to Myofiber Death in Idiopathic Inflammatory Myopathies

Idiopathic inflammatory myopathies (IIMs) include several distinct entities: dermatomyositis (DM), amyopathic DM (ADM), and immune-mediated necrotizing myopathy (IMNM). Not only do DM and IMNM show different clinical manifestations and pathologic features, but animal studies indicate that DM and IMNM have differing pathogeneses. While muscle damage is a prominent feature of all IIMs, the underlying mechanism behind this damage has not been fully clarified. Some researchers have suggested, however, that necroptosis (programmed necrosis that has been associated with many types of diseases affecting the tissue) may be behind the damage.

p. 1048

Initiators of necroptosis include death receptors, pathogen-recognition receptors, and the nucleic-acid–sensing protein ZBP1.

In this issue, Peng et al (p. 1048) report the results of the first attempt to investigate the dysregulation of necroptosis in IIMs. Their data demonstrate that overactivated necroptosis contributes to muscle damage in IIM (both DM and IMNM). The team analyzed muscle biopsy samples from 26 patients with confirmed IIM and identified elevated expression of receptor-interacting protein 3 and mixed-lineage kinase domain–like proteins. The researchers also found elevated expression of high mobility group box chromosomal protein 1, a protein released extracellularly during necroptotic cell death in the muscle tissue of patients with IIM. Taken together, their results indicate that the muscle tissues of IIM patients not only had significant features of myofiber necrosis but also had high levels of expression of key molecules that participate in the necroptosis machinery.

The investigators then performed in vitro cell culture experiments in which they used tumor necrosis factor to induce necroptosis in C2C12 myoblasts in the presence of the pan-caspase inhibitor Z-VAD. They found that when they inhibited necroptosis, they were able to prevent necroptosis-induced cell death of C2C12 cells. The authors suggest that necroptosis inhibitors could represent a new therapeutic target in the treatment of IIMs.

Journal Club

A monthly feature designed to facilitate discussion on research methods in rheumatology.

Nintedanib in Patients with Autoimmune Disease–Related Progressive Fibrosing ILDs: Subgroup Analysis of the INBUILD Trial

Matteson et al, *Arthritis Rheumatol* 2022;74:1039–1047

Interstitial lung disease (ILD) is a common manifestation of systemic autoimmune diseases. Progression of ILD is associated with a poor prognosis. Nintedanib is a tyrosine kinase inhibitor that has been shown to slow the decline in forced vital capacity (FVC) in patients with idiopathic pulmonary fibrosis (IPF), other fibrosing ILDs with a progressive phenotype, and fibrosing ILD associated with systemic sclerosis (SSc). The INBUILD trial investigated the efficacy and safety of nintedanib compared to placebo in 663 patients with progressive fibrosing ILDs other than IPF. To be eligible to enter the INBUILD trial, patients needed to have >10% extent of fibrosing ILD on a high-resolution computed tomography (HRCT) scan and to have shown progression of their ILD, based on a worsening of FVC, symptoms, or fibrotic abnormalities on HRCT, within the previous 2 years, despite management deemed appropriate in clinical practice.

This study presents data from the 170 patients with autoimmune disease–related ILDs who participated in the INBUILD trial. Results are presented for this subgroup on the annual rate of decline in FVC in ml/year over 52 weeks (i.e., the primary end point in the overall trial population and in patients with a usual interstitial pneumonia–like fibrotic pattern on HRCT), as well as on the proportions of patients with acute exacerbation of ILD or death, an absolute decline in FVC percent predicted of ≥10% or death, and death over the whole trial (i.e., after a mean exposure to trial medication of ~16 months). For the annual rate of decline in FVC, a *P* value for interaction was calculated as an indicator of the potential heterogeneity in the effect of nintedanib versus placebo across subgroups based on diagnosis (rheumatoid arthritis, SSc, mixed connective tissue disease, other autoimmune diseases). The safety and tolerability of nintedanib was assessed by examining the proportions of patients with adverse events and with adverse events leading to discontinuation of the trial drug, irrespective of causality.

Questions

1. **How easy would it be to use the inclusion criteria from this trial to identify patients with progressive ILD in clinical practice?**
2. **What do these results tell us about the effects of nintedanib in patients with autoimmune disease–related ILDs in general and in those with specific diseases?**
3. **How compelling are the findings on end points that were underpowered, such as the risk of acute exacerbations and death?**
4. **What evidence is there to support the use of other drugs in patients with ILD associated with autoimmune diseases other than SSc?**

Clinical Connections

Role of Lysine-Specific Demethylase 1 in Metabolically Integrating Osteoclast Differentiation and Inflammatory Bone Resorption Through Hypoxia-Inducible Factor 1α and E2F1

Doi et al, *Arthritis Rheumatol* 2022;74:948–960

CORRESPONDENCE
Koichi Murata, MD, PhD: kchm@kuhp.kyoto-u.ac.jp

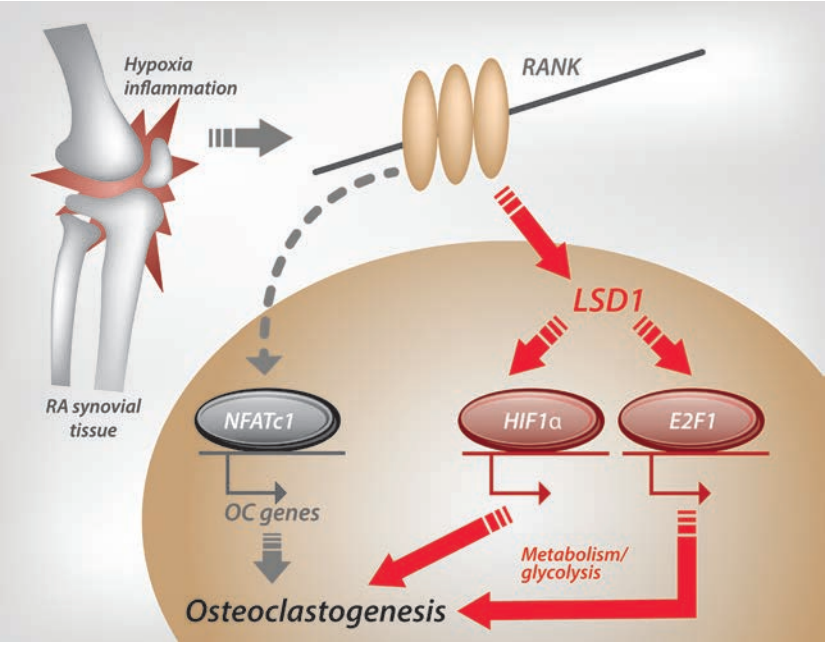

KEY POINTS

- LSD1 is a positive regulator for osteoclast differentiation.
- LSD1 promotes glycolysis via HIF-1α stabilization during osteoclast differentiation.
- Higher HIF-1α expression is associated with increased bone erosion in RA patients.
- LSD1 inhibition decreases pathologic bone resorption in inflammatory arthritis.

SUMMARY

Osteoclasts are the primary cells responsible for bone resorption in rheumatoid arthritis (RA). The combination of cellular hyperproliferation and infiltration in RA synovium increases oxygen demand and results in hypoxia. Osteoclast differentiation is considered an energy-demanding process, but the molecular mechanisms to meet energy demand in this harsh environment are not fully understood. Doi et al showed that lysine-specific demethylase 1 (LSD1) metabolically regulated osteoclast differentiation through hypoxia-inducible factor 1α (HIF-1α) and E2F1.

LSD1 was induced by RANKL in osteoclast precursor cells and was a positive regulator of osteoclast differentiation. RANKL-induced LSD1 stabilized HIF-1α protein, which is promptly degraded in a normoxic environment, thereby promoting glycolysis in conjunction with the up-regulation of E2F1, a transcription factor that mainly controls the cell cycle and promotes glycolysis during the early phases of osteoclastogenesis. Analysis of *cis*-acting expression quantitative trait loci revealed that higher HIF-1α expression was associated with increased bone erosion in RA patients. LSD1 inhibition decreased pathologic bone resorption in mouse models of inflammatory arthritis and osteolysis.

Rituximab Impairs B Cell Response But Not T Cell Response to COVID-19 Vaccine in Autoimmune Diseases

Bitoun et al, *Arthritis Rheumatol* 2022;74:927–933

CORRESPONDENCE
Xavier Mariette, MD, PhD: xavier.mariette@aphp.fr

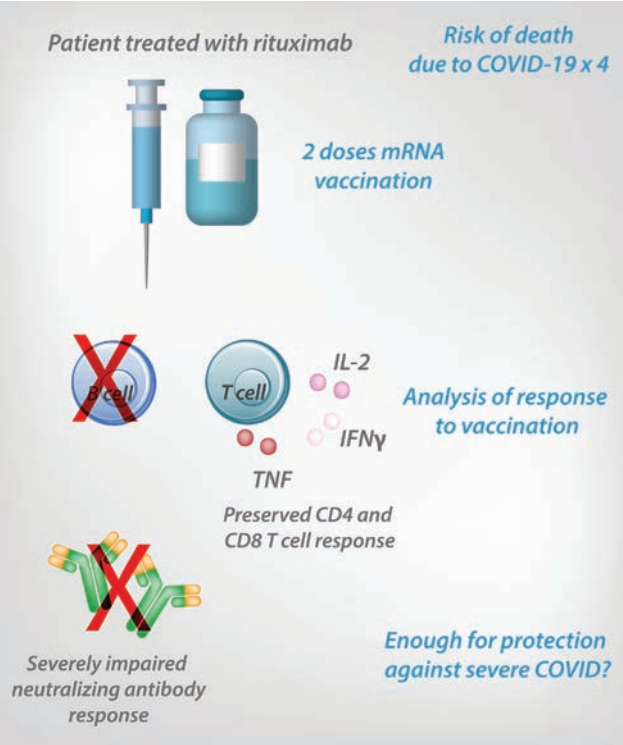

KEY POINTS

- Only 29% of patients treated with RTX develop a neutralizing humoral response after the BNT162b2 mRNA vaccine.
- CD4 and CD8 T cell functional spike-specific response in patients with autoimmune diseases is similar in RTX-treated patients and healthy controls.
- Preserved T cell response suggests that all RTX-treated patients should be vaccinated against COVID-19, even if they were treated recently.

SUMMARY

Rituximab (RTX) increases the risk of severe SARS–CoV-2 infection in patients with autoimmune diseases. Bitoun et al demonstrate that RTX-treated patients have an impaired antibody response to the SARS–CoV-2 messenger RNA (mRNA) vaccine after 2 doses. The neutralizing response is both delayed and diminished in RTX-treated patients (29% of response) compared to patients with autoimmune diseases treated with other immunomodulatory or immunosuppressant agents (80% of response) and healthy controls (92% of response). This defect is mainly influenced by the time between the last RTX infusion and the first vaccine injection. No patients treated with RTX in the last 6 months showed a humoral response.

The functional cytokine response in CD4 and CD8 T cells 1 month after the second vaccine dose was assessed. Intracellular staining for interferon-γ (IFNγ), tumor necrosis factor (TNF), and interleukin-2 (IL-2) upon stimulation with spike peptide pools was the technique used for the T cell response. There was no significant difference in the T cell response when comparing RTX-treated patients, patients treated with other immunosuppressants, and healthy controls. In the RTX group, there was no difference when comparing the CD4 and CD8 T cell response between responders and nonresponders.

In conclusion, RTX leads to an impaired neutralizing antibody response after COVID-19 mRNA vaccination. The T cell response is not different in RTX-treated patients compared to healthy controls and patients treated with other immunosuppressants. Since treatment with RTX is the main risk factor of severe COVID and death in patients with autoimmune diseases, the preserved T cell response after vaccination provides incentive to vaccinate all RTX-treated patients. More studies are needed to determine whether this T cell response is enough to protect patients against severe COVID-19.

Arthritis & Rheumatology
Vol. 74, No. 6, June 2022, pp 915–926
DOI 10.1002/art.42092

American College of Rheumatology
Empowering Rheumatology Professionals

EXPERT PERSPECTIVES ON CLINICAL CHALLENGES

Expert Perspective: An Approach to Refractory Lupus Nephritis

Swati Arora[1] and Brad H. Rovin[2]

Systemic lupus erythematosus affects the kidneys in ~50% of all patients, and lupus nephritis (LN) is the most common manifestation of kidney involvement. Despite prompt diagnosis and treatment with aggressive immunosuppression, a significant proportion of LN patients do not respond to treatment and are considered to have refractory LN. Several factors other than drug resistance, such as nonadherence to treatment, undertreatment with conventional drugs, the effects of accumulated chronic damage, and genetic factors, may contribute to a poor response to treatment and should be considered. We define refractory LN as no change in (or worsening of) proteinuria and/or estimated glomerular filtration rate in response to 2 different standard-of-care induction regimens after 4–6 months in patients who are adherent to treatment. For patients who have LN that is truly refractory to standard of care, B cell–targeted therapy, specifically rituximab (RTX), is the most common next step. There is limited evidence available on alternative rescue therapies that may be used when there is no response to RTX. These include anti-CD38, leflunomide, intravenous immunoglobulin, plasma exchange, autologous stem cell transplantation, chimeric antigen receptor T cell therapy, anticomplement therapy, and interleukin-2 therapy.

The clinical challenge

The patient, a 29-year-old woman with a 5-year history of systemic lupus erythematous (SLE) manifested by arthralgia, skin rash, positive anti–double-stranded DNA antibodies, and low levels of complement components C3 and C4, who was receiving low-dose prednisone and hydroxychloroquine, presented with new-onset nephrotic-range proteinuria (3.5 gm/day). Her serum creatinine concentration was 0.6 mg/dl. A kidney biopsy showed class IV lupus nephritis (LN) with wire loop–like lesions, endocapillary hypercellularity, mesangial hypercellularity, 1 glomerulus with karyorrhectic debris, and mild interstitial fibrosis (Figure 1). National Institutes of Health (NIH) activity and chronicity indices (1) were 7/24 and 1/12, respectively. She was initially treated with 3 intravenous doses of methylprednisolone totaling 2 gm followed by prednisone 0.5 mg/kg/day with a tapering schedule, and intravenous cyclophosphamide (CYC) 500 mg every 2 weeks for 6 doses. CYC was to be followed by mycophenolate mofetil (MMF) maintenance (2 gm/day), but at her 12-week follow-up visit proteinuria was 3.4 gm/day and the serum creatinine concentration was 0.8 mg/dl. Given this lack of response, MMF was started at 3 gm/day, tacrolimus 1 mg twice a day was added, and prednisone was recycled to 0.5 mg/kg/day and the taper restarted. Despite these medication changes, the patient had persistent proteinuria (3 gm/day) and hypocomplementemia 6 months later. The patient was given two 1-gm doses of rituximab (RTX) and MMF was continued. Some progress was noted, with improved complement levels, but the patient developed leukopenia and MMF had to be reduced to 500 mg/day. Voclosporin became available around this time and was added. The patient's proteinuria decreased to 500 mg/day.

Background

SLE affects the kidneys in ~50% of all patients (2). LN, the most common manifestation of kidney involvement in lupus, typically occurs within the first 6–36 months after diagnosis, and in 25–50% of patients LN is the initial presentation of SLE (3). Despite prompt diagnosis and treatment with aggressive immunosuppression, it has been reported that 14–33% of patients fail to respond and have LN that is refractory to treatment (4,5).

If no response to a single course of one standard therapy is considered refractory disease, then we suspect that the reported

Dr. Rovin's work was supported by the NIH (grant R01-AR-071947).
[1]Swati Arora, MD: Allegheny Health Network, Pittsburgh, Pennsylvania; [2]Brad H. Rovin, MD: The Ohio State University Wexner Medical Center, Columbus.
Author disclosures are available at https://onlinelibrary.wiley.com/action/downloadSupplement?doi=10.1002%2Fart.42092&file=art42092-sup-0001-Disclosureform.pdf.

Address correspondence to Brad H. Rovin, MD, Ohio State University Nephrology, 1664 Neil Avenue, Columbus, OH 34201. Email: Rovin.1@osu.edu.
Submitted for publication December 13, 2021; accepted in revised form February 9, 2022.

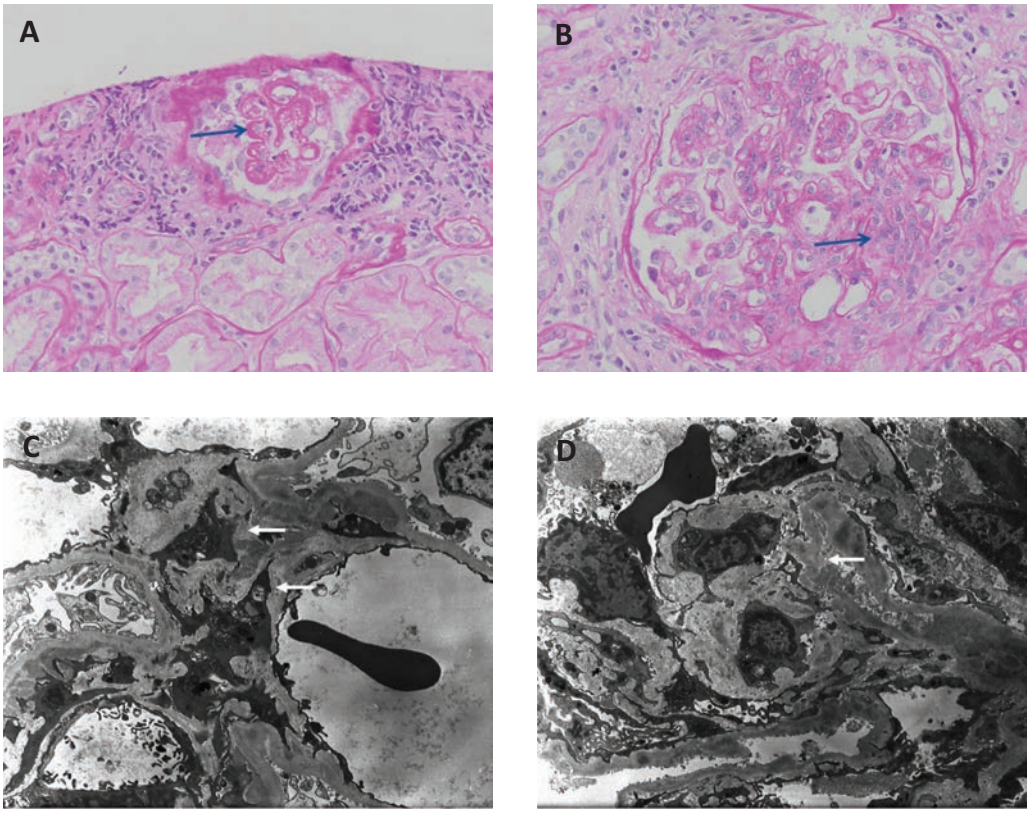

Figure 1. Kidney biopsy specimen from a patient with refractory lupus nephritis. **A** and **B**, Light microscopy images demonstrating wire loop–like lesions (**arrow** in **A**) and endocapillary hypercellularity (**arrow** in **B**). **C** and **D**, Electron micrographs showing mesangial (**arrows** in **C**) and subendothelial (**arrow** in **D**) immune complex deposits. Original magnification × 100 in **A**; × 400 in **B**; × 4,900 in **C**; × 3,800 in **D**.

or perceived frequency of refractory LN is largely overestimated. Several factors besides drug resistance contribute to a poor response to treatment and should be excluded before labeling a patient as treatment resistant. For example, nonadherence to prescribed treatment is very common among patients with autoimmune diseases. Using a Medicaid Database, treatment adherence was assessed in >4,000 patients with SLE during their first year of therapy using the criterion of medication refilled >80% of the time as "adherent." Fewer than 25% of patients met this metric (6). Female sex, younger age, Black race, and Hispanic ethnicity were associated with higher odds of noncompliance. Other important barriers identified were health literacy, financial issues, access to healthcare, perceived treatment inefficacy, and side effects (7). It is therefore prudent to assess adherence before changing treatment plans or adding additional immunosuppression. Obtaining pharmacy refill records, doing pill counts, and monitoring drug levels may help in ascertaining adherence. Monitoring hydroxychloroquine levels also does seem to improve adherence (8). Hydroxychloroquine has a long, 40–50-day half-life, and serum levels do not fluctuate much, so an undetectable hydroxychloroquine level suggests long-term nonadherence (9). Once nonadherence is revealed, a nonjudgmental conference with the patient (and their family) should be pursued, incorporating open discussion to identify and address barriers, improve disease understanding, and if possible, simplify the treatment regimen and decrease pill burden (10).

Although standard-of-care regimens for LN are well-established, adequate drug dosing can be challenging. Most patients start treatment within prescribed dose ranges, but how an individual metabolizes a specific drug is generally not known a priori. Additionally, dosing is often decreased in response to reported side effects, and this may affect efficacy. Ideally, treatment adequacy for individual patients would be determined by monitoring blood drug levels, but the therapeutic range for most standard LN drugs has not been established (11). Furthermore, therapeutic drug monitoring can be challenging in the clinical setting. Measurement of the area under the concentration–time curve (AUC) is the most accurate determination of an individual's exposure to a drug, but involves obtaining blood samples repeatedly over time. Trough concentrations are more convenient, and sometimes do correlate with a drug's AUC (12). MMF dose adjustment could be considered in nonresponsive patients if predose levels are consistently <3–4.5 mg/liter (11,12). Therapeutic drug monitoring of the calcineurin inhibitors cyclosporine and tacrolimus is more helpful for monitoring adherence and toxicity than efficacy (11). Voclosporin levels do not need to be monitored (13), and most clinical laboratories do not offer testing. Pharmacodynamic effects based on a drug's specific mechanism of

action may be used in lieu of blood levels. For example, the efficacy of RTX in LN seems to depend on achieving complete peripheral B cell depletion (14).

Patients with LN must be given sufficient time to achieve a kidney response. The European Alliance of Associations for Rheumatology (EULAR) guidelines point out that patients with nephrotic-range proteinuria at baseline may need an additional 6–12 months to achieve complete clinical response (15). On the other hand, continuing an ineffective therapy for many months waiting for a complete response will likely result in chronic damage to the kidneys. Determining the balance between sufficient duration of treatment and prolonging exposure of the kidneys to inflammatory injury may be guided by the observation that early, albeit partial, response to treatment is associated with complete response later. A decline in proteinuria of ≥25% at 8 weeks has been shown to associate with a 50% reduction in proteinuria after 6 months of therapy (16), and a decrease in proteinuria of ≥50% after 6 months of therapy predicts good long-term kidney survival (17). Patients who have a reduction in proteinuria of ≥25% after 2–3 months of treatment are expected to continue to show improvement and may not need to switch therapy; on the other hand, patients who do not show improvement are candidates for a change in treatment. It is important to emphasize that these thresholds are only intended to provide a starting point for decision-making and are not rigid. Some patients who did not meet these thresholds went on to have good long-term responses, and conversely, some patients who did achieve these metrics did not do well (16,17). Monitoring LN should be a continuous process using real-time data for flexible decision-making.

While there is no consensus definition of a complete kidney response, most clinical trials require proteinuria to decrease to ≤700–500 mg/day and serum creatinine level or estimated glomerular filtration rate (eGFR) to be within 10–25% of baseline (16,18). Ideally, a complete kidney response based on these clinical thresholds would reflect resolution of intrarenal inflammation, but there is considerable discordance between clinical and histologic responses (19–21). Proteinuria and serum creatinine levels reflect both acute inflammatory kidney injury and chronic kidney damage. Therefore, persistent proteinuria and/or an elevated serum creatinine level must be correctly interpreted. This is particularly difficult in LN patients who have had their disease for a long time, or who have experienced multiple LN flares, and in whom accumulated chronic damage may result in proteinuria and kidney function that will never meet complete clinical response criteria. Persistence of proteinuria or an abnormal eGFR in patients who have been treated for longer than 18–24 months therefore does not always represent ongoing immune-mediated kidney injury that has evaded treatment (22). A kidney biopsy may be needed to differentiate active disease from chronic damage and resolved inflammation in such cases (19,20). A kidney biopsy may also demonstrate an unanticipated process, such as antiphospholipid nephropathy, that would require a different intervention.

Finally, kidney disease in LN patients may progressively worsen despite adequate therapy because of genetic factors, giving the appearance of nonresponsiveness. For example, the genetic variations of apolipoprotein L1 that predispose patients of African ancestry to end-stage kidney disease (ESKD) (23) are found in patients with LN and are associated with ESKD and a shorter timeline to ESKD (24). Progressive kidney failure in such individuals may not be due to treatment resistance (25). Alternatively, some genetic conditions, such as autoinflammatory disorders characterized by increased type I interferon production, may have similar clinical and pathologic findings as LN, but do not respond well to conventional LN treatments (26).

Approach

Once a patient with LN is diagnosed as treatment-resistant they often are exposed to more and more potent immunosuppressive treatments, sequentially or in parallel (27,28), and are at ever-increasing risk of serious short- and long-term adverse events. After standard treatments are exhausted, the evidence of efficacy for any of the proposed salvage therapies is very limited. Given the paucity of evidence for alternative therapies, and keeping in mind the previously discussed situations that may mimic treatment resistance, we consider refractory LN to be no change in (or worsening of) proteinuria and/or eGFR in response to 2 different standard-of-care induction regimens after 4–6 months in patients who are taking their prescribed medications in doses that are generally believed to be therapeutic. This approach is operationalized in Figure 2.

The proposed algorithm takes into account patient adherence and therapeutic drug monitoring, and tries to balance duration of treatment against accumulating chronic kidney injury. These attributes are evidence-based, at least to the extent that there is evidence. However, the proposal to try 2 different standard-of-care induction regimens sequentially is more opinion-based, and finds rationale in the heterogeneity of LN. Not every patient is expected to respond to the same medication. Over half the patients enrolled in all contemporary clinical trials of LN, even those considered successful, did not achieve a complete clinical response by the end of the trial. It seems reasonable to try another established regimen before reaching for rescue therapies. This approach is consistent with the independent LN guidelines from the EULAR, American College of Rheumatology, and Kidney Disease: Improving Global Outcomes consortium (15,29).

The LN guidelines suggest that adherent patients who are first treated with MMF plus glucocorticoids should be switched to the Euro-Lupus Nephritis Trial (EuroLupus) (17) or NIH dosing (29) of CYC plus glucocorticoids and vice versa. We suggest that after poor response to the first therapy used, strong consideration

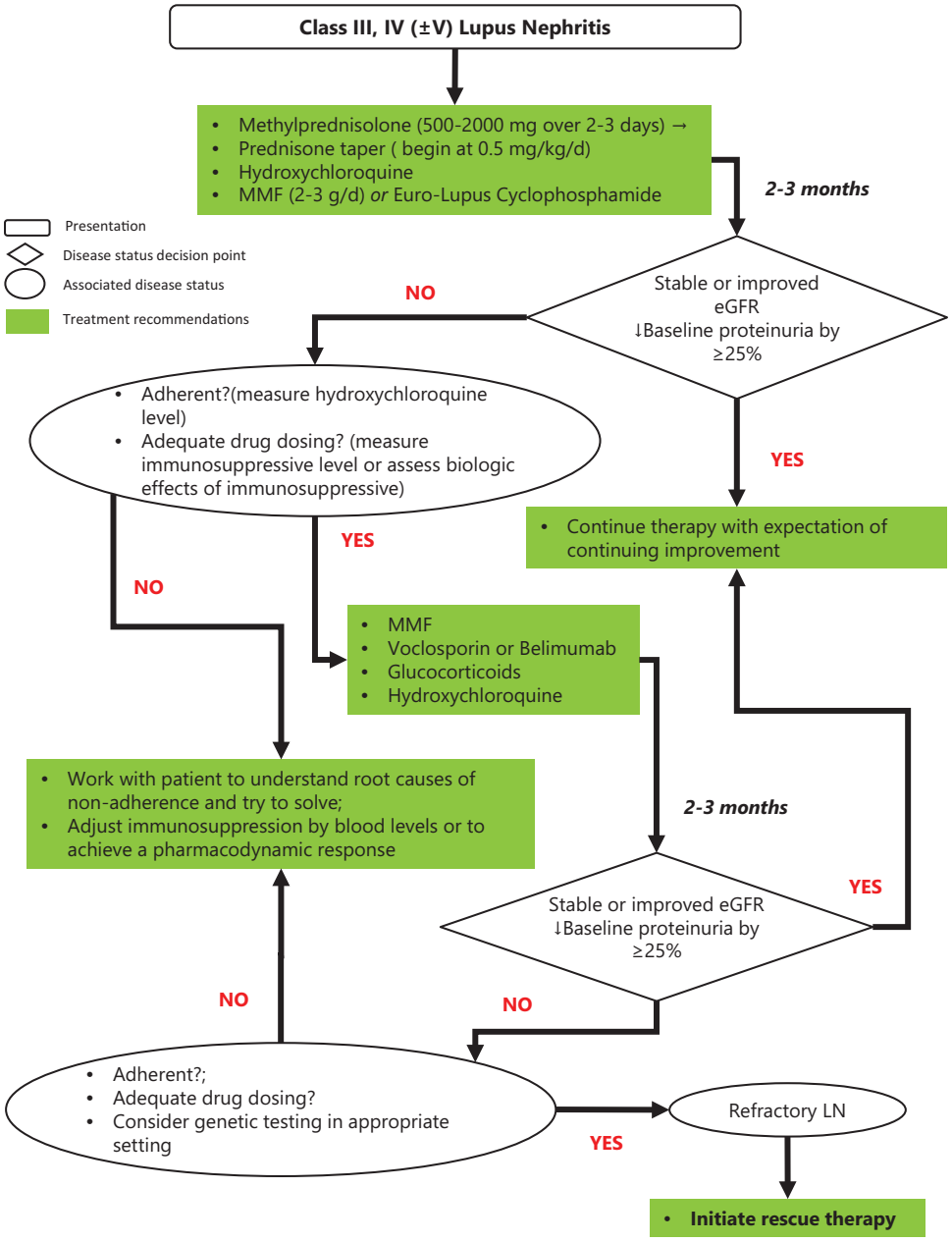

Figure 2. Approach to the diagnosis of refractory lupus nephritis (LN). MMF = mycophenolate mofetil; Euro-Lupus = Euro-Lupus Nephritis Trial dosing regimen; eGFR = estimated glomerular filtration rate.

be given to switching to a regimen that adds voclosporin or belimumab, one of the newly approved LN therapies, to standard therapy. The addition of each of these drugs to background standard of care significantly increased the number of patients with a good treatment response (30,31). Voclosporin responses were better in patients who were already receiving MMF when they entered the trial, and belimumab showed a larger beneficial effect in patients experiencing a relapse compared to those with de novo LN (32,33). These observations suggest that both of these novel therapies improve response rates in patients who have already been exposed to some immunosuppression. Of note, belimumab may be less effective in patients with proteinuria ≥3 gm/day, and voclosporin should be used cautiously or not at all in patients with a significantly impaired GFR of <45 ml/minute (30,31). If voclosporin is not available, tacrolimus could be considered, assuming a calcineurin inhibitor class effect (34,35).

Given that belimumab and voclosporin are new tools for LN management, there may be an inclination to use these medications as rescue therapies for refractory LN. However, neither drug has been systematically evaluated in patients with refractory disease, and such patients were excluded from the pivotal trials of voclosporin and belimumab. Interestingly, there are reports that the addition of a calcineurin inhibitor (tacrolimus or cyclosporine) to MMF may result in a response in refractory or

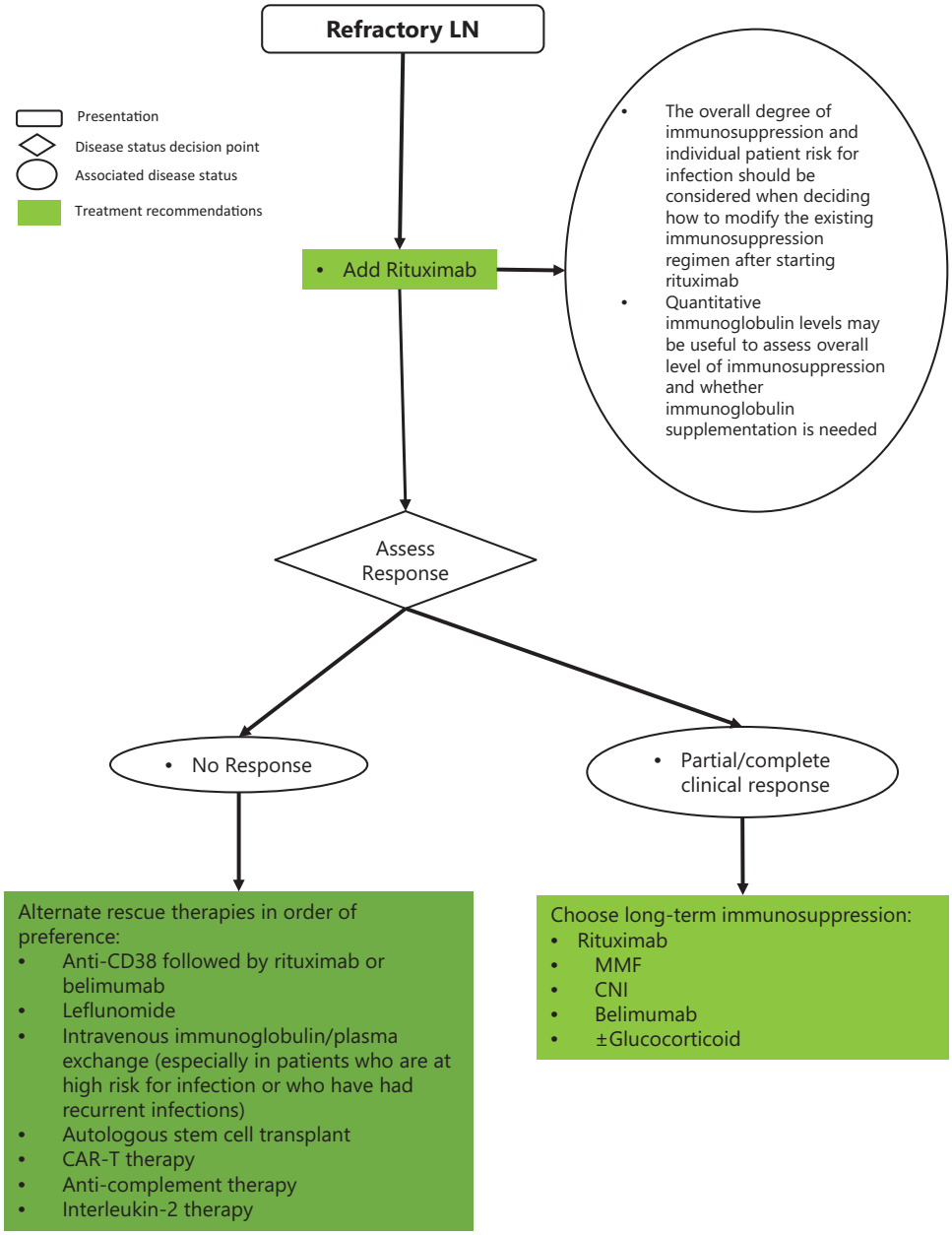

Figure 3. Therapeutic approach to patients with refractory lupus nephritis (LN). CAR T = chimeric antigen receptor T cell; MMF = mycophenolate mofetil; CNI = calcineurin inhibitor.

relapsing LN, but these have been small uncontrolled studies (34,36).

Once a diagnosis of treatment-resistant LN has been established, the most common next step has been the addition of B cell–targeted therapy, specifically RTX. A fair amount of data on the response of patients with LN refractory to RTX has been published, and while generally of poor-to-modest quality, provide some evidence for its use. Evidence for any particular therapy in the case of RTX failure is severely limited. The risk/benefit ratio of increasing immunosuppression in these patients must be assessed. In such cases it is prudent to assess the status of the patient's immune system and bone marrow by measuring quantitative immunoglobulin levels and leukocyte subset levels (37). If uncontrolled LN has been going on for a while, it is often useful to do a kidney biopsy and assess chronic damage. Patients with severe interstitial fibrosis, tubular atrophy, and global glomerulosclerosis have irreversible kidney damage and will inevitably need dialysis. The amount of viable kidney parenchyma left to save, and the likelihood of a need for kidney replacement therapy even if this parenchyma is saved, will figure importantly in calculating the risk/benefit ratio of intensifying immunosuppression further.

Of note, although race and ethnicity may be associated with an increased likelihood of developing refractory LN, once it has

been determined that a patient has refractory disease, as defined above, we do not choose subsequent rescue therapies based on race or ethnicity. Treatment options are too few and evidence for differential efficacy by race or ethnicity too sparse to make this feasible.

Our patient was compliant with therapy. Despite treatment with EuroLupus dosing of CYC, MMF, and tacrolimus, the patient did not respond. Our approach to rescue therapy for patients such as this is shown in Figure 3. The evidence supporting this approach is discussed below.

Evidence

Rituximab. In the development of LN, B cells play a central role in producing pathogenic autoantibodies, initiating release of cytokines such as interleukin-6 (IL-6) and tumor necrosis factor, and activating T cells by providing costimulatory support. B cell–directed biologics deplete or impair the function of B cells. Although RTX does not deplete plasma cells directly, it prevents repletion of plasma cells by depleting precursor B cells (38).

RTX, which is directed against the B cell surface molecule CD20, is a chimeric mouse/human monoclonal antibody. Many uncontrolled studies and open-label observational studies have reported efficacy of RTX in patients with refractory LN with response rates of 50–80% (39–46). Table 1 summarizes these RTX data. Of note, in these studies there was significant variation in how refractory LN was defined, and patients with relapsing disease were frequently clustered with patients with refractory disease. Concomitant therapies and duration of follow-up also varied considerably between studies.

Based on a systematic analysis of 26 studies that described 300 patients with refractory LN, defined as being unresponsive to previous therapy with ≥1 immunosuppressive agent, the addition of RTX resulted in 40% of the patients with refractory LN having a complete clinical kidney response, and 34% having a partial response (47). In the studies selected for that systematic review, an RTX dosing regimen of 4 infusions of 375 mg/m^2 each given 1 week apart was most commonly used (49%), followed by 2 doses of 1,000 mg given 2 weeks apart in 37% of patients. Thirty percent of cases received CYC along with RTX, 25% received MMF, 7% received azathioprine, and 4% received methotrexate (47). Treatment responses were more common in patients with class III LN and less frequent in patients with class IV or class V LN. Another meta-analysis of 31 studies described 1,112 patients with refractory lupus, of which 10 studies including 223 patients with refractory LN showed that 46% and 32% of patients achieved a complete and partial kidney response, respectively, after RTX was added. Refractory disease was defined as resistance to traditional therapy; use of prior therapies was not described (48). Further large, well-designed multicenter randomized controlled trials are warranted to establish the role of RTX in refractory LN. In the future, obinutuzumab, an anti-CD20 monoclonal antibody similar to RTX, but more potent, may be evaluated in refractory LN, but at present it is in a phase III trial after a successful phase II trial (49).

Several other approaches to refractory LN treatment have been reported (Table 2). In general, the evidence supporting these therapies is minimal and of low quality. Nonetheless, depending on a patient's specific situation, it may be necessary to consider these alternatives.

Anti–plasma cell therapy. An underlying pathogenic mediator of refractory LN could be long-lived autoreactive plasma cells that are resistant to commonly used immunosuppressive therapies (50). Bortezomib, a proteasome inhibitor, eliminates plasma cells, thereby reducing autoantibody production, blocks T cell–dependent inflammatory responses, and decreases interferon-α induction by disrupting Toll-like receptor signaling in dendritic cells (51).

A series of 12 patients with LN resistant to induction therapy with CYC, steroids, MMF, and RTX were treated with bortezomib plus dexamethasone. A complete clinical kidney response was achieved in 1 patient, and 11 patients had a partial response with improvement in proteinuria, serum creatinine level, and serologic markers after a mean of 6 bortezomib cycles (52). Similarly, a series of 5 patients with refractory LN also showed reduction in proteinuria and improved kidney function with 4 cycles of bortezomib plus glucocorticoids. Over 6–24 months of follow-up, 3 patients achieved a complete response, 1 had a partial response, and 1 patient progressed and required kidney replacement therapy (53). Like other B cell therapies, bortezomib may cause hypogammaglobinemia requiring intravenous immunoglobulin (IVIG) rescue (52,54). Also concerning, patients receiving bortezomib may develop a disabling peripheral neuropathy, although the incidence of this adverse event is decreased if subcutaneous dosing is used (55).

Another approach to plasma cell depletion is through the anti-CD38 monoclonal antibody daratumumab, which kills plasma cells and modulates Teff cell responses (56). A recent case report of 2 patients with life-threatening, refractory SLE, one of whom had LN, described excellent clinical and serologic responses to daratumumab given weekly for 4 weeks followed by longer-term belimumab (56). The LN patient had an improvement in proteinuria from >6 gm/day to ~1 gm/day and normalization of serum creatinine levels during the 12-month follow-up period.

While that report, which describes only 2 patients, provides low-quality evidence within the hierarchy of types of clinical investigation, it offers potential mechanistic insights into refractory LN. Both of these patients with refractory lupus had been treated with bortezomib prior to daratumumab, but did not achieve satisfactory responses. This finding suggests that, at least for some patients, depleting long-lived plasma cells will not be sufficient to

Table 1. Selected studies of rituximab for the treatment of refractory LN*

Author, year (ref.)	No. of patients	Study population	Duration of follow-up, months	Rituximab dosing regimen	Response to rituximab
Gunnarsson et al, 2007 (39)	7	CYC-resistant LN	6	4 infusions of 375 mg/m^2 each given 1 week apart	SLEDAI scores improved, decrease in the renal activity index on repeat biopsy at 6 months
Goswami et al, 2019 (40)	14	Refractory or relapsing LN	6	Not specified	CR in 71.4%; PR in 28.6%
Davies et al, 2013 (41)	18	All patients had severe, active disease that had failed to respond to conventional therapy, including MMF and CYC	6	2 infusions of 1 gm each given 2 weeks apart	CR in 61.1%; PR in 11.1%
Melander et al, 2009 (14)	20	18 (90%) had already received ≥1 conventional therapy, including intravenous CYC in 15 patients with a median cumulative dose of 6 gm	22	4 infusions of 375 mg/m^2 each given 1 week apart	CR in 35%; PR in 25%
Contis et al, 2016 (42)	17	All patients had refractory LN defined as resistant to standard treatment with CYC	12	4 infusions of 375 mg/m^2 each given 1 week apart (in 10 patients) or 2 infusions of 1 gm each given on day 0 and day 15 (in 7 patients)	CR or PR in 53%
Jónsdóttir et al, 2013 (43)	25	23 patients had disease refractory to conventional therapy, including CYC and/or MMF	12	4 infusions of 375 mg/m^2 each given 1 week apart	CR in 64%; PR in 24%
Lindholm et al, 2008 (44)	17	Signs of active kidney inflammation despite ongoing treatment with CYC (n = 14) or MMF (n = 3)	6–12	4 infusions of 375 mg/m^2 each given 1 week apart	CR in 12%; PR in 53%
Iwata et al, 2018 (45)	63 with SLE, 36 with LN	All had disease refractory to high-dose steroids and various conventional therapies, including CYC (54%), MMF (16%), and CNI (14%)	12	2 infusions of 500 mg each given 1 week apart (on days 1 and 8) in 22 patients; 4 infusions of 500 mg each (on days 1, 8, 15, and 22) in 9 patients; 2 infusions of 1,000 mg each given 2 weeks apart (on days 1 and 15) in 7 patients; 4 infusions of 1,000 mg each (on days 1, 15, 168, and 182) in 25 patients	BILAG score improved in 83.3%; UPCR decreased significantly
Iaccarino et al, 2015 (46)	145 with SLE, 68 with LN	All had failed to respond to ≥1 immunosuppressant	12	2 infusions of 1 gm each given 2 weeks apart in 118 patients; 4 infusions of 375 mg/m^2 each given 1 week apart in 27 patients, followed in 10 by 2 further doses, after 1 and 2 months	CR in 30.9%; PR in 63.2%

* CYC = cyclophosphamide; LN = lupus nephritis; SLEDAI = Systemic Lupus Erythematosus Disease Activity Index; CR = complete response; PR = partial response; MMF = mycophenolate mofetil; SLE = systemic lupus erythematosus; CNI = calcineurin inhibitor; BILAG = British Isles Lupus Assessment Group; UPCR = urine protein-to-creatinine ratiio.

Table 2. Therapies other than rituximab tried for refractory LN*

Author, year (ref.)	Therapy	No. of patients	Study population	Duration of follow-up	Response
Choi et al, 2018 (34)	MMF plus tacrolimus	29	12 with refractory and 17 with relapsing LN	12 months	CR in 25.9%; PR in 29.6%
Jesus et al, 2018 (36)	MMF plus tacrolimus	17	MMF-resistant patients	6 months	CR in 35%; PR in 35%
Segarra et al, 2020 (52)	Bortezomib plus dexamethasone	12	Refractory LN	9–30 months	CR in 8.3%; PR in 83.3%
Zhang et al, 2017 (53)	Bortezomib plus dexamethasone	6	Refractory LN	6–24 months	CR in 60%; PR in 20%
Ostendorf et al, 2020 (56)	Daratumumab	1	Refractory LN	12 months	Proteinuria improved
Tam et al, 2006 (59)	Leflunomide	17	Refractory to or intolerant of conventional treatment	12 months	CR in 29%; PR in 47%
Levy et al, 2000 (62)	IVIG	7	Refractory LN, patients who failed to respond to CYC	6 months	Decreased proteinuria in all patients
Monova et al, 2002 (64)	IVIG	58	Refractory LN	7 years	CR in 30%; PR in 40%
Zhang et al, 2021 (66)	IL-2 therapy	10	Refractory to ≥2 conventional treatments	6 months	Decreased proteinuria
Pickering et al, 2015 (68)	Eculizumab	1	Refractory to CYC, rituximab, MMF, and tacrolimus	18 months	Decreased proteinuria, improved renal function
Mougiakakos et al, 2021 (69)	CAR-T	1	Refractory to CYC, MMF, tacrolimus, rituximab, and belimumab	1.5 months	CR achieved

* MMF = mycophenolate mofetil; LN = lupus nephritis; CR = complete response; PR = partial response; IVIG = intravenous immunoglobulin; CYC = cyclophosphamide; IL-2 = interleukin-2; CAR T = chimeric antigen receptor T cell.

control lupus activity. A deeper dive into potential cellular targets for daratumumab showed that in addition to plasma cells, CD38 is expressed on plasmablasts, mature B cells, and plasmacytoid dendritic cells in lupus patients, and that CD38-expressing T cells are expanded (56). Thus, targeting CD38-expressing cells of various types may have contributed to the effect of daratumumab.

An immunoproteasome inhibitor, KZR-616, is currently under investigation for LN, but not specifically for refractory LN (57).

It is important to keep in mind that bortezomib and daratumumab only transiently deplete plasma cells; this effect must be maintained using additional immunosuppression to prevent autoreactive B cell precursors from developing into autoreactive plasma cells (56). This was the rationale for following up daratumumab with belimumab after lupus was controlled (56).

Leflunomide. Leflunomide, an inhibitor of dihydroorotate dehydrogenase, targets lymphocytes and has antiproliferative and antiinflammatory actions. A meta-analysis comparing leflunomide to CYC suggested a better safety profile and improved efficacy for leflunomide in LN, but similar effects on the SLE Disease Activity Index (SLEDAI) (58). Leflunomide was used to treat 17 LN patients who had refractory disease or were intolerant of conventional immunosuppression (59). Subsequently, 76% of the patients achieved a response (complete in 29% and partial in 47%). More extensive evaluation of leflunomide will be needed before it can be recommended for refractory LN.

Intravenous immunoglobulin. IVIG is a biologic therapy comprised of polyclonal antibodies derived from the plasma of a large pool of healthy donors. In addition to being used to treat hypogammaglobulinemia, it has the potential to treat inflammatory diseases, cancer, and autoimmune diseases. IVIG tips the balance of activating and inhibitory immune responses by neutralizing autoantibodies through antiidiotype binding, up-regulating inhibitory Fc receptors, and increasing clearance of pathogenic autoantibodies via the reticuloendothelial system (60,61). Seven patients with biopsy-proven class IV or class V LN and nephrotic syndrome who had failed to respond to therapy with CYC and prednisone showed an improvement in proteinuria with 1–6 courses of high-dose IVIG (62). Beneficial effects of IVIG have also been shown in a small Italian cohort of patients with refractory SLE (n = 12) and a Bulgarian cohort of patients with treatment-refractory chronic glomerulonephritis (n = 58) (63,64). The main advantage of IVIG is that it is not immunosuppressive, and may therefore be useful in patients who have been overimmunosuppressed and are at risk of infection.

Interleukin-2 therapy. Low-dose IL-2 has been used to influence the balance of T cells in SLE patients away from conventional (effector) phenotypes to regulatory phenotypes (65). A small series of 10 patients with refractory or relapsed LN was treated with low-dose, recombinant IL-2, and after 12 weeks, 7 patients had a reduction in proteinuria of ≥50%, and 2 of these had a complete renal response (66). This was accompanied by a significant expansion of peripheral Treg cells (66). IL-2 immunotherapy to restore T cell regulatory homeostasis in LN may be a novel therapeutic approach for resistant LN, but needs to be tested in larger randomized controlled trials.

Anticomplement therapy. The importance of the complement system in the pathogenesis of kidney injury in LN has been well-established in experimental models, and is believed to translate to human disease (67). Since refractory LN is characterized by persistent kidney inflammation, anticomplement therapies may be useful in controlling this inflammation, especially if complement-driven. While there are now several complement-targeted therapeutics in various stages of development, eculizumab, a monoclonal antibody that binds to complement component C5 and prevents formation of C5a and the membrane-attack complex (C5b–9), has had the longest clinical exposure. Most of the reports of eculizumab and SLE/LN have been in the context of concomitant thrombotic microangiopathy. However, a report detailed the successful use of eculizumab for the treatment of a patient with severe LN without thrombotic microangiopathy who had failed to respond to CYC, MMF, RTX, and tacrolimus. During 18 months of follow-up, the patient achieved a sustained and rapid improvement in kidney function and proteinuria (68). While much more evidence will be needed, understanding in whom uncontrolled disease is mediated by complement would facilitate the application of anticomplement therapies in resistant LN.

Chimeric antigen receptor T cell (CAR T cell) therapy. The principle of CAR T cell technology is to engineer autologous T cells to express a specific antigen receptor so the modified T cells can recognize and only kill those cells that express the antigen (69). This targeted effect of T cells is much faster and longer lasting compared to monoclonal antibody therapy. CAR T cells have mostly been developed to recognize CD19 and other B cell surface antigens for use in refractory or relapsed B cell malignancies. Harnessing B cell–directed CAR T cells to treat SLE has garnered attention as a way to deplete autoreactive B cells completely and for a long duration (69).

A recent case report described a 20-year-old patient with refractory SLE/LN treated with CAR T cells after lymphodepletion was achieved with fludarabine and CYC. Proteinuria decreased dramatically, and the SLEDAI score fell from 16 at baseline to 0 at follow-up (69). Another case report described a 41-year-old patient with stage IV diffuse large B cell lymphoma (DLBCL) and a 20-year history of SLE who was treated with CD19–BCMA compound CAR T cells with dual targeting of CD19 on B cells and BCMA (CD269) on plasma cells (70). The patient's SLE remained stable and DLBCL remained in remission for >23 months despite receiving no additional immunosuppressive therapy or chemotherapy.

Anifrolumab. Anifrolumab, recently approved by the US Food and Drug Administration for the treatment of SLE, is a fully human, IgG1κ monoclonal antibody to the type I interferon receptor subunit 1, and inhibits signaling by all type I interferons (71,72). Anifrolumab is currently being evaluated for LN, and results from a phase II trial will be available later this year (73). While there are no current data regarding the use of anifrolumab in refractory LN, a transcriptomic analysis of protocol kidney biopsies after induction therapy showed that interferon pathway transcripts remained upregulated in the kidneys of patients who did not respond to therapy, but declined in patients who had a complete clinical response after induction (74). These data raise the possibility that LN patients who do not respond to standard treatment may have ongoing intrarenal interferon activity that could respond to an interferon antagonist.

Plasma exchange. Like IVIG, plasma exchange can be administered without significantly immunosuppressing patients, if plasma rather than an albumin solution is added back. However, the evidence for plasma exchange or immunoadsorption in refractory LN is minimal, consisting mostly of single case reports and small observational studies. In contrast, a well-designed randomized controlled trial of plasma exchange added to standard therapy in patients with severe (not necessarily refractory) LN did show improved clinical outcomes (75).

Hematopoietic stem cell transplantation. Autologous stem cell transplantation temporarily resets the adaptive immune system and depletes autoreactive immunologic memory (76). In 2 large studies of patients with SLE, the probability of 5-year disease-free survival was 50% after autologous stem cell transplantation (77,78). More recently, 22 patients with refractory/relapsing LN underwent autologous stem cell transplantation. At a median of 72 months of follow-up, 18 patients were in complete clinical remission (79). The relapse rate was 27%, and treatment-related mortality was 5%. Given the higher risk of short-term mortality associated with autologous stem cell transplantation, and the risk of recurrence after transplant, we consider this approach only when other options are exhausted.

Mesenchymal stem cell (MSC) transplantation. MSCs have immunomodulatory properties and have shown therapeutic benefits when given to patients with autoimmune conditions. In patients with LN and in mouse models of LN, transplantation of MSCs has been shown to suppress autoimmunity and restore kidney function (80). MSC transplantation induces regulatory immune cells and suppresses Th1, Th17, T follicular helper cell, and B cell responses (80). Although several single-arm studies have shown a therapeutic benefit of MSCs in patients with LN refractory to conventional treatments, when tested in a randomized double-blind trial, albeit in a small cohort, an additional benefit of MSCs over standard of care was not observed (81). Better designed, larger randomized controlled trials are needed to evaluate the role of MSCs in the treatment of LN patients.

Discussion

The management of LN that is truly refractory to standard of care is challenging diagnostically and therapeutically. There is no standard definition or specific laboratory test for refractory disease, and because nonresponse to treatment may have several etiologies, refractory LN is a diagnosis of exclusion. It is critical to understand all of the contributing factors to nonresponse before labeling a patient as treatment resistant, because the consequence of this diagnosis is generally piling on more immunosuppression and increasing the risk of adverse iatrogenic outcomes. We suggest that the most common causes of nonresponse in the lupus and LN populations are nonadherence to treatment and undertreatment with conventional drugs. While adherence issues can be difficult to address, and titrating standard therapies is difficult without established therapeutic levels for most drugs, neither requires escalating immunosuppression. For patients with LN resistant to standard treatments, the choice of what should be used next is based on evidence that is of low-to-modest quality. There have been no randomized clinical trials of rescue therapies for LN. As such, the studies supporting regimens for refractory disease are mainly observational, uncontrolled, and are limited by the inclusion of a heterogeneous group of patients previously treated with variable immunosuppression.

Of all the therapeutic approaches to refractory disease, treatment with the anti-CD20 biologic RTX has garnered the most attention. There have been a sufficient number of such studies that several systematic analyses have shown improved outcomes in patients with treatment-resistant LN after the addition of RTX. The fact that there appears to be a favorable signal for anti-CD20 suggests this may be a reasonable first approach to refractory disease, and eliminating autoreactive B cells that may not have been depleted by other therapies fits into most pathogenic constructs of SLE. Nonetheless, it would be prudent to study anti-CD20 biologics in refractory LN in a well-controlled trial of patients with uniformly defined refractory disease. The role of newly approved LN drugs and drugs that are in development remains to be seen. The possibility that molecular evaluation of the kidneys from patients with refractory disease may provide clues to inflammatory pathways not controlled by conventional treatments is exciting, and suggests that in the future patients with refractory disease may be able to be treated more precisely, thereby avoiding immunosuppressive roulette.

Finally, given the ongoing SARS–COV-2 pandemic, it cannot be overstated that many of the approaches to refractory disease will put these patients at high risk of severe infection, and may prevent adequate protection from vaccination. We suggest that preexposure monoclonal antibodies be given to patients with refractory disease, and that all other safety measures, including social distancing and masking, be maintained.

AUTHOR CONTRIBUTIONS

Drs. Arora and Rovin drafted the article, revised it critically for important intellectual content, and approved the final version to be published.

REFERENCES

1. Austin HA III, Boumpas DT, Vaughan EM, Balow JE. Predicting renal outcomes in severe lupus nephritis: contributions of clinical and histologic data. Kidney Int 1994;45:544–550.
2. Parikh SV, Almaani S, Brodsky S, Rovin BH. Update on lupus nephritis: core curriculum 2020. Am J Kidney Dis 2020;76:265–81.
3. Maroz N, Segal MS. Lupus nephritis and end-stage kidney disease. Am J Med Sci 2013;346:319–23.
4. Anders HJ, Hiepe F. Treatment options for refractory lupus nephritis. Clin J Am Soc Nephrol 2019;14:653–5.
5. Moroni G, Ponticelli C. The multifaceted aspects of refractory lupus nephritis. Expert Rev Clin Immunol 2015;11:281–8.
6. Feldman CH, Collins J, Zhang Z, Xu C, Subramanian SV, Kawachi I, et al. Azathioprine and mycophenolate mofetil adherence patterns and predictors among Medicaid beneficiaries with systemic lupus erythematosus. Arthritis Care Res (Hoboken) 2019;71:1419–24.
7. Garcia Popa-Lisseanu MG, Greisinger A, Richardson M, O'Malley KJ, Janssen NM, Marcus DM, et al. Determinants of treatment adherence in ethnically diverse, economically disadvantaged patients with rheumatic disease. J Rheumatol 2005;32:913–9.
8. Durcan L, Clarke WA, Magder LS, Petri M. Hydroxychloroquine blood levels in systemic lupus erythematosus: clarifying dosing controversies and improving adherence. J Rheumatol 2015;42:2092–7.
9. Rainsford KD, Parke AL, Clifford-Rashotte M, Kean WF. Therapy and pharmacological properties of hydroxychloroquine and chloroquine in treatment of systemic lupus erythematosus, rheumatoid arthritis and related diseases [review]. Inflammopharmacology 2015;23:231–69.
10. Costedoat-Chalumeau N, Houssiau FA. Improving medication adherence in patients with lupus nephritis. Kidney Int 2021;99:285–7.
11. Mok CC. Therapeutic monitoring of the immuno-modulating drugs in systemic lupus erythematosus. Expert Rev Clin Immunol 2017;13:35–41.
12. Luszczynska P, Pawinski T. Therapeutic drug monitoring of mycophenolic acid in lupus nephritis: a review of current literature. Ther Drug Monit 2015;37:711–7.
13. Van Gelder T, Huizinga RB, Noukens J, Lisk L, Solomons N. Use of therapeutic drug monitoring does not add clinical value for voclosporin in patients with lupus nephritis [abstract]. J Am Soc Nephrol 2020;31:594.
14. Melander C, Sallée M, Trolliet P, Candon S, Belenfant X, Daugas E, et al. Rituximab in severe lupus nephritis: early B-cell depletion affects long-term renal outcome. Clin J Am Soc Nephrol 2009;4:579–87.
15. Fanouriakis A, Kostopoulou M, Cheema K, Anders HJ, Aringer M, Bajema I, et al. 2019 update of the joint European League Against Rheumatism and European Renal Association-European Dialysis and Transplant Association (EULAR/ERA-EDTA) recommendations for the management of lupus nephritis. Ann Rheum Dis 2020;79:713–23.
16. Dall'Era M, Stone D, Levesque V, Cisternas M, Wofsy D. Identification of biomarkers that predict response to treatment of lupus nephritis with mycophenolate mofetil or pulse cyclophosphamide. Arthritis Care Res (Hoboken) 2011;63:351–7.
17. Houssiau FA, Vasconcelos C, D'Cruz D, Sebastiani GD, de Ramon Garrido E, Danieli MG, et al. Early response to immunosuppressive therapy predicts good renal outcome in lupus nephritis: lessons from

long-term followup of patients in the Euro-Lupus Nephritis Trial. Arthritis Rheum 2004;50:3934–40.

18. Mackay M, Dall'Era M, Fishbein J, Kalunian K, Lesser M, Sanchez-Guerrero J, et al. Establishing surrogate kidney end points for lupus nephritis clinical trials: development and validation of a novel approach to predict future kidney outcomes. Arthritis Rheumatol 2019;71: 411–9.
19. Pagni F, Galimberti S, Goffredo P, Basciu M, Malachina S, Pilla D, et al. The value of repeat biopsy in the management of lupus nephritis: an international multicentre study in a large cohort of patients. Nephrol Dial Transplant 2013;28:3014–23.
20. Narváez J, Ricse M, Gomà M, Mitjavila F, Fulladosa X, Capdevila O, et al. The value of repeat biopsy in lupus nephritis flares. Medicine (Baltimore) 2017;96:e7099.
21. Alvarado AS, Malvar A, Lococo B, Alberton V, Toniolo F, Nagaraja HN, et al. The value of repeat kidney biopsy in quiescent Argentinian lupus nephritis patients. Lupus 2014;23:840–7.
22. Malvar A, Pirruccio P, Alberton V, Lococo B, Recalde C, Fazini B, et al. Histologic versus clinical remission in proliferative lupus nephritis. Nephrol Dial Transplant 2017;32:1338–44.
23. Freedman BI, Limou S, Ma L, Kopp JB. APOL1-associated nephropathy: a key contributor to racial disparities in CKD. Am J Kidney Dis 2018;72:S8–16.
24. Freedman BI, Langefeld CD, Andringa KK, Croker JA, Williams AH, Garner NE, et al. End-stage renal disease in African Americans with lupus nephritis is associated with APOL1. Arthritis Rheumatol 2014; 66:390–6.
25. Vajgel G, Lima SC, Santana DJ, Oliveira CB, Costa DM, Hicks PJ, et al. Effect of a single apolipoprotein L1 gene nephropathy variant on the risk of advanced lupus nephritis in Brazilians. J Rheumatol 2020;47:1209–17.
26. Frémond ML, Nathan N. COPA syndrome, 5 years after: where are we? Joint Bone Spine 2021;88:105070.
27. Kalloo S, Aggarwal N, Mohan P, Radhakrishnan J. Lupus nephritis: treatment of resistant disease. Clin J Am Soc Nephrol 2013;8: 154–61.
28. Ripoll È, Merino A, Grinyó JM, Torras J. New approaches for the treatment of lupus nephritis in the 21st century: from the laboratory to the clinic. Immunotherapy 2013;5:1089–101.
29. Kidney Disease: Improving Global Outcomes (KDIGO) Glomerular Diseases Work Group. KDIGO 2021 clinical practice guideline for the management of glomerular diseases. Kidney Int 2021;100:S1–276.
30. Furie R, Rovin BH, Houssiau F, Malvar A, Teng YK, Contreras G, et al. Two-year, randomized, controlled trial of belimumab in lupus nephritis. N Engl J Med 2020;383:1117–28.
31. Rovin BH, Teng YK, Ginzler EM, Arriens C, Caster DJ, Romero-Diaz J, et al. Efficacy and safety of voclosporin versus placebo for lupus nephritis (AURORA 1): a double-blind, randomised, multicentre, placebo-controlled, phase 3 trial. Lancet 2021;397:2070–80.
32. Rovin BH, Furie R, Teng YK, Contreras G, Malvar A, Yu X, et al. A secondary analysis of the belimumab international study in lupus nephritis trial examined effects of belimumab on kidney outcomes and preservation of kidney function in patients with lupus nephritis. Kidney Int 2022;101:403–13.
33. Anders HJ, Rovin B, Zhao MH, Malvar A, Hiromura K, Jones-Leone AR, et al. Effects of belimumab (bel) on renal outcomes in patients (pts) with relapsed and newly diagnosed active lupus nephritis (ln) [abstract]. J Am Soc Nephrol Suppl 2021;32:46–49.
34. Choi CB, Won S, Bae SC. Outcomes of multitarget therapy using mycophenolate mofetil and tacrolimus for refractory or relapsing lupus nephritis. Lupus 2018;27:1007–11.
35. Cortes-Hernandez J, Torres-Salido MT, Medrano AS, Tarres MV, Ordi-Ros J. Long-term outcomes–mycophenolate mofetil treatment for lupus nephritis with addition of tacrolimus for resistant cases. Nephrol Dial Transplant 2010;25:3939–48.
36. Jesus D, Rodrigues M, da Silva JA, Inês L. Multitarget therapy of mycophenolate mofetil and cyclosporine A for induction treatment of refractory lupus nephritis. Lupus 2018;27:1358–62.
37. Barmettler S, Ong MS, Farmer JR, Choi H, Walter J. Association of immunoglobulin levels, infectious risk, and mortality with rituximab and hypogammaglobulinemia. JAMA Netw Open 2018;1:e184169.
38. Leandro MJ. B-cell subpopulations in humans and their differential susceptibility to depletion with anti-CD20 monoclonal antibodies. Arthritis Res Ther 2013;15:S3.
39. Gunnarsson I, Sundelin B, Jónsdóttir T, Jacobson SH, Henriksson EW, van Vollenhoven RF. Histopathologic and clinical outcome of rituximab treatment in patients with cyclophosphamide-resistant proliferative lupus nephritis. Arthritis Rheum 2007;56:1263–72.
40. Goswami RP, Sircar G, Sit H, Ghosh A, Ghosh P. Cyclophosphamide versus mycophenolate versus rituximab in lupus nephritis remission induction: a historical head-to-head comparative study. J Clin Rheumatol 2019;25:28–35.
41. Davies RJ, Sangle SR, Jordan NP, Aslam L, Lewis MJ, Wedgwood R, et al. Rituximab in the treatment of resistant lupus nephritis: therapy failure in rapidly progressive crescentic lupus nephritis. Lupus 2013; 22:574–82.
42. Contis A, Vanquaethem H, Truchetet ME, Couzi L, Rigothier C, Richez C, et al. Analysis of the effectiveness and safety of rituximab in patients with refractory lupus nephritis: a chart review. Clin Rheumatol 2016; 35:517–22.
43. Jónsdóttir T, Zickert A, Sundelin B, Henriksson EW, van Vollenhoven RF, Gunnarsson I. Long-term follow-up in lupus nephritis patients treated with rituximab—clinical and histopathological response. Rheumatology (Oxford) 2013;52:847–55.
44. Lindholm C, Börjesson-Asp K, Zendjanchi K, Sundqvist AC, Tarkowski A, Bokarewa M. Longterm clinical and immunological effects of anti-CD20 treatment in patients with refractory systemic lupus erythematosus. J Rheumatol 2008;35:826–33.
45. Iwata S, Saito K, Hirata S, Ohkubo N, Nakayamada S, Nakano K, et al. Efficacy and safety of anti-CD20 antibody rituximab for patients with refractory systemic lupus erythematosus. Lupus 2018;27: 802–11.
46. Iaccarino L, Bartoloni E, Carli L, Ceccarelli F, Conti F, De Vita S, et al. Efficacy and safety of off-label use of rituximab in refractory lupus: data from the Italian Multicentre Registry. Clin Exp Rheumatol 2015; 33:449–56.
47. Weidenbusch M, Römmele C, Schröttle A, Anders HJ. Beyond the LUNAR trial. Efficacy of rituximab in refractory lupus nephritis. Nephrol Dial Transplant 2013;28:106–11.
48. Alshaiki F, Obaid E, Almuallim A, Taha R, El-Haddad H, Almoallim H. Outcomes of rituximab therapy in refractory lupus: a meta-analysis. Eur J Rheumatol 2018;5:118–26.
49. Furie RA, Aroca G, Cascino MD, Garg JP, Rovin BH, Alvarez A, et al. B-cell depletion with obinutuzumab for the treatment of proliferative lupus nephritis: a randomised, double-blind, placebo-controlled trial. Ann Rheum Dis 2022;81:100–7.
50. Hiepe F, Dörner T, Hauser AE, Hoyer BF, Mei H, Radbruch A. Long-lived autoreactive plasma cells drive persistent autoimmune inflammation. Nat Rev Rheumatol 2011;7:170–8.
51. Ichikawa HT, Conley T, Muchamuel T, Jiang J, Lee S, Owen T, et al. Beneficial effect of novel proteasome inhibitors in murine lupus via dual inhibition of type I interferon and autoantibody-secreting cells. Arthritis Rheum 2012;64:493–503.
52. Segarra A, Arredondo KV, Jaramillo J, Jatem E, Salcedo MT, Agraz I, et al. Efficacy and safety of bortezomib in refractory lupus nephritis: a single-center experience. Lupus 2020;29:118–25.

53. Zhang H, Liu Z, Huang L, Hou J, Zhou M, Huang X, et al. The short-term efficacy of bortezomib combined with glucocorticoids for the treatment of refractory lupus nephritis. Lupus 2017;26:952–8.
54. Singh M, Thomas VM, Mulay S. Bortezomib-induced motor neuropathy: a case report. J Oncol Pharm Pract 2020;26:1549–52.
55. Moreau P, Pylypenko H, Grosicki S, Karamanesht I, Leleu X, Grishunina M, et al. Subcutaneous versus intravenous administration of bortezomib in patients with relapsed multiple myeloma: a randomised, phase 3, non-inferiority study. Lancet Oncol 2011;12:431–40.
56. Ostendorf L, Burns M, Durek P, Heinz GA, Heinrich F, Garantziotis P, et al. Targeting CD38 with daratumumab in refractory systemic lupus erythematosus. N Engl J Med 2020;383:1149–55.
57. Kezar Life Sciences, sponsor. A study of KZR-616 in patients with SLE with and without lupus nephritis (MISSION). ClinicalTrials.gov identifier: NCT03393013; 2022.
58. Cao H, Rao Y, Liu L, Lin J, Yang H, Zhang X, et al. The efficacy and safety of leflunomide for the treatment of lupus nephritis in Chinese patients: systematic review and meta-analysis. PLoS One 2015;10:e0144548.
59. Tam LS, Li EK, Wong CK, Lam CW, Li WC, Szeto CC. Safety and efficacy of leflunomide in the treatment of lupus nephritis refractory or intolerant to traditional immunosuppressive therapy: an open label trial. Ann Rheum Dis 2006;65:417–8.
60. Wenderfer SE, Thacker T. Intravenous immunoglobulin in the management of lupus nephritis. Autoimmune Dis 2012;2012:589359.
61. Samuelsson A, Towers TL, Ravetch JV. Anti-inflammatory activity of IVIG mediated through the inhibitory Fc receptor. Science 2001;291:484–6.
62. Levy Y, Sherer Y, George J, Rovensky J, Lukac J, Rauova L, et al. Intravenous immunoglobulin treatment of lupus nephritis. Semin Arthritis Rheum 2000;29:321–7.
63. Francioni C, Galeazzi M, Fioravanti A, Gelli R, Megale F, Marcolongo R. Long-term i.v. Ig treatment in systemic lupus erythematosus. Clin Exp Rheumatol 1994;12:163–8.
64. Monova D, Belovezhdov N, Altunkova I, Monov S. Intravenous immunoglobulin G in the treatment of patients with chronic glomerulonephritis: clinical experience lasting 15 years. Nephron 2002;90:262–6.
65. Suárez-Fueyo A, Bradley SJ, Klatzmann D, Tsokos GC. T cells and autoimmune kidney disease. Nat Rev Nephrol 2017;13:329–43.
66. Zhang X, Feng R, Shao M, Wang Y, Sun X, He J. Low-dose interleukin-2 as an alternative therapy for refractory lupus nephritis. Rheumatol Ther 2021;8:1905–14.
67. Sekine H, Ruiz P, Gilkeson GS, Tomlinson S. The dual role of complement in the progression of renal disease in NZB/W F(1) mice and alternative pathway inhibition. Mol Immunol 2011;49:317–23.
68. Pickering MC, Ismajli M, Condon MB, McKenna N, Hall AE, Lightstone L, et al. Eculizumab as rescue therapy in severe resistant lupus nephritis. Rheumatology (Oxford) 2015;54:2286–8.
69. Mougiakakos D, Kronke G, Volkl S, Kretschmann S, Aigner M, Kharboutli S, et al. CD19-targeted CAR T cells in refractory systemic lupus erythematosus. N Engl J Med 2021;385:567–9.
70. Zhang W, Feng J, Cinquina A, Wang Q, Xu H, Zhang Q, et al. Treatment of systemic lupus erythematosus using BCMA-CD19 compound CAR. Stem Cell Rev Rep 2021;17:2120–3.
71. Morand EF, Furie R, Tanaka Y, Bruce IN, Askanase AD, Richez C, et al. Trial of anifrolumab in active systemic lupus erythematosus. N Engl J Med 2020;382:211–21.
72. Furie R, Morand E, Bruce I, Manzi S, Kalunian K, Vital E, et al. Type I interferon inhibitor anifrolumab in active systemic lupus erythematosus (TULIP-1): a randomized, controlled, phase 3 trial. Lancet Rheumatol 2019;1:e208–19.
73. Jayne D, Rovin B, Mysler EF, Furie RA, Houssiau FA, Trasieva T, et al. Phase II randomised trial of type I interferon inhibitor anifrolumab in patients with active lupus nephritis. Ann Rheum Dis 2022;81:496–506.
74. Parikh SV, Malvar A, Song H, Alberton V, Lococo B, Vance J, et al. Molecular imaging of the kidney in lupus nephritis to characterize response to treatment. Transl Res 2017;182:1–13.
75. Lewis EJ, Hunsicker LG, Lan SP, Rohde RD, Lachin JM. A controlled trial of plasmapheresis therapy in severe lupus nephritis. The lupus nephritis collaborative study group. N Engl J Med 1992;326:1373–9.
76. Alexander T, Thiel A, Rosen O, Massenkeil G, Sattler A, Kohler S, et al. Depletion of autoreactive immunologic memory followed by autologous hematopoietic stem cell transplantation in patients with refractory SLE induces long-term remission through de novo generation of a juvenile and tolerant immune system. Blood 2009;113:214–23.
77. Jayne D, Passweg J, Marmont A, Farge D, Zhao X, Arnold R, et al, and European Group for Blood and Marrow transplantation; European League Against Rheumatism Registry. Autologous stem cell transplantation for systemic lupus erythematosus. Lupus 2004;13:168–76.
78. Burt RK, Traynor A, Statkute L, Barr WG, Rosa R, Schroeder J, et al. Nonmyeloablative hematopoietic stem cell transplantation for systemic lupus erythematosus. JAMA 2006;295:527–35.
79. Huang X, Chen W, Ren G, Zhao L, Guo J, Gong D, et al. Autologous hematopoietic stem cell transplantation for refractory lupus nephritis. Clin J Am Soc Nephrol 2019;14:719–27.
80. Li W, Chen W, Sun L. An update for mesenchymal stem cell therapy in lupus nephritis [review]. Kidney Dis (Basel) 2021;7:79–89.
81. Deng D, Zhang P, Guo Y, Lim TO. A randomised double-blind, placebo-controlled trial of allogeneic umbilical cord-derived mesenchymal stem cell for lupus nephritis. Ann Rheum Dis 2017;76:1436–9.

Arthritis & Rheumatology
Vol. 74, No. 6, June 2022, pp 927–933
DOI 10.1002/art.42058

American College of Rheumatology
Empowering Rheumatology Professionals

Rituximab Impairs B Cell Response But Not T Cell Response to COVID-19 Vaccine in Autoimmune Diseases

Samuel Bitoun,[1] Julien Henry,[2] Delphine Desjardins,[3] Christelle Vauloup-Fellous,[4] Nicolas Dib,[2] Rakiba Belkhir,[2] Lina Mouna,[4] Candie Joly,[3] Marie Bitu,[3] Bineta Ly,[3] Juliette Pascaud,[3] Raphaèle Seror,[1] Anne-Marie Roque Afonso,[4] Roger Le Grand,[3] and Xavier Mariette[1]

Objective. Antibody response to the messenger RNA (mRNA) COVID-19 vaccine has been shown to be diminished in rituximab (RTX)–treated patients. We undertook this study to compare humoral and T cell responses between healthy controls, patients with autoimmune diseases treated with RTX, and those treated with other immunosuppressants, all of whom had been vaccinated with 2 doses of the mRNA COVID-19 vaccine.

Methods. We performed anti-spike IgG and neutralization assays just before and 28 days after the second BNT162b2 (Pfizer-BioNTech) vaccine dose. The specific T cell response was assessed in activated CD4 and CD8 T cells using intracellular flow cytometry staining of cytokines (interferon-γ, tumor necrosis factor, and interleukin-2) after stimulation with SARS–CoV-2 spike peptide pools.

Results. A lower proportion of responders with neutralizing antibodies to the vaccine was observed in the RTX group (29%; n = 24) compared to the other immunosuppressants group (80%; n = 35) ($P = 0.0001$) and the healthy control group (92%; n = 26) ($P < 0.0001$). No patients treated with RTX in the last 6 months showed a response. Time since last infusion was the main factor influencing humoral response in RTX-treated patients. The functional CD4 and CD8 cellular responses to SARS–CoV-2 peptides for each single cytokine or polyfunctionality were not different in the RTX group compared to the other immunosuppressants group or the control group. In RTX-treated patients, the T cell response was not different between patients with and those without a humoral response.

Conclusion. RTX induced a diminished antibody response to the mRNA COVID-19 vaccine, but the functional T cell response was not altered compared to healthy controls and autoimmune disease patients treated with other immunosuppressants. Further work is needed to assess the clinical protection granted by a functionally active T cell response in the absence of an anti-spike antibody response.

INTRODUCTION

Immunosuppressed patients have experienced an increased mortality rate during the COVID-19 pandemic. Particularly, patients with autoimmune diseases treated with rituximab (RTX) have an odds ratio of death of 4.04 (95% confidence interval 2.32–7.03) (1). The global COVID-19 pandemic is starting to be controlled by countries having benefited from mass vaccination. Unfortunately, RTX treatment that increases the risk of death in patients with autoimmune diseases also diminishes the immune response to the COVID-19 vaccine, with only ~40% of patients showing detectable humoral response (2–4). Other treatments such as mycophenolate mofetil (MMF) and steroids have also been shown to diminish antibody response to COVID-19 vaccine (5). There is still controversy regarding the T cell response, with preliminary studies showing preserved T cell response among patients treated with RTX (3,4,6,7),

Supported by the Infectious Disease Models and Innovative Therapies (IDMIT) research infrastructure (Programme Investissements d'Avenir; no. ANR-11-INBS-0008).

[1]Samuel Bitoun, MD, PhD, Raphaèle Seror, MD, PhD, Xavier Mariette, MD, PhD: Hôpital Bicêtre, AP-HP, FHU CARE, and Université Paris-Saclay, INSERM UMR 1184, CEA, Center for Immunology of Viral, Auto-immune, Hematological and Bacterial Diseases (IMVA-HB/IDMIT), Paris, France; [2]Julien Henry, MD, Nicolas Dib, Rakiba Belkhir, MD: Hôpital Bicêtre, AP-HP, FHU CARE, Paris, France; [3]Delphine Desjardins, PharmD PhD, Candie Joly, PharmD, PhD, Marie Bitu, MSc, Bineta Ly, MSc, Juliette Pascaud, MSc, Roger Le Grand, VetD, PhD: Université Paris-Saclay, INSERM UMR 1184, CEA, Center for Immunology of Viral, Auto-immune, Hematological and Bacterial Diseases (IMVA-HB/IDMIT), Paris, France; [4]Christelle Vauloup-Fellous, MD, PhD, Lina Mouna, PharmD, PhD, Anne-Marie Roque Afonso, MD, PhD: Université Paris Saclay, INSERM U1193, AP-HP, Paris, France, and Hôpital Paul Brousse, Villejuif, France.

Drs. Bitoun, Henry, Desjardins, and Valoup-Fellous contributed equally to this work.

Author disclosures are available at https://onlinelibrary.wiley.com/action/downloadSupplement?doi=10.1002%2Fart.42058&file=art42058-sup-0001-Disclosureform.pdf.

Address correspondence to Xavier Mariette, MD, PhD, Hôpital Bicêtre, Rheumatology Department, 78 Avenue du Général Leclerc, 94270, Le Kremlin Bicêtre, France. Email: xavier.mariette@aphp.fr.

Submitted for publication October 15, 2021; accepted in revised form December 22, 2021.

while others have shown that the T cell response was impaired upon RTX treatment (8). Notably, those studies used either interferon-γ (IFNγ) release assay bulk measurement (6–8) or IFNγ enzyme-linked immunospot (ELISpot) assays (4,5). These techniques can detect an overall T cell response to IFNγ only but do not have high sensitivity and lack the fine-tuning provided by the characterization of the production of multiple cytokines by specific T cells.

The objective of this study was to assess humoral and cellular responses (using cytokine production of CD4 and CD8 T cells) to the messenger RNA (mRNA) COVID-19 vaccine in a population of patients with autoimmune diseases treated with RTX and to compare them to healthy controls and patients treated with other immunosuppressive or immunomodulatory agents.

PATIENTS AND METHODS

Study patients. Consecutive patients with autoimmune diseases treated in a single tertiary rheumatology center, the National Reference Center for Rare Systemic Autoimmune Diseases, were included between January and March 2021. Patients were divided into 2 groups: 1) patients who had received an RTX infusion in the previous year, and 2) patients who had been treated with other immunosuppressive or immunomodulatory agents. Healthy controls were age- and sex-matched to the included patients.

All patients and controls provided informed consent. The study was approved by the Ethics Committee "CPP Sud Méditérrannée" (no. 2020-A00509-30). All patients received a BNT162b2 (Pfizer-BioNTech) vaccine injection on days 0 and 28, according to local guidelines at the time. Participants with a detectable response against the SARS–CoV-2 nucleocapsid at any time were excluded, as it is a hallmark of previous SARS–CoV-2 infection. Humoral response was assessed on day 28 and 1 month after the second dose, on day 56. The cellular response was assessed on day 56.

Patient and public involvement. Due to the urgency and time constraints of such a study, patients were not involved in the design, conduct, or reporting of data. They will be involved in the research dissemination plan, where results will be provided to patient advocacy groups and findings applied during therapeutic education sessions.

SARS–CoV-2 serology. Elecsys anti–SARS–CoV-2 and Elecsys anti–SARS–CoV-2 S immunoassays (Roche Diagnostics) were used for the qualitative detection of total antibodies to nucleocapsid protein and the quantitative determination of antibodies to the spike protein receptor-binding domain (RBD), respectively. In this assay, both neutralizing and non-neutralizing anti-spike antibodies were detected. Anti-nucleocapsid antibodies were considered detected when the assay index result was >1 unit; the quantification range of anti-spike antibodies was 0.4–250 units. Results <0.4 units were considered nonreactive, and anti-spike titers higher than the quantification range were expressed as 250 units.

Surrogate virus neutralization assay. The iFlash-2019-nCoV neutralizing antibody assay (Shenzhen YHLO Biotech) allows for the quantitative determination of total anti-spike antibodies able to block the interaction between soluble angiotensin-converting enzyme 2 and RBD peptides (neutralizing antibodies) coated on microparticles, in an automated immunoassay format. Surrogate neutralizing antibody titers are expressed in IU/ml. According to the manufacturer, results ≥24 IU/ml are considered reactive.

T cell response. We analyzed the T cell response in samples collected 1 month after the second vaccine dose. The percentages of cytokine-secreting cells among activated T cells (CD4+CD154+ and CD8+CD137+) were assessed using frozen human peripheral blood mononuclear cells (PBMCs) from immunized patients. Cytokine production of T cells was assessed after stimulation with peptide pools spanning the wild-type sequence of SARS–COV-2 spike. Briefly, PBMCs were thawed and rested for 1 hour in complete medium (RPMI 1640 GlutaMax [Gibco] supplemented with 10% fetal calf serum, 1% penicillin/streptomycin, and 2% HEPES 1 m*M* [Ozyme]) at 37°C in a CO_2 incubator. Live PBMCs were then counted and stimulated at 1×10^6 per ml with the PepMix SARS–COV-2 spike glycoprotein (JPT Peptide Technologies). Two pools of 15-mer peptides overlapping by 11 amino acids were used for the stimulation of PBMCs (spike 1 domain [S1] and spike 2 domain [S2]) at 2 μg/ml for 18 hours at 37°C in a 5% CO_2 incubator. Brefeldin A (Sigma) was added to the PBMCs at 5 μg/ml 2 hours after the beginning of the incubation. Control cells were treated with phorbol 12-myristate 13-acetate (62 ng/ml; Sigma) and ionomycin (720 ng/ml; Sigma) (positive control), or with complete medium only (unstimulated). After 2 washing steps with phosphate buffered saline (PBS) 1× (Lonza), PBMCs were stained with a viability marker (Live/Dead Near-IR; ThermoFisher) for 20 minutes at 4°C.

Next, PBMCs were fixed and permeabilized for 20 minutes using a Cytofix/Cytoperm kit according to the guidelines of the manufacturer (BD Biosciences). PBMCs were then stained with a panel of antibodies targeting surface markers and cytokines: CD3 BV605, CD8 BV771, CD4 BV421, CD154 PercPCy5.5, CD137 PEDazzle594, tumor necrosis factor (TNF) PECy7, IFNγ allophycocyanin, perforin fluorescein isothiocyanate (all from BioLegend), and granzyme B Alexa Fluor 700 (BD Bioscience), in Perm/Wash buffer supplemented with 10 μl of Fc blocking reagent (Miltenyi) and 10 μl of Brilliant Buffer Plus (BD Biosciences) for 30 minutes at 4°C. Finally, PBMCs were washed in Perm/Wash buffer and resuspended in PBS 1% paraformaldehyde (Sigma) until sample acquisition on a Fortessa Flow Cytometer (BD Biosciences). Data were analyzed using FlowJo software, version 10. Percentages of activated cytokine-secreting CD4 and CD8 T cells were obtained for each of the S1 and S2 pools. For comparison to the nonstimulated condition, values of the S1 and S2 peptide pools were summed. For comparison between groups, the percentage of the

Table 1. Demographic and clinical characteristics of the subjects*

	Controls (n = 26)	RTX-treated patients (n = 24)	Patients treated with other immunosuppressants (n = 35)
Female	20 (78)	22 (92)	23 (66)
Age, median (range) years	60 (26–97)	62 (42–91)	64 (28–94)
Diagnosis			
Rheumatoid arthritis	–	12 (50)	14 (40)
Sjögren's syndrome	–	9 (38)	6 (17)
Myositis	–	1 (4)	1 (3)
SLE	–	1 (4)	3 (8)
Vasculitis	–	0 (0)	2 (6)
GCA	–	0 (0)	3 (8)
PMR	–	0 (0)	1 (3)
Systemic sclerosis	–	1 (4)	2 (6)
Psoriatic arthritis	–	0 (0)	1 (3)
Ankylosing spondylitis	–	0 (0)	1 (3)
Renal transplant recipient	–	0 (0)	1 (3)
Treatment			
Glucocorticoids	–	5 (21)	15 (43)
Mean dose (mg/day)	–	2.9	3.1
RTX			
Time between last infusion of RTX and first vaccine injection, median (range) days	–	162 (0–295)	–
DMARDs			
MTX	–	10 (42)	12 (34)
bDMARDs			
TNFi	–	0 (0)	4 (11)
Tocilizumab	–	0 (0)	3 (9)
Tofacitinib	–	0 (0)	1 (3)
Belimumab	–	0 (0)	1 (3)
Other immunosuppressants			
MMF	–	1 (4)	7 (20)
Bendamustine	–	1 (4)	0 (0)
Gammaglobulinemia (<8 gm/liter)	–	3 (12.5)	–

* Except where indicated otherwise, values are the number (%) of subjects. RTX = rituximab; SLE = systemic lupus erythematosus; GCA = giant cell arteritis; PMR = polymyalgia rheumatica; DMARDs = disease-modifying antirheumatic drugs; MTX = methotrexate; bDMARDs = biologic DMARDs; TNFi = tumor necrosis factor inhibitors; MMF = mycophenolate mofetil.

nonstimulated condition was subtracted from each stimulated peptide pool. The plotted percentages were the sum of percentages of the S1 and S2 pools.

Statistical analysis. Continuous variables are expressed as the mean ± SD. Categorical variables were compared using Fisher's exact test, correlations were assessed using Spearman's test, continuous variables were compared using the Mann–Whitney U test, and multiple comparisons of continuous variables were performed using the Kruskal-Wallis test. Analyses were performed using GraphPad Prism, version 9.

RESULTS

Patient characteristics. Two patients in the control group, 2 in the RTX group, and 2 in the other immunosuppressant group were excluded because of positive anti-nucleocapsid antibodies, which indicate previous SARS–CoV-2 infection. Thus, we included 26 controls and 59 patients with autoimmune diseases (24 in the RTX group and 35 in the other immunosuppressant group) (Table 1).

Delayed and diminished antibody and neutralizing response in RTX-treated patients. On day 28, there was a significantly diminished anti-spike antibody response in both the RTX group (mean ± SD 16.64 ± 52 units/ml) and the other immunosuppressant group (26.75 ± 58 units/ml) compared to the control group (83.79 ± 92 units/ml) (Figure 1A). This highlights a significantly delayed response among most autoimmune disease patients. On day 56, one month after the second vaccine injection, only the RTX group (mean ± SD 69 ± 110 units/ml) had lower levels of anti-spike antibody response compared to healthy controls (235 ± 58 units/ml) and those in the other immunosuppressant group (180 ± 100 units/ml) (Figure 1B). The neutralization assay on day 56 showed that the RTX group (mean ± SD 480 ± 1,064 IU/ml) had much lower levels of neutralizing

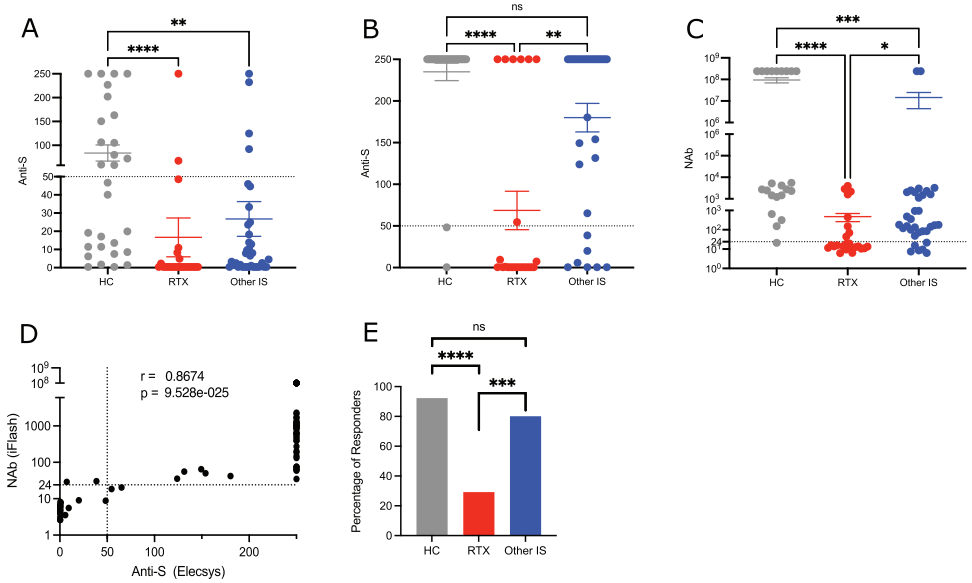

Figure 1. Humoral response after mRNA vaccination against COVID-19. **A** and **B**, Anti-spike (anti-S) antibody response on day 28 (n = 90) (**A**) and day 56 (n = 87) (**B**) after the first injection with the BNT162b2 (Pfizer-BioNTech) vaccine, in healthy controls (HC), rituximab (RTX)–treated patients, and patients treated with other immunosuppressants (IS). **C**, Neutralizing antibody (Nab) response on day 56 after the first injection with the BNT162b2 vaccine (n = 80). **D**, Correlation between anti-spike antibody and neutralizing antibody titers that were used to set the threshold of response. **E**, Percentages of responders, defined as subjects with an anti-spike antibody level of ≥50 units/ml (n = 78). In **A–C**, symbols represent individual subjects; bars show the mean ± SD. In **A–D**, the dotted line indicates the cutoff value. * = $P < 0.05$; ** = $P < 0.01$; *** = $P < 0.001$; **** = $P < 0.0001$. NS = not significant. Color figure can be viewed in the online issue, which is available at http://onlinelibrary.wiley.com/doi/10.1002/art.42058/abstract.

antibodies compared to healthy controls ($9.4 \times 10^8 \pm 1.2 \times 10^9$ IU/ml; $P < 0.0001$) and the other immunosuppressant group ($1.5 \times 10^8 \pm 5.8 \times 10^8$ IU/ml; $P = 0.042$) (Figure 1C). The other immunosuppressant group also had significantly reduced levels of neutralizing antibodies compared to healthy controls ($P = 0.001$) (Figure 1C).

There was a strong correlation between neutralizing antibody titers and anti-spike antibody titers (r = 0.87, $P < 0.0001$) (Figure 1D). Ninety-seven percent of patients with detectable neutralizing antibodies (>24 IU/ml) had an anti-spike concentration >50 units/ml. Antibody responders were defined as such if they met this anti-spike concentration threshold, indicating that they were very likely to have detectable neutralizing antibodies. On day 56, 29.2% of patients in the RTX group were responders, compared to 80% in the other immunosuppressant group ($P = 0.0001$) and 92.3% in the healthy control group ($P < 0.0001$) (Figure 1E).

Impact of B cell depletion on anti-spike response among RTX-treated patients. Demographic factors and cumulative dosing of RTX did not influence antibody responses, as shown in Supplementary Table 1 (available on the *Arthritis & Rheumatology* website at https://onlinelibrary.wiley.com/doi/10.1002/art.42058). However, we identified that in RTX-treated patients, significantly more time had passed since the last infusion for responders (mean ± SD 233 ± 48 days) compared to nonresponders (106 ± 93 days) (Figure 2A). No patient who received an infusion in the last 6 months showed a response. There was also a strong correlation between the number of B cells and the anti-spike antibody response (Figure 2B).

Preservation of functional specific T cell response in RTX-treated patients compared to healthy controls and patients treated without RTX. We analyzed the T cell response using percentages of cytokine-secreting cells among

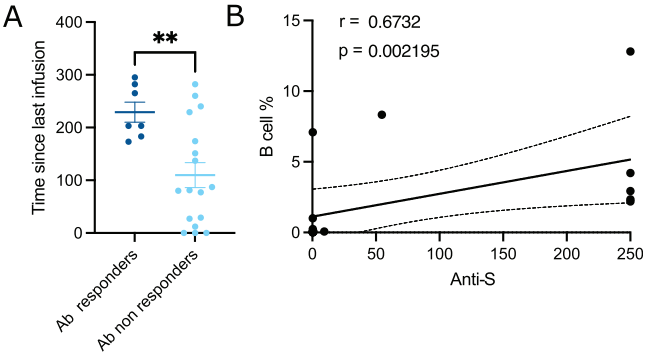

Figure 2. Factors influencing the humoral response in the RTX-treated group. **A**, Time between the last infusion of RTX and the first vaccination in responders and nonresponders. Symbols represent individual subjects; bars show the mean ± SD. **B**, Correlation between percentage of B cells and anti-spike antibody (Ab) response (n = 24). ** = $P < 0.01$. See Figure 1 for other definitions. Color figure can be viewed in the online issue, which is available at http://onlinelibrary.wiley.com/doi/10.1002/art.42058/abstract.

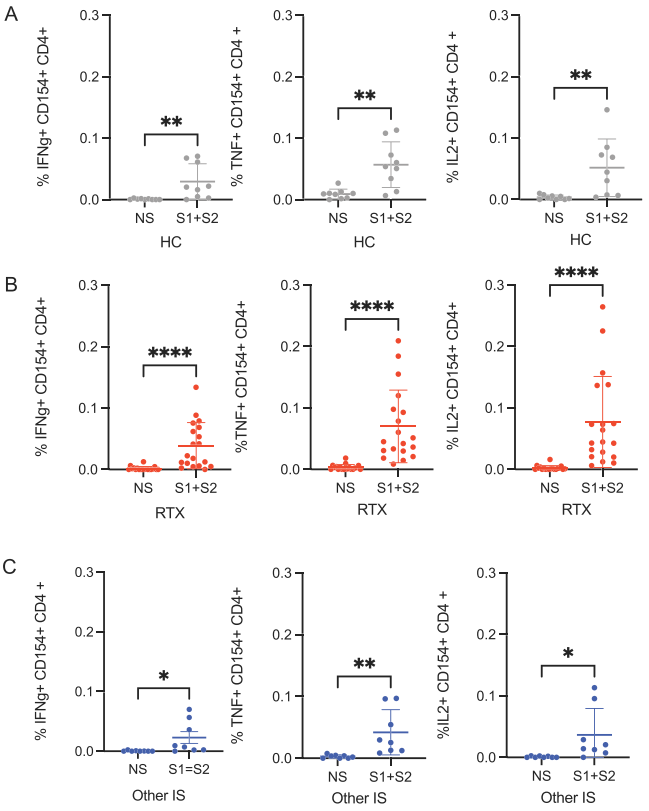

Figure 3. Comparison of unstimulated (NS) and spike peptide–stimulated cytokine secretion in CD4 T cells. In peripheral blood mononuclear cells from healthy controls (HC) (n = 9) (**A**), rituximab (RTX)–treated patients (n = 19) (**B**), and patients treated with other immunosuppressants (IS) (n = 8) (**C**), the T cell response was measured as the percentage of activated CD154+ T cells secreting cytokines (interferon-γ [IFNγ], tumor necrosis factor [TNF], and interleukin-2 [IL-2]) following stimulation with spike peptides (S1 + S2) or in unstimulated conditions. Values in the stimulated samples are the sum of the percentages of cells stimulated by the S1 and S2 pools. Symbols represent individual subjects; bars show the mean ± SD. * = $P < 0.05$; ** = $P < 0.01$; **** = $P < 0.0001$.

activated T cells (CD4+CD154+ and CD8+CD137+) in 9 healthy controls, 19 RTX-treated patients, and 8 patients treated with other immunosuppressants. In all groups, the percentage of CD4+CD154+ T cells producing IFNγ, TNF, and interleukin-2 (IL-2) were significantly higher in response to anti-spike peptide pools (S1 + S2) compared to the unstimulated condition (Figure 3). This validated the specificity of the T cell response detected by our assay. The specific anti-spike CD8 T cell response was significantly different compared to the unstimulated condition for all 3 cytokines in the RTX group, 2 cytokines (IFNγ and TNF) in the healthy control group, and only TNF in the other immunosuppressant group (Supplementary Figure 1, available on the *Arthritis & Rheumatology* website at https://onlinelibrary.wiley.com/doi/10.1002/art.42058). T cell response was not influenced by the age of the participants (data not shown).

Between the 3 groups, there was no difference in the CD4 T cell response in cells secreting IFNγ, TNF, or IL-2 (Figure 4A). Similarly, cytokine-secreting activated spike-specific CD8 T cells were not different between the healthy controls (n = 9), RTX-treated patients (n = 19), and patients treated with other immunosuppressants (n = 8) (Figure 4B). We did not observe any specific granzyme B or perforin response.

Finally, we studied the ability of the CD4 and CD8 T cells to secrete multiple cytokines upon stimulation with spike peptides.

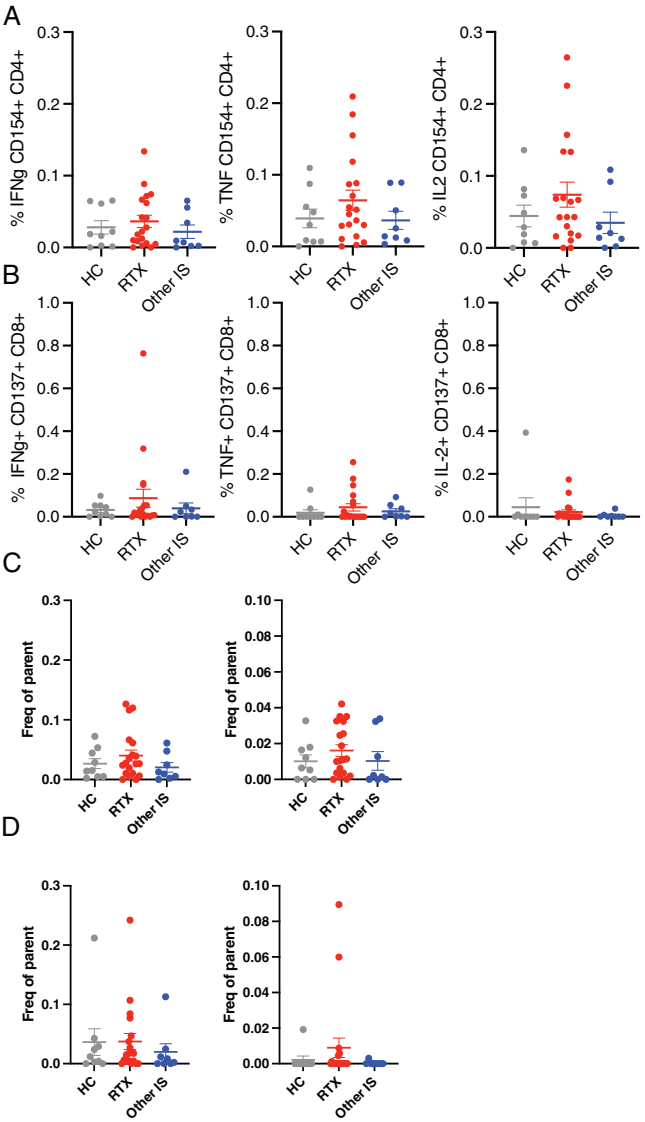

Figure 4. Comparison of specific CD4 and CD8 T cell responses between groups. **A,** Percentage of activated CD154+ cytokine-secreting cells among CD4 T cells. **B**, Percentage of activated CD137+ cytokine-secreting cells among CD8 T cells, minus the percentage among CD8 T cells in the unstimulated condition. Percentages in the stimulated samples are the sum of the percentages of cells stimulated by the S1 and S2 pools. **C** and **D**, Percentages of activated CD154+ cells among CD4 T cells (**C**) and activated CD137+ cells among CD8 T cells (**D**) that secreted 2 cytokines (left) or 3 cytokines (right) at the same time (polyfunctionality). Symbols represent individual subjects; bars show the mean ± SD. No *P* values obtained by Kruskal-Wallis test were significant. See Figure 3 for definitions.

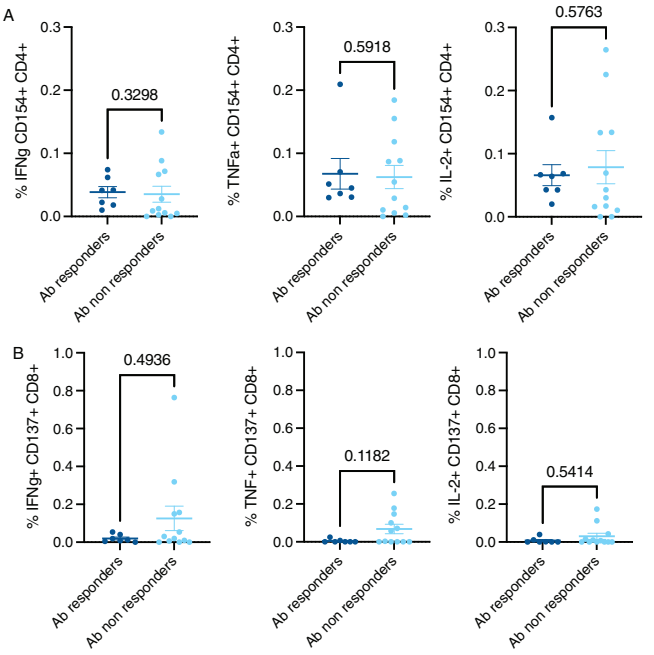

Figure 5. Relationship between cellular and humoral response in RTX-treated patients. Comparisons of percentages of activated CD154+ cytokine-secreting CD4 T cells (**A**) and activated CD137+ cytokine-secreting CD8 T cells (**B**) between antibody (Ab) responders and nonresponders in the RTX-treated group (n = 19) are shown. Symbols represent individual subjects; bars show the mean ± SD. *P* values show comparisons between indicated groups. See Figure 3 for other definitions. Color figure can be viewed in the online issue, which is available at http://onlinelibrary.wiley.com/doi/10.1002/art.42058/abstract.

Once again, we did not find any significant difference in the percentages of polyfunctional CD4 T cells (Figure 4C) or CD8 T cells (Figure 4D) between healthy controls, RTX-treated patients, and patients treated with other immunosuppressants.

Similar T cell response in antibody responders and nonresponders among RTX-treated patients. To assess whether the T cell response was different in patients with versus those without an antibody response to the vaccine, we compared the percentages of cytokine-secreting cells stimulated by spike peptides. No difference in the CD4 or CD8 T cell response was observed when comparing antibody responders and nonresponders in the RTX group for IFNγ, TNF, or IL-2 (Figure 5). Notably, there was a trend toward a better CD8 T cell TNF response against spike peptides in patients without a humoral response ($P = 0.11$) (Figure 5B).

DISCUSSION

This single-center prospective study confirmed the diminished anti-spike antibody and neutralizing antibody response to mRNA COVID-19 vaccines in patients with autoimmune diseases who are being treated with RTX, compared to patients treated with other immunosuppressants and healthy controls. Detailed analysis of the CD4 and CD8 T cell responses using intracellular cytokine staining (ICS) revealed a preserved response in RTX-treated patients compared to healthy controls and patients treated with other immunosuppressants, even in those lacking a humoral response.

To provide a clinically relevant level of neutralizing response, we identified a cutoff of 50 units/ml for the anti-spike antibody assay, which guarantees optimal specificity in detecting neutralizing antibodies. Using this threshold, less than one-third of patients treated with RTX had an effective humoral response to the vaccine, which is consistent with findings from previous studies. We and others (3,4,8) have identified that the time since last infusion and not the cumulative dose of RTX is an important risk factor for nonresponse. This could help to guide clinicians, since we showed, like Spiera et al (3), that no patient had a humoral response if the last infusion of RTX had been conducted in the previous 6 months.

A key finding of our study relies on the maintenance of the T cell response against the vaccine, regardless of the humoral response. Data on the cellular response against the COVID-19 vaccine in patients treated with RTX remain controversial. Our results are consistent with other studies (3,4,6,7) that also provide evidence of a similar T cell response in controls as in patients treated with RTX, but they are in opposition to a recent publication that identified a diminished T cell response in RTX-treated patients, using an IFN release assay (8). In the latter study, patients in the RTX group were co-treated with other immunosuppressants such as steroids (75%), MMF or azathioprine (42%), and calcineurin inhibitors (33%), versus only 4% in our study who were co-treated with MMF.

The main difference between our study and previous studies is the technique used for assessing T cell response. ICS is the reference technique used by Pfizer-BioNTech to address the question of cellular response in the general population (9). Most published studies used the IFNγ release assay, which measures secretion from all cells in the tube (6–8), or IFNγ ELISpot (4,5). These techniques can detect an overall T cell response to IFNγ only but lack the fine-tuning provided by ICS that allows for assessment of several cytokines secreted specifically by activated CD4 and CD8 T cells. ICS also allows for detection of polyfunctional T cells, which can secrete 2 or 3 cytokines at the same time. Again, there was no difference in the percentage of polyfunctional T cells between healthy controls, RTX-treated patients, and patients treated with other immunosuppressants.

Studies have shown a correlation between polyfunctional T cells and control of HIV infection (10). Restricting our analysis of T cell response to activated and cytokine-secreting T cells greatly enhanced the specificity. This provides a more stringent method of assessing the cellular response. We confirmed the ability of autoimmune disease patients to build a specific CD4 T cell response to BNT162b2. Autoimmune disease patients showed similar percentages of cytokine-specific CD4 T cells compared to a study performed in healthy controls by Pfizer-BioNTech using the same ICS technique (9). We also confirmed, both in healthy

controls and patients, a lower response for IL-2 in the CD8 T cells, as previously described by Sahin et al (9). Spike-specific CD8 T cells are known to be less frequently detected compared to CD4 T cells (11) in convalescent patients.

Studies in rhesus macaques showed that depletion of CD8 T cells in animals with low titers of neutralizing antibodies leads to higher viral replication in rechallenge experiments (12). We did not find diminished cytokine secretion of spike-specific CD8 T cells in the RTX group compared to the other groups, and conversely, observed a trend toward a better CD8 T cell TNF response in RTX-treated patients without a humoral response. Interestingly, a recent study in multiple sclerosis patients treated with anti-CD20 demonstrated an increase in spike-specific CD8 T cells compared to controls (13).

This study has a number of limitations. Fewer patients were analyzed in the T cell experiments compared to those using antibody assays. This is due to the time and cost constraints of the ICS technique that requires nonautomated processing, staining, acquisition, and analysis of the samples. Notably, the number of samples analyzed is similar to the reference article using the same technique (9). Therefore, our study may be underpowered to demonstrate a higher T cell response in antibody nonresponders. However, we are confident that there is no difference in T cell response between antibody responders and nonresponders. Finally, our study did not assess other cytokines such as IL-21, which can be secreted by CD4 Tfh, and Th17, which can play a role in antiviral defense.

Further human studies are needed to assess whether this preserved T cell response, despite the impaired humoral response to the COVID-19 vaccine, will be sufficient to protect these RTX-treated patients from severe forms of COVID-19 and to decrease the excess mortality observed in these patients when infected. Taken together, our findings highlight the probable usefulness of vaccination in RTX-treated patients, even if they do not develop a humoral response.

ACKNOWLEDGMENTS

We warmly thank Sylvie Miconnet, Asmaa Mamoune, Isabelle Bonnet, Elodie Rivière, and Marie-Armelle Roudault for their involvement in the patient vaccination process. We thank the Equipements de Recherche Mutualisés (Université Paris-Saclay) and the Île de France Region for funding upgrades and new machines for our flow cytometry facility.

AUTHOR CONTRIBUTIONS

All authors were involved in drafting the article or revising it critically for important intellectual content, and all authors approved the final version to be published. Dr. Bitoun had full access to all of the data in the study and takes responsibility for the integrity of the data and the accuracy of the data analysis.

Study conception and design. Bitoun, Henry, Seror, Roque Afonso, Le Grand, Mariette.

Acquisition of data. Bitoun, Henry, Desjardins, Vauloup-Fellous, Dib, Belkhir, Mouna, Joly, Bitu, Ly, Pascaud, Mariette.

Analysis and interpretation of data. Bitoun, Henry, Desjardins, Vauloup-Fellous, Dib, Belkhir, Mouna, Joly, Seror, Roque Afonso, Le Grand, Mariette.

REFERENCES

1. Strangfeld A, Schäfer M, Gianfrancesco MA, Lawson-Tovey S, Liew JW, Ljung L, et al. Factors associated with COVID-19-related death in people with rheumatic diseases: results from the COVID-19 Global Rheumatology Alliance physician-reported registry. Ann Rheum Dis 2021;80:930–42.
2. Furer V, Eviatar T, Zisman D, Peleg H, Paran D, Levartovsky D, et al. Immunogenicity and safety of the BNT162b2 mRNA COVID-19 vaccine in adult patients with autoimmune inflammatory rheumatic diseases and in the general population: a multicentre study. Ann Rheum Dis 2021;80:1330–8.
3. Spiera R, Jinich S, Jannat-Khah D. Rituximab, but not other antirheumatic therapies, is associated with impaired serological response to SARS-CoV-2 vaccination in patients with rheumatic diseases. Ann Rheum Dis 2021;80:1357–9.
4. Mrak D, Tobudic S, Koblischke M, Graninger M, Radner H, Sieghart D, et al. SARS-CoV-2 vaccination in rituximab-treated patients: B cells promote humoral immune responses in the presence of T-cell-mediated immunity. Ann Rheum Dis 2021;80:1345–50.
5. Izmirly PM, Kim MY, Samanovic M, Fernandez-Ruiz R, Ohana S, Deonaraine KK, et al. Evaluation of immune response and disease status in systemic lupus erythematosus patients following SARS–CoV-2 vaccination. Arthritis Rheumatol 2022;74:284–94.
6. Bonelli MM, Mrak D, Perkmann T, Haslacher H, Aletaha D. SARS-CoV-2 vaccination in rituximab-treated patients: evidence for impaired humoral but inducible cellular immune response. Ann Rheum Dis 2021;80:1355–6.
7. Prendecki M, Clarke C, Edwards H, McIntyre S, Mortimer P, Gleeson S, et al. Humoral and T-cell responses to SARS-CoV-2 vaccination in patients receiving immunosuppression. Ann Rheum Dis 2021;80:1322–9.
8. Moor MB, Suter-Riniker F, Horn MP, Aeberli D, Amsler J, Möller B, et al. Humoral and cellular responses to mRNA vaccines against SARS-CoV-2 in patients with a history of CD20 B-cell-depleting therapy (RituxiVac): an investigator-initiated, single-centre, open-label study. Lancet Rheumatol 2021;3:e789–97.
9. Sahin U, Muik A, Vogler I, Derhovanessian E, Kranz LM, Vormehr M, et al. BNT162b2 vaccine induces neutralizing antibodies and polyspecific T cells in humans. Nature 2021;595:572–7.
10. Brenchley JM, Knox KS, Asher AI, Price DA, Kohli LM, Gostick E, et al. High frequencies of polyfunctional HIV-specific T cells are associated with preservation of mucosal CD4 T cells in bronchoalveolar lavage. Mucosal Immunol 2008;1:49–58.
11. Grifoni A, Weiskopf D, Ramirez SI, Mateus J, Dan JM, Moderbacher CR, et al. Targets of T cell responses to SARS-CoV-2 coronavirus in humans with COVID-19 disease and unexposed individuals. Cell 2020;181:1489–1501.
12. McMahan K, Yu J, Mercado NB, Loos C, Tostanoski LH, Chandrashekar A, et al. Correlates of protection against SARS-CoV-2 in rhesus macaques. Nature 2021;590:630–4.
13. Apostolidis SA, Kakara M, Painter MM, Goel RR, Mathew D, Lenzi K, et al. Cellular and humoral immune responses following SARS-CoV-2 mRNA vaccination in patients with multiple sclerosis on anti-CD20 therapy. Nat Med 2021:1–12.

Arthritis & Rheumatology
Vol. 74, No. 6, June 2022, pp 934–947
DOI 10.1002/art.42060

American College of Rheumatology
Empowering Rheumatology Professionals

B Cell Numbers Predict Humoral and Cellular Response Upon SARS–CoV-2 Vaccination Among Patients Treated With Rituximab

Ana-Luisa Stefanski,[1] Hector Rincon-Arevalo,[2] Eva Schrezenmeier,[3] Kirsten Karberg,[4] Franziska Szelinski,[1] Jacob Ritter,[5] Bernd Jahrsdörfer,[6] Hubert Schrezenmeier,[6] Carolin Ludwig,[6] Arne Sattler,[7] Katja Kotsch,[7] Yidan Chen,[1] Anne Claußnitzer,[7] Hildrun Haibel,[7] Fabian Proft,[7] Gabriela Guerra,[8] Pawel Durek,[8] Frederik Heinrich,[8] Marta Ferreira-Gomes,[8] Gerd R. Burmester,[1] Andreas Radbruch,[8] Mir-Farzin Mashreghi,[8] Andreia C. Lino,[8] and Thomas Dörner[1]

Objective. Patients with autoimmune inflammatory rheumatic diseases receiving rituximab (RTX) therapy are at higher risk of poor COVID-19 outcomes and show substantially impaired humoral immune response to anti–SARS–CoV-2 vaccine. However, the complex relationship between antigen-specific B cells and T cells and the level of B cell repopulation necessary to achieve anti-vaccine responses remain largely unknown.

Methods. Antibody responses to SARS–CoV-2 vaccines and induction of antigen-specific B and CD4/CD8 T cell subsets were studied in 19 patients with rheumatoid arthritis (RA) or antineutrophil cytoplasmic antibody–associated vasculitis receiving RTX, 12 patients with RA receiving other therapies, and 30 healthy controls after SARS–CoV-2 vaccination with either messenger RNA or vector-based vaccines.

Results. A minimum of 10 B cells per microliter (0.4% of lymphocytes) in the peripheral circulation appeared to be required for RTX-treated patients to mount seroconversion to anti-S1 IgG upon SARS–CoV-2 vaccination. RTX-treated patients who lacked IgG seroconversion showed reduced receptor-binding domain–positive B cells ($P = 0.0005$), a lower frequency of Tfh-like cells ($P = 0.0481$), as well as fewer activated CD4 ($P = 0.0036$) and CD8 T cells ($P = 0.0308$) compared to RTX-treated patients who achieved IgG seroconversion. Functionally relevant B cell depletion resulted in impaired interferon-γ secretion by spike-specific CD4 T cells ($P = 0.0112$, $r = 0.5342$). In contrast, antigen-specific CD8 T cells were reduced in both RA patients and RTX-treated patients, independently of IgG formation.

Conclusion. In RTX-treated patients, a minimum of 10 B cells per microliter in the peripheral circulation is a candidate biomarker for a high likelihood of an appropriate cellular and humoral response after SARS–CoV-2 vaccination. Mechanistically, the data emphasize the crucial role of costimulatory B cell functions for the proper induction of CD4 responses propagating vaccine-specific B cell and plasma cell differentiation.

INTRODUCTION

Infectious diseases and associated complications are an important cause of morbidity and mortality in patients with autoimmune inflammatory rheumatic diseases (1). Increased susceptibility to infectious diseases in these patients is most likely due to an immunosuppressive effect of the disease itself and/or related to immunosuppressive treatment (2). COVID-19, caused

Dr. Stefanski's work was supported by the German Society of Rheumatology. Mr. Rincon-Arevalo's work was supported by a COLCIENCIAS scholarship (award 727, 2015). Dr. E. Schrezenmeier's work was supported by the Federal Ministry of Education and Research (grant BCOVIT, 01KI20161), and the Berlin Institute of Health (BIH)–Charité Clinician Scientist Program funded by the Charité Universitätsmedizin Berlin and the BIH. Mr. Ritter's work was supported by an MD scholarship from the BIH. Dr. H. Schrezenmeier's work was supported by the Ministry for Science, Research, and Arts of Baden-Württemberg, Germany (CORE-Project) and the European Commission (award HORIZON2020 Project SUPPORT-E, no. 101015756). Dr. Chen's work was supported by a state scholarship fund organized by the China Scholarship Council. Dr. Mashreghi's work was supported by the state of Berlin and the European Regional Development Fund (award ERDF 2014–2020, EFRE 1.8/11, DRFZ), the BIH Starting Grant Multi-Omics Characterization of SARS-CoV-2 infection (Project 6, Identifying immunological targets in Covid-19), and the Senate of Berlin (Modulation of the mucosal immune response in order to prevent severe COVID-19). Dr. Dörner's work was supported by the German Research Foundation (TRR 130/project 24, Do491/7-5, and Do 491/10-1).

[1]Ana-Luisa Stefanski, MD, Franziska Szelinski, MSc, Yidan Chen, MSc, Gerd R. Burmester, MD, Thomas Dörner, MD: Charité Universitätsmedizin Berlin and Deutsches Rheumaforschungszentrum, Berlin, Germany; [2]Hector Rincon-Arevalo, MSc: Charité Universitätsmedizin Berlin and Deutsches Rheumaforschungszentrum, Berlin, Germany, and Universidad de Antioquia, Medellín, Colombia; [3]Eva Schrezenmeier, MD: Charité Universitätsmedizin, Berlin, Deutsches Rheumaforschungszentrum, Berlin, and Berlin Institute of Health BIH Academy, Berlin, Germany; [4]Kirsten Karberg, MD: RheumaPraxis Steglitz, Berlin, Germany; [5]Jacob Ritter, BS: Charité Universitätsmedizin Berlin and Berlin Institute of Health, BIH Academy, Berlin, Germany;

by SARS–CoV-2, requires particular consideration in patients with autoimmune inflammatory rheumatic diseases. Rituximab (RTX), an anti-CD20 monoclonal antibody leading to B cell depletion and used in autoimmune inflammatory rheumatic diseases like rheumatoid arthritis (RA) and antineutrophil cytoplasmic antibody–associated vasculitis (AAV), has been found to be a risk factor for poor COVID-19–associated outcomes (3,4). Since a suitable treatment for COVID-19 has not been developed yet, vaccination is of crucial importance to protect these vulnerable patients. Meanwhile, various phase III clinical trials have demonstrated the efficacy and safety of messenger RNA (mRNA)–based vaccines (BNT162b2 [Pfizer-BioNTech] [5,6] and mRNA-1273 [Moderna] [7]) and viral vector–based vaccines (ChAdOx1 [AstraZeneca] [8] and Ad26.COV2.S [Johnson & Johnson] [9]) to prevent severe COVID-19 disease or death.

In patients with autoimmune inflammatory rheumatic diseases, vaccination is generally regarded as safe and efficacious (10). However, in patients receiving B cell–depleting therapy with RTX in particular, hampered humoral and cellular responses following influenza, pneumococcal, and hepatitis B vaccination have been reported (11–16). Available data on the SARS–CoV-2 vaccine response in RTX-treated patients with autoimmune inflammatory rheumatic diseases reveal substantially impaired humoral (17–19), but partly inducible cellular, immune responses (20). However, little is known about the complex mechanisms of interaction between T cells, B cells, and plasma cells, or the level of B cell repopulation necessary for proper vaccine response among RTX-treated patients.

In this study, we investigated the characteristics of humoral and cellular antigen-specific CD4/CD8 and B cell immune response upon SARS–CoV-2 vaccination in patients treated with RTX compared to healthy controls and RA patients receiving other therapies.

PATIENTS AND METHODS

Study participants. Outpatients with rheumatic disease treated with RTX who received SARS–CoV-2 vaccination according to federal and Berlin state recommendations between February and May 2021 were asked to participate in this study. We included 16 patients who had RA according to the American College of Rheumatology/European Alliance of Associations for Rheumatology 2010 classification criteria (21) and 3 patients with AAV defined as described by the Chapel Hill Consensus Conference Nomenclature (22), all of whom were receiving RTX. In addition, 12 patients with RA who were receiving other therapies and 30 healthy controls were included as control groups. All participants gave written informed consent in accordance with the approval of the ethics committee at the Charité University Hospital Berlin (EA2/010/21, EA4/188/20).

Peripheral blood samples were obtained using EDTA anticoagulant or serum tubes (BD Vacutainer System; BD Diagnostics) 6–9 days (referred to hereafter as day 7) after vaccination with either 2 doses of BNT162b2, 2 doses of ChAdOx1, or 1 dose of ChAdOx1 followed by 1 dose of BNT162b2. Serologic and B cell data for healthy controls have partially been published (23). Samples obtained 3–4 weeks after the second vaccination (referred to hereafter as day 21) were available for 19 RTX-treated patients and 12 RA controls. One RTX-treated patient (who had RA) had concomitant chronic lymphocytic leukemia (CLL); cellular data for this patient were excluded from the analyses of B cells, CD4 T cells, and the relationships between humoral immune responses, cell subsets, and demographic characteristics. Limited baseline T cell, B cell, and natural killer cell data were available for 16 of the 19 patients receiving RTX (2 AAV patients and 14 RA patients), 11 of the 12 RA patients, and 16 of the 30 healthy controls. Regarding the absolute numbers of B cells, CD4 cells, and CD8 cells, there was no difference between baseline and day 7 after the second vaccination (data not shown). Participant characteristics are summarized in Table 1, with more detailed information provided in Supplementary Table 1, available on the *Arthritis & Rheumatology* website at http://onlinelibrary.wiley.com/doi/10.1002/art.42060.

Enzyme-linked immunosorbent assay and surrogate SARS–CoV-2 neutralization test. The assays were performed according to the manufacturer's instructions, as previously described (23). Briefly, serum samples were diluted at 1:100 in sample buffer, pipetted onto strips of 8 single wells of a 96-well microtiter plate, and precoated with recombinant SARS–CoV-2 spike or nucleocapsid proteins. Calibrators, a positive control, and a negative control were carried out on each plate. After incubation for 60 minutes at 37°C, wells were washed 3 times and peroxidase-labeled anti-IgG or anti-IgA antibody solution was added, followed by a second incubation step for 30 minutes. After 3 additional washing steps, substrate solution was added and the samples were incubated for 15–30 minutes in the dark. Optical density (OD) values were measured on a POLARstar Omega plate reader (BMG Labtech) at 450 nm and at 620 nm.

[6]Bernd Jahrsdörfer, MD, Hubert Schrezenmeier, MD, Carolin Ludwig, MLT: Ulm University, Ulm, Germany, Institute for Clinical Transfusion Medicine and Immunogenetics, German Red Cross Blood Transfusion Service Baden-Württemberg–Hessen, and University Hospital Ulm, Ulm, Germany; [7]Arne Sattler, PhD, Katja Kotsch, PhD, Anne Claußnitzer, MD, Hildrun Haibel, MD, Fabian Proft, MD: Charité Universitätsmedizin Berlin, Berlin, Germany; [8]Gabriela Guerra, MSc, Pawel Durek, PhD, Frederik Heinrich, PhD, Marta Ferreira-Gomes, PhD, Andreas Radbruch, PhD, Mir-Farzin Mashreghi, PhD, Andreia C. Lino, PhD: Deutsches Rheumaforschungszentrum, Berlin, Germany.

Dr. Stefanski and Mr. Rincon-Arevalo contributed equally to this work.

Author disclosures are available at https://onlinelibrary.wiley.com/action/downloadSupplement?doi=10.1002%2Fart.42060&file=art42060-sup-0001-Disclosureform.pdf.

Address correspondence to Thomas Dörner, MD, Department of Rheumatology and Clinical Immunology, Charité Universitätsmedizin Berlin, Charitéplatz 1, 10117 Berlin, Germany. Email: thomas.doerner@charite.de

Submitted for publication August 16, 2021; accepted in revised form December 22, 2021.

Table 1. Characteristics of the study participants*

	Healthy controls (n = 30)	RA controls (n = 12)	RTX-treated patients (n = 19)†
Age, years			
Median (IQR)	57 (46.25–79.5)	68 (63–79.5)	58 (56.5–65)
No. <50	9	1	3
No. 50–69	12	5	13
No. >69	9	6	3
Sex, no. female/male	15/15	9/3	14/5
Vaccine, no.			
2× BNT162b2	24	11	14
2× mRNA-1273	0	0	1
2× ChAdOx1	3	1	1
1× ChAdOx1, 1× BNT162b2	3	0	3
Immunosuppression, no.			
MTX	–	8	4
Leflunomide	–	1	0
Sulfasalazine	–	0	1
AZA	–	0	1
JAK inhibitor	–	4	2
TNF inhibitor	–	1	0
Abatacept	–	2	1
Prednisolone‡	–	3	8
DAS28, median (IQR)	–	2.58 (1.70–3.99)	2.65 (1.96–3.41)
Time since last RTX treatment, median (IQR) months	–	–	9 (6–13.5)
Duration of RTX treatment, median (IQR) years	–	–	3 (2–6)

* IQR = interquartile range; MTX = methotrexate; AZA = azathioprine; TNF = tumor necrosis factor; DAS28 = Disease Activity Score in 28 joints.
† Included 16 patients with rheumatoid arthritis (RA) and 3 patients with antineutrophil cytoplasmic antibody–associated vasculitis.
‡ The maximum prednisolone dosage was 5 mg/day in the RA group and 7.5 mg/day in the rituximab (RTX) group.

Finally, OD ratios were calculated based on the sample and calibrator OD values. To identify individuals who had previously been infected with SARS–CoV-2, we measured antibodies against the nucleocapsid protein (not a vaccine component) on day 7 after the second vaccination (Supplementary Figure 1, available on the *Arthritis & Rheumatology* website at http://onlinelibrary.wiley.com/doi/10.1002/art.42060).

Isolation and staining of peripheral blood mononuclear cells (PBMCs). PBMCs were prepared by density-gradient centrifugation using Ficoll-Paque Plus solution (GE Healthcare Biosciences). For antigen-specific T cell analysis, PBMCs were cryopreserved at –80°C. For surface staining, 1–3 × 10^6 cells were suspended in 50 μl of phosphate buffered saline (PBS)/0.5% bovine serum albumin/EDTA and 10 μl Brilliant Buffer (BD Horizon). Cells were stained for 15 minutes on ice and washed afterwards with Dulbecco's PBS containing 1% fetal calf serum (FCS; Biowest) (810*g*, for 8 minutes at 4°C). For intracellular staining after T cell stimulation, cells were first stained for 30 minutes with 1:1,000 BUV395 Live/Dead (Invitrogen) in PBS, followed by 5 minutes with 2.5 μl Fc Block (Miltenyi Biotech) in 50 μl resuspended cells. Cells were fixed in Lyse/Fix (Becton Dickinson), permeabilized with FACS Perm II solution (Becton Dickinson), and intracellularly stained.

Staining of antigen-specific B cells. To identify receptor-binding domain (RBD)–specific B cells, recombinant purified RBD (DAGC149; Creative Diagnostics) was labeled with either Alexa Fluor 647 or Alexa Fluor 488 as previously described (23). Double-positive cells were considered antigen-specific. A blocking experiment using unlabeled RBD at 100-fold concentration was performed to ensure specificity of detection.

Peptide stimulation of antigen-specific T cells. For each stimulation, 2 × 10^6 PBMCs obtained from 15 healthy controls, 12 RA controls, and 19 RTX-treated patients were thawed and washed twice in prewarmed RPMI 1640 medium (containing 0.3 mg/ml glutamine, 100 units/ml penicillin, 0.1 mg/ml streptomycin, 10% FCS, and 25 units/ml DNase I [Roche International]), rested for 1 hour in culture medium (RPMI 1640 with glutamine, antibiotics, and 10% FCS) and stimulated with SARS–CoV-2 spike (PepMix SARS–CoV-2 [S B.1.1.7]; JPT) (24) or T Cell TransAct (Miltenyi Biotech) in the presence of allophycocyanin (APC)–conjugated anti-CD107a (clone H4A3; BioLegend) for 16 hours. Brefeldin A (10 μg/ml; Sigma-Aldrich) was added after 2 hours. Due to cell number limitations, T Cell TransAct stimulation was not carried out for all participants. CD4 T cells coexpressing CD154 and CD137 were considered antigen-specific. Spike-specific CD8 T cells were identified based on activation-dependent coexpression of CD137 and

interferon-γ (IFNγ) and CD107a and IFNγ, respectively. Subjects whose samples showed an increase in frequency after stimulation of at least 2-fold compared to unstimulated control were defined as responders.

Analytical methods. All flow cytometric analyses were performed using a BD FACS Fortessa (BD Biosciences). To ensure comparable mean fluorescence intensities over the time of the analyses, Cytometer Setup and Tracking beads (BD Biosciences) and Rainbow Calibration Particles (BD Biosciences) were used. For flow cytometric analysis, the following fluorochrome-labeled antibodies were used: BUV737-conjugated anti-CD11c (clone B-ly6; BD), BUV395-conjugated anti-CD14 (clone M5E2; BD), BUV395-conjugated anti-CD3 (clone UCHT1; BD), BV786-conjugated anti-CD27 (clone L128; BD), BV711-conjugated anti-CD19 (clone SJ25C1; BD), BV605-conjugated anti-CD24 (clone ML5; BD), BV510-conjugated anti-CD10 (clone HI10A; BD), BV421-conjugated anti-CXCR5 (clone RF8B2; BD), phycoerythrin (PE)–Cy7–conjugated anti-CD95 (clone APO-1/Fas; ThermoFisher), PE-CF594–conjugated anti-IgD (clone IA6-2; BioLegend), APC-Cy7–conjugated anti-CD38 (clone HIT2; BioLegend), PE–Cy7–conjugated anti-IgG (clone G18-145; BD), biotin-conjugated anti-IgA (clone G20-359; BD), BV650-conjugated anti-IgM (clone MHM-88; BD), fluorescein isothiocyanate (FITC)–conjugated anti-HLA–DR (clone L234; BioLegend), PE-conjugated anti-CD21 (clone B-ly4; BD), APC-conjugated anti-CD22 (clone S-HCL-1; BD), FITC-conjugated anti–tumor necrosis factor (anti-TNF) (clone Mab11; BioLegend), BV650-conjugated anti-IFNγ (clone 4S.B3; BD), BV786-conjugated anti-CD40L (clone 24-31; BioLegend), and PE-CF594–conjugated anti-CD137 (clone 4B4-1; BioLegend). The absolute number of B cells was measured with Trucount (BD), and samples were processed according to the manufacturer's instructions (B cells were defined as CD19+CD45+CD3–CD14–CD16–CD56– lymphocytes).

Sorting of plasmablasts, B cells, and T cells from peripheral blood for single-cell analysis. As previously described (23), cells were enriched from peripheral blood using StraightFrom Whole Blood CD19, CD3, and CD138 MicroBeads (Miltenyi Biotec) according to the manufacturer's instructions. Sorted populations were identified as plasmablasts (DAPI–CD3–CD14–CD16–CD38++CD27++), memory B cells (DAPI–CD3–CD14–CD16–CD38–CD27+), and activated T cells (DAPI–CD3+CD14–CD16–CD38++HLA–DR+). The 3 sorted populations were pooled and further processed for single-cell RNA sequencing.

Single-cell RNA library preparation and single-cell transcriptome sequencing. Sequencing was performed on a NextSeq500 device (Illumina) using High Output v2 Kits (150 cycles) with the recommended sequencing conditions for 5′ GEX libraries and as previously described (23). In particular, transcriptome profiles were merged and normalized, variable genes were detected, and Uniform Manifold Approximation and Projection (UMAP) was performed with default parameter settings using FindVariableGenes, RunPCA, and RunUMAP with 30 principal components. Expression values are represented as ln (10,000 × UMIsGene) /UMIsTotal +1). Transcriptionally similar clusters were identified using shared nearest neighbor (SNN) modularity optimization, SNN resolutions ranging from 0.1 to 1.0 in 0.1 increments were computed, or gating was performed manually using Loupe Browser (10x Genomics). Data from transcriptome and immune profiling were merged using the same cellular barcodes.

Statistical analysis. All samples included in the final analyses had at least 1×10^6 events with a minimum threshold for CD19+ cells of 5,000 events, apart from RTX-treated patients: minimum recorded CD19+ events in the RTX group were 16 and 45 events, in 2 different patients, of >1 million total recorded events. Flow cytometric data were analyzed by FlowJo software version 10.7.1 (TreeStar). GraphPad Prism software version 5 was used for statistical analysis. For comparison of multiple groups, two-way analysis of variance with Šidák's post test for multiple comparisons or Kruskal-Wallis with Dunn's post test was used. Spearman's correlation coefficient was calculated to detect possible associations between parameters or disease activity. *P* values less than 0.05 were considered significant. Data on cellular subsets for 1 patient receiving RTX who had concomitant CLL were excluded from the analyses of B cells, CD4 T cells, and the relationships between humoral immune responses, cell subsets, and demographic characteristics. For 1 patient receiving RTX and 6 healthy controls there was not enough material to perform fluorescence-activated cell sorting T cell staining for activated T cells. A correlation matrix was calculated using the base R and corrplot package (R Foundation for Statistical Computing) using the Spearman method (n = 17 for the RTX group; 1 patient excluded due to concomitant CLL and 1 patient excluded due to partially missing T cell data).

Data and materials availability. All data, code, and materials used in the analysis are available at https://datadryad.org/stash/. In particular, the genetic data are available in a gene bank.

RESULTS

Cohorts and participant characteristics. This study recruited 19 patients receiving RTX (16 patients with RA and 3 patients with AAV [RTX group]), 30 healthy controls, and 12 patients with RA receiving other therapies as an additional control group (RA group). Most study participants were vaccinated twice with the mRNA vaccine BNT162b2; 1 RTX-treated patient was vaccinated twice with mRNA-1273. Three healthy controls, 1 RA control, and 1 RTX-treated patient were vaccinated twice with the viral vector vaccine ChAdOx1. According to national recommendations, 3 RTX-treated patients and 3 healthy

controls received 1 dose of ChAdOx1 followed by a heterologous vaccination with 1 dose of BNT162b2.

Regarding demographic characteristics, healthy controls were age-matched to RTX-treated patients and were younger than RA patients. As is typical for patients with rheumatic diseases, the majority of RA patients and RTX-treated patients were women. Disease activity at the time of first vaccination was comparable between the RA control group and RTX group. At the time of vaccination, median time since the last RTX treatment was 9 months. RTX-treated patients had received B cell–depleting therapy on average for 3 years, and presented with a range of circulating B cell numbers of 0–484/μl blood. Demographic characteristics and additional treatments for all study participants are summarized in Table 1. (Further details on the patient cohorts are provided in Supplementary Table 1, available on the *Arthritis & Rheumatology* website at http://onlinelibrary.wiley.com/doi/10.1002/art.42060.)

Impaired humoral immune response upon SARS–CoV-2 vaccination in RA patients and RTX-treated patients. Antibody responses to SARS–CoV-2 vaccines were assessed in all individuals on day 7 after the second vaccination. All healthy controls became positive for anti–spike S1 (anti-S1) IgG and IgA and showed >90% SARS–CoV-2 neutralization. Notably, IgA and IgG anti-vaccine titers were significantly diminished on day 7 after the second vaccination in the RA control group, and especially in the RTX group, compared to the healthy control group (Figure 1A). Anti-S1 IgG antibodies were detected in 8 (66.7%) of 12 patients in the RA group and 8 (42.1%) of 19 patients in the RTX group. Simultaneously, 5 (41.7%) of 12 patients in the RA group and 9 (47.4%) of 19 patients in the RTX group developed anti-S1 IgA antibodies. Virus-neutralizing antibodies were found in only 8 (66.7%) of the 12 RA control patients and 9 (47.4%) of the 19 RTX-treated patients (Figure 1A).

Two RTX-treated patients with unknown prior infection (identified as anti-nucleocapsid protein positive) (Supplementary Figure 1, available on the *Arthritis & Rheumatology* website at http://onlinelibrary.wiley.com/doi/10.1002/art.42060) developed high titers of anti-S1 IgG, IgA, and neutralizing-antibodies comparable with the titers in healthy controls.

Delayed serologic response in RTX-treated patients. As previously reported (25), patients with autoimmune inflammatory rheumatic diseases may show a delayed humoral immune response after vaccination. To address this possibility, we obtained additional blood samples from patients in the RA and RTX groups 3–4 weeks (day 21) after the second vaccination (Figure 1B). Two RA patients and 5 RTX-treated patients developed positive IgG antibodies; IgA was detected in 2 patients in the RA group and 1 patient in the RTX group 3–4 weeks after the second vaccination. Neutralizing antibodies were detected in 2 patients in the RA group and 6 patients in the RTX group at this later time point. Among the RTX-treated patients who did not show seroconversion on day 7 after the second vaccination, there was a significant increase in IgG and neutralizing-antibody formation at the later time point (Figure 1C). Notably, IgG titers correlated with neutralizing antibodies ($r = 0.8957$, $P < 0.0001$) (Figure 1D). Thus, and considering the delayed vaccine response, 10 (83.3%) of 12 RA patients and 13 (68.4%) of 19 RTX-treated patients showed IgG seroconversion with neutralizing antibodies after SARS–CoV-2 vaccination, even though at lower titers compared to those in healthy controls.

Interestingly, the data suggested that RTX-treated patients had a potential dichotomous response: 13 of 19 RTX-treated patients showed seroconversion to IgG (RTX IgG+), while 6 of 19 did not (RTX IgG–). To identify potential factors resulting in IgG seroconversion among RTX-treated patients, further study addressed potential differences between the 2 groups. With regard to comedication, we found a negative correlation between prednisolone dose and IgG formation as well as B cell counts, while there was no significant relationship with the use of methotrexate (Supplementary Figures 2A–C, available on the *Arthritis & Rheumatology* website at http://onlinelibrary.wiley.com/doi/10.1002/art.42060). There was no association between the Disease Activity Score in 28 joints in RA and vaccine-induced humoral response (Supplementary Figure 2D).

Requirement of a minimum of 10 B cells per microliter in the peripheral circulation for specific IgG induction. We analyzed the B cell compartment (gating strategy shown in Figure 2A) and RBD-specific B cells (Figure 2B) among the different groups. RTX-treated patients presented with significantly lower relative and absolute B cell numbers compared to healthy controls and RA controls (Figure 2C). Notably, a significant difference in the frequency and absolute number of B cells was also found between IgG+ RTX-treated patients and RTX-treated patients who did not show seroconversion (Figure 2D). In our RTX cohort, 10 B cells per microliter in the peripheral circulation (or 0.4% of lymphocytes accordingly) was identified as the minimum needed to mount seroconversion to anti-S1 IgG among RTX-treated patients (Figure 2D).

In the RTX group, there was a direct relationship between B cell numbers and humoral anti-vaccine response, as indicated by the significant correlations of the absolute number of B cells (Figure 2E) and B cell frequency (Supplementary Figure 3A, available on the *Arthritis & Rheumatology* website at http://onlinelibrary.wiley.com/doi/10.1002/art.42060) with anti-S1 IgG titers ($r = 0.5975$, $P = 0.0044$ and $r = 0.6391$, $P = 0.0021$, respectively) and the even stronger correlations of absolute number of B cells and B cell frequency with neutralizing antibodies ($r = 0.7296$, $P = 0.0003$ and $r = 0.7744$, $P < 0.0001$, respectively). These findings clearly suggest that humoral protection elicited by vaccination is dependent on the critical availability of B cells in RTX-treated patients. In the RA and healthy control groups we did not find a significant

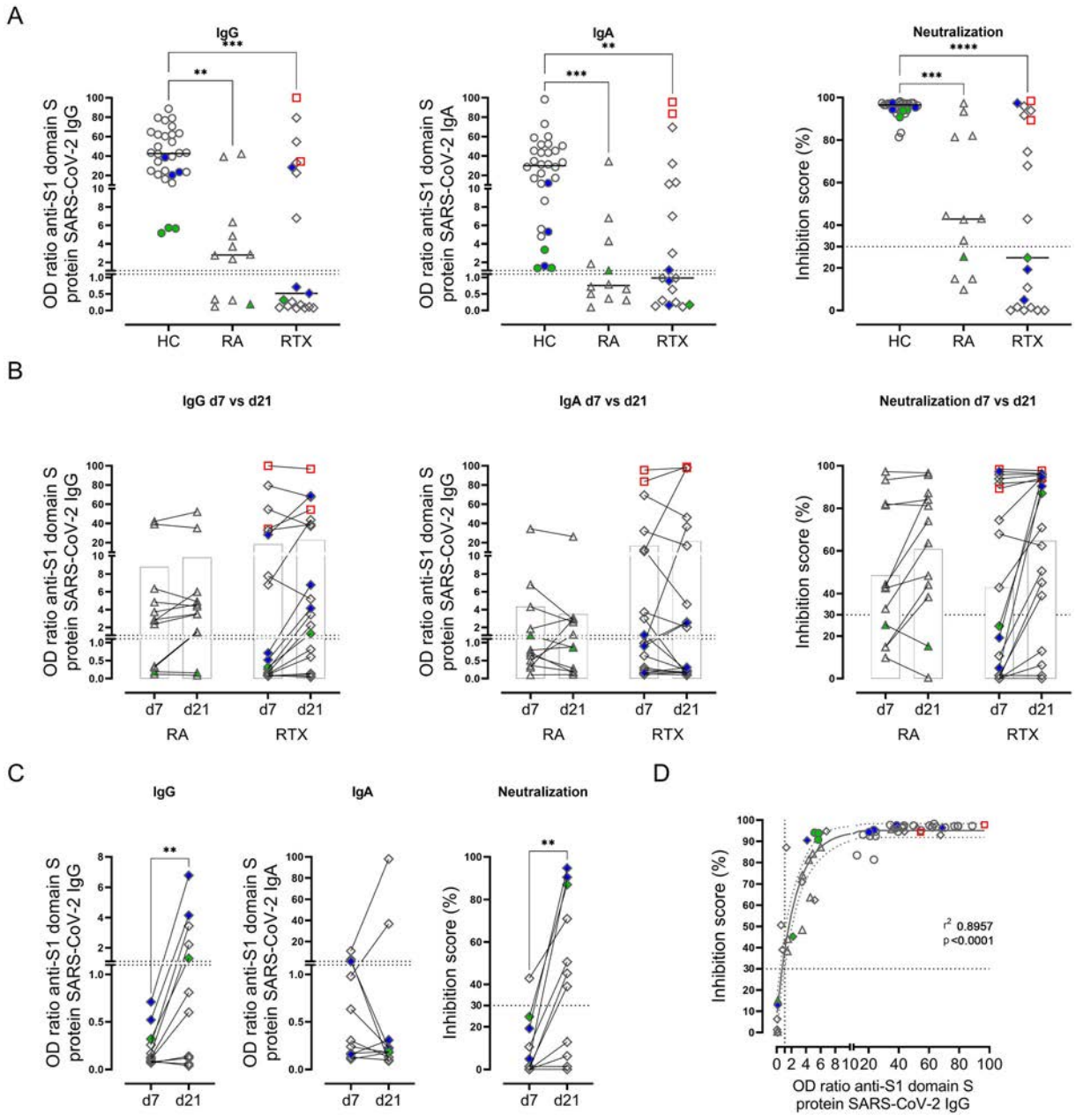

Figure 1. Reduced and delayed humoral immune response to SARS–CoV-2 vaccination in patients with rheumatoid arthritis (RA) and patients treated with rituximab (RTX). **A**, Anti-S1 IgG antibody titer, anti-S1 IgA antibody titer, and inhibition score indicating antibody neutralization, determined by enzyme-linked immunosorbent assay (ELISA) for spike protein S1 IgG, ELISA for spike protein S1 IgA, and blocking ELISA for virus neutralization, respectively, in peripheral blood samples obtained from healthy controls (HCs; n = 30), RA controls (n = 12), and RTX-treated patients (n = 19) on day 7 after the second SARS–CoV-2 vaccination. Symbols represent individual subjects; horizontal lines show the mean. **B**, Anti-S1 IgG antibody titer, anti-S1 IgA antibody titer, and antibody neutralization in serum samples obtained from 12 RA patients and 19 RTX-treated patients on day 7 after (d7) and 3–4 weeks after (d21) the second vaccination. Linked symbols represent individual subjects; open bars show the mean. Two-way analysis of variance with Šidák's post test was used for comparisons. The interaction effect was not significant. **C**, Delayed IgG response on day 21 in 5 of the 11 RTX-treated patients who did not initially show seroconversion (on day 7 after the second vaccination). Linked symbols represent individual subjects. **D**, Significant correlation, determined by Spearman's correlation test, between IgG titers and inhibition score of antibody neutralization among RTX-treated patients. Solid and dotted curved lines show the sigmoidal model with 95% confidence bands. Red indicates previously infected subjects; green indicates subjects who were vaccinated twice with ChAdOx1; blue indicates subjects who received 1 dose of ChAdOx1 followed by a heterologous vaccination with 1 dose of BNT162b2. Dotted lines indicate the upper limit of normal. ** = $P < 0.01$; *** = $P < 0.001$; **** = $P < 0.0001$, by Kruskal-Wallis with Dunn's post test in **A**, by Mann-Whitney test in **C**.

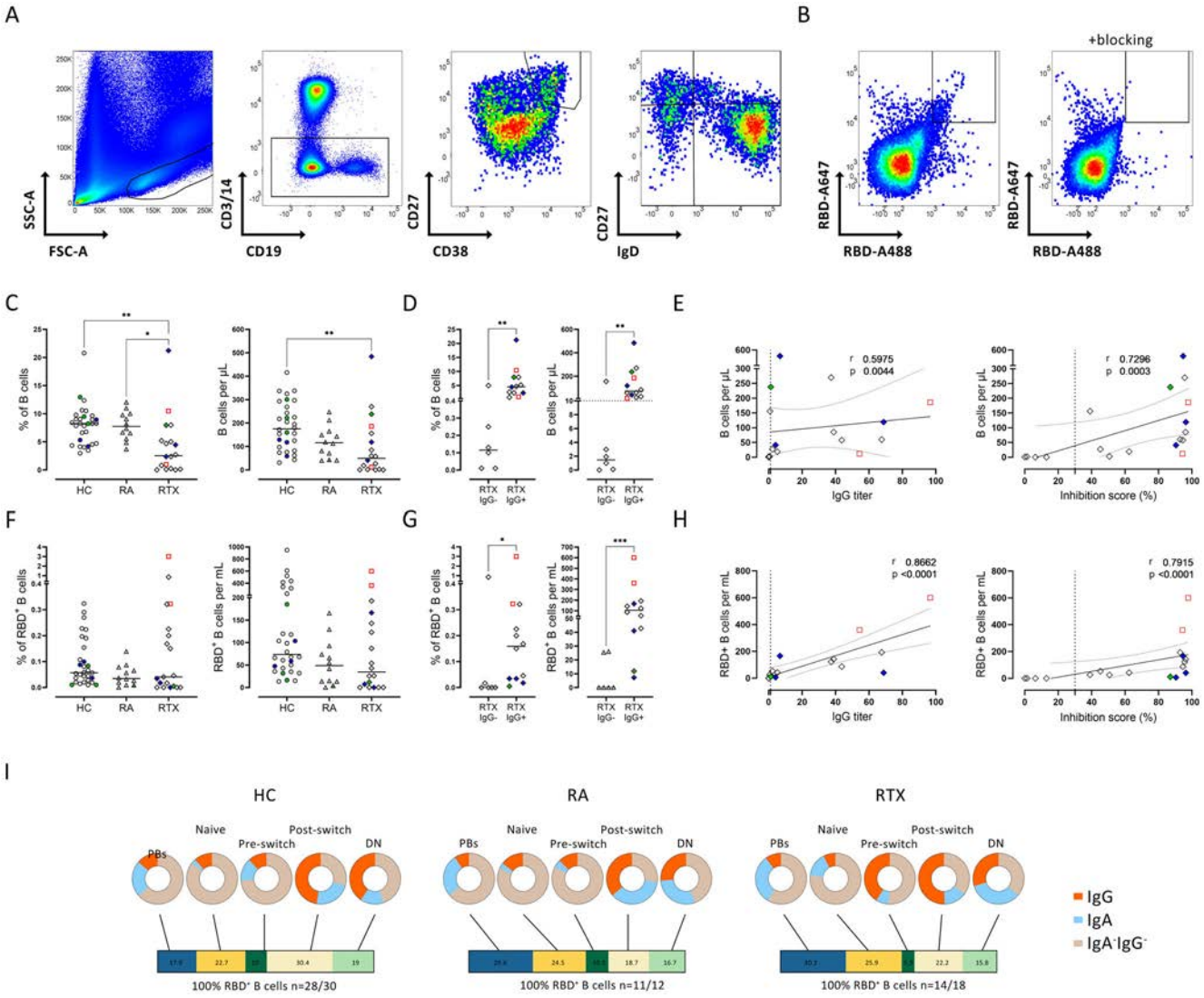

Figure 2. Reduction in the frequencies and numbers of total B cells and antigen-specific B cells in RTX-treated patients, and correlation of B cell numbers with humoral immune response. **A**, Representative flow cytometry plots of receptor-binding domain (RBD)–positive B cells, plasmablasts (PBs), and non-plasmablast B cell subsets based on IgD/CD27 classification. **B**, Representative flow cytometry plots of RBD+ B cells before and after blocking with unlabeled RBD. **C** and **D**, Frequency and absolute number of CD19+ B cells in healthy controls, RA controls, and RTX-treated patients (**C**) and in IgG+ RTX-treated patients compared to IgG– RTX-treated patients (**D**) on day 7 after the second SARS–CoV-2 vaccination. Dotted line in **D** indicates the minimum number of B cells needed to mount seroconversion to anti-S1 IgG. **E**, Correlations between the number of CD19+ B cells and humoral immune response, as indicated by IgG formation and neutralizing capacity, in RTX-treated patients. **F** and **G**, Frequency and absolute number of RBD+ cells among total CD19+ B cells in healthy controls, RA controls, and RTX-treated patients (**F**) and in IgG+ RTX-treated patients compared to IgG– RTX-treated patients (**G**) on day 7 after the second vaccination. **H**, Correlations between the number of RBD+ B cells and humoral immune response, as indicated by IgG formation and neutralizing capacity, in RTX-treated patients. **I**, Frequencies of RBD+ B cell subsets (bars) and Ig isotype distribution (pie charts) in healthy controls, RA controls, and RTX-treated patients on day 7 after the second vaccination. DN = double negative. In **C**, **D**, **F**, and **G**, symbols represent individual subjects; horizontal lines show the mean. In **E** and **H**, vertical lines indicate the upper limit of normal; dotted lines show the 95% confidence interval. Red indicates previously infected subjects; green indicates subjects who were vaccinated twice with ChAdOx1; blue indicates subjects who received 1 dose of ChAdOx1 followed by a heterologous vaccination with 1 dose of BNT162b2. * = $P < 0.05$; ** = $P < 0.01$; *** = $P < 0.001$. See Figure 1 for other definitions.

correlation between B cell numbers and serologic response (data not shown), suggesting that the correlation between B cell numbers and IgG response is restricted to patients with B cell counts below the lower limits of normal.

Significantly lower frequencies and numbers of antigen-specific B cells in RTX-treated IgG nonresponders. Next, we studied SARS–CoV-2–specific B cell responses in RTX-treated patients, using flow cytometry to

quantify RBD-specific B cells in peripheral blood (23) (gating strategy shown in Figure 2B). While no significant difference was seen between healthy controls, RA patients, and RTX-treated patients (Figure 2F), RTX-treated patients who did not show seroconversion after the second vaccination (RTX IgG–) had significantly reduced frequencies and absolute numbers of RBD+ specific B cells compared to IgG+ RTX-treated patients (Figure 2G). The number (Figure 2H) and frequency (Supplementary Figure 3A) of RBD+ B cells in RTX-treated patients correlated significantly with the induction of IgG ($r = 0.8662$, $P < 0.0001$ and $r = 0.6898$, $P = 0.0008$ respectively) and neutralizing antibodies ($r = 0.7915$, $P < 0.0001$ and $r = 0.5674$, $P = 0.0070$, respectively).

Subsequent analyses addressed the distribution of RBD-specific B cells among B cell subsets (5 RTX-treated patients were excluded from the analysis due to very limited RBD+ B cell numbers, which did not permit a reliable analysis of the corresponding B cell subsets). As previously shown for healthy controls (23), RA control and RTX-treated patients who were able to mount RBD+ B cells were also able to generate IgG+ plasmablasts upon vaccination. We found no significant difference between the groups regarding RBD+ B cell subset distribution or Ig isotypes (Figure 2I and Supplementary Figures 3B and C).

Reduced frequencies of Tfh-like and activated CD4 and CD8 T cells in RTX-treated IgG nonresponders. We next investigated how the dynamics of CD4/8 T cell subsets interrelate with the induction of vaccine-specific B cells and IgG. In contrast to B cells, there was no significant difference regarding the frequency, absolute numbers, or memory formation of CD4 T cells (Supplementary Figures 4A and C, available on the *Arthritis & Rheumatology* website at http://onlinelibrary.wiley.com/doi/10.1002/art.42060) and CD8 T cells (Supplementary Figures 4B and D) between healthy controls, RA controls, and RTX-treated patients. A subsequent analysis addressed the differences between vaccine responders and nonresponders in the RTX group (representative gates shown in Figure 3A). Interestingly, patients who lacked anti-vaccine IgG antibodies showed significantly lower frequencies of circulating Tfh-like CD4 T cells, defined as CD4+CXCR5+PD1+, as well as of activated CD4/8 T cells coexpressing CD38+HLA–DR+ (Figure 3B). Activated CD4 T cell frequencies correlated significantly with absolute B cell numbers ($r = 0.5490$, $P = 0.0122$) (Figure 3C). These data suggest an impaired bidirectional T cell–B cell interaction in patients with gradual B cell depletion that results in insufficient vaccination-induced humoral immunity.

Impaired cytokine secretion of antigen-specific CD4 T cells is characteristic of IgG− RTX-treated patients and correlates with absolute B cell number. The overall occurrence of spike-specific CD4 T cells (representative gates shown in Figure 3D and Supplementary Figure 5A, available on the *Arthritis & Rheumatology* website at http://onlinelibrary.wiley.com/doi/10.1002/art.42060) in stimulated compared to unstimulated samples was found to be similar in all groups: 86.7% of healthy controls (13 of 15), 83% of RA controls (10 of 12), and 73.7% of RTX-treated patients (14 of 19) (Figure 3E). This finding was also consistent with a comparable magnitude of response between the groups (Figure 3F) as well as similar memory subset distribution (Supplementary Figure 5E). A more detailed study of the RTX group showed that the majority of IgG+ RTX-treated patients (10 [76.9%] of 13) versus 50% of IgG– RTX-treated patients (3 of 6) showed an appropriate increase in antigen-specific CD4 T cells upon stimulation. With regard to functional analyses of cytokine secretion by spike-specific CD4 T cells, RTX-treated patients who did not show seroconversion had significantly reduced TNF production (Figure 3G) and IFNγ production (Figure 3H) compared to IgG+ RTX-treated responders (representative gates shown in Supplementary Figure 5B).

Since most patients in the nonseroconverted RTX group had very low circulating B cell counts, we wondered if there was a relationship between reduced B cell numbers and impaired cytokine production by antigen-specific CD4+ T cells. Indeed, IFNγ production, but not TNF production, was significantly correlated with absolute B cell numbers ($r = 0.5342$, $P = 0.0112$ for IFNγ), suggesting the importance of B cell costimulatory functions for the proper and interactive induction of CD4 responses.

Lower antigen-specific CD8 responses in RA patients and RTX-treated patients. Compared to unstimulated samples, 93.3% of healthy control samples (14 of 15) but only 58.3% of RA control samples (7 of 12) and 57.9% of RTX-treated patient samples (11 of 19) showed an increase in spike-specific CD8 T cells coexpressing CD137 and IFNγ (representative gates shown in Figure 3J and Supplementary Figure 5C) upon stimulation (Figure 3K). To assess the degranulation function of CD8 T cells, we analyzed the coexpression of CD107a and IFNγ. The responder rate for CD8 T cells coexpressing CD107a and IFNγ after stimulation was low overall, with 60% in the healthy control group (9 of 15), 41.6% in the RA control group (5 of 12), and 42.1% in the RTX group (8 of 19) (data not shown). Regarding the amplitude of CD8 responses, the frequencies of spike-specific CD8 T cells coexpressing CD137 and IFNγ (Figure 3L), and CD107a and IFNγ (Supplementary Figure 5D), as well as their memory subset distribution, were comparable between all groups (Supplementary Figure 5E).

Correlation of antigen-specific and activated T cell subsets with RBD+ plasmablasts. To identify further predictive factors of IgG seroconversion in RTX-treated patients,

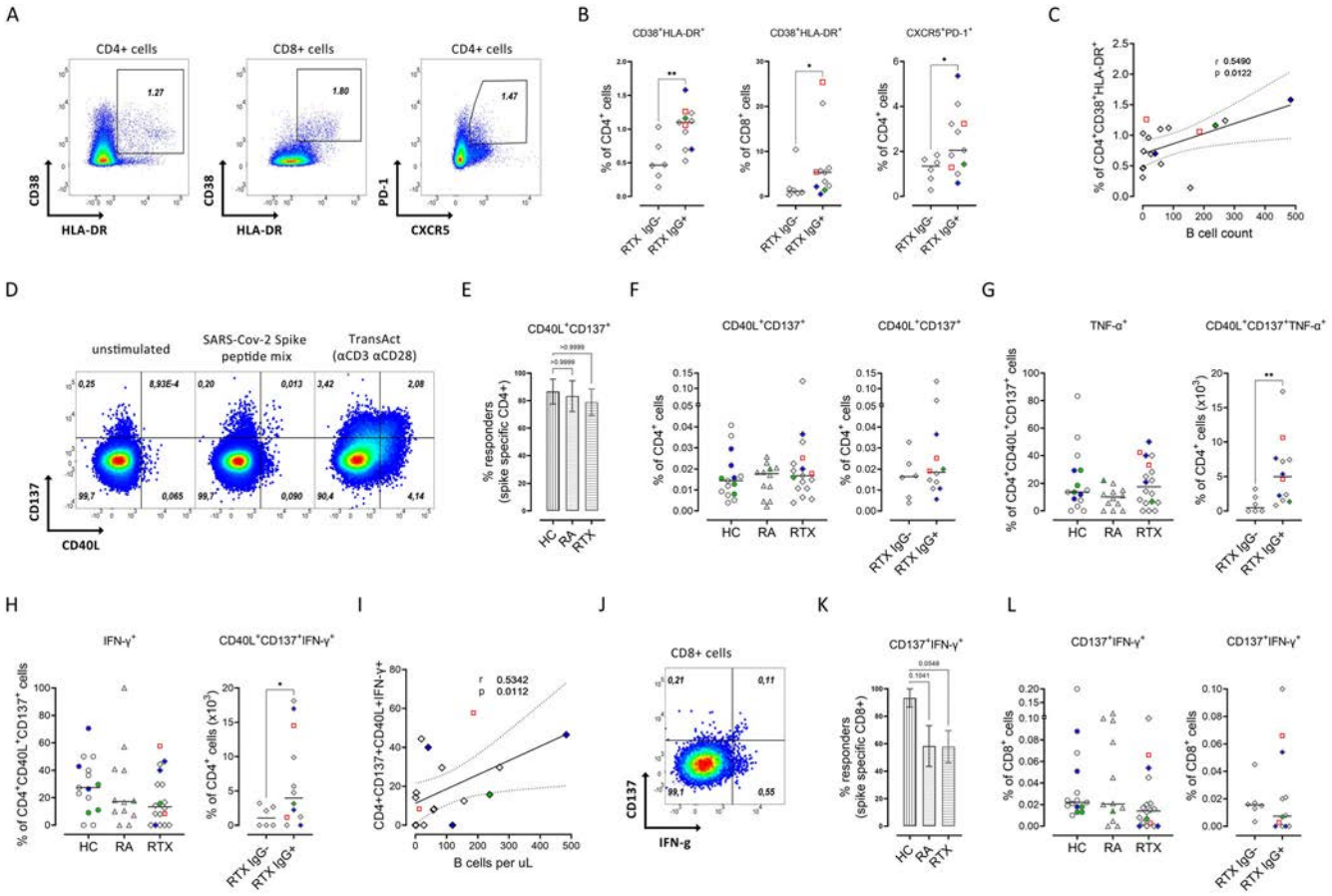

Figure 3. Correlation of the frequencies of activated CD4 T cells and interferon-γ (IFNγ)–positive antigen-specific CD4+ T cells with absolute B cell counts. **A**, Representative flow cytometry plots of activated CD4 and CD8 T cells and Tfh-like CD4 T cells. Values are the percent of cells. **B**, Significant decrease in the frequencies of the indicated cell types in RTX-treated patients who did not respond to SARS–CoV-2 vaccination (RTX IgG–). **C**, Correlation of the frequency of activated CD4 T cells with B cell count in RTX-treated patients. **D**, Representative flow cytometry plots of antigen-specific CD4 T cells (CD137+CD40L+) in peripheral blood mononuclear cells from a healthy control, left unstimulated, stimulated with SARS–Cov-2 spike peptide mix, or stimulated with TransAct. Values are the percent of cells. **E**–**G**, Responder rate (**E**) and frequency of antigen-specific CD4 T cells (**F**) after stimulation with B.1.1.7 SARS–CoV-2 spike peptide mix, and production of tumor necrosis factor (TNF)–positive (**G**) and IFNγ+ (**H**) spike-specific CD4+ T cells in healthy controls (n = 15), RA controls (n = 12), and RTX-treated patients (n = 18), and in IgG+ RTX-treated patients (n = 12) and IgG– RTX-treated patients (n = 6). **I**, Correlation of the frequency of IFNγ+ antigen-specific CD4 T cells with B cell count in RTX-treated patients. **J**, Representative flow cytometry plot of antigen-specific CD8 T cells (CD137+IFNγ+). **K** and **L**, Responder rate (**K**) and frequency of antigen-specific CD8+ T cells (**L**) after stimulation with B.1.1.7 SARS–CoV-2 spike peptide mix. In **B**, **F**–**H**, and **L**, symbols represent individual subjects; horizontal lines show the mean. In **C** and **I**, dotted lines show the 95% confidence interval. In **E** and **K**, bars show the mean ± SD. Red indicates previously infected subjects; green indicates subjects who were vaccinated twice with ChAdOx1; blue indicates subjects who received 1 dose of ChAdOx1 followed by a heterologous vaccination with 1 dose of BNT162b2. * = $P < 0.05$, ** = $P < 0.01$. See Figure 1 for other definitions.

we constructed a correlation matrix (Figure 4) including antigen-specific T cell and B cell subsets as well as demographic data. IgG titers and neutralizing antibodies correlated significantly with RBD+ plasmablasts and memory compartments, as we have previously shown (23). Furthermore, neutralizing antibodies correlated significantly with the frequency of activated CD38+HLA–DR+ CD4/8 T cells as well as with IFNγ- and TNF-producing antigen-specific CD4 T cells. Activated CD38+HLA–DR+ CD4/8 T cells also correlated significantly with RBD+ plasmablasts, while circulating Tfh-like CD4 T cells correlated significantly with total RBD+ B cells. Notably, there was a significant correlation of TNF- and IFNγ-producing antigen-specific CD4 T cells with RBD+ plasmablasts and switched memory B cells. There was no significant correlation of IgG titer with age or time since the last RTX infusion.

Interestingly, antigen-specific CD8 responses induced upon stimulation did not correlate significantly with humoral immunity, or with B cell or CD4 T cell subsets, suggesting an independent, more direct antigen-driven cellular immunity compared to the CD4–CD19 interaction required for IgG formation.

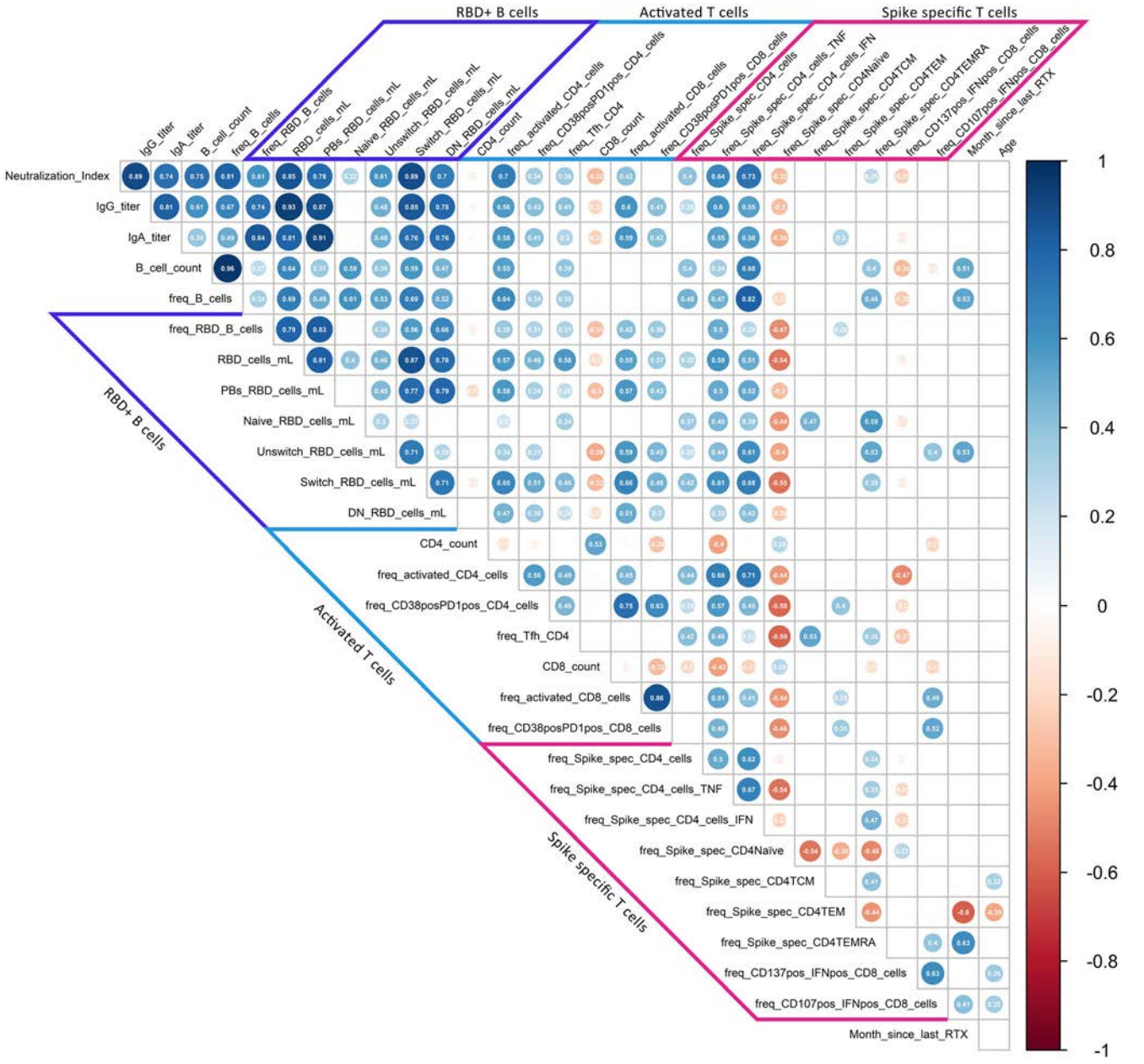

Figure 4. Correlation of humoral and cellular vaccine responses in rituximab (RTX)–treated patients. The Spearman's correlation matrix shows the relationships between humoral responses, receptor-binding domain (RBD)–positive B cell subsets, activated CD4 and CD8 T cells, antigen-specific CD4 and CD8 T cell response, month since last RTX dose, and demographic characteristics of the patients. A total of 17 RTX-treated patients were included in the analysis (due to partial missing data for 2 patients). Red circles indicate negative correlations; blue circles indicate positive correlations. Size and color intensity indicate the strength of correlation. Values inside the circles are the correlation coefficient. Only correlations with $P \leq 0.05$ are shown. PBs = plasmablasts; DN = double negative; TNF = tumor necrosis factor; IFN = interferon; TCM = central memory T cells; TEM = effector memory T cells; TEMRA = terminally differentiated effector memory T cells.

Reduced circulating follicular B cell frequency in IgG–RTX-treated patients. To further investigate the specific differences during SARS–CoV-2 vaccination in RTX-treated patients, we sorted CD27++CD38++ plasmablasts, CD27+ memory B cells, and HLA–DR+CD38+ activated T cells as indicators of the ongoing adaptive immune response after vaccination. The cytometrically enriched cells were subsequently analyzed using Drop-Seq single-cell RNA sequencing (23). Unsupervised analysis using UMAP for Dimension Reduction identified 15 distinct clusters: 4 B cell clusters, 3 plasmablast clusters, and 8 clusters of activated T cells (Figures 5A–C). Here, clusters 3 and 5 were of particular interest: cluster 3 is enriched with circulating follicular-like B cells expressing *CXCR5* and *CCR6* and cluster 5 contains *CD40LG*, *PDCD1*, and *ICOS* expressing Tfh-like CD4

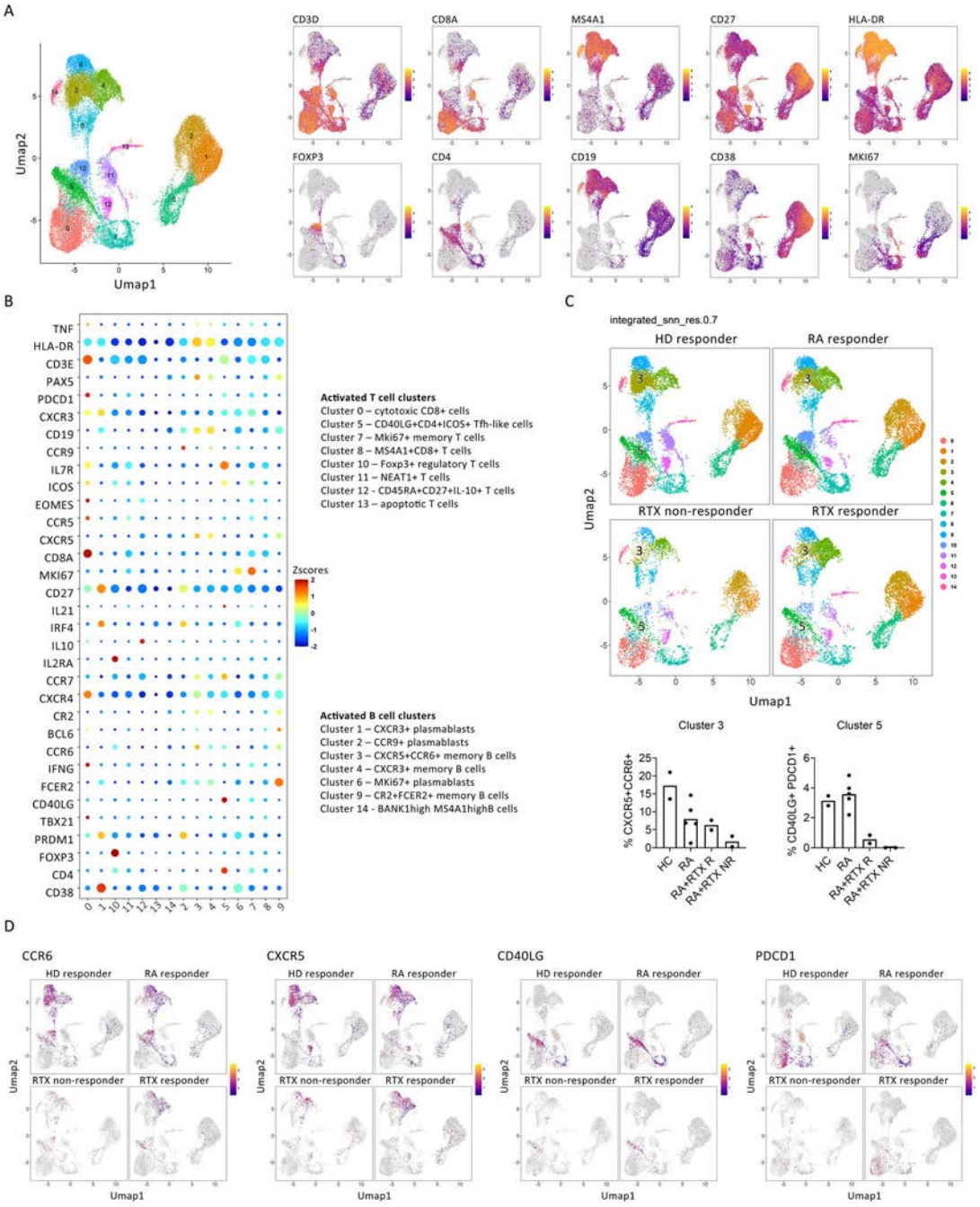

Figure 5. Diminished frequencies of follicular T and B cells in RTX-treated patients, determined by single-cell transcriptome and Cellular Indexing of Transcriptomes and Epitopes by Sequencing (CITE-seq) analyses. **A**, Uniform Manifold Approximation and Projection (UMAP) clustering of peripheral blood CD27++CD38++ plasmablasts, CD27+ memory B cells, and T cells. Samples from 2 healthy controls (healthy donors [HDs]), 4 RA controls, and 5 RTX-treated patients (3 responders [R] and 2 nonresponders [NR] to SARS–Cov-2 vaccine) were isolated and sorted by fluorescence-activated cell sorting for single-cell sequencing. **B**, Relative expression levels of selected signature genes in the 15 identified clusters (total number of cells sequenced 38,038). Larger circles indicate higher expression. **C**, UMAP clustering of cells in samples from 2 healthy controls, 4 RA controls, 2 IgG– RTX-treated patients (RTX nonresponders), and 3 IgG+ RTX-treated patients (RTX responders) (top) and cluster frequency comparison for clusters 3 and 5 (bottom). Symbols represent individual subjects; bars show the mean. **D**, UMAP representation of the expression levels of *CCR6*, *CXCR5*, *CD40LG*, and *PDCD1* in healthy controls, RA controls, and RTX-treated nonresponders and responders. See Figure 1 for other definitions. Color figure can be viewed in the online issue, which is available at http://onlinelibrary.wiley.com/doi/10.1002/art.42060/abstract.

T cells. Follicular B cells and *CD40LG+PD1+* Tfh cells were substantially reduced in RTX-treated patients, with the reduction most pronounced among IgG nonresponders in the RTX group (Figure 5D and Supplementary Figures 6 and 7, available on the *Arthritis & Rheumatology* website at http://onlinelibrary.wiley.com/doi/10.1002/art.42060).

DISCUSSION

SARS–CoV-2 vaccines have been approved based on their protection against COVID-19 in clinical trials (5–8). However, certain patient groups receiving immunosuppressive therapies appear to develop insufficient humoral and cellular responses (18,23,26,27), but limited data about the underlying impairments are available. Protection through immunization is achieved by an orchestrated immune response between different cellular subsets of innate immunity (antigen-presenting cells) and adaptive immunity, such as B cells and T cells. Anti–B cell therapies such as anti-CD20 antibodies (RTX, obinutuzumab, and ocrelizumab) and inhibitors of Bruton's tyrosine kinase are associated with poor humoral immune response to SARS–CoV-2 vaccination in patients with autoimmune inflammatory rheumatic diseases (17–20), multiple sclerosis (28), and CLL (29). Since B cell depletion enhances the risks of poor COVID-19 outcomes (3), but also can reduce anti–SARS–CoV-2 vaccine responses, it is of utmost importance to delineate the level of B cell repopulation necessary to achieve anti-vaccine responses and get insights into the complex relationship between antigen-specific B cells and T cells.

Therefore, we aimed to investigate humoral and cellular responses in RTX-treated patients versus controls. Consistent with previous data (17–19,25), serologic IgG conversion with formation of neutralizing antibodies was significantly lower and delayed in both RA controls and RTX-treated patients, with an even more pronounced effect in the RTX cohort, compared to healthy controls. This finding was closely linked to the availability of peripheral B cells, activated CD4/8 T cells, as well as circulating Tfh-like cells. Another risk factor identified for developing a substantially diminished vaccination response was the prednisolone dose. Ongoing antigen exposure through mRNA vaccines seems to permit prolonged germinal center (GC) maturation (30), which might be an explanation for the further increase in antibody titers over an additional period in some patients.

Besides the IgG nonresponders in the RTX group, 2 patients in the RA group with normal B cell numbers did not develop anti-S1 IgG antibodies. After completing the analysis, it appears that the underlying cause is most likely related to impaired T cell responses: in 1 patient due to inhibition of costimulation by abatacept, consistent with a prior report (18). The other patient, who was treated with a JAK inhibitor, lacked cytokine production by antigen-specific T cells after receiving 2 doses of the ChAdOx1 vaccine. Even though significantly lower IgG responses were reported after 2 doses of ChAdOx1 in healthy individuals (31), it remains to be delineated whether the treatment and/or selected vaccine may account for this finding. Induction of vaccine-specific IgG in individuals vaccinated with ChAdOx1/BNT162b2 was comparable with that in individuals vaccinated with 2 doses of BNT162b2. Interestingly, IgA formation was comparable across all groups, although the protective potency of IgA remains to be determined.

Of utmost importance, our RTX cohort showed a correlation between IgG seroconversion, neutralizing antibodies, and absolute B cell number. A minimum of 10 B cells per microliter in the peripheral circulation is a candidate biomarker for a high likelihood of an appropriate cellular and humoral vaccination response. Patients with B cell numbers below this range not only presented with lower antigen-specific B cells, but they also showed substantially diminished circulating Tfh-like CD4 T cells, reduced activated CD4/8 T cells coexpressing CD38 and HLA–DR, as well as impaired IFNγ secretion of spike-specific CD4 T cells. The frequency of IFNγ-secreting antigen-specific CD4 T cells also correlated with the absolute number of B cells, suggesting that these cells interact to achieve proper anti-S1 responses. Mechanistically, the current data suggest the critical role of available costimulatory B cell functions for the induction of proper CD4 Th response. This finding is consistent with observations of previously described impaired B cell–T cell crosstalk in RTX-treated patients (32–34), leading to reduced frequencies of activated T cells (34), down-regulation of CD40L in CD4 T cells (32,33), and reduced antigen-specific CD8 T cells after influenza vaccination (14).

With regard to the induction of antigen-specific CD8 T cells upon stimulation, the RTX and RA groups both showed a tendency toward reduced responder rates compared to the healthy control group, although it was not statistically significant. However, other than for antigen-specific CD4 T cells, neither B cell depletion nor IgG formation correlated with spike-specific CD8 T cells, suggesting that their induction occurred independently upon SARS–CoV-2 vaccination. It is not clear how these vaccine-specific CD8 T cells provide antiviral protection on clinical grounds.

The debate about what correlates with protection after vaccination against SARS–CoV-2 is ongoing, while it is widely accepted that neutralizing antibodies are a reliable surrogate of protection against virus variants (35,36). The threshold for protective SARS–CoV-2 IgG titer is still unknown, although non-human primate studies suggest that it is likely already very effective at low titers (37). Our study provides evidence that detection of RBD-specific B cells and spike-specific CD4 T cells may provide cellular correlates of this response, while the CD8 response occurred in an independent manner. The role of these 2 lines of vaccine response needs to be further delineated.

Limitations of this study are the small number of RA and RTX-treated patients and the heterogeneity of the groups (including different disease-modifying antirheumatic drug [DMARD] regimens and different vaccination strategies). In this regard, Mrak et al (38) analyzed the impact of comedication on vaccination response in 74 RTX-treated patients and did not observe differences in the levels of antibodies in the presence or absence of concomitant treatment with conventional synthetic DMARDs (csDMARDs) or prednisolone. This finding suggests that the impact of RTX on B cells is more relevant than the effect of csDMARDs.

Here, we present a first study investigating humoral as well as antigen-specific T cell and B cell responses in RTX-treated patients after SARS–CoV-2 vaccination. Mechanistically, the data

provide insights into the crucial role of available B cells equipped with proper costimulatory function to interactively cross-talk with CD4 T cells. These functions likely result in GC formation, plasma cell differentiation, and vaccine-specific IgG production. As a clinical consequence, we propose a range of absolute B cell numbers signifying expansion of vaccine responses after RTX treatment, which may support optimization of vaccination protocols among this vulnerable patient group.

ACKNOWLEDGMENTS

We kindly thank all study participants for taking part and all team members of the rheumatology outpatient office RheumaPraxis Steglitz, Berlin (Drs. Kirsten Karberg and Henning Christian Brandt) as well as of AGZ Rheumatology Charité Mitte Berlin (Dr. Anne Claußnitzer), for organization of patient schedules.

AUTHOR CONTRIBUTIONS

All authors were involved in drafting the article or revising it critically for important intellectual content, and all authors approved the final version to be published. Dr. Dörner had full access to all of the data in the study and takes responsibility for the integrity of the data and the accuracy of the data analysis.

Study conception and design. Stefanski, Rincon-Arevalo, E. Schrezenmeier, Radbruch, Lino, Dörner.

Acquisition of data. Stefanski, Karberg, Ritter, Jahrsdörfer, H. Schrezenmeier, Ludwig, Chen, Claußnitzer, Haibel, Proft.

Analysis and interpretation of data. Stefanski, Rincon-Arevalo, Szelinski, Jahrsdörfer, H. Schrezenmeier, Sattler, Kotsch, Guerra, Durek, Heinrich, Ferreira-Gomes, Burmester, Mashreghi, Lino, Dörner.

REFERENCES

1. Hsu CY, Ko CH, Wang JL, Hsu TC, Lin CY. Comparing the burdens of opportunistic infections among patients with systemic rheumatic diseases: a nationally representative cohort study. Arthritis Res Ther 2019;21:211.
2. Furer V, Rondaan C, Heijstek M, van Assen S, Bijl M, Agmon-Levin N, et al. Incidence and prevalence of vaccine preventable infections in adult patients with autoimmune inflammatory rheumatic diseases (AIIRD): a systemic literature review informing the 2019 update of the EULAR recommendations for vaccination in adult patients with AIIRD. RMD Open 2019;5:e001041.
3. Strangfeld A, Schäfer M, Gianfrancesco MA, Lawson-Tovey S, Liew JW, Ljung L, et al. Factors associated with COVID-19-related death in people with rheumatic diseases: results from the COVID-19 Global Rheumatology Alliance physician-reported registry. Ann Rheum Dis 2021;80:930–42.
4. Jones JM, Faruqi AJ, Sullivan JK, Calabrese C, Calabrese LH. COVID-19 outcomes in patients undergoing B cell depletion therapy and those with humoral immunodeficiency states: a scoping review. Pathog Immun 2021;6:76–103.
5. Polack FP, Thomas SJ, Kitchin N, Absalon J, Gurtman A, Lockhart S, et al. Safety and efficacy of the BNT162b2 mRNA Covid-19 vaccine. N Engl J Med 2020;383:2603–15.
6. Dagan N, Barda N, Kepten E, Miron O, Perchik S, Katz MA, et al. BNT162b2 mRNA Covid-19 vaccine in a nationwide mass vaccination setting. N Engl J Med 2021;384:1412–23.
7. Baden LR, El Sahly HM, Essink B, Kotloff K, Frey S, Novak R, et al. Efficacy and safety of the mRNA-1273 SARS-CoV-2 vaccine. N Engl J Med 2021;384:403–16.
8. Voysey M, Clemens SA, Madhi SA, Weckx LY, Folegatti PM, Aley PK, et al. Safety and efficacy of the ChAdOx1 nCoV-19 vaccine (AZD1222) against SARS-CoV-2: an interim analysis of four randomised controlled trials in Brazil, South Africa, and the UK. Lancet 2021;397:99–111.
9. Sadoff J, Gray G, Vandebosch A, Cárdenas V, Shukarev G, Grinsztejn B, et al. Safety and efficacy of single-dose Ad26.COV2.S vaccine against Covid-19. N Engl J Med 2021;384:2187–201.
10. Furer V, Rondaan C, Heijstek MW, Agmon-Levin N, van Assen S, Bijl M, et al. 2019 update of EULAR recommendations for vaccination in adult patients with autoimmune inflammatory rheumatic diseases. Ann Rheum Dis 2020;79:39–52.
11. Hua C, Barnetche T, Combe B, Morel J. Effect of methotrexate, anti-tumor necrosis factor α, and rituximab on the immune response to influenza and pneumococcal vaccines in patients with rheumatoid arthritis: a systematic review and meta-analysis. Arthritis Care Res (Hoboken) 2014;66:1016–26.
12. Huang Y, Wang H, Tam WW. Is rheumatoid arthritis associated with reduced immunogenicity of the influenza vaccination? A systematic review and meta-analysis. Curr Med Res Opin 2017;33:1901–8.
13. Bingham CO III, Looney RJ, Deodhar A, Halsey N, Greenwald M, Codding C, et al. Immunization responses in rheumatoid arthritis patients treated with rituximab: results from a controlled clinical trial. Arthritis Rheum 2010;62:64–74.
14. Graalmann T, Borst K, Manchanda H, Vaas L, Bruhn M, Graalmann L, et al. B cell depletion impairs vaccination-induced $CD8^+$ T cell responses in a type I interferon-dependent manner. Ann Rheum Dis 2021;80:1537–44.
15. Nazi I, Kelton JG, Larché M, Snider DP, Heddle NM, Crowther MA, et al. The effect of rituximab on vaccine responses in patients with immune thrombocytopenia. Blood 2013;122:1946–53.
16. Richi P, Alonso O, Martín MD, González-Hombrado L, Navío T, Salido M, et al. Evaluation of the immune response to hepatitis B vaccine in patients on biological therapy: results of the RIER cohort study. Clin Rheumatol 2020;39:2751–6.
17. Bonelli MM, Mrak D, Perkmann T, Haslacher H, Aletaha D. SARS-CoV-2 vaccination in rituximab-treated patients: evidence for impaired humoral but inducible cellular immune response. Ann Rheum Dis 2021;80:1355–6.
18. Furer V, Eviatar T, Zisman D, Peleg H, Paran D, Levartovsky D, et al. LB0003 immunogenicity and safety of the BNT162b2 mRNA COVID-19 vaccine in adult patients with autoimmune inflammatory rheumatic diseases and general population: a multicenter study. Ann Rheum Dis 2021;80 Suppl:200–1.
19. Deepak P, Kim W, Paley MA, Yang M, Carvidi AB, El-Qunni AA, et al. Glucocorticoids and B cell depleting agents substantially impair immunogenicity of mRNA Vaccines to SARS-CoV-2 [preprint]. medRxiv 2021.
20. Westhoff TH, Seibert FS, Anft M, Blazquez-Navarro A, Skrzypczyk S, Doevelaar A, et al. Correspondence on 'SARS-CoV-2 vaccination in rituximab-treated patients: evidence for impaired humoral but inducible cellular immune response.' Ann Rheum Dis 2021;80:e162.
21. Aletaha D, Neogi T, Silman AJ, Funovits J, Felson DT, Bingham CO III, et al. 2010 rheumatoid arthritis classification criteria: an American College of Rheumatology/European League Against Rheumatism collaborative initiative. Arthritis Rheum 2010;62:2569–81.
22. Jennette JC, Falk RJ, Bacon PA, Basu N, Cid MC, Ferrario F, et al. 2012 revised International Chapel Hill Consensus Conference Nomenclature of Vasculitides. Arthritis Rheum 2013;65:1–11.
23. Rincon-Arevalo H, Choi M, Stefanski AL, Halleck F, Weber U, Szelinski F, et al. Impaired humoral immunity to SARS-CoV-2 BNT162b2 vaccine in kidney transplant recipients and dialysis patients. Sci Immunol 2021;6:eabj1031.
24. Sattler A, Schrezenmeier E, Weber UA, Potekhin A, Bachmann F, Straub-Hohenbleicher H, et al. Impaired humoral and cellular

immunity after SARS-CoV2 BNT162b2 (tozinameran) prime-boost vaccination in kidney transplant recipients. J Clin Invest 2021;131: e150175.

25. Simon D, Tascilar K, Fagni F, Krönke G, Kleyer A, Meder C, et al. SARS-CoV-2 vaccination responses in untreated, conventionally treated and anticytokine-treated patients with immune-mediated inflammatory diseases. Ann Rheum Dis 2021 80:1312–6.
26. Geisen UM, Berner DK, Tran F, Sümbül M, Vullriede L, Ciripoi M, et al. Immunogenicity and safety of anti-SARS-CoV-2 mRNA vaccines in patients with chronic inflammatory conditions and immunosuppressive therapy in a monocentric cohort. Ann Rheum Dis 2021;80: 1306–11.
27. Haberman RH, Herati R, Simon D, Samanovic M, Blank RB, Tuen M, et al. Methotrexate hampers immunogenicity to BNT162b2 mRNA COVID-19 vaccine in immune-mediated inflammatory disease. Ann Rheum Dis 2021;80:1339–44.
28. Apostolidis SA, Kakara M, Painter MM, Goel RR, Mathew D, Lenzi K, et al. Cellular and humoral immune responses following SARS-CoV-2 mRNA vaccination in patients with multiple sclerosis on anti-CD20 therapy. Nat Med 2021;27:1990–2001.
29. Herishanu Y, Avivi I, Aharon A, Shefer G, Levi S, Bronstein Y, et al. Efficacy of the BNT162b2 mRNA COVID-19 vaccine in patients with chronic lymphocytic leukemia. Blood 2021;137: 3165–73.
30. Turner JS, O'Halloran JA, Kalaidina E, Kim W, Schmitz AJ, Zhou JQ, et al. SARS-CoV-2 mRNA vaccines induce persistent human germinal centre responses. Nature 2021;596:109–113.
31. Liu X, Shaw R, Stuart A, Greenland M, Dinesh T, Provstgaard-Morys S, et al. Safety and immunogenicity report from the Com-COV study: a single-blind randomised non-inferiority trial comparing heterologous and homologous prime-boost schedules with an adenoviral vectored and mRNA COVID-19 vaccine. Lancet 2021;398:856–69.
32. Antonopoulos I, Daoussis D, Lalioti ME, Markatseli TE, Drosos AA, Taraviras S, et al. B cell depletion treatment decreases CD4+IL4+ and CD4+CD40L+ T cells in patients with systemic sclerosis. Rheumatol Int 2019;39:1889–98.
33. Sfikakis PP, Boletis JN, Lionaki S, Vigklis V, Fragiadaki KG, Iniotaki A, et al. Remission of proliferative lupus nephritis following B cell depletion therapy is preceded by down-regulation of the T cell costimulatory molecule CD40 ligand: an open-label trial. Arthritis Rheum 2005; 52:501–13.
34. Ramwadhdoebe TH, van Baarsen LG, Boumans MJ, Bruijnen ST, Safy M, Berger FH, et al. Effect of rituximab treatment on T and B cell subsets in lymph node biopsies of patients with rheumatoid arthritis. Rheumatology (Oxford) 2019;58:1075–85.
35. Khoury DS, Cromer D, Reynaldi A, Schlub TE, Wheatley AK, Juno JA, et al. Neutralizing antibody levels are highly predictive of immune protection from symptomatic SARS-CoV-2 infection. Nat Med 2021;27: 1205–11.
36. Hall VJ, Foulkes S, Charlett A, Atti A, Monk EJ, Simmons R, et al. SARS-CoV-2 infection rates of antibody-positive compared with antibody-negative health-care workers in England: a large, multicentre, prospective cohort study (SIREN). Lancet 2021;397:1459–69.
37. McMahan K, Yu J, Mercado NB, Loos C, Tostanoski LH, Chandrashekar A, et al. Correlates of protection against SARS-CoV-2 in rhesus macaques. Nature 2021;590:630–4.
38. Mrak D, Tobudic S, Koblischke M, Graninger M, Radner H, Sieghart D, et al. SARS-CoV-2 vaccination in rituximab-treated patients: B cells promote humoral immune responses in the presence of T-cell-mediated immunity. Ann Rheum Dis 2021;80:1345–50.

American College of Rheumatology
Empowering Rheumatology Professionals

Arthritis & Rheumatology
Vol. 74, No. 6, June 2022, pp 948–960
DOI 10.1002/art.42074

Role of Lysine-Specific Demethylase 1 in Metabolically Integrating Osteoclast Differentiation and Inflammatory Bone Resorption Through Hypoxia-Inducible Factor 1α and E2F1

Kohei Doi,[1] Koichi Murata,[2] Shuji Ito,[3] Akari Suzuki,[4] Chikashi Terao,[5] Shinichiro Ishie,[1] Akio Umemoto,[1] Yoshiki Murotani,[1] Kohei Nishitani,[1] Hiroyuki Yoshitomi,[1] Takayuki Fujii,[1] Ryu Watanabe,[1] Motomu Hashimoto,[1] Kosaku Murakami,[1] Masao Tanaka,[1] Hiromu Ito,[1] Kyung-Hyun Park-Min,[6] Lionel B. Ivashkiv,[6] Akio Morinobu,[1] and Shuichi Matsuda[1]

Objective. Hypoxia occurs in tumors, infections, and sites of inflammation, such as in the affected joints of patients with rheumatoid arthritis (RA). It alleviates inflammatory responses and increases bone resorption in inflammatory arthritis by enhancing osteoclastogenesis. The mechanism by which the hypoxia response is linked to osteoclastogenesis and inflammatory bone resorption is unclear. This study was undertaken to evaluate whether the protein lysine-specific demethylase 1 (LSD1) metabolically integrates inflammatory osteoclastogenesis and bone resorption in a state of inflammatory arthritis.

Methods. LSD1-specific inhibitors and gene silencing with small interfering RNAs were used to inhibit the expression of LSD1 in human osteoclast precursor cells derived from CD14-positive monocytes, with subsequent assessment by RNA-sequencing analysis. In experimental mouse models of arthritis, inflammatory osteolysis, or osteoporosis, features of accelerated bone loss and inflammatory osteolysis were analyzed. Furthermore, in blood samples from patients with RA, *cis*-acting expression quantitative trait loci (*cis*-eQTL) were analyzed for association with the expression of hypoxia-inducible factor 1α (HIF-1α), and associations between HIF-1α allelic variants and extent of bone erosion were evaluated.

Results. In human osteoclast precursor cells, RANKL induced the expression of LSD1 in a mechanistic target of rapamycin–dependent manner. Expression of LSD1 was higher in synovium from RA patients than in synovium from osteoarthritis patients. Inhibition of LSD1 in human osteoclast precursors suppressed osteoclast differentiation. Results of transcriptome analysis identified several LSD1-mediated hypoxia and cell-cycle pathways as key genetic pathways involved in human osteoclastogenesis. Furthermore, HIF-1α protein, which is rapidly degraded by the proteasome in a normoxic environment, was found to be expressed in RANKL-stimulated osteoclast precursor cells. Induction of LSD1 by RANKL stabilized the expression of HIF-1α protein, thereby promoting glycolysis, in conjunction with up-regulation of the transcription factor E2F1. Analyses of *cis*-eQTL revealed that higher HIF-1α expression was associated with increased bone erosion in patients with RA. Inhibition of LSD1 decreased pathologic bone resorption in mice, both in models of accelerated osteoporosis and models of arthritis and inflammatory osteolysis.

Conclusion. LSD1 metabolically regulates osteoclastogenesis in an energy-demanding inflammatory environment. These findings provide potential new therapeutic strategies targeting osteoclasts in the management of inflammatory arthritis, including in patients with RA.

Dr. Murata's work was supported by the KANAE Foundation for the Promotion of Medical Science, Takeda Science Foundation, Inamori Foundation, and JSPS KAKENHI (grants 17H06816 and 18H02926). Research conducted in the US at the Hospital for Special Surgery was supported by the NIH (grant DE-019420).

[1]Kohei Doi, MD, Shinichiro Ishie, MD, Akio Umemoto, MD, Yoshiki Murotani, MD, Kohei Nishitani, MD, PhD, Hiroyuki Yoshitomi, MD, Takayuki Fujii, MD, PhD, Ryu Watanabe, MD, PhD, Motomu Hashimoto, MD, PhD, Kosaku Murakami, MD, PhD, Masao Tanaka, MD, PhD, Hiromu Ito, MD, PhD, Akio Morinobu, MD, PhD, Shuichi Matsuda, MD, PhD: Kyoto University Graduate School of Medicine, Kyoto, Japan; [2]Koichi Murata, MD, PhD: Kyoto University Graduate School of Medicine, Kyoto, Japan, and Hospital for Special Surgery, New York, New York; [3]Shuji Ito, MD: RIKEN Center for Integrative Medical Sciences, Yokohama, Japan, and Shimane University Faculty of Medicine, Shimane, Japan; [4]Akari Suzuki, PhD: RIKEN Center for Integrative Medical Sciences, Yokohama, Japan; [5]Chikashi Terao, MD, PhD: RIKEN Center for Integrative Medical Sciences, Yokohama, Japan, and Shizuoka General Hospital and University of Shizuoka, Shizuoka, Japan; [6]Kyung-Hyun Park-Min, PhD, Lionel B. Ivashkiv, MD: Hospital for Special Surgery, New York, New York.

INTRODUCTION

Bone destruction is a hallmark and serious consequence of various skeletal diseases, including osteoporosis and inflammatory arthritis. It affects the quality of life of patients and increases the risk of disability and mortality. Osteoclasts are multinucleated bone-resorbing cells derived from myeloid lineage cells. Excessive generation of osteoclasts and/or increased osteoclast activity in these patients results in pathologic bone resorption (1,2). Antiresorptive therapies, including bisphosphonates and anti-RANKL monoclonal antibodies (denosumab), have become the first-line treatments for osteoporosis; of note, denosumab is also currently available for the treatment of rheumatoid arthritis (RA), with the aim of suppressing progressive bone erosion in RA patients (3,4). These agents effectively reduce bone resorption and limit bone loss. However, these types of treatment still face problems associated with long-term usage and drug discontinuation (5).

Macrophage colony-stimulating factor (M-CSF) and RANKL are key cytokines in the processes of osteoclast differentiation and survival. During osteoclast differentiation, the binding of RANKL to its receptor, RANK, activates various transcription factors, including MYC, NF-κB, AP-1, CREB, and NFATc1, which work in a complex network to promote osteoclast differentiation (6). Effective osteoclastogenesis requires both glycolysis and oxidative phosphorylation for energy generation (7–13). We previously showed that E2F1, a transcription factor that mainly controls the cell cycle, is induced by stimulation with RANKL in nonproliferative human osteoclast precursor cells (OCPs) and promotes glycolysis during the early phases of osteoclastogenesis (14). Hypoxia-inducible factor 1 (HIF-1) appears to be another factor responsible for the induction of glycolytic genes during osteoclastogenesis, as demonstrated by observations of up-regulated expression of GLUT1, VEGF, and glycolytic enzymes, the well-known target genes of HIF-1, during osteoclastogenesis, even in conditions of normoxia (15). However, HIF-1α, a subunit of HIF-1, is unstable in a normoxic environment, because of its rapid degradation by O_2-dependent prolyl hydroxylation (PHD) and von Hippel-Lindau (VHL) protein–dependent proteasomal degradation (15). However, the association between RANKL signaling and HIF-1 has not been completely elucidated.

Lysine-specific demethylase 1 (LSD1; also known as KDM1A, BHC110, and AOF2) catalyzes the demethylation of mono- and dimethylated forms of histone 3 lysine 4 (H3K4me1 and H3K4me2, respectively) for transcriptional repression and mono- and dimethylated forms of H3K9 (H3K9me1 and H3K9me2, respectively) for gene activation. LSD1 regulates not only histone substrates but also the methylation dynamics of nonhistone proteins, including E2F1, DNMT1, HIF-1α, and STAT3, which play a crucial role in a wide range of cellular processes, including stem cell pluripotent regulation, metabolism, cell proliferation, embryonic development, and human cancer development (16). However, the mechanisms by which LSD1 affects inflammatory responses and osteoclastogenesis remain unclear.

In the present study, we showed that LSD1 is essential for osteoclastogenesis in vivo and in vitro. LSD1 was induced by RANKL in a manner that was dependent on the activity of mechanistic target of rapamycin (mTOR). Induction of LSD1 by RANKL stabilized the expression levels of HIF-1α protein even in conditions of normoxia, and, in conjunction with the transcription factor E2F1, mediated metabolic pathways. LSD1 was up-regulated in RA patient synovium and was induced by stimulation with tumor necrosis factor (TNF). Analysis of expression quantitative trait loci (eQTL) in human blood revealed that higher HIF-1α expression was associated with increased bone erosion in patients with RA. Inhibition of LSD1 suppressed pathologic bone resorption in a mouse model of accelerated osteoporosis and in mouse models of arthritis and inflammatory osteolysis. These results suggest that targeting LSD1 may be an attractive therapeutic strategy for the prevention of pathologic bone resorption in inflammatory arthritis, including in the affected joints of patients with RA.

MATERIALS AND METHODS

Details on the methods used for RNA interference experiments, RNA-sequencing (RNA-seq) analysis, glycolytic rate analysis, immunofluorescence staining, immunohistochemistry, analyses of DNA in RA patient blood, and micro–computed tomography (micro-CT) are described in the Supplementary Methods (available on the *Arthritis & Rheumatology* website at https://onlinelibrary.wiley.com/doi/10.1002/art.42074).

Reagents. Human and murine M-CSF, soluble RANKL, and TNF were purchased from PeproTech. A variety of specific inhibitors, including SP2509, RN-1, ORY-1001, and Torin1, were purchased from Cayman Chemical. The following antibodies were used: antibodies to LSD1, phosphorylated NF-κB p65, phosphorylated eukaryotic translation initiation factor 4E-binding protein 1 (phospho–4E-BP1), HIF-1α, E2F1, and PHD-2 (all from Cell Signaling Technologies), p38 and c-Myc (both from BioLegend), and horseradish peroxidase–conjugated swine anti-rabbit immunoglobulins (Dako).

Cell culture. Human peripheral blood mononuclear cells (PBMCs) were obtained from leukoreduction filters (purchased

Author disclosures are available at https://onlinelibrary.wiley.com/action/downloadSupplement?doi=10.1002%2Fart.42074&file=art42074-sup-0001-Disclosureform.pdf.

Address correspondence to Koichi Murata, MD, PhD, Department of Advanced Medicine for Rheumatic Diseases, Kyoto University Graduate School of Medicine, 54 Kawahara-cho, Shogoin, Sakyo, Kyoto 606-8507, Japan. Email: kchm@kuhp.kyoto-u.ac.jp.

Submitted for publication May 4, 2021; accepted in revised form January 21, 2022.

from the Japanese Red Cross Society) using a lymphocyte separation solution (density 1.077; Nacalai Tesque), in accordance with a protocol approved by the ethics committee of Kyoto University Graduate School and Faculty of Medicine. CD14-positive monocytes were isolated from the PBMCs with anti-CD14 magnetic beads (Miltenyi Biotec).

To obtain RANK-expressing OCPs, CD14-positive monocytes were cultured overnight in α-modified essential medium (Sigma) with 10% fetal bovine serum (MP Biomedicals) and penicillin, streptomycin, and L-glutamine (all from Nacalai Tesque), supplemented with 20 ng/ml M-CSF (PeproTech). For analyses of osteoclast differentiation, OCPs were cultured with 20 ng/ml M-CSF and 40 ng/ml RANKL, and then stained with tartrate-resistant acid phosphatase (TRAP) using a Sigma TRAP kit.

For cell experiments in conditions of hypoxia, cells were placed in an incubator (WakenBtech) containing 4% oxygen to establish an hypoxic environment. An MTT assay for cell viability (Cayman Chemical) was performed in accordance with the manufacturer's protocol. The in vitro resorption activity of osteoclasts was measured using a bone resorption assay plate (PG Research). Cells were seeded in the plates and cultured in the presence of M-CSF and RANKL. After 5 days of culture with RANKL, cells were removed, in accordance with the manufacturer's protocol.

Assessment of the in vivo mouse bone phenotype. All animal studies were conducted in accordance with the principles of the Kyoto University Committee of Animal Resources, which are based on the International Guiding Principles for Biomedical Research Involving Animals. The experimental sample size was determined on the basis of observations from our previous studies (14). All of the purchased mice were of a similar age and were randomly assigned to a treatment group; no randomization allocation sequence was assigned.

For a mouse model of experimental arthritis, 8-week-old female SKG mice were purchased from Clea Japan. Arthritis was induced by intraperitoneal injection of 20 mg mannan (Sigma). SP2509 (25 mg/kg) was administered intraperitoneally twice per week for 3 weeks. The severity of arthritis in each paw was scored in a blinded manner by 3 investigators (KD, KM, and AU) using a 3-point scale, as previously described (14). To evaluate osteoclast formation as a primary outcome measure, TRAP staining of histologic sections from the calcaneocuboid and tarsometatarsal joints was evaluated.

For a mouse model of inflammatory osteolysis, we used an established model of TNF-induced supracalvarial osteolysis in mice (17), with minor modifications. TNF (PeproTech) was administered on days 0, 2, and 4 to 6-week-old female C57BL/6N mice (Clea Japan). SP2509 (25 mg/kg) was administered intraperitoneally on days 0 and 3. On day 4, mice were killed at 6 hours after injection of TNF, and calvarial bones were collected for sectioning.

For a mouse model of enhanced osteoporosis, 14–16-week-old male C57BL/6N mice were purchased from Clea Japan and were fed a low-calcium diet (<0.01%) or a control diet (purchased from Clea Japan). SP2509 was administered intraperitoneally at 25 mg/kg twice per week for 3 weeks. Bone samples were collected for sectioning at 2 weeks after initiation of the inhibitor treatment. After 3 weeks, samples were obtained for micro-CT analysis.

Statistical analysis. Statistical analysis was performed using JMP Pro version 13.0.0 (SAS Institute). In experiments with only 2 conditions, we compared groups using a 2-tailed unpaired *t*-test. In experiments with >2 conditions, we compared groups using Tukey's test for multiple comparisons. *P* values less than 0.05 were considered statistically significant.

Data availability. RNA-seq data for this project have been deposited in the NCBI Gene Expression Omnibus database (no. GSE166559).

RESULTS

Essential role of LSD1 for osteoclast differentiation. First, we tested the effects of LSD inhibition on osteoclast differentiation using human blood–derived OCPs, a strategy that provides the following advantages: the effects of the inhibitor on osteoclastogenesis can be studied separately from its effects on cell proliferation, and cells directly relevant for human diseases can be used (18). We observed that treatment with an LSD1-specific inhibitor, SP2509, inhibited the differentiation of OCPs into multinucleated TRAP-positive cells, in a dose-dependent manner (Figure 1A; see also Supplementary Figure 1, available on the *Arthritis & Rheumatology* website at https://onlinelibrary.wiley.com/doi/10.1002/art.42074). Accordingly, inhibition of LSD1 with SP2509 suppressed, in a dose-dependent manner, the RANKL-induced expression of osteoclast-related genes, including the cathepsin K gene *CTSK* and β3 integrin gene *ITGB3* (Figure 1B). RANKL induction of *NFATc1*, which is essential for osteoclast differentiation and the expression of many osteoclast genes, was also suppressed by SP2509.

We directly tested the role of LSD1 in osteoclastogenesis by silencing LSD1 with small interfering RNA (siRNA). LSD1 silencing in human OCPs suppressed RANKL-induced osteoclast differentiation and reduced the relative expression of the osteoclast-related genes *ITGB3* and *CTSK* (Figures 1C–E; see also Supplementary Figure 2, available on the *Arthritis & Rheumatology* website at https://onlinelibrary.wiley.com/doi/10.1002/art.42074). The siRNA-mediated knockdown of LSD1 expression in OCPs also suppressed RANKL-induced expression of *NFATc1*. These results indicate that LSD1 is a positive regulator of osteoclast differentiation.

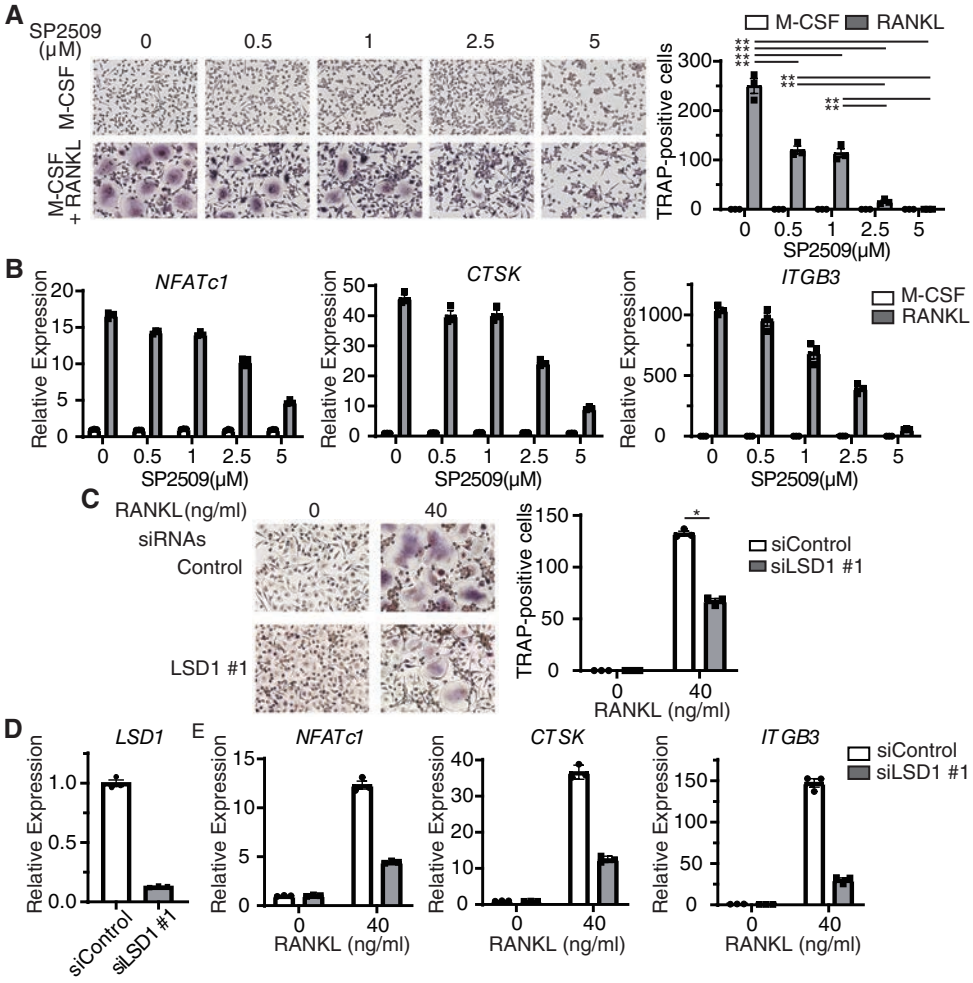

Figure 1. Effects of lysine-specific demethylase 1 (LSD1) on osteoclast differentiation. **A**, Osteoclast precursor cells (OCPs) derived from human CD14-positive monocytes were cultured with 20 ng/ml macrophage colony-stimulating factor (M-CSF) or M-CSF plus 40 ng/ml RANKL and treated with the LSD1-specific inhibitor SP2509. Left, OCPs were stained with tartrate-resistant acid phosphatase (TRAP) for detection of osteoclasts. Representative results from 1 of 3 independent donors are shown (original magnification × 10). Right, The number of TRAP-positive multinucleated cells was counted. Data are the mean ± SEM results of triplicate experiments in samples from 3 independent donors. **B**, OCPs were cultured with RANKL for 48 hours and treated with SP2509. Expression levels of osteoclast-related genes (normalized to the values for TBP mRNA) were analyzed by quantitative reverse transcription–polymerase chain reaction (qRT-PCR). Data are the mean ± SEM results of triplicate experiments. Representative results from 1 of 3 independent donors are shown. **C**, Human CD14-positive monocytes were nucleotransfected with LSD1-specific small interfering RNA (siRNA) (siLSD1 #1) or scrambled control siRNA (siControl) and stimulated with RANKL. Left, Osteoclasts were detected by TRAP staining. Representative results from 1 of 3 independent donors are shown (original magnification × 10). Right, The number of TRAP-positive multinucleated cells was counted. Data are the mean ± SEM results of triplicate experiments in samples from 3 independent donors. **D**, Following siRNA transfection and RANKL stimulation of monocytes, expression levels of osteoclast-related genes were analyzed by qRT-PCR. Data are the mean ± SEM results of triplicate experiments. Representative results from 1 of 3 independent donors are shown. * = $P < 0.05$, by Tukey-Kramer test. Color figure can be viewed in the online issue, which is available at http://onlinelibrary.wiley.com/doi/10.1002/art.42074/abstract.

Induction of LSD1 by RANKL and TNF in OCPs, and high expression of LSD1 in RA patient synovium. To determine how LSD1 expression is regulated in inflammatory bone resorption, human OCPs were stimulated with RANKL. The stimulation of OCPs with RANKL resulted in slightly up-regulated levels of *LSD1* mRNA at both 24 and 48 hours (Figure 2A). Immunohistochemical analyses revealed that the protein levels of LSD1 in OCPs were significantly up-regulated in the nucleus at 48 hours after RANKL stimulation (Figure 2B). These results suggest that LSD1 expression is substantially induced by RANKL at the protein level, with a more attenuated effect at the mRNA level.

Because we previously showed that RANKL stimulation up-regulates mTOR complex 1 (mTORC1), a key positive regulator of translation (14), we tested whether mTORC1 activity has a role in LSD1 protein expression. Stimulation of OCPs with RANKL up-regulated the phosphorylation of eukaryotic translation initiation factor 4E-binding protein 1 (4E-BP1) and LSD1 (Figure 2C).

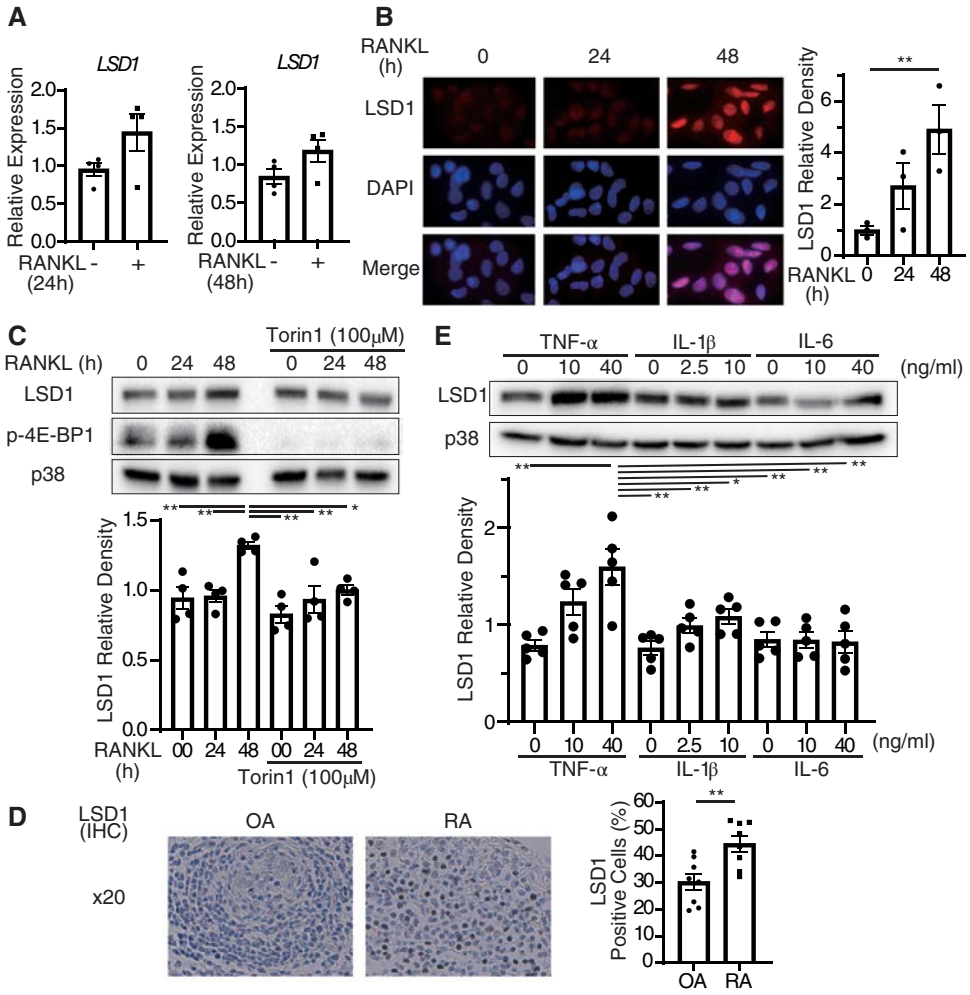

Figure 2. Induction of LSD1 expression by RANKL and tumor necrosis factor (TNF) in OCPs, and elevated levels of LSD1 in synovium from patients with rheumatoid arthritis (RA). **A**, *LSD1* mRNA levels (normalized to the values for TBP mRNA) were determined by qRT-PCR in human OCPs left unstimulated or stimulated with RANKL for 24 or 48 hours. **B**, Left, OCPs were treated with RANKL for 24 or 48 hours, and subcellular localization of LSD1 was analyzed by immunofluorescence microscopy. Representative images from 1 of 3 donors are shown (original magnification × 40). Merged images show LSD1 staining (red) and DAPI nuclear staining (blue). Right, The relative fluorescence intensity of LSD1 staining of OCPs from 3 different donors was assessed. Bars show the mean ± SEM. **C**, OCPs were cultured with RANKL and treated with 100 μ*M* of Torin1, an inhibitor of the mechanistic target of rapamycin complex 1, for 24 or 48 hours. Top, Whole-cell lysates were analyzed by immunoblotting for detection of LSD1 and phosphorylated eukaryotic translation initiation factor 4E-binding protein 1 (p-4E-BP1); p38 antibodies served as a loading control. Representative blots from 1 of 4 independent donors are shown. Bottom, The relative density of LSD1-positive cells in samples from 4 donors was quantified. Bars show the mean ± SEM. **D**, Left, Synovium from a patient with osteoarthritis (OA) and a patient with RA was analyzed by immunohistochemistry (IHC) for detection of LSD1. Representative results from 1 of 8 patients are shown. Right, Percentages of LSD1-positive cells in the synovium of OA and RA patients (n = 8 per group) are shown. Bars show the mean ± SEM. **E**, OCPs were treated with TNF, interleukin-1β (IL-1β), or IL-6. Top, Whole-cell lysates were analyzed by immunoblotting for LSD1 (with p38 antibodies as a loading control). Representative blots from 1 of 5 donors are shown. Bottom, The relative density of LSD1-positive cells was determined in samples from 5 donors. Bars show the mean ± SEM. * = $P < 0.05$; ** = $P < 0.01$, by 2-tailed, unpaired *t*-test in **D**, and by Tukey-Kramer test in **B**, **C**, and **E**. See Figure 1 for other definitions. Color figure can be viewed in the online issue, which is available at http://onlinelibrary.wiley.com/doi/10.1002/art.42074/abstract.

Furthermore, treatment with Torin1, an mTORC1 inhibitor, suppressed the RANKL-induced expression of both LSD1 and phospho–4E-BP1, suggesting that LSD1 protein expression is mTOR-dependent.

We next investigated the level of LSD1 expression in RA patient synovium. Immunohistochemical analyses of synovial tissue samples revealed that LSD1 expression was higher in synovium from RA patients than in synovium from osteoarthritis patients (Figure 2D).

We also stimulated OCPs with the proinflammatory cytokines TNF, IL-1β, and IL-6. The expression of LSD1 protein was significantly up-regulated following stimulation of the cells with TNF, but not with IL-1β or IL-6 (Figure 2E). These data suggest that LSD1 expression is induced in human OCPs in the presence

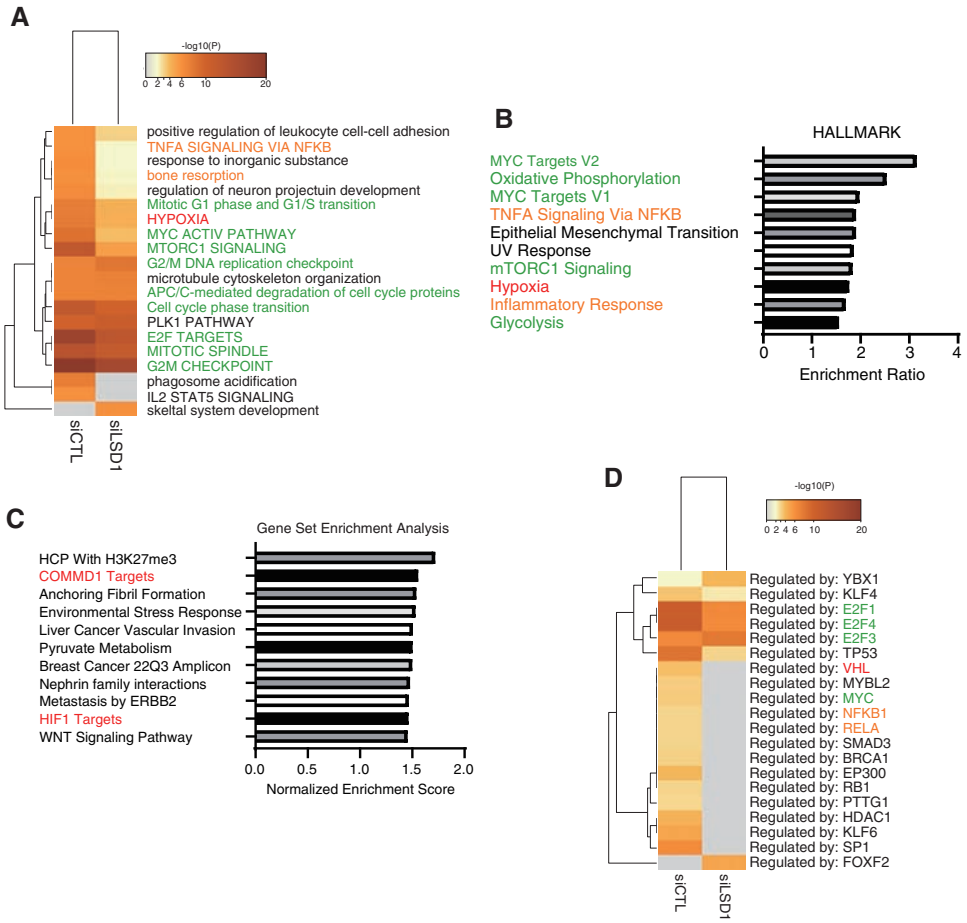

Figure 3. Regulation of metabolic pathways by LSD1 in RANKL-stimulated human OCPs. **A**, OCPs were transfected with LSD1-specific siRNA or scrambled control siRNA and stimulated with RANKL for 0, 24, or 48 hours. The top 20 pathways that were differentially enriched in RANKL-stimulated OCPs subjected to siRNA-mediated LSD1 knockdown, relative to that in scrambled control siRNA–treated OCPs, were assessed based on genes showing a >2-fold increase in expression at 48 hours compared to 0 hours. **B** and **C**, Gene set enrichment analysis was used to assess RANKL-inducible genes in OCPs transfected with LSD1-specific siRNA, relative to that in scrambled control siRNA–treated OCPs. Genes whose expression was up-regulated by RANKL (>1.5-fold increase) and suppressed by LSD1 siRNA (<1.5-fold decrease) after 48 hours of RANKL stimulation, and genes not up-regulated by LSD1 siRNA in the absence of RANKL treatment, were analyzed. **D**, The top 20 transcription factors differentially enriched in OCPs treated with RANKL are shown. Genes described in **A** were used for this analysis. Green indicates the gene set for the metabolic and cell-cycle pathways, orange indicates the inflammatory NF-κB signaling pathway, and red indicates the hypoxia pathway. See Figure 1 for other definitions. Color figure can be viewed in the online issue, which is available at http://onlinelibrary.wiley.com/doi/10.1002/art.42074/abstract.

of RANKL and TNF, and that the levels of LSD1 are elevated in the synovial tissue of patients with inflammatory RA.

Regulation of metabolic pathways by LSD1 in RANKL-stimulated OCPs. The known nonhistone substrates of LSD1 demethylation are p53, DNMT1, E2F1, MYC, MYPT1, STAT3, ERa, HIF-1α, MTA, and AGO2 (16). We previously found that E2F1 and MYC are important factors in the process of osteoclastogenesis linked to metabolism (7,14). In the present study, inhibition of LSD1 by SP2509 and siRNA silencing of LSD1 inhibited RANKL-induced MYC expression and translocation to the nucleus (Supplementary Figures 3A–C, available on the *Arthritis & Rheumatology* website at https://onlinelibrary.wiley.com/doi/10.1002/art.42074). RANKL-induced expression of E2F1 and E2F1 target genes was also suppressed by SP2509 (Supplementary Figures 3D–F).

We performed RNA-seq and bioinformatics analyses to identify genes that were regulated by LSD1 in RANKL-stimulated human OCPs (Supplementary Figure 4, available on the *Arthritis & Rheumatology* website at https://onlinelibrary.wiley.com/doi/10.1002/art.42074). Pathways enriched in RANKL-inducible genes were identified in cultures of OCPs transfected with LSD1-specific siRNA as compared to scrambled control siRNA–treated cells, after stimulation with RANKL for 24 or 48 hours. In addition, pathways associated with the cell cycle (i.e., those associated with anabolic metabolism) as well as pathways linked to

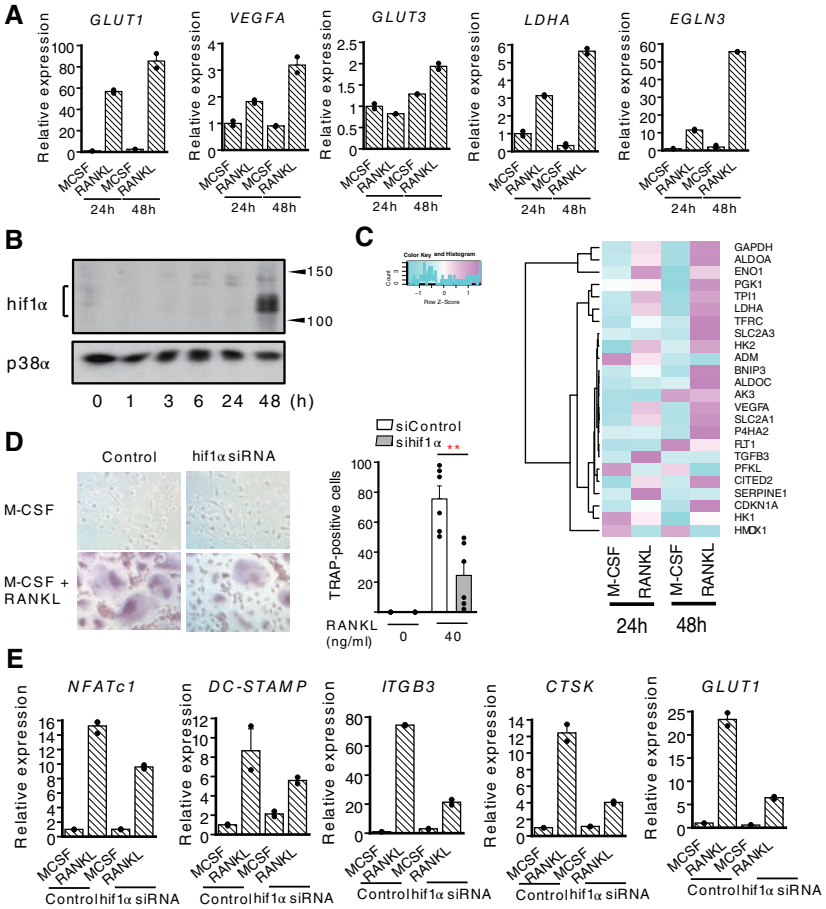

Figure 4. Regulation of osteoclast differentiation by hypoxia-inducible factor 1α (HIF-1α) in normoxic conditions. **A**, Expression of HIF-1α target genes (relative to the values for TBP mRNA) was analyzed by qRT-PCR in OCPs cultured for 24 or 48 hours with M-CSF or RANKL. Bars show the mean ± SEM from 1 of 2 experiments using samples from 3 different donors. **B**, OCPs were stimulated with RANKL for the indicated number of hours, and whole-cell lysates were analyzed by immunoblotting for detection of HIF-1α; p38 antibodies were used as a loading control. A representative blot from 1 of 5 experiments with different donors is shown. **C**, Heatmaps show the results of RNA-sequencing (RNA-seq) analysis of OCPs for expression of HIF-1α target genes (assessed as fragments per kilobase of transcript per million mapped reads). RNA-seq data are deposited at the Gene Expression Omnibus database (no. GSE99987). **D**, Left, Human CD14-positive monocytes were cultured for 48 hours with M-CSF or M-CSF plus RANKL and nucleotransfected with HIF-1α—specific siRNA or scrambled control siRNA. TRAP staining was performed for detection of osteoclasts. Representative results from 1 of 6 independent experiments are shown (original magnification × 10). Right, TRAP-positive multinucleated cells in the absence or presence of RANKL were counted. Results are the mean ± SEM of triplicate experiments in samples from 6 independent donors. **E**, Expression of osteoclast-related genes, relative to the values for TBP mRNA, was evaluated by qRT-PCR. Results are the mean ± SEM of duplicate experiments. Representative results from 1 of 3 different donors are shown. ** = $P < 0.01$ by Tukey-Kramer test. See Figure 1 for other definitions. Color figure can be viewed in the online issue, which is available at http://onlinelibrary.wiley.com/doi/10.1002/art.42074/abstract.

metabolism, inflammatory NF-κB, and hypoxia were altered after silencing of LSD1 (Figure 3A).

Results of gene set enrichment analysis (GSEA) consistently revealed that LSD1 regulated metabolic pathways, including the MYC, oxidative phosphorylation, mTORC1, and glycolysis pathways, as well as pathways of inflammation (Figure 3B). Furthermore, LSD1 mediated the hypoxia and COMMD1 pathways (linked to inflammation, metabolism, and hypoxia) (Figures 3B and C). Analysis of transcription factors regulated by LSD1 showed that E2F1, E2F3, E2F4, and MYC (linked to cell cycle and metabolism) were highly enriched (Figure 3D). The GSEA analyses also revealed that RELA, NF-κB1 (linked to inflammation), and VHL (linked to hypoxia) were highly enriched.

The cell-cycle and hypoxia pathways are associated with anabolic metabolism. We previously showed that COMMD1 is an important factor in the enhancement of osteoclastogenesis under conditions of hypoxia, acting via the HIF, E2F, and NF-κB/metabolism-mediated axis through E3 ubiquitination of HIF-1α and NF-κB (14). Findings from our RNA-seq analysis suggest that LSD1 also has an integrative role in inflammation, hypoxia, and metabolism.

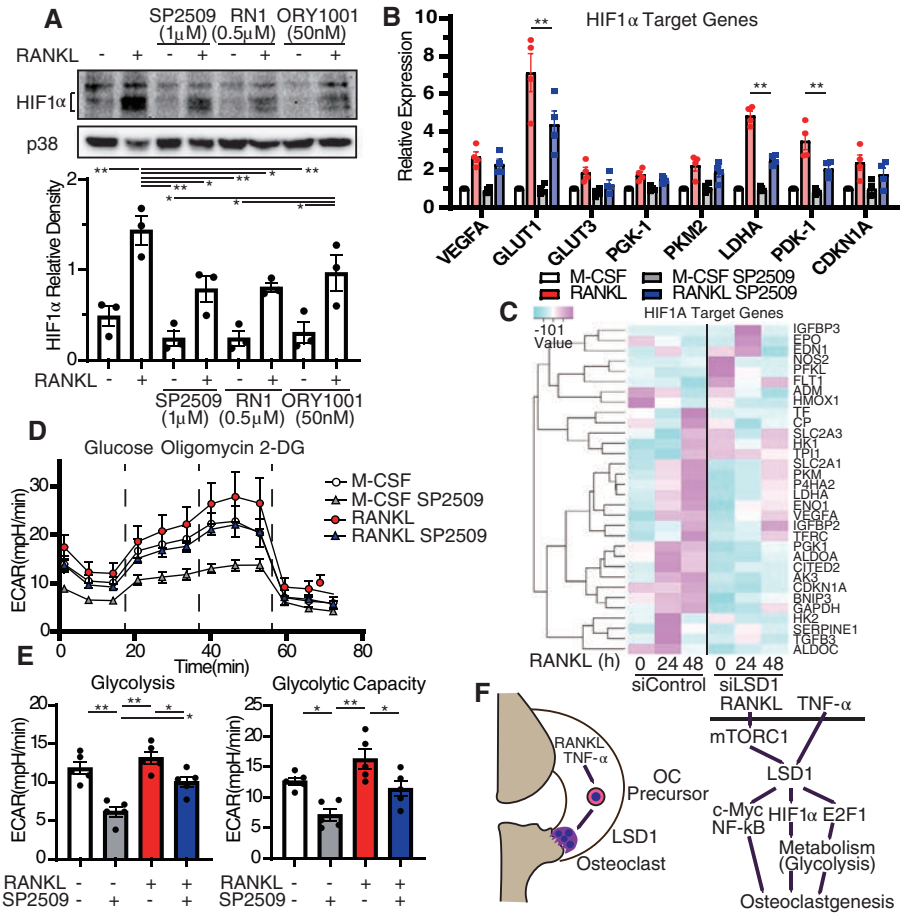

Figure 5. Promotion of glycolysis by LSD1 via hypoxia-inducible factor 1α (HIF-1α). **A**, Human CD14-positive monocytes were cultured with M-CSF and left untreated or treated with the LSD1 inhibitors SP-2509, RN1, or ORY 1001, and then stimulated with RANKL for 48 hours. Top, Whole-cell lysates were assessed by immunoblotting for detection of HIF-1α; p38 antibodies were used as a loading control. Representative blots from 1 of 3 different donors are shown. Bottom, Results of densitometry analyses of HIF-1α are shown. Data are the mean ± SEM of samples from 3 donors. **B**, Expression of HIF-1α target gene expression, relative to the values for TBP mRNA, was analyzed in the cells by qRT-PCR. Data are the mean ± SEM results in samples from 4 independent donors. **C**, Heatmaps show the results of RNA-sequencing analysis of gene expression in human OCPs following RANKL stimulation for the indicated number of hours and transfection with LSD1 siRNA, relative to that in scrambled control siRNA–treated cells. **D** and **E**, The extracellular acidification rate (ECAR) of OCPs under each condition was recorded. The ECAR was normalized to the relative cell counts. Representative ECAR time-course data are shown (**D**), and assessments of glycolysis and the glycolytic capacity of human OCPs based on the ECAR are shown (n = 5 per group). **F**, The schematic diagram depicts the LSD1-mediated pathways during osteoclastogenesis. Data are the mean ± SEM. * = $P < 0.05$; ** = $P < 0.01$, by Tukey-Kramer test. See Figure 1 for other definitions.

Regulation of osteoclast differentiation by HIF-1α in conditions of normoxia. Osteoclast formation and bone resorption are regarded as energy-demanding processes that require active metabolic reprogramming, although these processes have not been studied extensively (12). During osteoclastogenesis, the expression of glucose transporter (GLUT) genes—including *GLUT1* (SLC2A1) and *GLUT3* (SLC2A3)—is known to be up-regulated (Figure 4A), and glycolysis is increased (11,15). HIF-1α is a strong inducer of glycolysis, which targets these genes, and is suspected to have a critical role in osteoclastogenesis; however, the association between RANKL signaling and HIF-1α remains unclear. The HIF-1α protein is unstable because of the hydroxylation by PHD in conditions of normoxia.

In human CD14-positive monocytes cultured with M-CSF and stimulated with RANKL, HIF-1α mRNA levels remained unchanged after 24 hours of stimulation, and increased slightly at 48 hours (Supplementary Figure 5, available on the *Arthritis & Rheumatology* website at https://onlinelibrary.wiley.com/doi/10.1002/art.42074). Surprisingly, however, immunoblotting showed that the expression of HIF-1α protein could be detected at 48 hours after RANKL stimulation in conditions of normoxia, although it could not be observed within 24 hours of RANKL stimulation (Figure 4B). Concomitantly, expression of HIF-1α target genes, including *VEGFA*, *PHD3*, and *LDHA*, as well as *GLUT1* and *GLUT3*, was induced 48 hours after RANKL treatment (Figures 4A and C). Furthermore, siRNA-mediated knockdown

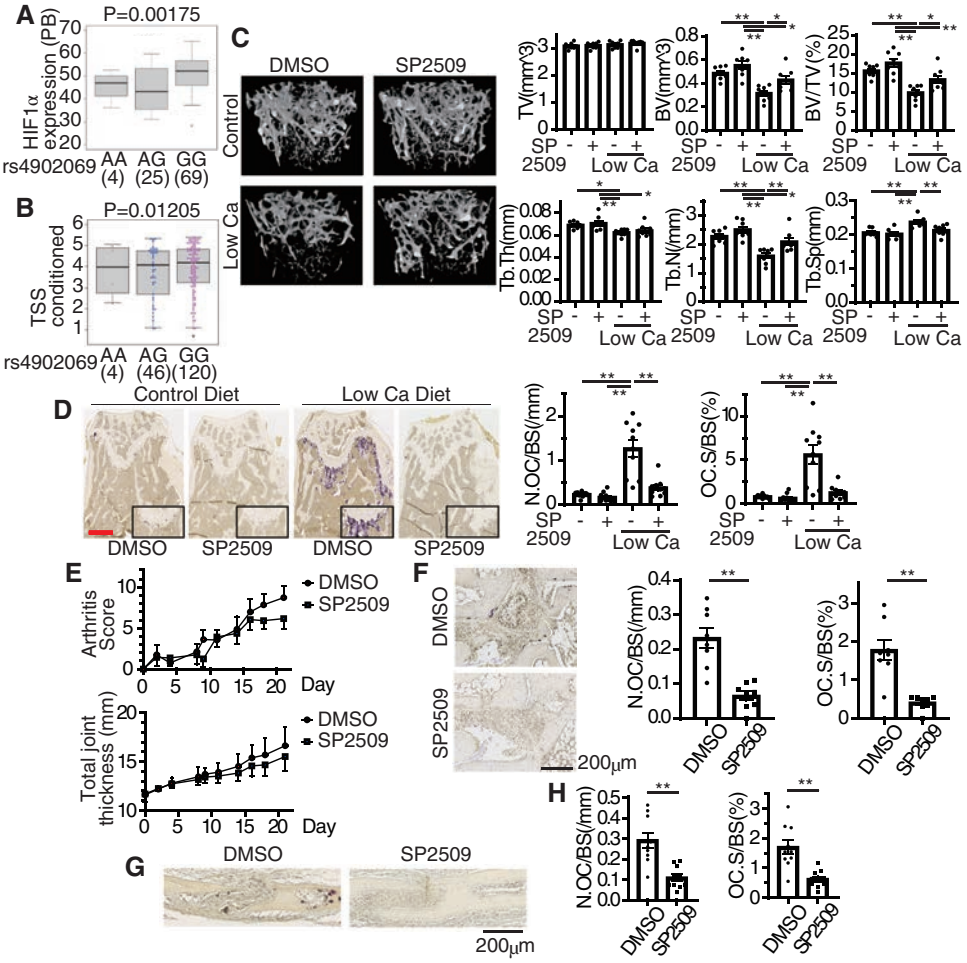

Figure 6. Positive effects of hypoxia-inducible factor 1α (HIF-1α) and LSD1 on bone erosion in inflammatory arthritis. **A**, Associations between the *cis*-acting expression quantitative trait locus at rs4902069 (AA, AG, GG) and HIF-1α expression were assessed in healthy donors. **B**, The modified Sharp/van der Heijde score (TSS conditioned) of radiographic disease severity was assessed in the hand joints of rheumatoid arthritis patients according to the 3 genotypes of rs4902069. Data in **A** and **B** are shown as box plots. Each box represents the 25th to 75th percentiles. Lines inside the boxes represent the median. Lines outside the boxes represent the 10th and 90th percentiles. **C**, Male C57BL/6N mice were fed a control diet or a low-calcium diet (<0.01% calcium), and were treated with DMSO or SP2509. The distal femurs of mice in each group were assessed by micro–computed tomography (micro-CT) (left). Micro-CT measures included the total volume (TV), bone volume (BV), ratio of BV to TV, trabecular thickness (Tb.Th), trabecular number (Tb.N), and trabecular separation (Tb.Sp) (right). Results are the mean ± SEM from 10 mice in 3 independent experiments. **D**, Left, Histologic sections from the distal femurs of mice in each group were stained with tartrate-resistant acid phosphatase (TRAP) for histomorphometric analysis (bar = 500 μm; **insets** show higher-magnification views). Right, Results are expressed as the mean ± SEM osteoclast number per bone surface (N.OC/BS) and osteoclast surface area per bone surface (OC.S/BS) (n = 8 mice from 2 experiments). **E** and **F**, Arthritis was induced with mannan in SKG mice, followed by treatment with DMSO or SP2509. The time course of changes in the arthritis severity score and joint swelling are shown (**E**). Histologic sections from the calcaneocuboid and tarsometatarsal joints of mice were stained with TRAP (**F**; left) and assessed for histologic features (**F**; right). Data are the mean ± SEM (n = 8 mice from 2 experiments). **G** and **H**, In the mouse model of tumor necrosis factor–induced supracalvarial osteolysis, histologic sections of the calvaria of mice were stained with TRAP (**G**) and assessed for histologic features (**H**). Data are the mean ± SEM (n = 10 mice from 2 experiments). * = $P < 0.05$; ** = $P < 0.01$, by 2-tailed, unpaired *t*-test in **F** and **H**, and by Tukey-Kramer test in **C** and **D**. See Figure 1 for other definitions. Color figure can be viewed in the online issue, which is available at http://onlinelibrary.wiley.com/doi/10.1002/art.42074/abstract.

of HIF-1α suppressed osteoclastogenesis and the expression of osteoclast-related genes, including *TRAP*, *CTSK*, *ITGB3*, and *DC-STAMP*, in conditions of normoxia (Figures 4D and E). These results suggest that RANKL-induced osteoclastogenesis is metabolically regulated by HIF-1α, even in an environment of normoxia.

Promotion of glycolysis by LSD1 via HIF-1α. To gain additional insights into the mechanism by which LSD1 regulates metabolism through the HIF-1α pathway, we analyzed the expression of RANKL-induced HIF-1α, whose protein expression is known to be stabilized by demethylation activity of LSD1 in other cell systems (19,20). In cultures of human CD14-positive

monocytes stimulated with M-CSF, the LSD1 inhibitors SP2509 and RN1 significantly suppressed RANKL-induced HIF-1α protein expression (Figure 5A), whereas treatment with the SP2509 inhibitor and silencing of LSD1 with siRNA only minimally decreased the expression of HIF-1α mRNA (Supplementary Figures 6A and B, available on the *Arthritis & Rheumatology* website at https://onlinelibrary.wiley.com/doi/10.1002/art.42074). Concordantly, the expression of HIF-1α target genes, which were up-regulated by RANKL, was suppressed by treatment with SP2509 and siRNA-mediated silencing of LSD1 (Figures 5B and C). RANKL induced the expression of PHD2, which prompted the degradation of HIF-1α through mediation of HIF-1α hydroxylation. However, treatment with SP2509 did not inhibit RANKL-induced expression of PHD2 (Supplementary Figure 6C).

Finally, we evaluated the level of glycolysis after RANKL stimulation of the cells. Treatment with SP2509 significantly suppressed glycolysis and glycolytic capacity in the cell cultures (Figures 5D and E). These results suggest that LSD1 regulates osteoclast differentiation by controlling glycolysis via the stabilization of HIF-1α expression, in conjunction with the activity of the transcription factor E2F1 (Figure 5F).

Suppression of osteoclastogenesis by LSD1 inhibition in conditions of hypoxia. In addition to the effects on osteoclastogenesis in a normoxic environment, we confirmed that LSD1 inhibition by SP2509 suppressed osteoclast differentiation in conditions of hypoxia (Supplementary Figure 7A, available on the *Arthritis & Rheumatology* website at https://onlinelibrary.wiley.com/doi/10.1002/art.42074). Suppression of LSD1 by SP2509 (at a dose of 1 μ*M*) did not strongly suppress the level of *NFATc1* mRNA (Figure 1B; see also Supplementary Figure 3B); however, induction of HIF-1α target genes by RANKL in conditions of hypoxia was effectively suppressed by SP2509 (Supplementary Figure 7C). These results suggest that LSD1 has a metabolically important role in the hypoxic enhancement of osteoclastogenesis.

Furthermore, HIF-1α is known to promote bone resorption even under normoxia (11). We confirmed that siRNA-mediated knockdown of LSD1 inhibited bone resorption and the down-regulation of HIF-1α (Supplementary Figure 7D [https://onlinelibrary.wiley.com/doi/10.1002/art.42074]), suggesting that LSD1 could also promote bone resorption.

Evidence supporting LSD1 as a potential therapeutic target for pathologic bone resorption. We investigated whether LSD1 could be a potential therapeutic target for achieving attenuation of the severity of pathologic bone resorption in patients with RA. We tested the relationship between LSD1 allelic variants that affect gene expression and the progression of bone loss in RA patients. We identified significant associations between eQTL and the expression of HIF-1α and LSD1 (based on a *P* value threshold of <0.05, as determined in a previously published large eQTL study using a healthy donor [21]). In total, 4 single-nucleotide polymorphisms (SNPs) (rs646193, rs2092933, rs12137132, and rs10917219) were found to be associated with LSD1 expression; the first 2 SNPs were observed in CD4-positive cells, while the latter 2 were observed in monocytes. Three SNPs (rs912619, rs2252267, and rs4902069) were associated with HIF-1α expression; the first 2 SNPs were observed in B cells, and the last was located in peripheral blood. Our results did not demonstrate a significant relationship between LSD1 allelic variants and bone erosion in RA patients. However, among the SNPs linked to associations between *cis*-eQTL and HIF-1α, allelic variant rs4902069 (G) was significantly associated with higher expression of HIF-1α in healthy control subjects ($P = 0.0017$) (Figure 6A). Presence of this SNP was also associated with increased bone erosion of the hand joints in RA patients ($P = 0.01$) (Figure 6B).

We next used a mouse model to examine the effect of LSD1 on accelerated bone loss in mice fed a low-calcium diet. Micro-CT analysis of the mouse bones revealed that a low-calcium diet decreased bone mass, and that LSD1 inhibition by SP2509 significantly suppressed the low calcium–induced bone loss relative to that in mice treated with DMSO (Figure 6C).

Histomorphometric analysis of sections of calvaria from the mice showed that treatment with SP2509 decreased the numbers of osteoclasts and osteoclast surface area, supporting the notion that LSD1 is crucial for osteoclastogenesis and pathologic bone resorption (Figure 6D).

Finally, we tested the effect of LSD1 on inflammatory bone resorption. Mannan-induced arthritis in ZAP70-mutated SKG mice, which develop T cell–mediated autoimmune arthritis, represents a disease model that is clinically and immunologically similar to human RA (22). Inhibition of LSD1 by SP2509 treatment in this mouse model resulted in a minor decrease in the arthritis severity score, which was not significantly different from that in DMSO-treated mice (Figure 6E). In an SKG mouse model of arthritis, LSD1 inhibition significantly suppressed osteoclast numbers in the periarticular bone (Figure 6F), and inhibited the decrease in bone volume of the calcaneus without affecting LSD1 expression (Supplementary Figures 8A–D, available on the *Arthritis & Rheumatology* website at https://onlinelibrary.wiley.com/doi/10.1002/art.42074).

Similarly, in a mouse model of TNF-induced supracalvarial osteolysis, treatment with SP2509 strongly inhibited osteoclastogenesis and the associated bone erosion in vivo (Figure 6G; see also Supplementary Figure 8E [https://onlinelibrary.wiley.com/doi/10.1002/art.42074]). Histomorphometric analysis showed decreased osteoclast numbers per bone surface and decreased osteoclast surface area per bone surface (Figure 6H). These results suggest that LSD1 is a potential therapeutic target for prevention of metabolic energy–demanding pathologic bone resorption in patients with RA.

DISCUSSION

Previous studies have highlighted the importance of functions and drivers of metabolic reprogramming, especially glycolysis, during osteoclastogenesis; however, the process of metabolic reprogramming in osteoclastogenesis is still not completely understood (12,13). We investigated the mechanisms by which LSD1 mediates osteoclastogenesis. The results of this study show that RANKL-induced LSD1 stabilizes the levels of HIF-1α protein, even in normoxia. LSD1, along with HIF-1α and E2F1, mediates glycolysis. Furthermore, inhibition of LSD1 suppresses energy-demanding pathologic bone resorption.

In RA patient synovium, synovial proliferation and leukocyte extravasation outstrip the oxygen supply and create a hypoxic microenvironment (15). Abnormal cellular metabolism and mitochondrial dysfunction increase production of reactive oxygen species and worsen the extent of inflammation. Hypoxia is also known to enhance osteoclast differentiation (14). It is noteworthy that the hypoxic response is involved in osteoclast differentiation, even under normoxic conditions, and that LSD1 integrates its response.

HIF-1α, which increases glycolysis and decreases mitochondrial function in response to hypoxic stimuli, is unstable in normoxia. However, stimulation with cytokines, growth factors, and vascular hormones can also lead to the induction and activation of HIF-1α in different cell types (23–26). These factors mostly regulate HIF-1α at the transcriptional, posttranscriptional, or translational levels (27,28). We showed that RANKL stabilized HIF-1α protein under conditions of normoxia, and that HIF-1α was important for human osteoclastogenesis even under normoxia. Because of the complexity and difficulty in detecting the protein expression of HIF-1α, cells depleted of HIF-1α tend to be used in a normoxic environment, without showing protein expression and the mechanism of stabilization of HIF-1α. A recent study using HIF-1α–depleted neuroblastoma cells demonstrated that metabolic processes are regulated by HIF-1α even in conditions of normoxia (29), without confirming that HIF-1α protein was expressed in the cells in normoxia. Although we showed that the stabilization of HIF-1α protein under normoxia during osteoclastogenesis was partly attributable to its modification by LSD1, HIF-1α protein expression in normoxia was also shown to be regulated by the increased expression of HIF-1α mRNA and mTOR activity (27). RANKL could also induce the expression of HIF-1α mRNA and increase mTOR activity in our model. Although it was not investigated in this study, it has been suggested that a non-hypoxic simulator regulates HIF-1α expression through microRNAs (28). Whether the RANKL–LSD1 axis stabilizes HIF-1α via microRNAs needs to be investigated in further study.

In this study, LSD1 was induced via the RANKL–mTOR pathway, resulting in the induction of the HIF-1α and E2F1 pathways. We previously demonstrated the importance of RANKL-mediated induction of anabolic, cell-cycle, and E2F-mediated pathways using nonproliferating human OCPs: the effects of RANKL on cell proliferation and energy production using proliferating mouse OCPs are difficult to distinguish (14). E2F target genes regulate many anabolic pathway genes. Human OCPs use the cell-cycle pathway to prepare for the high energy demand for terminal differentiation, just as proliferating cells utilize the cell-cycle pathway to prepare the energy required for cell division. Recent investigations of stepwise events during the process of osteoclastogenesis, determined using single-cell RNA-seq analysis in mice, demonstrated findings supporting this idea of involvement of the cell-cycle pathway (30). This study provides new insights into how RANKL stimulates metabolic reprogramming mediating the activities of HIF-1α and E2F1.

LSD1 targets both histone and nonhistone proteins with demethylase enzymatic activity (16). In HIF-1α, Set9 histone methyltransferase induces HIF-1α methylation at lysine 32 or lysine 391, and LSD1 reverses this process, in that it protects HIF-1α against ubiquitin-mediated protein degradation (19,31). LSD1 also inhibits HIF-1α hydroxylation by PHD2 in cancer cell lines. SP2509 blocks LSD1 methylase function allosterically; that is, SP2509 interrupts the binding of the partner protein by binding with the H3 pocket within LSD1. RN1 and ORY1001 are *trans*-2-phenylcyclopropylamine derivatives that inhibit LSD1 methylase activity as covalent adducts through a flavin loop, which is a cofactor during catalysis of demethylation (32,33). Through these processes, RANKL-induced HIF-1α protein stabilization is considered to be suppressed by these inhibitors (as shown in Figure 5A).

The inhibition of LSD1 successfully suppressed bone loss in mice fed a low-calcium diet. We used SP2509 at a dose that was used in a previous study (34). However, we still need to study whether SP2509 at this dose could effectively suppress pathologic bone resorption in vivo or might have some toxic effects. Furthermore, inhibition of LSD1 was shown to increase BMP2, WNT7B, and RUNX2 expression in osteoblasts, and mice lacking LSD1 in mesenchymal cells exhibit increased bone mass (35,36). Treatment with an LSD1 inhibitor for bone loss may have dual effects on the bone via an increase in bone formation and reduction in bone resorption.

SP2509 did not effectively suppress inflammatory arthritis. Elevated LSD1 expression is a characteristic that has been observed in patients with various cancers and is closely related to many cellular effects, including malignant transformation, epithelial–mesenchymal cell transition, and cell proliferation and differentiation (33). Thus, it is considered a promising therapeutic target for malignant tumors. It is reasonable to think that SP2509, an LSD1 inhibitor, suppresses inflammatory arthritis because it suppresses the cell-cycle and metabolic pathways, which are essential for the proliferation of inflammatory synovial cells (37). In fact, disease severity was alleviated in mice with collagen-induced arthritis when LSD1 was knocked down (38); however, this effect was not confirmed in the present study.

Possible reasons for this discrepancy include 1) inflammation induced in SKG mice was fulminant or 2) SP2509 was insufficient to control arthritis. However, bone erosion was suppressed in SKG mice. Therefore, LSD1 remains a promising therapeutic target in strategies aimed at alleviating both arthritis and the severity of bone erosion, with variations in the type and dose of inhibitors.

One of the limitations of this study is the lack of epigenetic analysis. Because LSD1 mediates transcriptional repression by demethylation of H3K4me1/2 and transcriptional activation by demethylation of H3K9me1/2, determining which genes are epigenetically regulated in RANKL-induced osteoclast differentiation may be a challenging task when using histone modification analysis, and it is reasonable to investigate the LSD1-regulated pathway by siRNA silencing. Another limitation is that the specificity and toxicity of SP2509 are not reported herein. SP2509 has been shown to have a weak effect in the inhibition of D-lactate dehydrogenase, glucose oxidase, cytochrome P450s, and the hERG gene (39). A transcriptomic analysis using a Ewing sarcoma cell line also showed that the expression pattern of the SP2509-regulated genes mimicked those regulated by LSD1 knockdown (40). However, further studies are still needed before SP2509 could be applied for the treatment of human diseases.

In summary, we identified the integrative role of LSD1 in osteoclastogenesis. LSD1 stabilizes RANKL-induced HIF-1α protein even in conditions of normoxia, which promotes osteoclast differentiation via an anabolic pathway. During osteoclastogenesis, LSD1 is induced via the RANKL-induced mTOR pathway. TNF is also a factor that induces LSD1 expression. Inhibition of LSD1 effectively suppresses osteoclastogenesis and bone loss in mice with accelerated osteoporosis as well as in mouse models of inflammatory osteolysis and arthritis. These findings indicate that LSD1 plays a crucial role in osteoclastogenesis under challenging, metabolic energy–demanding inflammatory conditions. Thus, targeting the activity of LSD1 in osteoclasts may be an attractive therapeutic strategy for the treatment of inflammatory arthritis, including in the affected joints of patients with RA.

ACKNOWLEDGMENT

We thank the staff at Editage for providing English language editing of the manuscript.

AUTHOR CONTRIBUTIONS

All authors were involved in drafting the article or revising it critically for important intellectual content, and all authors approved the final version to be published. Dr. Murata had full access to all of the data in the study and takes responsibility for the integrity of the data and the accuracy of the data analysis.

Study conception and design. Doi, Murata.

Acquisition of data. Doi, Murata, Ito, Suzuki, Terao, Ishie, Umemoto, Murotani, Nishitani, Yoshitomi, Fujii, Watanabe, Hashimoto, Murakami, Tanaka, Ito.

Analysis and interpretation of data. Doi, Murata, Park-Min, Ivashkiv, Morinobu, Matsuda.

REFERENCES

1. Mbalaviele G, Novack DV, Schett G, Teitelbaum SL. Inflammatory osteolysis: a conspiracy against bone. J Clin Invest 2017;127:2030–9.
2. Walsh MC, Takegahara N, Kim H, Choi Y. Updating osteoimmunology: regulation of bone cells by innate and adaptive immunity [review]. Nat Revi Rheumatol 2018;14:146–56.
3. Black DM, Rosen CJ. Clinical practice: postmenopausal osteoporosis. N Engl J Med 2016;374:254–62.
4. Takeuchi T, Tanaka Y, Soen S, Yamanaka H, Yoneda T, Tanaka S, et al. Effects of the anti-RANKL antibody denosumab on joint structural damage in patients with rheumatoid arthritis treated with conventional synthetic disease-modifying antirheumatic drugs (DESIRABLE study): a randomised, double-blind, placebo-controlled phase 3 trial. Ann Rheum Dis 2019;78:899–907.
5. Tsourdi E, Zillikens MC, Meier C, Body JJ, Gonzalez Rodriguez E, Anastasilakis AD, et al. Fracture risk and management of discontinuation of denosumab therapy: a systematic review and position statement by ECTS. J Clin Endocrinol Metab 2020;26:dgaaa756.
6. Tsukasaki M, Takayanagi H. Osteoimmunology: evolving concepts in bone-immune interactions in health and disease [review]. Nat Rev Immunol 2019;19:626–42.
7. Bae S, Lee MJ, Mun SH, Giannopoulou EG, Yong-Gonzalez V, Cross JR, et al. MYC-dependent oxidative metabolism regulates osteoclastogenesis via nuclear receptor ERRα. J Clin Invest 2017;127:2555–68.
8. Nishikawa K, Iwamoto Y, Kobayashi Y, Katsuoka F, Kawaguchi S, Tsujita T, et al. DNA methyltransferase 3a regulates osteoclast differentiation by coupling to an S-adenosylmethionine-producing metabolic pathway. Nat Med 2015;21:281–7.
9. Lemma S, Sboarina M, Porporato PE, Zini N, Sonveaux P, Di Pompo G, et al. Energy metabolism in osteoclast formation and activity. Int J Biochem Cell Biol 2016;79:168–80.
10. Jin Z, Wei W, Yang M, Du Y, Wan Y. Mitochondrial complex I activity suppresses inflammation and enhances bone resorption by shifting macrophage-osteoclast polarization. Cell Metab 2014;20:483–98.
11. Indo Y, Takeshita S, Ishii KA, Hoshii T, Aburatani H, Hirao A, et al. Metabolic regulation of osteoclast differentiation and function. J Bone Miner Res 2013;28:2392–9.
12. Park-Min KH. Metabolic reprogramming in osteoclasts. Semin Immunopathol 2019;41:565–72.
13. Ivashkiv LB. Metabolic-epigenetic coupling in osteoclast differentiation. Nat Med 2015;21:212–3.
14. Murata K, Fang C, Terao C, Giannopoulou EG, Lee YJ, Lee MJ, et al. Hypoxia-sensitive COMMD1 integrates signaling and cellular metabolism in human macrophages and suppresses osteoclastogenesis. Immunity 2017;47:66–79.
15. Palazon A, Goldrath AW, Nizet V, Johnson RS. HIF transcription factors, inflammation, and immunity. Immunity 2014;41:518–28.
16. Gu F, Lin Y, Wang Z, Wu X, Ye Z, Wang Y, et al. Biological roles of LSD1 beyond its demethylase activity. Cell Mol Life Sci 2020;77:3341–50.
17. Kitaura H, Zhou P, Kim HJ, Novack DV, Ross FP, Teitelbaum SL. M-CSF mediates TNF-induced inflammatory osteolysis. J Clin Invest 2005;115:3418–27.
18. Sorensen MG, Henriksen K, Schaller S, Henriksen DB, Nielsen FC, Dziegiel MH, et al. Characterization of osteoclasts derived from CD14+ monocytes isolated from peripheral blood. J Bone Miner Metab 2007;25:36–45.
19. Lee JY, Park JH, Choi HJ, Won HY, Joo HS, Shin DH, et al. LSD1 demethylates HIF1α to inhibit hydroxylation and ubiquitin-mediated degradation in tumor angiogenesis. Oncogene 2017;36:5512–21.

20. Sacca CD, Gorini F, Ambrosio S, Amente S, Faicchia D, Matarese G, et al. Inhibition of lysine-specific demethylase LSD1 induces senescence in glioblastoma cells through a HIF-1alpha-dependent pathway. Biochim Biophys Acta Gene Regul Mech 2019;1862:535–46.
21. Ishigaki K, Kochi Y, Suzuki A, Tsuchida Y, Tsuchiya H, Sumitomo S, et al. Polygenic burdens on cell-specific pathways underlie the risk of rheumatoid arthritis. Nat Genet 2017;49:1120–5.
22. Takeuchi Y, Hirota K, Sakaguchi S. Impaired T cell receptor signaling and development of T cell-mediated autoimmune arthritis [review]. Immunol Rev 2020;294:164–76.
23. Dery MA, Michaud MD, Richard DE. Hypoxia-inducible factor 1: regulation by hypoxic and non-hypoxic activators. Int J Biochem Cell Biol 2005;37:535–40.
24. McInturff AM, Cody MJ, Elliott EA, Glenn JW, Rowley JW, Rondina MT, et al. Mammalian target of rapamycin regulates neutrophil extracellular trap formation via induction of hypoxia-inducible factor 1 α. Blood 2012;120:3118–25.
25. Finlay DK, Rosenzweig E, Sinclair LV, Feijoo-Carnero C, Hukelmann JL, Rolf J, et al. PDK1 regulation of mTOR and hypoxia-inducible factor 1 integrate metabolism and migration of CD8+ T cells. J Exp Med 2012;209:2441–53.
26. Rius J, Guma M, Schachtrup C, Akassoglou K, Zinkernagel AS, Nizet V, et al. NF-κB links innate immunity to the hypoxic response through transcriptional regulation of HIF-1α. Nature 2008;453:807–11.
27. Hayashi Y, Yokota A, Harada H, Huang G. Hypoxia/pseudohypoxia-mediated activation of hypoxia-inducible factor-1α in cancer [review]. Cancer Sci 2019;110:1510–7.
28. Kuschel A, Simon P, Tug S. Functional regulation of HIF-1α under normoxia—is there more than post-translational regulation? J Cell Physiol 2012;227:514–24.
29. Cimmino F, Avitabile M, Lasorsa VA, Montella A, Pezone L, Cantalupo S, et al. HIF-1 transcription activity: HIF1A driven response in normoxia and in hypoxia. BMC Med Genet 2019;20:37.
30. Tsukasaki M, Huynh NC, Okamoto K, Muro R, Terashima A, Kurikawa Y, et al. Stepwise cell fate decision pathways during osteoclastogenesis at single-cell resolution. Nat Metab 2020;2:1382–90.
31. Kim Y, Nam HJ, Lee J, Park DY, Kim C, Yu YS, et al. Methylation-dependent regulation of HIF-1α stability restricts retinal and tumour angiogenesis. Nat Commun 2016;7:10347.
32. Zheng YC, Ma J, Wang Z, Li J, Jiang B, Zhou W, et al. A systematic review of histone lysine-specific demethylase 1 and its inhibitors. Med Res Rev 2015;35:1032–71.
33. Fang Y, Liao G, Yu B. LSD1/KDM1A inhibitors in clinical trials: advances and prospects. J Hematol Oncol 2019;12:129.
34. Fiskus W, Sharma S, Shah B, Portier BP, Devaraj SG, Liu K, et al. Highly effective combination of LSD1 (KDM1A) antagonist and pan-histone deacetylase inhibitor against human AML cells. Leukemia 2014;28:2155–64.
35. Munehira Y, Yang Z, Gozani O. Systematic analysis of known and candidate lysine demethylases in the regulation of myoblast differentiation. J Mol Biol 2017;429:2055–65.
36. Sun J, Ermann J, Niu N, Yan G, Yang Y, Shi Y, et al. Histone demethylase LSD1 regulates bone mass by controlling WNT7B and BMP2 signaling in osteoblasts. Bone Res 2018;6:14.
37. Falconer J, Murphy AN, Young SP, Clark AR, Tiziani S, Guma M, et al. Synovial cell metabolism and chronic inflammation in rheumatoid arthritis [review]. Arthritis Rheumatol 2018;70:984–99.
38. Liu W, Fan JB, Xu DW, Zhu XH, Yi H, Cui SY, et al. Knockdown of LSD1 ameliorates the severity of rheumatoid arthritis and decreases the function of CD4 T cells in mouse models. Int J Clin Exp Pathol 2018;11:333–41.
39. Sorna V, Theisen ER, Stephens B, Warner SL, Bearss DJ, Vankayalapati H, et al. High-throughput virtual screening identifies novel N'-(1-phenylethylidene)-benzohydrazides as potent, specific, and reversible LSD1 inhibitors. J Med Chem 2013;56:9496–508.
40. Pishas KI, Drenberg CD, Taslim C, Theisen ER, Johnson KM, Saund RS, et al. Therapeutic targeting of KDM1A/LSD1 in Ewing sarcoma with SP-2509 engages the endoplasmic reticulum stress response. Mol Cancer Ther 2018;17:1902–16.

Arthritis & Rheumatology
Vol. 74, No. 6, June 2022, pp 961–971
DOI 10.1002/art.42072

American College of Rheumatology
Empowering Rheumatology Professionals

Antibodies to Cartilage Oligomeric Matrix Protein Are Pathogenic in Mice and May Be Clinically Relevant in Rheumatoid Arthritis

Changrong Ge,[1] Dongmei Tong,[1] Erik Lönnblom,[1] Bibo Liang,[2] Weiwei Cai,[1] Cecilia Fahlquist-Hagert,[3] Taotao Li,[1] Alf Kastbom,[4] Inger Gjertsson,[5] Doreen Dobritzsch,[6] and Rikard Holmdahl[2]

Objective. Cartilage oligomeric matrix protein (COMP) is an autoantigen in rheumatoid arthritis (RA) and experimental models of arthritis. This study was undertaken to investigate the structure, function, and relevance of anti-COMP antibodies.

Methods. We investigated the pathogenicity of monoclonal anti-COMP antibodies in mice using passive transfer experiments, and we explored the interaction of anti-COMP antibodies with cartilage using immunohistochemical staining. The interaction of the monoclonal antibody 15A11 in complex with its specific COMP epitope P6 was determined by x-ray crystallography. An enzyme-linked immunosorbent assay and a surface plasma resonance technique were used to study the modulation of calcium ion binding to 15A11. The clinical relevance and value of serum IgG specific to the COMP P6 epitope and its citrullinated variants were evaluated in a large Swedish cohort of RA patients.

Results. The murine monoclonal anti-COMP antibody 15A11 induced arthritis in naive mice. The crystal structure of the 15A11–P6 complex explained how the antibody could bind to COMP, which can be modulated by calcium ions. Moreover, serum IgG specific to the COMP P6 peptide and its citrullinated variants was detectable at significantly higher levels in RA patients compared to healthy controls and correlated with a higher disease activity score.

Conclusion. Our findings provide the structural basis for binding a pathogenic anti-COMP antibody to cartilage. The recognized epitope can be citrullinated, and levels of antibodies to this epitope are elevated in RA patients and correlate with higher disease activity, implicating a pathogenic role of anti-COMP antibodies in a subset of RA patients.

INTRODUCTION

Rheumatoid arthritis (RA) is a chronic autoimmune disease characterized by inflammation and damage in synovial joints. It affects 0.5–1% of the population worldwide (1–3). RA is caused by a complex set of genes and environmental factors, although none of these have been firmly defined or functionally understood (4–6). There is increasing evidence that environmental exposures, such as silica dust, bacterial stimuli, and tobacco smoking, cause chronic mucosal inflammation, possibly contributing to RA development (7–9). However, the mechanisms by which chronic inflammation triggers adaptive autoimmunity, in particular a B cell response to citrullinated proteins and later toward joint proteins, are not yet well understood (10).

Cartilage oligomeric matrix protein (COMP) is a noncollagenous matrix glycoprotein that belongs to the thrombospondin family of extracellular calcium-binding proteins (11). It is predominantly expressed in cartilage and is also found in other tissue, such as tendons, bones, blood vessels, and synovial membrane (12). COMP is a pentameric protein with each monomer consisting of an N-terminal domain followed by 4 epidermal growth factor (EGF)–like domains, 8 type III thrombospondin domains, and a C-terminal globular domain (13). The specific function of COMP is still undefined, but it appears to play a structural role in the assembly and

Supported by The Swedish Foundation for Strategic Research, Knut and Alice Wallenberg Foundation, Academy of Finland, the Finnish Cultural Foundation, the National Doctoral Programme in Informational and Structural Biology, and the Swedish Research Council. The research leading to this study received funding from the European Union's Seventh Framework Programme (FP7/2007-2013) under BioStruct-X (grant no. 283570).

[1]Changrong Ge, PhD, Dongmei Tong, PhD, Erik Lönnblom, PhD, Weiwei Cai, PhD, Taotao Li, PhD: Karolinska Institute, Stockholm, Sweden; [2]Bibo Liang, PhD, Rikard Holmdahl, MD, PhD: Karolinska Institute, Stockholm, Sweden, and Southern Medical University, Guangzhou, China; [3]Cecilia Fahlquist-Hagert, PhD: Karolinska Institute, Stockholm, Sweden, and University of Turku, Turku, Finland; [4]Alf Kastbom, MD, PhD: Linköping University, Linköping, Sweden; [5]Inger Gjertsson, MD, PhD: University of Gothenburg, Gothenburg, Sweden; [6]Doreen Dobritzsch, PhD: Uppsala University, Uppsala, Sweden.

Author disclosures are available at https://onlinelibrary.wiley.com/action/downloadSupplement?doi=10.1002%2Fart.42072&file=art42072-sup-0001-Disclosureform.pdf.

Address correspondence to Rikard Holmdahl, MD, PhD, Biomedicum, Quarter 9D Solnavägen 9, Solna, Sweden. Email: rikard.holmdahl@ki.se.

Submitted for publication August 19, 2021; accepted in revised form January 18, 2022.

stabilization of the extracellular matrix (ECM) through its interactions with collagen fibrils and other matrix components, such as proteoglycans and fibronectin (14).

The functional importance of COMP in cartilage is indicated by its association with several joint diseases (14). As a marker of cartilage turnover, elevated COMP levels are found in the serum and synovial fluid from patients with joint diseases such as RA and osteoarthritis (OA) (15). Because it reflects the specific metabolic activities of cartilage tissue, it has been suggested that COMP is a potential diagnostic and prognostic biomarker in joint diseases (15). Interestingly, circulating COMP fragments bind C3b and could be both an inhibitor and an initiator of complement activation in RA, but not in OA (16).

Cartilage damage and degradation in chronic joint disease are believed to promote an autoimmune reaction to cartilage components. We previously demonstrated that homologous COMP could induce arthritis in certain animal strains, highlighting its pathogenic role in experimental arthritis (17,18). In addition, disease can be transferred from arthritic mice to healthy recipients via affinity-purified COMP-specific polyclonal antibodies as well as with monoclonal antibodies alone or in combination with other cartilage-binding antibodies (19,20), indicating that B cells are involved in disease development. We previously reported that mouse monoclonal antibodies (mAb) raised against COMP were not only able to promote arthritis when combined with anti–type II collagen (CII) antibody, but were also capable of inducing joint pain in naive mice (19,21). These data collectively indicate that both COMP and its autoantibodies play pathogenic roles in experimental arthritis and further indicate that they may have a potentially important role in RA. Indeed, antibodies to COMP were detected in synovium and serum from RA patients (22).

COMP plays an essential role in matrix assembly by interacting with many extracellular and cell surface proteins (14). We have previously shown that there are several epitopes, mainly located in the EGF-like repeats of COMP, that can be targeted by autoantibodies, such as 15A11 and 16B5, generated using mice with COMP-induced arthritis (19). Understanding the molecular basis for the interaction of autoantibodies with COMP as well as whether and how this interaction influences the structural features of the ECM, thereby causing cartilage damage, will thus further our understanding of the pathogenesis of rheumatic diseases. Therefore, in the present study we aimed to investigate the pathogenesis of anti-COMP antibodies in experimental arthritis at the molecular level as well as the functional role of COMP as an autoantigen in human RA.

MATERIALS AND METHODS

Reagents and more detailed methods for enzyme-linked immunosorbent assay (ELISA), histologic assessment, and surface plasma resonance measurement are described in the Supplementary Materials and Methods (available on the *Arthritis & Rheumatology* website at http://onlinelibrary.wiley.com/doi/10.1002/art.42072).

Animals. C57BL mice with an H-2^q congenic fragment (denoted B10.Q) were used in all experiments, as this genetically defined background is used as a standard background (23). In some experiments (neonatal injections), a B10.Q mouse with a *Mus musculus* Fc receptor locus (24) was used as the congenic fragment, which likely did not affect the results. All mice were housed and bred in a climate-controlled specific pathogen–free environment on 12-hour light/dark cycles, housed in polystyrene cages containing wood shavings in the animal facility of the Division of Medical Inflammation Research at the Karolinska Institute and the Central Animal Laboratory of the University of Turku. Mice were provided with standard rodent chow and water ad libitum. All experiments were performed in 8–10-week-old mice under standard conditions. The experiments were approved by the Stockholm ethics committee (approval nos. N490/12 and H2014-483) and the National Animal Experiment Board in Finland (approval no. ESAVI/439/04.10.07/2017).

Passive transfer of antibodies. Three groups of B10.Q mice were injected intravenously with either 9 mg M2139 (specific to type II collagen/Col2) (25); 9 mg 15A11 (specific to COMP) (19); or a combination of M2139 and 15A11 (4.5 mg of each). On day 5, each mouse was intraperitoneally administered 25 μg lipopolysaccharide (LPS) from the *Escherichia coli* serotype O55:B5 (Sigma-Aldrich) to increase the severity of developing arthritis. Arthritis development was monitored daily in a blinded manner for 12 days using an extended scoring protocol. Briefly, clinical arthritis was defined as swelling and redness in the joint and was scored as follows: 1 point was assigned for each swollen or red toe, 1 point was assigned for each swollen joint (metatarsophalangeal joints, metacarpophalangeal joints, proximal interphalangeal joints, and distal interphalangeal joints), and 5 points were assigned for a swollen ankle (maximum score per limb 15 points, maximum score per mouse 60 points).

Crystallization, data collection, and structure determination. Purified 15A11 Fab fragment (final concentration 10 mg/ml in 20 m*M* Tris HCl, pH 7.4, 50 m*M* NaCl) was mixed with P6 peptide with a rat-specific sequence at a molar ratio of 1:1.2. Screening for crystallization conditions was performed in a sitting-drop vapor diffusion setup at 20°C using Crystal Screen HT (Hampton Research), with 0.3-μl drops equilibrated against 60-μl reservoirs. Crystals appeared under several conditions and were tested for diffraction. The data used for structure determination were collected from a crystal obtained with screening condition C6 (30% polyethylene glycol 8000, 0.2*M* ammonium sulfate) and a drop mixed at a 2:1 ratio with protein and reservoir solution. The crystal was briefly soaked in a cryoprotectant consisting of

reservoir solution supplemented with 15% (volume/volume) glycerol before it was flash-frozen in liquid N_2. Crystallographic data were collected at 100K at Beamline I03 of the Diamond Light Source, indexed and integrated on-site with XIA2-3d, and scaled using Aimless from the CCP4 suite of programs (26–32).

The initial estimates of phases were obtained by molecular replacement using the program Phaser (33). We performed manual model building using Coot (34) alternating with translation, liberation, and screw-motion and restrained refinement in REFMAC5 (35). A set including 5% of randomly selected reflections was used to monitor R_{free}. Water molecules were added in Coot. Molecular surfaces were analyzed with the Protein Interfaces, Surfaces and Assemblies service at the European Bioinformatics Institute (36). Crystal structure images were prepared with PyMOL (37). The crystallographic coordinates and structure factors of the 15A11 Fab–P6 complex have been deposited in the Protein Data Bank (PDB) (no. 6SF6).

Patient cohorts. In the present study, we used the prospective observational Early Intervention in RA second cohort (TIRA-2) consisting of 504 RA patients, and healthy subjects from the Western Region Initiative to Gather Information on Atherosclerosis cohort were used as controls (n = 290). Between 2006 and 2009, RA patients enrolled in the TIRA-2 fulfilled the American College of Rheumatology 1987 criteria for RA (38) or at least the criteria of morning stiffness for ≥60 minutes, symmetric arthritis, and arthritis in the small joints (39). The study protocols were approved by the regional ethics review boards in Linköping (approval nos. TIRA-2, M168-05, and 2005-12-14) and Gothenburg (approval nos. WINGA, 676-08, and T953-15).

Luminex immunoassay. The detection of autoantibody responses using Luminex technology has been described previously (40–42). Briefly, all biotinylated peptides were captured on beads via recognition of NeutrAvidin (ThermoFisher Scientific), which was immobilized on the beads with amine coupling. Human serum samples were diluted 1:100 (v/v) in assay buffer (3% bovine serum albumin, 5% milk powder, 0.1% ProClin 300, 0.05% Tween 20, 100 μg/ml NeutrAvidin in phosphate buffered saline [PBS]) and incubated for 60 minutes at room temperature. Then the serum samples were transferred to a 384-well plate containing peptide-coated beads, with a liquid handler (CyBio Selma). After incubation at room temperature on a shaker for 75 minutes, all beads were washed with PBS-Tween (PBST) on a plate washer (no. EL406; BioTek) and resuspended in a solution containing secondary anti-human phycoerythrin-conjugated IgG Fcγ (Jackson ImmunoResearch). After 40 minutes of incubation, the beads were washed with PBST and subsequently measured in a Flexmap 3D system (Luminex). The median fluorescence intensity was used to quantify the interaction of serum antibody with given peptides.

Statistical analysis. Quantitative data from the animal experiments are expressed as the mean ± SEM. We compared antibody responses in Luminex immunoassays using a nonparametric Mann-Whitney U test. *P* values less than 0.05 were considered significant. The cutoff for assessing the reactivity of a given peptide in the Luminex immunoassay is the median + 5× the mean absolute deviation from healthy controls. To assess the correlation of Disease Activity Score in 28 joints (DAS28) (43) with the reactivity of P6–CIT247 at different time points, we performed a linear regression analysis by adjusting for the effects of sex, age, and shared epitope status of the patients. All statistical calculations were performed with R and various R packages (44).

RESULTS

Arthritis induction by COMP-specific antibodies in mice. We previously mapped the 15A11 binding site in the fourth EGF-like domain of murine COMP (Figure 1A) (19). The epitope comprises residues 232–252 and was designated P6. The primary sequence of the rat COMP epitope (GSPSPCHEKADCILERDGSRS) differs at 3 positions compared to human COMP (Figure 1A). Nevertheless, mAb 15A11 binds equally well to both mouse and human COMP protein (19).

It has been shown that mAb 15A11, in combination with a subarthritogenic dose of Col2-specific mAb M2139, can increase the severity of induced acute arthritis in naive mice (19). To assess the arthritogenicity of 15A11 itself, we performed antibody-induced arthritis experiments in B10.Q mice by single-dose injection of mAb 15A11. As shown in Figure 1B, a single dose of 9 mg mAb 15A11 or mAb M2139 induced arthritis, whereas, an irrelevant isotype IgG1 antibody did not induce arthritis if administered at a dose of 4 mg (Supplementary Figure 1, http://onlinelibrary.wiley.com/doi/10.1002/art.42072). Based on our previous results (19), we assumed that arthritis induction in this experiment was due to recognition of COMP by 15A11. We also observed signs of arthritis before LPS challenge in the group injected with mAb 15A11 and mAb M2139 together (Figures 1B and C), implying high arthritogenicity of these mAb in the B10.Q mouse strain.

To confirm the correlation with clinical observations, we performed a histologic assessment of synovial membrane and cartilage by examining the paws of arthritic mice after termination of the experiments. The findings indicated that synovitis, pannus formation, hyperplasia, and proteoglycan loss were present in mice with arthritis (Supplementary Figure 2, http://onlinelibrary.wiley.com/doi/10.1002/art.42072).

Cartilage binding of 15A11. To investigate whether 15A11 can bind directly to COMP in cartilage in vivo, we injected a biotinylated antibody into neonatal mice and prepared frozen sections of whole paws for immunostaining. For both in vitro and in vivo staining, we used 2-day-old neonates to avoid decalcification, which could redistribute antibodies in in vivo binding assays,

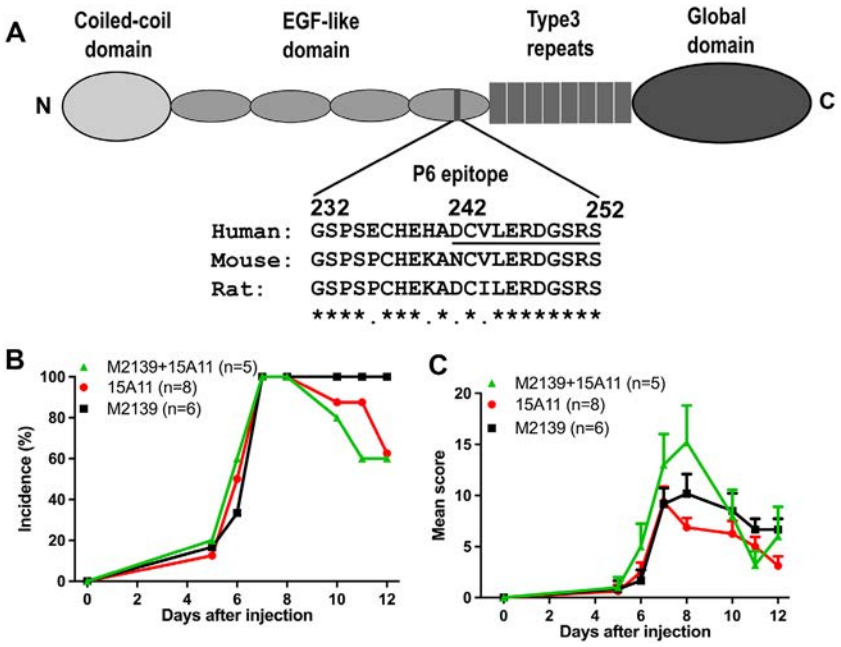

Figure 1. Arthritogenicity of cartilage oligomeric matrix protein (COMP)–specific monoclonal antibody (mAb) 15A11 in mice. **A**, Schematic presentation of the location of P6 in COMP. **B** and **C**, Incidence (**B**) and severity (**C**) of arthritis induced by passive transfer of antibodies to mice. Two-month-old naive male B10.Q mice were injected intravenously with either 9 mg of an equal combination of mAb M2139 and mAb 15A11, 9 mg of mAb M2139 alone, or 9 mg of mAb 15A11 alone. Each mouse was administered lipopolysaccharide (25 μg/mouse) intraperitoneally on day 5, and arthritis was scored daily for 12 days. Values in **C** are the mean ± SEM. EGF = epidermal growth factor. Color figure can be viewed in the online issue, which is available at http://onlinelibrary.wiley.com/doi/10.1002/art.42072/abstract.

as previously reported (45). Notably, injected antibodies can only target the cartilage surface in vivo, as the antibodies cannot penetrate very deeply into cartilage (45). For in vitro staining, all cartilage in the tissue section is accessible for staining; hence, it can be targeted by antibodies. As seen in Figure 2, we found that mAb 15A11 and anti-Col2 mAb M2139 demonstrated specific in vivo staining patterns on the lining of the articular cavity in native cartilage tissue. In contrast, tissue samples from control mice injected with PBS showed no staining. Furthermore, to investigate the binding capacity of 15A11 to cartilage in vitro, we performed an immunohistochemical analysis using frozen sections from naive neonatal mice. As seen in Figure 2, we observed strong widespread staining on cartilage for both 15A11 and M2139, while no staining was detectable in control samples. Taken together, these data show that COMP is accessible to antibodies on the cartilage surface in vivo.

Overall structure of the 15A11 Fab fragment in complex with COMP P6. In order to reveal the molecular basis of the interaction between 15A11 and COMP, we determined the crystal structure of the complex between the 15A11 Fab fragment and P6 peptide at 1.9Å resolution using molecular replacement. Data collection and refinement statistics are summarized in Supplementary Table 1 (http://onlinelibrary.wiley.com/doi/10.1002/art.42072).

The crystal structure belongs to space group $P2_12_12_1$ and contains 2 Fab–peptide complexes per asymmetric unit. Clear and continuous electron density was visible for residues 1–216 of the light chain and residues 1–137 and 142–222 of the heavy chain in the 15A11 Fab fragments.

Clearly defined electron density was only observed in the 11 C-terminal amino acids in the P6 peptide (^{242}DCILERDGSRS^{252}), which adopt a β-hairpin–like structure in the groove formed by the complementarity-determining regions (CDRs) of the 15A11 antibody (Figure 3B). An extension of the visible density of the side chain of C243 indicated that it is oxidized to *S*-hydroxy cysteine in the crystal used for structure determination. The β-hairpin conformation of P6 is stabilized by a total of 7 intrapeptide hydrogen bonds that primarily involve main chain atoms (Supplementary Table 2, http://onlinelibrary.wiley.com/doi/10.1002/art.42072). S252 alone formed 4 of these bonds, 2 with I244 via its backbone amide and carbonyl group, respectively, and the other 2 with D248 and E246 via its side chain hydroxyl group. In addition to the latter, E246 formed main chain atom-mediated hydrogen bonds with G249 and S250, while the seventh hydrogen bond linked the side chain of D248 with the backbone amide of S250. The N-terminal half of P6, which extended out of the binding groove into the surrounding solvent, can adopt multiple different conformations as indicated by the complete lack of electron density.

Interactions between the 15A11 Fab fragment and P6. Formation of the antibody–antigen complex covered ~47%

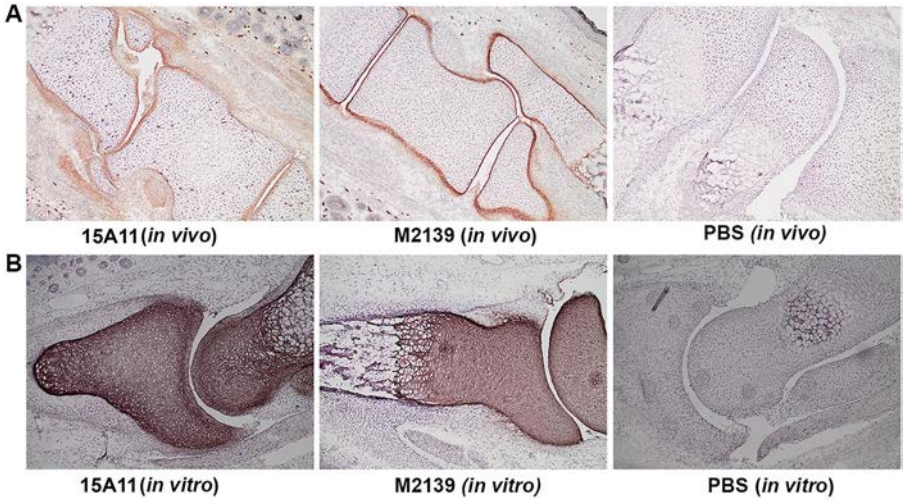

Figure 2. Specificity of mAb 15A11 binding to joint cartilage in vivo and in vitro. **A**, For histologic detection of the binding of mAb 15A11 to cartilage in vivo, a single dose of 100 μg of biotinylated anti-COMP mAb 15A11 was injected into 2-day-old neonatal BQ.Cia9i mice, and limbs were collected after 48 hours to make 5-μm cryosections. **B**, For in vitro analysis of the interaction between mAb 15A11 and cartilage, an immunohistochemical assay was performed on the 5-μm limb cryosections. Staining was performed with diaminobenzidine using ExtrAvidin–peroxidase as a detection system. Mice injected with biotinylated anti-Col2 mAb (M2139) and phosphate buffered saline (PBS) were used as a positive reference and blank control, respectively. Results shown are representative of 2–3 mice per group. Original magnification × 10. See Figure 1 for other definitions.

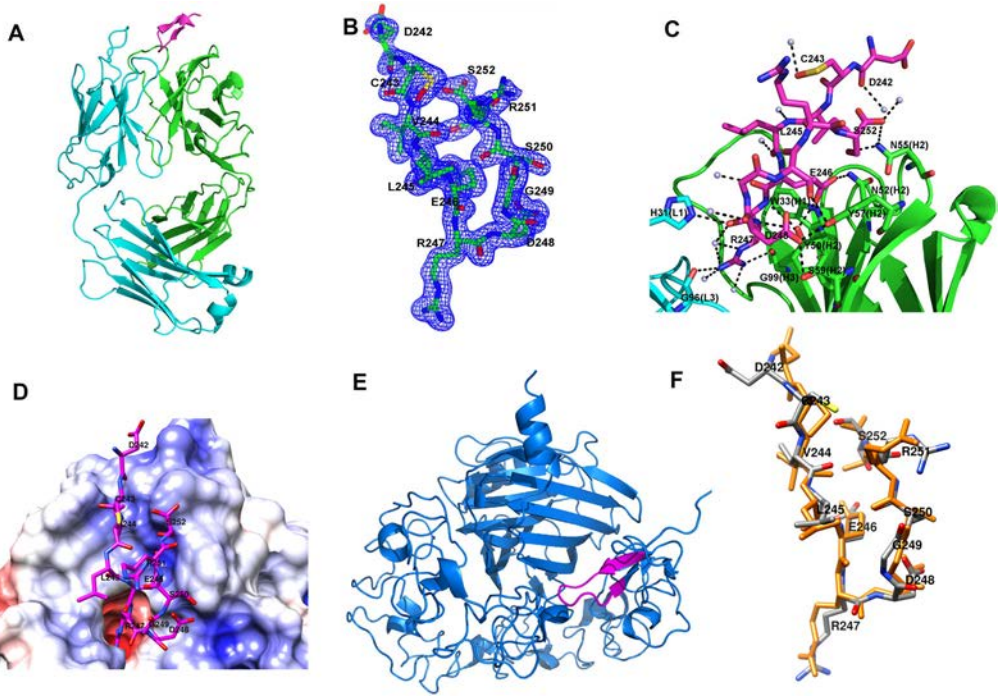

Figure 3. Crystal structure of the mAb 15A11–Fab complex. **A**, Overall complex of 15A11 Fab bound to COMP P6 peptide. The 15A11 Fab light chain (cyan) and heavy chain (green) are shown. **B**, Electron density map for the P6 peptide. The final $2F_o$–F_c difference map is contoured at a contour level of 1σ. **C**, Close-up stereoscopic view of the 15A11 paratope with bound P6 peptide. Fab residues and peptide residues (black) are distinguished by color. Water molecules (red) and hydrogen bonds (broken lines) are shown. **D**, Close-up stereoscopic view of the 15A11 paratope in surface presentation, with bound peptide shown. Colors of the paratope surface indicate the electrostatic potential as calculated using PyMOL. P6 residue R247 is deeply buried in a narrow pocket. **E**, P6 epitope–based superimposition of the crystal structure of truncated COMP (Protein Data Bank entry no. 3FBY [blue] with the P6 epitope [magenta]). **F**, Comparison of the conformations of 15A11-bound P6 peptide (yellow carbon atoms) and the P6 epitope within crystallized truncated COMP (magenta carbon atoms). See Figure 1 for other definitions.

(~640Å^2) and 2.5 % (~470Å^2) of the solvent-accessible surface area of the P6 peptide and the 15A11 Fab, respectively (Supplementary Tables 3 and 4, http://onlinelibrary.wiley.com/doi/10.1002/art.42072). The ^{244}ILERD^{248} motif of the peptide contributed the most to the interface, with additional significant contributions by C243, G249, S250, and S252, while D242 contacted the Fab exclusively via a water-mediated hydrogen bond to N55 from the heavy chain (Figure 3C). The only peptide residue with clearly visible electron density that was not involved in interactions with the 15A11 Fab fragment was R251. It was entirely solvent exposed and thus accessible to residues of a symmetry-related Fab fragment, with which it formed 3 hydrogen bonds via its main chain atoms. In the 15A11 Fab fragment, all CDRs except L2 were involved in epitope recognition, and H2 and H3 are the primary contact regions.

P6 epitope binding by Fab led to the formation of 11 direct and 7 water-mediated hydrogen bonds (Figure 3C and Supplementary Table 2, http://onlinelibrary.wiley.com/doi/10.1002/art.42072), as well as several hydrophobic and van der Waals interactions. These interactions were centered around E246 and R247, which are both entirely buried upon interface formation. The long side chain of R247 was inserted into a narrow, deep pocket in the center of the binding groove. Its entrance was formed by hydrophobic residues from both heavy chain and light chain CDRs, while increasing polarity and placement of E39 (light chain) at its deepest point provided shape and charge complementarity for recognition of R247 (Figure 3D). However, the depth of the pocket led to the formation of 2 water-mediated hydrogen bonds rather than a salt bridge with E39, which may explain why the mAb also efficiently recognized citrullinated P6 epitopes (see below). In addition, R247 was linked to G96 (L3), Y50 (H2), G99 (H3), H31 (L1), and W108 (H3) via direct or water-mediated hydrogen bonds, accounting for 8 of 18 total polar contacts between the P6 peptide and 15A11 Fab. Recognition of P6–E246 was mediated by an additional 4 hydrogen bonds, N52 and Y50 from the H2 CDR, W33 from H1, and H31 from the L1 CDR.

Of the P6 positions contacted by the mAb 15A11, all but 1 were conserved in rat, mouse, and human COMP sequences, explaining the observed cross-recognition (Figure 1A). The exception was I244, which was conservatively exchanged by valine in human COMP and mouse COMP. However, the absence of the additional methyl group likely has little influence on binding specificity and strength, as it indicates a more solvent-exposed region of the paratope and thus most likely does not significantly contribute to the interactions.

Structure of the P6 epitope in native COMP. To understand why mAb 15A11 can bind to native COMP and the P6 peptide, we compared the structure of the 15A11-bound peptide (rat sequence) to the native epitope within human COMP (PDB no. 3FBY). As shown in Figure 3E, the P6 epitope was located near the N-terminal of the crystallized truncated construct, which contained the last EGF-like repeat, the type III repeats, and the C-terminal domain of human COMP. As in the 15A11 Fab complex, it adopted a β-hairpin conformation (Figure 3F). The backbone root mean square deviation of the superimposition of the Cα atoms of residues 242–252 of the 15A11-bound and native P6 epitope was 0.63–0.80Å, which indicates that the conformation of the epitope itself remains largely unaltered upon interaction with mAb 15A11, allowing direct recognition both in vivo and in vitro. However, binding of 15A11 would require conformational changes in COMP to make the P6 epitope more accessible than in the crystallized construct, as serious clashes occur between the Fab and the C-terminal domains of the COMP protein superimposed peptides in both crystal structures. It has been suggested that the positioning/orientation and the conformation of this domain in COMP protein are affected by cations (46).

Modulation of 15A11 binding to COMP by calcium ions. Since binding of calcium ions to COMP alters the conformation of the individual domains and thereby the interaction between COMP and various substrates (46), we hypothesized that this might also affect binding of mAb 15A11 to native COMP. Therefore, we performed an ELISA to measure the binding behavior of 15A11 at different Ca^{2+} concentrations. As shown in Figure 4A, mAb 15A11 binding to COMP was calcium dependent, while binding of another COMP-specific mAb, 16B, was calcium independent.

We also measured the binding affinity of mAb 15A11 for COMP by surface plasmon resonance with or without the addition of 10 m*M* Ca^{2+}. Since the algorithm we used could not fit our experimental data with the default parameter values, we could not obtain reliable kinetics values. However, we obtained the steady-state affinity (K_d) value by fitting the binding curves shown in Figures 4B and C. The mAb 15A11 showed slightly stronger binding to COMP in the absence of calcium (K_d = 173.6 n*M*) than in the presence of calcium (K_d = 413.8 n*M*). In particular, the level of binding response (resonance units) in the presence of calcium ions was significantly higher than without calcium (Figures 4B and C), indicating that there were more COMP molecules captured by the 15A11-immobilized sensor chip. These data demonstrate that the Ca^{2+} concentration can modulate the binding strength of mAb 15A11 to COMP, most likely by affecting the conformation of the fourth EGF-like repeat, making the P6 epitope more accessible. Interestingly, we found that 15A11 had comparable binding capability toward P6–CIT247 and P6–R247 (Figure 4D), which can be explained by the negatively charged binding pocket in residue 247.

Identification of P6 as an immunodominant B cell epitope in RA patients. To assess the prevalence of anti-P6 antibodies and their association with RA, we measured antibody

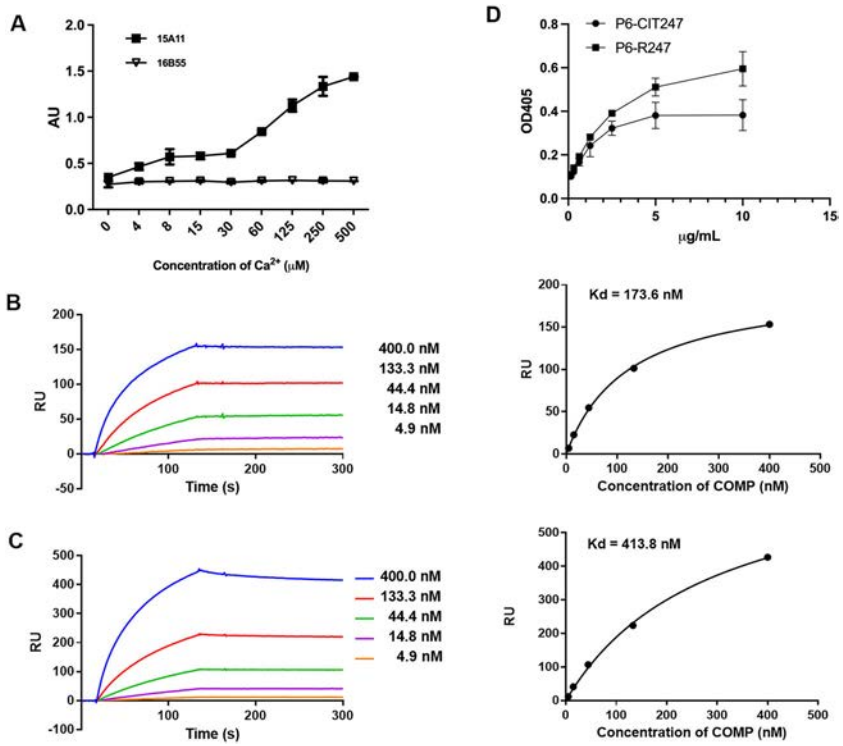

Figure 4. Modulation of binding by calcium. **A**, Influence of calcium ions on the interaction between mAb 15A11 and COMP, measured by enzyme-linked immunosorbent assay (ELISA). COMP-specific mAb 16B was used as a control. **B** and **C**, Association and dissociation curves for the interaction of 15A11 with COMP with (**C**) or without (**B**) 10 m*M* $CaCL_2$, measured by surface plasmon resonance. **D**, Binding of 15A11 to P6–CIT247 or P6–R247, measured by ELISA. Values in **A** and **D** are the mean ± SEM. RU = resonance unit (see Figure 1 for other definitions). Color figure can be viewed in the online issue, which is available at http://onlinelibrary.wiley.com/doi/10.1002/art.42072/abstract.

responses to the P6 peptide in a Swedish cohort consisting of 504 patients with early untreated RA and 290 healthy controls, using Luminex immunoassay. Both linear and cyclic P6 unmodified peptides (P6–R-R and P6–R247, respectively) were immobilized on magnetic beads to measure antibody responses. Similarly, to study the citrulline dependence of the antibody response to this epitope, we also analyzed 3 citrullinated linear peptides (P6–R-CIT, P6–CIT-R, and P6–CIT-CIT) and 1 citrullinated cyclic peptide (P6–CIT247). As shown in Figure 5, statistically significant antibody reactivity toward all P6 peptide variants was detected in RA patients compared to healthy controls ($P < 0.001$). Regarding the linear forms of the P6 epitope, autoantibody responses to the 3 citrullinated variants P6–R-CIT ($P = 1.13 \times 10^{-10}$), P6–CIT-R ($P = 6.37 \times 10^{-10}$), and P6–CIT-CIT ($P = 4.11 \times 10^{-9}$) were more significant than the response to the unmodified form P6–R-R ($P = 8.24 \times 10^{-3}$). Similarly, the cyclic form of the citrullinated P6 epitope P6–CIT247 demonstrated much higher reactivity in RA patients than its unmodified form P6–R247 ($P = 5.72 \times 10^{-3}$ and $P = 2.47 \times 10^{-33}$, respectively).

Among all peptides, P6–CIT247 had the highest prevalence (38%). In comparison, we also measured the prevalence of antibody responses to 2 classic citrullinated peptides, citrullinated peptide 1 (CCP-1) and citrullinated α-enolase peptide 1 (CEP-1), in the same cohort. CCP-1 and CEP-1 were found in 57% and 56% of patients, respectively, which is comparable to previously reported results (47,48). Although most RA patients who were positive for P6–CIT247 antibody were also positive for CEP-1 and CCP-1, ~8% of the patients were positive for P6–CIT247 only (Figure 6). Interestingly, the cyclic form of the P6 epitope demonstrated much higher reactivity than the corresponding linear form, possibly because the β-hairpin conformation required for recognition is better stabilized in cyclic peptides (see above).

More importantly, we evaluated potential associations between autoantibody specificity and DAS28 scores over time using multivariate regression analysis with adjustment for the effects of sex, age, and shared epitope allele status. As shown in Supplementary Table 5 (http://onlinelibrary.wiley.com/doi/10.1002/art.42072), patients who responded to P6–CIT247 appeared to have more severe disease activity at 12 months ($P = 0.051$) and 24 months ($P = 0.029$) after diagnosis compared to those who did not respond to P6–CIT247.

DISCUSSION

In this study, we investigated the properties of a COMP-specific antibody that recognizes native COMP protein in joint cartilage, causing arthritis after injection into mice. The pathogenicity of anti-COMP antibodies is likely relevant in humans, and the

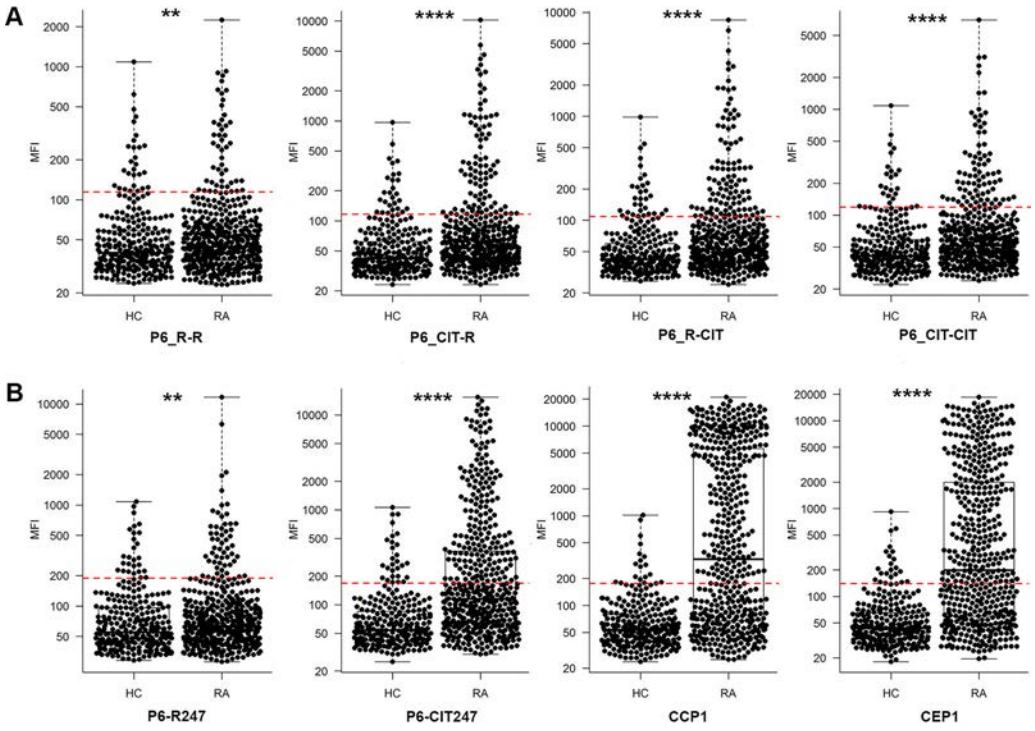

Figure 5. Human serum IgG response to P6 peptide variants in patients with rheumatoid arthritis (RA) compared to healthy controls (HC). IgG responses to linear (**A**) and cyclic (**B**) forms of the P6 epitope are shown. Citrullinated peptides P6–R-CIT, P6–CIT-R, P6–CIT-CIT, and P6–CIT247 showed higher positive responses than the noncitrullinated peptides P6–R-R (linear) and P6–R247 (cyclic). IgG levels were measured by Luminex assay. Symbols represent the reactivity of individual serum samples with the indicated peptide; bars show the mean ± SEM. Boxed areas denote box plots, where the boxes represent the 25th to 75th percentiles, the lines within the boxes represent the median, and the lines outside the boxes represent the 10th and 90th percentiles. Dashed red lines show the cutoffs for positivity, defined as the median + 5× the mean absolute deviation in median fluorescence intensity (MFI) values in the healthy controls. ** = $P < 0.01$; **** = $P < 0.0001$, by Mann-Whitney U test. CCP-1 = citrullinated peptide 1; CEP-1 = citrullinated α-enolase peptide 1. Color figure can be viewed in the online issue, which is available at http://onlinelibrary.wiley.com/doi/10.1002/art.42072/abstract.

antibody cross-reacts with human COMP. Furthermore, antibodies reacting with both native and citrullinated variants of COMP are indeed detectable in RA. To elucidate the molecular determinants by which arthritogenic mAb 15A11 specifically recognizes COMP in joint cartilage, we determined the crystal structure of its Fab fragment in complex with the P6 epitope, which according to findings from our previous epitope mapping study, spans residues 232–252 of mouse COMP (19). The interactions observed

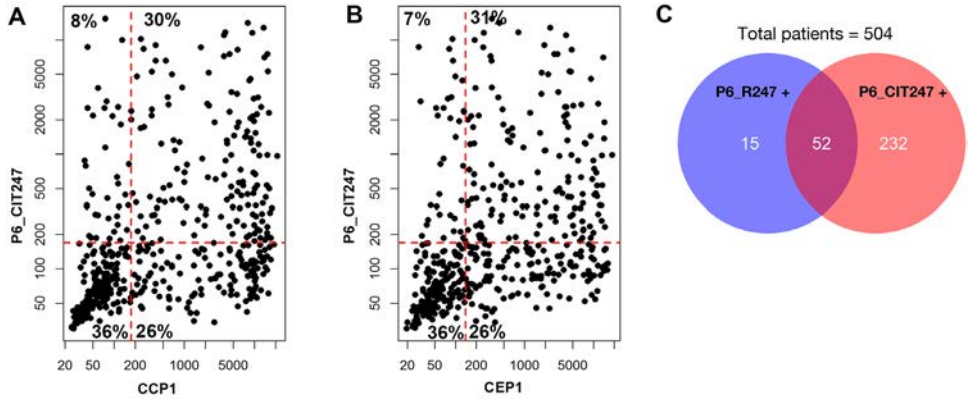

Figure 6. Autoantibodies against P6–CIT247 are highly associated with autoantibodies toward other citrullinated peptides. **A** and **B**, Rheumatoid arthritis patient–derived autoantibodies reactive with P6–CIT247 in relation to those responding to either citrullinated peptide 1 (CCP-1) (**A**) or citrullinated α-enolase peptide 1 (CEP-1) (**B**). Dashed lines show the cutoffs for positivity, defined as the median + 5× the mean absolute deviation from corresponding healthy controls. **C**, Venn diagram showing overlap of responses to P6–R247 and to P6–CIT247. Color figure can be viewed in the online issue, which is available at http://onlinelibrary.wiley.com/doi/10.1002/art.42072/abstract.

between the 15A11 antibody and P6 epitope in the crystal structure explain how this antibody can cross-react with the native COMP protein, thereby binding cartilage in vivo and efficiently inducing arthritis and joint pain. Binding is mainly governed by paratope shape–complementarity to the epitope in a β-hairpin conformation and the availability of a deep, narrow, and appropriately charged binding pocket for residue R247 of P6. When the structure of the P6 peptide bound to the 15A11 Fab fragment is superimposed onto the corresponding sequence in the COMP crystal structure, it becomes apparent that recognition of native COMP by mAb requires an increase in accessibility more than conformational changes in the epitope. The sequence dependency of epitope recognition is further highlighted by the fact that almost all residues of P6 visible in the crystal structure are conserved in human, mouse, and rat COMP, with the only exception representing a conservative exchange of residues.

Degradation of COMP and associated ECM constituents is mainly mediated by ADAMTS proteins and matrix metalloproteinase 13 (14) targeting the 4 evolutionarily conserved EGF-like repeats (49,50). Also, other COMPs interact with the EGF-like domain. Their interaction with cells through integrins could potentially affect cell adhesion during immune responses as well as in apoptosis (51,52).

It has also been shown that injection of a set of monoclonal IgG antibodies against COMP induces arthritis and enhances the development of cartilage antibody–induced arthritis when combined with anti-Col2 IgG antibodies (19). This study shows that a single injection of mAb 15A11 alone is sufficient to mount an immune response in naive mice and induce severe arthritis. This supports the notion that autoantibodies to COMP can play a pathogenic role in experimental arthritis by directly binding to exposed surface epitopes of COMP in joint cartilage, resulting in tissue damage (see Figure 2 and Supplementary Figure 1, http://onlinelibrary.wiley.com/doi/10.1002/art.42072). Hence, COMP antibodies act similarly to autoantibodies toward Col2, which are also well known to be pathogenic in mice by interacting directly with the native triple-helical conformation of Col2 in cartilage (53).

In addition to its pathogenic role in mice, COMP might also be important as a biomarker for disease activity and joint destruction in RA (15). Increased COMP fragments are detectable in serum and synovial fluid in RA and other inflammatory and degenerative diseases such as OA and systemic sclerosis (15). However, our current knowledge about autoimmunity to COMP in RA is limited.

Since the P6 epitope is a major pathogenic epitope in COMP-induced arthritis in mice and is conserved in humans, we tested the antibody response in RA. Interestingly, we detected a significant response not only to the native epitope but also to the citrullinated P6 epitope. Similar to Col2, antibodies recognizing native COMP epitopes are less frequently observed compared to their citrullinated counterparts. The higher frequency of citrullinated COMP–reactive antibodies may explain in part why antibodies specifically interacting with citrulline could promiscuously respond to many different peptides (54,55). However, a minor, potentially pathogenic fraction of antibodies could more specifically recognize citrullinated and native COMP within cartilage and thereby mediate arthritis.

Interestingly, COMP fragments are released into body fluids such as synovial fluid and blood (15). Joint synovium and synovial fluid contain peptidylarginine deiminases (PADs), which catalyze the modification of arginine to citrulline (56). Hence, the P6 epitope (and probably other unknown COMP fragments) are more likely to be modified by extracellular PADs, leading to neoantigens providing targets for antibodies.

The observed critical role of Ca^{2+} ions in the 15A11–COMP interaction was dose dependent. It is most likely mediated via conformational changes in COMP, as in silico docking of 15A11 Fab onto the P6 epitope in the crystal structure of (truncated) COMP in the absence of Ca^{2+} ions revealed that the epitope would otherwise be inaccessible to mAb 15A11. It has been shown that the pentameric form of COMP exists in a more compact conformation in the presence of Ca^{2+} (14,44). Interestingly, this finding raises the possibility that an increased extracellular level of calcium in inflamed joints could lead to increased accessibility of targeted epitopes of native COMP and increased in situ citrullination. This could lead to the joint-specific formation of local immune complexes playing essential roles in increasing joint pain and inducing arthritis.

In summary, our findings provide a structural basis for understanding the pathogenic effect of an autoantibody that specifically targets a selected protein domain in native COMP accessible in joints. This could also have functional importance in RA, as this antibody, together with antibodies to citrullinated variants of the same epitope, are detectable in RA serum and may be associated with increased disease activity. These findings warrant further study of anti-COMP antibodies as potential biomarkers in RA.

AUTHOR CONTRIBUTIONS

All authors were involved in drafting the article or revising it critically for important intellectual content, and all authors approved the final version to be published. Dr. Holmdahl had full access to all of the data in the study and takes responsibility for the integrity of the data and the accuracy of the data analysis.

Study conception and design. Ge, Holmdahl.

Acquisition of data. Ge, Tong, Lönnblom, Liang, Cai, Fahlquist-Hagert, Li, Kastbom, Gjertsson, Dobritzsch, Holmdahl.

Analysis and interpretation of data. Ge, Tong, Lönnblom, Liang, Cai, Fahlquist-Hagert, Li, Kastbom, Gjertsson, Dobritzsch, Holmdahl.

ACKNOWLEDGMENTS

We thank Diamond Light Source for providing access to synchrotron radiation (proposal mx8492) and thank the staff at Beamline I03 for assistance with data collection. We are also grateful to personnel at the Protein Science Facility at Karolinska Institute/SciLifeLab for assistance with part of the study.

REFERENCES

1. McInnes IB, Schett G. The pathogenesis of rheumatoid arthritis [review]. N Engl J Med 2011;365:2205–19.
2. Sangha O. Epidemiology of rheumatic diseases. Rheumatology (Oxford) 2000;39 Suppl:3–12.
3. Klareskog L, Catrina AI, Paget S. Rheumatoid arthritis. Lancet 2009; 373:659–72.
4. Stastny P. Association of the B-cell alloantigen DRw4 with rheumatoid arthritis. N Engl J Med 1978;298:869–71.
5. Tuomi T, Heliovaara M, Palosuo T, Aho K. Smoking, lung function, and rheumatoid factors. Ann Rheum Dis 1990;49:753–6.
6. Okada Y, Wu D, Trynka G, Raj T, Terao C, Ikari K, et al. Genetics of rheumatoid arthritis contributes to biology and drug discovery. Nature 2014;506:376–81.
7. Thorn J. The inflammatory response in humans after inhalation of bacterial endotoxin: a review. Inflamm Res 2001;50:254–61.
8. Christiani DC, Wang XR, Pan LD, Zhang HX, Sun BX, Dai H, et al. Longitudinal changes in pulmonary function and respiratory symptoms in cotton textile workers. A 15-yr follow-up study. Am J Respir Crit Care Med 2001;163:847–53.
9. Stolt P, Kallberg H, Lundberg I, Sjogren B, Klareskog L, Alfredsson L, et al. Silica exposure is associated with increased risk of developing rheumatoid arthritis: results from the Swedish EIRA study. Ann Rheum Dis 2005;64:582–6.
10. Scherer HU, Huizinga TW, Kronke G, Schett G, Toes RE. The B cell response to citrullinated antigens in the development of rheumatoid arthritis. Nat Rev Rheumatol 2018;14:157–69.
11. Oldberg A, Antonsson P, Lindblom K, Heinegård D. COMP (cartilage oligomeric matrix protein) is structurally related to the thrombospondins. J Biol Chem 1992;267:22346–50.
12. Smith R, Zunino L, Webbon P, Heinegård D. The distribution of cartilage oligomeric matrix protein (COMP) in tendon and its variation with tendon site, age and load. Matrix Biol 1997;16:255–71.
13. Tan K, Duquette M, Joachimiak A, Lawler J. The crystal structure of the signature domain of cartilage oligomeric matrix protein: implications for collagen, glycosaminoglycan and integrin binding. FASEB J 2009;23:2490–501.
14. Acharya C, Yik JH, Kishore A, Van Dinh V, Di Cesare PE, Haudenschild DR. Cartilage oligomeric matrix protein and its binding partners in the cartilage extracellular matrix: interaction, regulation and role in chondrogenesis. Matrix Biol 2014;37:102–11.
15. Tseng S, Reddi AH, Di Cesare PE. Cartilage Oligomeric Matrix Protein (COMP): a biomarker of arthritis. Biomark Insights 2009;4: 33–44.
16. Happonen KE, Saxne T, Aspberg A, Mörgelin M, Heinegård D, Blom AM. Regulation of complement by cartilage oligomeric matrix protein allows for a novel molecular diagnostic principle in rheumatoid arthritis. Arthritis Rheum 2010;62:3574–83.
17. Carlsén S, Hansson AS, Olsson H, Heinegård D, Holmdahl R. Cartilage oligomeric matrix protein (COMP)-induced arthritis in rats. Clin Exp Immunol 1998;114:477–84.
18. Carlsen S, Nandakumar KS, Bäcklund J, Holmberg J, Hultqvist M, Vestberg M, et al. Cartilage oligomeric matrix protein induction of chronic arthritis in mice. Arthritis Rheum 2008;58:2000–11.
19. Geng H, Nandakumar KS, Pramhed A, Aspberg A, Mattsson R, Holmdahl R. Cartilage oligomeric matrix protein specific antibodies are pathogenic. Arthritis Res Ther 2012;14:R191.
20. Li Y, Tong D, Liang P, Lonnblom E, Viljanen J, Xu B, et al. Cartilage-binding antibodies initiate joint inflammation and promote chronic erosive arthritis. Arthritis Res Ther 2020;22:120.
21. Farinotti AB, Wigerblad G, Nascimento D, Bas DB, Urbina CM, Nandakumar KS, et al. Cartilage-binding antibodies induce pain through immune complex-mediated activation of neurons. J Exp Med 2019;216:1904–24.
22. Souto-Carneiro MM, Burkhardt H, Muller EC, Hermann R, Otto A, Kraetsch HG, et al. Human monoclonal rheumatoid synovial B lymphocyte hybridoma with a new disease-related specificity for cartilage oligomeric matrix protein. J Immunol 2001;166:4202–8.
23. Ahlqvist E, Ekman D, Lindvall T, Popovic M, Forster M, Hultqvist M, et al. High-resolution mapping of a complex disease, a model for rheumatoid arthritis, using heterogeneous stock mice. Hum Mol Genet 2011;20:3031–41.
24. Vaartjes D, Klaczkowska D, Cragg MS, Nandakumar KS, Backdahl L, Holmdahl R. Genetic dissection of a major haplotype associated with arthritis reveal FcγR2b and FcγR3 to act additively. Eur J Immunol 2021;51:682–93.
25. Raposo B, Dobritzsch D, Ge C, Ekman D, Xu B, Lindh I, et al. Epitope-specific antibody response is controlled by immunoglobulin V(H) polymorphisms. J Exp Med 2014;211:405–11.
26. Winter G. Xia2: an expert system for macromolecular crystallography data reduction. J Appl Crystallogr 2010;43:186–90.
27. Zhang Z, Sauter NK, van den Bedem H, Snell G, Deacon AM. Automated diffraction image analysis and spot searching for high-throughput crystal screening. J Appl Crystallogr 2006;39:112–9.
28. Sauter NK, Grosse-Kunstleve RW, Adams PD. Robust indexing for automatic data collection. J Appl Crystallogr 2004;37:399–409.
29. Kabsch W. Xds. Acta Crystallogr D Biol Crystallogr 2010;66:125–32.
30. Evans P. Scaling and assessment of data quality. Acta Crystallogr D Biol Crystallogr 2006;62:72–82.
31. Collaborative Computational Project N. The CCP4 suite: programs for protein crystallography. Acta Crystallogr D Biol Crystallogr 1994;50:760–3.
32. Evans PR, Murshudov GN. How good are my data and what is the resolution? Acta Crystallogr D Biol Crystallogr 2013;69:1204–14.
33. Mccoy AJ, Grosse-Kunstleve RW, Adams PD, Winn MD, Storoni LC, Read RJ. Phaser crystallographic software. J Appl Crystallogr 2007; 40:658–74.
34. Emsley P, Lohkamp B, Scott WG, Cowtan K. Features and development of Coot. Acta Crystallogr D Biol Crystallogr 2010;66:486–501.
35. Murshudov GN, Vagin AA, Dodson EJ. Refinement of macromolecular structures by the maximum-likelihood method. Acta Crystallogr D Biol Crystallogr 1997;53:240–55.
36. Krissinel E, Henrick K. Inference of macromolecular assemblies from crystalline state. J Mol Biol 2007;372:774–97.
37. DeLano WL. The PyMOL molecular graphics system, version 1.2r3pre, Schrödinger, LLC. 2002.
38. Arnett FC, Edworthy SM, Bloch DA, McShane DJ, Fries JF, Cooper NS, et al. The American Rheumatism Association 1987 revised criteria for the classification of rheumatoid arthritis. Arthritis Rheum 1988;31: 315–24.
39. Svärd A, Skogh T, Alfredsson L, Ilar A, Klareskog L, Bengtsson C, et al. Associations with smoking and shared epitope differ between IgA- and IgG-class antibodies to cyclic citrullinated peptides in early rheumatoid arthritis. Arthritis Rheumatol 2015;67:2032–7.
40. Ayoglu B, Haggmark A, Khademi M, Olsson T, Uhlen M, Schwenk JM, et al. Autoantibody profiling in multiple sclerosis using arrays of human protein fragments. Mol Cell Proteomics 2013;12:2657–72.
41. Schwenk JM, Gry M, Rimini R, Uhlen M, Nilsson P. Antibody suspension bead arrays within serum proteomics. J Proteome Res 2008;7: 3168–79.
42. Hamsten C, Neiman M, Schwenk JM, Hamsten M, March JB, Persson A. Recombinant surface proteomics as a tool to analyze humoral immune responses in bovines infected by mycoplasma mycoides subsp mycoides small colony type. Mol Cell Proteomics 2009;8:2544–54.

43. Prevoo ML, van 't Hof MA, Kuper HH, van Leeuwen MA, van de Putte LB, van Riel PL. Modified disease activity scores that include twenty-eight–joint counts: development and validation in a prospective longitudinal study of patients with rheumatoid arthritis. Arthritis Rheum 1995;38:44–8.
44. Team RC. R: a language and environment for statistical computing. Vienna, Austria: R Foundation for Statistical Computing; 2021.
45. Holmdahl R, Jansson L, Larsson A, Jonsson R. Arthritis in DBA/1 mice induced with passively transferred type II collagen immune serum. Immunohistopathology and serum levels of anti-type II collagen auto-antibodies. Scand J Immunol 1990; 31:147–57.
46. Thur J, Rosenberg K, Nitsche DP, Pihlajamaa T, Ala-Kokko L, Heinegard D, et al. Mutations in cartilage oligomeric matrix protein causing pseudoachondroplasia and multiple epiphyseal dysplasia affect binding of calcium and collagen I, II, and IX. J Biol Chem 2001; 276:6083–92.
47. Lundberg K, Kinloch A, Fisher BA, Wegner N, Wait R, Charles P, et al. Antibodies to citrullinated α-enolase peptide 1 are specific for rheumatoid arthritis and cross-react with bacterial enolase. Arthritis Rheum 2008;58:3009–19.
48. Schellekens GA, de Jong BA, van den Hoogen FH, van de Putte LB, van Venrooij WJ. Citrulline is an essential constituent of antigenic determinants recognized by rheumatoid arthritis-specific autoantibodies. J Clin Invest 1998;101:273–81.
49. Liu CJ, Kong W, Xu K, Luan Y, Ilalov K, Sehgal B, et al. ADAMTS-12 associates with and degrades cartilage oligomeric matrix protein. J Biol Chem 2006;281:15800–8.
50. Liu CJ, Kong W, Ilalov K, Yu S, Xu K, Prazak L, et al. ADAMTS-7: a metalloproteinase that directly binds to and degrades cartilage oligomeric matrix protein. FASEB J 2006;20:988–90.
51. Kansas GS, Saunders KB, Ley K, Zakrzewicz A, Gibson RM, Furie BC, et al. A role for the epidermal growth factor-like domain of P-selectin in ligand recognition and cell adhesion. J Cell Biol 1994; 124:609–18.
52. Park SY, Kim SY, Jung MY, Bae DJ, Kim IS. Epidermal growth factor-like domain repeat of stabilin-2 recognizes phosphatidylserine during cell corpse clearance. Mol Cell Biol 2008;28:5288–98.
53. Holmdahl R, Mo JA, Jonsson R, Karlstrom K, Scheynius A. Multiple epitopes on cartilage type II collagen are accessible for antibody binding in vivo. Autoimmunity 1991;10:27–34.
54. Ge C, Holmdahl R. The structure, specificity and function of anti-citrullinated protein antibodies [review]. Nat Rev Rheumatol 2019;75: 503–8.
55. Ge C, Xu B, Liang B, Lönnblom E, Lundström SL, Zubarev RA, et al. Structural basis of cross-reactivity of anti-citrullinated protein antibodies. Arthritis Rheumatol 2019;71:210–21.
56. Kinloch A, Lundberg K, Wait R, Wegner N, Lim NH, Zendman AJ, et al. Synovial fluid is a site of citrullination of autoantigens in inflammatory arthritis. Arthritis Rheum 2008;58:2287–95.

Arthritis & Rheumatology
Vol. 74, No. 6, June 2022, pp 972–983
DOI 10.1002/art.42065

American College of Rheumatology
Empowering Rheumatology Professionals

Central Role of Semaphorin 3B in a Serum-Induced Arthritis Model and Reduced Levels in Patients With Rheumatoid Arthritis

Ana Igea,[1] Tiago Carvalheiro,[2] Beatriz Malvar-Fernández,[3] Sara Martinez-Ramos,[4] Carlos Rafael-Vidal,[4] Ellis Niemantsverdriet,[5] Jezabel Varadé,[1] Andrea Fernández-Carrera,[1] Norman Jimenez,[4] Trudy McGarry,[6] Angela Rodriguez-Trillo,[7] Douglas Veale,[8] Ursula Fearon,[6] Carmen Conde,[7] Jose M. Pego-Reigosa,[4] África González-Fernández,[1] Kris A. Reedquist,[2] Timothy R. D. J. Radstake,[2] Annette van der Helm-Van Mil,[5] and Samuel García[3]

Objective. Semaphorin 3B (Sema3B) decreases the migratory and invasive capacities of fibroblast-like synoviocytes (FLS) in rheumatoid arthritis (RA) and suppresses expression of matrix metalloproteinases. We undertook this study to examine the role of Sema3B in a mouse model of arthritis and its expression in RA patients.

Methods. Clinical responses, histologic features, and FLS function were examined in wild-type (WT) and Sema3B$^{-/-}$ mice in a K/BxN serum transfer model of arthritis. Protein and messenger RNA expression of Sema3B in mouse joints and murine FLS, as well as in serum and synovial tissue from patients with arthralgia and patients with RA, was determined using enzyme-linked immunosorbent assay, immunoblotting, quantitative polymerase chain reaction, and RNA sequencing. FLS migration was determined using a wound closure assay.

Results. The clinical severity of serum-induced arthritis was significantly higher in Sema3B$^{-/-}$ mice compared to WT mice. This was associated with increased expression of inflammatory mediators and increased migratory capacity of murine FLS. Administration of recombinant mouse Sema3B reduced the clinical severity of serum-induced arthritis and the expression of inflammatory mediators. Sema3B expression was significantly lower in the synovial tissue and serum of patients with established RA compared to patients with arthralgia. Serum Sema3B levels were elevated in patients with arthralgia that later progressed to RA, but not in those who did not develop RA; however, these levels drastically decreased 1 and 2 years after RA development.

Conclusion. Sema3B expression plays a protective role in a mouse model of arthritis. In RA patients, expression levels of Sema3B in the serum depend on the disease stage, suggesting different regulatory roles in disease onset and progression.

Dr. Carvalheiro's work was supported by the Portuguese National Funding Agency for Science, Research, and Technology (grants SFRH/BD/93526/2013 and SFRH/BD/116082/2016). Dr. Martinez-Ramos and Mr. Rafael-Vidal's work was supported by Xunta de Galicia (award IN606A-2021/024 to Dr. Martinez-Ramos and award IN606A-2020/043 to Mr. Rafael-Vidal). Dr. González-Fernández work was supported by the Xunta de Galicia Grupo Referencia Competitiva (grant ED431C 2016/041) and Centro de Investigaciones Biomedicas (co-financed by the European Regional Development Fund Operative Program ERDF Galicia 2014-2020 grant ERDF OP ED431G/02). Dr. García's work was supported by the Pfizer 2017 ASPIRE Dutch I CRP competitive grant program (grant WI229944), the Instituto de Salud Carlos III (project PI20/01472, co-funded by the European Regional Development Fund), and the Instituto de Salud Carlos III and European Social Fund Miguel Servet program (award CP19/00005).

[1]Ana Igea, PhD, Jezabel Varadé, PhD, Andrea Fernández-Carrera, PhD, África González-Fernández, MD, PhD: Universidade de Vigo, Campus Universitario Lagoas Marcosende, and Galicia Sur Health Research Institute, Servicio Galego de Saúde Universidade de Vigo, Vigo, Spain; [2]Tiago Carvalheiro, MSc, PhD, Kris A. Reedquist, PhD, Timothy R. D. J. Radstake, MD, PhD: University of Utrecht, Utrecht, The Netherlands; [3]Beatriz Malvar-Fernández, BSc, Samuel García, PhD: University of Utrecht, Utrecht, The Netherlands, and Galicia Sur Health Research Institute and University Hospital Complex of Vigo, Vigo, Spain; [4]Sara Martinez-Ramos, DVM, Carlos Rafael-Vidal, MSc, Norman Jimenez, MSc, Jose M. Pego-Reigosa, MD, PhD: Galicia Sur Health Research Institute, Servicio Galego de Saúde Universidade de Vigo, and University Hospital Complex of Vigo, Vigo, Spain; [5]Ellis Niemantsverdriet, PhD, Annette van der Helm-Van Mil, MD, PhD: Erasmus Medical Center, Rotterdam, The Netherlands, and Leiden University Medical Center, Leiden, the Netherlands; [6]Trudy McGarry, PhD, Ursula Fearon, MD, PhD: St. Vincent's University Hospital and University College Dublin, and Trinity College Dublin, Dublin, Ireland; [7]Angela Rodriguez-Trillo, PhD, Carmen Conde, MD, PhD: Hospital Clínico Universitario de Santiago de Compostela, Servicio Galego de Saúde, Santiago de Compostela, Spain; [8]Douglas Veale, MD, PhD: St. Vincent's University Hospital and University College Dublin, Dublin, Ireland.

Author disclosures are available at https://onlinelibrary.wiley.com/action/downloadSupplement?doi=10.1002%2Fart.42065&file=art42065-sup-0001-Disclosureform.pdf.

Address correspondence to Samuel García, PhD, Rheumatology & Immune-mediated Diseases Iridis group, Galicia Sur Health Research Institute, Hospital Álvaro Cunqueiro, Estrada Clara Campoamor Number 341, 36312 Vigo, Pontevedra, Spain. Email: samuel.garcia@iisgaliciasur.es.

Submitted for publication October 19, 2020; accepted in revised form January 4, 2022.

INTRODUCTION

Rheumatoid arthritis (RA) is an immune-mediated rheumatic and musculoskeletal disease marked by persistent synovial inflammation and progressive joint destruction, leading to disability and loss of quality of life (1,2). Most RA patients respond to the current therapies and reduction in disease progression is achieved; however, in 20–25% of patients, low disease activity is not reached. Moreover, current therapies have moderate-to-severe side effects, including higher cardiovascular risk and immunosuppression (3,4). Therefore, there is still an ultimate need for therapeutic molecules that can be targeted to reduce inflammation and joint destruction.

Semaphorin 3B (Sema3B) is a secreted protein belonging to the semaphorin family involved in different biologic processes, such as apoptosis, angiogenesis, cell migration, and invasion (5–7). A recent study from our group implicated Sema3B in the pathogenesis of RA (8). We have shown that Sema3B expression is reduced in the synovium of patients with early RA compared to patients with undifferentiated arthritis. Sema3B expression negatively correlated with clinical disease parameters and the expression of inflammatory mediators. Recombinant Sema3B reduces the migration and invasive capacity of RA fibroblast-like synoviocytes (FLS) in vitro (8). Taken together, these findings suggest that Sema3B might be a potential therapeutic target in RA. In the current study, we examined the functional role of Sema3B in a mouse model of arthritis and determined the local and systemic levels of Sema3B during the progression of RA.

PATIENTS AND METHODS

Patients and collection of samples. Serum samples and synovial biopsy specimens were obtained at the St. Vincent's University Hospital in Dublin, Ireland from patients with established RA who had clinically active inflamed joints (n = 10) and from patients with arthralgia (n = 8). Patients with arthralgia were defined as subjects with symptoms of aches and pains without clinical signs of synovitis or increased C-reactive protein levels (mean C-reactive protein level <5 mg/liter) but who were positive for circulating rheumatoid factor (RF+) and anti–citrullinated protein antibodies (ACPAs). Synovial biopsy specimens were obtained by needle arthroscopy from the knee joints, as previously described (9). Additionally, serum samples were obtained from the Leiden clinically suspect arthralgia (CSA) cohort (10) (Leiden University Medical Center, Leiden, The Netherlands), which is composed of 20 CSA patients with disease that progressed to RA, with paired samples at CSA onset and at the time that clinical arthritis first developed, and serum samples from 20 CSA patients with disease that did not progress to clinical arthritis or RA, in which paired samples were obtained at presentation of CSA and after 2 years of follow-up.

All patients presented at the outpatient clinic with recent-onset (<1 year) arthralgia of the small joints without clinical arthritis and had disease that, according to the clinical expertise of the rheumatologist, was suspected to progress to RA. Baseline visits consisted of physical examination, blood sample collection, and questionnaires. At the time of study inclusion, the autoantibody status of each patient was not known, as, in accordance with Dutch clinical practice guidelines, general practitioners are not required to measure serum autoantibodies as part of the examination. Follow-up visits were scheduled at months 4, 12, and 24. When necessary, additional visits were planned—for example, when a patient's symptoms increased or when a patient experienced joint swelling. Patients were followed up until the development of clinical inflammatory arthritis, determined by the rheumatologist at the time of the physical examination. During follow-up (and before the primary outcome was reached) treatment with disease-modifying antirheumatic drugs (including steroids) was not allowed. The date of censoring was either the date that the medical records were reviewed or an earlier date in those cases in which the patient was lost to follow-up.

In 8 CSA patients with disease that progressed to RA, serum samples were also obtained 1 year after diagnosis, and in 4 of these patients, serum samples were also obtained 2 years after diagnosis. All subjects provided written informed consent, and the protocol was approved by local institutional medical ethics review boards prior to patient inclusion in this study. RA patients fulfilled the American College of Rheumatology /European Alliance of Associations for Rheumatology 2010 classification criteria for RA (11,12). Clinical characteristics of the patients are detailed in Supplementary Tables 1–3 (available on the *Arthritis & Rheumatology* website at http://onlinelibrary.wiley.com/doi/10.1002/art.42065/abstract).*

Serum-transfer arthritis and clinical scoring. K/BxN mouse serum was collected from 4–8-week-old arthritic K/BxN mice (provided by C. Benoist and D. Mathis [Harvard Medical School]). Arthritis was induced in wild-type (WT) and Sema3B$^{-/-}$ mice (The Jackson Laboratory), transferring 100 μl of K/BxN serum into 8–12-week-old mice by intraperitoneal (IP) injection on days 0 and 2. Alternatively, control phosphate buffered saline (PBS) vehicle, recombinant mouse Sema3B–Fc chimera protein, or mouse IgG2a isotype control (both 10 μg) (R&D Systems) were administered IP on days 0, 2, and 4 in WT mice. Serum was collected on days 0, 4, and 9, and mice were killed on day 9 after serum transfer. Arthritis severity was assessed in each of the 4 limbs every 2 days by 2 blinded observers (AI and SG for evaluation of WT and Sema3B$^{-/-}$ mice, and AR and CC for evaluation of recombinant Sema3B–treated mice) using a semiquantitative clinical score

*[Correction added on 12 May 2022, after first online publication: In Supplementary Table 1, the number (%) of patients with arthralgia receiving NSAIDs was changed from "0 (25)" to "2 (25)."]

(0 = no swelling, 1 = slight swelling and erythema of the ankle, wrist, or digits, 2 = moderate swelling and erythema, 3 = severe swelling and erythema, and 4 = maximal inflammation with joint rigidity for a maximum possible score of 16 points per mouse).

Histologic analysis. The hind limbs from mice killed on day 9 were prepared for histology by dissecting the skin and muscle and then sectioning the ankle joints. Specimens were fixed in formalin for 24 hours and were demineralized in Osteosoft (Merck Millipore) for 30 days. Ankle joints were embedded in paraffin, cut, and stained with hematoxylin and eosin to evaluate inflammation and bone erosion. Toluidine blue was used for analysis of cartilage damage.

Synovial inflammation was graded according to the following index, where 0 = no inflammation, 1 = slight thickening of the synovial cell layer and/or some inflammatory cells in the sublining, 2 = thickening of the synovial lining and moderate infiltration of the sublining, 3 = thickening of the synovial lining and marked infiltration, and 4 = thickening of the synovial lining and severe infiltration. Cartilage damage was evaluated using a 0–4–point scale, where 0 = normal cartilage, 1 = cartilage surface irregularities and loss of metachromasia adjacent to superficial chondrocytes, 2 = fibrillation of cartilage with minor loss of surface cartilage, 3 = moderate cartilage abnormalities, including loss of superficial cartilage and moderate multifocal chondrocyte loss, and 4 = marked cartilage destruction with extension of fissures close to subchondral bone. Bone erosions were scored on a 0–4–point scale, where 0 = normal bone, 1 = small resorption areas, 2 = more numerous resorption areas, 3 = obvious resorption, and 4 = full-thickness resorption areas in the bone.

Mouse FLS culture and stimulation. Mouse FLS were isolated from WT and Sema3B$^{-/-}$ mice. Synovial tissue was minced and incubated with 1 mg/ml of collagenase in serum-free Dulbecco's modified Eagle's medium (DMEM) (Invitrogen) at 37°C for 3 hours. After digestion, FLS were passed through a nylon cell strainer (BD Falcon), washed, and cultured in 10% fetal bovine serum (FBS) (BioWest) and 10,000 units/ml of penicillin/streptomycin (ThermoFisher Scientific). After culture overnight, nonadherent cells were removed, and adherent cells were cultured in DMEM–10% FBS and used between passages 4 and 6.

Sema3B and cytokine measurement. Sema3B (Biomatik) levels in the serum of patients with arthralgia and patients with RA, Sema3B (Abbexa) levels in the serum of arthritic mice, and interleukin-6 (IL-6) (eBioscience) and tumor necrosis factor (TNF) (R&D Systems) levels in cell-free assay supernatants of mouse FLS were measured using an enzyme-linked immunosorbent assay, according to the manufacturer's instructions.

Bulk messenger RNA (mRNA) sequencing protocol. Sequencing was performed by the sequencing service provider Single Cell Discoveries, using an adapted version of the CEL-Seq protocol. Total RNA from mouse forepaws was extracted using an RNeasy kit and an RNase-Free DNase set (Qiagen) and was used for library preparation and sequencing. We processed mRNA as described previously, following an adapted version of the single-cell mRNA sequencing protocol of CEL-Seq (13,14). In brief, samples were barcoded with CEL-Seq primers during reverse transcription and were pooled after second-strand synthesis. The resulting complementary DNA (cDNA) was amplified with an overnight in vitro transcription reaction. From this amplified RNA, sequencing libraries were prepared with Illumina TruSeq small RNA primers.

Paired-end sequencing was performed on the Illumina NextSeq 500 platform. Read 1 was used to identify the Illumina library index and CEL-Seq sample barcode. Read 2 was aligned to the Mus musculus GRCm38 (mm10) mouse reference transcriptome using BWA (15). Reads that mapped equally well to multiple locations were discarded. Mapping and generation of count tables was conducted using the MapAndGo script (https://github.com/anna-alemany/transcriptomics/tree/master/mapandgo). Samples were normalized using reads per million–mapped reads normalization. The differential expression analysis based on the negative binomial was performed using R/Bioconductor package DESeq2 version 1.32. Negative binomial generalized linear model fitting and a paired Wald's test was used to assess the differentially expressed genes (DEGs), and *P* values were adjusted for multiple testing errors with a 5% false discovery rate according to the Benjamini-Hochberg method (16). DEGs were defined as those genes showing a ≥2 fold change in expression at an adjusted *P* value (P_{adj}) less than 0.05.

Real-time polymerase chain reaction (PCR) and quantitative PCR (qPCR). RNA from mouse forepaws, mouse FLS, and synovial tissue was isolated using an RNeasy Kit and an RNase-Free DNase Set (Qiagen). Total RNA was reverse-transcribed using iScript (Bio-Rad). Duplicate PCRs were performed using SYBR Green (Applied Biosystems) with a StepOnePlus Real-Time PCR detection system (Applied Biosystems). We amplified cDNA using specific primers (all from IDT) (see Supplementary Tables 4 and 5, http://onlinelibrary.wiley.com/doi/10.1002/art.42065/abstract). Relative levels of gene expression were normalized to the expression levels of 3 housekeeping genes (*B2M*, *RPL13*, and *RPL32* or *Hprt*, *β-actin*, and *B2m*). Relative expression was calculated using the formula $2^{-\Delta C_t} \times 1{,}000$.

Immunoblotting. FLS were lysed in Laemmli buffer and forepaws were lysed in radioimmunoprecipitation assay buffer. Protein content was quantified with a BCA Protein Assay kit (Pierce). An equal amount of total protein was subjected to electrophoresis on 4–12% NuPAGE Bis-Tris gels (Invitrogen), and

proteins were transferred to PVDF membranes (Millipore). Membranes were incubated overnight at 4°C with the following primary antibodies: antibodies specific to TNF (BD PharMingen); Sema3B, ERK, and β-actin antibodies (all from Abcam); neuropilin 1, plexin A2, and tubulin antibodies (all from R&D Systems); and H3 and protein ERK antibodies (Santa Cruz Biotechnology). Membranes were then washed and incubated in Tris buffered saline–Tween containing a horseradish peroxidase–conjugated secondary antibody. Protein was detected with Lumi-Light Plus Western blotting substrate (Roche Diagnostics) using a Chemi-Doc MP imaging system (Bio-Rad). Densitometry analysis was performed with ImageJ software. Relative protein expression was normalized to the values for H3, tubulin, or β-actin.

Migration assay. Cell migration was determined using a wound closure motility assay. A linear scratch was made on cultured mouse FLS plated at confluence using a 200-μl micropipette tip and then washed with PBS to remove unattached cells. Mouse FLS were placed in medium containing 1% or 10% FBS, and thereafter were either left unstimulated or stimulated with recombinant mouse Sema3B (100 ng/ml) (R&D Systems). Light microscopy images were obtained immediately (time point 0) and 24 hours after wounding. The mean number of migrated cells was determined from 3 10× field-of-view images and values were normalized to those in cultures with unstimulated cells.

Statistical analysis. A statistical analysis was performed using Windows GraphPad Prism version 8. Potential differences between patient groups were analyzed using a nonparametric 2-tailed Mann-Whitney test or a Kruskal-Wallis test, as appropriate. Potential differences between the mouse groups were

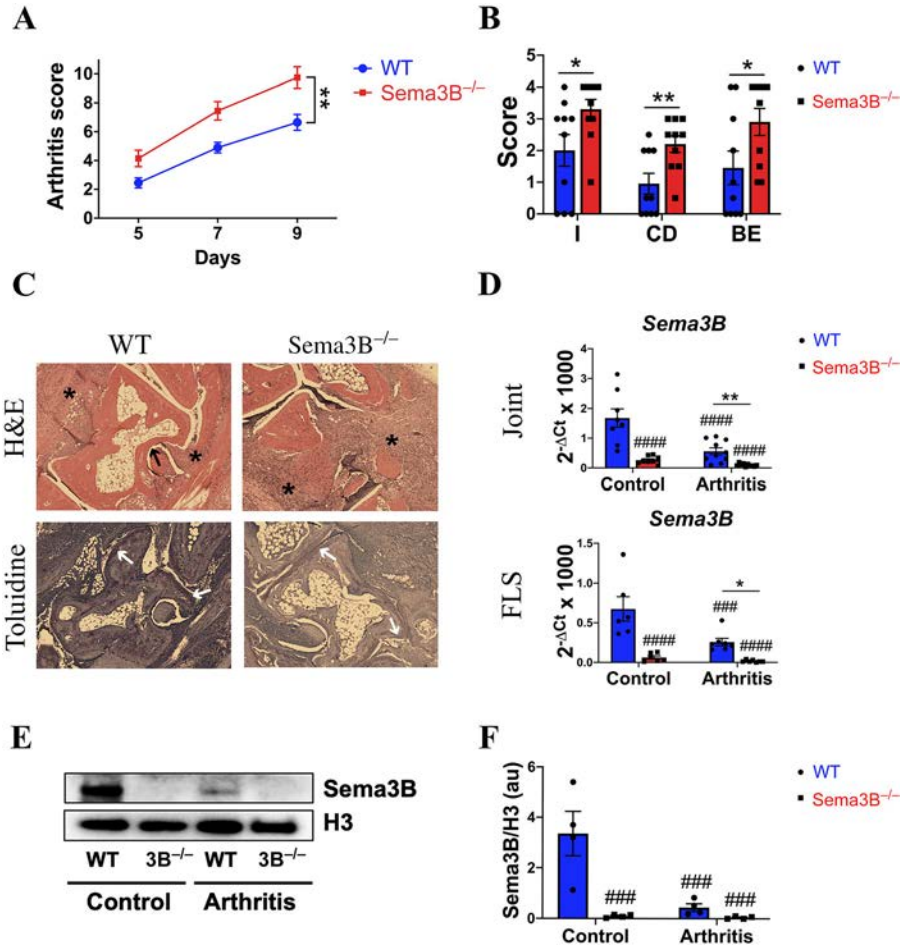

Figure 1. Semaphorin 3B (Sema3B) deficiency increases the severity of serum-induced arthritis. **A**, Daily global arthritis scores in wild-type (WT) mice (n = 10) and Sema3B$^{-/-}$ mice (n = 10). Values are the mean ± SEM. **B**, Inflammation (I) scores, cartilage damage (CD) scores, and bone erosion (BE) scores in mice in each group. **C**, Representative images of histologic features in the mouse joints, visualized using hematoxylin and eosin (H&E) and toluidine blue staining (n = 10). Synovial cell infiltration (**asterisks**), bone erosion (**black arrow**), and cartilage damage (**white arrows**) are shown. **D**, Expression of Sema3B mRNA in the joints and fibroblast-like synoviocytes (FLS) of WT mice (n = 6–8) and Sema3B$^{-/-}$ mice (n = 6–8). **E** and **F**, Representative immunoblot (**E**) and densitometric analysis (**F**) of Sema3B expression in FLS from WT mice (n = 4) and Sema3B$^{-/-}$ mice (n = 4). In **B**, **D**, and **F**, symbols represent individual mice; bars show the mean ± SEM. * = $P < 0.05$; ** = $P < 0.01$. ### = $P < 0.001$; #### = $P < 0.0001$, versus nonarthritic WT control mice.

analyzed using a parametric Student's 2-tailed paired *t*-test or analysis of variance, as appropriate. *P* values less than 0.05 were considered statistically significant.

RESULTS

Higher severity of arthritis in Sema3B$^{-/-}$ mice. We initially analyzed the role of Sema3B in K/BxN serum–induced arthritis and found that the clinical severity of arthritis was significantly higher in Sema3B$^{-/-}$ mice compared to the WT mice (Figure 1A). These differences were not sex dependent (Supplementary Figure 1A, http://onlinelibrary.wiley.com/doi/10.1002/art.42065/abstract). Histologic analysis of the tibiotalar and forefoot joints revealed significant increases in synovial inflammation, cartilage damage, and bone erosion in the Sema3B$^{-/-}$ mice (Figures 1B and C and Supplementary Figure 1B).

Next, we determined the expression of Sema3B in the total joints and FLS of mice. As expected, expression of Sema3B mRNA and protein was not detected in either the nonarthritic control group or the arthritic group of Sema3B$^{-/-}$ mice. Remarkably, among WT mice, expression of Sema3B was significantly lower in the arthritic group compared to the nonarthritic group (Figures 1D–F). Taken together, these data suggest that Sema3B may play a protective role in the K/BxN serum–induced arthritis model.

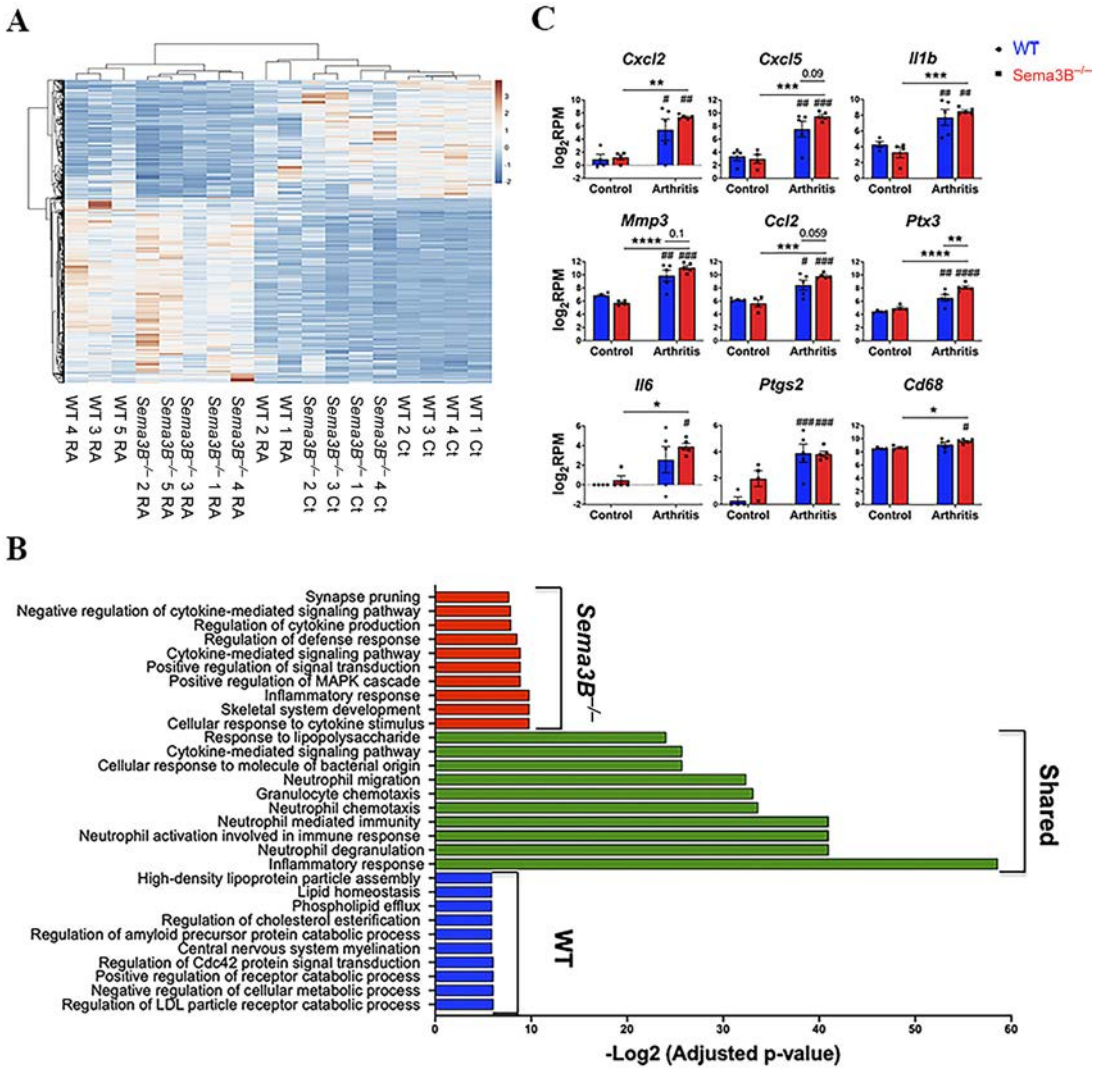

Figure 2. Sema3B deficiency enhances the activation of inflammatory pathways. **A**, Expression of differentially expressed gene (DEG) mRNA in the forepaws of WT or Sema3B$^{-/-}$ mice in a model of rheumatoid arthritis (RA) (n = 5 each) relative to that in nonarthritic control (Ct) mice (n = 4). Data are presented as a heatmap showing the lowest (blue) and highest (orange) mRNA expression levels. **B**, Gene Ontology analysis of the biologic processes associated with DEGs specific to arthritic WT mice, those specific to arthritic Sema3B$^{-/-}$ mice, or those shared between both groups. **C**, Expression of mRNA for inflammatory mediators, analyzed by RNA-Seq in the forepaws of nonarthritic control mice (n = 4) and arthritic WT mice or Sema3B$^{-/-}$ mice (n = 5). Symbols represent individual mice; bars show the mean ± SEM. * = $P < 0.05$; ** = $P < 0.01$; *** = $P < 0.001$; **** = $P < 0.0001$. # = $P < 0.05$; ## = $P < 0.01$; ### = $P < 0.001$; #### = $P < 0.0001$, versus nonarthritic WT control mice. LDL = low-density lipoprotein (see Figure 1 for other definitions). Color figure can be viewed in the online issue, which is available at http://onlinelibrary.wiley.com/doi/10.1002/art.42065/abstract.

Enhanced activation of inflammatory pathways in Sema3B$^{-/-}$ mice. To explore the mechanisms underlying increased arthritis severity in Sema3B$^{-/-}$ mice, we performed an RNA sequencing analysis in the joints of control mice and arthritic mice. A principal components analysis of the whole transcriptome showed a clearer distinction between the control and arthritic groups rather than between WT mice and Sema3B$^{-/-}$ mice (Supplementary Figure 2A, http://onlinelibrary.wiley.com/doi/10.1002/art.42065/abstract). In fact, there were no significant differences between WT and Sema3B$^{-/-}$ nonarthritic control mice, and we only observed a trend toward down-regulated expression of Sema3B mRNA in Sema3B$^{-/-}$ mice (fold change 0.06; P_{adj} = 0.078) (data not shown).

Next, we compared gene expression levels between WT and Sema3B$^{-/-}$ arthritic mice and, similar to the control groups, we did not observe major differences. In fact, only 2 genes (*Sema3b* and *Lrrn4cl*) were found to have significantly lower expression in Sema3B$^{-/-}$ mice compared to WT mice (Supplementary Table 6, http://onlinelibrary.wiley.com/doi/10.1002/art.42065/abstract).

We therefore compared the DEGs in WT or Sema3B$^{-/-}$ arthritic mice relative to WT control mice. The results revealed 197 DEGs in arthritic WT mice and 566 DEGs in arthritic Sema3B$^{-/-}$ mice that showed significant differences in expression compared to nonarthritic controls (Supplementary Tables 7 and 8, http://onlinelibrary.wiley.com/doi/10.1002/art.42065/abstract). A heatmap of the DEGs clearly distinguished the nonarthritic control mice and arthritic mice. Importantly, the Sema3B$^{-/-}$ arthritic mice clustered together, while the WT arthritic mice grouped in 2 different clusters, with 1 more similar to the Sema3B$^{-/-}$ arthritic mice and the other more similar to the nonarthritic mice (Figure 2A). Subsequently, we performed a venn diagram analysis (17) and we found that of all DEGs (606), 40 (6.6%) were specific to WT mice, 409 (67.5%) were specific to Sema3B$^{-/-}$ mice, and 157 (25.9%) were differentially expressed in both groups (Supplementary Figure 2B and Supplementary Table 9, http://onlinelibrary.wiley.com/doi/10.1002/art.42065/abstract). A Gene Ontology analysis of biologic processes did not show any relevant pathways in those DEGs

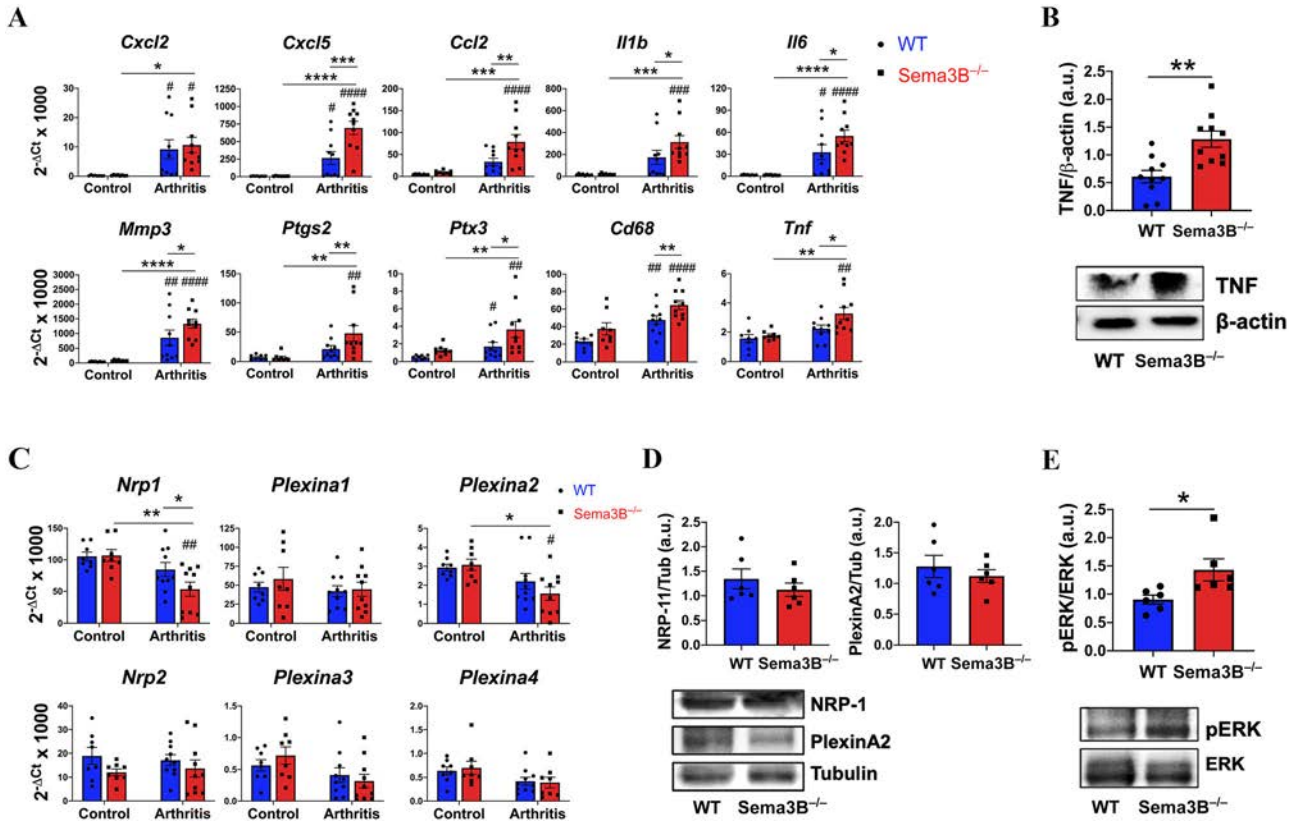

Figure 3. Sema3B deficiency enhances the activation of inflammatory pathways. **A**, Expression of mRNA for inflammatory mediators analyzed by quantitative PCR (qPCR) of the forepaws in nonarthritic control mice (n = 8) and arthritic WT mice or Sema3B$^{-/-}$ mice (n = 10). **B**, Densitometric analysis and representative immunoblot of tumor necrosis factor (TNF) in the joints of arthritic WT mice (n = 10) and arthritic Sema3B$^{-/-}$ mice (n = 10). **C**, Expression of Sema3B mRNA receptors analyzed by qPCR of the forepaws of nonarthritic control mice (n = 8) and arthritic WT mice or Sema3B$^{-/-}$ mice (n = 10 each). **D** and **E**, Densitometric analysis and representative immunoblot of neuropilin 1 (NRP-1) and plexin A2 expression (**D**) and ERK activation (**E**) in the joints of arthritic WT mice (n = 6) and arthritic Sema3B$^{-/-}$ mice (n = 6). Symbols represent individual mice; bars show the mean ± SEM. * = $P < 0.05$; ** = $P < 0.01$; *** = $P < 0.001$; **** = $P < 0.0001$. # = $P < 0.05$; ## = $P < 0.01$; ### = $P < 0.001$; #### = $P < 0.0001$, versus nonarthritic WT control mice. Tub = tubulin (see Figure 1 for other definitions). Color figure can be viewed in the online issue, which is available at http://onlinelibrary.wiley.com/doi/10.1002/art.42065/abstract.

specific to the WT arthritic group. As expected, the DEGs shared between both groups are related to processes involved in the pathogenesis of arthritis in this murine model, such as inflammatory responses, neutrophil activation and migration, and cytokine-mediated signaling pathways. In addition, the biologic processes specific to the Sema3B$^{-/-}$ mice were also related to cytokine and inflammatory responses (Figure 2B and Supplementary Table 10, http://onlinelibrary.wiley.com/doi/10.1002/art.42065/abstract).

We analyzed several DEGs common to WT and Sema3B$^{-/-}$ arthritic mice (*Cxcl2*, *Cxcl5*, *Il1b*, *Ccl2*, *Mmp3*, and *Ptx3*) and some specific to arthritic Sema3B$^{-/-}$ mice (*Il6*, *Ptgs2*, and *Cd68*), and we found elevated expression in the arthritic Sema3B$^{-/-}$ mice compared to arthritic WT mice, although only the difference in *Ptx3* expression was significant (Figure 2C). In order to confirm these data, we analyzed this subset of genes using single qPCR, as well as *Tnf*, due to the key role it plays in RA pathogenesis (2,18). We found up-regulation of *Cxcl5*, *Ccl2, Tnf, Il1*, *Il6*, *Mmp3, Ptgs2, Cd68*, and *Ptx3* in arthritic WT mice and arthritic Sema3B$^{-/-}$ mice compared to the nonarthritic control mice and significantly enhanced expression in arthritic Sema3B$^{-/-}$ mice compared to arthritic WT mice (Figure 3A). Finally, we also validated the increased expression of TNF at the protein level (Figure 3B).

Next, we investigated the possible molecular mechanisms involved in the elevated severity of arthritis in this murine model. First, we analyzed expression of the Sema3B receptors, the plexin A family members, and the coreceptors neuropilin 1 (NRP-1) and NRP-2 (5–7,19). We found that expression of *Nrp1* and *Plexina2* was significantly lower in the joints of arthritic

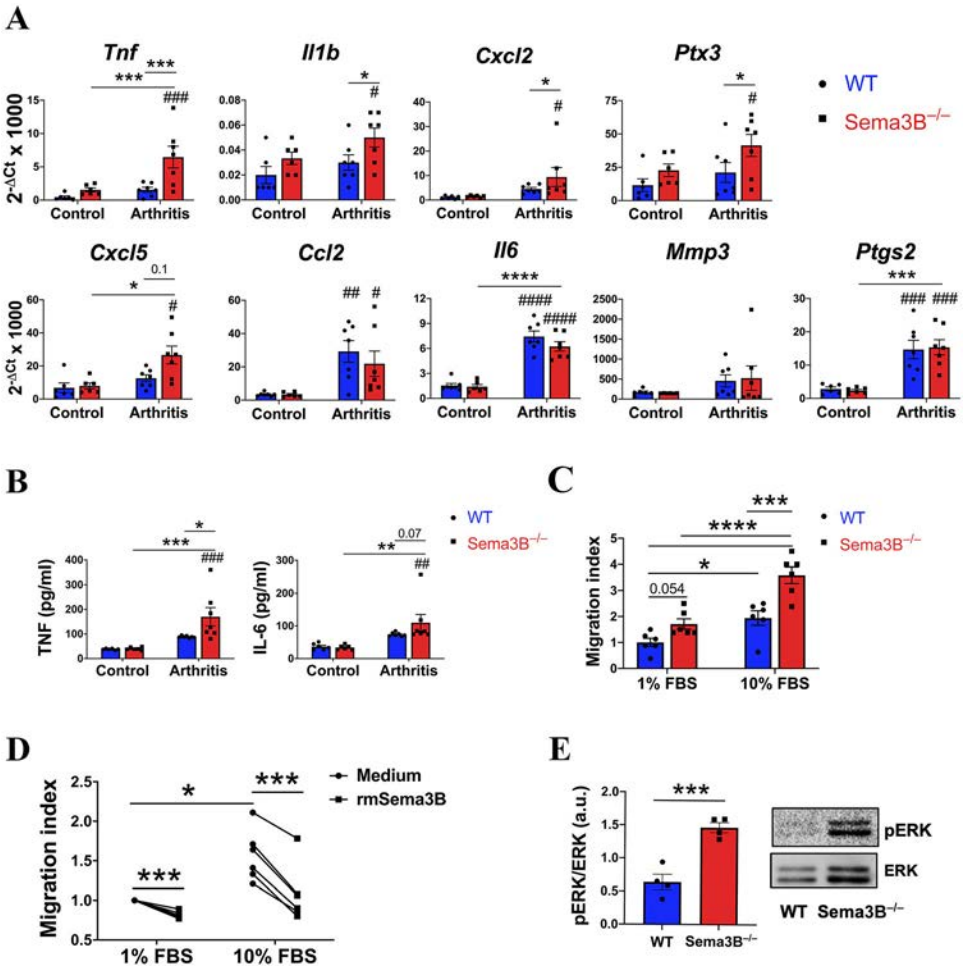

Figure 4. Sema3B deficiency enhances activation of inflammatory pathways and the migratory capacity of FLS. **A** and **B**, Expression of mRNA for inflammatory mediators (**A**) and tumor necrosis factor (TNF) and interleukin-6 (IL-6) protein secretion (**B**) in FLS (at passage 4) from nonarthritic control mice (n = 6) and arthritic WT mice or Sema3B$^{-/-}$ mice (n = 7). **C**, Migration of FLS (at passage 4) from arthritic WT mice and arthritic Sema3B$^{-/-}$ mice after culture in 1% or 10% fetal bovine serum (FBS) for 24 hours. **D**, Migration of mouse FLS (at passage 6) from arthritic Sema3B$^{-/-}$ mice stimulated with recombinant mouse Sema3B (rmSema3B) (100 ng/ml) after culture in 1% or 10% FBS for 24 hours. **E**, Densitometric analysis and representative immunoblot of ERK activation in FLS (at passage 4) from arthritic WT mice (n = 4) and arthritic Sema3B$^{-/-}$ mice (n = 4). In **A–C** and **E**, symbols represent individual mice; bars show the mean ± SEM. * = $P < 0.05$; ** = $P < 0.01$; *** = $P < 0.001$; **** = $P < 0.0001$. # = $P < 0.05$; ## = $P < 0.01$; ### = $P < 0.001$; #### = $P < 0.0001$, versus nonarthritic WT control mice. See Figure 1 for other definitions. Color figure can be viewed in the online issue, which is available at http://onlinelibrary.wiley.com/doi/10.1002/art.42065/abstract.

Sema3B$^{-/-}$ mice compared to the joints of WT and Sema3B$^{-/-}$ nonarthritic mice. In addition, expression of *Nrp1* was also diminished compared to levels in arthritic WT mice (Figure 3C). At the protein level, we observed slightly reduced expression of NRP-1 and plexin A2 in arthritic Sema3B$^{-/-}$ mice compared to arthritic WT mice, although this difference was not statistically significant (Figure 3D).

As Sema3B reduces ERK activation in FLS (8), we also evaluated the activation of this protein kinase in mouse FLS. In addition, 1 of the pathways found in the RNA-Seq data specific to arthritic Sema3B$^{-/-}$ mice was the positive regulation of the MAPK cascade (Figure 2B). Consistent with this finding, our results showed significantly increased ERK activation in arthritic Sema3B$^{-/-}$ mice compared to arthritic WT mice (Figure 3E).

Enhanced inflammatory and migratory phenotype of FLS in Sema3B$^{-/-}$ mice. In arthritic mouse FLS, we further analyzed expression of the gene targets in the joint tissue, since Sema3B is mainly expressed by FLS in the synovium (8). Our qPCR analysis showed increased *Tnf*, *Il1, Ptx3, Cxcl2*, and *Cxcl5* expression in FLS from arthritic Sema3B$^{-/-}$ mice compared to FLS from arthritic WT mice, but there were no differences in terms of the expression of *Ccl2*, *Il6*, *Mmp3*, or *Ptgs2* (Figure 4A). At the protein level, secretion of TNF and IL-6 was also increased in FLS from arthritic Sema3B$^{-/-}$ mice (Figure 4B).

Since Sema3B impairs the migratory capacity of RA FLS (8), we analyzed the migratory capacity of mouse FLS. We observed a trend toward increased spontaneous migration and significantly higher FBS-induced migration in FLS from Sema3B$^{-/-}$ mice compared to FLS from arthritic WT mice. Notably, the higher degree of migration of FLS from Sema3B$^{-/-}$ mice was reverted after stimulation with recombinant mouse Sema3B (Figures 4C and D).

Lastly, we determined ERK activation and, similar to the observations in the total joints of mice, ERK activation was significantly increased in the FLS from arthritic Sema3B$^{-/-}$ mice compared to WT mice (Figure 4E).

Protective role of Sema3B in a murine model of arthritis. To confirm that Sema3B plays a protective role in this model of arthritis, we determined the effect of treatment with a recombinant mouse Sema3B fusion protein in arthritic WT mice. Arthritis severity was significantly lower in recombinant mouse Sema3B–treated mice compared to mice in both control groups (PBS and isotype control IgG) (Figure 5A). Consistent with this, histologic analysis at day 9 showed a drastic reduction in synovial

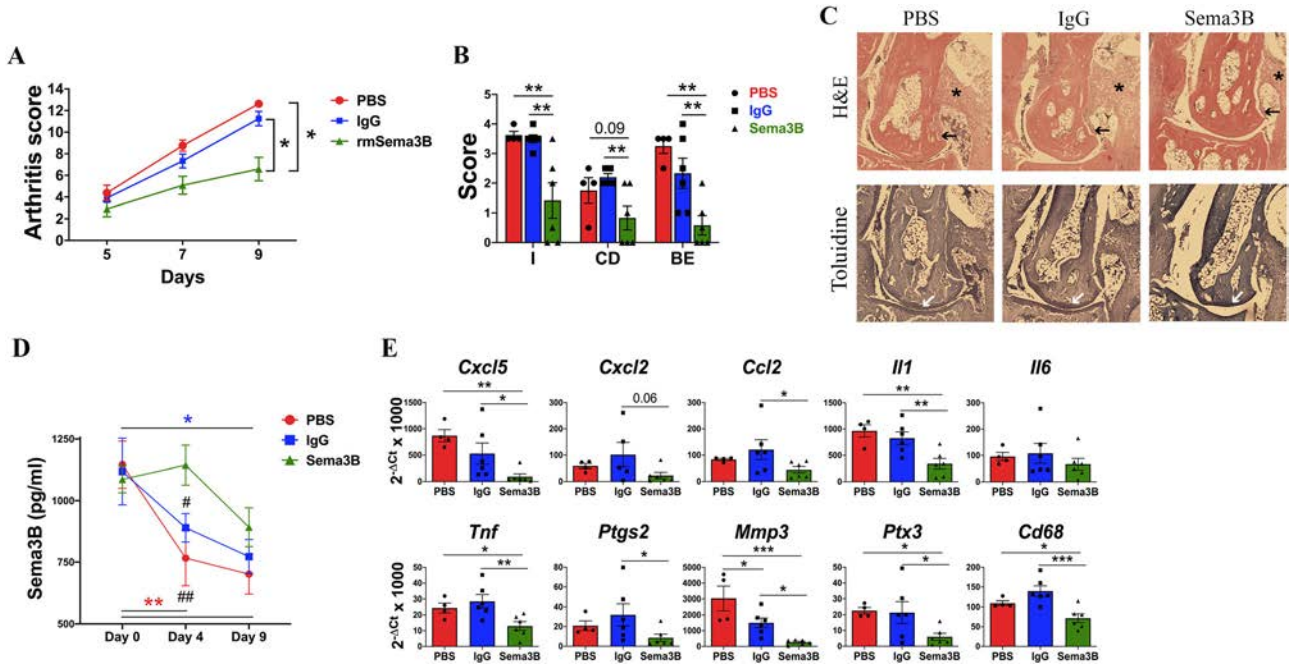

Figure 5. Sema3B reduces the severity of serum-induced arthritis. **A**, Daily global arthritis scores in arthritic WT mice treated on days 0, 2, and 4 with control phosphate buffered saline (PBS) (n = 4), isotype control IgG (10 μg) (n = 6), or recombinant mouse Sema3B (rmSema3B) (10 μg) (n = 6). Values are the mean ± SEM. **B**, Inflammation scores, cartilage damage scores, and bone erosion scores in mice in each group. **C**, Representative images of histologic features in the mouse joints visualized with H&E and toluidine blue staining. Synovial cell infiltration (**asterisks**), bone erosion (**black arrows**), and cartilage damage (**white arrows**) are shown. **D**, Longitudinal serum Sema3B levels in the mouse groups analyzed in **A**. **E**, Expression of mRNA for inflammatory mediators in the forepaws of mice analyzed in **A**. In **B** and **E**, symbols represent individual mice; bars show the mean ± SEM. * = $P < 0.05$; ** = $P < 0.01$; *** = $P < 0.001$. # = $P < 0.05$; ## = $P < 0.01$, versus Sema3B-treated mice on day 4. See Figure 1 for other definitions. Color figure can be viewed in the online issue, which is available at http://onlinelibrary.wiley.com/doi/10.1002/art.42065/abstract.

inflammation, cartilage damage, and bone erosion in recombinant mouse Sema3B–treated mice compared to those in both control groups (Figures 5B and C).

Findings from a longitudinal analysis demonstrated that serum Sema3B levels were significantly lower during the course of arthritis in the PBS and IgG groups. In the Sema3B-treated group, the levels of this protein on day 4 were similar to those observed on day 0 (before the induction of arthritis and administration of the recombinant mouse Sema3B), but were reduced on day 9, likely due to the final dose of recombinant mouse Sema3B administered on day 4. Importantly, also on day 4, levels of Sema3B were significantly higher in the Sema3B mouse group compared to the control groups (Figure 5D). Finally, analysis of the inflammatory mediators in the mouse joints demonstrated that recombinant mouse Sema3B administration resulted in significantly down-regulated expression of *Tnf*, *Il1*, *Ccl2*, *Cxcl5*, *Ptgs2*, *Ptx3*, *Cd68*, and *Mmp3* compared to the expression levels of these genes in the control groups (Figure 5E).

Disease stage dependence of Sema3B expression in human RA. Our previous findings (8) and results from the murine experiments suggest that Sema3B expression might be reduced in patients with established RA, but to date its expression in patients with arthralgia preceding the development of clinical arthritis and RA is unexplored. First, we examined the local and systemic expression of Sema3B in patients with arthralgia and those with RA. We found significantly lower Sema3B mRNA and protein expression in the synovial tissue and serum of patients with established RA compared to those with arthralgia (Figures 6A and B).

To better understand the expression levels at different disease stages, we measured Sema3B levels in 20 patients with CSA who had disease that progressed to RA (median time between presentation with CSA and the development of clinical arthritis 4 months [interquartile range 0.3–5]) and 20 patients with disease that did not progress to RA (samples collected at presentation with CSA and after 2 years). In patients with disease that progressed to RA, serum Sema3B levels were significantly elevated both at the time of presentation with CSA and at the time that clinical arthritis first developed, compared to the levels in the patients who had disease that did not progress to RA (Figure 6C).

These differences were independent of ACPA autoantibody status, as Sema3B levels were increased in the progressor patients in both the ACPA-negative and ACPA-positive groups. Interestingly, at the baseline visit and to a lower extent after 1 year of follow-up, levels of Sema3B were significantly higher in ACPA-positive patients compared to ACPA-negative patients, both in those with disease that progressed to RA and in those whose disease remained as arthralgia (Supplementary Figure 3 http://onlinelibrary.wiley.com/doi/10.1002/art.42065/abstract). Similar

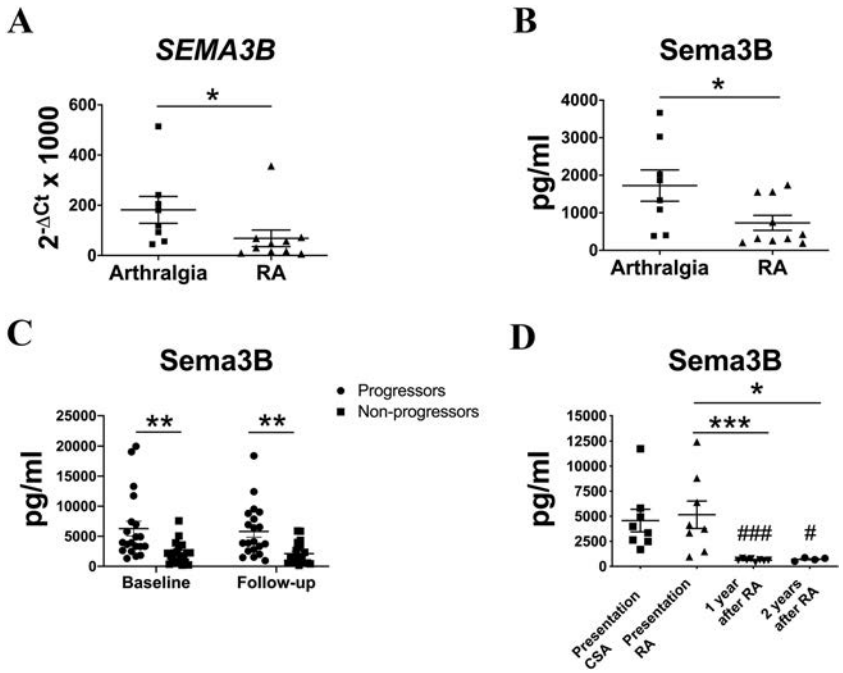

Figure 6. Semaphorin 3B (Sema3B) expression is reduced during the progression of rheumatoid arthritis (RA). **A** and **B**, Expression of Sema3B mRNA in synovial tissue (**A**) and Sema3B protein in serum (**B**) from patients with arthralgia (n = 8) and those with established RA (n = 10). **C**, Sema3B levels in a longitudinal cohort of patients with clinically suspect arthralgia (CSA) (n = 40) who had disease that progressed to RA (n = 20) or those whose disease remained as arthralgia after 2 years of follow-up (n = 20). **D**, Sema3B levels in a longitudinal cohort of patients with CSA at presentation of arthralgia (n = 8), at presentation of RA (n = 8), and 1 year (n = 8) and 2 years (n = 4) after RA diagnosis. Symbols represent individual patients; bars show the mean ± SEM. * = $P < 0.05$; ** = $P < 0.01$; *** = $P < 0.001$. # = $P < 0.05$, ### = $P < 0.001$, versus presentation.

to the previous set of patients with established RA, in 8 of the CSA patients with disease that progressed to RA, Sema3B levels were drastically reduced after 1 year of follow-up, and in 4 patients, levels remained lower after 2 years of follow-up (Figure 4D). Taken together, these data show that expression of Sema3B is disease stage–dependent and is associated with ACPA status.

DISCUSSION

In this study we found that Sema3B plays a protective role in a K/BxN mouse model of arthritis. The higher arthritis severity observed in Sema3B$^{-/-}$ mice was associated with 2 main effects. First, mRNA and protein analysis in Sema3B$^{-/-}$ mice showed higher expression of cytokines, chemokines, and matrix metalloproteinases, which are elevated in RA patients and play a key role in pathogenesis of the disease (18,20,21). Enrichment analysis of DEGs in both WT arthritic mice and Sema3B$^{-/-}$ arthritic mice showed induction of biologic pathways involved in the pathogenesis of arthritis in this model, as well as in RA patients. Specific pathways in Sema3B$^{-/-}$ mice were also related to these processes, indicating that Sema3B deficiency enhances the expression of inflammatory mediators, rather than regulating other biologic processes. We found that FLS are responsible for the enhanced expression of inflammatory mediators, although some mediators were up-regulated in total joints but not in FLS (*Il6*, *Ccl2*, *Mmp3*, *Ptgs2*), suggesting the involvement of other cell types. Neutrophils and macrophages are crucial in a K/BxN mouse model of arthritis, as they represent the main immune cells infiltrating the affected joints and release cytokines and chemokines, among other inflammatory mediators (22–24).

Increased synovial inflammation and higher expression of the macrophage marker CD68 in the joints of Sema3B$^{-/-}$ mice suggest that both neutrophils and macrophages are involved in the greater arthritis severity and in the production of inflammatory mediators found in these mice. Second, FLS from Sema3B$^{-/-}$ mice demonstrated an increased migratory capacity, consistent with the invasive and aggressive phenotype of RA FLS (8,25,26). In addition, the enhanced bone erosion observed in Sema3B$^{-/-}$ mice suggests that Sema3B also may be involved in bone erosion, which is consistent with findings from other studies that have shown that Sema3B promotes osteoblastic proliferation and differentiation (27,28).

In this study we also found lower expression of plexin A2 and the coreceptor NRP-1 in the joints of WT arthritic mice, and this reduction was more evident in the Sema3B$^{-/-}$ arthritic mice. These data, taken together with the low Sema3B levels, suggest that decreased plexin A2 and NRP-1 expression may be implicated in this arthritis model. In fact, plexin A2 and NRP-1 are crucial for appropriate Sema3B signaling in different cell types (8,29,30). In addition, Sema3A and Sema3F, which play protective roles in RA pathogenesis, also bind to plexin A2 and NRP-1. Therefore, Sema3B deficiency might also enhance arthritis severity through the impairment of the Sema3A and Sema3F protective pathways. (8,31,32).

Regarding the molecular pathways involved in enhanced arthritis severity, we found higher ERK activation both in the joints and in the FLS from Sema3B$^{-/-}$ arthritic mice, indicating that the protective role of Sema3B in RA pathogenesis may be due, at least in part, to inhibition of this molecular pathway. This notion is supported by previous findings of low ERK activation in Sema3B-stimulated RA FLS (8) and elevated ERK activation in synovial tissue from patients with RA, as well as from patients with early arthritis who develop erosive RA (33–35).

Notably, expression of Sema3B was reduced in arthritic WT mice during the course of arthritis, similar to the decreased Sema3B levels observed during RA progression. Of special interest, administration of Sema3B resulted in diminished arthritis severity, decreased expression of inflammatory mediators, and reduced migration of FLS, highlighting the important modulatory role of Sema3B in the K/BxN mouse model of arthritis.

We also found that local and systemic levels of Sema3B were lower in patients with established RA compared to patients with arthralgia; however, Sema3B levels were increased in patients with CSA who had disease that progressed to RA. These data suggest that expression of Sema3B is disease stage dependent and the elevated expression in patients with pre-RA may be a consequence of a counterregulatory mechanism, similar to the high levels of antiinflammatory mediators (IL-4, IL-5, IL-10, IL-13) observed in patients with RA (35–37). Due to the protective role of Sema3B, this counterregulation in the early stages of the disease may reduce the pathogenic processes that ultimately lead to joint destruction. However, further studies are needed to elucidate this mechanism. Eight of the CSA patients with disease that progressed to RA presented with remarkably low serum Sema3B levels 1 and 2 years after the date of diagnosis.

These data, along with our previous findings showing that Sema3B levels are lower in the synovium of patients with early RA compared to patients with undifferentiated arthritis (8), which is considered an early phase of RA (38), confirm that expression of Sema3B is down-regulated during the progression of the disease. The pathogenic mechanisms observed in very early RA might be responsible for this reduction. In fact, IL-1 and TNF levels are elevated in the synovial fluid of patients with early RA (37), and the expression levels of *IL1B* and *TNF* negatively correlate with *SEMA3B* expression in the synovium of patients with early RA. In addition, both IL-1 and TNF down-regulate Sema3B expression in RA FLS (8). Nevertheless, we cannot rule out the possibility that ACPAs are involved in Sema3B expression, as serum Sema3B levels are increased in ACPA-positive RA patients and several studies have shown that anticitrullinated antibodies induce the expression of inflammatory mediators (38–40).

Taken together, our data from the K/BxN mouse model and human patients suggest that administration of Sema3B may be a new therapeutic approach for RA. Multiple studies have shown

that early treatment can prevent RA progression (41–43). Since Sema3B levels are low during the first year of the disease, early administration of Sema3B could prevent or decelerate the progression of joint damage and therefore preclude irreversible disability. Further studies are needed to analyze the therapeutic effect of Sema3B administration.

ACKNOWLEDGMENT

We thank Single Cell Discoveries for their help with the project design, single-cell sequencing services, and data analysis.

AUTHOR CONTRIBUTIONS

All authors were involved in drafting the article or revising it critically for important intellectual content, and all authors approved the final version to be published. Dr. García had full access to all of the data in the study and takes responsibility for the integrity of the data and the accuracy of the data analysis.

Study conception and design. Veale, Fearon, Conde, Pego-Reigosa, González-Fernández, Reedquist, Radstake, van der Helm-Van Mil, García.

Acquisition of data. Igea, Carvalheiro, Malvar-Fernández, Martinez-Ramos, Rafael-Vidal, Niemantsverdriet, Varadé, Fernández-Carrera, McGarry, Rodriguez-Trillo, García.

Analysis and interpretation of data. Igea, Carvalheiro, Malvar-Fernández, Martinez-Ramos, Rafael-Vidal, Niemantsverdriet, Jimenez, Reedquist, Radstake, van der Helm-Van Mil, García.

REFERENCES

1. McInnes IB, Schett G. Pathogenetic insights from the treatment of rheumatoid arthritis. Lancet 2017;389:2328–37.
2. Smolen JS, Aletaha D, Barton A, Burmester GR, Emery P, Firestein GS, et al. Rheumatoid arthritis. Nat Rev Dis Prim 2018;4:1–23.
3. Aletaha D, Smolen JS. Diagnosis and management of rheumatoid arthritis: a review. JAMA 2018;320:1360–72.
4. Sparks JA. Rheumatoid arthritis. Ann Intern Med 2019;170:ITC1–15.
5. Garcia S. Role of semaphorins in immunopathologies and rheumatic diseases. Int J Mol Sci 2019;20:374.
6. Gaur P, Bielenberg DR, Samuel S, Bose D, Zhou Y, Gray MJ, et al. Role of class 3 semaphorins and their receptors in tumor growth and angiogenesis. Clin Cancer Res 2009;15:6763–70.
7. Worzfeld T, Offermanns S. Semaphorins and plexins as therapeutic targets. Nat Rev Drug Discov 2014;13:603–21.
8. Tang MW, Malvar Fernández B, Newsom SP, va Buul JD, Radstake TR, Baeten DL, et al. Class 3 semaphorins modulate the invasive capacity of rheumatoid arthritis fibroblast-like synoviocytes. Rheumatology (Oxford) 2018;57:909–20.
9. Ng CT, Biniecka M, Kennedy A, McCormick J, FitzGerald O, Bresnihan B, et al. Synovial tissue hypoxia and inflammation in vivo. Ann Rheum Dis 2010;69:1389–95.
10. Van Steenbergen HW, Mangnus L, Reijnierse M, Huizinga TW, van der Helm-van Mil AH. Clinical factors, anticitrullinated peptide antibodies and MRI-detected subclinical inflammation in relation to progression from clinically suspect arthralgia to arthritis. Ann Rheum Dis 2016;75:1824–30.
11. Aletaha D, Neogi T, Silman AJ, Funovits J, Felson DT, Bingham CO III, et al. 2010 rheumatoid arthritis classification criteria: an American College of Rheumatology/European League Against Rheumatism collaborative initiative. Arthritis Rheum 2010;62:2569–81.
12. Aletaha D, Neogi T, Silman AJ, Funovits J, Felson DT, Bingham CO III, et al. 2010 Rheumatoid arthritis classification criteria: an American College of Rheumatology/European League Against Rheumatism collaborative initiative. Ann Rheum Dis 2010;69:1580–88.
13. Simmini S, Bialecka M, Huch M, Kester L, Van De Wetering M, Sato T, et al. Transformation of intestinal stem cells into gastric stem cells on loss of transcription factor Cdx2. Nat Commun 2014;5:1–10.
14. Hashimshony T, Wagner F, Sher N, Yanai I. CEL-Seq: Single-Cell RNA-Seq by multiplexed linear amplification. Cell Rep 2012;2:666–73.
15. Li H, Durbin R. Fast and accurate long-read alignment with Burrows-Wheeler transform. Bioinformatics 2010;26:589–95.
16. Love MI, Huber W, Anders S. Moderated estimation of fold change and dispersion for RNA-seq data with DESeq2. Genome Biol 2014;15:1–21.
17. Oliveros J. Venny: an interactive tool for comparing lists with Venn's diagrams. 2015. URL: http://BioinfogpCnbCsicEs/Tools/Venny/IndexHtml 2015:2015.
18. McInnes IB, Buckley CD, Isaacs JD. Cytokines in rheumatoid arthritis: shaping the immunological landscape. Nat Rev Rheumatol 2015;12:63–8.
19. Sharma A, Verhaagen J, Harvey AR. Receptor complexes for each of the class 3 semaphorins. Front Cell Neurosci 2012;6:1–13.
20. Miyabe Y, Lian J, Miyabe C, Luster AD. Chemokines in rheumatic diseases: pathogenic role and therapeutic implications. Nat Rev Rheumatol 2019;15:731–46.
21. Lerner A, Neidhöfer S, Reuter S, Matthias T. MMP3 is a reliable marker for disease activity, radiological monitoring, disease outcome predictability, and therapeutic response in rheumatoid arthritis. Best Pract Res Clin Rheumatol 2018;32:550–62.
22. Solomon S, Rajasekaran N, Jeisy-Walder E, Snapper SB, Illges H. A crucial role for macrophages in the pathology of K/B × N serum-induced arthritis. Eur J Immunol 2005;35:3064–73.
23. Wipke BT, Allen PM. Essential role of neutrophils in the initiation and progression of a murine model of rheumatoid arthritis. J Immunol 2001;167:1601–8.
24. Monach PA, Nigrovic PA, Chen M, Hock H, Lee DM, Benoist C, et al. Neutrophils in a mouse model of autoantibody-mediated arthritis: critical producers of Fc receptor γ, the receptor for C5a, and lymphocyte function–associated antigen 1. Arthritis Rheum 2010;62:753–64.
25. Müller-Ladner U, Kriegsmann J, Franklin BN, Matsumoto S, Geiler T, Gay RE, et al. Synovial fibroblasts of patients with rheumatoid arthritis attach to and invade normal human cartilage when engrafted into SCID mice. Am J Pathol 1996;149:1607–15.
26. Lefèvre S, Knedla A, Tennie C, Kampmann A, Wunrau C, Dinser R, et al. Synovial fibroblasts spread rheumatoid arthritis to unaffected joints. Nat Med 2009;15:1414–20.
27. Xing Q, Feng J, Zhang X. Semaphorin3B promotes proliferation and osteogenic differentiation of bone marrow mesenchymal stem cells in a high-glucose microenvironment. Stem Cells Int 2021;2021:13–5.
28. Sang C, Zhang Y, Chen F, Huang P, Qi J, Wang P, et al. Tumor necrosis factor α suppresses osteogenic differentiation of MSCs by inhibiting semaphorin 3B via Wnt/β-catenin signaling in estrogen-deficiency induced osteoporosis. Bone 2016;84:78–87.
29. Sabag AD, Smolkin T, Mumblat Y, Ueffing M, Kessler O, Gloeckner CJ, et al. The role of the plexin-A2 receptor in Sema3A and Sema3B signal transduction. J Cell Sci 2014;127:5240–52.
30. Varshavsky A, Kessler O, Abramovitch S, Kigel B, Zaffryar S, Akiri G, et al. Semaphorin-3B is an angiogenesis inhibitor that is inactivated by furin-like pro-protein convertases. Cancer Res 2008;68:6922–31.
31. Catalano A. The neuroimmune semaphorin-3A reduces inflammation and progression of experimental autoimmune arthritis. J Immunol 2010;185:6373–83.
32. Teng Y, Yin Z, Li J, Li K, Li X, Zhang Y. Adenovirus-mediated delivery of Sema3A alleviates rheumatoid arthritis in a serum-transfer induced mouse model. Oncotarget 2017;8:66270–80.

33. Schett G, Tohidast-Akrad M, Smolen JS, Schmid BJ, Steiner CW, Bitzan P, et al. Activation, differential localization, and regulation of the stress-activated protein kinases, extracellular signal–regulated kinase, c-JUN N-terminal kinase, and p38 mitogen-activated protein kinase, in synovial tissue and cells in rheumatoid arthritis. Arthritis Rheum 2000;43:2501–12.
34. De Launay D, van de Sande MG, de Hair MJ, Grabiec AM, van de Sande GP, Lehmann KA, et al. Selective involvement of ERK and JNK mitogen-activated protein kinases in early rheumatoid arthritis (1987 ACR criteria compared to 2010 ACR/EULAR criteria): a prospective study aimed at identification of diagnostic and prognostic biomarkers as well as therapeutic targets. Ann Rheum Dis 2012;71:415–23.
35. Cush JJ, Splawski JB, Thomas R, Mcfarlin JE, Schulze-Koops H, Davis LS, et al. Elevated interleukin-10 levels in patients with rheumatoid arthritis. Arthritis Rheum 1995;38:96–104.
36. Bucht A, Larsson P, Weisbrot L, Thorne C, Pisa P, Smedegård G, et al. Expression of interferon-gamma (IFN-γ), IL-10, IL-12 and transforming growth factor-beta (TGF-β) mRNA in synovial fluid cells from patients in the early and late phases of rheumatoid arthritis (RA). Clin Exp Immunol 1996;103:357–67.
37. Raza K, Falciani F, Curnow SJ, Ross EJ, Lee CY, Akbar AN, et al. Early rheumatoid arthritis is characterized by a distinct and transient synovial fluid cytokine profile of T cell and stromal cell origin. Arthritis Res Ther 2005;7:R784–95.
38. Lu MC, Lai NS, Yu HC, Huang HB, Hsieh SC, Yu CL. Anti–citrullinated protein antibodies bind surface-expressed citrullinated Grp78 on monocyte/macrophages and stimulate tumor necrosis factor α production. Arthritis Rheum 2010;62:1213–23.
39. Dong X, Zheng Z, Lin P, Fu X, Li F, Jiang J, et al. ACPAs promote IL-1β production in rheumatoid arthritis by activating the NLRP3 inflammasome. Cell Mol Immunol 2020;17:261–71.
40. Clavel C, Nogueira L, Laurent L, Iobagiu C, Vincent C, Sebbag M, et al. Induction of macrophage secretion of tumor necrosis factor α through Fcγ receptor IIa engagement by rheumatoid arthritis–specific autoantibodies to citrullinated proteins complexed with fibrinogen. Arthritis Rheum 2008;58:678–88.
41. Van Nies JA, Tsonaka R, Gaujoux-Viala C, Fautrel B, Van Der Helm-Van Mil AH. Evaluating relationships between symptom duration and persistence of rheumatoid arthritis: does a window of opportunity exist? Results on the Leiden Early Arthritis Clinic and ESPOIR cohorts. Ann Rheum Dis 2015;74:806–12.
42. Van Der Linden MP, Le Cessie S, Raza K, Van Der Woude D, Knevel R, Huizinga TW, et al. Long-term impact of delay in assessment of patients with early arthritis. Arthritis Rheum 2010;62:3537–46.
43. Van Der Woude D, Young A, Jayakumar K, Mertens BJ, Toes RE, van der Heijde, et al. Prevalence of and predictive factors for sustained disease-modifying antirheumatic drug–free remission in rheumatoid arthritis: results from two large early arthritis cohorts. Arthritis Rheum 2009;60:2262–71.

American College of Rheumatology
Empowering Rheumatology Professionals

Arthritis & Rheumatology
Vol. 74, No. 6, June 2022, pp 984–991
DOI 10.1002/art.42064

Rheumatoid Factor and Anti–Modified Protein Antibody Reactivities Converge on IgG Epitopes

Aisha M. Mergaert,[1] Zihao Zheng,[1] Michael F. Denny,[1] Maya F. Amjadi,[1] S. Janna Bashar,[1] Michael A. Newton,[1] Vivianne Malmström,[2] Caroline Grönwall,[2] Sara S. McCoy,[1] and Miriam A. Shelef[3]

Objective. Rheumatoid arthritis (RA) patients often develop rheumatoid factors (RFs), antibodies that bind IgG Fc, and anti–modified protein antibodies (AMPAs), multireactive autoantibodies that commonly bind citrullinated, homocitrullinated, and acetylated antigens. Recently, antibodies that bind citrulline-containing IgG epitopes were discovered in RA, suggesting that additional undiscovered IgG epitopes could exist and that IgG could be a shared antigen for RFs and AMPAs. This study was undertaken to reveal new IgG epitopes in rheumatic disease and to determine if multireactive AMPAs bind IgG.

Methods. Using sera from patients with RA, systemic lupus erythematosus, Sjögren's disease (SjD), or spondyloarthropathy, IgG binding to native, citrulline-containing, and homocitrulline-containing linear epitopes of the IgG constant region was evaluated by peptide array, with highly bound epitopes further evaluated by enzyme-linked immunosorbent assay (ELISA). Binding of monoclonal AMPAs to IgG-derived peptides and IgG Fc was also evaluated by ELISA.

Results. Seropositive RA sera showed high IgG binding to multiple citrulline- and homocitrulline-containing IgG-derived peptides, whereas anti-SSA+ sera from SjD patients showed consistent binding to a single linear native epitope of IgG in the hinge region. Monoclonal AMPAs bound citrulline- and homocitrulline-containing IgG peptides and modified IgG Fc.

Conclusion. The repertoire of epitopes bound by AMPAs includes modified IgG epitopes, positioning IgG as a common antigen that connects the otherwise divergent reactivities of RFs and AMPAs.

INTRODUCTION

Two main types of autoantibodies with high diagnostic value and possible pathogenic roles exist in rheumatoid arthritis (RA): rheumatoid factors (RFs) and anti–citrullinated protein antibodies (ACPAs). RFs, which are antibodies of any isotype that bind the Fc portion of IgG, are common in RA but are also found less frequently in those with systemic lupus erythematosus (SLE), anti-SSA+ Sjögren's disease (SjD), ankylosing spondylitis, some infections, hematologic malignancy, or in smokers (1–6). RFs commonly bind to 2 conformational epitopes after antigen binding, enzymatic degradation, or other changes to the IgG molecule: 1 in the hinge region and 1 that includes parts of the C_H2 and C_H3 regions (5,7–9). In RA, additional epitopes are bound, affinity maturation occurs, and IgG-RF and IgA-RF are common (4,5,10), all of which show evidence of T cell help. However, it is unknown why tolerance against IgG is lost in T cells.

In addition to RFs, ~75% of RA patients develop ACPAs, autoantibodies against proteins containing arginines that were posttranslationally modified to citrullines (11). Unlike RFs, ACPAs

Supported by the National Heart, Lung, and Blood Institute, NIH (award T32 HL007899 to Dr. Mergaert), the National Institute on Aging, NIH (award T32 AG000213 to Ms. Amjadi), MSTP funding (award T32 GM140935 to Ms. Amjadi), the Clinical and Translational Science Award program through the National Center for Advancing Translational Sciences, NIH (awards UL1TR002373 and KL2TR002374 to Dr. McCoy), and the US Army Medical Research Acquisition Activity through the Peer Reviewed Medical Research Program (award W81XWH-18-1-0717), the University of Wisconsin-Madison, Office of the Vice Chancellor for Research and Graduate Education with funding from the Wisconsin Alumni Research Foundation (to Dr. Shelef). Monoclonal anti–modified protein antibody work was supported by the Swedish Research Council and the European Union/European Federation of Pharmaceutical Industries and Associations' Innovative Medicines Initiative 2 Joint Undertaking project (RTCure grant 777357).

[1]Aisha M. Mergaert, PhD, Zihao Zheng, Michael F. Denny, PhD, Maya F. Amjadi, BS, S. Janna Bashar, MS, Michael A. Newton, PhD, Sara S. McCoy, MD: University of Wisconsin-Madison; [2]Vivianne Malmström, PhD, Caroline Grönwall, PhD: Karolinska University Hospital, Stockholm, Sweden; [3]Miriam A. Shelef, MD, PhD: University of Wisconsin-Madison and William S. Middleton Memorial Veterans Hospital, Madison, Wisconsin.

Author disclosures are available at https://onlinelibrary.wiley.com/action/downloadSupplement?doi=10.1002%2Fart.42064&file=art42064-sup-0001-Disclosureform.pdf.

Address correspondence to Miriam A. Shelef, MD, PhD, 4130 UW Medical Foundation Centennial Building, 1685 Highland Avenue, Madison, WI 53705. Email: mshelef@medicine.wisc.edu.

Submitted for publication July 23, 2021; accepted in revised form January 4, 2022.

are highly specific to RA and are associated with shared epitope–containing HLA alleles (12), which may contribute to their development. In RA, autoantibodies that bind to epitopes in which lysines have been converted to homocitrullines, i.e., homocitrullinated (carbamylated) antigens, have also been identified (13). Moreover, individual ACPAs are often anti–modified protein antibodies (AMPAs), given their frequent reactivity to homocitrullinated and acetylated epitopes in addition to their multireactivity to many citrullinated targets (14–16). It is a long-standing mystery as to why AMPAs and RFs typically coexist in RA. Perhaps each autoantibody type enhances the other's production and/or a common antigen underlies the development of both autoantibodies (12,17).

Recently, IgG in RA sera was shown to bind to citrulline-containing linear peptides present in the constant region of the IgG heavy chain (18), suggesting the possibility that IgG could be a shared antigen for RFs and AMPAs. However, although RF is defined by its binding to IgG, the ability of AMPAs to recognize modified IgG epitopes is unknown. Moreover, the use of modern technology to discover new IgG epitopes in a few RA patients raised the possibility of additional unexplored IgG epitopes in RA and other rheumatic diseases with RF.

In this study, we evaluate the repertoire of IgG heavy chain–derived linear peptides bound by serum IgG from patients with rheumatic diseases and by monoclonal AMPAs to identify new IgG epitopes and to determine whether IgG is a common antigen for AMPAs and RFs.

PATIENTS AND METHODS

Subjects. Human subject research was approved by the University of Wisconsin Institutional Review Board and complied with the Declaration of Helsinki. Sera were obtained from the University of Wisconsin (UW) Rheumatology Biorepository (19,20), which has expanded to include SLE, SjD, and spondyloarthropathy. Subjects were ≥18 years old and received care at UW Health.

In this study, RA patients met the 2010 American College of Rheumatology (ACR)/European Alliance of Associations for Rheumatology (EULAR) diagnostic criteria for RA (21). Anti–cyclic citrullinated peptide–positive (anti-CCP+) RF-positive (RF+) RA patients had anti-CCP and RF levels more than twice the upper limit of normal, and anti-CCP–RF– RA patients tested negative for both markers in UW Health's clinical labs. Lupus patients met Systemic Lupus International Collaborating Clinics criteria (22). All SjD patients met the 2016 ACR/EULAR classification criteria for primary SjD (23), except for 2 patients: 1 with a positive SSA test result and the other with a minor salivary gland biopsy with a focus score >1, but both had incomplete medical record documentation for objective sicca. Patients with spondyloarthropathy were diagnosed by a rheumatologist as having ankylosing spondylitis, psoriatic arthritis, or inflammatory bowel disease associated arthritis, and all showed radiographic evidence of sacroiliitis. Controls were matched by age and sex and had none of the following diagnoses: RA, lupus, SjD, scleroderma, psoriasis, psoriatic arthritis, ankylosing spondylitis, reactive arthritis, ulcerative colitis, Crohn's disease, multiple sclerosis, type I diabetes mellitus, or hematologic malignancy. Subject characteristics can be found in Supplementary Tables 1–4 (available on the *Arthritis & Rheumatology* website at https://onlinelibrary.wiley.com/doi/10.1002/art.42064).

High-density peptide array. A high-density peptide array (Roche NimbleGen) was used to detect serum IgG that bound to overlapping 12–amino acid peptides derived from the constant region of the heavy chains of IgG1 (UniProt no. P01857), IgG2 (no. P01859), IgG3 (no. P01860), and IgG4 (no. P01861), as previously described (18). Peptides were included in 3 forms: native, all arginines replaced by citrullines, and all lysines replaced by homocitrullines.

Monoclonal AMPAs. Generation of the human monoclonal AMPAs from single B cells from RA patients has previously been described. Clones 1325:07E07 and 1325:04C03 were derived from synovial plasma cells (14), and clones 37CEPT1G09, 14CFCT3G09, and 37CEPF2C05 were derived from blood memory B cells (24). The monoclonal antibodies were recombinantly expressed as human IgG1, purified, and extensively quality-controlled (25). All AMPA clones bound CCP2 and multiple citrullinated peptides without native peptide reactivity and with reactivity against homocitrullinated antigens ranging from very limited to extensive (14,15,24,26,27). The negative control clone 1362:01E02 has not displayed any reactivity to any posttranslational modifications or control antigens (15,27).

Posttranslational modification of IgG Fc. IgG Fc (MilliporeSigma) was depleted of contaminating IgM and residual light chain using streptavidin magnetic beads (ThermoFisher Scientific) coated with biotin-conjugated goat IgG anti-human IgM, goat IgG anti-human kappa, and goat IgG anti-human lambda (Southern Biotech). IgG Fc was citrullinated by treatment with 2 μg of peptidylarginine deiminase type 2 (PAD2) and PAD4, per 1 mg of IgG Fc, in a buffer of 100 m*M* Tris HCl (pH 7.5), 1 m*M* dithiothreitol, and 5 m*M* CaCl2. IgG Fc was homocitrullinated by treatment with 0.1*M* KOCN in H_2O, stopping the reaction with 0.15*M* Tris (pH 8.8). Citrullination and homocitrullination are demonstrated in Supplementary Figure 1 (available on the *Arthritis & Rheumatology* website at https://onlinelibrary.wiley.com/doi/10.1002/art.42064).

Enzyme-linked immunosorbent assay (ELISA). For peptide ELISA, plates were coated with 5 μg/ml streptavidin (ThermoFisher Scientific) for 1 hour at room temperature, washed with phosphate buffered saline (PBS), and then coated with 0.125 μ*M* of peptide conjugated to biotin at the C terminus

(Biomatik) for 1 hour at room temperature. Peptides are listed in Supplementary Table 5 (available on the *Arthritis & Rheumatology* website at https://onlinelibrary.wiley.com/doi/10.1002/art.42064). For IgG Fc ELISA, plates were coated overnight at 4°C with 10 μg/ml IgG Fc in PBS in 4 forms: treated with PADs in buffer, treated with 0.1*M* KOCN in H_2O, diluted in citrullination buffer, and diluted in H_2O. After washing with PBS, plates were blocked for 1 hour at room temperature with 5% nonfat dried milk in 0.2% Tween 20 in PBS (serum ELISA block) or 1% bovine serum albumin in PBS (monoclonal AMPA ELISA block without 0.1% Tween 20). Sera diluted 1:200 or 1:2,000 in serum ELISA block or 1 μg/ml monoclonal AMPAs (14,24) in monoclonal AMPA ELISA block were applied to plates overnight at 4°C. After 3 washes, plates were incubated with mouse monoclonal anti-human IgG conjugated to horse radish peroxidase (HRP) (clone JDC-10; Southern Biotech) diluted 1:5,000 in serum ELISA block, or goat anti-human lambda and anti-human kappa IgG conjugated to HRP (Southern Biotech) diluted 1:5,000 in monoclonal AMPA ELISA block.

After one hour at room temperature, plates were washed 4 times, developed with 3,3′,5,5′-tetramethylbenzidine (ThermoFisher Scientific) for 10 minutes, then stopped with 0.18*M* sulfuric acid. Plates were read on a FilterMAX F3 (Molecular Devices) at an optical density of 450 nm and 562 nm, with 562-nm values subtracted from 450-nm values for each sample. For each sample, absorbance values for uncoated wells were subtracted from peptide- or Fc-coated wells to exclude nonspecific binding, and absorbance values for PAD-containing buffer were subtracted from wells coated with PAD-treated IgG Fc to exclude anti-PAD reactivity.

Each plate included a standard curve of purified human IgG ranging from 0.0169 to 1,000 ng/ml. To generate the human IgG standard curve, wells were coated with streptavidin as described above, followed by biotin-labeled goat IgG anti-human lambda and kappa capture antibodies at a 1:5,000 dilution. Following a blocking step, serially diluted purified human IgG (Bethyl Laboratories) in blocking buffer was added to the wells. The serially diluted human IgG was detected using the same method described above. The background-corrected absorbance values for the patient serum samples were converted to ng/ml of human IgG by applying a 4-parameter nonlinear curve fit to the wells containing the human IgG standards (elisaanalysis.com).

Statistical analysis. To avoid making distributional assumptions about the array measurements, we used nonparametric statistical tests. ELISA data for disease groups versus controls were compared by Mann-Whitney or Kruskal-Wallis tests. Analyses were performed using GraphPad Prism software, and *P* values less than 0.05 were considered significant. Categorical variables were compared using Pearson's chi-square and Fisher's exact tests, and continuous variables were compared using the Kruskal-Wallis rank test, with Stata version 16 (Supplementary Tables 1–4, available on the *Arthritis & Rheumatology* website at https://onlinelibrary.wiley.com/doi/10.1002/art.42064).

RESULTS

To evaluate IgG epitopes bound in RA and other rheumatic diseases, we quantified IgG binding to every 12–amino acid linear peptide derived from the constant region of the heavy chain of human IgG1–4 using a high-density peptide array (18) and sera from patients diagnosed as having RA (anti-CCP+RF+ and anti-CCP–RF–), lupus, SjD (anti-SSA+ and anti-SSA–), or spondyloarthropathy, as well as age- and sex-matched controls. Anti-CCP+RF+ RA serum IgG bound strongly to multiple citrulline- and homocitrulline-containing peptides derived from all IgG isotypes, with minimal binding to corresponding arginine- and lysine-containing native peptides (Figure 1 and Supplementary Figure 2, available on the *Arthritis & Rheumatology* website at https://onlinelibrary.wiley.com/doi/10.1002/art.42064). Serum IgG from patients with other diseases displayed very limited binding to linear IgG-derived peptides overall, although anti-SSA+ serum IgG from patients with SjD or spondyloarthropathy bound to native peptides in the hinge region. As expected (2), serum IgG from anti-CCP–RF– RA patients and anti-SSA– SjD patients showed no areas of high binding to IgG-derived peptides.

In a previous study that used an identical array with different RA patients (18), IgG binding to homocitrulline-containing epitopes was not as prominent. To identify a cause for this discrepancy, we more closely inspected the binding of serum IgG for each anti-CCP+RF+ RA patient in the previous study and in the current study (Supplementary Figure 3, available on the *Arthritis & Rheumatology* website at https://onlinelibrary.wiley.com/doi/10.1002/art.42064). We found similar maximum and minimum binding signals in both arrays, with more subjects in the current study displaying high binding to homocitrulline-containing epitopes.

We then selected regions of IgG1, the most abundant IgG subclass (28), that were highly bound in anti-CCP+RF+ RA based on our current array experiment (peptide sequences shown in Supplementary Table 5, available on the *Arthritis & Rheumatology* website at https://onlinelibrary.wiley.com/doi/10.1002/art.42064), for further evaluation of IgG binding by ELISA. Anti-CCP+RF+ RA sera showed increased binding, compared to control sera, to most of the homocitrulline-containing, citrulline-containing, and dually modified peptides, with only 1 native peptide bound more in RA than controls (Figure 2). Interestingly, the increased binding in RA patients versus controls was due to both increased binding in RA and reduced binding in controls to modified peptides (versus native peptides). Similar to array results (Supplementary Figure 3, available on the *Arthritis & Rheumatology* website at https://onlinelibrary.wiley.com/doi/10.1002/art.42064), some subjects showed high binding at specific epitopes while others did not. Anti-CCP–RF– RA sera showed no increased binding to any peptide (data not shown).

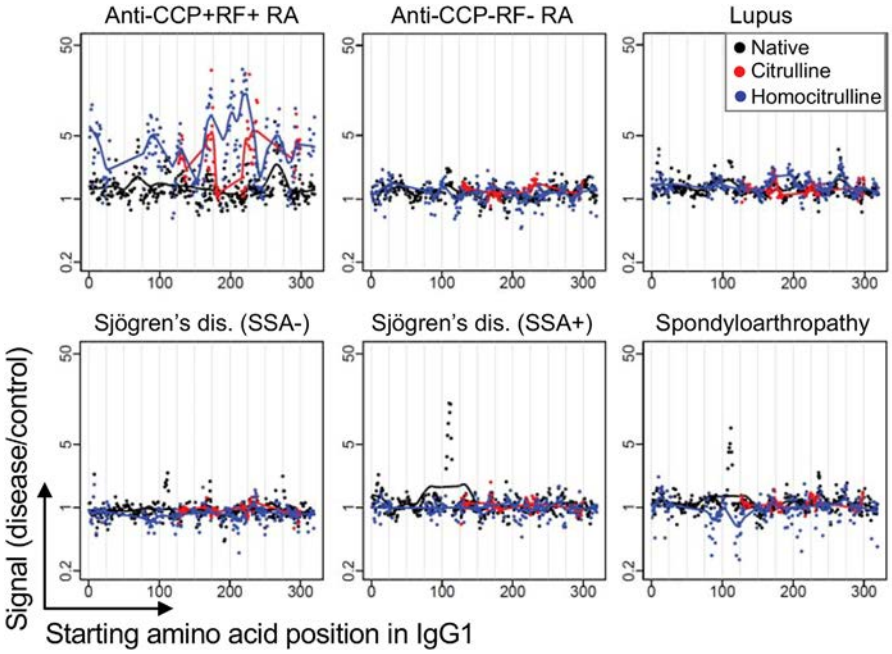

Figure 1. Serum IgG binding to IgG1-derived peptides in rheumatic diseases. Serum IgG binding was quantified for every 12–amino acid linear peptide derived from the constant region of the heavy chain of human IgG1, using a high-density peptide array and sera from patients diagnosed as having rheumatoid arthritis (RA) (anti–cyclic citrullinated peptide–positive [anti-CCP+] rheumatoid factor–positive [RF+] RA and anti-CCP–RF– RA), lupus, Sjögren's disease (anti-SSA+ and anti-SSA–), or spondyloarthropathy, relative to age- and sex-matched controls. IgG binding signal for each disease group (n = 8, except for lupus [n = 16]) was divided by control binding signal and graphed for each peptide according to its starting position in the constant region of the heavy chain of IgG1.

Previously, RA IgG and several monoclonal AMPAs were shown to commonly bind modified antigens if the citrulline was next to glycine or serine, or if the homocitrulline was next to glycine (14,15,18). Therefore, we investigated whether the highly bound IgG1-derived peptides in Figure 2 had similar motifs. Two of the 3 citrullines in highly bound peptides were next to serine, whereas only 1 of the 3 citrullines in poorly bound peptides was next to serine (Figure 3A). None of the 6 total citrullines were next to glycine, and no amino acid was more commonly next to citrulline than serine in the highly bound peptides. Of the 15 homocitrullines in highly bound IgG1-derived peptides, 5 homocitrullines were next to serine, whereas only 1 of the 13 homocitrullines in poorly bound peptides had a neighboring serine (Figure 3B). No amino acid neighbored homocitrulline

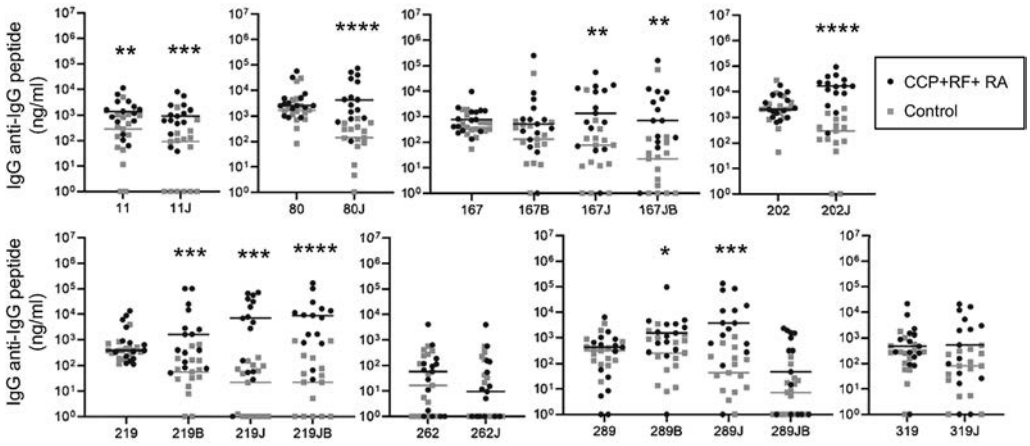

Figure 2. Multiple modified IgG-derived peptides are bound by IgG in anti-CCP+RF+ RA. Binding of IgG from anti-CCP+RF+ RA and control sera to native, citrulline (B)–containing, homocitrulline (J)–containing, and dually modified (JB) peptides (n = 15) starting at the indicated amino acid position of the constant region of the IgG1 heavy chain was quantified by enzyme-linked immunosorbent assay. Symbols represent individual subjects; horizontal lines show the median. * = $P < 0.05$; ** = $P < 0.01$; *** = $P < 0.001$; **** = $P < 0.0001$, versus controls, by Mann-Whitney test. See Figure 1 for other definitions.

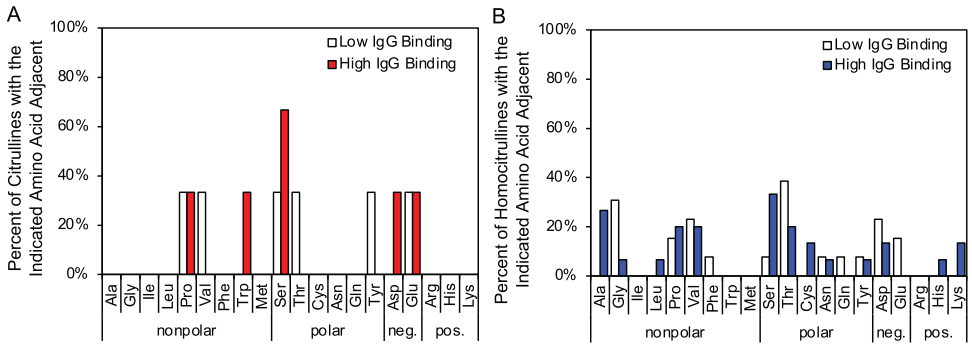

Figure 3. Serine is commonly next to citrulline and homocitrulline in IgG1-derived peptides highly bound by IgG in RA. **A**, Percentage of citrullines with each amino acid adjacent to the citrulline for the 3 citrullines in highly bound IgG1-derived peptides and the 3 citrullines in poorly bound IgG1-derived peptides. **B**, Percentage of homocitrullines with each amino acid in an adjacent position for the 15 homocitrullines in highly bound IgG1-derived peptides and the 13 homocitrullines in poorly bound IgG1-derived peptides. Ala = alanine; Gly = glycine; Ile = isoleucine; Leu = leucine; Pro = proline; Val = valine; Phe = phenylalanine; Trp = tryptophan; Met = methionine; Ser = serine; Thr = threonine; Cys = cysteine; Asn = asparagine; Gln = glutamine; Tyr = tyrosine; Asp = aspartic acid; Glu = glutamic acid; Arg = arginine; His = histidine; Lys = lysine (see Figure 1 for other definitions). Color figure can be viewed in the online issue, which is available at http://onlinelibrary.wiley.com/doi/10.1002/art.42064/abstract.

more commonly than serine in highly bound peptides, including glycine, which was next to only 1 of the 15 homocitrullines in highly bound peptides.

Using ELISA, we next evaluated a peptide from IgG1 in the hinge region starting at position 109, which appeared to be highly bound in non-RA rheumatic disease, as assessed by peptide array (Figure 1). Anti-SSA+ SjD serum IgG, but not lupus or spondyloarthropathy serum IgG, showed significantly increased binding to the hinge peptide compared to controls (Figure 4). There was a trend toward increased binding in anti-CCP+RF+ RA compared to controls, but no increased binding in anti-CCP–RF RA– (Figure 4). Taken together, our data demonstrate a wide range of binding to multiple citrulline- and homocitrulline-containing IgG epitopes in anti-CCP+RF+ RA, with binding to a single linear IgG epitope in SjD.

Given the different IgG epitopes bound in anti-CCP+RF+ RA compared to SjD, and the frequent coexistence of AMPAs and

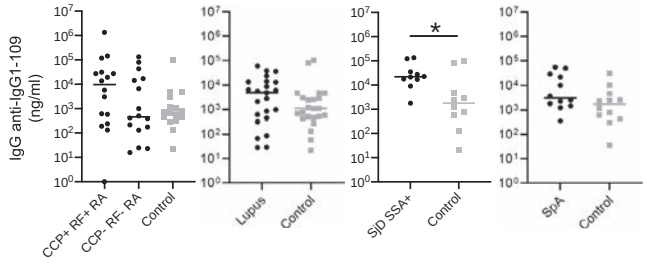

Figure 4. A native linear peptide from the hinge region of IgG1 is bound in Sjögren's disease (SjD). Binding of IgG to a hinge peptide (position 109) was quantified by enzyme-linked immunosorbent assay for anti-CCP+RF+ RA (n = 16), anti-CCP–RF– RA (n = 16), lupus (n = 23), anti-SSA+ primary SjD (n = 10), spondyloarthropathy (SpA; n = 12), and matched controls. Symbols represent individual subjects; horizontal lines show the median. * = $P < 0.05$ versus controls, by Kruskal-Wallis or Mann-Whitney test. See Figure 1 for other definitions.

RFs in RA, we next assessed whether multireactive monoclonal AMPAs could bind to the IgG epitopes highly bound in RA. Five patient-derived monoclonal AMPAs that were previously determined to have cross-reactivity against multiple citrulline-containing epitopes, varying levels of homocitrulline reactivity, and no reactivity with native antigens (14,15,24,26,27), as well as 1 negative control monoclonal antibody, were evaluated for binding to IgG-derived peptides using ELISA (Figure 5). The 3 monoclonal AMPAs (1325:04C03, 37CEPT1G09, and 37CEPTF2C05) previously shown to have homocitrulline multireactivity (14,15,26) showed binding to many modified (including all homocitrulline-containing peptides), but not native, IgG-derived peptides, with different patterns among clones (Figure 5A). The 2 monoclonal AMPA clones (1325:07E07 and 14CFCT3G09) previously shown to be primarily citrulline-restricted (14,15,26) showed very limited binding to IgG-derived peptides. Compared to the extensive binding to homocitrulline-containing peptides, binding to doubly modified peptides was less consistent, and binding to citrulline-containing peptides was comparatively low.

Finally, we evaluated monoclonal AMPA binding to native, citrullinated, and homocitrullinated IgG Fc protein. Two monoclonal AMPAs with high reactivity to modified IgG-derived peptides also bound to IgG Fc, particularly homocitrullinated Fc (Figure 5B). Taken together, these data demonstrate that monoclonal AMPAs, which bind many different modified epitopes (14,15,24), also bind IgG epitopes, bridging the divide between AMPAs and RFs.

DISCUSSION

In this study, we evaluated IgG binding to all possible linear epitopes of the constant region of IgG heavy chain to reveal several key features of autoantibody reactivity in rheumatic disease. First, we discovered several homocitrulline-containing

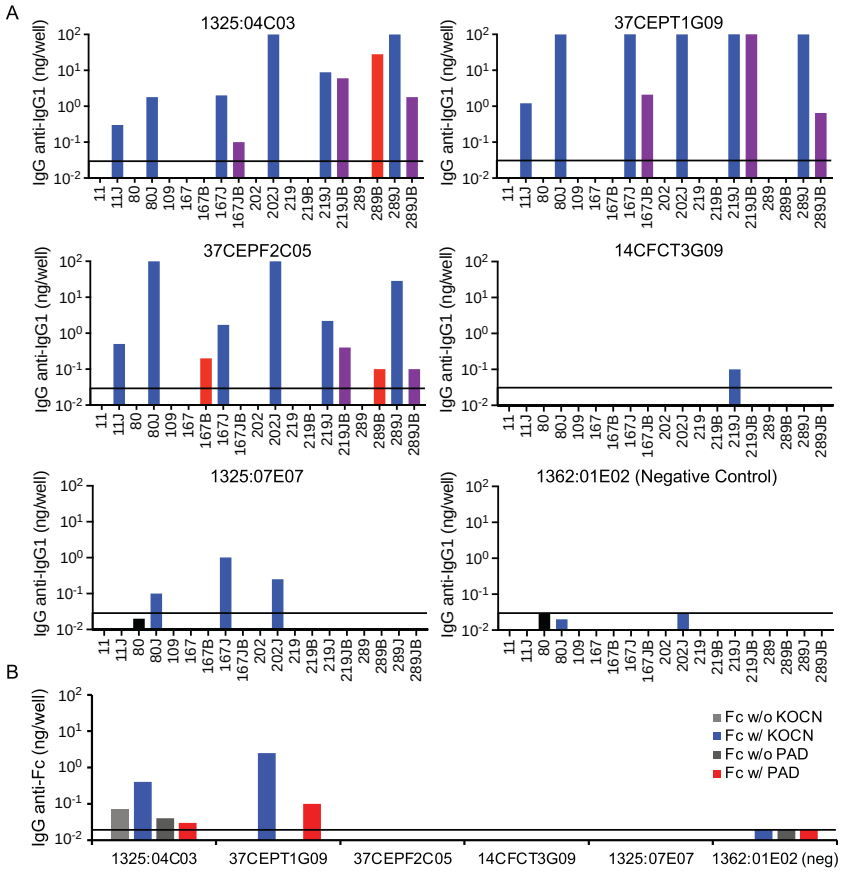

Figure 5. Anti–modified protein antibodies (AMPAs) bind citrulline- and homocitrulline-containing IgG-derived peptides and modified IgG Fc. Five patient-derived monoclonal AMPAs (clones 1325:04C03, 37CEPT1G09, 37CEPF2C05, 14CFCT3G09, and 1325:07E07) and 1 negative control monoclonal antibody (clone 1362:01E02) were assessed by enzyme-linked immunosorbent assay for binding to IgG1-derived peptides (**A**) and to human IgG Fc that was left unmodified (exposed to buffer alone) or was treated with peptidylarginine deiminases (PADs) to citrullinate or KOCN to homocitrullinate (**B**). Native peptides and proteins are shown in black or gray, citrulline (B)–containing peptides in red, homocitrulline (J)–containing peptides in blue, and dually modified (JB) peptides in purple. Numbers on the x-axis in **A** indicate the location of the first amino acid of the peptide in the constant region of the IgG1 heavy chain. Lines indicate the highest level of binding detected for the negative control monoclonal antibody.

IgG epitopes bound in anti-CCP+RF+ RA patients. These homocitrulline-containing epitopes were bound less prominently in a previous study, whereas binding to citrulline-containing IgG1 epitopes was comparable (18). Given the general reproducibility of this array (29), the discrepancy appears to be due to the wide range of reactivity to linear IgG epitopes in anti-CCP+RF+ RA patients (Figure 2 and Supplementary Figure 3, available on the *Arthritis & Rheumatology* website at https://onlinelibrary.wiley.com/doi/10.1002/art.42064). Similarly, the monoclonal AMPAs had different reactivities to IgG epitopes. Homocitrulline-containing epitopes were bound prominently by monoclonal AMPAs, but to varying extents by different clones. Interestingly, only 2 of 5 monoclonal AMPAs bound to citrulline-containing epitopes, perhaps due to the absence of glycine neighboring the citrullines, a previously identified binding motif for 3 of the monoclonal AMPAs (14,15). Minimal citrullination in the case of the Fc protein (Supplementary Figure 1, available on the *Arthritis & Rheumatology* website at https://onlinelibrary.wiley.com/doi/10.1002/art.42064) may have also contributed. Regardless of the cause, our findings suggest different AMPA and RF repertoires among RA patients with binding to homocitrullinated and citrullinated epitopes.

In addition to variability in IgG binding among subjects and monoclonal AMPAs, variability was observed among epitopes. Different citrulline- and homocitrulline-containing epitopes were not equally bound by RA sera, and reactivity to citrulline- and homocitrulline-containing epitopes did not guarantee reactivity with dually modified epitopes, supporting the idea that modification alone is insufficient for antibody binding across all individuals. However, a previously identified motif for IgG binding in RA, serine next to citrulline (18), was present for 2 of 3 citrullines in IgG-derived peptides highly bound by RA IgG in this study. Interestingly, homocitrulline next to serine was also commonly present in highly bound IgG-derived peptides. Homocitrulline–serine pairs have not been previously identified as a highly bound motif by IgG in RA (14,15,18). Despite the common presence of serine

next to homocitrulline or citrulline, a variety of amino acids neighbored the modified amino acids. Thus, additional unknown features of epitopes appear to drive modified antigen targeting in seropositive RA patients, which requires further investigation.

In contrast to the extensive binding of linear IgG epitopes in anti-CCP+RF+ RA, we demonstrated consistent IgG binding to only 1 linear IgG epitope in 1 non-RA disease: a hinge region epitope bound in anti-SSA+ SjD. Conformational epitopes in the hinge and C_H2/C_H3 regions of IgG have been described in RA, hematologic malignancy, lupus, and in healthy controls (5,7,9). Antibody binding to multiple linear epitopes may be a relatively unique feature of RA, consistent with observed reactivity against structurally disordered citrulline-containing and native epitopes (18). Notably, this difference in reactivity against some IgG epitopes in RA versus other rheumatic diseases could be leveraged to refine diagnostic testing.

Taken together, our findings expand on and partially merge the known reactivities of RFs and AMPAs (Figure 6). We have added 2 linear native epitopes (starting at amino acid positions 11 and 109 of IgG1) to the RF repertoire, as well as multiple citrulline- and homocitrulline-containing IgG epitopes to both the RF and AMPA repertoires, positioning IgG as a shared antigen for RFs and AMPAs. The binding of AMPAs to modified IgG epitopes allows for the possibility that IgG, potentially modified, conformationally altered, and/or degraded in vivo, could be a common antigen underlying the development of AMPAs and IgG-RFs in RA, as previously described (17). If true, then tolerance might be lost against modified IgG through a shared epitope–related mechanism, leading to AMPAs and IgG-RFs via epitope spreading. This mechanism may not lead to all IgG-RF, including IgG-RF in lupus (4), a disease without citrulline reactivity. Moreover, this mechanism would not lead to IgM-RF, a major portion of RF in RA, which may be a nonspecific response to inflammation (17). Consistent with this idea, IgM from RA patients positive or those negative for anti-CCP or RF had limited binding to citrulline- and homocitrulline-containing IgG epitopes as evaluated by peptide array (18).

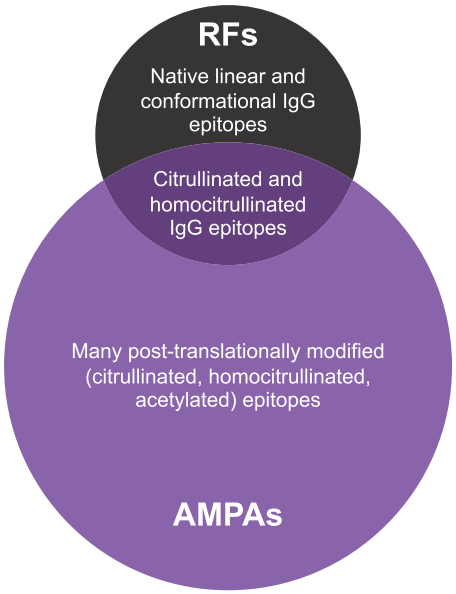

Figure 6. The reactivities of rheumatoid factors (RFs) and anti–modified protein antibodies (AMPAs) converge on IgG epitopes. The Venn diagram illustrates RF and AMPA reactivities. RFs bind native linear and conformational IgG epitopes, and AMPAs bind many different post-translationally modified epitopes. Antibodies that bind citrulline- and homocitrulline-containing IgG epitopes can be considered both an RF, an antibody that binds to the Fc region of IgG, and an AMPA, an antibody that binds posttranslationally modified epitopes. Color figure can be viewed in the online issue, which is available at http://onlinelibrary.wiley.com/doi/10.1002/art.42064/abstract.

Alternatively, AMPAs, perhaps with limited multireactivity, could develop first, followed by the development of anti–modified IgG antibodies and later RF possibly via epitope spreading, which would be consistent with the detection of ACPAs prior to RFs in preclinical RA (30–32), as well as the absence of anti-modified IgG antibodies in anti-CCP+RF- RA (18). Future studies that evaluate the timing of AMPA, RF, and anti-IgG antibody formation in preclinical RA may shed light on how autoantibodies develop. However, although pathophysiologic and mechanistic mysteries remain, the observation that IgG is a common antigen for RFs and AMPAs could underly the frequent coexistence of AMPAs and IgG-RF in RA.

In summary, we discovered new IgG epitopes in rheumatic disease and demonstrated that IgG epitopes are bound by AMPAs in addition to RFs. These findings provide new insights into the loss of tolerance against IgG and the development of autoantibodies in RA and other rheumatic diseases.

ACKNOWLEDGMENT

We thank Dr. Daniel Mueller for his contributions to monoclonal anti–citrullinated protein antibody development.

AUTHOR CONTRIBUTIONS

All authors were involved in drafting the article or revising it critically for important intellectual content, and all authors approved the final version to be published. Dr. Shelef had full access to all of the data in the study and takes responsibility for the integrity of the data and the accuracy of the data analysis.

Study conception and design. Shelef.

Acquisition of data. Mergaert, Denny, Amjadi, Bashar, Malmström, Grönwall, McCoy, Shelef.

Analysis and interpretation of data. Mergaert, Zheng, Denny, Newton, Shelef.

REFERENCES

1. Newkirk MM, Mitchell S, Procino M, Li Z, Cosio M, Mazur W, et al. Chronic smoke exposure induces rheumatoid factor and anti-heat shock protein 70 autoantibodies in susceptible mice and humans with lung disease. Eur J Immunol 2012;42:1051–61.
2. Harley JB, Alexander EL, Bias WB, Fox OF, Provost TT, Reichlin M, et al. Anti–Ro (SS-A) and anti–La (SS-B) in patients with Sjögren's syndrome. Arthritis Rheum 1986;29:196–206.

3. Moller P, Kleveland G, Egeland T, Vinje O, Mellbye OJ. IgA and rheumatoid factor in ankylosing spondylitis. Scand J Rheumatol Suppl 1988;75:276–7.
4. Jonsson T, Steinsson K, Jonsson H, Geirsson AJ, Thorsteinsson J, Valdimarsson H. Combined elevation of IgM and IgA rheumatoid factor has high diagnostic specificity for rheumatoid arthritis. Rheumatol Int 1998;18:119–22.
5. Artandi SE, Calame KL, Morrison SL, Bonagura VR. Monoclonal IgM rheumatoid factors bind IgG at a discontinuous epitope comprised of amino acid loops from heavy-chain constant-region domains 2 and 3. Proc Natl Acad Sci U S A 1992;89:94–8.
6. Watanabe K, Ohkubo Y, Funahashi Y, Nishimaki T, Moritoh T, Kasukawa R, et al. An investigation on rheumatoid factor of different immunoglobulin classes in hepatitis B virus carriers. Clin Rheumatol 1991;10:31–7.
7. Terness P, Kohl I, Hubener G, Battistutta R, Moroder L, Welschof M, et al. The natural human IgG anti-F(ab')2 antibody recognizes a conformational IgG1 hinge epitope. J Immunol 1995;154:6446–52.
8. Maibom-Thomsen SL, Trier NH, Holm BE, Hansen KB, Rasmussen MI, Chailyan A, et al. Immunoglobulin G structure and rheumatoid factor epitopes. PLoS One 2019;14:e0217624.
9. Falkenburg WJ, van Schaardenburg D, Ooijevaar-de Heer P, Tsang AS, Bultink IE, Voskuyl AE, et al. Anti-hinge antibodies recognize IgG subclass- and protease-restricted neoepitopes. J Immunol 2017; 198:82–93.
10. Borretzen M, Randen I, Zdarsky E, Forre O, Natvig JB, Thompson KM. Control of autoantibody affinity by selection against amino acid replacements in the complementarity-determining regions. Proc Natl Acad Sci U S A 1994;91:12917–21.
11. Schellekens GA, de Jong BA, van den Hoogen FH, van de Putte LB, van Venrooij WJ. Citrulline is an essential constituent of antigenic determinants recognized by rheumatoid arthritis-specific autoantibodies. J Clin Invest 1998;101:273–81.
12. Hedstrom AK, Ronnelid J, Klareskog L, Alfredsson L. Complex relationships of smoking, HLA–DRB1 genes, and serologic profiles in patients with early rheumatoid arthritis: update from a Swedish population-based case–control study. Arthritis Rheumatol 2019;71: 1504–11.
13. Shi J, Knevel R, Suwannalai P, van der Linden MP, Janssen GM, van Veelen PA, et al. Autoantibodies recognizing carbamylated proteins are present in sera of patients with rheumatoid arthritis and predict joint damage. Proc Natl Acad Sci U S A 2011;108:17372–7.
14. Steen J, Forsstrom B, Sahlstrom P, Odowd V, Israelsson L, Krishnamurthy A, et al. Recognition of amino acid motifs, rather than specific proteins, by human plasma cell–derived monoclonal antibodies to posttranslationally modified proteins in rheumatoid arthritis. Arthritis Rheumatol 2019;71:196–209.
15. Sahlstrom P, Hansson M, Steen J, Amara K, Titcombe PJ, Forsstrom B, et al. Different hierarchies of anti–modified protein autoantibody reactivities in rheumatoid arthritis. Arthritis Rheumatol 2020;72: 1643–57.
16. Kissel T, Reijm S, Slot LM, Cavallari M, Wortel CM, Vergroesen RD, et al. Antibodies and B cells recognising citrullinated proteins display a broad cross-reactivity towards other post-translational modifications. Ann Rheum Dis 2020;79:472–80.
17. Shelef MA. New relationships for old autoantibodies in rheumatoid arthritis [editorial]. Arthritis Rheumatol 2019;71:1396–9.
18. Zheng Z, Mergaert AM, Fahmy LM, Bawadekar M, Holmes CL, Ong IM, et al. Disordered antigens and epitope overlap between anti–citrullinated protein antibodies and rheumatoid factor in rheumatoid arthritis. Arthritis Rheumatol 2020;72:262–72.
19. Rebernick R, Fahmy L, Glover C, Bawadekar M, Shim D, Holmes CL, et al. DNA area and NETosis Analysis (DANA): a high-throughput method to quantify neutrophil extracellular traps in fluorescent microscope images. Biol Proced Online 2018;20:7.
20. Holmes CL, Peyton CG, Bier AM, Donlon TZ, Osman F, Bartels CM, et al. Reduced IgG titers against pertussis in rheumatoid arthritis: Evidence for a citrulline-biased immune response and medication effects. PLoS One 2019;14:e0217221.
21. Aletaha D, Neogi T, Silman AJ, Funovits J, Felson DT, Bingham CO III, et al. 2010 rheumatoid arthritis classification criteria: an American College of Rheumatology/European League Against Rheumatism collaborative initiative. Arthritis Rheum 2010;62:2569–81.
22. Petri M, Orbai AM, Alarcón GS, Gordon C, Merrill JT, Fortin PR, et al. Derivation and validation of the Systemic Lupus International Collaborating Clinics classification criteria for systemic lupus erythematosus. Arthritis Rheum 2012;64:2677–86.
23. Shiboski CH, Shiboski SC, Seror R, Criswell LA, Labetoulle M, Lietman TM, et al. 2016 American College of Rheumatology/European League Against Rheumatism classification criteria for primary Sjögren's syndrome: a consensus and data-driven methodology involving three international patient cohorts. Arthritis Rheumatol 2017;69:35–45.
24. Titcombe PJ, Wigerblad G, Sippl N, Zhang N, Shmagel AK, Sahlstrom P, et al. Pathogenic citrulline-multispecific B cell receptor clades in rheumatoid arthritis. Arthritis Rheumatol 2018;70:1933–45.
25. Amara K, Israelsson L, Stalesen R, Sahlstrom P, Steen J, Malmstrom V, et al. A refined protocol for identifying citrulline-specific monoclonal antibodies from single human B Cells from rheumatoid arthritis patient material. Bio Protoc 2019;9:e3347.
26. Gronwall C, Liljefors L, Bang H, Hensvold AH, Hansson M, Mathsson-Alm L, et al. A comprehensive evaluation of the relationship between different IgG and IgA anti-modified protein autoantibodies in rheumatoid arthritis. Front Immunol 2021;12:627986.
27. Lloyd KA, Wigerblad G, Sahlstrom P, Garimella MG, Chemin K, Steen J, et al. Differential ACPA binding to nuclear antigens reveals a PAD-independent pathway and a distinct subset of acetylation cross-reactive autoantibodies in rheumatoid arthritis. Front Immunol 2018; 9:3033.
28. Morell A, Skvaril F, Steinberg AG, Van Loghem E, Terry WD. Correlations between the concentrations of the four sub-classes of IgG and Gm Allotypes in normal human sera. J Immunol 1972;108: 195–206.
29. Zheng Z, Mergaert AM, Ong IM, Shelef MA, Newton MA. MixTwice: large-scale hypothesis testing for peptide arrays by variance mixing. Bioinformatics 2021;37:2637–43. E-pub ahead of print. DOI: https://doi.org/10.1093/bioinformatics/btab162.
30. Nielen MM, van Schaardenburg D, Reesink HW, van de Stadt RJ, van der Horst-Bruinsma IE, de Koning MH, et al. Specific autoantibodies precede the symptoms of rheumatoid arthritis: a study of serial measurements in blood donors. Arthritis Rheum 2004;50:380–6.
31. Kelmenson LB, Wagner BD, McNair BK, Frazer-Abel A, Demoruelle MK, Bergstedt DT, et al. Timing of elevations of autoantibody isotypes prior to diagnosis of rheumatoid arthritis. Arthritis Rheumatol 2020;72: 251–61.
32. Mikuls TR, Edison J, Meeshaw E, Sayles H, England BR, Duryee MJ, et al. Autoantibodies to malondialdehyde–acetaldehyde are detected prior to rheumatoid arthritis diagnosis and after other disease specific autoantibodies. Arthritis Rheumatol 2020;72:2025–9.

American College of Rheumatology
Empowering Rheumatology Professionals

Arthritis & Rheumatology
Vol. 74, No. 6, June 2022, pp 992–1000
DOI 10.1002/art.42076

Prevalence, Incidence, and Progression of Radiographic and Symptomatic Hand Osteoarthritis: The Osteoarthritis Initiative

Charles B. Eaton,[1] Lena F. Schaefer,[2] Jeff Duryea,[3] Jeff B. Driban,[4] Grace H. Lo,[5] Mary B. Roberts,[6] Ida K. Haugen,[7] Bing Lu,[3] Michael C. Nevitt,[8] Marc C. Hochberg,[9] Rebecca D. Jackson,[10] C. K. Kwoh,[11] and Timothy McAlindon[12]

Objective. To describe the prevalence, incidence, and progression of radiographic and symptomatic hand osteoarthritis (OA), and to evaluate differences according to age, sex, race, and other risk factors.

Methods. Participants were assessed for radiographic and symptomatic hand OA at baseline and year 4 to determine incident disease. A modified Poisson regression with a robust variance estimator was used to account for clustering of joints within fingers within persons to estimate the prevalence ratios and relative risk estimates associated with participant characteristics.

Results. Among 3,588 participants, the prevalence of radiographic hand OA was 41.4%, and the prevalence of symptomatic hand OA was 12.4%. The incidence over 48 months was 5.6% for radiographic hand OA and 16.9% for symptomatic hand OA. Over 48 months, 27.3% of the participants exhibited OA progression. We found complex differences by age, sex, and race, with increasing rates of prevalent hand OA with older age in both men and women, but with rates of incident disease peaking at ages 55–64 years in women. Women had higher rates of symptomatic hand OA, but only nonsignificantly higher rates of incident radiographic hand OA, than men. Women more frequently had distal interphalangeal joint disease, while men more frequently had metacarpophalangeal joint OA. Black men and women had lower rates of hand OA than White participants, but Black men had higher rates of prevalent hand OA than Black women at younger ages.

Conclusion. Hand OA is a heterogeneous disease with complex differences by age, sex, race, hand symptoms, and patterns of specific joints affected. Further research investigating the mechanisms behind these differences, whether mechanical, metabolic, hormonal, or constitutional, is warranted.

INTRODUCTION

Hand osteoarthritis (OA), a highly prevalent disorder that may lead to severe pain and disability (1,2), is a heterogeneous disease with involvement of different joints and varying degrees of symptoms. The prevalence and incidence of hand OA vary greatly depending on the definition used, population included, and whether symptomatic hand OA or radiographic hand OA is analyzed (1–16). Previous studies are limited by small sample sizes (5), inclusion of participants of only a single race (1,3,4,7,13) or sex (5) or of a limited age range (5,14), and a focus on either only radiographic hand OA (1,5,6,9,14) or only symptomatic hand OA (2). Thus, prior studies paint an incomplete picture of the descriptive epidemiology of hand OA. Unresolved questions

Supported by the NIH (National Institute of Arthritis and Musculoskeletal and Skin Diseases contract HHSN268201200032C) and the Tupper Research Fund at Tufts Medical Center.

[1]Charles B. Eaton, MD, MS: Alpert Medical School of Brown University, Providence, Rhode Island, Center for Primary Care and Prevention, Pawtucket, Rhode Island, and Brown University School of Public Health, Providence, Rhode Island; [2]Lena Schaefer, MD: South Nuremberg Hospital, Nuremberg, Germany; [3]Jeff Duryea, PhD, Bing Lu, MD, DrPH: Brigham and Women's Hospital and Harvard Medical School, Boston, Massachusetts; [4]Jeff B. Driban, PhD, ATC, CSCS: Tufts Medical Center, Boston, Massachusetts; [5]Grace H. Lo, MD, MS: Houston Health Services Research and Development Center of Excellence, Michael E. DeBakey VAMC, and Baylor College of Medicine, Houston, Texas; [6]Mary B. Roberts, MS: Center for Primary Care and Prevention, Pawtucket, Rhode Island; [7]Ida K. Haugen, MD, PhD: Diakonhjemmet Hospital, Oslo, Norway; [8]Michael C. Nevitt, PhD: University of California, San Francisco; [9]Marc C. Hochberg, MD, MPH, MACP, MACR: University of Maryland School of Medicine, Baltimore; [10]Rebecca D. Jackson, MD: The Ohio State University, Columbus; [11]C. K. Kwoh, MD: University of Arizona, Tucson; [12]Timothy E. McAlindon, MD, MPH: Tufts Medical Center, Boston, Massachusetts.

Author disclosures are available at https://onlinelibrary.wiley.com/action/downloadSupplement?doi=10.1002%2Fart.42076&file=art42076-sup-0001-Disclosureform.pdf.

Address correspondence to Charles B. Eaton, MD, MS, Center for Primary Care and Prevention, Alpert Medical School of Brown University, 111 Brewster Street, Pawtucket, Rhode Island 02860. Email: CBeaton51@gmail.com.

Submitted for publication December 15, 2020; accepted in revised form January 21, 2022.

include the extent to which women have hand OA more frequently than men, adjusting for age and age-by-sex interaction; whether the pattern of hand OA differs between men and women; whether Black individuals have hand OA more or less frequently than White individuals; and whether the risk factors for prevalent and incident disease and for progression are similar for radiographic hand OA and symptomatic hand OA. Obtaining a comprehensive picture of the epidemiology of hand OA will allow for a better understanding of the extent to which hand OA may be related to mechanical etiologies versus metabolic or systemic etiologies. We therefore performed a comprehensive analysis of the prevalence, incidence, progression, and specific joint patterns of hand OA and evaluated the association of age, race, sex, and risk factors with the risk of radiographic and symptomatic hand OA in a longitudinal cohort of diverse individuals with or at risk of symptomatic knee OA (the Osteoarthritis Initiative [OAI]).

PATIENTS AND METHODS

The OAI is a multicenter cohort study of 4,796 adults with or at risk of symptomatic knee OA. Four clinical sites (Memorial Hospital of Rhode Island, The Ohio State University, University of Maryland and Johns Hopkins University, and the University of Pittsburgh) recruited participants between February 2004 and May 2006. The eligibility criteria for the OAI were designed to enrich the cohort for individuals at risk of knee OA and to exclude individuals with end-stage knee OA or inflammatory rheumatic disease. OAI data and protocols are available for free public access (https://data-archive.nimh.gov/oai/). Institutional review boards at each OAI clinical site and the OAI coordinating center (University of California, San Francisco) approved the OAI study. All participants provided informed consent prior to participation.

Assessments. Posteroanterior radiographs of one or both hands were obtained at baseline and 48 months. Questions about hand pain were asked at both visits, referencing a homunculus. Interviewers asked, "During the past 30 days, which of these joints have had pain, aching, or stiffness on most days? By most days, we mean more than half the days of a month." If participants indicated hand pain and marked the homunculus accordingly (right, left, or bilateral), we defined them as having hand pain. We then matched the hand in which the participant indicated pain to the same-sided radiograph to define symptomatic hand OA.

Hand radiographs. Posteroanterior radiographs were evaluated for the presence and severity of OA in each of the second through the fifth distal interphalangeal (DIP) joints, the second through the fifth proximal interphalangeal (PIP) joints, the first through the fifth metacarpophalangeal (MCP) joints, the interphalangeal (IP) joint of the thumb, and the base of the thumb (carpometacarpal [CMC] and scaphotrapeziotrapezoid [STT]) joints. The dominant hand was assessed by OAI clinical staff in 95% of study participants. If a participant's hand dominance was unknown we used the hand radiograph available (4% of the sample), and if bilateral hand radiographs were available we used the radiograph of the hand ipsilateral to the foot the participant reported as using to kick a ball (1% of the sample).

One investigator (LFS) read the posteroanterior radiographs of the dominant hand using a custom software data entry tool, which blinded to time point and allowed 2 images to be viewed simultaneously. A graphical user interface allowed for electronic scoring. These joints were graded using a Kellgren/Lawrence (K/L) scale (17) based on the presence of individual radiographic OA features as follows: 0 = no OA (no osteophyte or joint space narrowing), 1 = questionable osteophyte or joint space narrowing, 2 = small osteophyte(s) or mild joint space narrowing, 3 = moderate osteophyte(s) or joint space narrowing, and 4 = large osteophyte(s) or joint space narrowing (3). The hand radiograph reading went through an extensive quality assessment process; a rheumatology fellow with extensive experience in hand OA scoring (LFS) reviewed the readings and flagged them for a musculoskeletal radiologist to review if any questions arose. To assess reproducibility, 100 randomly selected pairs of hand radiographs were read twice. Intrareader agreement was considered good, with weighted kappas of >0.84.

Definitions of hand OA. We assessed OA in the IP, metacarpal, and thumb base joints as defined by a K/L score of ≥2 at each joint. For descriptive purposes prevalence and incidence rates for each IP, metacarpal, CMC, and STT thumb base joint are shown by sex in Figures 1 and 2. In exploring etiologic associations, a person was classified as having radiographic hand OA if OA was present in ≥1 IP or metacarpal joint on ≥2 digits in that hand, excluding the thumb base, at baseline for prevalent radiographic hand OA, and at year 4 if not present at baseline for incident radiographic hand OA. We excluded OA of the thumb base since it is more common in the nondominant hand (18–22), which was not evaluated in the OAI, so any etiologic association of thumb base OA would be prone to error. In addition, the etiology of thumb base OA is well described and is associated with hypermobility in the nondominant hand (20–22), which we could not evaluate. We required that OA be present in 2 joints on different digits (rays) in order to exclude isolated trauma-related joint OA from our analysis of radiographic hand OA.

Prevalent symptomatic hand OA was defined as radiographic hand OA at baseline plus same-sided hand pain. Participants were considered to have incident symptomatic hand OA if they had radiographic hand OA accompanied by a new report of same-sided hand pain at the 48-month visit (i.e., not present at baseline), had hand pain symptoms without radiographic hand OA at baseline and developed same-sided radiographic hand OA at 48 months, or developed both same-sided hand pain and

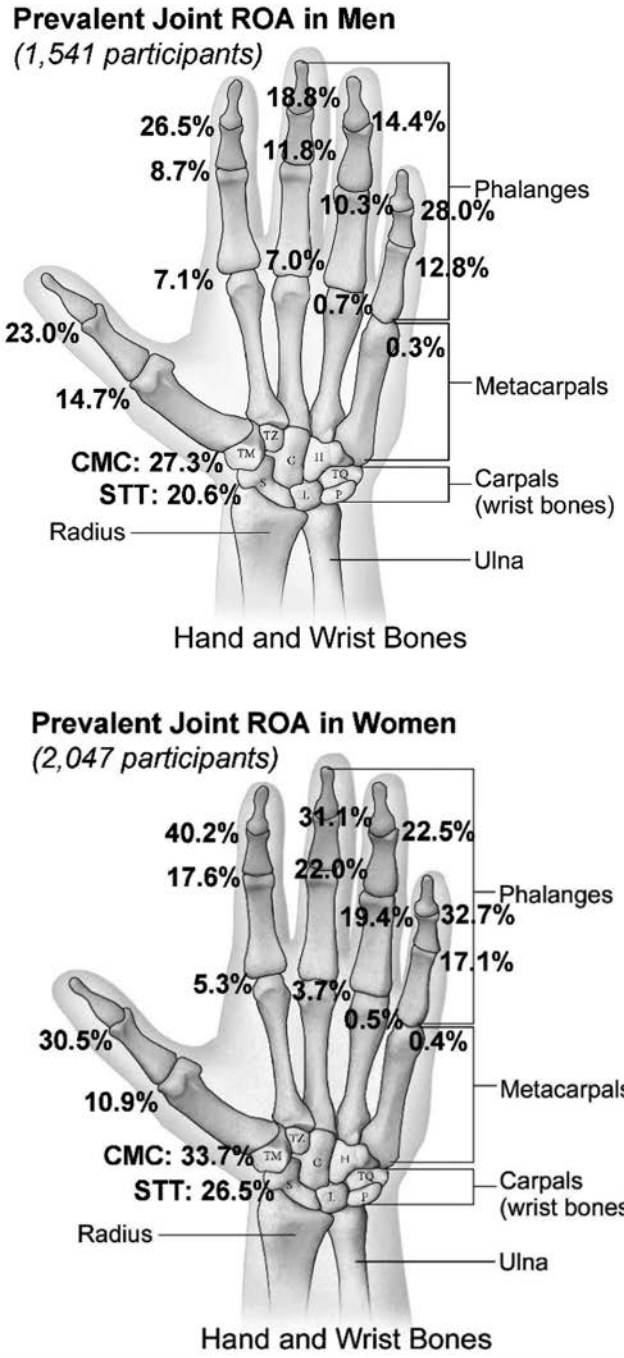

Figure 1. Rates of prevalent radiographic osteoarthritis (ROA) of the indicated hand joints in participants in the Osteoarthritis Initiative, by sex. CMC = carpometacarpal; STT = scaphotrapeziotrapezoid; TM = trapezium; TZ = trapezoid; S = scaphoid; C = capitate; H = hamate; L = lunate; TQ = triquetrum; P = pisiform. Adapted from Blausen.com staff. Medical gallery of Blausen Medical. WikiJournal of Medicine 2014. doi:10.15347/wjm/2014.010. URL: https://commons.wikimedia.org/w/index.php?curid=29849185.

radiographic hand OA at 48 months. We also calculated the progression of hand OA, defined as an increase in the sum of the K/L grades in the IP and metacarpal joints for an entire hand excluding the thumb base, for all participants.

Risk factors. Age, sex, self-reported race, and body mass index (BMI) were recorded at the baseline clinical visit. BMI in kg/m^2 was calculated based on height measured without shoes with a wall-mounted stadiometer and weight measured in

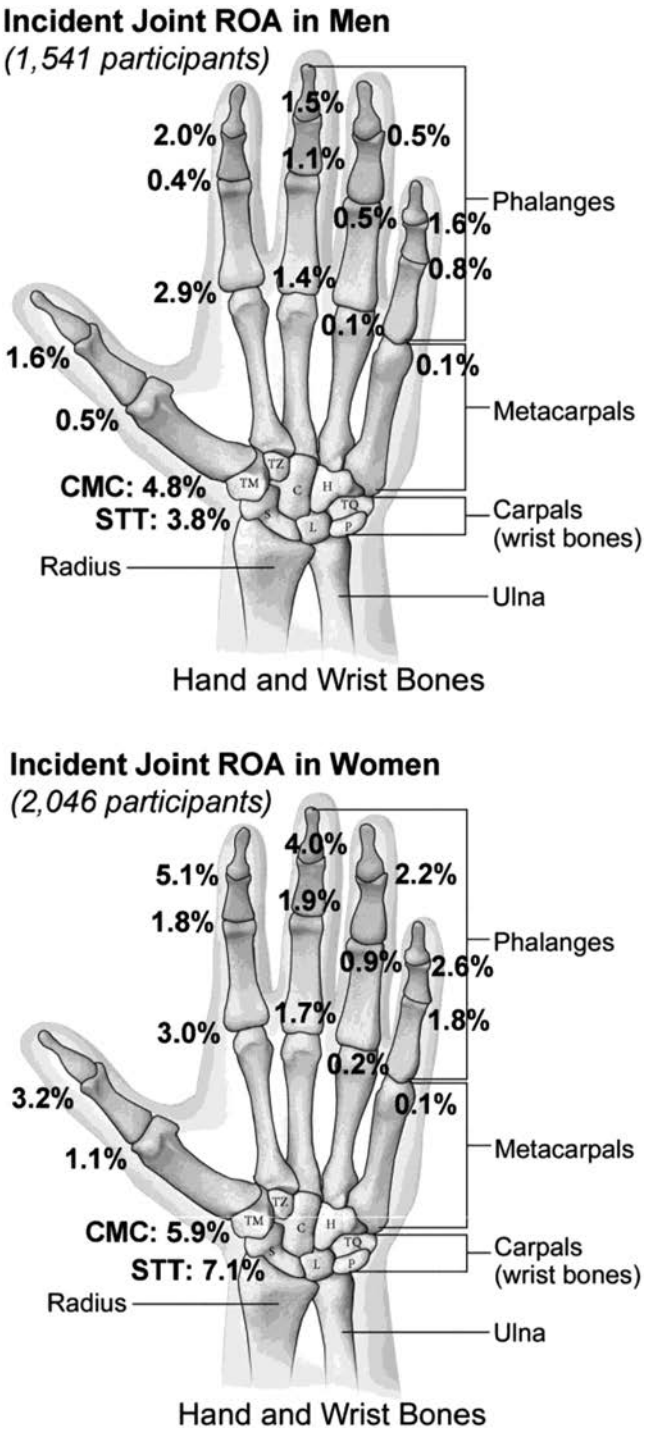

Figure 2. Rates of incident radiographic OA of the indicated hand joints in participants in the Osteoarthritis Initiative, by sex. Adapted from Blausen.com staff. Medical gallery of Blausen Medical. WikiJournal of Medicine 2014. doi:10.15347/wjm/2014.010. URL: https://commons.wikimedia.org/w/index.php?curid=29849185. See Figure 1 for definitions.

lightweight clothing and without shoes. Knee OA severity was based on baseline K/L scoring of knee radiographs (17).

Statistical analysis. Descriptive statistics were used to summarize the sample used for analysis and to compare it to the whole OAI cohort. The primary analysis used a modified Poisson regression with a robust variance estimator (23,24) to account for clustering of joints within fingers within persons to estimate the prevalence ratio (PR) for prevalent disease and relative risk (RR) estimates for incident disease and progression associated with participant characteristics. Multivariable adjusted models included age, sex, race, BMI, knee OA severity, and hand pain unless part of the outcome (symptomatic hand OA). We tested for interactions between sex and age; race and age; and age, sex, and race.

In order to characterize patterns in hand OA, we examined the associations of the various hand OA outcomes by the fingers (rays) and joint types (rows) in which they occurred. RRs were estimated using a modified Poisson regression as described above. Dummy variables were created for each ray and row such that 0 indicated no OA in any joints in the target ray/row and 1 indicated OA in ≥1 joint in the target ray/row. Risk estimates were adjusted for age, sex, race, and BMI. Interactions between sex and ray/row were also tested. All analyses were conducted using SAS version 9.4. *P* values less than or equal to 0.05 were considered significant.

RESULTS

Of the 4,796 participants in the OAI, 3,588 had evaluable hand radiographs at both baseline and the 48-month follow-up visit. We found no meaningful differences between our sample and the entire OAI cohort with regard to sociodemographic characteristics or risk factors for hand OA (Supplementary Table 1, available on the *Arthritis & Rheumatology* website at http://onlinelibrary.wiley.com/doi/10.1002/art.42076). Baseline characteristics of the participants with prevalent radiographic hand OA, prevalent symptomatic hand OA, incident radiographic hand OA, incident symptomatic hand OA, and hand OA progression are given in Table 1.

Hand OA prevalence, incidence, and progression rates. The prevalence of radiographic hand OA was 41.4 per 100 persons (95% confidence interval [95% CI] 39.8–43.0), and the prevalence of symptomatic hand OA was 12.4 per 100 persons (95% CI 11.3–13.5). The incidence over 4 years was 5.6 per 100 persons for radiographic hand OA (95% CI 4.7–6.7) and 16.9 per 100 persons for symptomatic hand OA (95% CI 15.6–18.2).

Table 1. Baseline characteristics of the participants with prevalent radiographic and symptomatic hand OA, incident radiographic and symptomatic hand OA, and hand OA progression*

Risk factor	All participants (n = 3,588)	Prevalent radiographic hand OA (n = 1,485)	Prevalent symptomatic hand OA (n = 443)	Incident radiographic hand OA (n = 118)	Incident symptomatic hand OA (n = 530)	Hand OA progression (n = 981)
Age, years						
45–54	1,065 (29.7)	120 (8.1)	30 (6.8)	40 (33.9)	63 (11.9)	187 (19.0)
55–64	1,187 (33.1)	454 (30.6)	153 (34.5)	53 (44.9)	176 (33.2)	347 (35.4)
65–79	1,336 (37.2)	911 (61.4)	260 (58.7)	25 (21.2)	291 (54.9)	447 (45.6)
Sex						
Male	1,541 (43.0)	563 (37.9)	116 (26.2)	51 (43.2)	197 (37.2)	329 (33.5)
Female	2,047 (57.1)	922 (62.1)	327 (73.8)	67 (56.8)	333 (62.8)	652 (66.5)
Race						
White	2,928 (81.6)	1,289 (86.8)	388 (87.6)	98 (83.1)	448 (84.5)	826 (84.2)
Black	556 (15.5)	160 (10.8)	41 (9.3)	18 (15.3)	66 (12.5)	120 (12.2)
Other	104 (2.9)	36 (2.4)	14 (3.2)	2 (1.7)	16 (3.0)	35 (3.6)
BMI						
Normal	871 (24.3)	335 (22.6)	101 (22.8)	32 (27.1)	136 (25.7)	250 (25.5)
Overweight	1,427 (39.8)	625 (42.1)	187 (42.2)	44 (37.3)	206 (38.9)	383 (39.0)
Obese	1,290 (36.0)	525 (35.4)	155 (35.0)	42 (35.6)	188 (35.5)	348 (35.5)
Knee OA severity, K/L score						
0	994 (27.7)	313 (21.1)	86 (19.4)	31 (26.3)	129 (24.3)	241 (24.6)
1	582 (16.2)	203 (13.7)	61 (13.8)	20 (17.0)	69 (13.0)	146 (14.9)
2	1,109 (30.9)	467 (31.5)	156 (35.2)	46 (39.0)	167 (31.5)	302 (30.8)
3	687 (19.2)	375 (25.3)	105 (23.7)	16 (13.6)	123 (23.2)	220 (22.4)
4	216 (6.0)	127 (8.6)	35 (7.9)	5 (4.2)	42 (7.9)	72 (7.3)
Hand pain						
No	2,797 (78.0)	1,042 (70.2)	–	85 (72.0)	–	676 (68.9)
Yes	791 (22.1)	443 (29.8)	–	33 (28.0)	–	305 (31.1)

* Values are the number (%). OA = osteoarthritis; BMI = body mass index; K/L = Kellgren/Lawrence.

Over 48 months, 27.3 per 100 persons (95% CI 25.9–28.8) exhibited OA progression, with an average increase in the sum of the hand joint K/L grades of 1.85 (95% CI 1.78–1.93). Crude prevalence and incidence rates for each joint are detailed by sex in Figures 1 and 2. Women had higher rates than men of prevalent OA at the IP joint of the thumb (30.5% versus 23%), DIP joint of the index finger (40.2% versus 26.5%), and DIP joint of the middle finger (31.1% versus 18.8%) (all $P < 0.01$). A similar pattern was found for incident IP joint OA, with women having higher rates than men in the thumb (3.2% versus 1.6%), index finger (5.1% versus 2.0%), and middle finger (4.0% versus 1.5%) (all $P < 0.01$). Men had higher rates of prevalent MCP joint OA in the thumb (14.7% versus 10.9%; $P = 0.001$), index finger (7.1% versus 5.3%; $P = 0.03$), and middle finger (7.0% versus 3.7%; $P < 0.001$), but the rates of incident MCP joint OA did not differ significantly by sex.

Risk factors for prevalent radiographic hand OA, prevalent symptomatic hand OA, incident radiographic hand OA, incident symptomatic hand OA, and progression. The PRs for an association of prevalent radiographic hand OA and prevalent symptomatic hand OA, and the RRs for an association of incident radiographic hand OA, incident symptomatic hand OA, and hand OA progression, with age, sex, BMI, knee OA severity, and hand pain (where appropriate) in multivariable adjusted analyses are shown in Table 2.

Age. A monotonically increasing risk of prevalent radiographic and symptomatic hand OA, as well as of incident symptomatic hand OA (3–5-fold increased risk), was observed with increasing age. Age was associated with a more modest increased risk of incident radiographic hand OA and progression (30–70%), with the greatest risk in those ages 55–64 years and not the oldest group (ages 65–79 years).

Sex. Compared to men, women had a greater risk of prevalent symptomatic hand OA (PR 2.16 [95% CI 1.76–2.64]) and, to a lesser extent, incident symptomatic hand OA (RR 1.41 [95% CI 1.20–1.66]) and progression (RR 1.59 [95% CI 1.37–1.84]) but had only a modestly increased risk of prevalent radiographic hand OA (PR 1.18 [95% CI 1.10–1.27]) and no increased risk of incident radiographic hand OA (RR 1.05 [95% CI 0.73–1.51]).

Race. Compared to White participants, Black participants had a lower risk of both prevalent radiographic hand OA (PR 0.72 [95% CI 0.63–0.81]) and prevalent symptomatic hand OA (PR 0.55 [95% CI 0.40–0.75]), incident symptomatic hand OA (RR 0.75 [95% CI 0.59–0.96]), and progression (RR 0.72

Table 2. Multivariable adjusted PRs for prevalent radiographic and symptomatic hand OA and RRs for incident radiographic and symptomatic hand OA and hand OA and progression*

Risk factor	Prevalent radiographic hand OA, PR (95% CI) (n = 1,485)	Prevalent symptomatic hand OA, PR (95% CI) (n = 443)	Incident radiographic hand OA, RR (95% CI) (n = 118)	Incident symptomatic hand OA, RR (95% CI) (n = 530)	Hand OA progression, RR (95% CI) (n = 981)
Age, years					
45–54	Reference	Reference	Reference	Reference	Reference
55–64	3.20 (2.66–3.84)	4.20 (2.87–6.15)	1.68 (1.13–2.49)	2.72 (2.06–3.58)	1.70 (1.40–2.05)
65–79	5.45 (4.58–6.48)	5.99 (4.12–8.69)	1.32 (0.82–2.14)	4.20 (3.23–5.47)	1.67 (1.38–2.01)
Sex					
Male	Reference	Reference	Reference	Reference	Reference
Female	1.18 (1.10–1.27)	2.16 (1.76–2.64)	1.05 (0.73–1.51)	1.41 (1.20–1.66)	1.59 (1.37–1.84)
Race					
White	Reference	Reference	Reference	Reference	Reference
Black	0.72 (0.63–0.81)	0.55 (0.40–0.75)	0.67 (0.41–1.09)	0.75 (0.59–0.96)	0.72 (0.58–0.89)
Other	0.85 (0.68–1.06)	1.11 (0.68–1.82)	0.46 (0.12–1.82)	1.09 (0.72–1.66)	1.04 (0.74–1.45)
BMI					
Normal	Reference	Reference	Reference	Reference	Reference
Overweight	1.11 (1.01–1.21)	1.21 (0.97–1.52)	0.93 (0.59–1.46)	0.97 (0.80–1.17)	1.00 (0.85–1.19)
Obese	1.14 (1.03–1.25)	1.19 (0.94–1.51)	0.88 (0.56–1.39)	1.04 (0.85–1.28)	0.88 (0.74–1.06)
Knee OA severity, K/L score					
0	Reference	Reference	Reference	Reference	Reference
1	0.95 (0.84–1.08)	1.05 (0.77–1.43)	1.08 (0.63–1.85)	0.82 (0.63–1.07)	0.96 (0.77–1.19)
2	1.13 (1.02–1.25)	1.38 (1.07–1.76)	1.64 (1.05–2.56)	1.08 (0.88–1.33)	1.05 (0.87–1.27)
3	1.26 (1.14–1.40)	1.33 (1.02–1.74)	1.14 (0.63–2.03)	1.15 (0.91–1.44)	1.14 (0.93–1.40)
4	1.34 (1.17–1.53)	1.53 (1.07–2.19)	1.11 (0.43–2.89)	1.32 (0.97–1.81)	1.41 (1.06–1.87)
Hand pain					
No	Reference	–	Reference	–	Reference
Yes	1.33 (1.24–1.43)	–	2.06 (1.40–3.03)	–	1.66 (1.44–1.91)

* Prevalence ratios (PRs) were adjusted for age, race, sex, body mass index (BMI), knee Kellgren/Lawrence (K/L) grade, and hand pain in participants without symptomatic disease. OA = osteoarthritis; RRs = relative risks; 95% CI = 95% confidence interval.

[95% CI 0.58–0.89]), but a nonsignificantly decreased risk of incident radiographic hand OA (RR 0.67 [95% CI 0.41–1.09]).

Age, sex, and race interactions. We found an age-by-sex interaction for prevalent symptomatic hand OA and incident radiographic hand OA. For symptomatic hand OA, while the risk increased for both men and women at older ages, it increased at a greater rate for women ($P < 0.01$). At older ages, men had higher rates of incident radiographic hand OA than women (8.4% versus 3.3%; $P = 0.02$). We found a race-by-sex interaction for prevalent radiographic hand OA, with a higher prevalence among Black men than among Black women (33.2% versus 26.7%), and a higher prevalence among White women than among White men (49.8% versus 37.0%; $P < 0.03$). We also found a 3-way interaction of age-by-race-by-sex for prevalent radiographic hand OA: at younger ages Black women had hand OA much less frequently than Black men (5.3% versus 14.5%), while White women had hand OA more frequently than White men (13.6% versus 10.9%) (Figure 3).

Obesity. Overweight and obesity were associated with an increased risk of prevalent radiographic hand OA (11–14%), a nonsignificantly increased risk of prevalent symptomatic hand OA (19–21%), and no increased risk of incident radiographic hand OA, incident symptomatic hand OA, or progression.

Knee OA. Knee OA severity (K/L score of ≥2) was associated with a monotonically increasing risk of prevalent radiographic and symptomatic hand OA, while only knee OA with a K/L score of 2 was associated with an increased risk of incident radiographic hand OA, and only knee OA with a K/L score of 4 was associated with an increased risk of hand OA progression.

Hand pain. Hand pain at baseline was associated with a 33% increased risk of prevalent radiographic hand OA, a 206% increased risk of incident radiographic hand OA, and a 66% increased risk of hand OA progression.

Patterns of prevalent and incident radiographic and symptomatic hand OA and hand OA progression by rays and rows. The patterns of prevalent and incident radiographic and symptomatic hand OA and progression by ray and row, adjusted for age, race, BMI, and sex, are given in Table 3.

The index finger had the strongest association with prevalent radiographic hand OA (PR 3.60 [95% CI 3.05–4.25]), prevalent symptomatic hand OA (PR 4.45 [95% CI 2.85–6.96]), incident symptomatic hand OA (RR 2.60 [95% CI 1.93–3.50]), and hand OA progression (RR 1.71 [95% CI 1.38–2.10]), while the ring finger had the strongest association with incident radiographic hand OA (RR 8.66 [95% CI 4.61–16.27]), compared to the thumb. Additionally, compared to the thumb (excluding thumb base), most rays had more joint OA. Regarding rows, compared to the MCP joints, the DIP joints had much greater rates of OA for all outcomes except for incident radiographic hand OA, where the PIP joints showed a greater risk (RR 7.04 [95% CI 4.28–11.56]).

DISCUSSION

This prospective cohort study in a large, well-characterized diverse population shows that prevalent radiographic hand OA, symptomatic hand OA, radiographic progression, and incident symptomatic hand OA are particularly common in older

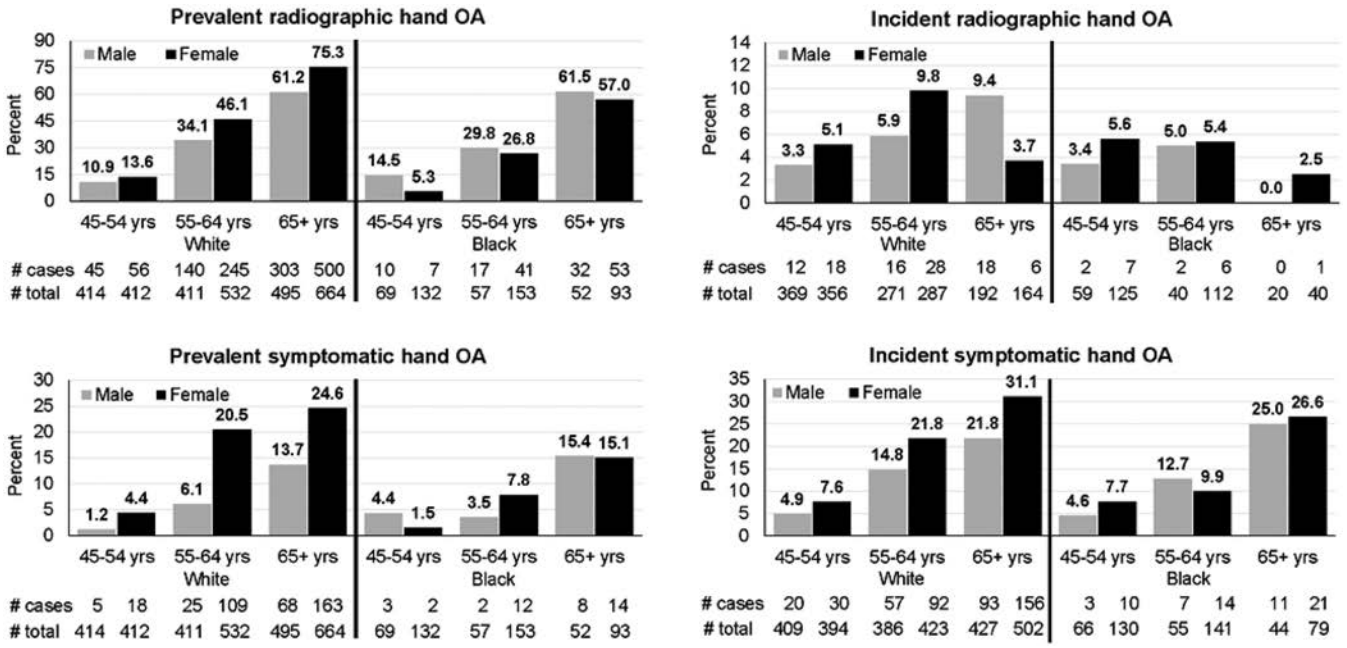

Figure 3. Rates of prevalent radiographic hand osteoarthritis (OA), incident radiographic hand OA, prevalent symptomatic hand OA, and incident symptomatic hand OA in participants in the Osteoarthritis Initiative, by age, race, and sex.

Table 3. Patterns of prevalent radiographic and symptomatic hand OA, incident radiographic and symptomatic hand OA, and hand OA progression, by individual finger and joint type after adjustment for age, race, sex, and BMI*

Joint	Prevalent radiographic hand OA, PR (95% CI)	Prevalent symptomatic hand OA, PR (95% CI)	Incident radiographic hand OA, RR (95% CI)	Incident symptomatic hand OA, RR (95% CI)	Hand OA progression, RR (95% CI)
Ray					
Thumb	Reference	Reference	Reference	Reference	Reference
Index	3.60 (3.05–4.25)	4.45 (2.85–6.96)	4.72 (2.85–7.80)	2.60 (1.93–3.50)†	1.71 (1.38–2.10)
Middle	1.86 (1.65–2.11)	2.31 (1.59–3.35)	6.42 (3.78–10.19)	2.28 (1.71–3.04)	1.22 (0.95–1.56)
Ring	1.05 (0.97–1.14)	1.29 (1.01–1.65)†	8.66 (4.61–16.27)	1.13 (0.92–1.39)	1.28 (1.03–1.60)
Pinky	1.72 (1.56–1.90)†	1.60 (1.19–2.14)	4.25 (2.59–6.99)	1.71 (1.34–2.18)	1.08 (0.87–1.34)
Row					
DIP joints	14.30 (10.93–18.71)†	17.04 (9.29–31.24)	5.19 (3.60–7.47)	8.27 (5.97–11.47)	2.02 (1.69–2.42)
PIP joints	1.84 (1.73–1.97)†	2.57 (2.11–3.14)	7.04 (4.28–11.56)	2.24 (1.90–2.65)	1.59 (1.36–1.86)
MCP joints	Reference	Reference	Reference	Reference	Reference

* OA = osteoarthritis; BMI = body mass index; PR = prevalence ratio; 95% CI = 95% confidence interval; RR = relative risk; DIP = distal interphalangeal; PIP = proximal interphalangeal; MCP = metacarpophalangeal.
† Significant interaction with sex ($P \leq 0.05$).

participants and in female participants. However, at older ages (≥65 years) men have a higher rate of incident radiographic hand OA than women, and at younger ages Black men have a higher rate of prevalent radiographic hand OA than Black women and rates similar to those seen among White women. The pattern of disease appears to have sex differences, with a female preponderance for DIP joint OA and a male preponderance for MCP joint OA. The strong inverse relationship between Black participants and White participants with regard to prevalent radiographic and symptomatic hand OA, incident symptomatic hand OA, and radiograhic progression of hand OA is noteworthy and a relatively novel finding. Knee OA severity showed a dose–response relationship with prevalent radiographic and symptomatic hand OA, whereas only K/L grade 2 knee OA was associated with incident radiographic hand OA only and K/L grade 4 knee OA was associated with radiographic hand OA progression.

Our findings show a strong association of hand OA with age, with a 3–5-fold increase in prevalent radiographic hand OA and a 2–4-fold increase in incident symptomatic hand OA in older participants compared to younger participants (ages 45–54 years) but with signficant age-by-sex and age-by-sex-by-race interactions, which are novel findings. The age-by-sex interactions may be related to endocrine-related aspects of the menopausal transition in women, with women having higher rates of radiographic hand OA during perimenopause but decreased rates by age 65 years (25).

Our findings of a modest association of hand OA with sex, with female predominance of prevalent radiograpic and symptomatic hand OA, incident symptomatic hand OA, and radiographic progression are consistent with most previous studies (3,7,8,9,11,12). The higher prevalence and incidence rates of symptomatic hand OA compared to radiographic disease in women compared to men are consistent with the findings of the Framingham Osteoarthritis study (3) and may be related to differential pain reporting, pain sensitivity, or cognitive or affective mechanisms (26). The higher rate of DIP row OA in women and higher prevalence of MCP joint OA in men was also observed in the Framingham Osteoarthritis study (3) and may be related to mechanical factors. MCP joint OA has been associated with heavy labor (27), and biomechanical experimental studies have demonstrated that greater forces are generated at the MCP joint than at the DIP joint when gripping (28). Our finding that the highest rate of joint OA occurred in the index ray is also consistent with the results of the Framingham Osteoarthritis study (3), as well as findings in a Chinese cohort (13), and may also be related to mechanical mechanisms.

The lack of association of incident hand OA with obesity has been reported in a smaller subsample of the OAI (n = 994) (10) and several other cohorts (29,30) and contradicts a meta-analysis that found that 10 of 15 hiqh-quality studies supported the notion of an association of obesity with hand OA (31). However, many of the studies in that meta-analysis were cross-sectional studies (31). Indeed, in our cross-sectional analysis we did find an association of obesity with prevalent radiograpic hand OA. The lack of association of obesity with incident hand OA may be related to potential collider bias, since individuals with obesity and prevalent disease were excluded from the incident analysis. An alternative explanation may be that obesity and its metabolic pertubations are not related to hand OA but only affect weight-bearing joints. A recent Mendelian randomization study in the UK Biobank showed a robust association of genetically determined BMI with OA of the knee and hip, which are weight-bearing joints, but not with OA of the hand (32).

Our findings that prevalent knee OA is associated with prevalent hand OA suggest that a subset of patients with polyarticular disease exists, consistent with the findings of other studies (11,33–36). While the association of prevalent radiographic hand OA with incident knee OA is well described (37,38) the association of baseline knee OA severity with incident hand OA is less well investigated.

Our finding of a lower risk of hand OA in Black participants is consistent with the findings of the Johnston County

study (15) but differs from those of a study of a young-to-middle-aged cohort in southeastern Michigan (5). A recent cross-sectional analysis of the OAI found lower odds of hand OA in Black participants, consistent with our findings for prevalent hand OA, and we now extend these findings to incidence and progression of radiographic and symptomatic hand OA (39).

This prospective study has several strengths, including the comprehensive assessment of hand OA using various definitions and evaluating prevalence, incidence, and progression. We had adequate statistical power to examine differences by age, sex, and race and to evaluate interactions by age, sex, and race. We observed consistent associations between progression and incidence for most of our findings, suggesting that collider or survivial bias did not affect our results in a significant manner, except perhaps for obesity.

Weaknesses of the study include potential selection bias for individuals with risk factors for knee OA, since this was part of the entry criteria for the OAI, including obesity, which may partially explain the lack of association with obesity with incident hand OA in our analysis. Our definition of symptomatic hand OA relied on using a homunuculus and included stiffness and aching as well as pain, which may lead to misclassification bias. As in any prospective cohort study, misclassification bias of the exposure and outcomes may be operative, but are likely to be random and thus bias the results toward the null.

Previous work has provided evidence of a familial association with hand OA (40,41), and the co-occurrence of multijoint OA suggests a possible systemic etiology of hand OA. Our findings that knee OA predicts incident hand OA, the differences noted by sex and race, and the strong association with aging suggest a nonmechanical etiology for hand OA, particularly in the DIP joints; altered metabolic pathways, genetic, or epigenetic factors may be operative. Pathologic aging associated with chronic oxidative stress and chronic low levels of inflammation may play an important role in the development of hand OA (42). Indeed, we and others have previously shown that shortened telomere length, known to be a measure of pathologic aging, was associated with incident radiographic hand OA (42,43). Future work further exploring pathomechanistic pathways for hand OA appears indicated.

AUTHOR CONTRIBUTIONS

All authors were involved in drafting the article or revising it critically for important intellectual content, and all authors approved the final version to be published. Dr. Eaton had full access to all of the data in the study and takes responsibility for the integrity of the data and the accuracy of the data analysis.

Study conception and design. Eaton, Driban, Lo, Haugen, Nevitt, Hochberg, Jackson, Kwoh, McAlindon.

Acquisition of data. Eaton, Schaefer, Duryea, Haugen, Nevitt, Hochberg, Jackson, Kwoh, McAlindon.

Analysis and interpretation of data. Eaton, Duryea, Driban, Lo, Roberts, Lu, McAlindon.

REFERENCES

1. Dahaghin S, Bierma-Zeinstra SM, Ginai AZ, Pols HA, Hazes JM, Koes BW. Prevalence and pattern of radiographic hand osteoarthritis and association with pain and disability (the Rotterdam study). Ann Rheum Dis 2005;64:682–7.
2. Schaefer LF, McAlindon TE, Eaton CB, Roberts MB, Haugen IK, Smith SE, et al. The associations between radiographic hand osteoarthritis definitions and hand pain: data from the osteoarthritis initiative. Rheumatol Int 2018;38:403–13.
3. Haugen IK, Englund M, Aliabadi P, Niu J, Clancy M, Kvien TK, et al. Prevalence, incidence and progression of hand osteoarthritis in the general population: the Framingham Osteoarthritis Study. Ann Rheum Dis 2011;70:1581–6.
4. Egger P, Cooper C, Hart DJ, Doyle DV, Coggon D, Spector TD. Patterns of joint involvement in osteoarthritis of the hand: the Chingford study. J Rheumatol 1995;22:1509–13.
5. Sowers M, Lachance L, Hochberg M, Jamadar D. Radiographically defined osteoarthritis of the hand and knee in young and middle-aged African American and Caucasian women. Osteoarthritis Cartilage 2000;8:69–77.
6. Zhang Y, Xu L, Nevitt MC, Niu J, Goggins JP, Aliabadi P, et al. Lower prevalence of hand osteoarthritis among Chinese subjects in Beijing compared with white subjects in the United States: the Beijing Osteoarthritis Study. Arthritis Rheum 2003;48:1034–40.
7. Haara MM, Manninen P, Kröger H, Arokoski JP, Kärkkäinen A, Knekt A, et al. Osteoarthritis of finger joints in Finns aged 30 or over: prevalence, determinants, and association with mortality. Ann Rheum Dis 2003;62:151–8.
8. Butler WJ, Hawthorne VM, Mikkelsen WM, Carman WJ, Bouthillier DL, Lamphiear DE, et al. Prevalence of radiologically defined osteoarthritis in the finger and wrist joints of adult residents of Tecumseh, Michigan, 1962–65. J Clin Epidemiol 1988;41:467–73.
9. Wilder FV, Barrett JP, Farina EJ. Joint-specific prevalence of osteoarthritis of the hand. Osteoarthritis Cartilage 2006;14:953–7.
10. Haugen IK, Magnusson K, Turkiewicz A, Englund M. The prevalence, incidence and progression of hand osteoarthritis in relation to body mass index, smoking and alcohol consumption. J Rheumatol 2017; 44:1402–9.
11. Prieto-Alhambra D, Judge A, Javaid A, Cooper C, Diez-Perez A, Arden NK. Incidence and risk factor for clinically diagnosed knee, hip and hand osteoarthritis affecting other joints. Ann Rheum Dis 2014; 73:1659–4.
12. Chaisson CE, Zhang Y, McAlindon TE, Hannan MT, Aliabadi P, Nailmark, et al. Radiographic hand osteoarthritis: incidence, patterns, influence of pre-existing disease in a population based sample. J Rheumatol 1997;24:1337–43.
13. Hunter DJ, Zhang Y, Nevitt MC, Xu L, Niu J, Lui LY, et al. Chopstick arthropathy: the Beijing osteoarthritis study. Arthritis Rheum 2004; 50:1495–500.
14. Niu J, Zhang Y, LaValley M, Chaisson CE, Aliabadi P, Felson DT. Symmetry and clustering of symptomatic hand osteoarthritis in elderly men and women: the Framingham study. Rheumatology (Oxford) 2003;42:343–8.
15. Qin J, Barbour KE, Murphy LB, Nelson AE, Schwartz TA, Helmick CG, et al. Lifetime risk of symptomatic hand osteoarthritis: the Johnston County Osteoarthritis Project. Arthritis Rheumatol 2017;69:1204–12.
16. Davis JE, Schaefer LF, McAlindon TE, Eaton CB, Roberts MB, Haugen IK, et al. Characteristics of accelerated hand osteoarthritis: data from the Osteoarthritis Initiative. J Rheumatol 2019;46:422–8.
17. Kellgren JH, Lawrence JS. Radiological assessment of osteo-arthrosis. Ann Rheum Dis 1957;16:494–502
18. Haara MM, Heliövaara M, Kröger H, Arokoski JP, Manninen P, Kärkkäinen, et al. Osteoarthritis in the carpometacarpal joint of

the thumb. Prevalence and associations with disability and mortality. J Bone Joint Surg Am 2004;86:1452–7.

19. Acheson RM, Chan YK, Clemett AR. New Haven survey of joint diseases. XII. Distribution and symptoms of osteoarthrosis in the hands with reference to handedness. Ann Rheum Dis 1970;29:275–86.
20. Jónsson H, Elíasson GJ, Jónsson A, Eiríksdóttir G, Sigurdsson S, Aspelund T, et al. High hand joint mobility is associated with radiological CMC1 osteoarthritis: the AGES-Reykjavik study. Osteoarthritis Cartilage 2009;17:592–5.
21. Jónsson H, Valtýsdóttir ST, Kjartansson O, Brekkan A. Hypermobility associated with osteoarthritis of the thumb base: a clinical and radiological subset of hand osteoarthritis. Ann Rheum Dis 1996;55:540–3.
22. Hunter DJ, Zhang Y, Sokolove J, Niu J, Aliabadi P, Felson DT. Trapeziometacarpal subluxation predisposes to incident trapeziometacarpal osteoarthritis (OA): the Framingham Study. Osteoarthritis Cartilage 2005;13:953–7.
23. McNutt LA, Wu C, Xue X, Hafner JP. Estimating the relative risk in cohort studies and clinical trials of common outcomes. Am J Epidemiol 2003;157:940–3.
24. Zou G. A modified poisson regression approach to prospective studies with binary data. Am J Epidemiol 2004;159:702–6.
25. Spector TD, Campion GD. Generalised osteoarthritis: a hormonally mediated disease. Ann Rheum Dis 1989;48:523–7.
26. Fillingim RB, King CD, Ribeiro-Dasilva MC, Rahim-Williams B, Riley JL III. Sex, gender, and pain: a review of recent clinical and experimental findings. J Pain 2009;10:447–85.
27. Williams WV, Cope R, Gaunt WD, Adelstein EH, Hoyt TS, Pressly TA, et al. Metacarpophalangeal arthropathy associated with manual labor (Missouri metacarpal syndrome). Clinical radiographic, and pathologic characteristics of an unusual degeneration process. Arthritis Rheum 1987;30:1362–71.
28. Cooney WP III, Chao EY. Biomechanical analysis of static forces in the thumb during hand function. J Bone Joint Surg Am 1977;59:27–36.
29. Magnusson K, Østerås N, Haugen IK, Mowinckel P, Nordsletten L, Natvig B, et al. No strong relationship between body mass index and clinical hand osteoarthritis: results from a population-based case-control study. Scand J Rheumatol 2014;43:409–15.
30. Magnusson K, Slatkowsky-Christensen B, van der Heijde D, Kvien TK, Hagen KB, Haugen IK. Body mass index and progressive hand osteoarthritis: data from the Oslo hand osteoarthritis cohort. Scand J Rheumatol 2015;44:331–6.
31. Yusuf E, Nelissen RG, Ioan-Facsinay A, Stojanovic-Susulic V, DeGroot J, van Osch G, et al. Association between weight or body mass index and hand osteoarthritis: a systematic review. Ann Rheum Dis 2010;69:761–5.
32. Funck-Bretano T, Nethander M, Moverare-Skrtic, Richette P, Ohisson C. Causal factors for knee, hip and hand osteoarthritis: a Mendelian randomization study in the UK Biobank. Arthritis Rheumatol 2019;71:1634–41.
33. Hirsch R, Lethbridge-Cejku M, Scott WW Jr, Reichle R, Plato CC, Tobin J, et al. Association of hand and knee osteoarthritis: evidence for a polyarticular disease subset. Ann Rheum Dis 1996;55:25–9.
34. Hochberg MC, Lane NE, Pressman AR, Genant HK, Scott JC, Nevitt MC. The association of radiographic changes of osteoarthritis of the hand and hip in elderly women. J Rheumatol 1995;22:2291–4.
35. Englund M, Paradowski PT, Lohmander LS. Association of radiographic hand osteoarthritis with radiographic knee osteoarthritis after meniscectomy. Arthritis Rheum 2004;50:469–75.
36. Cicuttini FM, Baker J, Hart DJ, Spector TD. Relation between Heberden's nodes and distal interphalangeal joint osteophytes and their role as markers of generalised disease. Ann Rheum Dis 1998;57:246–8.
37. Felson DT, Zhang Y, Hannan MT, Naimark A, Weissman B, Aliabadi P, et al. Risk factors for incident radiographic knee osteoarthritis in the elderly: the Framingham study. Arthritis Rheum 1997;40:728–33.
38. Dahaghin S, Bierma-Zeinstra SM, Reijman M, Pols HA, Hazes JM, Koes BW. Does hand osteoarthritis predict future hip or knee osteoarthritis? Arthritis Rheum 2005;52:3520–7.
39. Pishgar F, Kwee RM, Haj-Mirzaian A, Guermazi A, Haugen IK, Demehri S. Association between race and radiographic, symptomatic, and clinical hand osteoarthritis: a propensity score-matched study using Osteoarthritis Initiative data. Arthritis Rheumatol 2022;74:453–61.
40. Doherty M. Genetics of hand osteoarthritis. Osteoarthritis Cartilage 2000;8 Suppl:S8–10.
41. Spector TD, Cicuttini F, Baker J, Loughlin J, Hart D. Genetic influences on osteoarthritis in women: a twin study. BMJ 1996;312:940–3.
42. Zhai G, Aviv A, Hunter DJ, Hart DJ, Gardner JP, Kimura M, et al. Reduction of leucocyte telomere length in radiographic hand osteoarthritis: a population-based study Ann Rheum Dis 2006;65:1444–8.
43. McAlindon T, Roberts M, Driban J, Schaefer L, Haugen IK, Smith SE, et al. Incident hand OA is strongly associated with reduced peripheral blood leukocyte telomere length. Osteoarthritis Cartilage 2018;26:1651–7.

Arthritis & Rheumatology
Vol. 74, No. 6, June 2022, pp 1001–1012
DOI 10.1002/art.42068

American College of Rheumatology
Empowering Rheumatology Professionals

Antiphospholipid Antibodies Increase Endometrial Stromal Cell Decidualization, Senescence, and Inflammation via Toll-like Receptor 4, Reactive Oxygen Species, and p38 MAPK Signaling

Mancy Tong,[1] Teimur Kayani,[1] Deidre M. Jones,[2] Jane E. Salmon,[3] Shannon Whirledge,[1] Lawrence W. Chamley,[2] and Vikki M. Abrahams[1]

Objective. Miscarriage affects 1 in 7 pregnancies, and antiphospholipid autoantibodies (aPLs) are one of the biggest risk factors for recurrent pregnancy loss. While aPLs target the endometrial stroma, little is known about their impact. Endometrial stromal cells (EnSCs) undergo decidualization each menstrual cycle, priming the uterus to receive implanting embryos. Thus, appropriate decidualization and EnSC function is key for establishment of a successful pregnancy. This study was undertaken to explore the effects of aPL on EnSC decidualization, senescence, and inflammation.

Methods. EnSCs under decidualizing conditions were exposed to aPL or control IgG alone or in the presence of either a Toll-like receptor 4 (TLR-4) antagonist, a p38 MAPK inhibitor, a reactive oxygen species (ROS) inhibitor, low molecular weight heparin (LMWH), or acetyl salicylic acid. Secretion of decidualization markers and inflammatory interleukin-8 were quantified by enzyme-linked immunosorbent assay, and senescence-associated β-galactosidase activity was evaluated. In a mouse model of decidualization, aPL or control IgG was administered, and uterine expression levels of decidualization and inflammatory markers were quantified by real-time quantitative polymerase chain reaction.

Results. Antiphospholipid antibodies increased human EnSC decidualization, senescence, and inflammation. This phenotype was recapitulated in the mouse model. The decidualization and inflammatory responses were partially mediated by TLR-4 and p38 MAPK, while the decidualization and senescence responses were ROS-dependent. LMWH, commonly used to treat aPL-positive women at risk of obstetric complications, reduced the ability of aPL to increase EnSC decidualization and inflammation.

Conclusion. These findings shed new light on the pathogenesis of pregnancy complications in women with aPLs and underscore the benefit of heparin in preventing pregnancy loss in this high-risk population.

INTRODUCTION

Spontaneous miscarriage, defined as pregnancy loss prior to 20 weeks of gestation, affects 15% of clinically recognized pregnancies (1). While ~50% of cases are caused by chromosomal abnormalities of the embryo, the other 50% remain idiopathic and may be due to maternal factors such as endometrial dysfunction. With or without a diagnosis of antiphospholipid syndrome (APS), antiphospholipid antibodies (aPLs) that target phospholipid binding proteins, such as cardiolipin and β_2-glycoprotein I (β_2GPI), are the most identifiable cause of non-chromosomal pregnancy loss (2) and are a major risk factor for early recurrent pregnancy loss (RPL) (<10 weeks of gestation) (1,3). Depending upon the study cited, aPLs have been reported in 8–42% of women with RPL (3), compared to 1–5% in the general population (2), and the simultaneous presence of multiple aPL isotypes is

Dr. Tong's work was supported by the Lalor Foundation Postdoctoral Fellowship, the Yale James Hudson-Brown Fellowship, and the National Institute of Child Health and Human Development, NIH (grant K99-HD-101653). Dr. Abrahams' work was supported by the Paul Titus Fellowship.

[1]Mancy Tong, PhD, Teimur Kayani, BA, Shannon Whirledge, PhD, Vikki M. Abrahams, PhD: Yale School of Medicine, New Haven, Connecticut; [2]Deidre M. Jones, MS, Lawrence W. Chamley, PhD: The University of Auckland, New Zealand; [3]Jane E. Salmon, MD: Weill Cornell Medicine, New York, New York.

Author disclosures are available at https://onlinelibrary.wiley.com/action/downloadSupplement?doi=10.1002%2Fart.42068&file=art42068-sup-0001-Disclosureform.pdf.

Address correspondence to Vikki M. Abrahams, PhD, Department of Obstetrics, Gynecology & Reproductive Sciences, Yale School of Medicine, 310 Cedar Street, LSOG 305C, New Haven, CT 06510. Email: Vikki.abrahams@yale.edu.

Submitted for publication October 1, 2021; accepted in revised form January 12, 2022.

associated with the highest risk (4). Furthermore, women with APS are at an increased risk of pregnancy complications later in gestation, including fetal demise, preeclampsia, and intrauterine growth restriction (5).

Antiphospholipid antibodies specific for β_2GPI are the most pathologic in both thrombotic and obstetric APS. In obstetric APS, aPLs specific for β_2GPI target the placental trophoblast, the uterine endothelium, and the endometrial/decidual stroma, where high basal levels of β_2GPI are surface-expressed or bound (6–9). Unlike systemic APS, which is a thrombotic disorder, obstetric APS is associated with inflammation at the maternal–fetal interface, as well as poor placentation and vascular remodeling (5,10,11). Many studies have shown that aPL can deleteriously affect placental trophoblast function (systematically reviewed in [10]), including activation of trophoblast Toll-like receptor 4 (TLR-4) signaling to mediate inflammation (12,13). However, in addition to appropriate placental function, early pregnancy success is also dependent upon a functional and receptive endometrium that plays key roles in modulating trophoblast function, as well as local maternal immune responses to govern implantation. Thus, insufficient or inappropriate endometrial function may be a contributing underlying cause of reduced pregnancy success in women with aPLs.

The major cellular component of the endometrium are endometrial stromal cells (EnSCs). In humans, during the midluteal phase of each menstrual cycle, EnSCs undergo dramatic structural and biochemical changes, termed decidualization, in preparation for implantation. This process is triggered by the postovulatory rise in progesterone that increases intracellular cAMP levels. This causes EnSCs to transition from spindle-shaped fibroblasts to epithelioid-like decidual cells that secrete increased levels of insulin-like growth factor binding protein 1 (IGFBP-1) and prolactin, 2 classic decidualization markers (14), as well as a range of chemokines and cytokines that coordinate changes in the local immune cell composition, contribute to structural changes in the uterine epithelium, and regulate trophoblast invasion (14,15). Thus, aberrant decidualization can predispose a woman to pregnancy failure or associated obstetric complications. Indeed, in women with RPL, EnSCs respond aberrantly to deciduogenic signals, display prolonged and/or disordered inflammation (14,16), and exhibit premature senescence (cellular aging) (17,18).

Senescence is characterized by up-regulation of senescence-associated β-galactosidase (SA β-gal) activity, as well as a range of protein markers and an inflammatory SA secretory phenotype (SASP) that includes cytokines such as interleukin-6 (IL-6) and IL-8 (19). While acute decidual senescence and a transient SASP may be important for promoting tissue plasticity and endometrial function, remodeling, and repair, premature senescence can lead to secondary/bystander senescence of surrounding cells and may promote abnormal EnSC function and uncontrolled inflammation (14,18,20,21). Despite the importance of the endometrium/decidua to early pregnancy, very little is understood about how aPLs impact EnSC function. Therefore, this study aimed to determine the effects of aPL on EnSC decidualization, inflammation, and senescence, and the mechanisms involved. Furthermore, we examined whether the 2 standard therapies for pregnant women with APS, low molecular weight heparin (LMWH) and acetyl salicylic acid (ASA) (22), have any protective effects.

Using a combination of a human EnSC cell line, primary human EnSCs, and a mouse model of decidualization and APS, we demonstrated that aPL dramatically increased EnSC decidualization, accelerated EnSC senescence, and induced EnSC inflammation. The EnSC decidualization and inflammatory responses to aPL were mediated by activation of TLR-4 and p38 MAPK signaling, while increased EnSC reactive oxygen species (ROS) signaling was essential for the elevated decidualization and senescent responses to aPL. Finally, we report that LMWH was able to reduce aPL-mediated increases in EnSC decidualization and inflammation.

PATIENTS AND METHODS

Study approval. Deidentified endometrial tissues were collected from women undergoing hysterectomies or laparoscopic surgery for fibroids or voluntary sterilization, following informed written consent. All human subject research was carried out in accordance with the Declaration of Helsinki, and the protocol was approved by the Yale University's Research Protection Program (protocol no. 0607001625). All animal studies were conducted in accordance with the National Institutes of Health guide for the care and use of laboratory animals and were approved by Yale University's Institutional Animal Care and Use Committee (protocol no. 2019-11589). Mice were housed in standard cages at a specific pathogen–free animal facility following a 12-hour light/dark cycle and were provided with food and water ad libitum.

Antiphospholipid antibodies. The aPL used in this study was IIC5, a well-characterized mouse IgG1 anti-human β_2GPI monoclonal antibody (mAb). This antibody also binds to cardiolipin–β_2GPI complexes and is thus an anticardiolipin antibody. IIC5 also possesses lupus anticoagulant activity, making it a triple-positive aPL (23–25), which is most pathologic in obstetric APS (26). Specifically, IIC5 recognizes an epitope in domain V of β_2GPI and is an appropriate model for human aPL, since it has been validated to compete for binding with patient aPL (24,27) and acts in a similar fashion to patient-derived polyclonal aPL in vitro (12,13). As an isotype-matched control, mouse IgG1 clone 107.3 (BD Biosciences) was used throughout these studies. Human EnSCs were treated with aPL or the IgG isotype control at 20 μg/ml (13), while in vivo studies used aPL or control IgG at 1 mg (28).

EnSCs. A characterized telomerase-immortalized human EnSC cell line was used in this study (29). EnSCs were cultured in low-glucose Dulbecco's modified Eagle's medium supplemented with 10% fetal bovine serum (FBS), 2% penicillin/streptomycin, 2% HEPES, and 2% nonessential amino acids (Life Technologies) at 37°C in humidified 95% air/5% CO_2. Cells were passaged at a 1:3 ratio when 90% confluent, and cells used for this study were under 10 passages. Primary human EnSCs were isolated from endometrial tissue collected from women undergoing hysterectomies or laparoscopic surgery for fibroids or voluntary tubal ligation, following a previously published protocol (30). Briefly, tissue was dissected and incubated in digestion medium (0.1% collagenase B [Stemcell Technologies] and 0.01% DNAse I [Roche] in calcium-free Hanks' balanced salt solution) at 37°C for up to 1 hour, with vortexing every 10 minutes. Next, the supernatant was filtered through a 70-μm polypropylene cell strainer, and the flowthrough containing EnSCs was collected and cultured. EnSCs were used for experiments when 90% confluent and were all under 5 passages.

EnSC treatments. The EnSC cell line or primary EnSCs were either left undecidualized by culturing them in base medium which served as the no-treatment control (OptiMEM medium supplemented with 2% charcoal-stripped FBS [both from Life Technologies]) or decidualized by culturing them in decidualization medium (DM) (OptiMEM medium supplemented with 2% charcoal-stripped FBS, 10 n*M* estradiol [Sigma-Aldrich], 1 μ*M* medroxyprogesterone acetate [Sigma-Aldrich], and 0.5 m*M* 8-bromo-cAMP [Enzo Life Sciences]) (29), with medium changes every 48 hours. Cells were treated in DM in the presence or absence of aPL (20 μg/ml) or the isotype-matched control IgG (20 μg/ml).

In order to investigate the signaling pathways activated by aPL, in some experiments, EnSCs were pretreated for 30 minutes at 37°C prior to the addition of the DM with aPL or control IgG with the following: lipopolysaccharide from the photosynthetic bacterium *Rhodobacter sphaeroides* (LPS-RS), an antagonist that blocks the extracellular binding domain of TLR-4 (10 μg/ml; InvivoGen), SB203580, a p38 MAPK inhibitor (10 μg/ml; Selleckchem), or diphenyleneiodonium (DPI), an ROS inhibitor (5 μ*M*; Sigma-Aldrich). In other experiments, EnSCs were exposed to DM with aPL or control IgG in the presence of LMWH (10 μg/ml; enoxaparin sodium injection; Aventis Pharmaceuticals, Inc.) or ASA (10 μg/ml; Sigma-Aldrich), either alone or in combination. The doses of LMWH and ASA were based on a previous study and are equivalent to low-dose medications used in the clinical setting (31). Inhibitors, drugs, and aPL/IgG were kept in the culture system during the entire treatment process.

Secreted factors. EnSCs were treated for 48 hours prior to collecting the cell-free culture supernatants and storing them at –80°C until further analysis. Secretion of the markers of decidualization, IGFBP-1 and prolactin were measured by enzyme-linked immunosorbent assay (ELISA) (R&D Systems). The following cytokines/chemokines were quantified by multiplex analysis: granulocyte colony-stimulating factor (G-CSF)/CSF3, granulocyte–macrophage CSF (GM-CSF)/CSF2, growth-related oncogene α/CXCL1, IL-1β, IL-6, IL-8, IL-10, IL-12, IL-17, interferon-γ, interferon-γ–inducible 10-kd protein/CXCL10, monocyte chemotactic protein 1 (MCP-1)/CCL2, macrophage inflammatory protein 1α (MIP-1α)/CCL3, MIP-1β/CCL4, RANTES/CCL5, and tumor necrosis factor (all from Bio-Rad). EnSC IL-8 secretion was also measured by ELISA (R&D Systems).

F-actin staining. EnSCs were treated for 96 hours prior to washing and fixation with 4% paraformaldehyde for 10 minutes at room temperature and permeabilization with 0.1% Triton X-100 in phosphate buffered saline (PBS) for 5 minutes. Cells were washed thrice with PBS and then incubated in 3% bovine serum albumin in PBS for 1 hour at room temperature to block nonspecific binding. Next, rhodamine phalloidin (diluted 1:50 in blocking solution; Molecular Probes) was added for 20 minutes at room temperature. EnSCs were washed thrice in PBS before nuclei were labeled with DAPI (diluted 1:10,000 in PBS) (Life Technologies) and viewed on a Keyence BZ-X700 inverted fluorescence microscope. Images were captured and merged using BZ-X advanced analysis software (BZ-H3AE; Keyence).

SA β-gal activity. After treatment of EnSCs for 48 hours, cells were fixed in 0.5% glutaraldehyde in PBS for 5 minutes at room temperature. Cells were washed in PBS prior to incubation with the β-gal staining solution (1 m*M* $MgCl_2$, 1 mg/ml X-Gal, 5 m*M* potassium ferricyanide, 5 m*M* potassium ferrocyanide; pH 6.0) for 16 hours at 37°C with rocking. EnSCs were then washed in PBS, and SA β-gal staining was viewed using an Echo Revolve microscope, with images captured using EchoPRO software.

Western blot analysis. Total protein from treated EnSCs was extracted using Cell Lysis Buffer (no. 9803; Cell Signaling Technology), and Western blot analysis was performed as previously described (32). Membranes were probed with the following primary antibodies diluted in 1% nonfat milk powder/PBS–tween: apolipoprotein E receptor 2 (ApoER2)/low-density lipoprotein receptor–related protein 8 (LRP-8) (diluted 1:500; LS-B169; LifeSpan Biosciences), β-actin (diluted 1:2,500; A2066; Sigma-Aldrich), lamin B1 (diluted 1:500; 13435S; Cell Signaling Technology), phosphorylated S6 (diluted 1:1,000; 4858T; Cell Signaling Technology), and total S6 (diluted 1:1,000; 2217S; Cell Signaling Technology). Chemiluminescence was detected and images were captured using an Amersham Imager 680 (General Electric).

Real-time quantitative polymerase chain reaction (qPCR). Total RNA was extracted from uterine tissue using TRIzol (ThermoFisher Scientific), and complementary DNA synthesis

was performed using 1 μg of RNA and oligo(dT) primers, following the manufacturer's guidelines (SuperScript II kit; Invitrogen). Expression of markers of decidualization (*Bmp2, dPRP, Wnt4*), inflammation (*Il6, KC, Tnf*), and senescence (*p16, p21, p53*) were measured by real-time qPCR using a Kapa SYBR Fast qPCR kit (Kapa Biosystems), with GAPDH as the internal control. All primer sequences are listed in Supplementary Table 1 (available on the *Arthritis & Rheumatology* website at https://onlinelibrary.wiley.com/doi/10.1002/art.42068). Relative gene expression was calculated using the $2^{-\Delta\Delta C_t}$ method.

ROS production. For measurement of ROS production, EnSCs were treated for 1 hour, after which 20 μ*M* of 2′, 7′-dichlorodihydrofluorescein diacetate (Invitrogen) was added and the cells incubated at 37°C for 30 minutes. Without washing, fluorescence at 485/520 nm was measured using a Tecan Infinite M1000 Pro microplate reader (ThermoFisher Scientific).

Mouse model. This study combined 2 established mouse models with modifications: 1 study that was previously used to study APS-associated pregnancy loss by injecting pregnant mice with aPL specific for β_2GPI (28,33), and 1 that induced artificial decidualization in ovariectomized nonpregnant mice to study endometrial function (34). In the current study, female C57BL/6J mice ovariectomized at 6 weeks were purchased from The Jackson Laboratories (Bar Harbor, ME), and after acclimatization for 5–7 days in the institutional animal facility, decidualization was artificially induced as previously described (34). Briefly, at 7–8 weeks of age, mice were administered 100 ng of estradiol (E_2) subcutaneously for 3 days. After 2 days of rest, mice were administered 6.7 ng of E_2 and 1 mg of progesterone (P_4) subcutaneously for a total of 7 consecutive days. On day 3 of the administration of E_2 and P_4, mice were randomly chosen for administration of either PBS, aPL (1 mg), or control IgG (1 mg) intraperitoneally, as previously described (28). Six hours later, mice were anesthetized and a deciduogenic stimulus of 50 μl of sesame oil was injected into the right uterine horn. After recovery, mice continued to receive subcutaneous injections of the combined E_2 and P_4 daily for 4 days, with either PBS, aPL, or IgG also administered intraperitoneally on the second day post–deciduogenic stimulation. At the end of the 7 days of E_2 and P_4 injections, mice were euthanized, and the 2 uterine horns were dissected separately and snap-frozen for analysis. Tissue collection, RNA extraction, and qPCR were performed with the researcher blinded with regard to the mice's treatments. Only data from mice who demonstrated a clear morphologic change with decidualization in 1 uterine horn were included for analysis.

Statistical analysis. Each experiment was performed ≥3 times. The number of independent experiments that data were pooled from is indicated in the figure legends. All data are reported as the mean ± SEM. *P* values were determined using GraphPad Prism software and those less than 0.05 were considered significant. Whether data were normally distributed or not was determined using the Shapiro-Wilk test and the Kolmogorov-Smirnov test. For normally distributed data, significance was determined using either one-way analysis of variance with Dunnett's multiple comparison test, or a paired *t*-test or unpaired *t*-test with Welch's correction. For data not normally distributed, significance was determined using either the paired Friedman test or the Kruskal-Wallis test with Dunn's multiple comparisons test, or a paired Wilcoxon's matched pairs signed rank test or unpaired Mann-Whitney U test.

RESULTS

Antiphospholipid antibodies increased decidualization and senescence and induced inflammation in a human EnSC cell line. To determine how aPLs affect EnSC decidualization, EnSCs were treated with the base medium no-treatment control, DM, or DM with either control IgG or aPL. After 48 hours, DM increased the EnSC secretion of IGFBP-1 (Figure 1A) and prolactin (Figure 1B), compared to the no-treatment control, indicating the initiation of decidualization. Compared to DM alone, aPL further and significantly increased EnSC secretion of IGFBP-1 by a mean ± SEM change of 6.0 ± 2.2–fold ($P < 0.01$; Figure 1A) and prolactin by 2.3 ± 0.3–fold ($P < 0.01$; Figure 1B). This response was not observed with the IgG control, and there was a similarly significant difference in IGFBP-1 and prolactin secretion after aPL exposure, compared to control IgG (mean ± SEM change of 6.7 ± 2.3–fold for IGFBP-1; 2.3 ± 0.2–fold for prolactin) (Figures 1 A and B). Increased decidualization was confirmed by more rounded cell morphology in the aPL-treated cells (Figure 1D). In addition to elevating markers of decidualization, aPL also significantly increased EnSC secretion of inflammatory IL-8 by a mean ± SEM change of 3.5 ± 1.0–fold when compared to DM alone and by 3.6 ± 1.0–fold when compared to control IgG ($P < 0.05$; Figure 1C).

To determine which other EnSC-derived cytokines/chemokines were modulated by aPL, multiplex analysis was performed. Antiphospholipid antibodies significantly increased EnSC secretion of IL-6 (mean ± SEM change of 232.6 ± 154.2–fold compared to DM), IL-17 (1.9 ± 0.1–fold compared to IgG), MCP-1 (6.0 ± 3.4–fold compared to IgG), and vascular endothelial growth factor (VEGF) (2.7 ± 0.8–fold compared to IgG) (Figure 1E). While EnSC secretion of GM-CSF and IL-10 were also increased compared to control IgG, the fold changes were below 1.5 (Figure 1E). Some of these factors (IL-6, IL-8, MCP-1, VEGF) are part of the SASP (19). Indeed, when EnSC expression levels of markers of senescence were investigated, we observed that while low levels of SA β-gal activity were seen under decidualizing conditions (DM), exposure to aPL markedly up-regulated SA β-gal activity when compared to no treatment, treatment with DM,

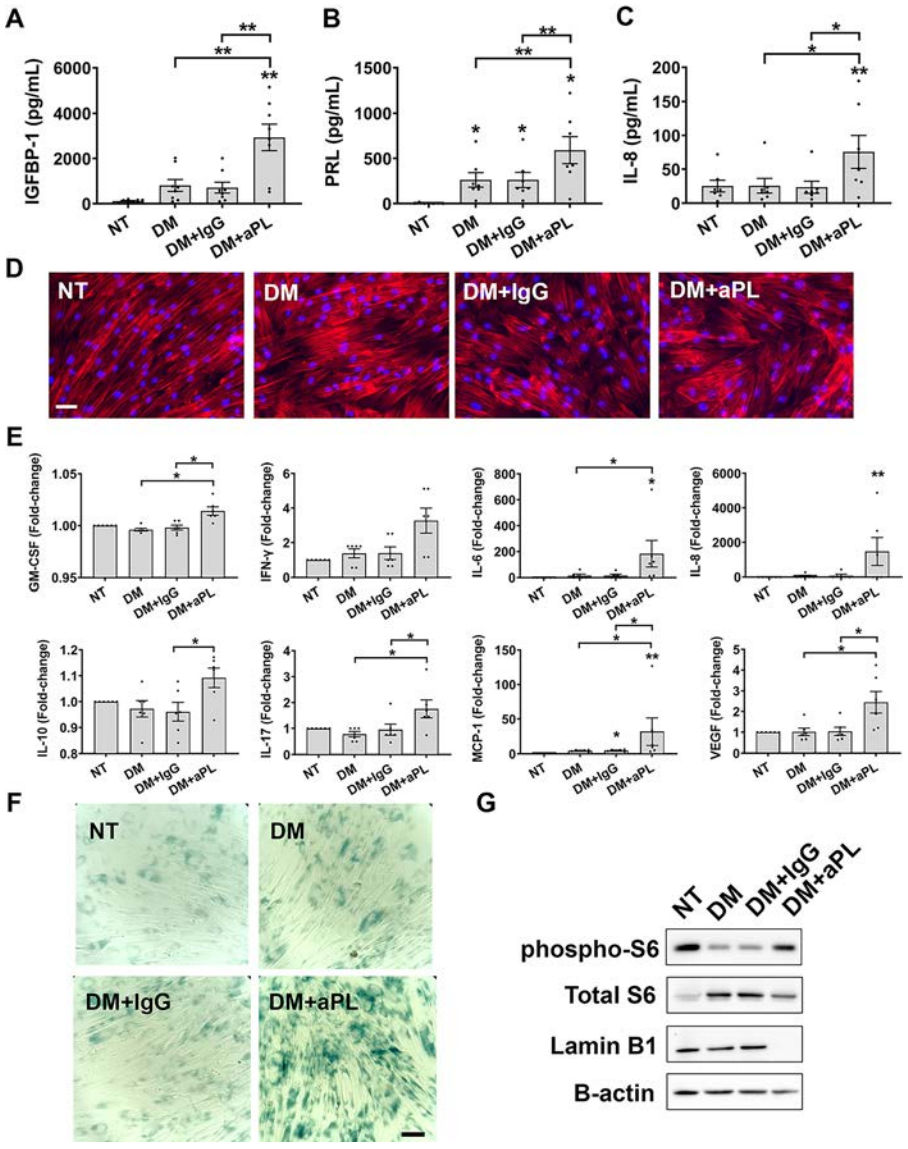

Figure 1. Antiphospholipid antibodies (aPLs) increased decidualization and senescence and induced inflammation in a human endometrial stromal cell (EnSC) line. EnSCs were cultured in decidualization medium (DM), either alone or together with control IgG or aPL. EnSCs cultured in base medium served as the no-treatment (NT) control. **A–C**, After 48 hours, EnSC secretion of insulin-like growth factor binding protein 1 (IGFBP-1) (n = 8 independent experiments) (**A**), prolactin (PRL) (n = 7 independent experiments) (**B**), and interleukin-8 (IL-8) (n = 7 independent experiments) (**C**) into supernatants was quantified by enzyme-linked immunosorbent assay. Bars show the mean ± SEM. **D**, After 96 hours, EnSC morphology was visualized after staining for F-actin (red) and counterstaining the nuclei with DAPI (blue) (n = 3 independent experiments). Results from 1 representative experiment are shown. Bar = 100 μm. **E**, After 48 hours, EnSC supernatants were examined for cytokine/chemokine secretion by multiplex analysis (n = 6 independent experiments). Bars show the mean ± SEM. **F**, After 48 hours, EnSCs were fixed and stained for senescence-associated β-galactosidase (SA β-gal) activity (blue) (n = 5 independent experiments). Results from 1 representative experiment are shown. Bar = 100 μm. **G**, After 48 hours, EnSCs were lysed for extraction of total protein, and Western blotting was performed for visualizing expression of the SA proteins S6 (phosphorylated and total) and lamin B1. β-actin served as a loading control (n = 3 independent experiments). Results from 1 representative experiment are shown. * = $P < 0.05$; ** = $P < 0.01$ for the indicated comparisons or versus no treatment. GM-CSF = granulocyte–macrophage colony-stimulating factor; IFNγ = interferon-γ; MCP-1 = monocyte chemotactic protein 1; VEGF = vascular endothelial growth factor.

and treatment with DM and IgG (Figure 1F). When compared to DM alone or control IgG, aPL also increased EnSC expression of phosphorylated S6 ribosomal protein relative to total S6 protein and reduced lamin B1 relative to β-actin expression (Figure 1G).

Antiphospholipid antibodies increased decidualization and senescence and induced inflammation in primary human EnSCs. To validate the observed effects of aPL on the human EnSC cell line, primary human EnSCs were exposed to base medium as the no-treatment control, DM, or DM with

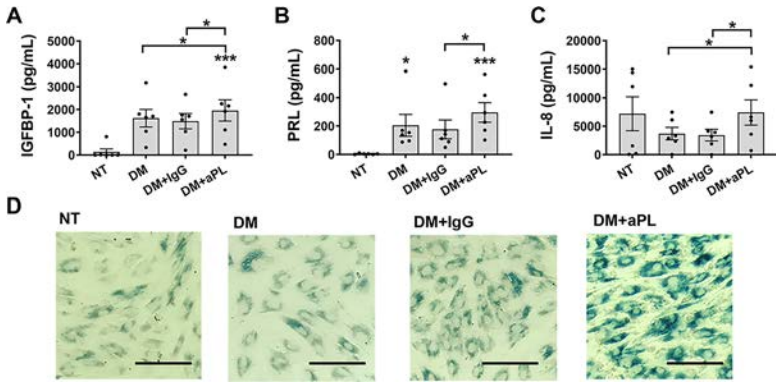

Figure 2. Antiphospholipid antibodies increased decidualization and senescence and induced inflammation in primary human EnSCs. Primary EnSCs were cultured in DM, either alone or together with control IgG or aPL. EnSCs cultured in base medium served as the no-treatment control. **A–C**, After 48 hours, supernatants were collected to measure the secretion of IGFBP-1 (n = 6 independent experiments) (**A**), prolactin (n = 6 independent experiments) (**B**), and IL-8 (n = 6 independent experiments) (**C**). Error bars show the mean ± SEM. **D**, After 48 hours, EnSCs were fixed and stained for SA β-gal activity (blue) (n = 5 independent experiments). Results from 1 representative experiment are shown. Bars = 100 μm. * = $P < 0.05$; *** = $P < 0.001$ for the indicated comparisons or versus no treatment. See Figure 1 for definitions. Color figure can be viewed in the online issue, which is available at http://onlinelibrary.wiley.com/doi/10.1002/art.42068/abstract.

either control IgG or aPL. Similar to the effects on the human EnSC cell line, under culture conditions with DM and exposure to aPL, primary EnSC secretion of IGFBP-1 significantly increased by a mean ± SEM change of 1.4 ± 0.2–fold (Figure 2A), prolactin by 2.0 ± 0.3–fold (Figure 2B), and IL-8 by 1.8 ± 0.4–fold (Figure 2C), compared to control IgG ($P < 0.05$). SA β-gal activity was also up-regulated compared to controls (Figure 2D). These findings demonstrate that the EnSC cell line served as an appropriate model of primary EnSCs and justified the use of the EnSC cell line for downstream mechanistic studies.

Antiphospholipid antibodies increased decidualization and induced uterine inflammation and senescence in a mouse model. To validate our in vitro findings with a physiologically relevant in vivo system, a mouse model of decidualization and APS was employed. Mice were ovariectomized, enabling manipulations of their circulating E_2 and P_4 levels, and they were induced to undergo decidualization by intrauterine oil injection into the right uterine horn. PBS, control IgG, or aPL was administered intraperitoneally on the same day as the induction of decidualization and then again 2 days later. On day 7 post–decidualization induction, mice were euthanized and tissues collected (Figure 3A). This model induced robust decidualization at the organ level (Figure 3B). The murine decidualization markers, *Bmp2*, *dPRP*, and *Wnt4* were detectable under PBS conditions in the decidualized uterine horns.

In mice administered aPL, *Bmp2* levels were significantly higher compared to mice administered control IgG (mean ± SEM change of 3.5 ± 0.3–fold) and higher compared to mice administered PBS (mean ± SEM change of 3.6 ± 0.3–fold) ($P < 0.01$; Figure 3C). While aPL significantly increased *Wnt4* expression compared to PBS-treated controls (mean ± SEM change of 4.5 ± 0.9–fold), there was no significant difference between *Wnt4* levels under aPL and control IgG conditions, and *dPRP* expression was not significantly different under any condition (Figure 3C). Administration of aPL also significantly increased uterine inflammatory *Il6* expression by a mean ± SEM change of 4.3 ± 1.0–fold compared to the IgG control ($P < 0.05$), and by a mean ± SEM change of 34.2 ± 8.1–fold compared to PBS-treated controls ($P < 0.01$; Figure 3D). Uterine expression of *KC*, the mouse equivalent of IL-8, and *Tnf* were not altered following aPL exposure (Figure 3D). To evaluate uterine senescence, expression levels of key cell cycle regulators *p16, p21*, and *p53* (35) were assessed. Exposure to aPL significantly reduced uterine *p53* expression by a mean ± SEM 21.3 ± 4.8% compared to IgG-treated controls and by 18.1 ± 5.0% compared to PBS-treated controls ($P < 0.05$), without affecting *p16* and *p21* expression (Figure 3E).

Antiphospholipid antibodies up-regulated EnSC decidualization and inflammation through, in part, TLR-4. We next sought to determine which receptor on human EnSCs is activated by aPL to mediate the elevated decidualization, inflammation, and senescence. We first investigated whether TLR-4 plays a role, because we have previously shown that aPL activation of TLR-4 in placental trophoblasts leads to inflammation (12,13). EnSCs and decidual stromal cells express TLR-4 (36,37). If TLR-4 is required for aPL-induced changes, then blockade of the extracellular ligand binding domain of TLR-4 with the antagonist LPS-RS would attenuate the effects of aPL. Treatment of EnSCs with LPS-RS significantly reduced aPL-induced EnSC secretion of IGFBP-1 by a mean ± SEM 19.4 ± 5.8% ($P < 0.001$; Figure 4A), prolactin by 12.9 ± 3.3% ($P < 0.05$; Figure 4B), and IL-8 by 20.2 ± 4.4% ($P < 0.001$; Figure 4C). However, LPS-RS had no effect on aPL-induced SA β-gal activity (Figure 4D).

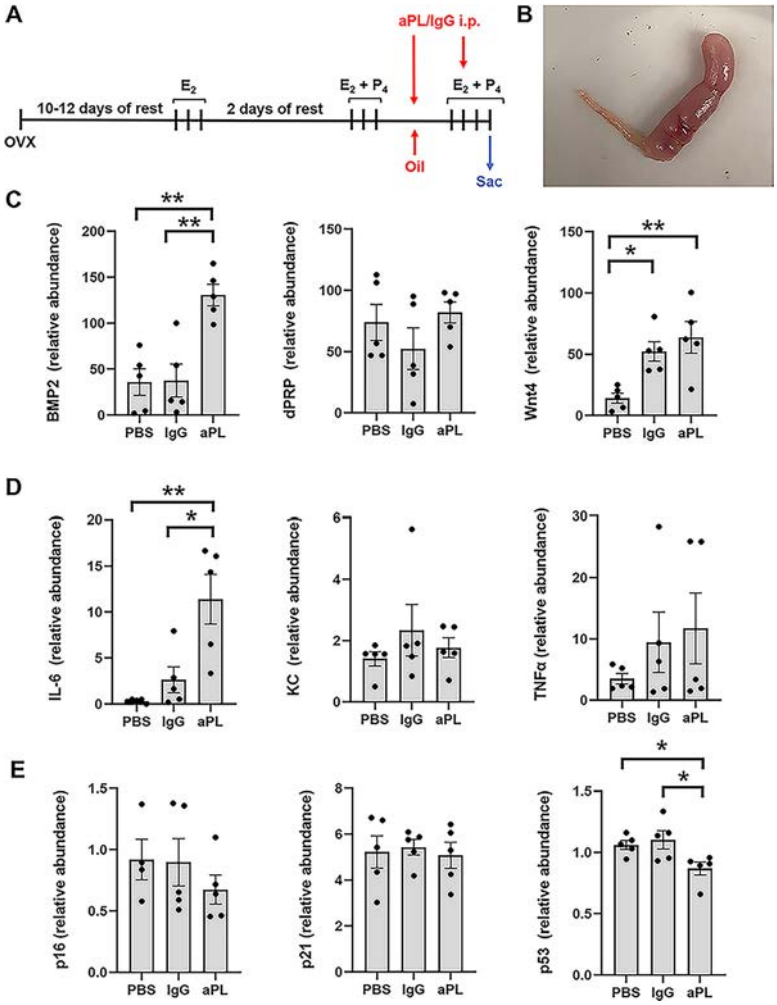

Figure 3. Antiphospholipid antibodies increased decidualization and induced uterine inflammation and senescence in a mouse model. **A**, Mice were ovariectomized (OVX) and then rested. Thereafter, estrogen (E_2) and progesterone (P_4) were replenished in a controlled manner, prior to induction of decidualization using intrauterine injection of sesame oil. Either phosphate buffered saline (PBS) (n = 5 mice), control IgG (n = 5 mice), or aPL (n = 5 mice) were administered intraperitoneally (i.p.) on the day of decidualization induction and again 2 days later. Uterine tissues were then collected 4 days after the induction of decidualization and 6 hours after the last hormone injection. Uterine horns were separated and portions snap-frozen for analysis. **B**, This model induced visually apparent robust decidualization (right horn received oil). **C–E**, Total RNA was extracted from the separated left uterine horns and real-time quantitative polymerase chain reaction was performed to detect markers of the following: decidualization (*Bmp2*, *dPRP*, *Wnt4*) (**C**), inflammation (*Il6*, *KC*, *Tnf*) (**D**), and senescence (*p16, p21*, *p53*) (**E**) (n = 5 independent experiments). Bars show the mean ± SEM. * = $P < 0.05$; ** = $P < 0.01$ for the indicated comparisons or versus PBS treatment. See Figure 1 for other definitions. Color figure can be viewed in the online issue, which is available at http://onlinelibrary.wiley.com/doi/10.1002/art.42068/abstract.

Another receptor that can be activated by aPL is ApoER2/LRP-8 (38,39). To investigate whether ApoER2 also mediated the aPL effect on EnSC function, ApoER2 expression was knocked down in EnSCs using small interfering RNA (siRNA). EnSCs confirmed to have successful ApoER2 knockdown by Western blotting (Supplementary Figure 1A, available on the *Arthritis & Rheumatology* website at https://onlinelibrary.wiley.com/doi/10.1002/art.42068) secreted similar levels of IGFBP-1, prolactin, and IL-8 (Supplementary Figures 1B–D) after stimulation with aPL under target siRNA conditions, compared to EnSCs transfected with control siRNA.

Antiphospholipid antibodies up-regulated EnSC decidualization and inflammation through, in part, p38 MAPK. In order to examine the downstream mechanism by which aPL up-regulated EnSC decidualization, inflammation, and senescence, we investigated whether p38 MAPK, a signaling pathway reported to be increased in trophoblasts exposed to aPL (40), was involved. The presence of the specific p38 MAPK inhibitor SB203580 significantly reduced the ability of aPL to increase EnSC secretion of IGFBP-1 by a mean ± SEM 62.9 ± 11.5% ($P < 0.05$; Figure 4E), prolactin by 48.8 ± 8.4% ($P < 0.01$; Figure 4F), and IL-8 by 41.8 ± 15.8% ($P < 0.05$; Figure 4G). The presence of SB203580 did not

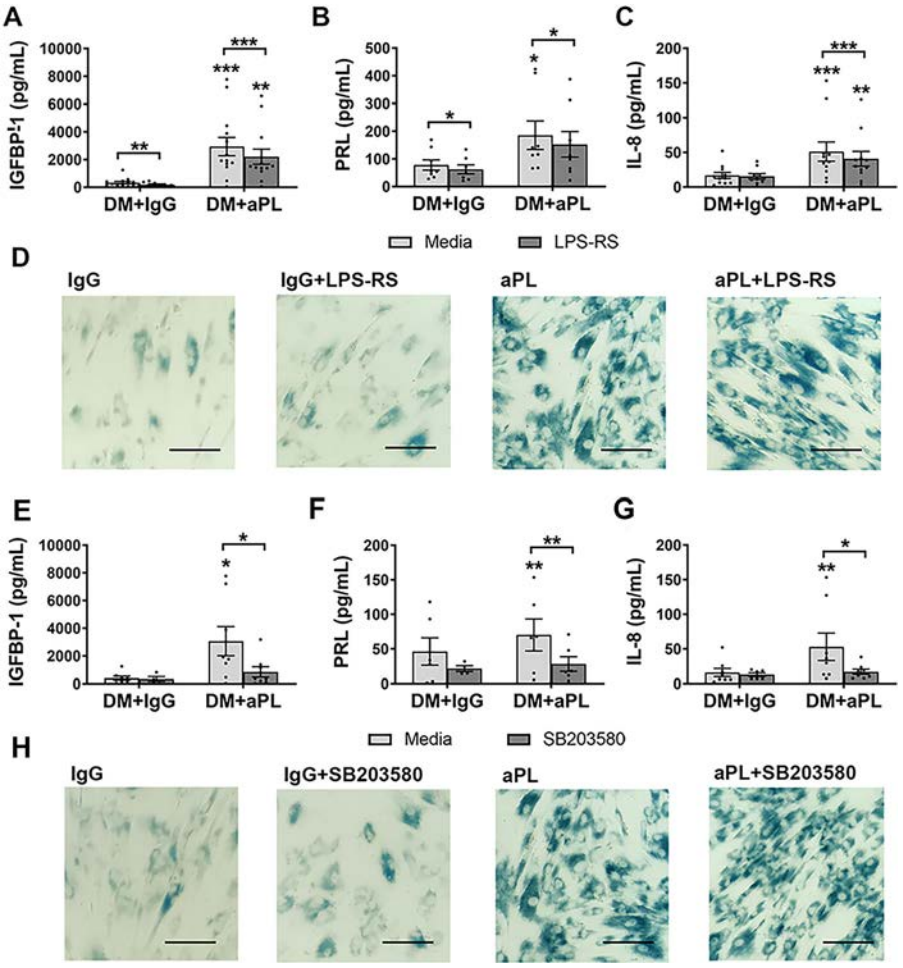

Figure 4. Antiphospholipid antibodies up-regulated EnSC decidualization and inflammation in part through Toll-like receptor 4 (TLR-4) and p38 MAPK. **A–C**, EnSCs were pretreated with medium or the TLR-4 antagonist *Rhodobacter sphaeroides* (LPS-RS) for 30 minutes, prior to the addition of DM with either control IgG or aPL (n = 8–13 independent experiments). After 48 hours, cell-free supernatants were collected to measure the secretion of IGFBP-1 (**A**), prolactin (**B**), and IL-8 (**C**). Error bars show the mean ± SEM. **D**, After 48 hours, cells were fixed and stained for SA β-gal activity (blue) (n = 10 independent experiments). Results from 1 representative experiment are shown. Bars = 100 μm. **E–H**, EnSCs were pretreated with medium or the p38 MAPK inhibitor SB203580 for 30 minutes, prior to the addition of DM with either control IgG or aPL (n = 8 independent experiments). After 48 hours, cell-free supernatants were collected to measure the secretion of IGFBP-1 (**E**), prolactin (**F**), and IL-8 (**G**). Error bars show the mean ± SEM. **H**, After 48 hours, cells were fixed and stained for SA β-gal activity (blue) (n = 10 independent experiments). Results from 1 representative experiment are shown. Bars = 100 μm. * = $P < 0.05$; ** = $P < 0.01$; *** = $P < 0.001$ for the indicated comparisons or versus DM + control IgG treatment. See Figure 1 for other definitions. Color figure can be viewed in the online issue, which is available at http://onlinelibrary.wiley.com/doi/10.1002/art.42068/abstract.

affect the ability of aPL to increase EnSC SA β-gal activity (Figure 4H).

Antiphospholipid antibodies up-regulated EnSC decidualization and senescence through ROS production. Since aPLs are able to induce placental ROS production (41) and ROS could contribute to inflammatory and senescent pathways, we investigated whether aPL could induce ROS production in EnSCs. Antiphospholipid antibodies significantly increased EnSC ROS production by a mean ± SEM change of 1.7 ± 0.2–fold compared to IgG-treated controls ($P < 0.05$) and by 1.5 ± 0.0–fold compared to DM-treated controls ($P < 0.01$; Figure 5A). Inhibition of ROS production using DPI significantly reduced the ability of aPL to increase EnSC IGFBP-1 by a mean ± SEM 46.0 ± 11.2% ($P < 0.05$; Figure 5B) and prolactin by 50.3 ± 8.4% ($P < 0.05$; Figure 5C), but had no effect on IL-8 secretion (Figure 5D). The presence of DPI markedly reduced aPL-induced EnSC SA β-gal activity (Figure 5E).

LMWH prevention of aPL up-regulation of EnSC decidualization and inflammation. Heparin (unfractionated or LMWH) with or without low-dose ASA are standard treatments for aPL-positive women at risk for obstetric complications (22). We assessed whether these 2 drugs, either alone or in combination, had any effects on the function of EnSCs exposed to aPL. LMWH alone significantly reduced the ability of aPL to increase

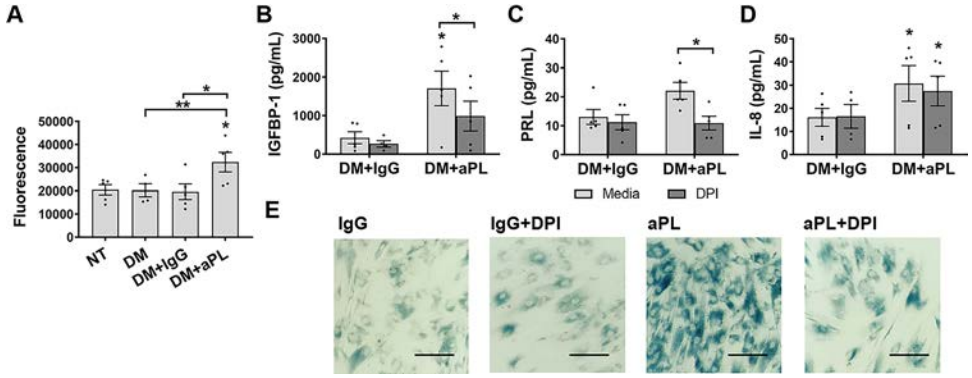

Figure 5. Antiphospholipid antibodies up-regulated EnSC decidualization and senescence through reactive oxygen species (ROS) production. **A**, EnSCs were exposed to base medium as a control or exposed to DM alone or DM together with either control IgG or aPL for 1 hour, after which ROS production was measured at 485/520 nm by H2DCFDA staining (n = 5 independent experiments). **B–D**, EnSCs were pretreated with either medium or the ROS inhibitor diphenyleneiodonium (DPI) for 30 minutes, prior to the addition of DM together with either control IgG or aPL (n = 5 independent experiments). After 48 hours, cell-free supernatants were collected to measure the secretion of IGFBP-1 (**B**), prolactin (**C**), and IL-8 (**D**). Error bars show the mean ± SEM. **E**, After 48 hours, cells were fixed and stained for SA β-gal activity (blue) (n = 3 independent experiments). Results from 1 representative experiment are shown. Bars = 100 μm. * = $P < 0.05$; ** = $P < 0.01$ for the indicated comparisons or versus no treatment in **A** and versus DM + control IgG treatment in **B–D**. See Figure 1 for other definitions. Color figure can be viewed in the online issue, which is available at http://onlinelibrary.wiley.com/doi/10.1002/art.42068/abstract.

EnSC secretion of IGFBP-1 by a mean ± SEM 18.4 ± 6.4% ($P < 0.05$; Figure 6A), prolactin by 19.5 ± 3.7% ($P < 0.05$; Figure 6B), and IL-8 by 18.4 ± 5.8% ($P < 0.05$; Figure 6C). In contrast, ASA did not significantly affect the capacity of aPL to increase EnSC secretion of IGFBP-1 or IL-8 (Figures 6A and C), but ASA did significantly reduce aPL-induced EnSC prolactin secretion by a mean ± SEM 22.6 ± 7.8% ($P < 0.05$; Figure 6B). Treatment with a combination of LMWH and ASA demonstrated similar statistically significant reductions in EnSC secretion of IGFBP-1 ($P < 0.05$; Figure 6A) and IL-8 ($P < 0.05$; Figure 6C), compared to treatment with LMWH alone, suggesting that ASA did not have any additive or synergistic effects. LMWH or ASA either alone or in combination had no demonstrable effect on aPL-induced EnSC SA β-gal activity (Figure 6D).

DISCUSSION

The presence of aPL is one of the single biggest maternal risk factors for recurrent miscarriage (1–3). While the deleterious effects of aPL on placental trophoblast function are well

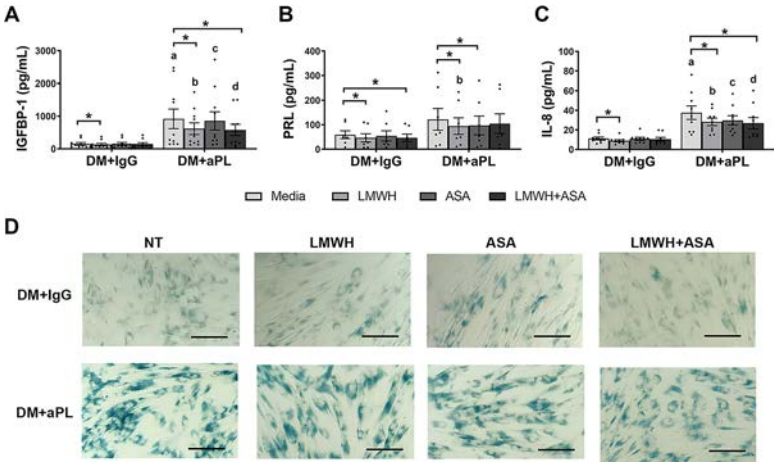

Figure 6. Low molecular weight heparin (LMWH) prevented aPL from up-regulating EnSC decidualization and inflammation. **A–C**, EnSCs were pretreated with either base medium, LMWH, acetyl salicylic acid (ASA), or both LMWH and ASA for 30 minutes, prior to the addition of DM together with either control IgG or aPL. After 48 hours, cell-free supernatants were collected to measure the secretion of IGFBP-1 (n = 10 independent experiments) (**A**), prolactin (n = 7 independent experiments) (**B**), and IL-8 (n = 9 independent experiments) (**C**). Error bars show the mean ± SEM. **D**, After 48 hours, cells were fixed and stained for SA β-gal activity (blue) (n = 3 independent experiments). Results from 1 representative experiment are shown. Bars = 100 μm. a = $P < 0.05$ versus medium pretreatment followed by DM + control IgG; b = $P < 0.05$ versus LMWH pretreatment followed by DM + control IgG; c = $P < 0.05$ versus ASA pretreatment followed by DM + control IgG; d = $P < 0.05$ versus LMWH + ASA pretreatment followed by DM + control IgG; * = $P < 0.05$ between the indicated groups. See Figure 1 for other definitions. Color figure can be viewed in the online issue, which is available at http://onlinelibrary.wiley.com/doi/10.1002/art.42068/abstract.

reported (10), how aPL affects the maternal endometrium/decidua remains unclear. Using a combination of a human EnSC cell line, primary human EnSCs, and a mouse model, we demonstrated that aPL elevated decidualization, triggered inflammation, and accelerated senescence in EnSCs. These effects were partially mediated by activation of TLR-4 and signaling through p38 MAPK and ROS. LMWH, a commonly prescribed therapeutic for aPL-positive women with RPL, was able to partially protect against aPL-induced increases in EnSC decidualization and inflammation, but not senescence, while ASA, another commonly prescribed therapeutic, did not have these protective effects.

The aPL we used in this study, IIC5, is a mouse mAb that reacts with domain V of β_2GPI (24). While aPLs reactive with domain I of β_2GPI have been considered more pathogenic, a task force on aPLs concluded that not all anti-β_2GPI antibodies detectable in APS patients target domain I, with significant subpopulations reacting against other β_2GPI epitopes (42). Furthermore, a systematic review found that only 44.3–45.4% of patients with APS (either alone or with systemic lupus erythematosus) had domain I anti-β_2GPI antibodies, and while the presence of anti-β_2GPI domain I antibodies doubles the risk for thrombotic events, no studies have shown an association with pregnancy morbidities (43). Another systematic review demonstrated that the most important feature of pathogenic aPLs in obstetric APS is triple positivity (26), and IIC5 is triple-positive by having anti-β_2GPI, anticardiolipin, and lupus anticoagulant activity (23–25).

In the presence of aPL under decidualizing conditions, markers of decidualization and senescence were elevated in EnSCs, along with an inflammatory response resembling an SASP (IL-6, IL-8, MCP-1, VEGF). The aPL-induced up-regulation in decidualization was different from what had previously been demonstrated in decidualizing EnSCs (7) and in decidualized cells at full term (44). In one study, treatment of decidualizing EnSCs with aPL reduced prolactin and IGFBP-1 secretion (7). These conflicting findings could be due to the use of an aPL that recognizes a distinct epitope in domain V of β_2GPI, as well as the cells, aPL concentration, and time point studied. In particular, it is recognized that small changes in aPL epitope specificity can have large functional and biologic effects (45). Conversely, the observed induction of EnSC inflammatory IL-8 secretion triggered by aPL corroborates findings from a previous study that showed that anti-β_2GPI aPL altered first trimester decidual cell gene expression by up-regulating pathways involved in developmental, inflammatory, immune, and stress responses (6).

We found that aPL-induced senescence was ROS-dependent, as was the aPL-mediated decidualization response, suggesting that these 2 processes may be connected. A recent bioinformatic study demonstrated that decidualizing EnSCs progress along a continuous trajectory toward senescence (18); particularly since we observed (in the presence of aPL under decidualizing conditions) that most EnSCs were senescent, it is interesting to hypothesize that aPL may accelerate this process, leading to altered uterine receptivity. In women who experience recurrent miscarriage, EnSCs have been reported to respond aberrantly to deciduogenic signals and exhibit signs of premature senescence (18). We validated our in vitro observations in vivo using a mouse model, and demonstrated that aPL can similarly affect conserved aspects of uterine/endometrial function in mice, despite species differences in decidualization between rodents and humans. Dysregulated decidualization and uterine inflammation induced by aPL may negatively impact downstream trophoblast invasion and placental growth, leading to implantation failure and early pregnancy loss.

In order to investigate the cell surface receptor that aPL could be signaling through to modulate human EnSC function, we investigated TLR-4 and ApoER2, both of which have been shown to be activated by aPL recognizing β_2GPI in placental trophoblasts (12,13,39). Inhibition of TLR-4 was able to reduce, but not abrogate, the effect of aPL on elevated EnSC decidualization and inflammation. In contrast, knockdown of ApoER2 had no effect. Since the inhibition of TLR-4 did not completely reverse the effects of aPL on EnSCs, another receptor may also be activated, such as TLR-2 (46) or another scavenger receptor for low-density lipoprotein (27). Mechanistically, we demonstrated that aPL further increased EnSC decidualization by activating p38 MAPK and ROS signaling, while the inflammatory response was mediated through p38 MAPK but not ROS. Strikingly, inhibition of p38 MAPK signaling completely abrogated aPL up-regulation of IGFBP-1, prolactin, and IL-8 secretion. This suggests that this is a major signaling pathway activated by aPL to up-regulate decidualization and inflammation, while a separate pathway of increased ROS signaling is responsible for the decidualization and senescence response. Interestingly, the observed IL-8 response was ROS-independent, suggesting that it is unrelated to the EnSC senescence response. Potentially, the amount of IL-8 secreted from EnSCs as an inflammatory response to aPL is much higher than that secreted as part of the SASP.

Finally, this study examined whether the standard therapeutics for women with obstetric APS, LMWH and ASA, could protect against the effect of aPL on EnSC function. While early treatment with heparin, alone or in combination with low-dose ASA, may increase the live birth rate in aPL-positive women to ~70%, this remains controversial due to a lack of large, well-controlled trials (2). A recent Cochrane systematic review demonstrated that, compared to ASA alone, heparin treatment together with ASA may increase live births and reduce the risk of pregnancy loss in aPL-positive women (47). In contrast, treatment of aPL-positive women with low-dose ASA was not beneficial in preventing obstetric complications (48,49). In a mouse model of obstetric APS, heparin was also shown to have protective effects against aPL-induced fetal loss, and this was related to inhibition of aPL-mediated complement activation at the maternal–fetal interface (50). Accordingly, in the present study, we demonstrated

that LMWH, with or without ASA, played a protective role against aPL-increased decidualization and inflammation, while ASA alone did not have these effects.

Appropriately controlled decidualization and function of EnSCs is key for successful implantation, placentation, and the establishment of a healthy pregnancy. Herein, we demonstrated that aPL significantly impacted EnSC function, leading to dysregulated decidualization, as well as a senescent and proinflammatory environment that could deleteriously affect their cross-talk with the implanting blastocyst and invading placental trophoblasts. This may dysregulate implantation, which could manifest as spontaneous miscarriage or obstetric complications later in gestation, such as preeclampsia or intrauterine growth restriction. Furthermore, LMWH appeared to have some protective effect on EnSC function in the context of aPL, providing further support for the use of this therapeutic in aPL-positive women with a history of recurrent miscarriage or obstetric APS. Together, these findings shed new light on the underlying pathogenesis of obstetric APS and underscore the potential benefit of heparin treatment for this high-risk population.

ACKNOWLEDGMENTS

The authors would like to thank Hugh Taylor, MD and Valerie Flores, MD for providing samples of human endometrial tissue for analysis.

AUTHOR CONTRIBUTIONS

All authors were involved in drafting the article or revising it critically for important intellectual content, and all authors approved the final version to be published. Dr. Abrahams had full access to all of the data in the study and takes responsibility for the integrity of the data and the accuracy of the data analysis.

Study conception and design. Tong, Salmon, Whirledge, Chamley, Abrahams.

Acquisition of data. Tong, Kayani, Jones.

Analysis and interpretation of data. Tong, Abrahams.

REFERENCES

1. Quenby S, Gallos ID, Dhillon-Smith RK, Podesek M, Stephenson MD, Fisher J, et al. Miscarriage matters: the epidemiological, physical, psychological, and economic costs of early pregnancy loss. Lancet 2021; 397:1658–67.
2. Schreiber K, Sciascia S, de Groot PG, Devreese K, Jacobsen S, Ruiz-Irastorza G, et al. Antiphospholipid syndrome. Nat Rev Dis Primers 2018;4:17103.
3. Practice Committee of the American Society for Reproductive Medicine. Evaluation and treatment of recurrent pregnancy loss: a committee opinion. Fertil Steril 2012;98:1103–11.
4. Antovic A, Sennstrom M, Bremme K, Svenungsson E. Obstetric antiphospholipid syndrome. Lupus Sci Med 2018;5:e000197.
5. Abrahams VM, Chamley LW, Salmon JE. Emerging treatment models in rheumatology: antiphospholipid syndrome and pregnancy: pathogenesis to translation. Arthritis Rheumatol 2017;69:1710–21.
6. Chighizola CB, Pregnolato F, Raschi E, Grossi C, Gentilini D, Borghi MO, et al. Antiphospholipid antibodies and infertility: a gene expression study in decidual stromal cells. Isr Med Assoc J 2016;18: 146–9.
7. Mak IY, Brosens JJ, Christian M, Hills FA, Chamley L, Regan L, et al. Regulated expression of signal transducer and activator of transcription, Stat5, and its enhancement of PRL expression in human endometrial stromal cells in vitro. J Clin Endocrinol Metab 2002;87:2581–8.
8. Meroni PL, Borghi MO, Grossi C, Chighizola CB, Durigutto P, Tedesco F. Obstetric and vascular antiphospholipid syndrome: same antibodies but different diseases? Nat Rev Rheumatol 2018;14: 433–40.
9. Agostinis C, Biffi S, Garrovo C, Durigutto P, Lorenzon A, Bek A, et al. In vivo distribution of β2 glycoprotein I under various pathophysiologic conditions. Blood 2011;118:4231–8.
10. Tong M, Viall CA, Chamley LW. Antiphospholipid antibodies and the placenta: a systematic review of their in vitro effects and modulation by treatment. Hum Reprod Update 2015;21:97–118.
11. Viall CA, Chamley LW. Histopathology in the placentae of women with antiphospholipid antibodies: a systematic review of the literature. Autoimmun Rev 2015;14:446–71.
12. Mulla MJ, Brosens JJ, Chamley LW, Giles I, Pericleous C, Rahman A, et al. Antiphospholipid antibodies induce a pro-inflammatory response in first trimester trophoblast via the TLR4/MyD88 pathway. Am J Reprod Immunol 2009;62:96–111.
13. Mulla MJ, Salmon JE, Chamley LW, Brosens JJ, Boeras CM, Kavathas PB, et al. A role for uric acid and the Nalp3 inflammasome in antiphospholipid antibody-induced IL-1β production by human first trimester trophoblast. PLoS One 2013;8:e65237.
14. Gellersen B, Brosens JJ. Cyclic decidualization of the human endometrium in reproductive health and failure. Endocr Rev 2014;35: 851–905.
15. Hannan NJ, Salamonsen LA. Role of chemokines in the endometrium and in embryo implantation. Curr Opin Obstet Gynecol 2007;19:266–72.
16. Salker MS, Nautiyal J, Steel JH, Webster Z, Sucurovic S, Nicou M, et al. Disordered IL-33/ST2 activation in decidualizing stromal cells prolongs uterine receptivity in women with recurrent pregnancy loss. PLoS One 2012;7:e52252.
17. Lucas ES, Dyer NP, Murakami K, Lee YH, Chan YW, Grimaldi G, et al. Loss of endometrial plasticity in recurrent pregnancy loss. Stem Cells 2016;34:346–56.
18. Lucas ES, Vrljicak P, Muter J, Diniz-da-Costa MM, Brighton PJ, Kong CS, et al. Recurrent pregnancy loss is associated with a pro-senescent decidual response during the peri-implantation window. Commun Biol 2020;3:37.
19. Coppe JP, Desprez PY, Krtolica A, Campisi J. The senescence-associated secretory phenotype: the dark side of tumor suppression. Annu Rev Pathol 2010;5:99–118.
20. Brighton PJ, Maruyama Y, Fishwick K, Vrljicak P, Tewary S, Fujihara R, et al. Clearance of senescent decidual cells by uterine natural killer cells in cycling human endometrium. Elife 2017;6.
21. Lucas ES, Dyer NP, Fishwick K, Ott S, Brosens JJ. Success after failure: the role of endometrial stem cells in recurrent miscarriage. Reproduction 2016;152:R159–66.
22. Arslan E, Branch DW. Antiphospholipid syndrome: diagnosis and management in the obstetric patient. Best Pract Res Clin Obstet Gynaecol 2020;64:31–40.
23. Chamley LW, Konarkowska B, Duncalf AM, Mitchell MD, Johnson PM. Is interleukin-3 important in antiphospholipid antibody-mediated pregnancy failure? Fertil Steril 2001;76:700–6.
24. Albert CR, Schlesinger WJ, Viall CA, Mulla MJ, Brosens JJ, Chamley LW, et al. Effect of hydroxychloroquine on antiphospholipid antibody-induced changes in first trimester trophoblast function. Am J Reprod Immunol 2014;71:154–64.
25. Viall CA, Chen Q, Stone PR, Chamley LW. Human extravillous trophoblasts bind but do not internalize antiphospholipid antibodies. Placenta 2016;42:9–16.

26. De Carolis S, Tabacco S, Rizzo F, Giannini A, Botta A, Salvi S, et al. Antiphospholipid syndrome: an update on risk factors for pregnancy outcome. Autoimmun Rev 2018;17:956–66.
27. Viall CA, Chen Q, Liu B, Hickey A, Snowise S, Salmon JE, et al. Antiphospholipid antibodies internalised by human syncytiotrophoblast cause aberrant cell death and the release of necrotic trophoblast debris. J Autoimmun 2013;47:45–57.
28. Girardi G, Berman J, Redecha P, Spruce L, Thurman JM, Kraus D, et al. Complement C5a receptors and neutrophils mediate fetal injury in the antiphospholipid syndrome. J Clin Invest 2003;112:1644–54.
29. Krikun G, Mor G, Alvero A, Guller S, Schatz F, Sapi E, et al. A novel immortalized human endometrial stromal cell line with normal progestational response. Endocrinology 2004;145:2291–6.
30. Yang H, Zhou Y, Edelshain B, Schatz F, Lockwood CJ, Taylor HS. FKBP4 is regulated by HOXA10 during decidualization and in endometriosis. Reproduction 2012;143:531–8.
31. Han CS, Mulla MJ, Brosens JJ, Chamley LW, Paidas MJ, Lockwood CJ, et al. Aspirin and heparin effect on basal and antiphospholipid antibody modulation of trophoblast function. Obstet Gynecol 2011; 118:1021–8.
32. Tong M, Potter JA, Mor G, Abrahams VM. Lipopolysaccharide-stimulated human fetal membranes induce neutrophil activation and release of vital neutrophil extracellular traps. J Immunol 2019;203: 500–10.
33. Holers VM, Girardi G, Mo L, Guthridge JM, Molina H, Pierangeli SS, et al. Complement C3 activation is required for antiphospholipid antibody-induced fetal loss. J Exp Med 2002;195:211–20.
34. Whirledge SD, Oakley RH, Myers PH, Lydon JP, DeMayo F, Cidlowski JA. Uterine glucocorticoid receptors are critical for fertility in mice through control of embryo implantation and decidualization. Proc Natl Acad Sci U S A 2015;112:15166–71.
35. Gomez-Lopez N, Romero R, Plazyo O, Schwenkel G, Garcia-Flores V, Unkel R, et al. Preterm labor in the absence of acute histologic chorioamnionitis is characterized by cellular senescence of the chorioamniotic membranes. Am J Obstet Gynecol 2017;217:592. e1–17.
36. Hirata T, Osuga Y, Hirota Y, Koga K, Yoshino O, Harada M, et al. Evidence for the presence of toll-like receptor 4 system in the human endometrium. J Clin Endocrinol Metab 2005;90:548–56.
37. Schatz F, Kayisli UA, Vatandaslar E, Ocak N, Guller S, Abrahams VM, et al. Toll-like receptor 4 expression in decidual cells and interstitial trophoblasts across human pregnancy. Am J Reprod Immunol 2012;68: 146–53.
38. Ramesh S, Morrell CN, Tarango C, Thomas GD, Yuhanna IS, Girardi G, et al. Antiphospholipid antibodies promote leukocyte-endothelial cell adhesion and thrombosis in mice by antagonizing eNOS via β2GPI and apoER2. J Clin Invest 2011;121:120–31.
39. Ulrich V, Gelber SE, Vukelic M, Sacharidou A, Herz J, Urbanus RT, et al. ApoE receptor 2 mediation of trophoblast dysfunction and pregnancy complications induced by antiphospholipid antibodies in mice. Arthritis Rheumatol 2016;68:730–9.
40. Krivokuća MJ, Rabi TA, Stefanoska I, Vrzić-Petronijević S, Petronijević M, Vićovac L. Immunoglobulins from sera of APS patients bind HTR-8/SVneo trophoblast cell line and reduce additional mediators of cell invasion. Reprod Biol 2017;17:389–95.
41. Zussman R, Xu LY, Damani T, Groom KM, Chen Q, Seers B, et al. Antiphospholipid antibodies can specifically target placental mitochondria and induce ROS production. J Autoimmun 2020;111: 102437.
42. Bertolaccini ML, Amengual O, Andreoli L, Atsumi T, Chighizola CB, Forastiero R, et al. 14th International Congress on Antiphospholipid Antibodies Task Force. Report on antiphospholipid syndrome laboratory diagnostics and trends. Autoimmun Rev 2014;13:917–30.
43. Radin M, Cecchi I, Roccatello D, Meroni PL, Sciascia S. Prevalence and thrombotic risk assessment of anti-β2 glycoprotein I domain I antibodies: a systematic review. Semin Thromb Hemost 2018;44: 466–74.
44. Pierro E, Andreani CL, Lazzarin N, Minici F, Apa R, Miceli F, et al. Effect of anticardiolipin antibodies on prolactin and insulin-like growth factor binding protein-1 production by human decidual cells. Am J Reprod Immunol 1999;41:209–16.
45. Chukwuocha RU, Zhu M, Cho CS, Visvanathan S, Hwang KK, Rahman A, et al. Molecular and genetic characterizations of five pathogenic and two non-pathogenic monoclonal antiphospholipid antibodies. Mol Immunol 2002;39:299–311.
46. Satta N, Kruithof EK, Fickentscher C, Dunoyer-Geindre S, Boehlen F, Reber G, et al. Toll-like receptor 2 mediates the activation of human monocytes and endothelial cells by antiphospholipid antibodies. Blood 2011;117:5523–31.
47. Hamulyak EN, Scheres LJ, Marijnen MC, Goddijn M, Middeldorp S. Aspirin or heparin or both for improving pregnancy outcomes in women with persistent antiphospholipid antibodies and recurrent pregnancy loss. Cochrane Database Syst Rev 2020;5:CD012852.
48. Amengual O, Fujita D, Ota E, Carmona L, Oku K, Sugiura-Ogasawara M, et al. Primary prophylaxis to prevent obstetric complications in asymptomatic women with antiphospholipid antibodies: a systematic review. Lupus 2015;24:1135–42.
49. Laskin CA, Spitzer KA, Clark CA, Crowther MR, Ginsberg JS, Hawker GA, et al. Low molecular weight heparin and aspirin for recurrent pregnancy loss: results from the randomized, controlled HepASA Trial. J Rheumatol 2009;36:279–87.
50. Girardi G, Redecha P, Salmon JE. Heparin prevents antiphospholipid antibody-induced fetal loss by inhibiting complement activation. Nat Med 2004;10:1222–6.

Arthritis & Rheumatology
Vol. 74, No. 6, June 2022, pp 1013–1026
DOI 10.1002/art.42061

American College of Rheumatology
Empowering Rheumatology Professionals

Interleukin-1β–Activated Microvascular Endothelial Cells Promote DC-SIGN–Positive Alternatively Activated Macrophages as a Mechanism of Skin Fibrosis in Systemic Sclerosis

Paôline Laurent,[1] Joelle Lapoirie,[2] Damien Leleu,[1] Emeline Levionnois,[1] Cyrielle Grenier,[1] Blanca Jurado-Mestre,[1] Estibaliz Lazaro,[3] Pierre Duffau,[3] Christophe Richez,[3] Julien Seneschal,[2] Jean-Luc Pellegrin,[2] Joel Constans,[2] Thierry Schaeverbeke,[2] Isabelle Douchet,[1] Dorothée Duluc,[1] Thomas Pradeu,[1] Carlo Chizzolini,[4] Patrick Blanco,[3] Marie-Elise Truchetet,[3] and Cécile Contin-Bordes,[3] on behalf of the Fédération Hospitalo-Universitaire ACRONIM and the Centre National de Référence des Maladies Auto-Immunes Systémiques Rares de l'Est et du Sud-Ouest (RESO)

Objective. To characterize the role of interleukin-1β (IL-1β) and microvascular endothelial cells (MVECs) in the generation of alternatively activated macrophages in the skin, and to explore their role in the development of skin fibrosis in patients with systemic sclerosis (SSc; scleroderma).

Methods. Conditioned medium prepared with MVECs purified from the skin of healthy donors and the skin of SSc patients was used to generate monocyte-derived macrophages. Flow cytometry, multiplex protein assessment, real-time quantitative polymerase chain reaction, and tissue immunofluorescence were used to characterize MVEC-induced polarization of alternatively activated macrophages. Coculture experiments were conducted to assess the role of MVEC-induced alternatively activated macrophages in fibroblast activation. Alternatively activated macrophages were characterized in the skin of healthy donors and SSc patients using multiparametric immunofluorescence and multiplex immunostaining for gene expression. Based on our in vitro data, we defined a supervised macrophage gene signature score to assess correlation between the macrophage score and clinical features in patients with SSc, using the Spearman's test.

Results. IL-1β–activated MVECs from SSc patients induced monocytes to differentiate into DC-SIGN+ alternatively activated macrophages producing high levels of CCL18, CCL2, and CXCL8 but low levels of IL-10. DC-SIGN+ alternatively activated macrophages showed significant enhancing effects in promoting the production of proinflammatory fibroblasts and were found to be enriched in perivascular regions of the skin of SSc patients who had a high fibrosis severity score. A novel skin transcriptomic macrophage signature, defined from our in vitro findings, correlated with the extent of skin fibrosis (Spearman's r = 0.6, $P = 0.0018$) and was associated with early disease manifestations and lung involvement in patients with SSc.

Conclusion. Our findings shed new light on the vicious circle implicating unabated IL-1β secretion, MVEC activation, and the generation of DC-SIGN+ alternatively activated macrophages in the development of skin fibrosis in patients with SSc.

Supported by la Fondation Arthritis and l'Association des Sclérodermiques de France.

[1]Paôline Laurent, PhD, Damien Leleu, PhD, Emeline Levionnois, MSc, Cyrielle Grenier, MD, Blanca Jurado-Mestre, MSc, Isabelle Douchet, MSc, Dorothée Duluc, PhD, Thomas Pradeu, PhD: Immunoconcept, CNRS UMR 5164, Bordeaux University, Bordeaux, France; [2]Joelle Lapoirie, MD, Julien Seneschal, MD, PhD, Jean-Luc Pellegrin, MD, PhD, Joel Constans, MD, PhD, Thierry Schaeverbeke, MD, PhD: University Hospital Centre Bordeaux, Bordeaux, France; [3]Estibaliz Lazaro, MD, PhD, Pierre Duffau, MD, PhD, Christophe Richez, MD, PhD, Patrick Blanco, MD, PhD, Marie-Elise Truchetet, MD, PhD, Cécile Contin-Bordes, PhD: Immunoconcept, CNRS UMR 5164, Bordeaux University, and University Hospital Centre Bordeaux, Bordeaux, France; [4]Carlo Chizzolini, MD, PhD: Geneva University, Geneva, Switzerland.

Drs. Truchetet and Contin-Bordes contributed equally to this work.

Author disclosures are available at https://onlinelibrary.wiley.com/action/downloadSupplement?doi=10.1002%2Fart.42061&file=art42061-sup-0001-Disclosureform.pdf.

Address correspondence to Cecile Contin-Bordes, PhD, Site de Carreire, Zone Nord, Bâtiment 1B, 146 Rue Léo Saignat. 33076 Bordeaux Cedex, France. Email: cecile.bordes@chu-bordeaux.fr.

Submitted for publication May 12, 2021; accepted in revised form December 22, 2021.

INTRODUCTION

Systemic sclerosis (SSc) is a rare autoimmune connective tissue disease characterized by microangiopathy and fibrosis (1). The pathophysiology of SSc is unclear, but it involves a complex network of interactions between the microvascular system, activation of autoimmune processes, and chronic activation of fibroblasts (2,3).

Monocyte-derived macrophages exhibit a wide spectrum of polarization states, which are determined by the local environment in which they differentiate. Based on in vitro stimulation and analysis of membrane and soluble markers, monocyte-derived macrophages are classified as inflammatory (M1-type) and alternatively activated macrophages (M2-type). M1-type macrophages originate in response to microbial factors, such as lipopolysaccharide (LPS) and proinflammatory cytokines (interferon-γ [IFNγ], tumor necrosis factor [TNF], and interleukin-1β [IL-1β]) (4). Alternatively activated macrophages comprise numerous cell subsets that may be distinguished on the basis of the milieu in which they differentiate: stimulation with IL-4 or IL-13 for the M2a macrophage phenotype, interaction of immune complexes with IL-1β or LPS for the M2b subtype, stimulation with IL-10, transforming growth factor β (TGFβ), or glucocorticoids for the M2c subtype, and stimulation with Toll-like receptors (TLRs) and IL-6 for the M2d subtype (4).

In analyses of circulating markers and immunohistochemistry (5,6), the role of alternatively activated macrophages in fibrosis during the course of SSc has been reinforced by transcriptomics and systems biology data (7,8). In mouse models of SSc, a cAMP-specific phosphodiesterase 4 blocker and the tyrosine kinase inhibitor nintedanib have been shown to alleviate the development of skin fibrosis by, in part, limiting polarization toward alternatively activated macrophages (9,10). Moreover, in the faSScinate trial (Safety and Efficacy of Subcutaneous Tocilizumab in Adults with SSc), molecular profiling of skin biopsy specimens and analysis of circulating cytokines revealed that IL-6 receptor blockade by tocilizumab down-regulated the alternatively activated macrophage signature in the skin of SSc patients (11). However, fibrinogenic monocytes harboring both M1 and M2 markers are present in patients with SSc and interstitial lung disease (12), and transcriptomic analysis of skin has revealed associated M1 and M2 signatures in early SSc (13). This suggests that the classic M1/M2 macrophage classification rapidly finds limitations as it does not reflect the diversity of tissue macrophages induced by dynamic and complex microenvironmental changes, which mediate long-term macrophage imprinting (trained innate immunity), polarization states, and plasticity (14). Taken together, these observations suggest that macrophages participate in fibrotic processes in mouse models of SSc and in human patients with SSc. However, the underlying mechanisms are still largely unknown, especially in humans.

Human studies (15,16) and animal models have highlighted the role of the inflammasome and the release of IL-1β in the development of lung and skin fibrosis (17–19). Our group recently reported that activated platelets promote the IL-1β–dependent production of thymic stromal lymphopoietin by microvascular endothelial cells (MVECs), which in turn activate dermal fibroblasts and enhance collagen deposition (20). In the present study, we evaluated whether IL-1β–activated MVECs indirectly favor fibrotic processes by promoting a microenvironment that modulates polarization of cutaneous macrophages during SSc.

PATIENTS AND METHODS

Patients with SSc who presented to the University Hospital of Bordeaux, France, between March 2014 and September 2016 were prospectively enrolled in the present study. All patients satisfied the 2013 American College of Rheumatology/European League of Associations for Rheumatology classification criteria for SSc (21). Patients were included in the Vasculopathy and Inflammation in Systemic Sclerosis (VISS) biomedical research project (22) and the study was approved by the University Hospital of Bordeaux institutional ethics committee (Comites de Protection des Personnes approval no. 2012-A00081-42). All participants provided written informed consent before inclusion. Age- and sex-matched healthy donors were recruited at the local Blood Transfusion Centre (Etablissement Français du sang, Bordeaux). Details on all patients' demographic and clinical features and laboratory test results are provided in the Supplementary Materials and Methods and Supplementary Table 1 (available on the *Arthritis & Rheumatology* website at http://onlinelibrary.wiley.com/doi/10.1002/art.42061).

Cell purification. Human dermal MVECs were obtained from the skin of healthy donors and patients with SSc as previously described (23) (Supplementary Table 2, available at http://onlinelibrary.wiley.com/doi/10.1002/art.42061). MVEC-conditioned medium (MVEC-CM) was produced by culturing MVECs with or without IL-1β (50 ng/ml; R&D Systems) for 24 hours in MV2 medium supplemented with 1% penicillin/streptomycin and 8% fetal calf serum (FCS) (PromoCell). Fibroblasts were cultured by incubating skin samples in Hanks' buffered salt solution containing 0.1% type I collagenase A (Sigma) for 3 hours at 37°C. Cell pellets were suspended in Dulbecco's modified Eagle's medium with 1% penicillin/streptomycin and 10% FCS (Gibco). Monocytes were obtained from the blood of healthy donors recruited at Bordeaux Blood Transfusion Centre. After separation with Ficoll (Eurobio), monocytes were purified by immunomagnetic sorting using CD14 microbeads (Miltenyi). Purity (>90%) was assessed by flow cytometry.

Generation of monocyte-derived macrophages. Monocytes were incubated for 6 days in 24-well flat-bottomed plates at a density of 5×10^4 cells/well in a 1:1 volume of complete RPMI medium (supplemented with 1% penicillin/streptomycin and

8% FCS) together with MV2 medium or MVEC-CM. Cultures were supplemented with 5 ng/ml granulocyte–macrophage colony-stimulating factor (GM-CSF) or 50 ng/ml M-CSF (Miltenyi Biotech) and fresh cytokines were added on day 3. When indicated, endothelin-1 receptor (ET-1R) antagonist (macitentan 100 ng/ml; Actelion), anti–interleukin-6 receptor (anti–IL-6R) (tocilizumab 100 ng/ml, Roche), anti–IL-1β antibodies (canakinumab 150 μg/ml; Novartis), recombinant IL-6 (100 ng/ml), or recombinant ET-1 (10 ng/ml) were added to the cultures. To potentiate blockade of the receptors, ET-1R antagonist and anti–IL-6R were preincubated with monocytes for 1 hour before the addition of MVEC-CM. To prevent quick engagement of IL-1β receptor by IL-1β contained in the MVEC-CM, blocking anti–IL-1β was preincubated with MVEC-CM for 1 hour before being cultured with monocytes.

Flow cytometry. STAT1 and STAT3 phosphorylation were assessed in monocytes after incubation for 20 minutes with MVEC-CM with the use of a dedicated flow cytometry kit from Miltenyi Biotec. Macrophage membrane marker expression was evaluated by flow cytometry using PerCP-labeled CD14, allophycocyanin (APC)–labeled CD206, VioBlue-labeled CD209, APC–Cy7-labeled CCR2, phycoerythrin (PE)–Cy7-labeled CCR7 (Miltenyi), and PE-labeled CD163 (BD Biosciences). Cells were analyzed using a FACSCanto II flow cytometer with FACSDiva software (BD Biosciences), and data analysis was performed using FlowJo software version 10.1.

Cytokine and chemokine assays. IL-6, CXCL8, CXCL10, platelet-derived growth factor BB (PDGF-BB), interleukin-1 receptor antagonist (IL-1Ra), GM-CSF, granulocyte colony-stimulating factor (G-CSF), CCL2, CCL5, IL-12p40, TNF, and IFNγ were quantified using a multiplex assay (BioLegend) in MVEC, macrophage, and fibroblast supernatants. IL-10 and ET-1 (Abcam) were assessed by enzyme-linked immunosorbent assay. To ensure the specificity of cytokine/chemokine measurements in macrophage culture supernatants, cytokine/chemokine levels were also quantified in MVEC-CM cultured without macrophages for 6 days and were deduced from the total levels in macrophage culture supernatant.

Fibroblast and macrophage cocultures. Macrophages were washed intensively (3 times with 10 ml of phosphate buffered saline) to eliminate any remaining cytokines/chemokines from the supernatant and were then seeded at a density of 3×10^4 in the lower chambers of Transwell microplates. Fibroblasts were seeded at a density of 3×10^4 in the upper chambers of Transwell microplates and cultured for 24 hours. *Col1A1*, *Col1A2*, *MMP1*, *MMP2*, *TIMP1*, *TIMP2*, *CCL2*, *IL6*, *CXCL10*, *CCL5*, *IL1R*, and *CFS3* messenger RNA (mRNA) expression was quantified using quantitative reverse transcriptase–polymerase chain reaction (qRT-PCR) as previously described (20). For details on the probes used in qRT-PCR see the Supplementary Materials and Methods, available on the *Arthritis & Rheumatology* website at http://onlinelibrary.wiley.com/doi/10.1002/art.42061.

Quantification of mRNA expression in healthy donor and SSc skin tissue sections. NanoString nCounter gene expression assay was performed with RNA that had been isolated from formalin-fixed paraffin-embedded (FFPE) skin sections from healthy donors (n = 10) and patients with SSc (n = 24), using a High-Pure FFPET RNA Isolation kit (Roche). The enriched gene signature comprised mRNAs of *CD68*, *CD163*, *CD209* (*DC-SIGN*), *MRC1* (*CD206*), *c-Maf*, *STAT3*, *IL10*, *CCL18*, *CCL2*, *CXCL8*, *CX_3CL1*, *CX_3CR1*, *CSF1R*, *CCR2*, *CFS1*, *IL1R1*, and *IL1RA*. Natural logarithm–transformed expression values of genes were scaled and visualized as a clustergram with the use of the R package heatmap. The macrophage score was determined for each sample as previously described (24), and the fold change between each patient with SSc and the healthy donor group was computed.

Immunofluorescence analysis of healthy donor and SSc skin tissue sections. FFPE skin sections (3-μm–thick) from 4 healthy donors and 8 patients with SSc were used in immunohistochemical analyses. For multiplex staining of macrophages, the sections were incubated for 1 hour at room temperature with mouse anti-human DC-SIGN and visualized with an Alexa Fluor 647 Tyramide SuperBoost kit and goat anti-rabbit IgG, in accordance with the manufacturer's instructions. Primary/secondary antibody complexes were stripped by heat-induced epitope retrieval and the sections were stained with mouse anti-human CD68 and rabbit anti-human c-MAF primary antibodies, and with goat anti-mouse Alexa Fluor 568 and Alexa Fluor 488 Tyramide SuperBoost kit goat anti-rabbit IgG secondary antibodies. Whole-tissue sections were scanned using a NanoZoomer 2.0-HT (Hamamatsu). Microscopy was performed at the Bordeaux Imaging Center. For details on the immunofluorescence reagents used, see the Supplementary Materials and Methods, available on the *Arthritis & Rheumatology* website at http://onlinelibrary.wiley.com/doi/10.1002/art.42061.

Statistical analysis. Statistical analysis was performed using GraphPad Prism. For distributions that satisfied the Shapiro-Wilk normality test, Student's 2-tailed *t*-test for unpaired or paired samples and one-way repeated-measures analysis of variance (ANOVA) followed by Bonferroni correction were used to compare populations. When the normality test was not satisfied, the Mann-Whitney or Wilcoxon test was used. Correlations were analyzed by Spearman's test. *P* values less than 0.05 were considered significant. Results are reported as the mean ± SEM.

Data availability. All data supporting the findings of this study are available within the article and/or its supplementary materials.

RESULTS

Differentiation of monocytes into DC-SIGN+ alternatively activated macrophages in vitro in MVEC-CM cultures derived from healthy donors. Alternatively activated macrophages play a pivotal role in the development of fibrosis in the setting of scleroderma. However, the mechanisms underlying the polarization of alternatively activated macrophages in affected tissues are unknown. We evaluated whether IL-1β–activated MVECs from healthy donors modulated the polarization of monocyte-derived macrophages. As shown in Figure 1A, IL-1β–activated MVEC-CM induced a

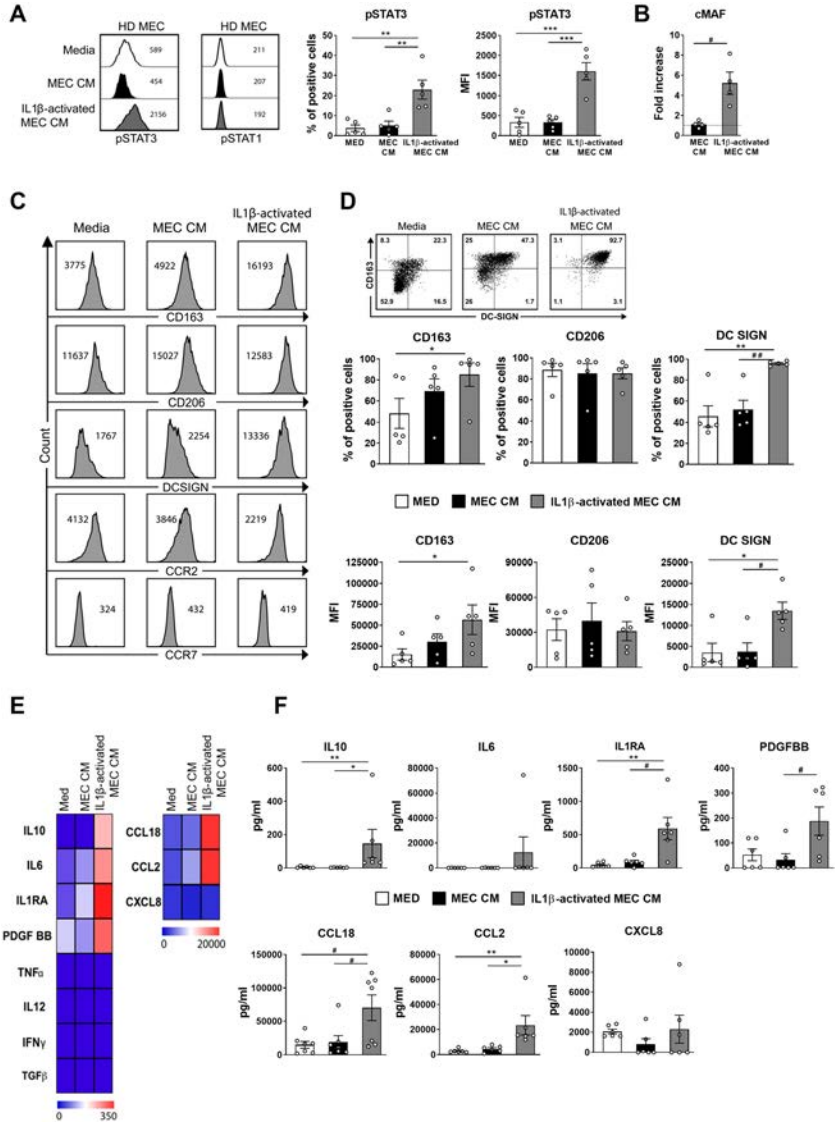

Figure 1. Induction of polarization of DC-SIGN+ c-MAF+ alternatively activated macrophages by interleukin-1β (IL-1β)–activated microvascular endothelial cells (MVECs) from healthy donors (HDs). Monocytes or macrophages from healthy donors were incubated with medium alone (MED), with nonactivated MVEC-conditioned medium (MEC CM), or with IL-1β–activated MVEC-conditioned medium. **A**, Histograms show expression levels of pSTAT3 and pSTAT1 in monocytes under each culture condition (left), with results expressed as the percentage of positive cells and mean fluorescence intensity (MFI) (right). **B**, The fold increase in *cMaf* mRNA expression in healthy donor macrophages under each culture condition was assessed on day 6; data are from 3 independent experiments. **C** and **D**, Histograms show macrophage expression of CD163, CD206, DC-SIGN, CCR2, and CCR7 (**C**), and flow cytometry dot plots show macrophage expression of CD163, CD206, and DC-SIGN (**D**; top) under each culture condition, with results expressed as the percentage of positive cells and MFI (**D**; bottom). Data in **C** and **D** are from 5 independent experiments. **E** and **F**, Levels of cytokines and chemokines were measured on day 6 in macrophage supernatants under each culture condition. Expression levels of cytokines and chemokines are shown as heatmaps (**E**) and presented as cumulative data from 5 independent experiments (**F**). In **A**, **B**, **D**, and **F**, symbols represent individual experiments; bars show the mean ± SEM. * or # = $P < 0.05$; ** or ## = $P < 0.01$; *** = $P < 0.001$, by *t*-test or analysis of variance. IL-1Ra = IL-1 receptor antagonist; PDGF-BB = platelet-derived growth factor BB; TNF = tumor necrosis factor; IFNγ = interferon-γ; TGFβ = transforming growth factor β.

significant increase in the expression of phosphorylated STAT3 (pSTAT3), in terms of both the percentage of positive cells and the mean fluorescence intensity (MFI) of expression, compared to that with medium alone or that with nonactivated MVEC-CM. The expression of pSTAT1 was not detected under any condition (Figure 1A). The transcription factor c-Maf, which regulates the expression of numerous alternative and tumor-associated macrophage–related genes in mice and humans (25), was significantly up-regulated on day 6 in macrophages generated in the presence of IL-1β–activated MVEC-CM compared to nonactivated CM ($P = 0.028$) (Figure 1B).

Compared to macrophages cultured with medium alone, macrophages cultured with IL-1β–activated MVECs showed a significant up-regulation in the surface expression of CD163; there was a nonsignificant trend toward increased expression of CD163 in macrophages cultured with IL-1β–activated MVECs in CM compared to macrophages cultured with nonactivated MVECs in CM ($P = 0.06$) (Figures 1C and D). The same observation held true for MFI. The alternatively activated macrophage–associated marker CD206 was induced under all conditions, as expected, considering the presence of GM-CSF in the culture. DC-SIGN expression (percentage of positive cells and MFI) was significantly increased in macrophages derived from monocytes cultured in the presence of IL-1β–activated MVEC-CM compared to medium alone and nonactivated MVEC-CM ($P = 0.008$ for the percentage of positive cells; and $P = 0.03$ for MFI).

In contrast, the M1 macrophage marker CCR7 was not detected, and CCR2 expression was unchanged under all conditions (Figure 1C and data not shown). Neither blockade of IL-1β in IL-1β–activated MVEC-CM nor the addition of recombinant IL-1β to nonactivated MVEC-CM modified DC-SIGN or CD163 expression (Supplementary Figure 1A, available on the *Arthritis & Rheumatology* website at http://onlinelibrary.wiley.com/doi/10.1002/art.42061), which ruled out a direct effect of IL-1β. Expression of CD163 and DC-SIGN was similar under GM-CSF or M-CSF conditions (Supplementary Figure 2, available on the *Arthritis & Rheumatology* website at http://onlinelibrary.wiley.com/doi/10.1002/art.42061), which excluded a specific effect of GM-CSF.

Irrespective of the stimulation conditions, IFNγ, TNF, IL-12p40, and TGFβ (Figure 1E and data not shown) were not detected in macrophage supernatants. IL-6 was not detected in macrophage supernatant induced by MVEC-CM, and levels of the chemokine ligand CXCL8 were comparable under all conditions tested (Figures 1E and F). In contrast, macrophages generated in the presence of IL-1β–activated MVEC-CM produced significantly greater levels of IL-10 ($P = 0.016$), IL-1Ra ($P = 0.015$), PDGF-BB ($P = 0.05$), CCL18 ($P = 0.017$), and CCL2 ($P = 0.045$) compared to nonactivated MVEC-CM (Figure 1F). IL-1β was not directly responsible for the increased cytokine/chemokine production (see Supplementary Figure 1B, available on the *Arthritis & Rheumatology* website at http://onlinelibrary.wiley.com/doi/10.1002/art.42061). Therefore, CM prepared with IL-1β–activated MVECs promotes the generation of pSTAT3+ DC-SIGN+ alternatively activated macrophages, which produce IL-10 and high levels of CCL2 and CCL18.

Generation of SSc MVEC DC-SIGN+ macrophages with distinct functional capabilities. We next determined if MVECs purified from the skin of SSc patients would induce similar or distinctive macrophages. CM prepared with IL-1β–activated MVECs from patients with SSc increased expression of pSTAT3 compared to MVEC-CM from healthy donors (Figure 2A). The magnitude of pSTAT3 induction was significantly increased in CM prepared with IL-1β–activated MVECs from SSc patients, both in terms of the percentage of positive cells and the MFI. In contrast, there was no significant difference in pSTAT3 expression between healthy donor–derived MVEC-CM and CM prepared with nonactivated MVECs from SSc patients (Figure 2B). CM prepared with IL-1β–activated MVECs from SSc patients significantly increased the macrophage expression of c-Maf (Figure 2C) and DC-SIGN (Figure 2D) when compared to that observed in cultures with nonactivated MVEC-CM derived from SSc patients. No difference in macrophage expression of c-Maf and DC-SIGN was observed between IL-1β–activated MVEC-CM derived from healthy donors and MVEC-CM derived from patients with SSc. CD163 and CD206 expression was comparable between the SSc patient–derived and healthy donor–derived MVEC-CM cultures (Figure 2D), with similar results seen for CCR7 and CCR2 expression in these cultures (data not shown).

Although the production of CCL18, IL-1Ra, and PDGF-BB by macrophages was increased in the presence of IL-1β–activated MVECs from healthy donors and SSc patients, consistent with that in the presence of alternatively activated macrophages, CCL2 was markedly up-regulated ($P = 0.038$). Surprisingly, despite induction with c-Maf, IL-10 was not produced by macrophages generated in the presence of IL-1β–activated MVECs from patients with SSc compared to macrophages cultured in the presence of MVECs from healthy donors ($P = 0.009$). Of note, although it was barely detectable in MVECs from healthy donors irrespective of stimulation, IL-1β–activated MVECs from SSc patients strongly up-regulated the production of the M1-associated marker CXCL8 ($P = 0.009$) (Figure 2E).

Taken together, these data demonstrate that IL-1β–stimulated MVECs from patients with SSc promoted the generation of DC-SIGN+ alternatively activated macrophages, which did not produce IL-10 but did generate high levels of CCL2 and CXCL8 compared to MVECs from healthy donors. Thus, patients with SSc had a mixed phenotype of alternatively activated macrophages and M1 macrophages.

IL-6 and endothelin-1 in the generation of DC-SIGN+ macrophages. To identify soluble factors responsible for the skewing of normal monocytes toward alternatively activated

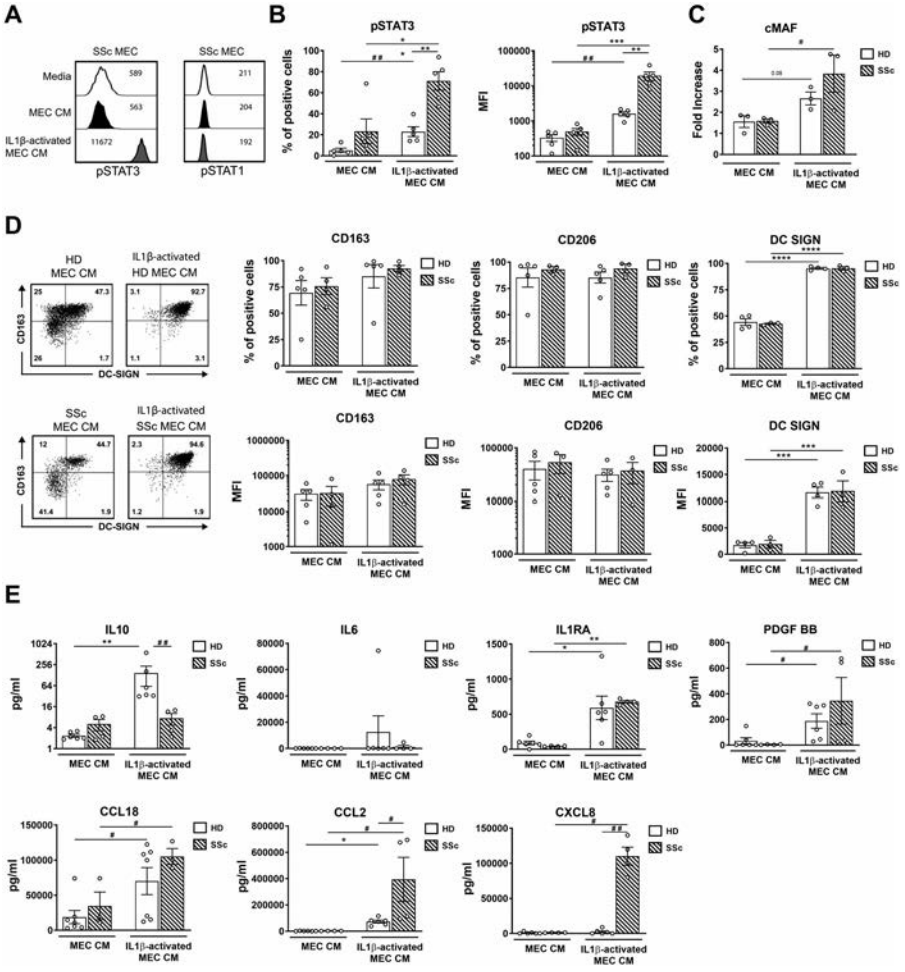

Figure 2. Induction of expression of DC-SIGN+ alternatively activated macrophages and altered chemokine and cytokine production in cultures of IL-1β–activated MVECs from patients with systemic sclerosis (SSc). Monocytes or macrophages from patients with SSc and healthy donors were incubated with medium alone, with nonactivated MVEC-conditioned medium, or with IL-1β–activated MVEC-conditioned medium. **A** and **B**, The expression of pSTAT3 and pSTAT1 was assessed in monocytes from SSc patients under each culture condition, with results shown in flow cytometry histograms (**A**) and as percentages of pSTAT3-positive cells and MFI (**B**); data are from 5 independent experiments. **C**, The fold increase in *cMaf* expression in SSc and healthy donor macrophages was assessed on day 6 under each culture condition; data are from 3 independent experiments. **D**, Representative flow cytometry dot plots (left) and quantification of the results (right) show expression of CD163, CD206, and DC-SIGN in SSc and healthy donor macrophages under each culture condition. **E**, Cytokine and chemokine levels were assessed on day 6 in macrophage culture supernatants under each condition; data are from 5 independent experiments, with different cells in each experiment. Symbols represent individual experiments; bars show the mean ± SEM. * or # = $P < 0.05$; ** or ## = $P < 0.01$; *** = $P < 0.001$; **** = $P < 0.0001$, by *t*-test or analysis of variance. See Figure 1 for other definitions.

macrophages, we measured the levels of several soluble promoters of macrophage polarization in MVEC-CM. While IL-4, IL-13, eotaxin, GM-CSF, M-CSF, TNF, and IFNγ were not detectable, or were barely detectable, in all CM tested (data not shown), IL-6 was strongly induced in the presence of IL-1β but was not detected in CM prepared with nonactivated MVECs (Figure 3A). Interestingly, the level of IL-6 was higher in the CM prepared with IL-1β–activated MVECs from SSc patients. Although it was not statistically significant, we observed a trend toward increased production of ET-1 in the CM of IL-1β–activated MVECs (Figure 3B).

We tested whether IL-6 receptor blockade by tocilizumab in IL-1β–activated MVEC-CM would affect macrophage differentiation. IL-6 blockade significantly reduced the percentage of cells expressing pSTAT3 and DC-SIGN (Figures 3C and D), and also reduced the MFI of expression of pSTAT3 and DC-SIGN (data not shown).

ET-1, a key mediator in the development of SSc, has been found to be involved in the polarization of alternatively activated macrophages (26). The addition of macitentan (inhibitor of ET-1 receptors A and B) to CM from IL-1β–activated MVECs slightly, but significantly, decreased both the percentage of DC-SIGN+ cells and the MFI of DC-SIGN expression in macrophages (data not shown) ($P = 0.0003$ and $P = 0.002$, respectively). The proportion of pSTAT3+ cells decreased significantly

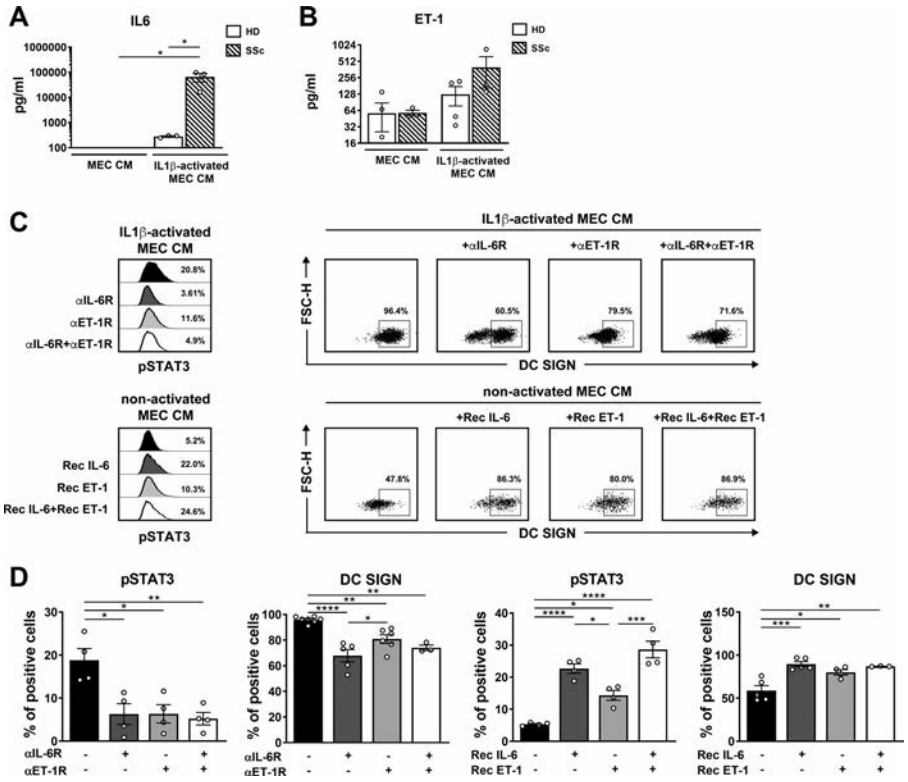

Figure 3. Production of IL-6 and endothelin-1 (ET-1) in cultures of IL-1β–activated MVECs from SSc patients triggers polarization of DC-SIGN+ alternatively activated macrophages. **A** and **B**, Production of IL-6 (**A**) and ET-1 (**B**) was assessed in cultures of nonactivated or IL-1β–activated MVECs from healthy donors (n = 4) and patients with SSc (n = 3). **C** and **D**, Monocytes (**C**) or macrophages (**D**) were preincubated with an IL-6 receptor (IL-6R) blocking antibody (tocilizumab), an ET-1 receptor (ET-1R) blocking antibody (macitentan), or both antibodies, followed by the addition of IL-1β–activated IL-1β–activated MVEC-conditioned medium, or were preincubated with nonactivated MVEC-conditioned medium supplemented with or without recombinant IL-6 (Rec IL-6) or Rec ET-1 or both. Following treatment, cells were assessed for the expression of pSTAT3 and DC-SIGN. Data are from at least 4 independent experiments in each experimental setting. Symbols represent individual experiments; bars show the mean ± SEM. * = $P < 0.05$; ** = $P < 0.01$; *** = $P < 0.001$; **** = $P < 0.0001$, by analysis of variance or *t*-test. See Figure 1 for other definitions.

(Figures 3C and D), but the MFI was unchanged (data not shown).

As shown in Figures 3C and D, the addition of recombinant IL-6 or ET-1 to nonactivated MVEC-CM significantly increased DC-SIGN and p-STAT3 expression. IL-6 and ET-1 redundantly, but not synergistically, enhanced STAT3 phosphorylation (Figure 3D). Therefore, IL-1β promotes the production of IL-6 and ET-1 by MVECs, favoring the polarization of monocytes toward DC-SIGN+ alternatively activated macrophages.

Promotion of proinflammatory fibroblasts by alternatively activated macrophages following induction in CM containing IL-1β–activated MVECs from SSc patients. To analyze their role in fibrosis and inflammation, we cocultured DC-SIGN+ alternatively activated macrophages with healthy donor fibroblasts in Transwells. After 24 hours, fibroblasts were harvested and the levels of mRNA for proinflammatory genes (*CCL2*, *IL1RA*, *IL6*, *CXCL10*, *CCL5*, *CFS3*), matrix-remodeling genes (*MMP1*, *MMP2*, *TIMP1*), and genes encoding extracellular matrix proteins (*COL1A1* and *COL1A2*) were assessed. Additionally, global cytokine and chemokine production was quantified in the coculture supernatants.

Expression of *COL1A1*, *COL1A2*, *MMP2*, and *TIMP1* by fibroblasts was unchanged irrespective of the stimulation conditions and origin of the MVECs (see Supplementary Figure 3, available on the *Arthritis & Rheumatology* website at http://onlinelibrary.wiley.com/doi/10.1002/art.42061). In contrast, strong and reproducible increases in *MMP1* and *CCL2* mRNA expression were observed in healthy donors and patients with SSc (Figure 4A and Supplementary Figure 3, available on the *Arthritis & Rheumatology* website at http://onlinelibrary.wiley.com/doi/10.1002/art.42061). Although macrophages induced in the presence of IL-1β–activated MVECs from patients with SSc and healthy donors resulted in similar levels of *MMP1* mRNA, levels of CCL2 were reproducibly and significantly higher in CM prepared with IL-1β–activated MVECs from SSc patients, at the level of both mRNA and protein expression ($P = 0.04$ and $P = 0.017$, respectively) (Figures 4A and B).

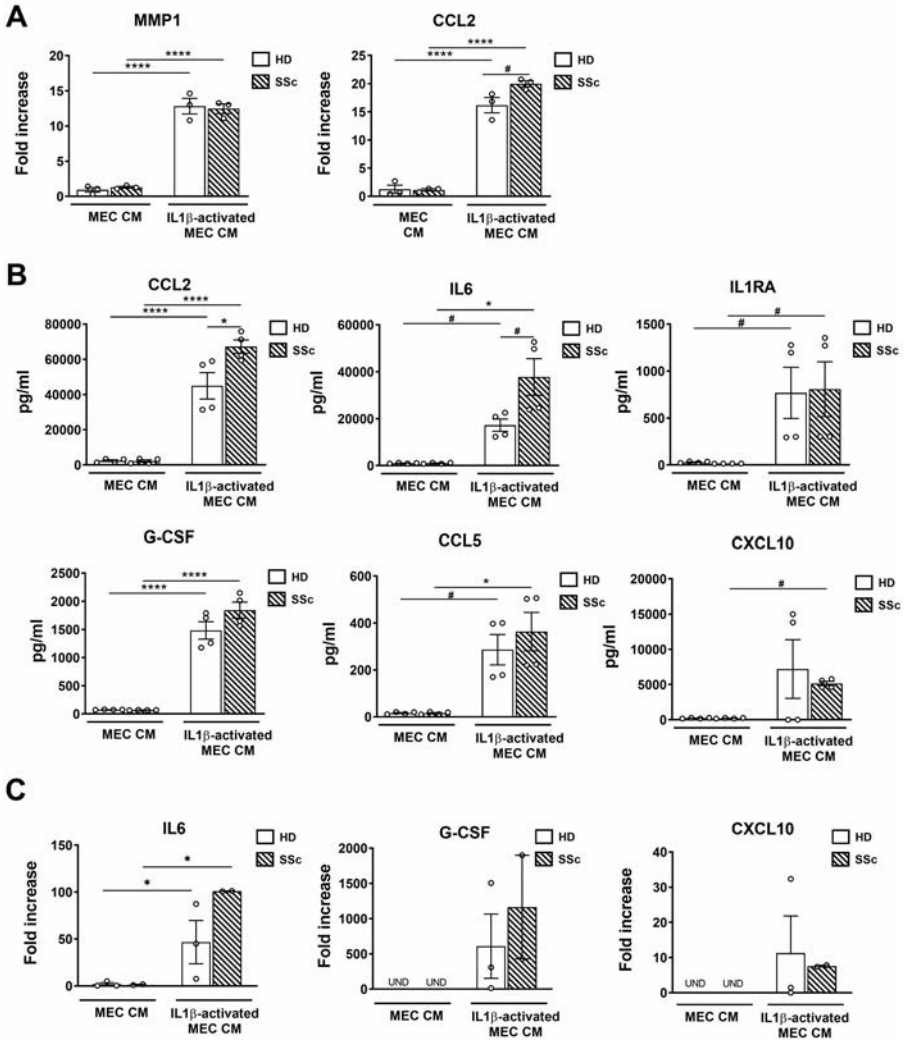

Figure 4. Proinflammatory and proremodeling effects on fibroblasts in cultures with macrophages differentiated in the presence of IL-1β–activated MVECs. Fibroblasts were incubated with macrophages that had been stimulated with nonactivated or IL-1β–activated MVECs from healthy donors or patients with systemic sclerosis (SSc). **A**, The fold increase in *MMP1* and *CCL2* expression was assessed by quantitative reverse transcriptase–polymerase chain reaction (qRT-PCR) analysis in fibroblasts under each culture condition. **B**, Global cytokine/chemokine production was assessed in fibroblasts under each culture condition. **C**, The fold increase in expression of IL-6, granulocyte colony-stimulating factor (G-CSF), and CXCL10 transcripts was assessed by qRT-PCR in fibroblasts under each culture condition. Data are from 3 independent experiments. Symbols represent individual experiments; bars show the mean ± SEM. * or # = $P < 0.05$; **** = $P < 0.0001$, by analysis of variance or *t*-test. UND = undetectable (see Figure 1 for other definitions).

The IL-6 protein level was also found to be significantly higher in the presence of macrophages induced by IL-1β–activated MVECs from SSc patients compared to CM prepared with MVECs from healthy donors ($P = 0.028$) (Figure 4B). IL-6 mRNA expression was up-regulated in fibroblasts cultured with IL-1β–activated MVEC–derived macrophages irrespective of the source of the MVECs (Figure 4C), which suggests that both macrophages and fibroblasts contributed to the increased protein production observed in culture supernatants from IL-1β–activated MVEC-CM.

Finally, CCL5, CXCL10, G-CSF, and IL-1Ra protein levels were also increased in IL-1β–activated MVEC-CM, irrespective of the source of the MVECs (Figure 4B). IL1-Ra and CCL5 transcripts were undetectable irrespective of the condition tested (data not shown), suggesting that both proteins were produced by macrophages. In sharp contrast, G-CSF expression was strongly up-regulated in fibroblasts cultured in the presence of macrophages generated in CM with IL-1β–activated MVECs both from healthy donors and from SSc patients (Figure 4C), confirming the contribution of fibroblasts to the production of G-CSF. Interestingly, CXCL10 expression was reproducibly increased in fibroblasts from cultures of macrophages generated with IL-1β–activated MVECs from SSc patients, while results from cultures of CM prepared with MVECs from healthy donors were more inconsistent (Figure 4B).

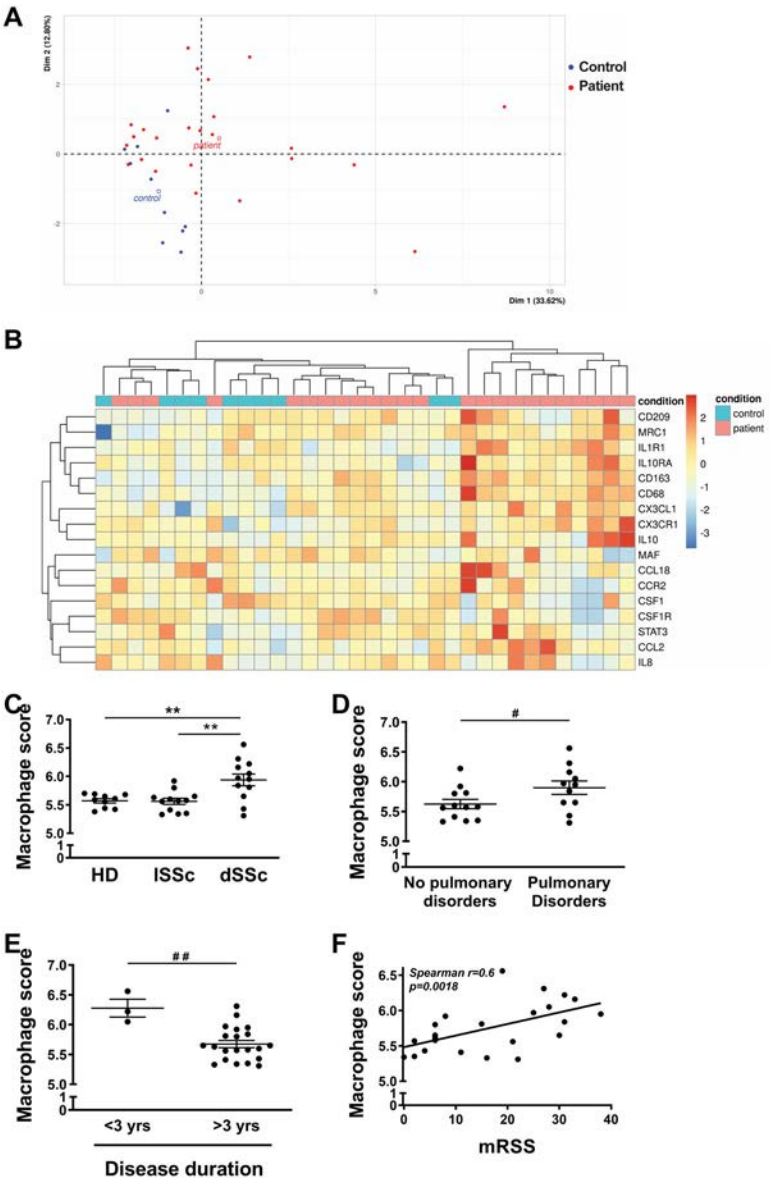

Figure 5. Enriched DC-SIGN+ alternatively activated macrophage gene signature in the skin of patients with early systemic sclerosis (SSc), and correlation with severity of fibrosis. **A** and **B**, Results of principal components analysis (**A**) and a heatmap of macrophage marker gene expression (**B**) in the skin of 24 patients with SSc and 10 healthy donors (HDs) are shown. **C–E**, A macrophage score based on the mean $\log_2$ fold change in gene expression was assessed in the skin of healthy donors, patients with limited SSc (lSSc), and patients with diffuse SSc (dSSc) (**C**), the skin of patients with or without pulmonary disorders (**D**), and the skin of patients with SSc with a disease duration of <3 years or >3 years (**E**). Symbols represent individual subjects; bars show the mean ± SEM. **F**, Correlation between the macrophage score in the skin of patients with SSc and the extent of fibrosis (measured using the modified Rodnan skin thickness score [MRSS]) was assessed. # = $P < 0.05$; ** or ## = $P < 0.01$, by analysis of variance or *t*-test.

Taken together, these results show that IL-1β–activated MVECs from patients with SSc promote the up-regulated expression of DC-SIGN+ alternatively activated macrophages. This process, in turn, prompts fibroblasts to adopt a proinflammatory phenotype.

A transcriptomic skin signature involving DC-SIGN+ alternatively activated macrophages as a marker of early disease and high fibrosis severity score. We next evaluated whether a specific macrophage transcriptomic signature could be used to classify the severity and systemic involvement of SSc. We quantified mRNA expression in skin biopsy samples from 10 healthy donors and 24 patients with SSc using NanoString technology. *CD68* mRNA expression was significantly up-regulated in patients with SSc compared to healthy donors ($\log_2$ fold change 0.75; adjusted $P = 0.03$). The fold change in *CD68* mRNA expression significantly correlated with the extent of cutaneous fibrosis assessed by the modified

Rodnan skin thickness score (MRSS) (r = 0.5, $P = 0.008$) (27). Moreover, the fold change in *CD68* mRNA expression significantly correlated with the fold change in mRNA levels of *CD163* (r = 0.92, $P < 0.0001$) and *DC-SIGN* (r = 0.57, $P < 0.0033$), but not with the fold change in *IL10* mRNA levels (see Supplementary Figures 4A–D, available on the *Arthritis & Rheumatology* website at http://onlinelibrary.wiley.com/doi/10.1002/art.42061).

Using our in vitro data, we then defined a supervised macrophage gene signature comprising *CD68*, *CD163*, *CD209* (*DC-SIGN*), *MRC1* (*CD206*), *c-Maf*, *STAT3*, *IL10*, *CCL18*, *CCL2*, *CXCL8*, *CX_3CL1*, *CX_3CR1*, *CSF1R*, *CCR2*, *CFS1*, *IL1R1*, and *IL1RA* mRNA. Principal components analysis and unsupervised clustering of enriched macrophage marker genes enabled differentiation between the SSc patients and healthy donors. Interestingly, the macrophage gene signature of some SSc patients clustered with that of healthy donors, but others did not (Figures 5A and B).

To evaluate whether the signature was associated with clinical features of SSc, we calculated a macrophage score based on the mean $\log_2$ fold change in gene expression, as previously described (24). The macrophage score was increased in patients with diffuse cutaneous SSc compared to those with limited cutaneous SSc (Figure 5C) and in patients with pulmonary fibrosis compared to those without pulmonary fibrosis (Figure 5D). Patients with a shorter disease duration had a significantly higher score than those with a longer disease duration (Figure 5E); however, this needs to be confirmed due to the small number of patients who had a shorter disease duration. Moreover, the macrophage score was strongly correlated with the MRSS (r = 0.6, $P = 0.0018$) (Figure 5F).

Taken together, our findings suggest that the DC-SIGN+ alternatively activated macrophage gene signature we identified is associated with the clinical characteristics of SSc. Indeed, a high macrophage score was associated with severe skin and lung fibrosis and a shorter disease duration in patients with SSc.

Perivascular localization and enrichment of DC-SIGN+ and CD68+ macrophages in the skin and the extent of skin fibrosis in patients with SSc. To confirm the presence of DC-SIGN+ and CD68+ alternatively activated macrophages and gain insight into their localization, we performed immunofluorescence analysis of skin biopsy samples from 8 patients with SSc and 4 healthy donors. We first analyzed global cutaneous CD68+ macrophage infiltration and their topographic location (within the dermis and around the vessels [morphologically determined]). As shown in Figure 6A, CD68+ macrophages were detected in the skin of healthy donors and patients with SSc. However, the topographic distribution of CD68+ macrophages in the skin of SSc patients differed from that in the skin of healthy donors, and also differed between individual skin samples within the SSc group.

In 4 SSc skin samples (e.g., patients SSc1 and SSc3 [Figure 6A]), CD68+ macrophages were present in the dermis, as in healthy donors. In the 4 other skin samples from SSc patients (e.g., patients SSc5 and SSc6 [Figure 6A]), CD68+ macrophages were enriched in perivascular areas. The total number of CD68+ macrophages quantified using automated counting was significantly increased in patients with an MRSS of >10 compared to those with an MRSS of <10 and compared to healthy donors (Figure 6B). This result was consistent with NanoString data as the 4 patients with a high MRSS had greater fold increases in *CD68* mRNA expression compared to that in the 4 patients with a low MRSS, whose *CD68* mRNA levels were similar to those in healthy donors ($P = 0.029$) (see Supplementary Figure 4E, available on the *Arthritis & Rheumatology* website at http://onlinelibrary.wiley.com/doi/10.1002/art.42061). This was the result of an increased number and proportion of perivascular CD68+ macrophages in skin samples from individuals with a high MRSS (Figure 6D).

We also analyzed the expression of DC-SIGN and c-Maf in CD68+ macrophages in skin sections. Perivascular CD68+ macrophages from patients with SSc with a high MRSS (SSc patients 5–8) expressed DC-SIGN, whereas patients with SSc with a low MRSS (SSc patients 1–4) had no or barely detectable DC-SIGN+ and CD68+ macrophages, similar to findings in the healthy donors (Figure 6E and Supplementary Figure 5, available on the *Arthritis & Rheumatology* website at http://onlinelibrary.wiley.com/doi/10.1002/art.42061). The transcription factor c-Maf was not detected in CD68+ macrophages in skin sections from healthy donors and was inconsistently expressed in CD68+ macrophages from patients with SSc (Figure 6E and Supplementary Figure 5).

In patients with SSc who had a high MRSS, not only were DC-SIGN+ and CD68+ macrophages increased in the dermis, they were also significantly enriched in perivascular areas, as compared to the expression profiles in healthy donors and patients with SSc with a low fibrosis severity score (Figure 6F). Patients with barely detectable DC-SIGN+ and CD68+ macrophages (Figure 6E) clustered with healthy donors in heatmap analyses of expression of each macrophage subset (Figure 5B). In contrast, the DC-SIGN and CD68 expression profiles in macrophages from patients with a high MRSS did not cluster with those of healthy donors (Figure 5B). SSc patients with a high MRSS exhibited greater CD68+ macrophage infiltration and showed enhanced perivascular DC-SIGN+ and CD68+ macrophage expression (Figures 6C–F).

These findings indicate that DC-SIGN+ and CD68+ macrophages are enriched in the perivascular areas of the skin of patients with SSc who have a high MRSS, supporting a role for SSc endothelial cells in the generation of DC-SIGN+ alternatively activated macrophages whose expression levels correlate with the severity of skin fibrosis. Moreover, use of the macrophage gene signature could be a useful tool for differentiating SSc

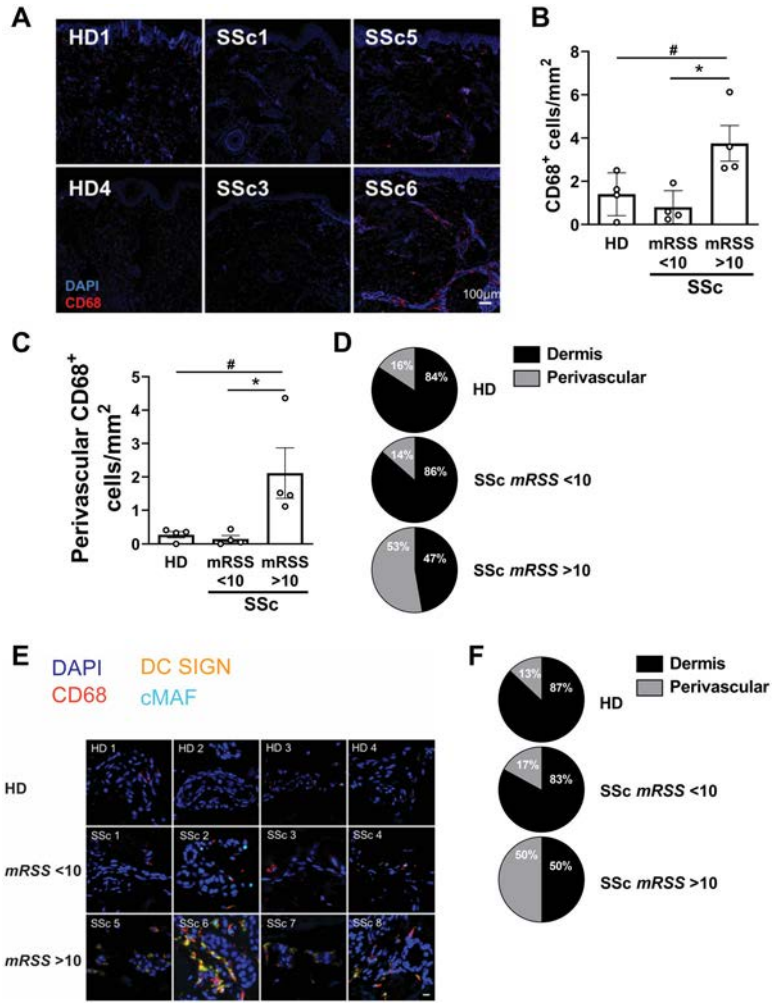

Figure 6. Enrichment of DC-SIGN+ CD68+ macrophages in perivascular areas of severely fibrotic skin from systemic sclerosis (SSc) patients. **A**, CD68+ macrophages were identified by staining of skin sections from healthy donors (left panels), SSc patients with a low modified Rodnan skin thickness score (MRSS) (score <10) (middle panels), and SSc patients with a high MRSS (score ≥10) (right panels). Representative samples are shown. **B**, Density of dermal CD68+ macrophages was assessed in skin sections from 4 healthy donors, 4 SSc patients with a low MRSS, and 4 SSc patients with a high MRSS. **C** and **D**, Automated quantification was performed to assess the number of perivascular CD68+ macrophages in skin sections from healthy donors, SSc patients with a low MRSS, and SSc patients with a high MRSS. Data are expressed as the number of cells/mm^2 (**C**) or percentage of dermis or perivascular area staining positive for CD68 (**D**). **E**, Expression of CD68, c-Maf, and DC-SIGN in skin sections from 4 healthy donors and 8 patients with SSc was assessed by immunostaining using multiplex immunofluorescence assay of the skin tissue. **F**, DC-SIGN+ CD68+ cells were assessed as the percentage of dermis or perivascular area of the skin staining positive for CD68 in healthy donors, SSc patients with a low MRSS, and SSc patients with a high MRSS. In **B** and **C**, symbols represent individual subjects; bars show the mean ± SEM. * or # = $P < 0.05$, by analysis of variance or *t*-test.

patients with skin-infiltrating, DC-SIGN+ alternatively activated macrophages from SSc patients with other phenotypes.

DISCUSSION

Our findings provide insight into the role of MVECs in the polarization of macrophages in the setting of SSc. In in vitro, in situ, and transcriptomic analyses, we showed that IL-1β prompts MVECs from SSc patients to induce differentiation of monocytes into DC-SIGN+ CCL18^{high}CCL2^{high}CXCL8^{high}IL-10^{low} alternatively activated macrophages, which are associated with the development of skin fibrosis in SSc.

Animal models have highlighted the role of the inflammasome and IL-1β in lung and skin fibrosis. IL-1 receptor type I (IL-1RI)–knockout mice showed reduced fibrosis in both cutaneous and deep tissue wounds (28), and IL-1β transient overexpression induced by an adenoviral gene promoted severe progressive tissue fibrosis in the rat lung (19). In a murine model of fibrosis induced by silica exposure, blocking production of IL-1β in *nlrp3*-null mice alleviated fibrosis (17). In bleomycin-induced lung injury, a model of idiopathic pulmonary fibrosis,

specific blockade of IL-1RI reduced inflammation and fibrosis, and exogenous IL-1β administration alone was sufficient to mimic bleomycin-induced lung pathology (18).

In human SSc, studies have shown associations between elevated levels of IL-1β and skin or lung fibrosis (29–31). These data suggest that IL-1β is an important mediator of lung and skin inflammation and fibrosis but the precise mechanisms are still unclear, notably in human settings. Proposed mechanisms related to the role of IL-1β in fibrosis include induction of myofibroblast differentiation and collagen production following IL-1β augmentation of microRNA-55 expression (29), as well as endothelial-to-mesenchymal cell transition in the presence of IL-1β together with IL-6 and TGFβ2 (32).

Finally, the use of IL-1β blockers for the treatment of fibrosis in mouse models of SSc (19,33) and human patients with SSc (34) is rare and has yielded conflicting results, thus suggesting that the effect of IL-1β inhibition is time- and context-dependent. Consistent with these findings, recent transcriptomic analysis of biopsy specimens from the Prospective Registry for Early Systemic Sclerosis cohort of patients with early diffuse SSc showed that IL-1β was one of the 3 most highly expressed cytokines, suggesting a role in the early phases of SSc (13).

M-CSF alone or in combination with IL-4, CSF-1, and IL-1β induced DC-SIGN in human and mouse macrophages (35–37); in contrast, GM-CSF suppresses DC-SIGN expression (36). In this study, up-regulation of DC-SIGN was independent of IL-4 and M-CSF, because IL-4 was not detected in MVEC-CM or differentiated macrophages and was induced in the absence of M-CSF but in the presence of GM-CSF. Rather, MVEC-derived IL-6 and endothelin-1 contributed to up-regulation of DC-SIGN in macrophages, even in the presence of GM-CSF. Importantly, and contrary to the findings in a prior study, IL-1β had no direct effect on DC-SIGN induction (37).

Enhanced proinflammatory and profibrotic CCL2, IL-6, CXL10, and CXCL8 levels have been described in the setting of SSc, but the precise mechanisms contributing to their production are still unclear (38–40). In the present study, we showed that DC-SIGN+ alternatively activated macrophages induced by MVECs from patients with SSc not only produced increased levels of CCL2 and CXCL8, but also facilitated the production of CCL2, IL-6, and CXCL10 by fibroblasts, thus highlighting a new dynamic interplay contributing to sustained inflammation in SSc.

The role of increased matrix metalloproteinase 1 (MMP-1) expression is paradoxical. In a mouse model of SSc and bleomycin-induced fibrosis, treatment with an MMP inhibitor prevented experimental fibrosis by increasing MMP-2 and MMP-9 activity (41). Interestingly, MMP-1 expression is increased in fibroblasts from patients with early SSc and decreased in fibroblasts from patients with late SSc (42), suggesting that increased MMP-1 activity contributes to fibrosis in early SSc.

In a mouse model of allograft kidney rejection, DC-SIGN+ Ly6C^{low} macrophages induced expansion of FoxP3-expressing regulatory T cells and suppressed proliferation of CD8+ T cells, in part by releasing IL-10 in a manner dependent on DC-SIGN and TLR-4 triggering (35). Jeljeli et al recently reported that repeated injection of a low dose of LPS reduced disease severity associated with the induction of inducible costimulator ligand, DC-SIGN, and IL-10 production by dermal macrophages (43). In contrast, we showed that perivascular DC-SIGN+ and CD68+ macrophages are associated with fibrosis in patients with SSc. Interestingly, we provide in vitro evidence of a lack of IL-10 production by DC-SIGN+ alternatively activated macrophages induced by MVECs from SSc patients despite c-Maf induction, which may contribute to enhanced inflammation and fibrosis in tissue.

Hsa-miR-106a and tristetraprolin RNA-binding molecule have been involved in the posttranscriptional degradation of IL-10 mRNA in human myeloid cells and mouse macrophages, respectively (44,45). The reason that DC-SIGN+ alternatively activated macrophages induced by MVECs from SSc patients failed to produce IL-10 remains to be determined, and it is not yet known whether it could be attributed to posttranscriptional alterations. Although the NanoString analysis showed that some patients with SSc exhibited high levels of *IL10* mRNA in the skin, there was no correlation between *CD68* and *IL10* mRNA levels in the skin, suggesting that IL-10 was not being produced by skin macrophages, in contrast to DC-SIGN expression.

Following inflammation and tissue damage, large amounts of carbohydrates are released, including those containing mannose or fucose residues or LewisX, which are potent DC-SIGN agonists (46). Hence, liberation of carbohydrates by dying MVECs or neutrophils in the vicinity of DC-SIGN+ macrophages modulates their immune function during the development of SSc. Whether triggering DC-SIGN in macrophages affects their immune functions and restores their IL-10 secretion is unknown.

Finally, we developed a new DC-SIGN+ alternatively activated macrophage gene signature based on in vitro data to distinguish patients according to their skin fibrosis score. Of note, the signature only shares CD163, CX_3CR1, and IL-10Ra with the M2 macrophage subnetwork defined by Mahoney et al (7). Patients with high scores had more severe fibrosis, a shorter disease duration, and pulmonary complications.

In conclusion, our work sheds new light on the vicious circle implicating sustained IL-1β secretion, activation of MVECs, and the generation of DC-SIGN+ alternatively activated macrophages, which trigger proinflammatory fibroblasts, in the development of fibrotic processes in scleroderma. Targeting this pathophysiologic loop may create new perspectives on potential therapeutic interventions in SSc. These findings may also be relevant to other autoimmune and inflammatory fibrotic diseases.

Our findings provide insight into the role of MVECs in the development of fibrosis through the induction of M2 macrophages, a process that leads to the production of peculiar cytokines and the induction of proinflammatory fibroblasts. However,

our study had several limitations, including that the limited number of different endothelial cells from SSc patients for macrophage induction and testing did not allow for the definition of potential subgroups. We did not assess the functional consequences of altered cytokine/chemokine production by DC-SIGN+ alternatively activated macrophages induced by IL-1β–activated MVECs from SSc patients, and further studies are warranted to determine how this production of altered cytokines/chemokines mechanistically relates to SSc, particularly within skin tissue. Moreover, a more detailed phenotypic and functional characterization of perivascular cutaneous DC-SIGN+ macrophages by immunofluorescence and/or single-cell RNA-Seq analysis is needed to better understand their contribution to the fibrotic process.

ACKNOWLEDGMENTS

We are grateful to the Groupe de Recherche en Immunologie Clinique at Bordeaux University Hospital for assistance with the nanostring analysis. We thank Sébastien Marais from the Bordeaux Imagine Center for help with image analysis and Macha Nikolski's group for bioinformatics analysis.

AUTHOR CONTRIBUTIONS

All authors were involved in drafting the article or revising it critically for important intellectual content, and all authors approved the final version to be published. Drs. Contin-Bordes and Truchetet jointly supervised the study, and both had full access to all of the data and take responsibility for the integrity of the data and the accuracy of the data analysis.

Study conception and design. Chizzolini, Contin-Bordes.

Acquisition of data. Laurent, Lapoirie, Leleu, Levionnois, Grenier, Jurado-Mestre, Lazaro, Duffau, Richez, Seneschal, Pellegrin, Constans, Schaeverbeke, Douchet.

Analysis and interpretation of data. Laurent, Lapoirie, Levionnois, Duluc, Pradeu, Blanco, Truchetet, Contin-Bordes.

REFERENCES

1. Denton CP, Khanna D. Systemic sclerosis. Lancet 2017;390: 1685–99.
2. Asano Y. Systemic sclerosis. J Dermatol 2018;45:128–38.
3. Cutolo M, Soldano S, Smith V. Pathophysiology of systemic sclerosis: current understanding and new insights. Expert Rev Clin Immunol 2019;15:753–64.
4. Murray PJ, Allen JE, Biswas SK, Fisher EA, Gilroy DW, Goerdt S, et al. Macrophage activation and polarization: nomenclature and experimental guidelines. Immunity 2014;41:14–20.
5. Manetti M. Deciphering the alternatively activated (M2) phenotype of macrophages in scleroderma. Exp Dermatol 2015;24:576–8.
6. Nakayama W, Jinnin M, Makino K, Kajihara I, Makino T, Fukushima S, et al. Serum levels of soluble CD163 in patients with systemic sclerosis. Rheumatol Int 2012;32:403–7.
7. Mahoney JM, Taroni J, Martyanov V, Wood TA, Greene CS, Pioli PA, et al. Systems level analysis of systemic sclerosis shows a network of immune and profibrotic pathways connected with genetic polymorphisms. PLoS Comput Biol 2015;11:e1004005.
8. Taroni JN, Greene CS, Martyanov V, Wood TA, Christmann RB, Farber HW, et al. A novel multi-network approach reveals tissue-specific cellular modulators of fibrosis in systemic sclerosis. Genome Med 2017;9:27.
9. Huang J, Maier C, Zhang Y, Soare A, Dees C, Beyer C, et al. Nintedanib inhibits macrophage activation and ameliorates vascular and fibrotic manifestations in the Fra2 mouse model of systemic sclerosis. Ann Rheum Dis 2017;76:1941–8.
10. Maier C, Ramming A, Bergmann C, Weinkam R, Kittan N, Schett G, et al. Inhibition of phosphodiesterase 4 (PDE4) reduces dermal fibrosis by interfering with the release of interleukin-6 from M2 macrophages. Ann Rheum Dis 2017;76:1133–41.
11. Khanna D, Denton CP, Jahreis A, van Laar JM, Frech TM, Anderson ME, et al. Safety and efficacy of subcutaneous tocilizumab in adults with systemic sclerosis (faSScinate): a phase 2, randomised, controlled trial. Lancet 2016;387:2630–40.
12. Trombetta AC, Soldano S, Contini P, Tomatis V, Ruaro B, Paolino S, et al. A circulating cell population showing both M1 and M2 monocyte/macrophage surface markers characterizes systemic sclerosis patients with lung involvement. Respir Res 2018;19:186.
13. Skaug B, Khanna D, Swindell WR, Hinchcliff ME, Frech TM, Steen VD, et al. Global skin gene expression analysis of early diffuse cutaneous systemic sclerosis shows a prominent innate and adaptive inflammatory profile. Ann Rheum Dis 2020;79:379–86.
14. Locati M, Curtale G, Mantovani A. Diversity, mechanisms, and significance of macrophage plasticity. Annu Rev Pathol 2020;15:123–47.
15. De Luca G, Cavalli G, Campochiaro C, Bruni C, Tomelleri A, Dagna L, et al. Interleukin-1 and systemic sclerosis: getting to the heart of cardiac involvement. Front Immunol 2021;12:653950.
16. Xu D, Mu R, Wei X. The roles of IL-1 family cytokines in the pathogenesis of systemic sclerosis. Front Immunol 2019;10:2025.
17. Cassel SL, Eisenbarth SC, Iyer SS, Sadler JJ, Colegio OR, Tephly LA, et al. The Nalp3 inflammasome is essential for the development of silicosis. Proc Natl Acad Sci U S A 2008;105:9035–40.
18. Gasse P, Mary C, Guenon I, Noulin N, Charron S, Schnyder-Candrian S, et al. IL-1R1/MyD88 signaling and the inflammasome are essential in pulmonary inflammation and fibrosis in mice. J Clin Invest 2007; 117:3786–99.
19. Kolb M, Margetts PJ, Anthony DC, Pitossi F, Gauldie J. Transient expression of IL-1β induces acute lung injury and chronic repair leading to pulmonary fibrosis. J Clin Invest 2001;107:1529–36.
20. Truchetet ME, Demoures B, Guimaraes JE, Bertrand A, Laurent P, Jolivel V, et al. Platelets induce thymic stromal lymphopoietin production by endothelial cells: contribution to fibrosis in human systemic sclerosis. Arthritis Rheumatol 2016;68:2784–94.
21. Van den Hoogen F, Khanna D, Fransen J, Johnson SR, Baron M, Tyndall A, et al. 2013 classification criteria for systemic sclerosis: an American College of Rheumatology/European League Against Rheumatism collaborative initiative. Arthritis Rheum 2013;65:2737–47.
22. University Hospital Bordeaux, sponsor. Vasculopathy, inflammation, and systemic sclerosis (VISS). ClinicalTrials.gov identifier: NCT02562079; 2015.
23. Henrot P, Laurent P, Levionnois E, Leleu D, Pain C, Truchetet ME, et al. A method for isolating and culturing skin cells: application to endothelial cells, fibroblasts, keratinocytes, and melanocytes from punch biopsies in systemic sclerosis skin. Front Immunol 2020;11: 566607.
24. Danaher P, Warren S, Dennis L, D'Amico L, White A, Disis ML, et al. Gene expression markers of tumor infiltrating leukocytes. J Immunother Cancer 2017;5:18.
25. Liu M, Tong Z, Ding C, Luo F, Wu S, Wu C, et al. Transcription factor c-Maf is a checkpoint that programs macrophages in lung cancer. J Clin Invest 2020;130:2081–96.
26. Soldano S, Pizzorni C, Paolino S, Trombetta AC, Montagna P, Brizzolara R, et al. Alternatively activated (M2) macrophage phenotype

is inducible by endothelin-1 in cultured human macrophages. PLoS One 2016;11:e0166433.

27. Clements PJ, Lachenbruch PA, Ng SC, Simmons M, Sterz M, Furst DE. Skin score: a semiquantitative measure of cutaneous involvement that improves prediction of prognosis in systemic sclerosis. Arthritis Rheum 1990;33:1256–63.
28. Thomay AA, Daley JM, Sabo E, Worth PJ, Shelton LJ, Harty MW, et al. Disruption of interleukin-1 signaling improves the quality of wound healing. Am J Pathol 2009;174:2129–36.
29. Artlett CM, Sassi-Gaha S, Hope JL, Feghali-Bostwick CA, Katsikis PD. Mir-155 is overexpressed in systemic sclerosis fibroblasts and is required for NLRP3 inflammasome-mediated collagen synthesis during fibrosis. Arthritis Res Ther 2017;19:144.
30. Artlett CM, Sassi-Gaha S, Rieger JL, Boesteanu AC, Feghali-Bostwick CA, Katsikis PD. The inflammasome activating caspase 1 mediates fibrosis and myofibroblast differentiation in systemic sclerosis. Arthritis Rheum 2011;63:3563–74.
31. Martinez-Godinez MA, Cruz-Dominguez MP, Jara LJ, Dominguez-Lopez A, Jarillo-Luna RA, Vera-Lastra O, et al. Expression of NLRP3 inflammasome, cytokines and vascular mediators in the skin of systemic sclerosis patients. Isr Med Assoc J 2015;17:5–10.
32. Maleszewska M, Moonen JR, Huijkman N, van de Sluis B, Krenning G, Harmsen MC. IL-1β and TGFβ2 synergistically induce endothelial to mesenchymal transition in an NFκB-dependent manner. Immunobiology 2013;218:443–54.
33. Birnhuber A, Crnkovic S, Biasin V, Marsh LM, Odler B, Sahu-Osen A, et al. IL-1 receptor blockade skews inflammation towards Th2 in a mouse model of systemic sclerosis. Eur Respir J 2019;54.
34. Mantero JC, Kishore N, Ziemek J, Stifano G, Zammitti C, Khanna D, et al. Randomised, double-blind, placebo-controlled trial of IL1-trap, rilonacept, in systemic sclerosis: a phase I/II biomarker trial. Clin Exp Rheumatol 2018;36 Suppl 113:146–9.
35. Conde P, Rodriguez M, van der Touw W, Jimenez A, Burns M, Miller J, et al. DC-SIGN+ macrophages control the induction of transplantation tolerance. Immunity 2015;42:1143–58.
36. Dominguez-Soto A, Sierra-Filardi E, Puig-Kroger A, Perez-Maceda B, Gomez-Aguado F, Corcuera MT, et al. Dendritic cell-specific ICAM-3-grabbing nonintegrin expression on M2-polarized and tumor-associated macrophages is macrophage-CSF dependent and enhanced by tumor-derived IL-6 and IL-10. J Immunol 2011;186:2192–200.
37. Schenk M, Fabri M, Krutzik SR, Lee DJ, Vu DM, Sieling PA, et al. Interleukin-1β triggers the differentiation of macrophages with enhanced capacity to present mycobacterial antigen to T cells. Immunology 2014;141:174–80.
38. Carvalheiro T, Horta S, van Roon JA, Santiago M, Salvador MJ, Trindade H, et al. Increased frequencies of circulating CXCL10-, CXCL8- and CCL4-producing monocytes and Siglec-3-expressing myeloid dendritic cells in systemic sclerosis patients. Inflamm Res 2018;67:169–77.
39. Codullo V, Baldwin HM, Singh MD, Fraser AR, Wilson C, Gilmour A, et al. An investigation of the inflammatory cytokine and chemokine network in systemic sclerosis. Ann Rheum Dis 2011;70:1115–21.
40. Schmidt K, Martinez-Gamboa L, Meier S, Witt C, Meisel C, Hanitsch LG, et al. Bronchoalveoloar lavage fluid cytokines and chemokines as markers and predictors for the outcome of interstitial lung disease in systemic sclerosis patients. Arthritis Res Ther 2009;11:R111.
41. Corbel M, Lanchou J, Germain N, Malledant Y, Boichot E, Lagente V. Modulation of airway remodeling-associated mediators by the antifibrotic compound, pirfenidone, and the matrix metalloproteinase inhibitor, batimastat, during acute lung injury in mice. Eur J Pharmacol 2001;426:113–21.
42. Kuroda K, Shinkai H. Gene expression of types I and III collagen, decorin, matrix metalloproteinases and tissue inhibitors of metalloproteinases in skin fibroblasts from patients with systemic sclerosis. Arch Dermatol Res 1997;289:567–72.
43. Jeljeli M, Riccio LG, Doridot L, Chene C, Nicco C, Chouzenoux S, et al. Trained immunity modulates inflammation-induced fibrosis. Nat Commun 2019;10:5670.
44. Sharma A, Kumar M, Aich J, Hariharan M, Brahmachari SK, Agrawal A, et al. Posttranscriptional regulation of interleukin-10 expression by hsa-miR-106a. Proc Natl Acad Sci U S A 2009;106:5761–6.
45. Stoecklin G, Tenenbaum SA, Mayo T, Chittur SV, George AD, Baroni TE, et al. Genome-wide analysis identifies interleukin-10 mRNA as target of tristetraprolin. J Biol Chem 2008;283:11689–99.
46. Van Liempt E, Bank CM, Mehta P, Garcia-Vallejo JJ, Kawar ZS, Geyer R, et al. Specificity of DC-SIGN for mannose- and fucose-containing glycans. FEBS Lett 2006;580:6123–31.

Arthritis & Rheumatology
Vol. 74, No. 6, June 2022, pp 1027–1038
DOI 10.1002/art.42063

American College of Rheumatology
Empowering Rheumatology Professionals

Involvement of Multiple Variants of Soluble CD146 in Systemic Sclerosis: Identification of a Novel Profibrotic Factor

Marie Nollet,[1] Richard Bachelier,[1] Ahmad Joshkon,[1] Waël Traboulsi,[1] Amandine Mahieux,[1] Anais Moyon,[2] Alexandre Muller,[1] Indumathi Somasundaram,[3] Stéphanie Simoncini,[1] Franck Peiretti,[1] Aurélie S. Leroyer,[1] Benjamin Guillet,[2] Brigitte Granel,[4] Françoise Dignat-George,[1] Nathalie Bardin,[1] Alexandrine Foucault-Bertaud,[1] and Marcel Blot-Chabaud[1]

Objective. Systemic sclerosis (SSc) is an autoimmune disorder characterized by excessive fibrosis, immune dysfunction, and vascular damage, in which the expression of many growth factors is deregulated. CD146 was recently described as a major actor in SSc. Since CD146 also exists as a circulating soluble form (sCD146) that acts as a growth factor in numerous angiogenic- and inflammation-related pathologies, we sought to identify the mechanisms underlying the generation of sCD146 and to characterize the regulation and functions of the different variants identified in SSc.

Methods. We performed in vitro experiments, including RNA-Seq and antibody arrays, and in vivo experiments using animal models of bleomycin-induced SSc and hind limb ischemia.

Results. Multiple forms of sCD146, generated by both shedding and alternative splicing of the primary transcript, were discovered. The shed form of sCD146 was generated from the cleavage of both long and short membrane isoforms of CD146 through ADAM-10 and TACE metalloproteinases, respectively. In addition, 2 novel sCD146 splice variants, I5-13-sCD146 and I10-sCD146, were identified. Of interest, I5-13-sCD146 was significantly increased in the sera of SSc patients ($P < 0.001$; n = 117), in particular in patients with pulmonary fibrosis ($P < 0.01$; n = 112), whereas I10-sCD146 was decreased ($P < 0.05$; n = 117). Further experiments revealed that shed sCD146 and I10-sCD146 displayed proangiogenic activity through the focal adhesion kinase and protein kinase Cε signaling pathways, respectively, whereas I5-13-sCD146 displayed profibrotic effects through the Wnt-1/β-catenin/WISP-1 pathway.

Conclusion. Variants of sCD146, and in particular the novel I5-13-sCD146 splice variant, could constitute novel biomarkers and/or molecular targets for the diagnosis and treatment of SSc and other angiogenesis- or fibrosis-related disorders.

INTRODUCTION

CD146 is a transmembrane glycoprotein that is primarily expressed on the vascular system. It has numerous functions related to vascular permeability, inflammation, and angiogenesis (1,2). Recently, it has been shown to be a coreceptor for vascular endothelial growth factor receptor 2 (VEGFR-2) (3). Two membrane-bound CD146 isoforms have been described. In endothelial cells, the long isoform is a component of the endothelial junction primarily involved in the control of cell–cell cohesion, vascular permeability, and tissue architecture (4). In contrast, the short isoform is expressed at the apical membrane and displays angiogenic functions (4). In addition to these 2 membrane isoforms, a soluble form (sCD146) that is modulated in different pathologies (4–7) has been described by our team (5). Soluble CD146 can be generated by shedding of CD146 membrane isoforms and has

Supported by INSERM, Aix-Marseille University, Agence Nationale de la Recherche, and MSD Avenir.

[1]Marie Nollet, PhD, Richard Bachelier, PhD, Ahmad Joshkon, PhD, Waël Traboulsi, PhD, Amandine Mahieux, MRes, Alexandre Muller, PhD, Stéphanie Simoncini, PhD, Franck Peiretti, PhD, Aurélie S. Leroyer, PhD, Françoise Dignat-George, PhD, PharmD, Nathalie Bardin, PhD, PharmD, Alexandrine Foucault-Bertaud, PhD, Marcel Blot-Chabaud, PhD: Aix-Marseille University, INSERM 1263, INRAE 1260, C2VN, Marseille, France; [2]Anais Moyon, PhD, Benjamin Guillet, PhD, PharmD: Aix-Marseille University, INSERM 1263, INRAE 1260, C2VN, and CERIMED, Aix-Marseille University, Marseille, France; [3]Indumathi Somasundaram, PhD: D. Y. Patil University, Kolhapur, India; [4]Brigitte Granel, PhD, MD: Aix-Marseille University, INSERM 1263, INRAE 1260, C2VN, and AP-HM, Marseille, France.

Drs. Foucault-Bertaud and Blot-Chabaud contributed equally to this work.

Author disclosures are available at https://onlinelibrary.wiley.com/action/downloadSupplement?doi=10.1002%2Fart.42063&file=art42063-sup-0001-Disclosureform.pdf.

Address correspondence to Marcel Blot-Chabaud, PhD, C2VN, 27 Boulevard J. Moulin, 13005 Marseille, France. E-mail: marcel.blot-chabaud@laposte.net.

Submitted for publication September 9, 2020; accepted in revised form January 4, 2022.

recently been shown to be involved in angiogenesis (8,9). At present, the mechanism of generation of sCD146 is unknown. It has been shown to depend on a GM6001-sensitive (10) and Ca^{2+}-dependent (11) mechanism. Of interest, for the avian homolog of CD146, gicerin, a soluble form generated by alternative splicing with retention of intron 11 has been described (12).

Deciphering the different molecules involved in angiogenesis and inflammation remains an important challenge and may provide new approaches for the treatment of many diseases. Along these lines, systemic sclerosis (SSc) is an autoimmune disease characterized by a defect in angiogenesis, excessive fibrosis, and immune dysfunction (11), for which efficient treatments are still lacking. In a recent study (13), we showed that sCD146 could constitute a novel biomarker for the assessment of disease activity and that sCD146 injections reduced disease severity in an animal model of SSc. Like VEGF, sCD146 is involved in angiogenesis (8,9) and could thus exist as different variants with different receptors and signaling pathways. However, to date little is known about this circulating molecule, its mechanisms of shedding, and the potential existence of splice variants and their involvement in SSc.

MATERIALS AND METHODS

Cells. Endothelial colony-forming cells (ECFCs), human umbilical vein endothelial cells (HUVECs), and HMEC-1 cells were cultured in endothelial growth medium 2 as previously described (13,14).

Mouse embryonic fibroblasts (MEFs) were isolated from 13-day-old CD146-knockout (CD146-KO) or wild-type mice and cultured as previously described (15). Human dermal microvascular endothelial cells (HDMECs) and human dermal fibroblasts (HDFs) were obtained from PromoCell. HDFs from SSc patients were obtained from B. Granel.

Endothelial cell tube formation in spheroids. Spheroid formation experiments were performed as previously described (16).

Coimmunoprecipitation experiments. Coimmunoprecipitation experiments were performed as previously described (17).

Chorioallantoic membrane assay. The chorioallantoic membrane of the chick embryo assay was performed according to the protocol described by Beckers et al (18) and briefly described in the Supplementary Methods, available on the *Arthritis & Rheumatology* website at http://onlinelibrary.wiley.com/doi/10.1002/art.42063.

Lipid raft preparation. Lipid rafts were isolated by sucrose density-gradient centrifugation of cells treated with nonionic detergents as previously described (19). Additional details on lipid raft preparation, as well as on other methods, are provided in the Supplementary Methods and Supplementary Tables 1 and 2, available on the *Arthritis & Rheumatology* website at http://onlinelibrary.wiley.com/doi/10.1002/art.42063.

RESULTS

Generation of different variants of sCD146 by CD146 membrane isoform shedding and alternative splicing in endothelial cells. Secretion of sCD146 was increased in endothelial cells in response to different stimuli, including tumor necrosis factor (TNF), VEGF, netrin, transforming growth factor β (TGFβ), and Wnt-5a (Figure 1A). Since TNF produced the highest effect, we analyzed sCD146 secretion under control conditions and after treatment with this cytokine. Experiments were performed in the absence or presence of the metalloprotease inhibitor GM6001 in order to estimate the relative contribution of the shed and splice forms (Figure 1B). Under both the control and TNF conditions, ~75% of total sCD146 secretion was GM6001 dependent, and 25% was GM6001 resistant.

In addition, we performed the same type of experiments in the presence of a furin convertase inhibitor (IF). We observed that, both under control conditions and after stimulation with TNF, IF inhibited sCD146 secretion. Of interest, the fraction of the secretion resistant to IF was similar under both conditions (Supplementary Figure 1A, available on the *Arthritis & Rheumatology* website at http://onlinelibrary.wiley.com/doi/10.1002/art.42063).

Finally, we used different tissue inhibitors of metalloproteinases (TIMPs) to inhibit sCD146 secretion (Supplementary Figure 1B). TIMP-1 (1 μg/ml) reduced sCD146 secretion both in cells treated with control and in cells treated with TNF, TIMP-3 (1 μg/ml) reduced sCD146 secretion only in cells treated with TNF, and no effect of TIMP-2 (1 μg/ml) was observed.

Generation of sCD146 by the long CD146 isoform through ADAM-10–dependent shedding in endothelial cells. We analyzed the influence of long and short CD146 small interfering RNA (siRNA) on sCD146 secretion in endothelial cells under control conditions. Whereas long CD146 siRNA reduced sCD146 secretion by ~75%, short CD146 siRNA had no effect (Figure 1C). This finding indicates that, under control conditions, only the long CD146 isoform is involved in sCD146 secretion through a shedding process.

In view of the inhibitory effects of TIMP-1 on sCD146 secretion under control conditions (Supplementary Figure 1B), we tested the effect of siRNAs targeting ADAM-10, membrane type 1 matrix metalloproteinase (MT1-MMP), and MMP-2. Supplementary Figures 2A and B, available on the *Arthritis & Rheumatology* website at http://onlinelibrary.wiley.com/doi/10.1002/art.42063, show the efficiency of siRNA. Only ADAM-10 siRNA inhibited sCD146 secretion, and the effect was similar to that of GM6001 (Figure 1D).

To confirm this result, we performed coimmunoprecipitation experiments and showed that, under control conditions, long

CD146 coimmunoprecipitated with ADAM-10 whereas short CD146 did not (Figure 1E). Accordingly, immunofluorescence experiments showed that long CD146 colocalized with ADAM-10, both at the junction of endothelial cells and in the perinuclear area, in confluent ECFCs. Long CD146 and ADAM-10 also colocalized in the intracellular compartment in nonconfluent ECFCs (Supplementary Figure 3A, available on the *Arthritis & Rheumatology* website at http://onlinelibrary.wiley.com/doi/10.1002/art.42063). In contrast, short CD146 did not colocalize with ADAM-10 in confluent cells (Supplementary Figure 3B). Colocalization of long CD146 and ADAM-10 was confirmed in another type of endothelial cell, HUVECs (Supplementary Figure 3C).

Since long CD146 is involved in paracellular permeability, we tested the effect of ADAM-10 silencing and overexpression on monolayer permeability. Transfection of ECFCs with ADAM-10 siRNA or with the ADAM-10–encoding plasmid decreased and increased, respectively, the permeability of ECFCs to dextran. In contrast, treatment with TACE siRNA or transfection with TACE plasmid did not modify it. These results were confirmed using a CRISPR/Cas9 knockout approach (Supplementary Figure 4A, available on the *Arthritis & Rheumatology* website at http://onlinelibrary.wiley.com/doi/10.1002/art.42063). To confirm the involvement of ADAM-10 in the shedding of long CD146, we expressed the long CD146 isoform in Chinese hamster ovary (CHO) cells by transfecting the plasmid. A stable clone expressing a high amount of the long CD146 isoform was selected (Supplementary Figure 5A, available on the *Arthritis & Rheumatology* website at http://onlinelibrary.wiley.com/doi/10.1002/art.42063). This clone was transiently transfected with a plasmid encoding for ADAM-10, and the effect on sCD146 secretion was observed. In the presence of ADAM-10, sCD146 secretion was significantly increased (Supplementary Figure 5B). Finally, the effect of ADAM-10 transfection on permeability was investigated. The permeability of CHO–long CD146 was significantly increased

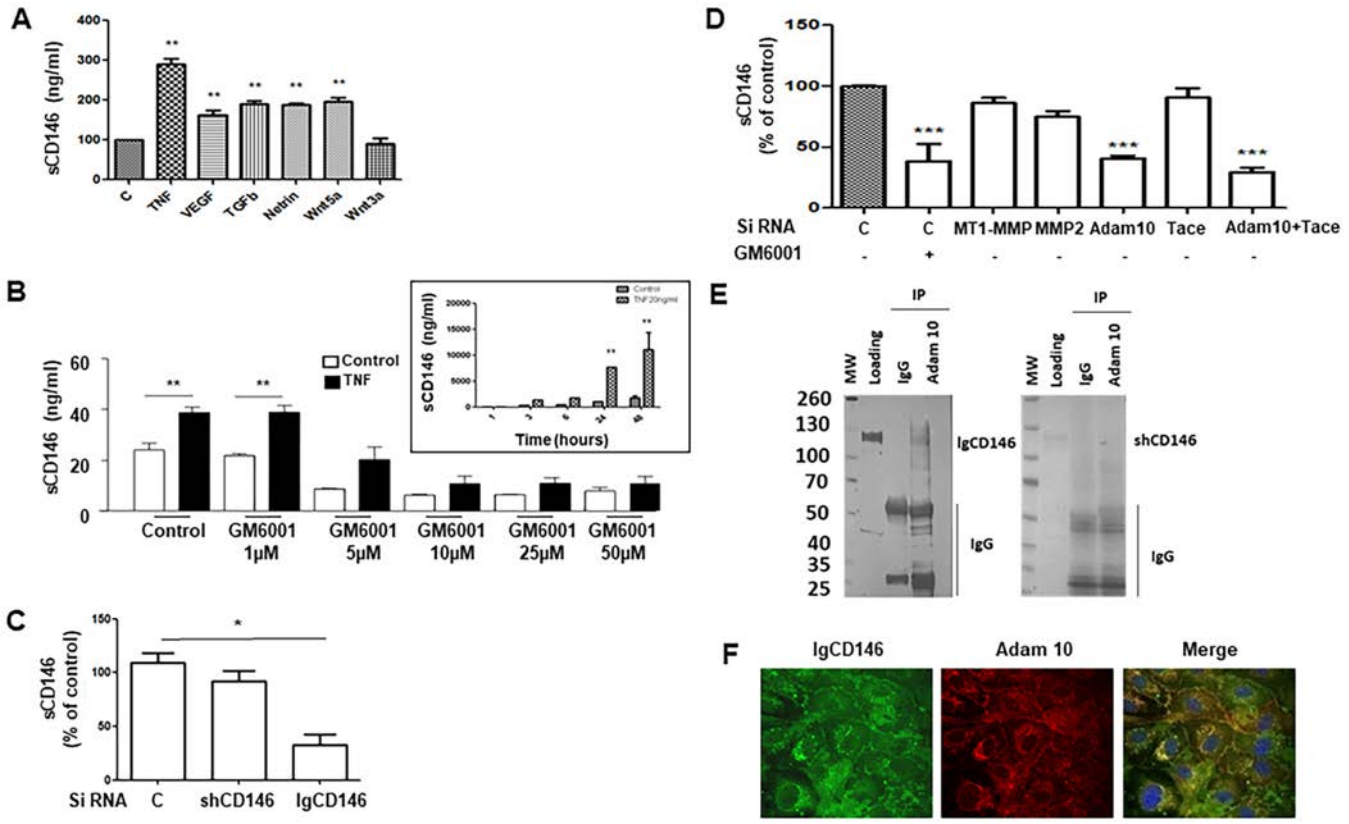

Figure 1. ADAM-10 sheds the long isoform of CD146 (lgCD146) in endothelial cells. **A**, Secretion of soluble CD146 (sCD146) in endothelial colony-forming cells (ECFCs) after 24 hours of treatment with tumor necrosis factor (TNF) or vascular endothelial growth factor (VEGF) (20 ng/ml each), transforming growth factor β (TGFβ; 5 ng/ml), or netrin, Wnt-5a, or Wnt-3a (50 ng/ml each). **B**, Effect of GM6001 on sCD146 secretion in ECFCs treated with 20 ng/ml TNF for 24 hours. **Inset** shows sCD146 secretion in control (C) and TNF-treated cells at the indicated time points. **C**, Secretion of sCD146 in ECFCs transfected with small interfering RNA (siRNA) targeting the short isoform of CD146 (shCD146) or lgCD146. **D**, Secretion of sCD146 in ECFCs transfected with siRNA targeting membrane type 1 matrix metalloproteinase (MT1-MMP), MMP-2, ADAM-10, or TACE. **E**, Western blot analysis. ADAM-10 was immunoprecipitated (IP) in ECFCs under basal conditions, and control immunoprecipitations were performed with IgG. The long and short isoforms of CD146 were then detected by Western blotting. **F**, Colocalization of the long isoform of CD146 and ADAM-10, visualized by immunofluorescence in confluent ECFCs. Original magnification × 40. In **A**–**D**, bars show the mean ± SEM from 3–7 experiments. * = $P < 0.05$; ** = $P < 0.01$; *** = $P < 0.001$ versus control, by analysis of variance in **A**, **C**, and **D**; by Mann-Whitney test in **B**.

in the presence of ADAM-10 whereas there was no effect of ADAM-10 on control CHO (Supplementary Figure 5C).

Generation of sCD146 by the short CD146 isoform through TACE-dependent shedding in endothelial cells. We analyzed the influence of long CD146 siRNA and short CD146 siRNA on sCD146 secretion after 24 hours of treatment with 20 ng/ml TNF. We confirmed that, under control conditions, only long CD146 siRNA reduced sCD146 secretion and observed that, with TNF treatment, both long CD146 siRNA and short CD146 siRNA reduced sCD146 secretion, by ~60% and 25%, respectively (Figure 2A). We then used different siRNAs to identify the proteinases involved in short CD146 shedding. In view of the effects of TIMP-1 and TIMP-3 on sCD146 secretion under TNF stimulation, we tested the effect of siRNA targeting ADAM-10, MT1-MMP, and TACE. Both ADAM-10 siRNA and TACE siRNA inhibited sCD146 secretion, with an additive effect when added simultaneously (Figure 2B). Of interest, ADAM-10 siRNA and TACE siRNA reduced sCD146 secretion by 60% and 25%, respectively, as observed with long CD146 siRNA and short CD146 siRNA. This result suggested that, since long CD146 was shed by ADAM-10, short CD146 could be shed by TACE.

To confirm this hypothesis, we performed coimmunoprecipitation experiments and showed that under TNF stimulation, short CD146 coimmunoprecipitated with TACE, whereas long CD146 coimmunoprecipitated with ADAM-10 (Figure 2C and Supplementary Figure 6A, available on the *Arthritis & Rheumatology* website at http://onlinelibrary.wiley.com/doi/10.1002/art.42063). Similarly, immunofluorescence experiments showed that short CD146 colocalized with TACE in ECFCs treated with TNF. In confluent cells, short CD146 colocalized with TACE at the membrane and in the nucleus (Figure 2D), whereas in nonconfluent cells, they essentially colocalized around the nucleus and at the membrane ruffles of migrating cells (Supplementary Figure 6B). In contrast,

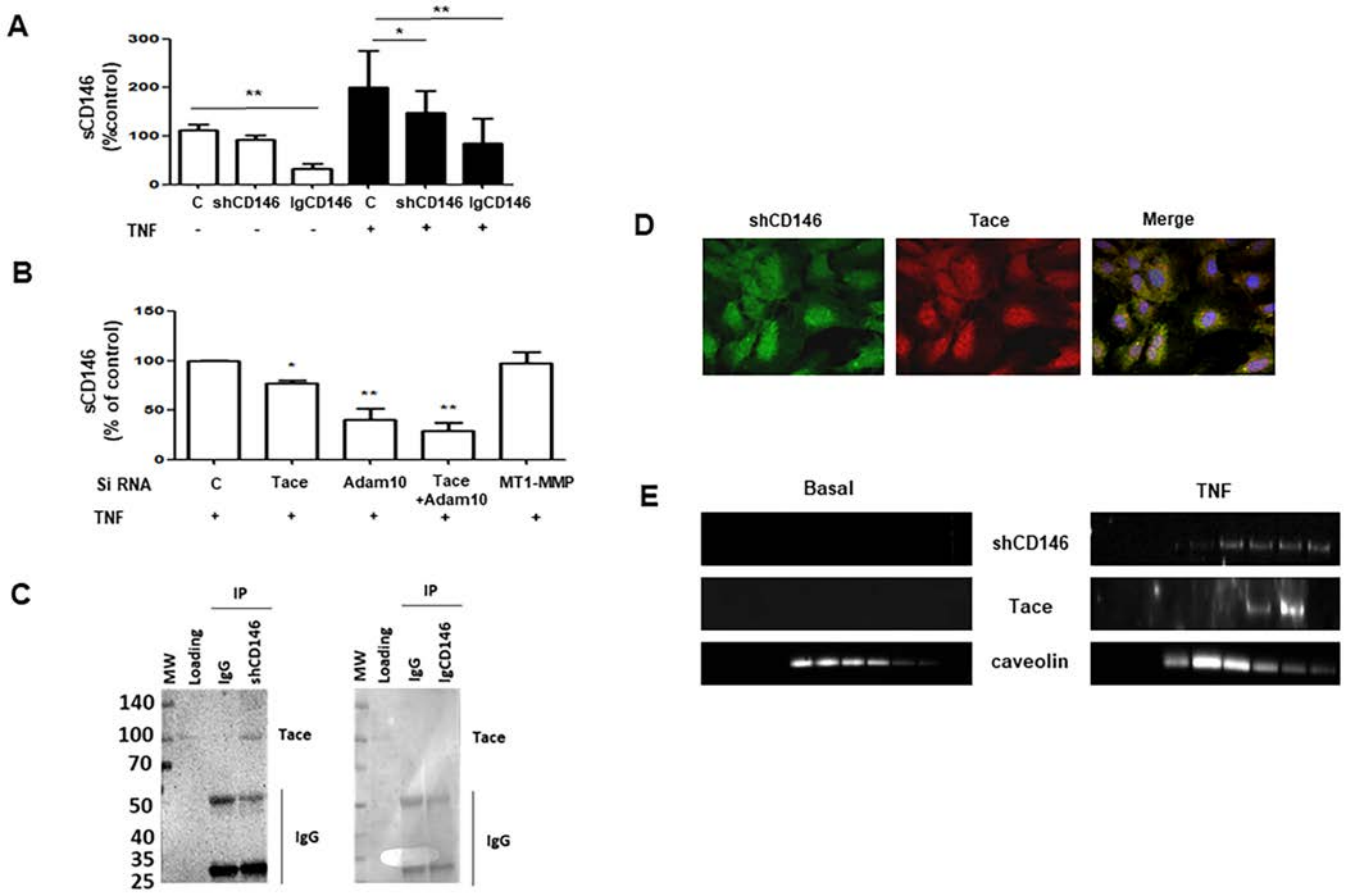

Figure 2. TACE sheds the short isoform of CD146 in endothelial cells. **A**, Secretion of sCD146 in ECFCs left untreated (basal condition) or treated with 20 ng/ml TNF for 24 hours and transfected with siRNA targeting the short or long isoforms of CD146. **B**, Secretion of sCD146 in ECFCs treated with TNF for 24 hours and transfected with siRNA targeting TACE, ADAM-10, or MT1-MMP. **C**, Immunoprecipitation of the long and short isoforms of CD146 in ECFCs after 24 hours of treatment with 20 ng/ml TNF. Control immunoprecipitation was performed with IgG. TACE was detected by Western blotting. **D**, Colocalization of the short isoform of CD146 and TACE, visualized in confluent and nonconfluent ECFCs. **E**, Lipid raft fractions prepared from ECFCs cultured under basal conditions or with 20 ng/ml TNF for 24 hours. Each line of the gel corresponds to one lipid fraction. Specific antibodies against the short isoform of CD146, TACE, and caveolin were used. In **A** and **B**, bars show the mean ± SEM from 3–5 experiments. * = $P < 0.05$; ** = $P < 0.01$ versus control, by analysis of variance. See Figure 1 for definitions.

long CD146 did not colocalize with TACE in confluent cells (Supplementary Figure 6C).

Since short CD146 and TACE are present in lipid rafts of endothelial cells (20), we analyzed lipid rafts of ECFCs under control conditions and ECFCs stimulated with TNF. In these experiments, 10 μ*M* GM6001 was added to the cells in order to prevent the shedding of the molecule (Figure 2E). Under control conditions, short CD146 was not detected in lipid rafts. In contrast, both short CD146 and TACE were present in this cellular fraction when cells were treated with TNF. Since we have

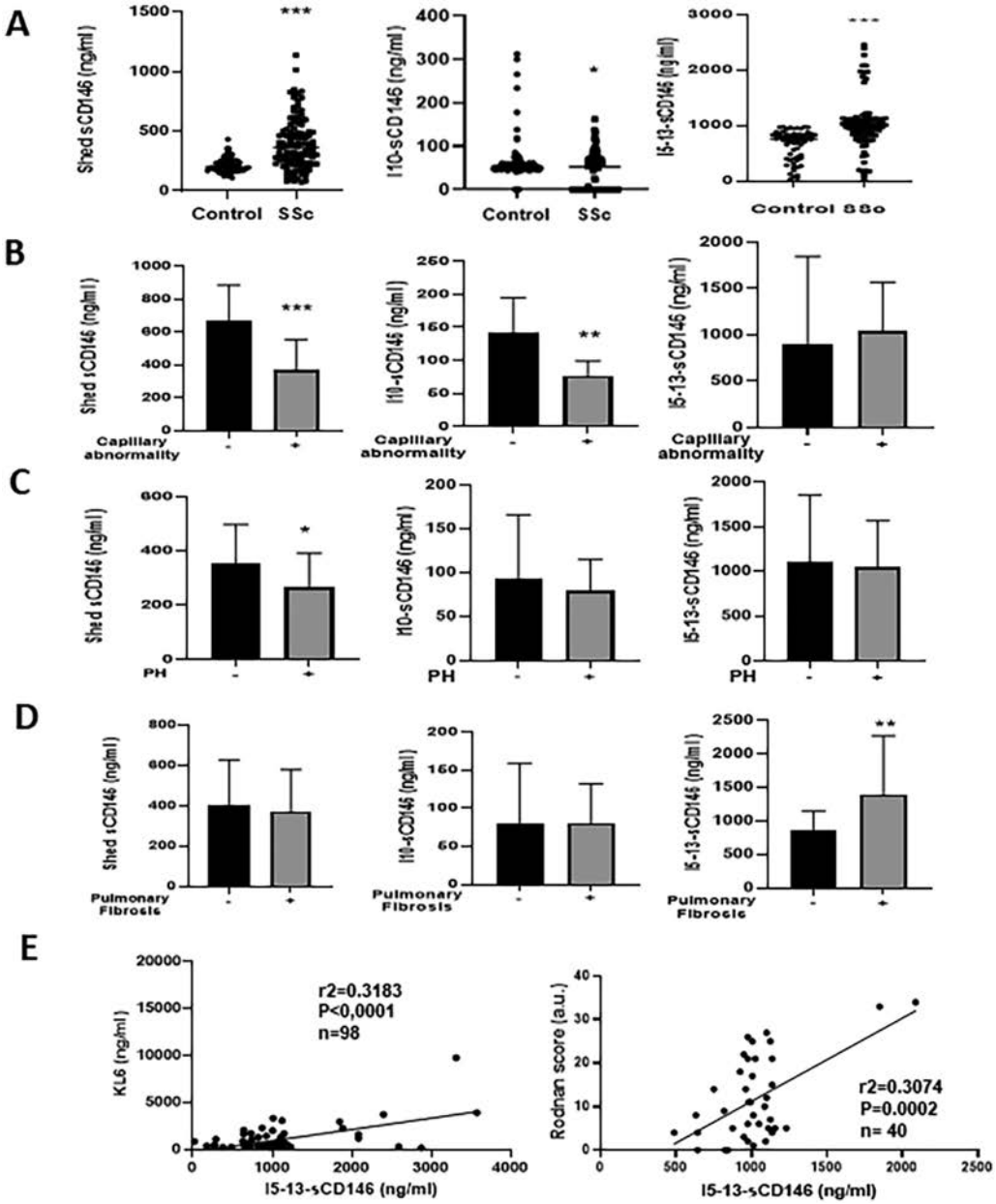

Figure 3. Evaluation of the concentrations of shed soluble CD146 (sCD146), the CD146 isoform retaining intron 10 (I10-sCD146), and the CD146 isoform retaining introns 5–13 (I5-13-sCD146) in sera from patients with systemic sclerosis (SSc). **A**, Shed sCD146, I10-sCD146, and I5-13-sCD146 concentrations in patients with SSc (n = 117) and matched controls (n = 81). Symbols represent individual subjects; horizontal lines show the mean. **B**, Shed sCD146, I10-sCD146, and I5-13-sCD146 concentrations in SSc patients with capillary abnormality (n = 46) and those without capillary abnormality (n = 34), as determined by nailfold videocapillaroscopy. Nailfold videocapillaroscopy was not performed in 37 patients. **C** and **D**, Shed sCD146, I10-sCD146, and I5-13-sCD146 concentrations in SSc patients with pulmonary hypertension (PH; n = 27) and those without pulmonary hypertension (n = 86) (**C**) and in SSc patients with pulmonary fibrosis (n = 40) and those without pulmonary fibrosis (n = 72) (**D**). Pulmonary hypertension was not determined in 4 patients; pulmonary fibrosis was not determined in 5 patients. **E**, Correlations between I5-13-sCD146 concentration and KL-6 (n = 98) and between I5-13-sCD146 concentration and modified Rodnan skin thickness score (n = 40). KL-6 was not determined in 19 patients; modified Rodnan skin thickness score was not determined in 77 patients. In **B**–**D**, bars show the mean ± SEM. * = $P < 0.05$; ** = $P < 0.01$; *** = $P < 0.001$ versus controls, by analysis of variance.

previously described a TNF-induced increase in endothelial cell migration (10) and the involvement of short CD146, but not long CD146, in this migration process (4), we tested the effect of TACE silencing on ECFC migration in the presence of TNF. Treatment of ECFCs with TNF increased cell migration, and TACE siRNA or CRISPR/Cas9 deletion increased their migration. Knockdown or knockout of TACE by siRNA or CRISPR/Cas9 approaches increased ECFC migration, unlike those targeting ADAM-10, which did not modify it (Supplementary Figure 4B).

To confirm the involvement of TACE in short CD146 shedding, we expressed the short CD146 isoform in CHO cells. A stable clone expressing a high amount of short CD146 was selected (Supplementary Figure 7A, available on the *Arthritis & Rheumatology* website at http://onlinelibrary.wiley.com/doi/10.1002/art.42063). This clone was transiently transfected with a plasmid encoding for TACE, and the effect on sCD146 secretion was observed. In the presence of TACE, sCD146 secretion was significantly increased (Supplementary Figure 7B).

Identification of 2 new variants of sCD146 generated by alternative splicing in endothelial cells. Since a fraction of sCD146 secretion was insensitive to GM6001, we performed RNA-Seq on ECFCs to identify additional isoforms of sCD146 generated by alternative splicing. One of these isoforms retained intron 10 of the molecule (I10-sCD146 isoform). Another one retained introns 5 and 13 of the molecule (I5-13-sCD146 isoform). A schematic representation of these 2 isoforms and the sequences of these newly identified isoforms are shown in Supplementary Figure 8A and Supplementary Tables 3 and 4, available on the *Arthritis & Rheumatology* website at http://onlinelibrary.wiley.com/doi/10.1002/art.42063.

Both transcripts are present in ECFCs and HUVECs (Supplementary Figure 8B) and expressed as proteins, as demonstrated by immunofluorescence (Supplementary Figure 8C) and Western blot analysis (Supplementary Figure 8D). We tested the effects of the different stimuli that did affect membrane CD146 shedding (see Figure 1A) on the expression of messenger RNA (mRNA) for the 2 splice variants. I5-13-sCD146 was up-regulated at the mRNA level by TNF and Wnt-5a, while the shed form of CD146, VEGF, TGFβ, netrin, and Wnt-3a failed to modify its mRNA expression. In contrast, I10-sCD146 was not up-regulated at the mRNA level by these different factors. The levels of mRNA for the I10-sCD146 variant were even down-regulated by VEGF, netrin, and Wnt-3a (Supplementary Figure 8E).

We also analyzed the levels of mRNA for the newly identified sCD146 variants using a tissue array (Supplementary Figure 9, available on the *Arthritis & Rheumatology* website at http://onlinelibrary.wiley.com/doi/10.1002/art.42063). Whereas many organs did not express I5-13-sCD146 or I10-sCD146, the lungs, lymph nodes, and rectum highly expressed these 2 isoforms of sCD146. Of interest, peripheral blood lymphocytes expressed high levels of I5-13-sCD146 but did not express I10-sCD146.

Differential modulation of I5-13-sCD146, I10-sCD146, and shed sCD146 in patients with SSc. We analyzed the expression of the newly identified soluble splice variants in SSc. The concentrations of shed sCD146, I5-13-sCD146, and I10-sCD146 were determined in sera from SSc patients and healthy controls (Figure 3A). Shed sCD146 and I5-13-sCD146 were significantly increased in patients with SSc, whereas I10-sCD146 was decreased. Of interest, the concentrations of shed sCD146 and I10-sCD146, but not of I5-13-sCD146, were decreased in patients with capillary abnormality as detected by nailfold videocapillaroscopy (Figure 3B), and concentrations of shed sCD146 were decreased in patients with pulmonary hypertension (Figures 3C). In addition, we observed that I5-13-sCD146 concentrations were significantly increased in sera from patients with pulmonary fibrosis, as compared to patients without pulmonary disease (Figure 3D), whereas shed sCD146 and I10-sCD146 were not modified. Finally, I5-13-sCD146 was positively correlated with the fibrosis marker KL-6 and with the modified Rodnan skin thickness score (21) (Figure 3E), whereas shed sCD146 and I10-sCD146 were not (data not shown).

Differential profibrotic effects of I5-13-sCD146 and I10-sCD146/shed sCD146 in a CD146-KO mouse model of SSc induced by bleomycin. We used an animal model of SSc induced by bleomycin (13) to further analyze the effects of the different forms of sCD146. Because CD146-KO mice have a higher sensitivity to bleomycin than wild-type mice do, and to prevent interactions with soluble forms of CD146 produced by the animals, CD146-KO mice treated with bleomycin were subcutaneously injected with shed sCD146, I5-13-sCD146, or I10-sCD146. Bleomycin treatment led to an increase in dermal thickness. Treatment of bleomycin-injected animals with sCD146 or I10-sCD146, but not with I5-13-sCD146, significantly reduced this dermal thickness to an extent comparable to that in control animals (Figure 4A). To confirm these results, we performed sirius red staining to analyze the expression of collagen under the different experimental conditions. Bleomycin increased collagen content in the dermis of mice (Figure 4B). Of interest, whereas bleomycin and I5-13-sCD146 led to a decrease in the content of thick/organized collagen fibers (red) and an increase in the content of thin/lowly organized collagen fibers (orange, yellow, and green, indicating progressively less organized fibers), I10-sCD146 and shed sCD146 maintained collagen fiber content very similar to that observed under the control condition.

We also performed immunoperoxidase-based immunohistochemistry experiments to analyze the number of fibroblastic cells expressing α-smooth muscle actin (α-SMA) under the different experimental conditions. We observed that the number of fibroblastic cells expressing α-SMA was increased in animals treated with bleomycin, as compared to control animals (Figure 4C). Shed sCD146 and I10-sCD146 reduced the number of fibroblastic cells

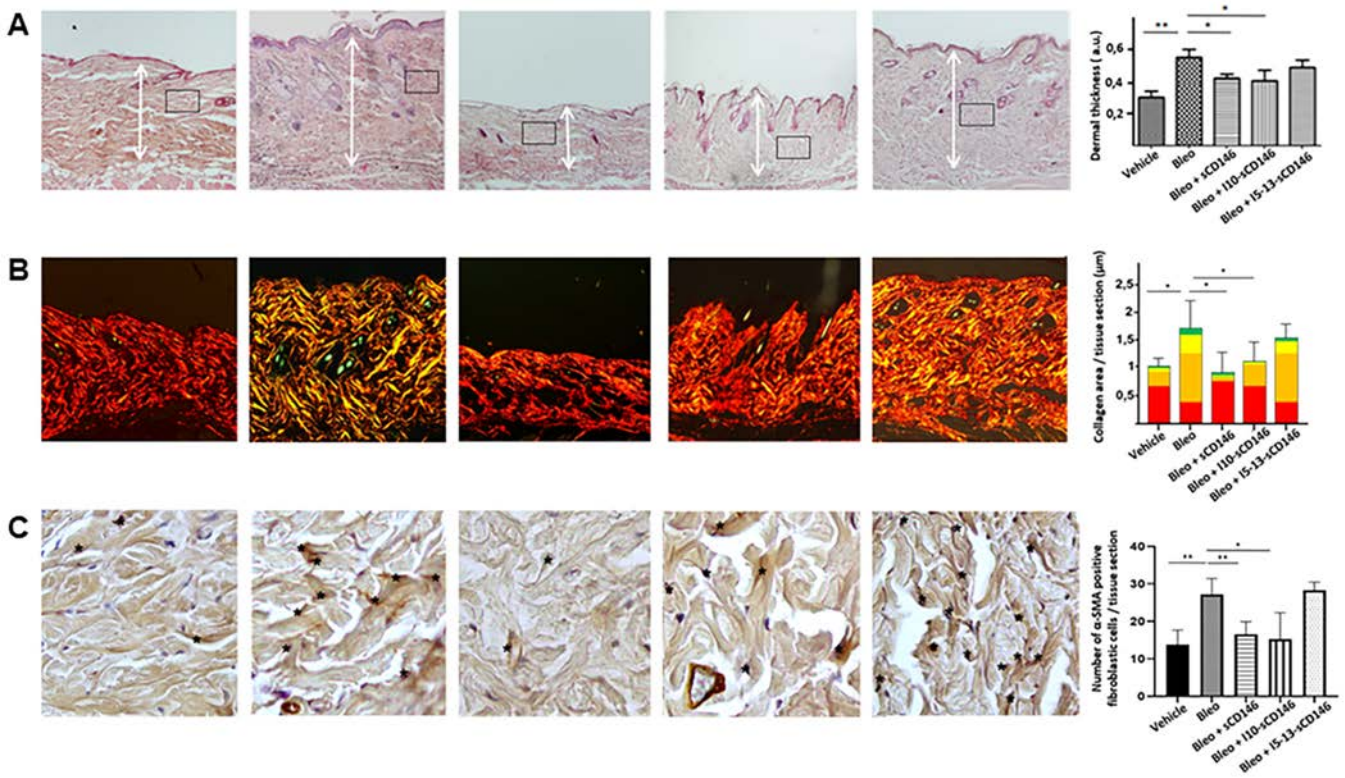

Figure 4. Effect of shed sCD146, I5-13-sCD146, and I10-sCD146 in a CD146-knockout (CD146-KO) mouse model of SSc induced by subcutaneous injection of bleomycin (Bleo). **A**, Left, Dermal thickness (**arrows**) in CD146-KO mice treated with vehicle, bleomycin alone, or bleomycin plus shed sCD146, I0-sCD146, or I5-13-sCD146. Representative results from 5 different animals are shown. Boxed areas show the location of tissues shown in **C**. Original magnification × 10. Right, Quantification of dermal thickness in mice treated as indicated. Bars show the mean ± SEM. **B**, Left, Sirius red staining of collagen content in biopsy specimens from CD146-KO mice treated with vehicle, bleomycin alone, or bleomycin and shed sCD146, I10-sCD146, or I5-13-sCD146. The quantification of the collagen area, as observed under polarized light, was performed on 4–7 slides from 3–5 animals. Original magnification × 10. Right, Quantification of collagen area in mice treated as indicated. Bars show the mean ± SEM. Red indicates thick/organized collagen fibers; orange, yellow, and green indicate progressively thinner/less organized collagen fibers. **C**, Staining for α-smooth muscle actin (α-SMA) (**asterisks**) in fibroblastic cells from CD146-KO mice treated with vehicle, bleomycin alone, or bleomycin and shed sCD146, I10-sCD146, or I5-13-sCD146. The number of fibroblastic cells expressing α-SMA was estimated on 4–7 slides from 3–5 animals. Selected zones are indicated by the boxed areas in **A**. Original magnification × 40. Right, Quantification of α-SMA–positive cells in mice treated as indicated. Bars show the mean ± SEM. * = $P < 0.05$; ** = $P < 0.01$ by analysis of variance in **A**; by Mann-Whitney test in **B** and **C**. See Figure 3 for other definitions.

compared to bleomycin injection only, whereas I5-13-sCD146 did not.

Proangiogenic effects of shed sCD146 and I10-sCD146 in vitro and in vivo. Since ECFCs constitute a model for ex vivo angiogenesis studies, we evaluated the effect of the different sCD146 forms on ECFC proliferation and migration. To this end, we used recombinant proteins. Recombinant human I10-sCD146 (rh-I10-sCD146) and rh-shed sCD146 increased endothelial cell proliferation (Figure 5A) and migration (Figure 5B) whereas rh-I5-13-sCD146 did not. To confirm these results, we analyzed the effects of the different forms on the proliferation of HDMECs. We observed that both shed sCD146 and I10-sCD146 increased the proliferation of HDMECs, whereas I5-13-sCD146 did not (Figure 5C). Likewise, HDMEC proliferation was lower in the presence of SSc patient sera depleted of 10-sCD146 or shed sCD146, but not in the presence of sera depleted of I5-13-sCD146 (Figure 5C), as compared to nondepleted patient sera. In experiments of 3-dimensional capillary-like formation, shed sCD146 and I10-sCD146 increased the ability to generate pseudo-capillaries, as measured by the cumulative sprout length, whereas I5-13-sCD146 did not (Figure 5D). Shed sCD146 and I10-sCD146 increased vascularization in a chorioallantoic membrane assay, whereas I5-13-sCD146 did not (Supplementary Figure 10, available on the *Arthritis & Rheumatology* website at http://onlinelibrary.wiley.com/doi/10.1002/art.42063).

Finally, in another in vivo approach, we used a mouse model of hind limb ischemia to evaluate the proangiogenic effects of the 3 sCD146 forms. Ischemic mice were treated with rh-sCD146, rh-I10-sCD146, rh-I5-13-sCD146, or VEGF for 28 days, and vessel density on the ischemic tissue was estimated. Labeling of

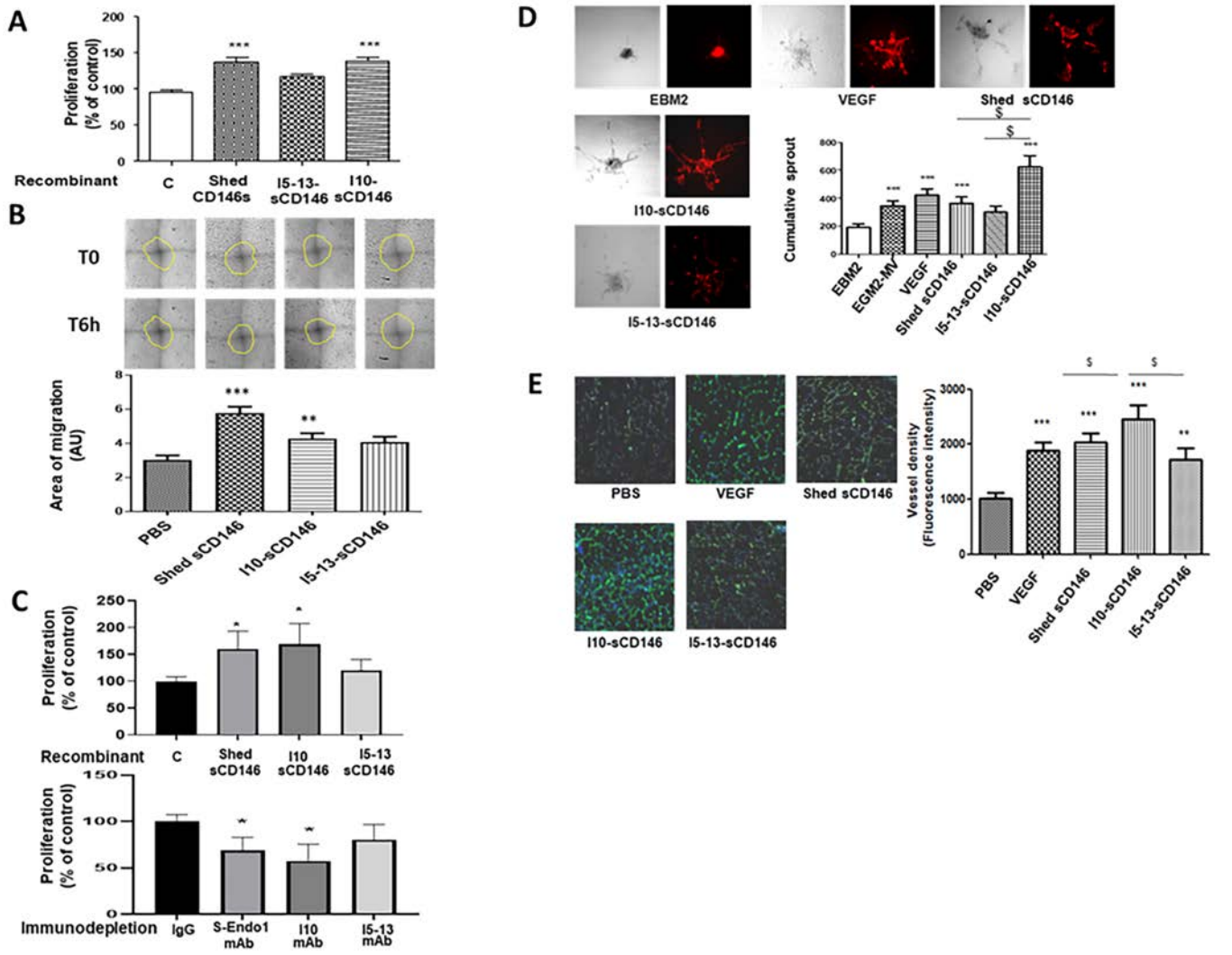

Figure 5. Effect of the different sCD146 variants on angiogenesis. **A**, Effect of recombinant proteins shed sCD146, I5-13-sCD146, and I10-sCD146 (50 ng/ml each) on the proliferation of endothelial colony-forming cells (ECFCs) after 24 hours of treatment. **B**, Effect of recombinant proteins shed sCD146, I10-sCD146, and I5-13-sCD146 (50 ng/ml each) on the migration of ECFCs after 6 hours of treatment. Results of cell migration assays (top) and quantification of migration area (bottom) are shown. Encircled areas show the limit of cell migration. **C**, Effect of recombinant proteins shed sCD146, I10-sCD146, and I5-13-sCD146 (50 ng/ml each) (top) and SSc patient sera immunodepleted with S-endo-1 monoclonal antibody (mAb), I10-sCD146 mAb, or I5-13-sCD146 mAb, as compared to nondepleted sera (top), on the proliferation of human dermal microvascular endothelial cells. **D**, Effect of recombinant shed sCD146, I10-sCD146, and I5-13-sCD146 (50 ng/ml each) on the cumulative sprout length in spheroid experiments realized with ECFCs after 24 hours of treatment. Brightfield imaging of spheroids labeled with DAPI (blue) or phalloidin (red) (top and left) and quantification of cumulative sprout length (right) are shown. EBM2 = endothelial basal medium 2; EGM2-MV = microvascular endothelial cell growth medium 2. **E**, Isolectin B4 labeling of blood vessels (left) and quantification of vessel density (right) in hind limb muscle sections from mice treated with control (phosphate buffered saline [PBS]), vascular endothelial growth factor (VEGF), shed sCD146, I10-sCD146, or I5-13-sCD146 28 days after hind limb ischemia. Representative results from 5 different animals are shown. Bars show the mean ± SEM. * = $P < 0.05$; ** = $P < 0.01$; *** = $P < 0.001$ versus controls; $ = $P < 0.05$ for the indicated comparisons, by analysis of variance. See Figure 3 for other definitions.

muscle with isolectin B4 showed that vascularization was highly increased in animals treated with rh-I10-sCD146, rh-sCD146, and VEGF. In contrast, it was minimally increased in those treated with rh-I5-13-sCD146 (Figure 5E).

To investigate the mechanism of action of these different sCD146 forms, we performed an antibody array. The shed form of sCD146 specifically increased the phosphorylation of focal adhesion kinase (FAK) on Tyr576 and Tyr861 (Supplementary Figures 11A and B, available on the *Arthritis & Rheumatology* website at http://onlinelibrary.wiley.com/doi/10.1002/art.42063). Likewise, I5-13-sCD146 specifically increased the phosphorylation of Akt on Tyr326 (Supplementary Figure 11C), whereas I10-sCD146 increased the phosphorylation of protein kinase Cε (PKCε) on Ser729 (Supplementary Figure 11D).

Profibrotic effects of I5-13-sCD146 in vitro and in vivo. In order to better characterize the role of the newly identified sCD146 isoforms in SSc fibrogenesis, we analyzed their effects on the regulation of the β-catenin pathway in MEFs using a synthetic construct containing β-catenin/T cell factor (TCF). We first showed that MEFs from CD146-KO mice were more sensitive to bleomycin than MEFs from wild-type mice (Figure 6A). We thus used MEFs from CD146-KO mice to analyze the effects of shed sCD146, I10-sCD146, and I5-13-sCD146. As shown in Figure 6A, sCD146 and I10-sCD146 decreased β-catenin/TCF transcription activity, whereas I5-13-sCD146 increased it. We also analyzed the effects of the different forms on the expression of vimentin in HDFs. In a first series of experiments, we analyzed the effects of the recombinant molecules and observed that I5-13-sCD146 increased vimentin expression, whereas shed sCD146 and I10-sCD146 did not (Figure 6B). In another series of experiments, we analyzed the effects of SSc patient sera immunodepleted of the different forms. In these experiments, S-endo-1 depleted sera of the 3 forms. As compared to nondepleted sera, sera depleted of I5-13-sCD146 decreased vimentin

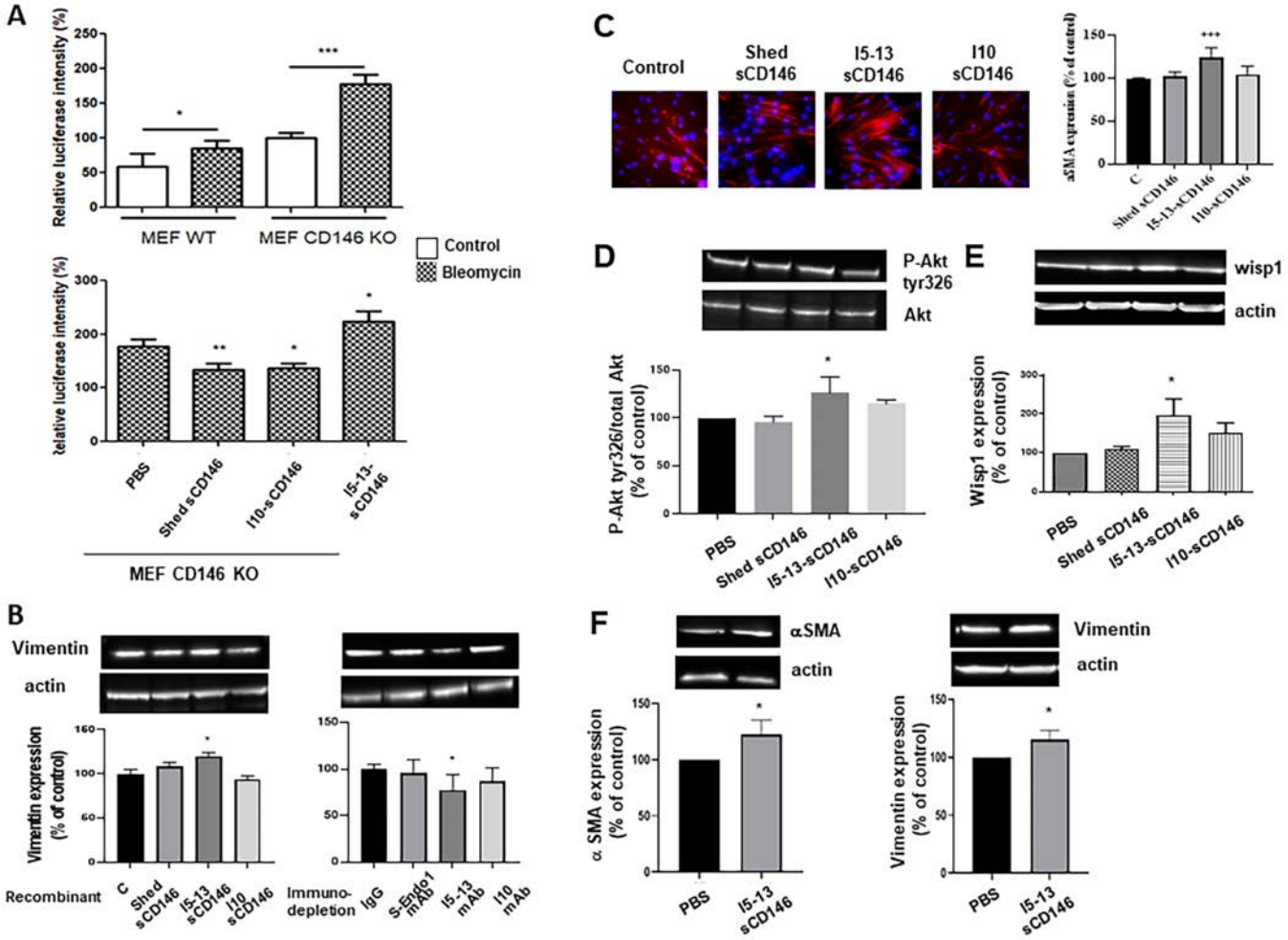

Figure 6. Differential effects of I10-sCD146 and I5-13-sCD146 in mouse embryonic fibroblasts (MEFs). **A**, Sensitivity of wild-type (WT) and CD146-knockout (CD146-KO) MEFs to bleomycin (top) and activation of canonical Wnt signaling (β-catenin/T cell factor transcription activity) in MEFs from CD146-KO and WT mice treated as indicated (bottom). **B**, Western blot (top) and quantification (bottom) of the expression of vimentin by human dermal fibroblasts (HDFs) after 48 hours of treatment with the recombinant proteins shed sCD146, I5-13-sCD146, or I0-sCD146 (50 ng/ml each) (left) or with SSc patient sera immunodepleted with S-endo-1 monoclonal antibody (mAb), I5-13-sCD146 mAb, or I10-sCD146 mAb (right). **C**, Immunofluorescence images (left) and quantification (right) of α-smooth muscle actin (α-SMA) expression by SSc HDFs after 48 hours of treatment with the recombinant proteins shed sCD146, I5-13-sCD146, or I10-sCD146 (50 ng/ml each). Results are representative of 4–6 samples from 2 SSc patients for each culture condition. **D**, Western blot (top) and quantification (bottom) of the expression of p-Akt phosphorylated on Tyr326 compared to total Akt in MEFs after 6 hours of treatment with shed sCD146, I5-13-sCD146, or I10-sCD146 (50 ng/ml each). **E**, Western blot (top) and quantification (bottom) of the expression of WISP-1 in MEFs after 6 hours of treatment with shed sCD146, I5-13-sCD146, or I10-sCD146 (50 ng/ml each). **F**, Western blot (top) and quantification (bottom) of the expression of α-SMA (left) and vimentin (right) in MEFs after 48 hours of treatment with I5-13-sCD146 (50 ng/ml). Bars show the mean ± SEM of 3–5 experiments. * = $P < 0.05$; ** = $P < 0.01$; *** = $P < 0.001$ versus control, by analysis of variance. PBS = phosphate buffered saline (see Figure 3 for other definitions).

expression in HDFs, whereas sera depleted of I10-sCD146 did not (Figure 6B). The specific effect of I5-13-sCD146 was also observed on α-SMA expression in immunofluorescence experiments with HDFs obtained from SSc patients (Figure 6C).

Since the antibody array (Supplementary Figures 11A and C) showed a specific effect of I5-13-sCD146 on the phosphorylation of Akt on Tyr326 in ECFCs, we analyzed its effect on MEFs and confirmed the activation of this pathway (Figure 6D). WISP-1 is frequently described as a major protein mediating pulmonary fibrosis (22), and I5-13-sCD146 was significantly increased in SSc patients with pulmonary fibrosis (see Figure 3D). We thus compared the effects of the 3 forms on WISP-1 expression. WISP-1 was specifically increased by I5-13-sCD146 (Figure 6E). Since WISP-1 is a Wnt-1–inducible signaling protein and Wnt-1/β-catenin signaling is important in mediating fibrosis, we analyzed the effect of I5-13-sCD146 on Wnt-1 expression and phosphorylation of β-catenin on Ser552. They were both increased by I5-13-sCD146 (Supplementary Figures 12A and B, available on the *Arthritis & Rheumatology* website at http://onlinelibrary.wiley.com/doi/10.1002/art.42063). At 48 hours, the activation of these different pathways led to an increase in α-SMA and vimentin expression in MEFs (Figure 6F). Of interest, after 48 hours of treatment with I5-13-sCD146, an increase in α-SMA and vimentin expression was also observed in the microvascular cell line HMEC-1 (Supplementary Figure 13, available on the *Arthritis & Rheumatology* website at http://onlinelibrary.wiley.com/doi/10.1002/art.42063).

DISCUSSION

In this study, we demonstrated that multiple isoforms of sCD146 are present in the sera of patients with SSc. We then identified these isoforms, their mechanism of generation, and their variations in patients with SSc, and determined their properties.

Concerning the shed form of CD146, it can be generated by 2 different ADAMs, ADAM-10 and TACE, for long and short isoforms, respectively. Of note, we have recently shown that the short isoform of CD146 displayed complete proteolytic processing with the shedding of the extracellular part followed by the shedding of the intracellular part through presenilin 1, generating an intracellular domain (short CD146 intracellular domain) with transcriptional effects. Of interest, TACE and presenilin 1 are often associated to generate sequential shedding of proteins, as reported for Notch (23). In addition to the shed form of CD146, our study showed that 2 other isoforms are generated by alternative splicing. In patients with SSc, we showed that shed sCD146 and I5-13-sCD146 were significantly increased, whereas I10-sCD146 was significantly decreased, as compared to healthy controls. Of interest, low levels of shed sCD146 and I10-sCD146 were associated with capillary abnormality as determined by nailfold videocapillaroscopy, but no association was found with pulmonary hypertension. In contrast, high levels of I5-13-sCD146 were associated with pulmonary fibrosis and were correlated with high modified Rodnan skin thickness scores, but no association was found with capillary abnormality. These data are consistent with the proangiogenic role of shed sCD146 and I10-sCD146 and the profibrotic role of I5-13-sCD146 demonstrated in our in vitro and in vivo experiments. Of interest, I10-sCD146 was decreased by Wnt-3A and VEGF, and was decreased in SSc. The observed decrease in I10-sCD146 in the sera of patients is thus consistent with the described increase in Wnt-3a and VEGF in SSc patients.

Finally, using an in vivo mouse model of SSc induced by bleomycin, we showed that shed sCD146 and I10-sCD146 reduced dermal thickness, whereas I5-13-sCD146 did not, a result that can be attributed, at least in part, to the proangiogenic role of these molecules. In addition, we showed that shed sCD146 and I10-sCD146 reduced the collagen deposition and disorganization of collagen fibers seen with bleomycin treatment, as observed with sirius red under polarized light (24). In contrast, I5-13-sCD146 did not. These findings are consistent with previous results from our group showing a protective effect of shed sCD146 on fibrosis development in SSc (13).

Different angiogenic factors have been shown to exist as different isoforms, as reported for VEGF (25). These isoforms bind different receptors that can be expressed in distinct cells and affect angiogenesis/lymphangiogenesis (26,27). Further studies will be necessary to determine if the different sCD146 variants bind different receptors. Recently, both proangiogenic and antiangiogenic isoforms of VEGF have been described (28). Of interest, one antiangiogenic splice variant of VEGF, VEGF165b, has been shown to be potentially involved in the pathogenesis of SSc since it is associated with the severity of nailfold capillary loss (29,30). Further studies will also be necessary to investigate whether antiangiogenic splice variants of sCD146 also exist and whether they play a role in SSc.

Concerning the I5-13-sCD146 isoform, we have shown that, in contrast to shed sCD146 and I10-sCD146, it is involved in the control of fibrosis. Indeed, I5-13-sCD146 stimulated the transition of HDFs toward myofibroblasts that were able to express vimentin and α-SMA, and secrete collagen, whereas shed sCD146 and I10-sCD146 did not. In addition, whereas shed sCD146 and I10-sCD146 also reduced β-catenin/TCF transcription activity in the in vitro model of MEF, suggesting a potential down-regulation of the Wnt canonical pathway, I5-13-sCD146 significantly increased it. Abnormalities in many factors have been reported in this disease (31). In this study, we showed that the I5-13-sCD146 splice variant was increased by Wnt-5a and TNF, and that this form of sCD146 was significantly enhanced in the sera of SSc patients, in particular in patients with pulmonary fibrosis, and was correlated with the modified Rodnan skin thickness score. Of interest, the expression of I5-13-sCD146 was correlated with another fibrotic marker, which is also highly increased in pulmonary fibrosis, KL-6. Here again, the observed increase in

l5-13-sCD146 in the sera of patients is consistent with the described increase in TNF levels in SSc patients.

We further investigated the mechanism of action of these different forms and showed that shed sCD146 was specifically able to induce FAK phosphorylation on 2 tyrosines (Tyr576 and Tyr861), consistent with the major effect of shed sCD146 on the migration of endothelial cells. In contrast, l10-sCD146 specifically increased PKCε phosphorylation on Ser729. The fact that PKCε stimulation has been demonstrated to promote angiogenesis and modulate VEGF activity (32) is consistent with the proangiogenic role of l10-sCD146. Finally, l5-13-sCD146 specifically increased the tyrosine phosphorylation of Akt (Tyr326). Since SSc fibroblasts have been demonstrated to display an enhanced activation of Akt (33), we explored the effect of l5-13-sCD146 on MEFs and confirmed this specific effect of the molecule on the Tyr326 phosphorylation of Akt. Of interest, phosphorylation of β-catenin by Akt has been shown to promote β-catenin transcriptional activity (34). In addition, this effect was accompanied by a specific effect of the molecule on the fibrosis-induced protein WISP-1. Of interest, WISP-1 in turn has been shown to be activated by Wnt-1 and β-catenin, as observed in our experiments (35), and to induce pulmonary fibrosis (22). In another study (36), authors showed that blocking Wnt/β-catenin decreased bleomycin-induced pulmonary fibrosis in a murine model. l5-13-sCD146 could thus induce fibrosis by an activation of fibroblasts into myofibroblast, as demonstrated by the induced expression of α-SMA and vimentin, through β-catenin– and Wnt1-meditated induction of WISP-1.

Notably, whereas myofibroblasts derived from fibroblasts are mostly responsible for the fibrotic process in many fibrotic disorders, recent studies have demonstrated that endothelial cells constitute another source of activated myofibroblasts through a process known as endothelial-to-mesenchymal transition (EndoMT), which is a phenomenon similar to epithelial–mesenchymal transition (EMT) (37). Of interest, EMT has been shown to participate in the pathogenesis of SSc (38). In our study, the specific effect of l5-13-sCD146 observed on α-SMA and vimentin expression in HMEC-1 cells also supports the notion of a role of this variant in the induction of fibrosis through EndoMT.

The limitations of this study include the fact that receptors of the newly identified splice variants of sCD146 are not yet known, precluding the deciphering of the whole signaling pathways.

In conclusion, our study identified the 2 proteinases involved in the shedding of the 2 membrane isoforms of CD146 and identified 2 new isoforms of sCD146 generated by alternative splicing that are differentially modulated in SSc (Supplementary Figure 11) and could constitute novel biomarkers and targets in SSc.

ACKNOWLEDGMENT

The authors thank BioCytex for providing rh-sCD146 and enzyme-linked immunosorbent assay kits.

AUTHOR CONTRIBUTIONS

All authors were involved in drafting the article or revising it critically for important intellectual content, and all authors approved the final version to be published. Dr. Blot-Chabaud had full access to all of the data in the study and takes responsibility for the integrity of the data and the accuracy of the data analysis.

Study conception and design. Nollet, Bachelier, Joshkon, Traboulsi, Mahieux, Moyon, Muller, Somasundaram, Simoncini, Peiretti, Guillet, Granel, Foucault-Bertaud, Blot-Chabaud.

Acquisition of data. Nollet, Bachelier, Joshkon, Traboulsi, Mahieux, Moyon, Muller, Somasundaram, Simoncini, Peiretti, Foucault-Bertaud.

Analysis and interpretation of data. Nollet, Bachelier, Joshkon, Traboulsi, Mahieux, Muller, Somasundaram, Peiretti, Leroyer, Dignat-George, Bardin, Foucault-Bertaud, Blot-Chabaud.

REFERENCES

1. Stalin J, Nollet M, Dignat-George F, Bardin N, Blot-Chabaud M. Therapeutic and diagnostic antibodies to CD146: thirty years of research on its potential for detection and treatment of tumors. Antibodies 2017;6:17.
2. Zeng Q, Wu Z, Duan H, Jiang X, Tu T, Lu D, et al. Impaired tumor angiogenesis and VEGF-induced pathway in endothelial CD146 knockout mice. Protein Cell 2014;5:445–56.
3. Jiang T, Zhuang J, Duan H, Luo Y, Zeng Q, Fan K, et al. CD146 is a coreceptor for VEGFR-2 in tumor angiogenesis. Blood 2012;120:2330–9.
4. Kebir A, Harhouri K, Guillet B, Liu JW, Foucault-Bertaud A, Lamy E, et al. CD146 short isoform increases the proangiogenic potential of endothelial progenitor cells in vitro and in vivo. Circ Res 2010;107:66–75.
5. Bardin N, Moal V, Anfosso F, Daniel L, Brunet P, Sampol J, et al. Soluble CD146, a novel endothelial marker, is increased in physiopathological settings linked to endothelial junctional alteration. Thromb Haemost 2003;90:915–20.
6. Bardin N, Reumaux D, Geboes K, Colombel JF, Blot-Chabaud M, Sampol J, et al. Increased expression of CD146, a new marker of the endothelial junction in active inflammatory bowel disease. Inflamm Bowel Dis 2006;12:16–21.
7. Stalin J, Nollet M, Garigue P, Fernandez S, Vivancos L, Essaadi A, et al. Targeting soluble CD146 with a neutralizing antibody inhibits vascularization, growth and survival of CD146-positive tumors. Oncogene 2016;35:5489–500.
8. Stalin J, Harhouri K, Hubert L, Subrini C, Lafitte D, Lissitzky JC, et al. Soluble melanoma cell adhesion molecule (sMCAM/sCD146) promotes angiogenic effects on endothelial progenitor cells through angiomotin. J Biol Chem 2013;288:8991–9000.
9. Harhouri K, Kebir A, Guillet B, Foucault-Bertaud A, Voytenko S, Piercecchi-Marti MD, et al. Soluble CD146 displays angiogenic properties and promotes neovascularization in experimental hind-limb ischemia. Blood 2010;115:3843–51.
10. Bardin N, Blot-Chabaud M, Despoix N, Kebir A, Harhouri K, Arsanto JP, et al. CD146 and its soluble form regulate monocyte transendothelial migration. Arterioscler Thromb Vasc Biol 2009;29:746–53.
11. Boneberg EM, Illges H, Legler DF, Fürstenberger G. Soluble CD146 is generated by ectodomain shedding of membrane CD146 in a calcium-induced, matrix metalloprotease-dependent process. Microvasc Res 2009;78:325–31.
12. Vainio O, Dunon D, Aïssi F, Dangy JP, McNagny KM, Imhof BA. HEMCAM, an adhesion molecule expressed by c-kit+ hemopoietic progenitors. J Cell Biol 1996;135:1655–68.
13. Kaspi E, Heim X, Granel B, Guillet B, Stalin J, Nollet M, et al. Identification of CD146 as a novel molecular actor involved in systemic sclerosis. J Allergy Clin Immunol 2017;140:1448–51.

14. Delorme B, Basire A, Gentile C, Sabatier F, Monsonis F, Desouches C, et al. Presence of endothelial progenitor cells, distinct from mature endothelial cells, within human CD146+ blood cells. Thromb Haemost 2005;94:1270–9.
15. Xu J. Preparation, culture, and immortalization of mouse embryonic fibroblasts. Curr Protoc Mol Biol 2005;Chapter 28:Unit 28.1.
16. Korff T, Kimmina S, Martiny-Baron G, Augustin HG. Blood vessel maturation in a 3-dimensional spheroidal coculture model: direct contact with smooth muscle cells regulates endothelial cell quiescence and abrogates VEGF responsiveness. FASEB J 2001;15: 447–57.
17. Stalin J, Harhouri K, Hubert L, Garrigue P, Nollet M, Essaadi A, et al. Soluble CD146 boosts therapeutic effect of endothelial progenitors through proteolytic processing of short CD146 isoform. Cardiovasc Res 2016;111:240–51.
18. Beckers M, Gladis-Villanueva M, Hamann W, Schmutzler W, Zwadlo-Klarwasser G. The use of the chorio-allantoic membrane of the chick embryo as test for anti-inflammatory activity. Inflamm Res 1997;46: 29–30.
19. Tellier E, Canault M, Rebsomen L, Bonardo B, Juhan-Vague I, Nalbone G, et al. The shedding activity of ADAM17 is sequestered in lipid rafts. Exp Cell Res 2006;312:3969–80.
20. Tellier E, Canault M, Poggi M, Bonardo B, Nicolay A, Alessi MC, et al. HDLs activate ADAM17-dependent shedding. J Cell Physiol 2008; 214:687–93.
21. Clements PJ, Lachenbruch PA, Ng SC, Simmons M, Sterz M, Furst DE. Skin score: a semiquantitative measure of cutaneous involvement that improves prediction of prognosis in systemic sclerosis. Arthritis Rheum 1990;33:1256–63.
22. Königshoff M, Kramer M, Balsara N, Wilhelm J, Amarie OV, Jahn A, et al. WNT1-inducible signaling protein-1 mediates pulmonary fibrosis in mice and is upregulated in humans with idiopathic pulmonary fibrosis. J Clin Invest 2009;119:772–87.
23. Gudey SK, Sundar R, Mu Y, Wallenius A, Zang G, Bergh A, et al. TRAF6 stimulates the tumor-promoting effects of TGFβ type I receptor through polyubiquitination and activation of presenilin 1. Sci Signal 2014;7:ra2.
24. Lattouf R, Younes R, Lutomski D, Naaman N, Godeau G, Senni K, et al. Picrosirius red staining: a useful tool to appraise collagen networks in normal and pathological tissues. J Histochem Cytochem 2014;62:751–8.
25. Guyot M, Pagès G. VEGF splicing and the role of VEGF splice variants: from physiological-pathological conditions to specific pre-mRNA splicing. Methods Mol Biol 2015;1332:3–23.
26. Jussila L, Alitalo K. Vascular growth factors and lymphangiogenesis. Physiol Rev 2002;82:673–700.
27. Fearnley GW, Smith GA, Abdul-Zani I, Yuldasheva N, Mughal NA, Homer-Vanniasinkam S, et al. VEGF-A isoforms program differential VEGFR2 signal transduction, trafficking and proteolysis. Biol Open 2016;5:571–83.
28. Biselli-Chicote PM, Oliveira AR, Pavarino EC, Goloni-Bertollo EM. VEGF gene alternative splicing: pro- and anti-angiogenic isoforms in cancer. J Cancer Res Clin Oncol 2012;138:363–70.
29. Manetti M, Guiducci S, Romano E, Ceccarelli C, Bellando-Randone S, Conforti ML, et al. Overexpression of VEGF165b, an inhibitory splice variant of vascular endothelial growth factor, leads to insufficient angiogenesis in patients with systemic sclerosis. Circ Res 2011;109: 14–26.
30. Manetti M, Guiducci S, Romano E, Bellando-Randone S, Lepri G, Bruni C, et al. Increased plasma levels of the VEGF165b splice variant are associated with the severity of nailfold capillary loss in systemic sclerosis. Ann Rheum Dis 2013;72:1425–7.
31. Hummers LK, Hall A, Wigley FM, Simons M. Abnormalities in the regulators of angiogenesis in patients with scleroderma. J Rheumatol 2009;36:576–82.
32. Monti M, Donnini S, Morbidelli L, Giachetti A, Mochly-Rosen D, Mignatti P, et al. PKCε activation promotes FGF-2 exocytosis and induces endothelial cell proliferation and sprouting. J Mol Cell Cardiol 2013;63:107–17.
33. Jun JB, Kuechle M, Min J, Shim SC, Kim G, Montenegro V, et al. Scleroderma fibroblasts demonstrate enhanced activation of Akt (protein kinase B) in situ. J Invest Dermatol 2005;124:298–303.
34. Fang D, Hawke D, Zheng Y, Xia Y, Meisenhelder J, Nika H, et al. Phosphorylation of β-catenin by AKT promotes β-catenin transcriptional activity. J Biol Chem 2007;282:11221–9.
35. Xu L, Corcoran RB, Welsh JW, Pennica D, Levine AJ. WISP-1 is a Wnt-1- and β-catenin-responsive oncogene. Genes Dev 2000;14: 585–95.
36. Kim TH, Kim SH, Seo JY, Chung H, Kwak HJ, Lee SK, et al. Blockade of the Wnt/β-catenin pathway attenuates bleomycin-induced pulmonary fibrosis. J Exp Med 2011;223:45–54.
37. Piera-Velazquez S, Mendoza FA, Jimenez SA. Endothelial to mesenchymal transition (EndoMT) in the pathogenesis of human fibrotic diseases. J Clin Med 2016;5:45.
38. Nikitorowicz-Buniak J, Denton CP, Abraham D, Stratton R. Partially evoked epithelial-mesenchymal transition (EMT) is associated with increased TGFβ signaling within lesional scleroderma skin. PLoS One 2015;10:e0134092.

American College of Rheumatology
Empowering Rheumatology Professionals

Arthritis & Rheumatology
Vol. 74, No. 6, June 2022, pp 1048–1058
DOI 10.1002/art.42071

Contribution of Necroptosis to Myofiber Death in Idiopathic Inflammatory Myopathies

Qing-Lin Peng,[1] Ya-Mei Zhang,[1] Yan-Chun Liu,[2] Lin Liang,[1] Wen-Li Li,[1] Xiao-Lan Tian,[1] Lu Zhang,[1] Hong-Xia Yang,[1] Xin Lu,[1] and Guo-Chun Wang[1]

Objective. Myofiber necrosis is a significant pathologic characteristic of idiopathic inflammatory myopathies (IIMs), and its molecular mechanism is largely unknown. Necroptosis is a recently identified form of regulated necrotic cell death, and its activation might have crucial biologic consequences. The aim of the present study was to investigate the role of necroptosis in IIM muscle damage.

Methods. Western blot and immunohistochemistry analyses were performed to examine the expression of receptor-interacting protein 3 (RIP-3) and mixed-lineage kinase domain–like (MLKL) proteins in 26 IIM patients and 4 healthy controls, as well as necroptosis-related damage–associated molecular pattern molecules. Tumor necrosis factor (TNF) was used to stimulate cultured C2C12 myoblasts, and the involvement of necroptosis in cell death of C2C12 cells was studied in vitro.

Results. The expression of RIP-3 and MLKL proteins and their phosphorylated forms was significantly increased in the muscle tissue of IIM patients compared to that of healthy controls. The expression levels of RIP-3 and MLKL proteins were associated with the severity of muscle damage in patients with IIM. Significant colocalization of MLKL with high mobility group box chromosomal protein 1 in necrotizing myofibers was observed in muscle biopsy tissue from patients with IIM. Stimulation of C2C12 myoblasts with TNF and a pan-caspase inhibitor, Z-VAD, resulted in the overactivation of necroptosis and significantly increased necrotic cell death. Strategies involving either inhibition of necroptosis with necrostatin-1 or knockdown of MLKL expression successfully prevented necroptosis-induced cell death of C2C12 cells.

Conclusion. These findings demonstrate that overactivated necroptosis contributes to muscle damage in IIMs and suggest that necroptosis inhibitors could represent a new therapeutic target in the treatment of IIMs.

INTRODUCTION

Idiopathic inflammatory myopathy (IIM) is a heterogeneous family of systemic autoimmune disorders characterized by muscle weakness, decreased muscle endurance, and inflammatory infiltrates in the skeletal muscle tissue (1). Muscle damage is a significant feature of IIM; however, the molecular mechanism of muscle damage remains to be elucidated.

Apoptosis is absent in muscle affected by myositis, which may be attributed to the up-regulation of antiapoptotic proteins (2). Previous studies have revealed that overactivation of endoplasmic reticulum stress and TRAIL-mediated autophagy in myositis skeletal muscle are potential nonimmune mechanisms of muscle damage (3,4). Pandya et al demonstrated that $CD28^{null}$ T cells induced significant myotoxicity in patients with polymyositis, which is mediated by directed perforin-dependent killing (5). More recently, anti–signal recognition particle (anti-SRP) and anti–hydroxymethylglutaryl-coenzyme A reductase (anti-HMGCR) autoantibodies were found to be pathogenic toward muscle tissue in vitro and in vivo, providing novel clues for the mechanism of muscle damage in myositis (6,7). These studies indicate that multiple factors may contribute to the pathogenesis of muscle involvement in myositis, including both immune-related and nonimmune mechanisms. Further elucidation of the underlying

Supported by the National Natural Science Foundation of China (awards 82171788, 81971531, and 82072359), the Elite Medical Professionals project of China-Japan Friendship Hospital (award ZRJY2021-GG13), and the Beijing Municipal Science & Technology Commission (awards Z181100001718063 and Z191100006619012).

[1]Qing-Lin Peng, PhD, Ya-Mei Zhang, MD, Lin Liang, MD, Wen-Li Li, PhD, Xiao-Lan Tian, MD, Lu Zhang, MD, PhD, Hong-Xia Yang, MSc, Xin Lu, MD, PhD, Guo-Chun Wang, MD, PhD: Department of Rheumatology, Key Laboratory of Myositis, China-Japan Friendship Hospital, Beijing, China; [2]Yan-Chun Liu, MSc: NMPA Key Laboratory for Quality Evaluation of In Vitro Diagnostics, Beijing Institute of Medical Device Testing, Beijing, China.

Author disclosures are available at https://onlinelibrary.wiley.com/action/downloadSupplement?doi=10.1002%2Fart.42071&file=art42071-sup-0001-Disclosureform.pdf.

Address correspondence to Guo-Chun Wang, MD, PhD, Department of Rheumatology, Key Laboratory of Myositis, China-Japan Friendship Hospital, Beijing 100029, China. Email: guochunwang@hotmail.com.

Submitted for publication August 11, 2021; accepted in revised form January 18, 2022.

pathologic mechanism of muscle damage may provide insights into new therapeutic targets.

Myofiber necrosis is frequently seen in myositis muscle biopsy tissue and is considered a significant form of muscle fiber death in IIMs. Necrosis has traditionally been thought to be a passive and unregulated form of cell death. Interestingly, and contrary to traditional belief, with the discovery of necroptosis as a form of regulated necrotic cell death, necrosis began to be considered programmed, rather than just an accident (8). Key effector molecules involved in the execution of necroptosis include receptor-interacting protein 1 (RIP-1), RIP-3, and mixed-lineage kinase domain–like (MLKL) protein, which constitute the necrosome (8). As late events in necroptosis, RIP-3 and MLKL are phosphorylated in the necrosome and translocated to the plasma membrane, where the complex mediates membrane permeabilization.

In the process of necroptotic cell death, damage-associated molecular pattern (DAMP) molecules including interleukin-33 (IL-33) and high mobility group box chromosomal protein 1 (HMGB1) are released extracellularly, consequently eliciting tissue inflammation (8,9). Examination of muscle biopsy tissue has revealed that myofiber necrosis and inflammatory infiltrates are prominent pathologic features of IIM; however, the mechanism by which necrosis occurs remains unelucidated. To determine whether necroptosis contributes to muscle damage in myositis, we investigated the expression of key molecules involved in the machinery of necroptosis and the involvement of necroptosis in the cell death of cultured myoblasts in vitro.

PATIENTS AND METHODS

Patients. This study was approved by the Human Ethics Board of the China-Japan Friendship Hospital (approval no. 2019-25-K19). All patient data were used anonymously and written informed consent was obtained from all participating individuals. A total of 26 patients with confirmed IIM from China-Japan Friendship Hospital were enrolled in this study from 2017 to 2019. Diagnosis was based on the 2017 European League Against Rheumatism/American College of Rheumatology classification criteria for adult and juvenile IIMs and their major subgroups (10). Five patients were diagnosed as having dermatomyositis (DM) and 4 patients were diagnosed as having amyopathic DM (ADM), according to the classification criteria. In addition, 17 patients who fulfilled the European Neuro Muscular Centre criteria (11) were diagnosed as having immune-mediated necrotizing myopathy (IMNM). Muscle biopsy was performed and diagnosis was histopathologically confirmed in all patients. For the healthy control group, samples of muscle tissue were obtained from 4 trauma patients without muscle disease.

Histologic review of muscle biopsy samples. Histopathologic features of the muscle biopsy tissue from all subjects were reviewed in a blinded manner, and analyzed using a validated international juvenile DM biopsy scoring tool (12,13). In IIM patients, myofiber necrosis scores were defined as 0 (no muscle cell necrosis), 1 (necrotic cell percentage ranging 1–5%), or 2 (necrotic cell percentage ≥5%).

Western blot analysis. Total protein extracted from muscle tissue or in vitro cultured cells was loaded onto 12% or 15% sodium dodecyl sulfate–polyacrylamide gel electrophoresis gels and transferred onto polyvinylidene difluoride membranes. After blocking with 5% nonfat dry milk in Tris buffered saline containing 0.1% Tween 20, the membranes were immunoblotted with appropriate primary antibodies. Following overnight incubation, the membranes were incubated with secondary antibodies. ImageJ software was used to quantify band intensity. The following antibodies were used for Western blot analysis: anti–RIP-3 polyclonal antibody (product no. 27-361; ProSci), anti-MLKL monoclonal antibody (product no. ab184718; Abcam), anti–RIP-3 (phospho-S227) monoclonal antibody (product no. ab209384; Abcam), anti-MLKL (phospho-S358) monoclonal antibody (product no. ab187091; Abcam), anti-MLKL monoclonal antibody (product no. 66675-1-Ig; Proteintech), anti-mouse MLKL (phospho-S345) monoclonal antibody (product no. ab196436; Abcam), and anti-GAPDH monoclonal antibody (product no. ab8245; Abcam).

Immunohistochemistry analysis. Unfixed cryostat muscle sections (8-μm–thick) were subjected to immunohistochemical staining as previously described (14). The following antibodies were used for immunohistochemical staining: anti–RIP-3 polyclonal antibody (product no. 27-361; ProSci), anti-MLKL monoclonal antibody (product no. ab184718; Abcam), anti–RIP-3 (phospho-S227) monoclonal antibody (product no. ab209384; Abcam), anti-MLKL (phospho-S358) monoclonal antibody (product no. ab187091; Abcam), anti-dystrophin monoclonal antibody (product no. NCL-DYS1; Leica Biosystems), anti-C5b-9+C5b-8 monoclonal antibody (product no. ab66768; Abcam), anti-HMGB1 polyclonal antibody (10829-1-AP; Proteintech), and anti–IL-33 monoclonal antibody (product no. ab207737; Abcam).

Irrelevant rabbit polyclonal IgG (product no. ab37415; Abcam), rabbit monoclonal IgG (product no. ab172730; Abcam), and mouse IgG (product no. ab18415; Abcam) were used as isotype controls for the primary antibodies when appropriate. Horseradish peroxidase–conjugated goat anti-rabbit IgG (product no. ab6721; Abcam) and goat anti-mouse IgG (ab6789, Abcam) were used as secondary antibodies. Myofiber necrosis was evaluated using a combination of eosin and dystrophin immunohistochemical staining as previously described by Allenbach et al (15). Necrotic myofiber was defined as pale and/or hyalinized muscle fiber combined with the loss of sarcolemmal integrity/coarse appearance.

Cell culture and treatment. The C2C12 mouse myoblast cell line (ATCC) was cultured in Dulbecco's modified Eagle's medium (Gibco) supplemented with 10% fetal bovine serum (Gibco), 100 units/ml of penicillin, and 100 μg/ml of streptomycin in 5% CO_2 at 37°C. Reagents used for cell treatment included recombinant tumor necrosis factor (TNF) proteins (BioLegend) at 100 ng/ml, Z-VAD-FMK (Promega) at 40 μ*M*, and necrostatin-1s (Nec-1s) (BioVision) at 50 μ*M*.

Cell death assay. Cell death was assessed using a CellTiter-Glo luminescent cell viability assay (Promega). Briefly, C2C12 cells were seeded onto opaque-walled 96-well plates at a density of 1×10^4 cells/well and were treated with reagents for 24 hours. CellTiter-Glo reagent was added to each well at a volume of 100 μl. The plate was then shaken on an orbital shaker to induce cell lysis, and then incubated at room temperature for 10 minutes to stabilize the luminescent signal. Luminescence was detected using a multimode microplate reader (Tecan). Cell viability data were presented as percentages of the control.

Flow cytometry analysis. Cultured C2C12 cells were treated with reagents, harvested, and incubated with propidium iodide (PI) staining solution (BD PharMingen) according to the manufacturer's instructions. After 20 minutes of incubation at room temperature, C2C12 cells were centrifuged, washed, and suspended in 500 μl of phosphate buffered solution for flow cytometry. Samples were processed on a FACSJazz instrument (BD Biosciences) and the results were analyzed using FACS software.

MLKL gene knockdown in C2C12 cells. The clustered regularly interspaced short palindromic repeat (CRISPR)/Cas9 gene editing system was used to knock down MLKL in C2C12 cells, as described previously (16). The single-guide RNA (sgRNA) used in the present study was 5′-GTCTCTGGAGAGGCTGTAGC-3′. The annealed sgRNAs were cloned into PX458 plasmid, and

Table 1. Demographic and clinical characteristics and laboratory findings in patients with idiopathic inflammatory myopathies and healthy controls*

Participant/ age/sex	Diagnosis	Myositis autoantibody	Creatine kinase, IU/liter	MMT-8 score	Time from muscle symptom onset to muscle biopsy, months
Patients					
1/41/F	ADM	PL-7	58	80	–
2/33/F	ADM	MDA-5	31	80	–
3/76/F	ADM	–	65	80	–
4/43/M	ADM	–	22	80	–
5/55/F	DM	Mi-2	3,059	40	36
6/33/F	DM	TIF1γ	6,193	38	2
7/50/F	DM	TIF1γ	331	30	10
8/47/F	DM	TIF1γ	2,776	50	2
9/61/F	DM	TIF1γ	714	56	3
10/63/M	IMNM	HMGCR	1,476	80	4
11/52/F	IMNM	SRP	13,514	66	12
12/37/F	IMNM	SRP	629	80	72
13/18/F	IMNM	SRP	247	80	35
14/44/M	IMNM	HMGCR	861	80	36
15/32/F	IMNM	SRP	810	65	3
16/26/M	IMNM	SRP	8,905	45	36
17/62/F	IMNM	HMGCR	5,992	44	1
18/18/M	IMNM	HMGCR	6,494	29	21
19/55/F	IMNM	SRP	318	66	36
20/81/F	IMNM	SRP	2,353	54	8
21/25/M	IMNM	–	6,533	50	24
22/53/F	IMNM	SRP	7,697	42	4
23/50/F	IMNM	–	4,645	80	7
24/51/M	IMNM	SRP	1,969	60	1
Healthy controls					
1/48/M	–	–	–	–	–
2/64/F	–	–	–	–	–
3/55/F	–	–	–	–	–
4/37/F	–	–	–	–	–

* MMT-8 = Manual Muscle Testing in 8 muscles; ADM = amyopathic dermatomyositis; MDA-5 = melanoma differentiation–associated protein 5; DM = dermatomyositis; TIF1γ = transcriptional intermediary factor 1γ; IMNM = immune-mediated necrotizing myopathy; SRP = signal recognition particle; HMGCR = hydroxymethylglutaryl-coenzyme A reductase.

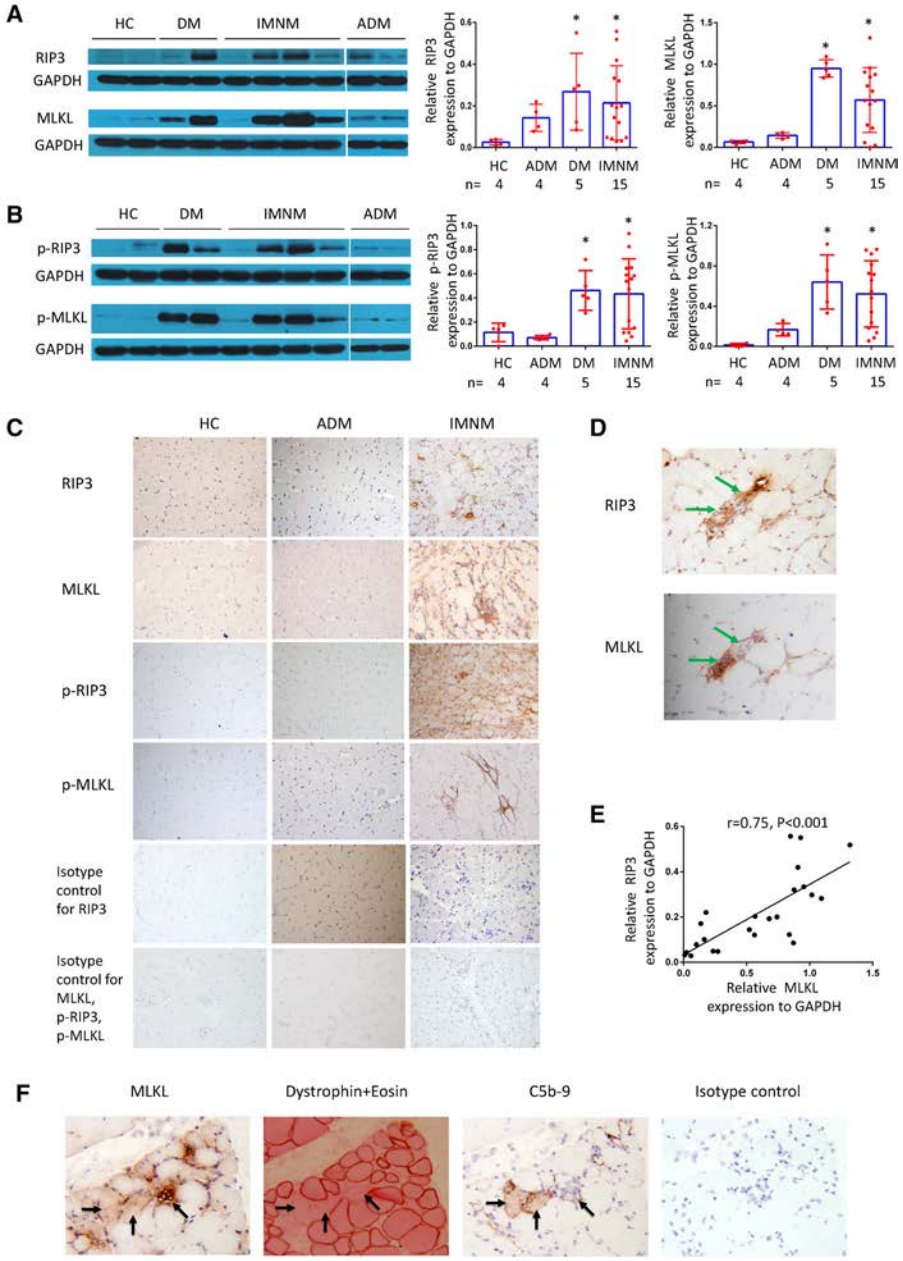

Figure 1. Expression of receptor-interacting protein 3 (RIP-3) and mixed-lineage kinase domain–like (MLKL) proteins in muscle tissue of patients with idiopathic inflammatory myopathies (IIMs). **A** and **B**, Western blot analysis revealed higher levels of RIP-3 and MLKL (**A**), and phosphorylated RIP-3 (p-RIP-3) and phosphorylated MLKL (p-MLKL) (**B**) in patients with dermatomyositis (DM) and patients with immune-mediated necrotizing myopathy (IMNM) compared to healthy controls (HCs). Symbols represent individual subjects; bars show the mean ± SD. * = adjusted $P < 0.05$ versus controls. **C**, Immunohistochemistry analysis of RIP-3, MLKL, p-RIP-3, and p-MLKL was performed in the muscle of patients with IIM. **D**, Immunohistochemistry analysis of serial muscle sections revealed colocalized expression of RIP-3 and MLKL (**arrows**). **E**, Pearson's correlation analysis revealed correlations between the relative expression levels of RIP-3 and MLKL in total protein lysate of muscle affected by myositis. **F**, Serial sections of muscle tissue were immunohistochemically stained for MLKL, dystrophin combined with eosin, and C5b–9. **Arrows** indicate necrotic myofibers staining positive for MLKL and C5b–9. Original magnification × 200.*

recombinant plasmids were transfected into C2C12 cells using Lipofectamine LTX (Invitrogen). The fluorescent cells were sorted using the FACSAria III system (BD Biosciences). MLKL protein expression in the sorted polyclonal cells was confirmed by Western blotting, and these MLKL–down-regulated C2C12 cells were then used in MLKL knockdown studies.

*[Correction added on 20 May 2022 after first online publication: In Figure 1E, "r = 0804" was changed to "r = 0.75."]

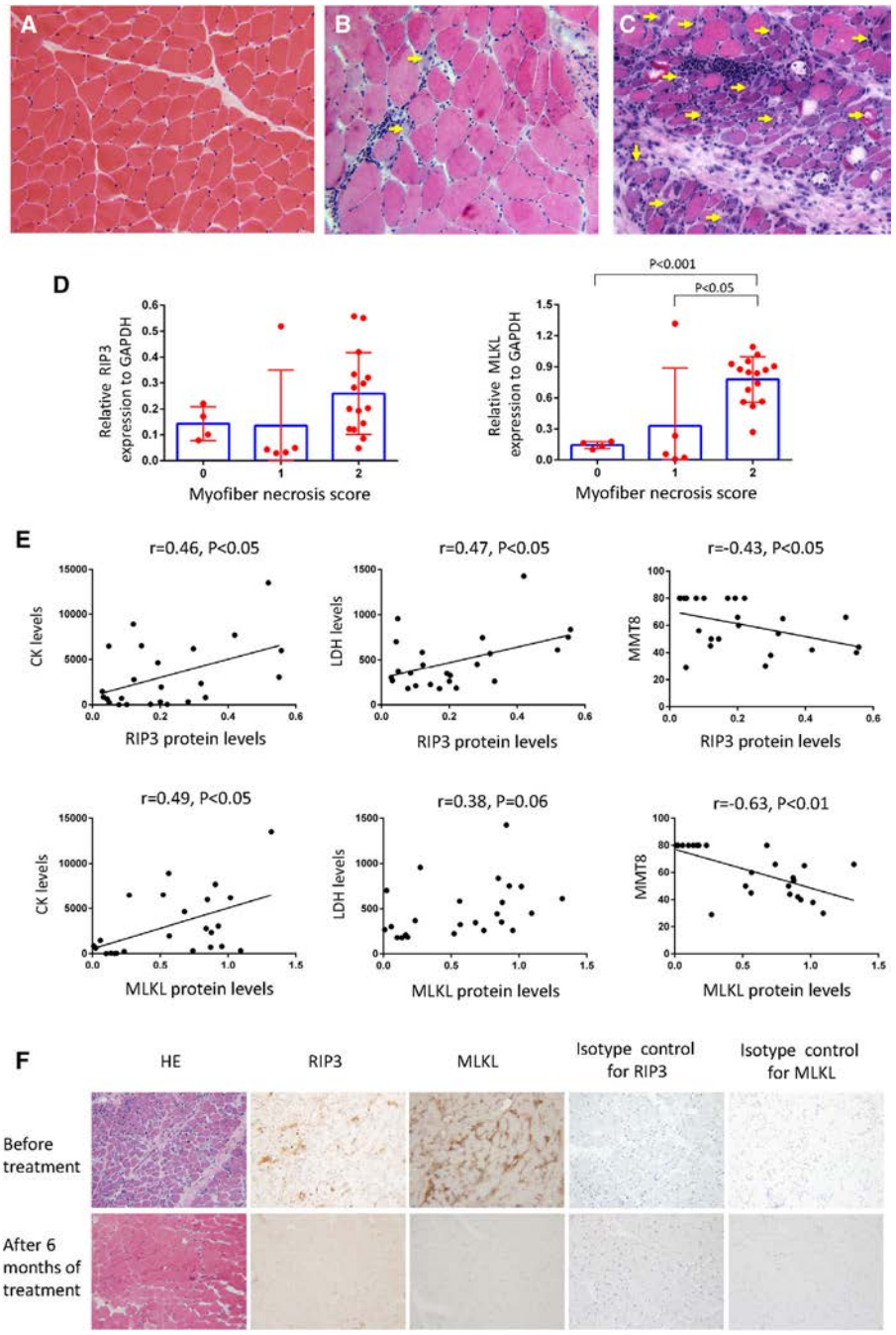

Figure 2. Correlation of RIP-3 and MLKL expression with histopathologic features of the muscle of patients with IIM. **A**–**C**, Representative hematoxylin and eosin (H&E) staining of muscle tissue from IIM patients with necrosis score 0 (**A**), necrosis score 1 (**B**), and necrosis score 2 (**C**) is shown. **Arrows** indicate necrotic myofibers. **D**, Patients with higher necrosis scores showed a trend toward increased expression of RIP-3 and MLKL in the muscle by Western blot analysis of patient groups with different necrosis scores; *P* values are adjusted for the false discovery rate. Symbols represent individual patients; bars show the mean ± SD. **E**, Expression levels of RIP-3 and MLKL protein positively correlated with serum creatine kinase (CK) and lactate dehydrogenase (LDH) levels in IIM patients, and inversely correlated with the Manual Muscle Testing in 8 muscles (MMT-8) score by Pearson's correlation. **F**, H&E staining and immunohistochemical analysis of RIP-3 and MLKL proteins were performed in muscle sections from a representative patient with IMNM before and after 6 months of combined treatment with glucocorticoid, tacrolimus, tocilizumab, and intravenous immunoglobulin. Original magnification × 200. See Figure 1 for other definitions.* Color figure can be viewed in the online issue, which is available at http://onlinelibrary.wiley.com/doi/10.1002/art.42071/abstract.

*[Correction added on 20 May 2022 after first online publication: In the legend of Figure 2E, "Spearman's correlation test" was changed to "Pearson's correlation."]

Statistical analysis. Statistical analyses were performed using GraphPad Prism software version 6.01. Normally distributed data were expressed as the mean ± SD and compared using an independent Student's *t*-test. Correction for multiple testing was done by adjusting for the false discovery rate. Pearson's correlation coefficient analyses were performed to test correlations.* *P* values less than or equal to 0.05 were considered significant.

RESULTS

Overactivation of necroptosis in myositis muscle. RIP-3 and MLKL are key molecules involved in necroptosis. To investigate the activation of necroptosis in the muscle of myositis patients, we first examined the expression of RIP-3 and MLKL in 24 patients with IIM (clinical and laboratory data are shown in Table 1). Western blot analyses showed that RIP-3 and MLKL proteins were highly expressed in muscle tissue samples from patients with DM and patients with IMNM, and were largely negative in muscle tissue from healthy controls and patients with ADM (Figure 1A). In addition, the expression of phosphorylated RIP-3 and MLKL was significantly increased in patients with DM and patients with IMNM compared to that in healthy controls or in patients with ADM (Figure 1B).

We further examined the localization of RIP-3 and MLKL in myositis muscle using immunohistochemistry analysis. In muscle tissue from patients with IMNM, we observed strong sarcoplasmic immunostaining of RIP-3 and MLKL, as well as their phosphorylated forms, which was not observed in healthy controls or in patients with ADM (Figure 1C). We then utilized serial muscle sections to determine the coexpression of RIP-3 and MLKL, and found significant colocalization of RIP-3 and MLKL proteins in muscle cells (Figure 1D). Interestingly, semiquantitative analysis by Western blotting of myositis muscle tissue in total protein lysates to evaluate RIP-3 and MLKL expression revealed that the expression levels of RIP-3 significantly correlated with those of MLKL ($r = 0.75$,* $P < 0.001$; $n = 24$) (Figure 1E).

Furthermore, immunohistochemical staining of serial muscle sections from myositis patients demonstrated that positively staining MLKL cells were mainly necrotic myofibers, characterized by a pale appearance and/or hyalinized features combined with a loss of sarcolemmal integrity (coarse appearance); intriguingly, in these myofibers, the C5b–9 marker was identified (Figure 1F). Taken together, these results demonstrate that RIP-3 and MLKL proteins are highly expressed and phosphorylated in muscle affected by myositis displaying significant necrotizing features, indicating an overactivation of necroptosis in necrotic myositis muscles.

Association of RIP-3 and MLKL expression levels with severe histopathologic features in the muscle. The degrees of myofiber necrosis in myositis patients were histologically graded as 0, 1, or 2, and representative muscle sections with necrosis scores of 0, 1, and 2 are shown in Figures 2A, B, and C, respectively. We then compared the expression levels of RIP-3 and MLKL proteins in the muscle by subdividing the patients into 3 groups according to their necrosis scores. The results showed that patients with a necrosis score of 2 exhibited significantly increased expression of MLKL proteins in the muscle compared to patients with necrosis scores of 0 and 1 (Figure 2D). The expression levels of RIP-3 also tended to be higher in patients with necrosis scores of 2 than in those with necrosis scores of 0 and 1; however, the difference did not reach statistical significance (Figure 2D).

In addition, we found that RIP-3 and MLKL protein levels positively correlated with serum creatine kinase and lactate dehydrogenase levels in IIM patients (Figure 2E). Moreover, RIP-3 and MLKL protein levels were inversely correlated with the Manual Muscle Testing in 8 muscles score ($r = -0.43$, $P < 0.05$ and $r = -0.63$, $P < 0.01$, respectively) (Figure 2E).

To investigate the expression of RIP-3 and MLKL proteins in follow-up samples, immunohistochemical staining was performed on repeated muscle biopsy samples from 2 additional IMNM patients whose disease responded to treatment (clinical and laboratory data on these 2 patients are presented in Supplementary Table 1, available on the *Arthritis & Rheumatology* website at http://onlinelibrary.wiley.com/doi/10.1002/art.42071). Intriguingly, RIP-3 and MLKL protein levels were dramatically decreased after 6 months of treatment (Figure 2F).

High expression of DAMPs in the necrotic myofibers in muscle tissue from IIM patients with overactivated necroptosis. A key biologic consequence of necroptotic cell death is the release of DAMPs including HMGB1 and IL-33 (9). We next investigated whether DAMPs were aberrantly expressed in the muscles affected by myositis. Immunohistochemical analysis showed strong sarcoplasmic immunostaining of HMGB1 and IL-33 in the muscle tissue of patients with IMNM or DM, while a largely negative sarcoplasmic signal was observed in the muscle tissue of healthy controls and ADM patients (Figure 3A). In addition, staining for HMGB1 yielded positive findings in the muscle nuclei and inflammatory infiltrating cells (Figure 3A). The expression pattern of IL-33 was similar to that of HMGB1. Immunohistochemical analysis of serial muscle sections revealed colocalization of MLKL and HMGB1 (Figure 3B), indicating a release of HMGB1 by MLKL-expressing necroptotic myofibers. In addition, we found a significant decrease of sarcoplasmic HMGB1 staining in the

*[Correction added on 20 May 2022 after first online publication: Under Statistical Analysis section, the sentence "Spearman's or Pearson's correlation coefficient analyses were performed to test correlations when appropriate." was changed to "Pearson's correlation coefficient analyses were performed to test correlations." While on the second paragraph of Results section, "r = 0.804" was changed to "r = 0.75".]

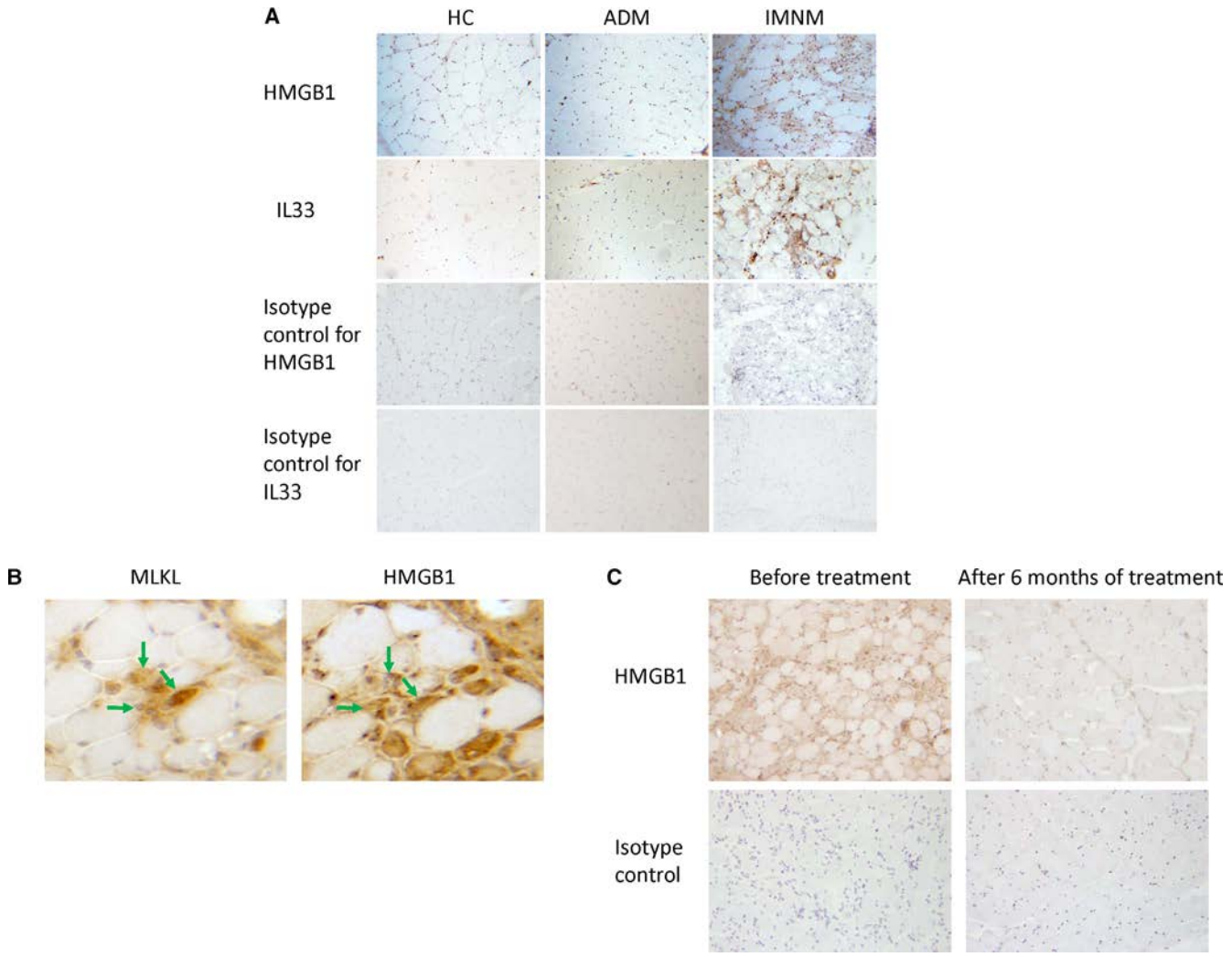

Figure 3. Expression of high mobility group box chromosomal protein 1 (HMGB1) and interleukin-33 (IL-33) in muscle tissue of patients with IIMs. **A**, Expression of HMGB1 and IL-33 in muscle tissue of patients with ADM, patients with IMNM, and healthy controls was analyzed using immunohistochemical staining. **B**, Immunohistochemistry analysis of serial sections revealed a colocalization of MLKL protein and HMGB1 in muscle cells (**arrows**). **C**, HMGB1 in muscle sections from a representative patient with IMNM was analyzed using immunohistochemical staining before and after 6 months of combined treatment with glucocorticoid, tacrolimus, tocilizumab, and intravenous immunoglobulin. Original magnification × 200. See Figure 1 for other definitions. Color figure can be viewed in the online issue, which is available at http://onlinelibrary.wiley.com/doi/10.1002/art.42071/abstract.

muscle tissue of patients with IMNM after 6 months of treatment (Figure 3C).

Promotion of cell death by TNF-induced necroptosis in C2C12 myoblasts. Since TNF is able to elicit necroptosis in various cell types in vitro, we used TNF to induce necrotic death in myoblasts. By stimulating C2C12 cells with TNF in the presence of a pan-caspase inhibitor, Z-VAD, we demonstrated obvious decreases in cell numbers using morphologic observation (Figure 4A). Cell viability assay showed that the survival percentage of C2C12 cells significantly decreased when the cells were stimulated with TNF and Z-VAD, whereas stimulation with either TNF alone or Z-VAD alone did not reduce cell survival (Figure 4B). We further used Nec-1s, an inhibitor of necroptosis, to rescue C2C12 cells stimulated with TNF and Z-VAD, and found that Nec-1s significantly increased cell survival (Figures 4A and B).

Consistently, using flow cytometry analysis, we observed that stimulation with TNF and Z-VAD caused a higher percentage of PI-positive cells, and treatment with the Nec-1s inhibitor reversed the augmented cell death induced by TNF (Figure 4C). In addition, Western blot analysis revealed that MLKL and phosphorylated MLKL proteins were dramatically up-regulated in C2C12 cells stimulated with TNF and Z-VAD, but did not increase with the addition of Nec-1s (Figures 4D and E). These results demonstrate that TNF induced the overactivation of necroptosis

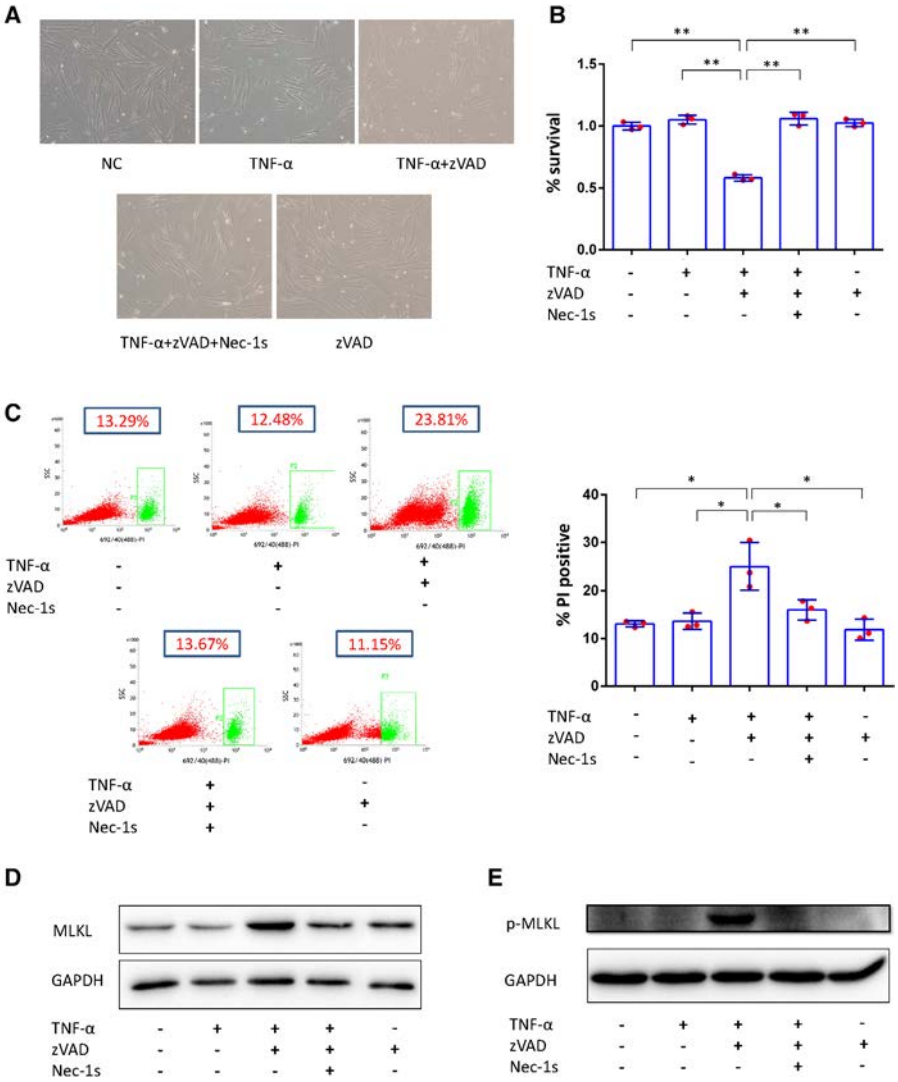

Figure 4. In vitro study of tumor necrosis factor (TNF)–induced necroptosis in C2C12 myoblast cells. Cultured C2C12 cells were treated with TNF, with TNF plus Z-VAD, with TNF plus Z-VAD plus necrostatin-1s (Nec-1s), or with Z-VAD alone. **A**, Cells were observed for morphologic changes at 24 hours after treatment. **B**, A cell viability assay showed that the percentage of surviving C2C12 cells significantly decreased when the cells were stimulated with TNF plus Z-VAD, compared to that in the negative controls (NC) or cells stimulated with TNF alone, with TNF plus Z-VAD plus Nec-1s, or with Z-VAD alone. **C**, Flow cytometry analysis revealed that stimulation of the C2C12 cells with TNF plus Z-VAD caused a higher percentage of cells staining positive for propidium iodide (PI) compared to that in the negative controls or cells stimulated with TNF alone, with TNF plus Z-VAD plus Nec-1s, or with Z-VAD alone. Symbols represent individual cell treatment; bars show the mean ± SD. **D** and **E**, Western blot analysis showed that MLKL and phosphorylated MLKL proteins were significantly up-regulated in C2C12 cells stimulated with TNF plus Z-VAD, compared to that in the negative controls or cells stimulated with TNF alone, with TNF plus Z-VAD plus Nec-1s, or with Z-VAD alone. * = adjusted $P < 0.05$; ** = adjusted $P < 0.001$. Color figure can be viewed in the online issue, which is available at http://onlinelibrary.wiley.com/doi/10.1002/art.42071/abstract.

in C2C12 myoblasts and consequently resulted in an increase in necrotic cell death.

MLKL-knockdown in C2C12 myoblasts and resistance to necroptosis. Next, we generated a C2C12 cell line with MLKL knockdown using the CRISPR/Cas9 gene editing system. As shown in Figure 5A, the expression of MLKL protein in sgRNA-MLKL–transfected C2C12 cells was significantly decreased. Treatment of MLKL-knockdown C2C12 cells with TNF in the presence of Z-VAD only slightly reduced cell survival compared to the reduction of survival in control cells with this treatment. Cell viability was significantly higher in MLKL-knockdown C2C12 cells than in control C2C12 cells when stimulated with TNF and Z-VAD (Figure 5B).

DISCUSSION

In the present study, we demonstrated that key molecules participating in necroptosis machinery were highly expressed in the muscle tissue of IIM patients with significant features of

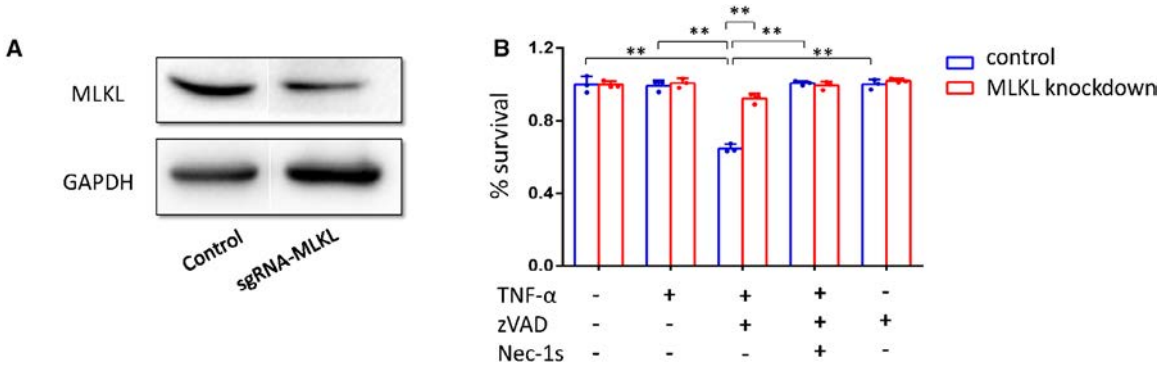

Figure 5. Resistance to necroptotic cell death observed among C2C12 myoblasts with knockdown of mixed-lineage kinase domain–like (MLKL) protein using single-guide RNA (sgRNA). **A**, The CRISPR/Cas9 gene editing system was used for MLKL gene knockdown in C2C12 cells. Western blot analysis revealed down-regulation of MLKL protein expression following sgRNA knockdown. **B**, Cell viability analysis showed higher cell survival rates among MLKL-knockdown C2C12 cells when the cells were stimulated with TNF plus Z-VAD, as compared to survival rates among control C2C12 cells receiving the same treatments. Symbols represent individual cell treatment; bars show the mean ± SD. ** = adjusted $P < 0.001$. Color figure can be viewed in the online issue, which is available at http://onlinelibrary.wiley.com/doi/10.1002/art.42071/abstract.

myofiber necrosis. The expression levels of RIP-3 and MLKL proteins were significantly correlated with the severity of clinical and pathologic muscle damage in patients with IIM. In vitro investigation of C2C12 myoblasts demonstrated that overactivation of necroptosis resulted in a significant increase in necrotic cell death. In addition, treatment with necroptosis inhibitor or knockdown of MLKL prevented C2C12 cells from undergoing necroptosis-induced cell death.

Muscle damage is a prominent feature of IIM; however, the underlying mechanism has not yet been fully clarified. Immune-related and nonimmune mechanisms have been highlighted in previous studies (17). Recently, mitochondrial dysfunction in muscle tissue was found to contribute to the pathogenesis of myositis (18,19). These studies suggest that the underlying mechanisms that mediate muscle damage and dysfunction are multiple and complex. Morphologically, there are 3 distinct major types of cell death: apoptosis, autophagic cell death, and necrosis (20). Although classic apoptotic cell death is rarely seen in muscle affected by myositis (2), overactivated autophagy has been demonstrated to be a mechanism mediating muscle damage in myositis (4). However, the molecular pathways that control myofiber necrosis have not been comprehensively studied. Recently, Liu et al reported that PKM2-dependent glycolysis could promote muscle cell pyroptosis, indicating a role of pyroptosis in the muscle damage characteristic of IIMs (21). In the present study, we investigated the recently well-characterized programmed cell death, necroptosis, and revealed its significant role in the myofiber necrosis of myositis.

Since the concept of programmed necrosis was raised and the term necroptosis was introduced (22), necrosis is no longer considered a purely accidental and passive cell death subroutine. Suppression of necroptosis is important for normal development and tissue homeostasis (8). Overactivated necroptosis has been reported in many types of diseases affecting the tissue, including ischemia–reperfusion injury, neurodegenerative diseases, and inflammation (8). Intriguingly, necroptosis has also recently been found to be dysregulated in autoimmune diseases (23–26), suggesting that necroptosis plays a vital role in autoimmune diseases by controlling the fate of a variety of cells.

To our knowledge, the present study is the first attempt to investigate the dysregulation of necroptosis in IIMs. In addition to the increased expression of RIP-3 and MLKL, we demonstrated up-regulation of phosphorylated RIP-3 and MLKL proteins, which are key executors of necroptosis and directly mediate necroptotic cell death, in muscle affected by myositis. Thus, our data provide significant evidence for the overactivation of necroptosis in IIMs. In addition, we demonstrated a significant correlation of RIP-3 and MLKL expression with the severity of clinical and pathologic muscle damage in patients with IIM. Notably, we found a dramatically decreased expression of RIP-3 and MLKL proteins in patients after 6 months of successful treatment. These data suggest that necroptosis-related molecules are promising biologic markers for IIMs, and that necroptosis has a crucial role in controlling myofiber necrosis.

DM and IMNM are believed to be 2 distinct entities in IIMs (10), which show different clinical manifestations and pathologic features. RNA-sequencing studies have demonstrated that interferon (IFN) pathways are differentially activated in different myositis subtypes. Within these subtypes, DM is characterized by high levels of IFN-inducible genes, while relatively low activation of the IFN pathway is shown in IMNM (27), therefore suggesting a different disease pathogenesis. Of note, a recent study using animal models demonstrated that the immune response to the DM-specific autoantigen transcriptional intermediary factor 1γ (TIF1γ) can result in experimental myositis (28). It was found that adoptive transfer of TIFγ-specific CD8+ T cells caused myositis in recipient mice, while transfer of TIFγ-specific IgG did not (28).

In contrast, passive transfer of IgG from IMNM patients with anti-SRP or anti-HMGCR autoantibodies successfully provoked

muscle deficiency in mice (7). Thus, these animal studies indicate that DM and IMNM have a different pathogenesis. However, in the present study, we observed no difference in the expression levels of RIP-3 and MLKL in muscle tissue from patients with DM compared to muscle tissue from patients with IMNM, suggesting that necroptosis has a similar extent of activation in DM and IMNM. It has also been reported that necroptosis is activated in mouse and human dystrophin-deficient muscles (29). Therefore, as a form of downstream cell death, necroptosis may be extensively activated in various types of myopathies. Our data suggest the broader possibility of targeting necroptosis as a therapeutic strategy for distinct subtypes of IIMs.

The initiators of necroptosis include death receptors, pathogen-recognition receptors, and nucleic acid–sensing protein ZBP1 (30). To date, TNF receptor type 1 (TNFRI)–initiated necroptosis is the most extensively characterized model of programmed necrosis. The association of TNFRI with TNF trimer leads to distinct cell fates, including cell survival, apoptosis, and necroptosis (8). Under conditions in which caspase 8 activity is inhibited, RIP-1 interacts with RIP-3 and MLKL; consequently, RIP-3 and MLKL are phosphorylated and translocated to the plasma membrane, leading to membrane permeabilization and activation of necroptosis.

In our in vitro cell culture experiments, we used TNF to induce C2C12 necroptosis in the presence of the pan-caspase inhibitor Z-VAD, which inhibits caspase 8 activity. As a result, we observed significantly decreased cell survival in C2C12 cells. In addition, TNF-induced C2C12 necroptosis could be prevented by treatment with Nec-1s or knockdown of MLKL expression. Together with early studies showing a high expression of TNF and its receptors (TNFRI and TNFRII) in the muscle tissue of IIM patients (31), our data indicate a role of TNF-induced necroptosis in IIM. Further clarification of the upstream pronecrotic signal transduction pathway may help define new therapeutic targets for the treatment of IIMs.

HMGB1 has been found to be highly expressed in the muscle of IIM patients (32), and has also been found to be significantly reduced after treatment with high-dose prednisolone (33). Additional in vitro studies have demonstrated that HMGB1 can accelerate muscle fatigue and induce major histocompatibility complex class I expression in muscle fibers by interacting with its receptor, Toll-like receptor 4 (34). More recently, Day et al showed that sarcoplasmic HMGB1 expression correlated with muscle weakness and histologic myonecrosis, inflammation, regeneration, and autophagy in patients with IIM (35). In the present study, we found similar patterns of HMGB1 expression in the muscle tissue of patients with IIM. Additionally, we observed significantly decreased sarcoplasmic HMGB1 expression after successful longitudinal treatment of muscles affected by IMNM. Using immunohistochemical staining of serial muscle sections, we demonstrated the colocalization of HMGB1 with MLKL, indicating a release of HMGB1 by muscle cells undergoing necroptotic death. As a prototypical DAMP, HMGB1 can be passively released by somatic cells undergoing necroptosis-caused cytoplasmic membrane destruction (36). Thus, our findings suggest that necroptotic muscle fibers are important sources of HMGB1, which may consequently mediate or accelerate muscle inflammation in IIM.

Our study has some limitations. First, a relatively small number of patients were examined for expression of RIP-3 and MLKL, and the protein expression profile may be heterogeneous among patients, especially the ADM group, due to their distinct serologic autoantibodies. Second, additional studies are needed to determine the upstream pronecrotic molecules that activate necroptosis in muscle affected by myositis. Another limitation is that our study did not include any disease controls; therefore we could not conclude whether necroptosis of myofibers is specific to patients with IIM.

Taken together, the findings of our study demonstrate that overactivated necroptosis significantly contributes to muscle damage in IIM. These findings provide novel insights into the pathologic mechanism of IIM-related myofiber necrosis and may open new therapeutic avenues for treating these diseases.

AUTHOR CONTRIBUTIONS

All authors were involved in drafting the article or revising it critically for important intellectual content, and all authors approved the final version to be published. Dr. Wang had full access to all of the data in the study and takes full responsibility for the integrity of the data and the accuracy of the data analysis.

Study conception and design. Peng, Wang.

Acquisition of data. Peng, Y. Zhang, Liu, Liang, Li, Tian, L. Zhang, Yang, Lu, Wang.

Analysis and interpretation of data. Peng, Y. Zhang, Liu, Liang, L. Zhang, Yang, Lu, Wang.

REFERENCES

1. Dalakas MC. Inflammatory muscle diseases. N Engl J Med 2015;372:1734–47.
2. Nagaraju K, Casciola-Rosen L, Rosen A, Thompson C, Loeffler L, Parker T, et al. The inhibition of apoptosis in myositis and in normal muscle cells. J Immunol 2000;164:5459–65.
3. Nagaraju K, Casciola-Rosen L, Lundberg I, Rawat R, Cutting S, Thapliyal R, et al. Activation of the endoplasmic reticulum stress response in autoimmune myositis: potential role in muscle fiber damage and dysfunction. Arthritis Rheum 2005;52:1824–35.
4. Alger HM, Raben N, Pistilli E, Francia DL, Rawat R, Getnet D, et al. The role of TRAIL in mediating autophagy in myositis skeletal muscle: a potential nonimmune mechanism of muscle damage. Arthritis Rheum 2011;63:3448–57.
5. Pandya JM, Venalis P, Al-Khalili L, Shahadat Hossain M, Stache V, Lundberg IE, et al. CD4+ and CD8+ CD28^{null} T cells are cytotoxic to autologous muscle cells in patients with polymyositis. Arthritis Rheumatol 2016;68:2016–26.
6. Arouche-Delaperche L, Allenbach Y, Amelin D, Preusse C, Mouly V, Mauhin W, et al. Pathogenic role of anti-signal recognition protein and anti-3-hydroxy-3-methylglutaryl-CoA reductase antibodies in necrotizing myopathies: myofiber atrophy and impairment of muscle regeneration in necrotizing autoimmune myopathies. Ann Neurol 2017;81:538–48.

7. Bergua C, Chiavelli H, Allenbach Y, Arouche-Delaperche L, Arnoult C, Bourdenet G, et al. In vivo pathogenicity of IgG from patients with anti-SRP or anti-HMGCR autoantibodies in immune-mediated necrotising myopathy. Ann Rheum Dis 2019;78:131–9.
8. Zhou W, Yuan J. Necroptosis in health and diseases. Semin Cell Dev Biol 2014;35:14–23.
9. Silke J, Rickard JA, Gerlic M. The diverse role of RIP kinases in necroptosis and inflammation. Nat Immunol 2015;16:689–97.
10. Lundberg IE, Tjärnlund A, Bottai M, Werth VP, Pilkington C, Visser M, et al. 2017 European League Against Rheumatism/American College of Rheumatology classification criteria for adult and juvenile idiopathic inflammatory myopathies and their major subgroups. Arthritis Rheumatol 2017;69:2271–82.
11. Hoogendijk JE, Amato AA, Lecky BR, Choy EH, Lundberg IE, Rose MR, et al. 119th ENMC international workshop: trial design in adult idiopathic inflammatory myopathies, with the exception of inclusion body myositis, 10–12 October 2003, Naarden, The Netherlands. Neuromuscul Disord 2004;14:337–345.
12. Varsani H, Charman SC, Li CK, Marie SK, Amato AA, Banwell B, et al. Validation of a score tool for measurement of histological severity in juvenile dermatomyositis and association with clinical severity of disease. Ann Rheum Dis 2015;74:204–10.
13. Wedderburn LR, Varsani H, Li CK, Newton KR, Amato AA, Banwell B, et al. International consensus on a proposed score system for muscle biopsy evaluation in patients with juvenile dermatomyositis: a tool for potential use in clinical trials. Arthritis Rheum 2007;57:1192–201.
14. Peng QL, Zhang YL, Shu XM, Yang HB, Zhang L, Chen F, et al. Elevated serum levels of soluble CD163 in polymyositis and dermatomyositis: associated with macrophage infiltration in muscle tissue. J Rheumatol 2015;42:979–87.
15. Allenbach Y, Arouche-Delaperche L, Preusse C, Radbruch H, Butler-Browne G, Champtiaux N, et al. Necrosis in anti-SRP(+) and anti-HMGCR(+) myopathies: role of autoantibodies and complement. Neurology 2018;90:e507–17.
16. Zhang L, Xia Q, Li W, Peng Q, Yang H, Lu X, et al. The RIG-I pathway is involved in peripheral T cell lymphopenia in patients with dermatomyositis. Arthritis Res Ther 2019;21:131.
17. Rayavarapu S, Coley W, Kinder TB, Nagaraju K. Idiopathic inflammatory myopathies: pathogenic mechanisms of muscle weakness. Skelet Muscle 2013;3:13.
18. Meyer A, Laverny G, Allenbach Y, Grelet E, Ueberschlag V, Echaniz-Laguna A, et al. IFN-β-induced reactive oxygen species and mitochondrial damage contribute to muscle impairment and inflammation maintenance in dermatomyositis. Acta Neuropathol 2017;134:655–66.
19. Boehler JF, Horn A, Novak JS. Mitochondrial dysfunction and role of harakiri in the pathogenesis of myositis. J Pathol 2019;249:215–26.
20. Green DR, Llambi F. Cell death signaling. Cold Spring Harb Perspect Biol 2015;7:a006080.
21. Liu D, Xiao Y, Zhou B, Gao S, Li L, Zhao L, et al. PKM2-dependent glycolysis promotes skeletal muscle cell pyroptosis by activating the NLRP3 inflammasome in dermatomyositis/polymyositis. Rheumatology (Oxford) 2021;60:2177–89.
22. Degterev A, Huang Z, Boyce M, Li Y, Jagtap P, Mizushima N, et al. Chemical inhibitor of nonapoptotic cell death with therapeutic potential for ischemic brain injury. Nat Chem Biol 2005;1:112–9.
23. Guo C, Fu R, Zhou M, Wang S, Huang Y, Hu H, et al. Pathogenesis of lupus nephritis: RIP3 dependent necroptosis and NLRP3 inflammasome activation. J Autoimmun 2019;103:102286.
24. Zhang M, Jie H, Wu Y, Han X, Li X, He Y, et al. Increased MLKL mRNA level in the PBMCs is correlated with autoantibody production, renal involvement, and SLE disease activity. Arthritis Res Ther 2020;22:239.
25. Schreiber A, Rousselle A, Becker JU, von Massenhausen A, Linkermann A. Necroptosis controls NET generation and mediates complement activation, endothelial damage, and autoimmune vasculitis. Proc Natl Acad Sci U S A 2017;114:E9618–25.
26. Polykratis A, Martens A, Eren RO, Shirasaki Y, Yamagishi M, Yamaguchi Y, et al. A20 prevents inflammasome-dependent arthritis by inhibiting macrophage necroptosis through its ZnF7 ubiquitin-binding domain. Nature Cell Biology 2019;21:731–42.
27. Pinal-Fernandez I, Casal-Dominguez M, Derfoul A, Pak K, Plotz P, Miller FW, et al. Identification of distinctive interferon gene signatures in different types of myositis. Neurology 2019;93:e1193–204.
28. Okiyama N, Ichimura Y, Shobo M, Tanaka R, Kubota N, Saito A, et al. Immune response to dermatomyositis-specific autoantigen, transcriptional intermediary factor 1γ can result in experimental myositis. Ann Rheum Dis 2021;80:1201–8.
29. Morgan JE, Prola A, Mariot V, Pini V, Meng J, Hourde C, et al. Necroptosis mediates myofibre death in dystrophin-deficient mice. Nat Commun 2018;9:3655.
30. Kist M, Vucic D. Cell death pathways: intricate connections and disease implications. The EMBO J 2021;40:e106700.
31. De Bleecker JL, Meire VI, Declercq W, Van Aken EH. Immunolocalization of tumor necrosis factor-α and its receptors in inflammatory myopathies. Neuromuscul Disord 1999;9:239–46.
32. Grundtman C, Bruton J, Yamada T, Ostberg T, Pisetsky DS, Harris HE, et al. Effects of HMGB1 on in vitro responses of isolated muscle fibers and functional aspects in skeletal muscles of idiopathic inflammatory myopathies. FASEB J 2010;24:570–8.
33. Ulfgren AK, Grundtman C, Borg K, Alexanderson H, Andersson U, Harris HE, et al. Down-regulation of the aberrant expression of the inflammation mediator high mobility group box chromosomal protein 1 in muscle tissue of patients with polymyositis and dermatomyositis treated with corticosteroids. Arthritis Rheum 2004;50:1586–94.
34. Zong M, Bruton JD, Grundtman C, Yang H, Li JH, Alexanderson H, et al. TLR4 as receptor for HMGB1 induced muscle dysfunction in myositis. Ann Rheum Dis 2013;72:1390–9.
35. Day J, Otto S, Cash K, Eldi P, Hissaria P, Proudman S, et al. Aberrant expression of high mobility group box protein 1 in the idiopathic inflammatory myopathies. Front Cell Dev Biol 2020;8:226.
36. Murao A, Aziz M, Wang H, Brenner M. Release mechanisms of major DAMPs. Apoptosis 2021;26:152–62.

Arthritis & Rheumatology
Vol. 74, No. 6, June 2022, pp 1059–1069
DOI 10.1002/art.42055

American College of Rheumatology
Empowering Rheumatology Professionals

Intensive Serum Urate Lowering With Oral Urate-Lowering Therapy for Erosive Gout: A Randomized Double-Blind Controlled Trial

Nicola Dalbeth,[1] Anthony J. Doyle,[2] Karen Billington,[3] Greg D. Gamble,[1] Paul Tan,[1] Kieran Latto,[1] Thrishila Parshu Ram,[1] Ravi Narang,[1] Rachel Murdoch,[1] David Bursill,[1] Borislav Mihov,[1] Lisa K. Stamp,[4] and Anne Horne[1]

Objective. To determine whether a therapeutic approach of intensive serum urate lowering results in improved bone erosion scores in patients with erosive gout.

Methods. We undertook a 2-year, double-blind randomized controlled trial of 104 participants with erosive gout who were receiving serum urate–lowering therapy orally and who had serum urate levels of ≥0.30 mmoles/liter at baseline. Participants were randomly assigned to either an intensive serum urate target of <0.20 mmoles/liter or a standard target of <0.30 mmoles/liter (considered the standard according to rheumatology guidelines). Oral serum urate–lowering therapy was titrated to target using a standardized protocol (with the maximum approved doses of allopurinol, probenecid, febuxostat, and benzbromarone). The primary end point was the total computed tomography (CT) bone erosion score. Outcome Measures in Rheumatology (OMERACT) gout core outcome domains were secondary end points.

Results. Although the serum urate levels were significantly lower in the intensive target group compared to the standard target group over the study period ($P = 0.002$), fewer participants in the intensive target group achieved the randomized serum urate target level by year 2 (62% versus 83% of patients in the standard target group; $P < 0.05$). The intensive target group required higher doses of allopurinol (mean ± SD 746 ± 210 mg/day versus 497 ± 186 mg/day; $P < 0.001$) and received more combination therapy ($P = 0.0004$) compared to the standard target group. We observed small increases in CT bone erosion scores in both serum urate target groups over 2 years, with no between-group difference ($P = 0.20$). OMERACT core outcome domains (gout flares, tophi, pain, patient's global assessment of disease activity, health-related quality of life, and activity limitation) improved in both groups over 2 years, with no between-group differences. Adverse event and serious adverse event rates were similar between the groups.

Conclusion. Compared to a serum urate target of <0.30 mmoles/liter, more intensive serum urate lowering is difficult to achieve with an oral urate-lowering therapy. Intensive serum urate lowering leads to a high medication burden and does not improve bone erosion scores in patients with erosive gout.

INTRODUCTION

Bone erosion is the most common feature of structural joint damage in severe gout (1), leading to joint deformity and disability (2,3). Monosodium urate (MSU) crystal deposition is strongly implicated in the development of bone erosion in gout. Advanced imaging studies have demonstrated a close relationship between MSU crystals and sites of bone erosion (4,5). In laboratory studies, MSU crystals have exhibited a profound inhibitory effect on the function and viability of bone-forming osteoblasts and osteocytes (6,7). Collectively, these findings indicate that dissolution of MSU crystals may be an important strategy to prevent or heal bone erosion in gout.

Australian New Zealand Clinical Trials Registry no.: 12615001219572.
Supported by the Health Research Council of New Zealand (grant 15-576).
[1]Nicola Dalbeth, MD, FRACP, Greg D. Gamble, MSc, Paul Tan, BSc, Kieran Latto, BSc, Thrishila Parshu Ram, MSc, Ravi Narang, MBChB, Rachel Murdoch, FRACP, David Bursill, FRACP, Borislav Mihov, BPhty, Anne Horne, MBChB: University of Auckland, Auckland, New Zealand; [2]Anthony J. Doyle, FRANZCR: Auckland District Health Board and University of Auckland, Auckland, New Zealand; [3]Karen Billington, MB BCh BAO: Auckland District Health Board, Auckland, New Zealand; [4]Lisa K. Stamp, PhD, FRACP: University of Otago, Christchurch, New Zealand.

Author disclosures are available at https://onlinelibrary.wiley.com/action/downloadSupplement?doi=10.1002%2Fart.42055&file=art42055-sup-0001-Disclosureform.pdf.
Address correspondence to Nicola Dalbeth, MD, FRACP, Department of Medicine, Faculty of Medical and Health Sciences, University of Auckland, 85 Park Road, Grafton, Auckland, New Zealand. Email: n.dalbeth@auckland.ac.nz.
Submitted for publication September 13, 2021; accepted in revised form December 16, 2021.

A previous clinical trial has shown that allopurinol dose escalation to achieve a serum urate target of <0.36 mmoles/liter (6 mg/dl) can reduce the progression of bone erosion in gout (8). However, improved erosion scores were not observed in that study. In contrast, there are emerging data indicating that intensive serum urate lowering may lead to healing of erosions in gout. In a small longitudinal study of patients receiving pegloticase, a treatment that leads to profound reductions in serum urate levels (9), filling-in of bone erosion was observed over a 1-year period (10). On plain radiography, bone erosion scores, but not joint space narrowing scores, significantly improved over this period. This effect was observed in patients with mean serum urate levels of <0.20 mmoles/liter (3.3 mg/dl) over the 1-year treatment period.

While promising, pegloticase is unlikely to be a widely adopted therapy for the management of erosive gout due to its lack of availability outside the US and the need for intravenous infusions every 2 weeks. Therefore, there is a clinical need to identify more feasible strategies for intensive urate-lowering therapy using oral medications, and it needs to be determined whether these strategies allow for structural improvement in patients with gout.

The 2012 American College of Rheumatology (ACR) gout management guidelines and the 2016 updated European Alliance of Associations for Rheumatology (EULAR) gout management guidelines both recommended that the serum urate target for patients with severe gout, including those with chronic arthropathy, is <0.30 mmoles/liter (5 mg/dl) (11,12). This serum urate target was also endorsed in the 2017 British Society for Rheumatology guideline for the management of gout (13). Achievement of this serum urate target leads to gradual reduction in MSU crystal deposition (14,15). The aim of this study was to determine whether intensive oral urate-lowering therapy to maintain serum urate concentrations of <0.20 mmoles/liter results in improved bone erosion scores in erosive gout, compared to the serum urate target of <0.30 mmoles/liter.

PATIENTS AND METHODS

Study design and approval. This was a 2-year, double-blind randomized controlled trial of 104 participants with erosive gout who were receiving oral urate-lowering therapy and had serum urate levels of ≥0.30 mmoles/liter. Participants were randomly assigned to reach a serum urate target of <0.20 mmoles/liter (intensive target group) or <0.30 mmoles/liter (standard target group as recommended in rheumatology society guidelines [11–13]). The primary end point was the total computed tomography (CT) bone erosion score.

The study was approved by the Southern Health and Disability Ethics Committee (approval no. 15/STH/108) and all participants provided written informed consent. The trial was also approved by the New Zealand Ministry of Health Standing Committee on Therapeutic Trials (approval no. 15/SCOTT/68). The study was prospectively registered as a clinical trial with the Australian New Zealand Clinical Trials Registry (ACTRN: 12615001219572).

Data availability. Following publication, data are available from the corresponding author upon reasonable request.

Participants. Participants were recruited from rheumatology clinics and hospitals and through advertising to general practitioners and the public in Tāmaki Makaurau/Auckland, Aotearoa/New Zealand. The first screening visit was February 23, 2016, and the final year 2 study visit was June 29, 2020. Inclusion criteria included gout, defined according to the 2015 ACR/EULAR classification criteria (16), at least 1 bone erosion on plain radiography of the feet, age >18 years, ability to provide informed consent, currently receiving treatment with an oral urate-lowering agent, and serum urate concentrations of ≥0.30 mmoles/liter.

Exclusion criteria included stage 4 or stage 5 chronic kidney disease (estimated glomerular filtration rate [eGFR] <30 ml/minute/1.73 m^2), current pregnancy or breastfeeding, an unstable systemic medical condition (e.g., New York Heart Association stage IV heart failure, recent myocardial infarction, advanced cancer), treatment with azathioprine (due to potential interactions with both allopurinol and febuxostat), treatment with warfarin, a diagnosis of rheumatoid arthritis (RA) or other erosive autoimmune arthritis, a diagnosis of Parkinson's disease, and presence of dementia.

Protocol. All study visits took place at a clinical research facility in a tertiary medical center. Potential participants attended a screening visit, and if they were considered eligible for the study, they attended the baseline study visit within 2 weeks of the screening visit. At the baseline visit, participants were randomized into either the intensive serum urate target group or standard serum urate target group using a random block randomization algorithm. All randomized participants began dose escalation/alteration of urate-lowering therapy according to a standardized protocol.

Urate-lowering therapy was adjusted according to the standard protocol to reach the target serum urate level of <0.20 mmoles/liter (intensive target group) or <0.30 mmoles/liter (standard target group), according to study group allocation. Participants attended monthly visits for serum urate testing, safety monitoring, and urate-lowering therapy intensification until the treatment target had been reached and maintained for 3 consecutive months. Thereafter, participants attended scheduled study visits every 3 months. Once the treatment target was maintained for 3 consecutive months, no further changes were made to the medication regimen, unless medication-related adverse events (AEs) developed. If changes to therapy during the escalation phase led to serum urate levels of <0.10 mmoles/liter in the intensive target group and <0.20 mmoles/liter in the standard target group, the medication dose was reduced.

The urate-lowering therapy escalation protocol was standardized as follows: 1) in those in whom allopurinol was well tolerated, the allopurinol dose was increased every month by 50–100 mg daily (increment dependent on the eGFR), to a maximum dose of 900 mg daily; 2) if the treatment target was not reached with maximum tolerated allopurinol monotherapy, probenecid was added at 500 mg twice daily, increasing to 1 gm twice daily after 1 month if needed to achieve the target; 3) if the treatment target was not reached with allopurinol/probenecid combination therapy, these treatments were replaced with febuxostat at 80 mg daily, increasing to a maximum dose of 120 mg daily; and 4) if the treatment target was not reached with febuxostat, benzbromarone was prescribed at 100 mg daily in combination with allopurinol, if tolerated (at the previously tolerated allopurinol dose). This protocol represented the maximum approved dosing of available oral urate-lowering therapies in Aotearoa/New Zealand. In the case of previous kidney stones, uricosuric therapy (probenecid and benzbromarone) was not used. Standard contraindications according to the prescribing information for each agent were assessed on an individual patient basis when considering changes to urate-lowering therapy, consistent with best clinical practice.

A protocol amendment occurred in November 2017, following the US Food and Drug Administration warning about the cardiovascular safety of febuxostat in response to the Cardiovascular Safety of Febuxostat and Allopurinol in Participants With Gout and Cardiovascular Comorbidities trial (17). Following this alert, febuxostat was only used when all other urate-lowering agents were not tolerated or were contraindicated. This resulted in 6 participants switching medications from febuxostat to another medication; 1 participant continued receiving febuxostat, as all other urate-lowering agents were not tolerated or were contraindicated.

In both groups, antiinflammatory prophylaxis against gout flares using colchicine (0.5 mg once daily) or naproxen (250 mg twice daily) was used for those who had experienced gout flares in the preceding 3 months and during dose escalation of urate-lowering therapy, in accordance with gout management guidelines (12,18). Under exceptional circumstances, low-dose prednisone (≤5 mg/day) was allowed as gout flare prophylaxis. The choice of antiinflammatory prophylaxis was at the discretion of the assessing clinician.

Patients were randomized using a random block randomization algorithm. Briefly, a random number (Microsoft Excel 2003) was assigned to each potential participant. Participants were sorted according to their random number within number blocks of random size to ensure that, should the trial terminate early, the potential for imbalance was kept to a minimum. Those with random numbers in the bottom half of the block were allocated to the intensive target group, and the rest to the standard target group.

To ensure blinding, only the statistician (GDG) and 1 study member (BM) who advised on dose adjustment according to the study protocol had access to the serum urate results and treatment allocation, and neither of these individuals had contact with participants. Participants and all other study staff were blinded with regard to the serum urate results and the serum urate target allocation throughout the trial.

Study end points. The primary end point was the degree of change from baseline in CT bone erosion score in both feet, measured at baseline, year 1, and year 2. Key secondary end points were mean serum urate concentration, percentage of participants who reached the allocated serum urate target, change from baseline in plain radiographic damage score, and frequency of AEs, including serious AEs (SAEs). Additional secondary end points were the degree of change from baseline in Outcome Measures in Rheumatology (OMERACT) core outcome domains for long-term gout studies (19) (area of up to 3 index tophi measured using digital Vernier calipers) (20), subcutaneous tophus count, number of gout flares in the preceding 3 months, pain (100-mm visual analog scale [VAS]) and patient's global assessment of disease activity (0–5–point Likert scale), health-related quality of life using the EuroQol 5-domain-3L (EQ-5D-3L) questionnaire (indexed to Aotearoa/New Zealand population norms [21]), and activity limitation using the Health Assessment Questionnaire II (22). Tophus measures and patient-reported outcomes were recorded every 6 months, and gout flare frequency was measured every 3 months.

Imaging acquisition and scoring. CT images of both feet were obtained at the beginning of the study and at the year 1 and year 2 visits. The participants were positioned feet first, supine, with the feet in a plantar flexion position. Both ankles and feet were scanned axially in one helical acquisition as previously described (23).

CT bone erosions were scored using a CT bone erosion scoring method, based on the RA Magnetic Resonance Imaging Score for erosion (24), and were validated for gout (23). The gout CT bone erosion scoring system includes erosions of the following bones scored on a semiquantitative scale of 0–10 in each foot: first metatarsal head, second, third, and fourth metatarsal base, cuboid, middle cuneiform, and distal tibia (maximum total score 140 points). Sets of CT scans from the baseline visit, year 1, and year 2 were scored in known order by 2 musculoskeletal radiologists (AJD and KB) who scored the scans separately and were blinded with regard to the treatment allocation and each other's scores. The mean scores from both readers were used in the analysis.

Plain radiography of the hands and both feet were obtained at the beginning of the study and at the year 1 and year 2 visits and were scored for erosions and joint space narrowing using a modified version of the Sharp/van der Heijde scoring method

(25) validated for gout (1). Sets of plain radiographs from the baseline visit, year 1, and year 2 were scored in known order by a rheumatologist (ND) and a musculoskeletal radiologist (KB) who scored radiographs separately and were blinded with regard to the treatment allocation and each other's scores. The mean scores from the 2 readers were used in the analysis.

Identification of AEs. At each study visit, patients were asked about the occurrence of AEs. AEs and SAEs were recorded and reported according to the Common Terminology Criteria for Adverse Events classification. The New Zealand Health Research Council Data Monitoring Core Committee provided independent data safety monitoring of the trial.

Calculation of sample size and study power. The primary end point for this study (change in the CT erosion score of the foot) was used in a previous 2-year randomized controlled trial of zoledronate for bone erosion in gout (26). In the zoledronate study, the SD for the mean change in CT erosion scores in those with baseline serum urate levels of <0.30 mmoles/liter was 0.555 units. These participants had a mean ± SD serum urate level of 0.25 ± 0.039 mmoles/liter. Accordingly, with a sample size of 104 participants (assuming 20% loss to follow-up over 2 years), a 0.41-point difference in the change in CT erosion score could be detected with 90% power at the 5% significance level. Based on the mean baseline CT scores of 12.1 units in participants with a serum urate level of <0.30 mmoles/liter in the zoledronate in gout study, this represented a 3.4% difference in CT erosion scores over 2 years. In an analysis of plain radiographic scores following pegloticase treatment, the mean improvement in plain radiographic erosion score was 17.3% over 1 year (10). We anticipated that in most participants in the intensive target group in the present study, serum urate levels of <0.20 mmoles/liter would be reached. However, we recognized that this target would not be achieved in all participants. In the event that the intensive target was achieved in only 50% of participants, the study was powered to detect a 0.61-point (5%) difference in the change in CT erosion score with 90% power at the 5% significance level. Sample size estimates were made using PASS 2002 and were verified with the power procedure of SAS version 9.4.

Statistical analysis. No interim efficacy analyses were performed. All outcome data recorded over the 2-year period were included in the models. All dependent variables were normal or were rendered normal by transformation. The intensive target group and standard target groups were compared using a mixed-model approach to repeated measures in order to model the difference in the change in CT erosion scores between groups. For analysis of the change from baseline, baseline scores were included as covariates (analysis of covariance [ANCOVA]). Each outcome was modeled with 3 covariance structures (first-order autoregressive, unstructured, or compound symmetry). The model with the smallest Akaike's information criterion was

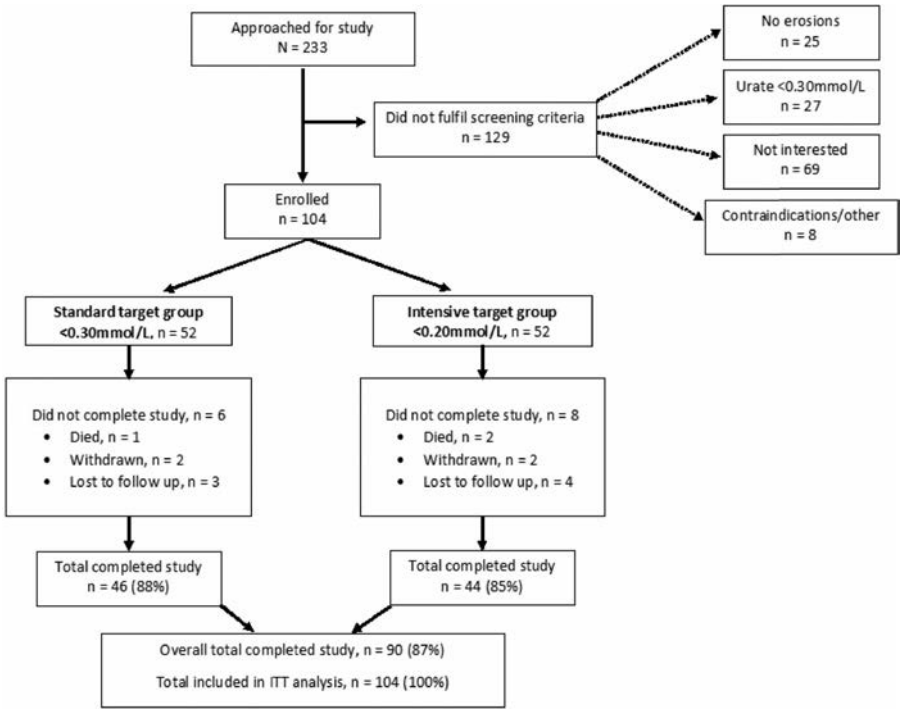

Figure 1. Disposition of the study participants throughout the trial. Included participants were randomized to either a standard serum urate–lowering target group or an intensive serum urate–lowering target group. ITT = intent-to-treat.

then chosen for analysis. If models produced Akaike's information criterion values within 2 units of each other, the simplest model (generally unstructured) was selected. Areas of up to 3 index tophi identified at the baseline visit in each participant were modeled over time using generalized estimating equations to take into account the correlation between successive measurements of the same tophus in an individual. Significant time-by-interaction effects were further investigated using prespecified comparisons between treatment groups at each time point with false discovery rate protection for multiple comparisons to maintain an overall 5% significance level for each outcome. Other than when indicated, no further adjustment for multiplicity was performed.

Sensitivity analyses were performed to investigate the influence of missing data, using a "last observation carried forward" approach and a Markov chain Monte Carlo imputation of 10 data sets. In these sensitivity analyses, data were assumed to be "missing at random."

Least squares–adjusted marginal means and 95% confidence intervals (95% CIs) from the mixed models are presented in the tables; observed means and 95% CIs or the median and interquartile range are shown in the figures. All tests were 2-tailed. Data analyses were performed on an intent-to-treat basis. Secondary per-protocol analyses were also performed, comprising only those participants with serum urate levels at the specified serum urate target at both year 1 and year 2. All data were analyzed using SAS version 9.4.

RESULTS

Participants. Disposition of the study participants is shown in Figure 1. A total of 233 patients were approached for inclusion in this study; 129 did not meet the inclusion criteria and were not recruited. There were 104 participants enrolled in the study, 52 in each group. A total of 90 participants completed the study: 44 in the intensive target group (85%) and 46 in the standard target group (88%). All participants were included in the primary intent-to-treat analysis.

Baseline demographic and clinical characteristics are shown in Table 1. The majority of participants were men, and the mean age was 61 years. The mean body mass index was >30 kg/m^2 in both groups. The mean disease duration was 19 years, and ~50% experienced a gout flare in the 3 months prior to enrollment.

Medications and serum urate lowering over the study period. Medications and serum urate data over the duration of the study are shown in Figures 2A and B. Medications at the end of the study are shown in Supplementary Table 1 (available on the *Arthritis & Rheumatology* website at http://onlinelibrary.wiley.com/doi/10.1002/art.42055). Mean and median serum urate levels at all study visits are shown in Supplementary Table 2 (http://onlinelibrary.wiley.com/doi/10.1002/art.42055).

Participants in the intensive target group experienced more changes in medication and required more combination therapy (P = 0.0004). At year 2, the mean ± SD number of medications was 1.3 ± 0.5 in the intensive target arm and

Table 1. Baseline characteristics of study participants randomized to the standard serum urate target group and those randomized to the intensive serum urate target group*

	Standard target (n = 52)†	Intensive target (n = 52)†
Age, years	62 ± 11	60 ± 14
Sex, no. (%) male	50 (96)	50 (96)
Self-reported ethnicity, no. (%) of patients		
Māori	5 (10)	7 (13)
NZ European	33 (63)	34 (65)
Other	5 (10)	4 (8)
Pacific peoples	9 (17)	7 (13)
Comorbidities, no. (%) of patients		
Type 2 diabetes	4 (8)	5 (10)
Hypertension	26 (50)	26 (50)
CVD	10 (19)	3 (6)
Kidney stones	6 (12)	6 (12)
BMI, kg/m^2	31.4 ± 5.8	32.3 ± 7.2
Gout disease duration, years	19 ± 13	19 ± 12
No. of gout flares in the preceding 3 months	1.48 ± 2.40	1.82 ± 2.61
No. (%) of patients who experienced a gout flare in the preceding 3 months	26 (50)	28 (54)
Presence of subcutaneous tophi, no. (%) of patients	33 (63)	37 (71)
No. of subcutaneous tophi	3.2 ± 4.7	4.8 ± 7.8
Index tophus area, mm^2‡	238 ± 259	214 ± 223
Pain, 100-mm VAS	1.1 ± 1.8	1.6 ± 2.5
Patient's global assessment of disease activity score	1.5 ± 1.0	1.8 ± 1.5
EQ-5D-3L index	0.72 ± 0.12	0.66 ± 0.19
HAQ-II score	0.33 ± 0.48	0.37 ± 0.52
Serum urate, mmoles/liter	0.37 ± 0.08	0.34 ± 0.10
Serum creatinine, μmoles/liter	96 ± 25	98 ± 23
eGFR, ml/minute/1.73 m^2	119 ± 49	124 ± 48
CT erosion score	8.9 ± 5.7	9.7 ± 6.9
Plain radiography erosion score	9.0 ± 9.4	11.2 ± 13.4
Plain radiography JSN score	6.4 ± 7.2	7.0 ± 8.0
Plain radiography damage score	15.4 ± 14.8	18.2 ± 20.0

* Except where indicated otherwise, values are the mean ± SD. NZ = New Zealand; CVD = cardiovascular disease; BMI = body mass index; VAS = visual analog scale; EQ-5D-3L = EuroQol 5-domain-3L; HAQ-II = Health Assessment Questionnaire II; eGFR = estimated glomerular filtration rate; CT = computed tomography; JSN = joint space narrowing.
† Standard target indicates a serum urate target of <0.30 mmoles/liter and intensive target indicates a serum urate target of <0.20 mmoles/liter.
‡ Index tophus area values are in those with at least 1 measurable index tophus at the baseline visit.

1.0 ± 0.1 in the standard target arm ($P = 0.0009$). The mean dose of allopurinol in the intensive target group was also significantly higher at week 26 ($P < 0.0001$) and remained higher throughout the trial. At the year 2 study visit, the mean ± SD dose of allopurinol was 746 ± 210 mg/day in the intensive target group and 497 ± 186 mg/day in the standard target group.

Over the study period, serum urate levels were significantly lower in the intensive target group compared to the standard target group ($P = 0.002$) (Figure 2C and Supplementary Table 2, http://onlinelibrary.wiley.com/doi/10.1002/art.42055). However, fewer participants in the intensive target group achieved the randomized serum urate target (at year 1, 53% versus 83% [$P < 0.01$]; at year 2, 62% versus 83% [$P < 0.05$]) (Figure 2D).

Primary and key secondary outcomes. Imaging outcomes for the primary intent-to-treat analysis are shown in Table 2, Figure 3, and Supplementary Table 3 (http://onlinelibrary.wiley.com/doi/10.1002/art.42055). Small increases (worsening) in CT erosion scores were observed in both groups over 2 years, with no between-group differences ($P = 0.20$). Similar findings were observed for the plain radiographic erosion scores ($P = 0.94$), plain radiographic joint space narrowing scores ($P = 0.27$), and the combined radiographic damage scores

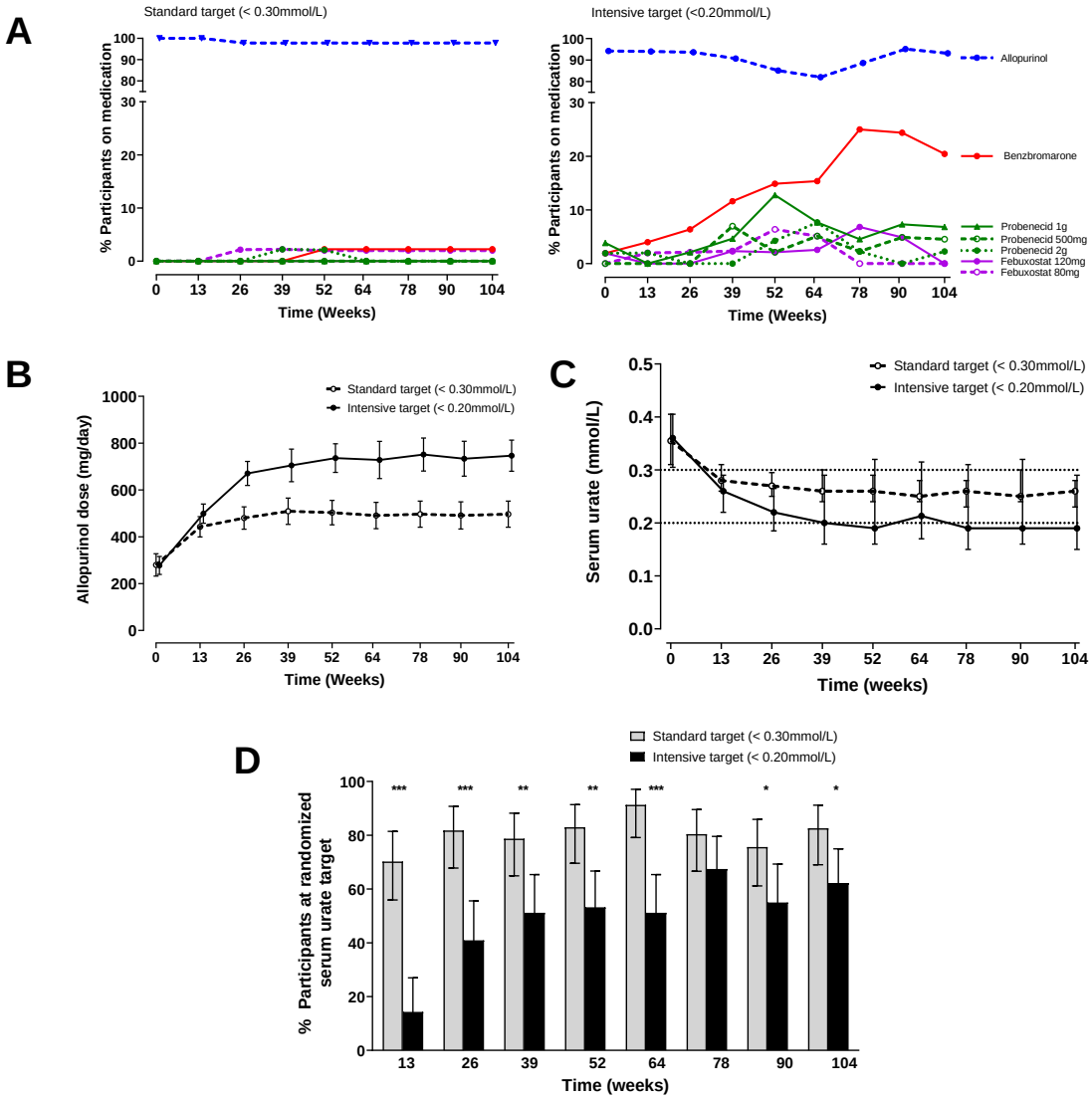

Figure 2. Medication usage and serum urate concentrations over the duration of the study. **A**, Medications in each treatment group. **B**, Allopurinol doses in the standard target group and intensive target group. Values are the observed mean and 95% confidence interval (95% CI). **C**, Serum urate concentration. Values are the observed median and interquartile range. **D**, Percentage (with 95% CI) of participants achieving randomized serum urate targets over time. * = $P < 0.05$; ** = $P < 0.01$; *** = $P < 0.001$.

Table 2. Change from baseline to year 1 and year 2 in outcomes in participants randomized to the standard serum urate target group and those randomized to the intensive serum urate target group*

	Standard target (n = 52)†	Intensive target (n = 52)†	Mean difference
CT erosion score			
Year 1	0.1 (−0.05, 0.25)	0.24 (0.09, 0.39)	0.14 (−0.07, 0.35)
Year 2	0.23 (0.07, 0.38)	0.46 (0.31, 0.62)	0.24 (0.02, 0.45)
Plain radiography erosion score			
Year 1	0.61 (0.27, 0.96)	0.66 (0.32, 1)	0.05 (−0.44, 0.53)
Year 2	0.93 (0.58, 1.28)	0.9 (0.55, 1.25)	−0.03 (−0.53, 0.46)
Plain radiography JSN score			
Year 1	0.22 (0.05, 0.39)	0.12 (−0.05, 0.29)	−0.1 (−0.34, 0.15)
Year 2	0.64 (0.46, 0.81)	0.4 (0.22, 0.57)	−0.24 (−0.49, 0.01)
Plain radiography damage score			
Year 1	0.82 (0.42, 1.23)	0.79 (0.39, 1.19)	−0.04 (−0.61, 0.54)
Year 2	1.57 (1.16, 1.99)	1.29 (0.87, 1.7)	−0.29 (−0.87, 0.3)
Gout flares in the preceding 3 months			
Year 1	−0.61 (−1, −0.21)	−0.79 (−1.19, −0.39)	−0.18 (−0.74, 0.38)
Year 2	−1.23 (−1.63, −0.83)	−1.24 (−1.65, −0.83)	−0.01 (−0.58, 0.57)
Tophus count			
Year 1	−0.38 (−0.9, 0.14)	−0.6 (−1.13, −0.08)	−0.22 (−0.96, 0.52)
Year 2	−1.45 (−1.98, −0.93)	−1.34 (−1.87, −0.81)	0.11 (−0.63, 0.86)
Index tophus area‡			
Year 1	−122 (−196, −48)	−112 (−179, −44)	10 (−90, 111)
Year 2	−185 (−270, −100)	−159 (−237, −82)	26 (−89, 141)
Pain, 100-mm VAS			
Year 1	0.05 (−0.38, 0.48)	−0.34 (−0.76, 0.09)	−0.39 (−1, 0.22)
Year 2	−0.46 (−0.89, −0.03)	−0.67 (−1.11, −0.23)	−0.21 (−0.82, 0.41)
Patient's global assessment of disease activity			
Year 1	−0.41 (−0.7, −0.12)	−0.5 (−0.78, −0.21)	−0.09 (−0.49, 0.32)
Year 2	−0.51 (−0.8, −0.22)	−0.51 (−0.8, −0.22)	0 (−0.41, 0.41)
EQ-5D-3L index score			
Year 1	0.01 (−0.02, 0.04)	0.01 (−0.02, 0.05)	0 (−0.04, 0.05)
Year 2	0.02 (−0.01, 0.05)	0.04 (0.01, 0.07)	0.02 (−0.03, 0.06)
HAQ-II score			
Year 1	−0.1 (−0.19, 0)	0.03 (−0.06, 0.12)	0.12 (−0.01, 0.25)
Year 2	−0.11 (−0.2, −0.02)	−0.08 (−0.17, 0.02)	0.03 (−0.1, 0.16)

* Values are the least squares–adjusted marginal mean (95% confidence interval). CT = computed tomography; JSN = joint space narrowing; VAS = visual analog scale; EQ-5D-3L = EuroQol 5-domain-3L; HAQ-II = Health Assessment Questionnaire II.
† Standard target indicates a serum urate target of <0.30 mmoles/liter and intensive target indicates a serum urate target of <0.20 mmoles/liter. The difference between groups was not statistically significant for any outcome measure, as assessed by analysis of covariance.
‡ Index tophus area values are in those with at least 1 measurable index tophus at the baseline visit.

(P = 0.63). Improved erosion scores were not observed in either group.

Sensitivity analyses were performed to investigate the influence of missing data. A "last observation carried forward" approach showed no time-by-treatment interaction effects for the change in CT erosion scores or the change in plain radiographic scores (P > 0.26 in all ANCOVA analyses), and no effects were demonstrated using Markov chain Monte Carlo imputation (P > 0.30 in all aggregated ANCOVA analyses).

Imaging results from the prespecified per-protocol analysis that included participants with randomized serum urate targets at year 1 and year 2 are shown in Supplementary Tables 4 and 5 (http://onlinelibrary.wiley.com/doi/10.1002/art.42055). This analysis included 19 participants in the intensive target group and 32 participants in the standard target group. These findings were similar to those in the primary intent-to-treat analysis. No differences in terms of the change in CT erosion scores or the change in plain radiographic scores were observed between the groups.

Additional secondary end points (OMERACT gout core outcome domains). Outcomes for the OMERACT gout core outcome domains (gout flares, tophi, pain, patient's global assessment of disease activity, health-related quality of life, and activity limitations) are shown in Table 2, Supplementary Table 3, and Supplementary Figures 1 and 2 (http://onlinelibrary.wiley.com/doi/10.1002/art.42055). All outcomes improved in both

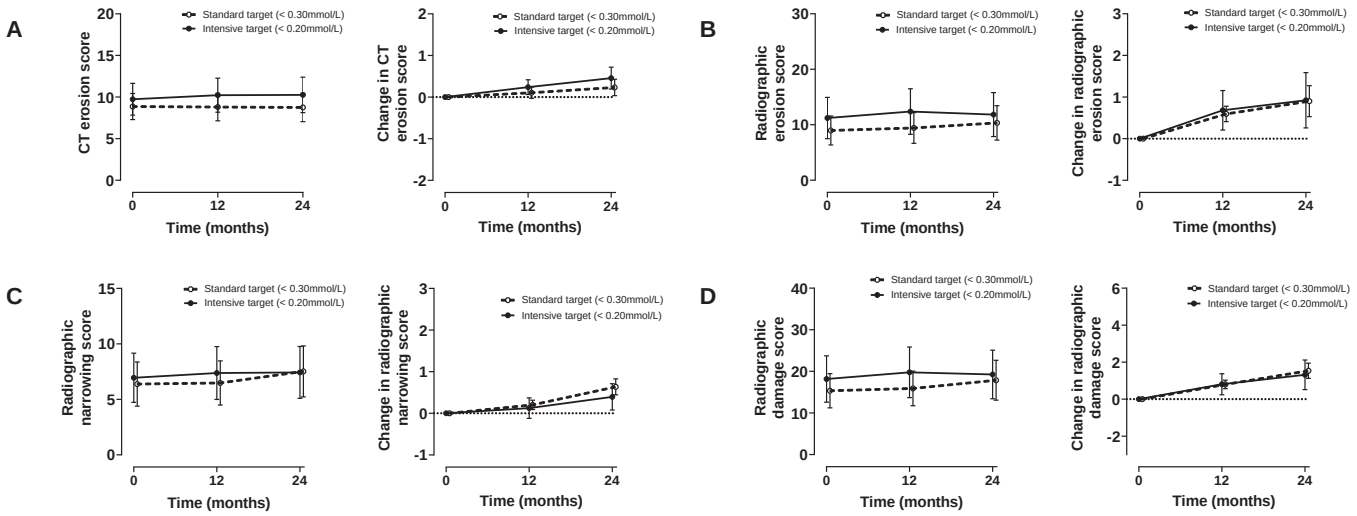

Figure 3. Imaging outcomes. **A**, Computed tomography (CT) bone erosion scores. **B**, Plain radiographic bone erosion scores. **C**, Plain radiographic joint space narrowing scores. **D**, Plain radiographic joint damage scores. Values are the observed mean and 95% confidence interval.

groups over the 2-year study period, with no between-group differences ($P > 0.29$ for all).

AEs. All AE data are shown in Table 3, and the number of participants with at least 1 SAE is shown in Supplementary Table 6 (http://onlinelibrary.wiley.com/doi/10.1002/art.42055). There were 3 medication-related AEs that required changes in therapy, all in the intensive target group: rash attributed to both allopurinol and febuxostat in the same participant and hot flashes and dizziness attributed to benzbromarone in another participant. There was no significant difference in AEs and SAEs between groups, although there were numerically more cardiac and circulatory system AEs and infection-related AEs in the intensive target group. Additional details regarding the number and sites of infections are shown in Supplementary Table 7 (http://onlinelibrary.wiley.com/doi/10.1002/art.42055). In the intensive target group, there were more infections affecting the skin, soft tissue, and urinary tract (though the increase was not statistically significant),

Table 3. AEs and SAEs in participants randomized to the standard serum urate target group and those randomized to the intensive serum urate target group

	Total AEs and SAEs, no. (%)			Patients with at least 1 AE or SAE, no. (%)		
	Standard target*	Intensive target*	Total	Standard target (n = 52)*	Intensive target (n = 52)*	Total
Cancer	3	3	6	3 (6)	3 (6)	6
Cardiac and circulatory system problems	10	25	35	7 (13)	11 (21)	18
Gastrointestinal disorders	27	24	51	21 (40)	17 (33)	38
Infection	82	140	222	37 (71)	45 (87)	82
Injury	42	43	85	25 (48)	27 (52)	52
Musculoskeletal disorders	29	32	61	21 (40)	19 (37)	40
Nervous system disorders	1	1	2	1 (2)	1 (2)	2
Other	37	36	73	21 (40)	20 (38)	41
Rash	17	21	38	16 (31)	13 (25)	29
Renal and urinary tract disorders	3	2	5	3 (6)	2 (4)	5
Respiratory system disorders	3	1	4	2 (4)	1 (2)	3
Any AE or SAE	253	328	581	48 (92)	49 (94)	97

* Standard target indicates a serum urate target of <0.30 mmoles/liter and intensive target indicates a serum urate target of <0.20 mmoles/liter. The difference between groups was not statistically significant for any adverse event (AE) or serious AE (SAE), as assessed by analysis of covariance.

as well as significantly more influenza and upper respiratory tract infections.

There were 9 participants (17%) in each group who had SAEs, with no between-group differences in the causes of the SAEs, including cardiac and circulatory system problems and infections. There were 2 deaths in the intensive target group (1 due to a perforated sigmoid colon [likely secondary to a colonic neoplasm] and 1 due to acute pulmonary edema [possibly secondary to myocardial infarction]) and 1 death in the standard target group (due to acute coronary syndrome and ventricular fibrillation cardiac arrest).

DISCUSSION

This randomized, double-blind clinical trial has shown that, compared to a standard serum urate target of <0.30 mmoles/liter, intensive urate-lowering therapy with oral medications to a target of <0.20 mmoles/liter does not improve bone erosion scores in patients with erosive gout. Furthermore, with oral medications, more medication is required to achieve the intensive serum urate target, and it is difficult to reach and maintain over time. Similar improvement in clinical outcomes in erosive gout, including gout flares, tophus size, activity limitation, and health-related quality of life, can be achieved with oral urate-lowering therapy at a standard serum urate target of <0.30 mmoles/liter.

The results of this trial can be compared to previous studies of erosive gout (8,10,26). In contrast to the small case series of patients receiving pegloticase, in which improvement in bone erosion scores was observed following treatment (10), clinical trials in patients receiving oral urate-lowering therapy have not demonstrated improvements in erosion scores (8,26). Importantly, in this study, difficulty achieving the intensive target with oral urate-lowering therapy may explain the differences compared to the results of the pegloticase studies. While the efficacy of pegloticase on bone erosion requires confirmation in future clinical trials, it seems likely that profound reductions in serum urate levels are required for erosion healing in gout. It is possible that with a longer duration of intensive urate lowering with oral medications, erosion healing might occur. However, our data indicate that once erosive gout has occurred, it cannot be easily reversed.

In this study, increases in CT scores and radiographic scores were observed over time despite urate-lowering therapy. Similar findings were observed in our previous trial examining allopurinol dose escalation, with some worsening in imaging outcomes, even in participants in the dose-escalation arm (8). Collectively, these findings indicate that, in gout, once joint damage is established, the processes driving this damage may continue despite control of the serum urate level. For this reason, earlier use of urate-lowering therapy to prevent the development of bone erosions in gout should be a priority.

The implications of the small changes in joint damage scores on imaging over the 2-year period are uncertain, given the improvement in other outcomes over the study period, including gout flares, tophi, and activity limitation. Our findings raise uncertainty regarding the clinical importance of small changes in joint damage observed on imaging, particularly when there is clinical improvement in other outcome domains with urate-lowering therapy use.

An important finding of this study is that in many participants, the serum urate target of <0.20 mmoles/liter could not be reached with oral therapy, but a target of <0.30 mmoles/liter was achievable for most participants receiving allopurinol monotherapy. The target of <0.30 mmoles/liter is recommended in patients with gouty arthropathy, and this trial shows that allopurinol monotherapy can be used to achieve this target in most patients. A mean allopurinol dose of ~500 mg/day was required to achieve the target of <0.30 mmoles/liter, which is a dose that is much higher than the 300-mg daily dose that is widely used in clinical practice (27). Together with findings from several other trials (17,28), these results provide evidence for the safety and efficacy of allopurinol escalated to doses of >300 mg/day.

AEs were broadly similar between the 2 groups. While there were more cardiac- and circulatory system–related AEs and infection-related AEs in the intensive target group, the number of participants with SAEs was similar in the 2 groups. A U-shaped mortality curve for serum urate levels has been reported for both all-cause and cardiovascular disease mortality (29), although large cardiovascular outcome trials have not demonstrated a clear relationship between intensity of serum urate lowering and cardiovascular events (17,30).

This is the first published randomized controlled trial designed specifically to examine different serum urate targets for gout management, and it provides a template for future double-blind randomized controlled trials examining different targets and treatment strategies in gout. While the serum urate target of <0.36 mmoles/liter (6 mg/dl) in gout patients receiving urate-lowering therapy (without severe disease) has been widely supported by rheumatology professional societies (12,18), it is unknown whether higher or lower serum urate targets have similar benefit to the widely recommended target of <0.36 mmoles/liter (6 mg/dl). This study demonstrates the feasibility of undertaking a double-blind randomized controlled trial to address this question.

Limitations of this study are that the study findings are not relevant to individuals without erosive disease or to health care systems without access to a broad range of urate-lowering agents. The Aotearoa/New Zealand population has a high prevalence of severe gout (31), so the study population may not be generalizable to other countries. However, in our view, the ethnically diverse study population is a strength of this study (32). Additional strengths of the study include the double-blind trial design, the use of validated imaging outcomes, and reporting of all OMERACT core outcome domains.

In summary, intensive serum urate lowering to a target of <0.20 mmoles/liter is difficult to achieve with oral urate-lowering therapy, leads to high medication burden, and does not improve bone erosion scores in patients with erosive gout. When using oral urate-lowering therapy, a serum urate target of <0.30 mmoles/liter is sufficient to achieve clinical benefit in this patient group.

ACKNOWLEDGMENTS

We thank the members of the Health Research Council of New Zealand Data Monitoring Core Committee for overseeing the trial. We also thank the staff of the Radiology Department at the Auckland District Health Board.

AUTHOR CONTRIBUTIONS

All authors were involved in drafting the article or revising it critically for important intellectual content, and all authors approved the final version to be published. Dr. Dalbeth had full access to all of the data in the study and takes responsibility for the integrity of the data and the accuracy of the data analysis.

Study conception and design. Dalbeth, Doyle, Gamble, Stamp, Horne.
Acquisition of data. Dalbeth, Doyle, Billington, Tan, Latto, Parshu Ram, Narang, Murdoch, Bursill, Mihov, Horne.
Analysis and interpretation of data. Dalbeth, Gamble, Stamp, Horne.

REFERENCES

1. Dalbeth N, Clark B, McQueen F, Doyle A, Taylor W. Validation of a radiographic damage index in chronic gout. Arthritis Rheum 2007; 57:1067–73.
2. Stewart S, Aati O, Horne A, Doyle AJ, Dalbeth N. Radiographic damage scores predict grip strength in patients with tophaceous gout. Rheumatology (Oxford) 2020;59:1440–2.
3. Stewart S, Rome K, Eason A, House ME, Horne A, Doyle AJ, et al. Predictors of activity limitation in people with gout: a prospective study. Clin Rheumatol 2018;37:2213–9.
4. Dalbeth N, Aati O, Kalluru R, Gamble GD, Horne A, Doyle AJ, et al. Relationship between structural joint damage and urate deposition in gout: a plain radiography and dual-energy CT study. Ann Rheum Dis 2015;74:1030–6.
5. Towiwat P, Doyle AJ, Gamble GD, Tan P, Aati O, Horne A, et al. Urate crystal deposition and bone erosion in gout: 'inside-out' or 'outside-in'? A dual-energy computed tomography study. Arthritis Res Ther 2016;18:208.
6. Chhana A, Callon KE, Pool B, Naot D, Watson M, Gamble GD, et al. Monosodium urate monohydrate crystals inhibit osteoblast viability and function: implications for development of bone erosion in gout. Ann Rheum Dis 2011;70:1684–91.
7. Chhana A, Pool B, Callon KE, Tay ML, Musson D, Naot D, et al. Monosodium urate crystals reduce osteocyte viability and indirectly promote a shift in osteocyte function towards a proinflammatory and proresorptive state. Arthritis Res Ther 2018;20:208.
8. Dalbeth N, Billington K, Doyle A, Frampton C, Tan P, Aati O, et al. Effects of allopurinol dose escalation on bone erosion and urate volume in gout: a dual-energy computed tomography imaging study within a randomized, controlled trial. Arthritis Rheumatol 2019;71:1739–46.
9. Sundy JS, Baraf HS, Yood RA, Edwards NL, Gutierrez-Urena SR, Treadwell EL, et al. Efficacy and tolerability of pegloticase for the treatment of chronic gout in patients refractory to conventional treatment: two randomized controlled trials. JAMA 2011;306:711–20.
10. Dalbeth N, Doyle AJ, McQueen FM, Sundy J, Baraf HS. Exploratory study of radiographic change in patients with tophaceous gout treated with intensive urate-lowering therapy. Arthritis Care Res (Hoboken) 2014;66:82–5.
11. Khanna D, Fitzgerald JD, Khanna PP, Bae S, Singh MK, Neogi T, et al. 2012 American College of Rheumatology guidelines for management of gout. Part 1: systematic nonpharmacologic and pharmacologic therapeutic approaches to hyperuricemia. Arthritis Care Res (Hoboken) 2012;64:1431–46.
12. Richette P, Doherty M, Pascual E, Barskova V, Becce F, Castañeda-Sanabria J, et al. 2016 updated EULAR evidence-based recommendations for the management of gout. Ann Rheum Dis 2017;76:29–42.
13. Hui M, Carr A, Cameron S, Davenport G, Doherty M, Forrester H, et al. The British Society for Rheumatology guideline for the management of gout. Rheumatology (Oxford) 2017;56:e1–20.
14. Perez-Ruiz F, Calabozo M, Pijoan JI, Herrero-Beites AM, Ruibal A. Effect of urate-lowering therapy on the velocity of size reduction of tophi in chronic gout. Arthritis Rheum 2002;47:356–60.
15. Perez-Ruiz F, Martin I, Canteli B. Ultrasonographic measurement of tophi as an outcome measure for chronic gout. J Rheumatol 2007; 34:1888–93.
16. Neogi T, Jansen TL, Dalbeth N, Fransen J, Schumacher HR, Berendsen D, et al. 2015 Gout classification criteria: an American College of Rheumatology/European League Against Rheumatism collaborative initiative. Arthritis Rheumatol 2015;67:2257–68.
17. White WB, Saag KG, Becker MA, Borer JS, Gorelick PB, Whelton A, et al. Cardiovascular safety of febuxostat or allopurinol in patients with gout. N Engl J Med 2018;378:1200–10.
18. FitzGerald JD, Dalbeth N, Mikuls T, Brignardello-Petersen R, Guyatt G, Abeles AM, et al. 2020 American College of Rheumatology guideline for the management of gout. Arthritis Rheumatol 2020;72:879–95.
19. Schumacher HR, Taylor W, Edwards L, Grainger R, Schlesinger N, Dalbeth N, et al. Outcome domains for studies of acute and chronic gout. J Rheumatol 2009;36:2342–5.
20. Dalbeth N, Schauer C, Macdonald P, Perez-Ruiz F, Schumacher HR, Hamburger S, et al. Methods of tophus assessment in clinical trials of chronic gout: a systematic literature review and pictorial reference guide. Ann Rheum Dis 2011;70:597–604.
21. Janssen MF, Szende A, Cabases J, Ramos-Goñi JM, Vilagut G, König HH. Population norms for the EQ-5D-3L: a cross-country analysis of population surveys for 20 countries. Eur J Health Econ 2019;20:205–16.
22. Wolfe F, Michaud K, Pincus T. Development and validation of the health assessment questionnaire II: a revised version of the health assessment questionnaire. Arthritis Rheum 2004;50:3296–305.
23. Dalbeth N, Doyle A, Boyer L, Rome K, Survepalli D, Sanders A, et al. Development of a computed tomography method of scoring bone erosion in patients with gout: validation and clinical implications. Rheumatology (Oxford) 2011;50:410–6.
24. Ostergaard M, Edmonds J, McQueen F, Peterfy C, Lassere M, Ejbjerg B, et al. An introduction to the EULAR-OMERACT rheumatoid arthritis MRI reference image atlas. Ann Rheum Dis 2005;64 Suppl:i3–7.
25. Van der Heijde DM, van Leeuwen MA, van Riel PL, Koster AM, van 't Hof MA, van Rijswijk MH, et al. Biannual radiographic assessments of hands and feet in a three-year prospective followup of patients with early rheumatoid arthritis. Arthritis Rheum 1992;35:26–34.
26. Dalbeth N, Aati O, Gamble GD, Horne A, House ME, Roger M, et al. Zoledronate for prevention of bone erosion in tophaceous gout: a randomised, double-blind, placebo-controlled trial. Ann Rheum Dis 2014;73:1044–51.
27. Becker MA, Fitz-Patrick D, Choi HK, Dalbeth N, Storgard C, Cravets M, et al. An open-label, 6-month study of allopurinol safety in gout: the LASSO study. Semin Arthritis Rheum 2015;45:174–83.

28. Stamp LK, Chapman PT, Barclay ML, Horne A, Frampton C, Tan P, et al. A randomised controlled trial of the efficacy and safety of allopurinol dose escalation to achieve target serum urate in people with gout. Ann Rheum Dis 2017;76:1522–8.
29. Cho SK, Chang Y, Kim I, Ryu S. U-shaped association between serum uric acid level and risk of mortality: a cohort study. Arthritis Rheumatol 2018;70:1122–32.
30. Mackenzie IS, Ford I, Nuki G, Hallas J, Hawkey CJ, Webster J, et al. Long-term cardiovascular safety of febuxostat compared with allopurinol in patients with gout (FAST): a multicentre, prospective, randomised, open-label, non-inferiority trial. Lancet 2020;396:1745–57.
31. Winnard D, Wright C, Taylor WJ, Jackson G, Te Karu L, Gow PJ, et al. National prevalence of gout derived from administrative health data in Aotearoa New Zealand. Rheumatology (Oxford) 2012;51:901–9.
32. Guillén AG, Te Karu L, Singh JA, Dalbeth N. Gender and ethnic inequities in gout burden and management. Rheum Dis Clin North Am 2020;46:693–703.

DOI 10.1002/art.42078

Clinical Images: Detection of titanium dioxide particles by Raman spectroscopy in synovial fluid from a swollen ankle

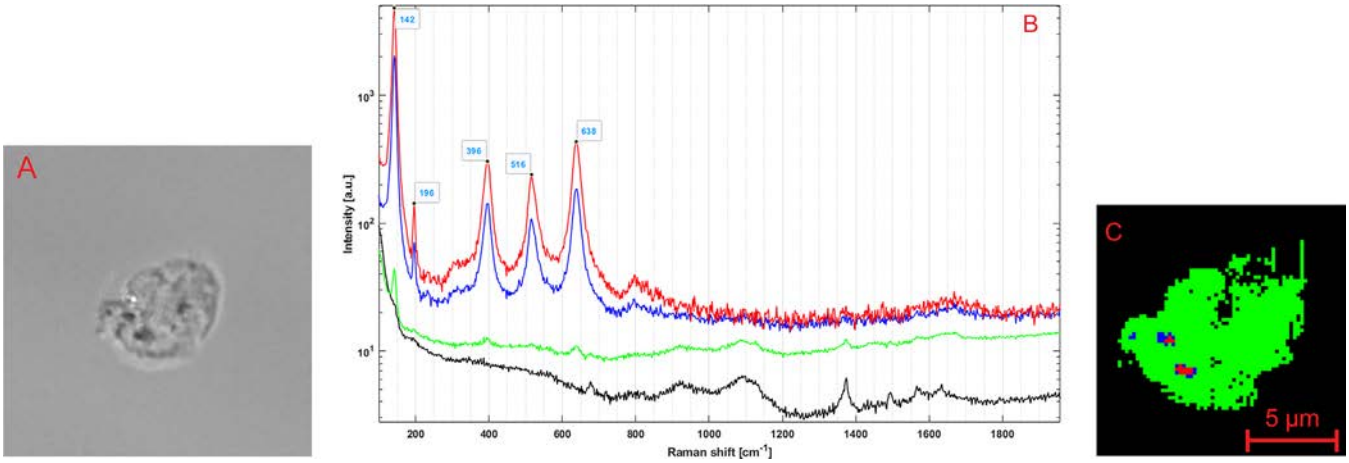

The patient, a 71-year-old man, presented with a swollen ankle joint. Review of the patient's history revealed gout flare in 2011 (diagnosed by a general practitioner) and receipt of titanium alloy hip implants in 2016. The general practitioner's diagnosis of suspected gout could not be confirmed by compensated polarized light microscopy. Brightfield microscopy of a synovial fluid specimen from the ankle joint showed dark, smooth objects inside a synovial leukocyte (**A**). We used Raman spectroscopy to measure the chemical composition of these objects. The red and blue spectra (**B** and **C**) are typical of anatase crystals, with peaks at 142, 196, 396, 516, and 638 cm^{-1} (1); anatase is a polymorph of titanium dioxide crystals (TiO_2). The black spectrum (**B** and **C**) has peaks at 676 and 1,374 cm^{-1}, which are linked to oxidized cytochrome b_{558}. Cytochrome b_{558} is part of the NADPH oxidase complex, which plays a critical role in inflammation. Anatase is a known component of paints, drugs, toothpaste, and ointments, and the release of titanium dioxide from dental and orthopedic implants is suggested (2). To our knowledge, this is the first example of anatase crystal detection in synovial fluid. Anatase has a low birefringence (±20% of the value for monosodium urate monohydrate crystals), and the morphology of crystal surfaces is smooth. Experiments have shown that TiO_2 endocytosis can trigger interleukin-1β release in cultures of leukocytes (3). Whether the anatase crystals contributed to the inflammation in this case is unknown. There were no clinical signs of metallosis or osteolysis. The patient responded well to prednisone (10 mg orally every other day for 6 weeks) and fully recovered.

The collaboration project is cofunded by a PPP allowance from Health-Holland, Top Sector Life Sciences & Health, to Stichting ReumaNederland, to stimulate public–private partnerships. Author disclosures are available at https://onlinelibrary.wiley.com/action/downloadSupplement?doi=10.1002%2Fart.42078&file=art42078-sup-0001-Disclosureform.pdf.

1. Ohsaka T, Izumi F, Fujiki Y. Raman spectrum of anatase, TiO_2. J Raman Spectrosc 1978;7:321–4.
2. Yao JJ, Lewallen EA, Trousdale WH, Xu W, Thaler R, Salib CG, et al. Local cellular responses to titanium dioxide from orthopedic implants. Biores Open Access 2017;6:94–103.
3. Vallés G, González-Melendi P, González-Carrasco JL, Saldaña L, Sánchez-Sabaté E, Munuera L, et al. Differential inflammatory macrophage response to rutile and titanium particles. Biomaterials 2006;27:5199–211.

Tom Niessink
Jasper Ringoot
Cees Otto, PhD
University of Twente
Enschede, The Netherlands
Matthijs Janssen, MD, PhD
VieCuri Medical Center
Venlo, The Netherlands
Tim L. Jansen, MD, PhD
University of Twente
Enschede, The Netherlands
and VieCuri Medical Center
Venlo, The Netherlands

American College of Rheumatology
Empowering Rheumatology Professionals

Arthritis & Rheumatology
Vol. 74, No. 6, June 2022, pp 1070–1082
DOI 10.1002/art.42052

Contribution of Interleukin-4–Induced Epithelial Cell Senescence to Glandular Fibrosis in IgG4-Related Sialadenitis

Sai-Nan Min,[1] Meng-Qi Zhu,[1] Xiang-Di Mao,[2] Wei Li,[1] Tai Wei,[1] Mei Mei,[1] Yan Zhang,[2] Li-Ling Wu,[2] Guang-Yan Yu,[1] and Xin Cong[2]

Objective. IgG4-related sialadenitis (IgG4-RS) is a chronic fibroinflammatory disease characterized by glandular fibrosis and hyposalivation. This study was undertaken to explore the role of cellular senescence in the pathogenesis of IgG4-RS–related fibrosis.

Methods. The expression of senescence markers and proinflammatory cytokines in the submandibular glands (SMGs) of IgG4-RS patients (n = 18) and controls (n = 14) was determined by proteomics, real-time polymerase chain reaction, Western blotting, and immunohistochemistry. After interleukin-4 (IL-4) treatment, high-throughput RNA sequencing was performed to identify the differentially expressed genes in SMG-C6 cells. A glandular fibrosis model was established by the intraglandular injection of IL-4 into mouse SMGs (n = 8 per group).

Results. Salivary acinar and ductal epithelial cells underwent senescence in IgG4-RS patients, as indicated by the elevated activity of senescence-associated β-galactosidase, lipofuscin accumulation, enhanced expression of senescence markers (p53 and $p16^{INK4A}$), and up-regulation of senescence-associated secretory phenotype factors. Moreover, there was a significant increase in IL-4 levels in SMGs from IgG4-RS patients ($P < 0.01$), which positively correlated with $p16^{INK4A}$ expression and the fibrosis score. Incubation with IL-4 exacerbated salivary epithelial cell senescence by increasing the expression of $p16^{INK4A}$ through the reactive oxygen species (ROS)/p38 MAPK pathway. Supernatant collected from IL-4–induced senescent SMG-C6 cells enhanced fibroblast activation and matrix protein production ($P < 0.05$). Furthermore, injecting mice with IL-4 promoted fibrosis and senescence phenotypes in SMGs in vivo.

Conclusion. The cellular senescence induced by IL-4 through the ROS/p38 MAPK-$p16^{INK4A}$ pathway promotes fibrogenesis in IgG4-RS. Our data suggest that cellular senescence could serve as a novel therapeutic target for treating IgG4-RS.

INTRODUCTION

IgG4-related disease (IgG4-RD) is a systemic fibroinflammatory disorder characterized by increased IgG4+ plasma cell infiltration and storiform fibrosis in multiple organs, such as the salivary glands, pancreas, lacrimal glands, and kidney (1). Salivary glands were found to be affected in nearly 27–58% of IgG4-RD patients, and this condition is referred to as "IgG4-related sialadenitis (IgG4-RS)" (2–4). IgG4-RS patients exhibit persistent and painless unilateral or bilateral enlargement of the salivary glands,

Supported by the National Natural Science Foundation of China (grants 81671005, 81974151, 81771093, 81991500, 81991502, and 82101037).

[1]Sai-Nan Min, PhD, Meng-Qi Zhu, MSc, Wei Li, MD, Tai Wei, PhD, Mei Mei, PhD, Guang-Yan Yu, DDS, PhD: Peking University School and Hospital of Stomatology, National Center of Stomatology, National Clinical Research Center for Oral Diseases, National Engineering Research Center of Oral Biomaterials and Digital Medical Devices, Beijing Key Laboratory of Digital Stomatology, Research Center of Engineering and Technology for Computerized Dentistry Ministry of Health, and NMPA Key Laboratory for Dental Materials, Beijing, China; [2]Xiang-Di Mao, BS, Yan Zhang, PhD, Li-Ling Wu, MSc, Xin Cong, PhD: Peking University School of Basic Medical Sciences, Key Laboratory of Molecular Cardiovascular Sciences, Ministry of Education, and Beijing Key Laboratory of Cardiovascular Receptors Research, Beijing, China.

Drs. Yu and Cong contributed equally to this work.

Author disclosures are available at https://onlinelibrary.wiley.com/action/downloadSupplement?doi=10.1002%2Fart.42052&file=art42052-sup-0001-Disclosureform.pdf.

Address correspondence to Guang-Yan Yu, DDS, PhD, Department of Oral and Maxillofacial Surgery, Peking University School and Hospital of Stomatology, No. 22, Zhongguancun South Avenue, Haidian District, Beijing 100081, China (email: gyyu@263.net); or to Xin Cong, PhD, Department of Physiology and Pathophysiology, Peking University School of Basic Medical Sciences, No. 38, Xueyuan Road, Haidian District, Beijing 100191, China (email: congxin@bjmu.edu.cn).

Submitted for publication August 24, 2021; accepted in revised form December 14, 2021.

which is accompanied by different degrees of hyposecretion due to progressive fibrosis (5).

In a cohort of 235 consecutive IgG4-RD patients in Japan, nine-tenths of the cases were diagnosed in 50–70-year-old individuals, suggesting that IgG4-RD mainly occurs in middle-aged and elderly individuals (6). The onset of this disease was more likely to be associated with strong lymphocytic activation in elderly patients (ages >70 years) than in younger patients (7). Recent studies have shown that serum interleukin-15 (IL-15) levels are increased in IgG4-RS patients. Furthermore, the number of memory CD28–CD4+ T cells, which proliferate in response to IL-15, also increased with age (8–10). Given that many chronic inflammatory diseases are considered to be aging-related disorders, it is notable that some features associated with aging, such as interstitial fibrosis, acinar atrophy, persistent inflammation, and loss of regenerative capability in salivary gland epithelial cells, are observed in IgG4-RS (5). These findings suggest that aging might be a contributing factor to the initiation and progression of IgG4-RS.

Accumulation of cellular senescence is a main feature of aged organisms, and refers to a state of irreversible growth arrest, which is triggered by pathogenic factors, such as inflammation caused by diverse inflammatory cytokines (e.g., interleukins, interferons, and chemokines), oxidative stress, oncogene activation, and DNA damage (11,12). The characteristics of senescent cells include growth arrest, increased lysosomal content, resistance to apoptosis, an enlarged and flattened morphology, and enhanced expression of cyclin-dependent kinase (CDK) inhibitor genes, such as $p16^{INK4A}$, p21, and p15 (13). Accumulation of senescent cells can further promote the release of proinflammatory cytokines, chemokines, growth factors, and proteases that are known as senescence-associated secretory phenotype (SASP) factors. SASP factors secreted by senescent cells reinforce and propagate senescence in an autocrine and paracrine manner; in addition, they attract immune cells and promote tissue repair (14).

Several studies have indicated that many proinflammatory cytokines, such as IL-18, transforming growth factor β (TGFβ), and IL-22, can induce cellular senescence and participate in various fibrotic diseases, such as idiopathic pulmonary fibrosis, liver fibrosis, and kidney fibrosis (15–17). Furthermore, cellular senescence has been observed and is related to the loss of salivary gland function in mice that received radiation in the head and neck, in primary Sjögren's syndrome, and in the senescence-accelerated mouse prone 1 line (18–22). However, whether the infiltrating lymphocytes and their secreted proinflammatory cytokines trigger cellular senescence in the salivary glands of patients with IgG4-RS remains unexplored. In this study, we aimed to understand the presence and role of cellular senescence in the pathogenesis of fibrosis in the salivary glands of patients with IgG4-RS, and further elucidate the underlying mechanism.

MATERIALS AND METHODS

Cell culture, animal models, Sudan Black B staining, senescence-associated (SA) β-galactosidase (β-gal) staining, TUNEL staining, Masson's trichrome staining, sirius red staining, lactate dehydrogenase (LDH) assay, cell cycle and proliferation assays, 5-ethynyl-2′-deoxyuridine assay, measurement of reactive oxygen species (ROS), migration assay, proteomics analysis, RNA sequencing, cytokine array, etc. are described in detail in the Supplementary Methods, available on the *Arthritis & Rheumatology* website at http://onlinelibrary.wiley.com/doi/10.1002/art.42052. All animal research has been reported according to Animals in Research: Reporting In Vivo Experiments guidelines (23).

Patients and samples. Submandibular gland (SMG) biopsy specimens were obtained from 18 patients who were diagnosed as having IgG4-RS according to the comprehensive diagnostic criteria (24) and had not been treated with steroids or immunosuppressants. SMG tissues from 4 patients with chronic sialadenitis (mean ± SD age 57.00 ± 8.29 years) were included for comparison. Control SMG tissues, confirmed to be normal on pathologic examination, were obtained from 14 individuals (mean ± SD age 62.50 ± 6.37 years) undergoing surgery for head or neck carcinoma. Immediately after surgery, a part of the specimen was frozen in liquid nitrogen for RNA and protein extraction, and the remainder was used for histochemical staining. Blood samples were obtained from IgG4-RS patients and healthy donors after an overnight fast. Following sample collection, serum was immediately separated by centrifugation and stored at −80°C. All patients signed an informed consent form. The study protocol was approved by the Ethics Committee of Peking University School and Hospital of Stomatology (No. PKUSSORB-2013008). The clinical characteristics and serologic features of the IgG4-RS patients are summarized in Supplementary Table 1, available on the *Arthritis & Rheumatology* website at http://onlinelibrary.wiley.com/doi/10.1002/art.42052.

Statistical analysis. Data were normalized and are expressed as the mean ± SEM. The significance of differences between groups was analyzed by Student's unpaired *t*-test or analysis of variance followed by Bonferroni test or Tukey's test using GraphPad software. Correlation was analyzed by Pearson's correlation coefficient analysis. *P* values less than 0.05 were considered significant.

RESULTS

Altered expression profile of aging-related proteins in the SMGs of patients with IgG4-RS. The protein profiles of SMG samples from IgG4-RS patients and controls were screened using proteomics. A total of 894 differentially expressed

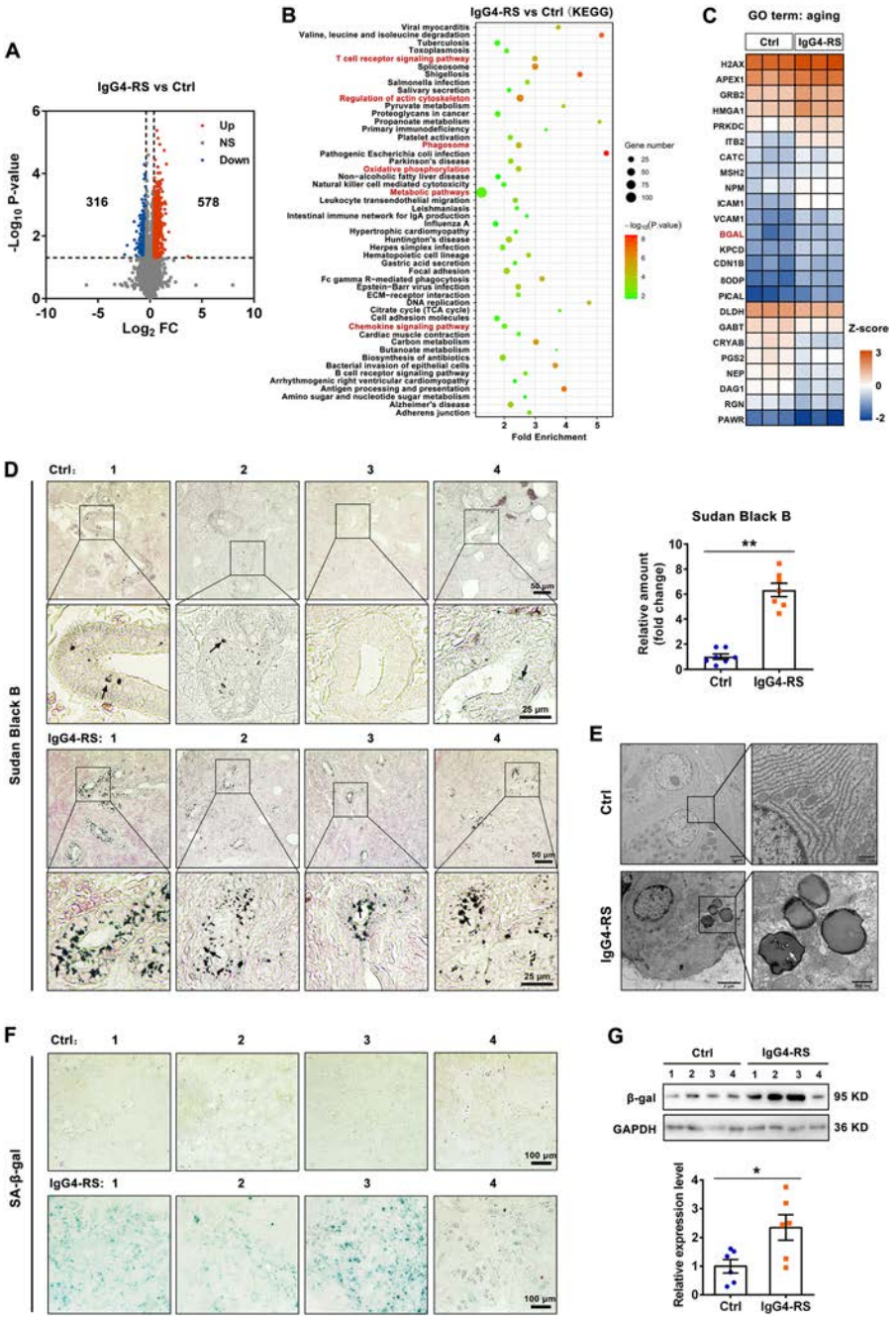

Figure 1. Cellular senescence in the submandibular glands (SMGs) of patients with IgG4-related sialadenitis (IgG4-RS). **A**, Volcano plot displaying differential expression of 894 proteins in IgG4-RS patients and controls (n = 3 per group). Proteins up-regulated (ratio of fold change [FC] ≥1.3) in IgG4-RS are shown in orange; proteins down-regulated (ratio of fold change ≤0.77) in IgG-RS are shown in blue. NS = not significant. **B**, The 50 most enriched KEGG pathways for the differentially expressed proteins in SMGs from IgG4-RS patients and controls. Pathways shown in red are related to aging and inflammatory processes. ECM = extracellular matrix; TCA = tricarboxylic acid. **C**, Heatmap depicting differentially expressed proteins in the Gene Ontology term "aging" in controls and IgG4-RS patients. Several aging-related proteins, such as β-galactosidase (β-gal), histone H2AX, and CDK inhibitor 1B were abnormally expressed in SMGs from IgG4-RS patients. Red text indicates β-gal, a cellular senescence marker. **D**, Left, Sudan Black B staining for lipofuscins in SMGs from 4 representative controls (n = 7) and 4 representative IgG4-RS patients (n = 7). Bottom panels show higher-magnification views (bars = 25 μm) of the boxed areas in the top panels (bars = 50 μm). **Arrows** indicate positive staining. Right, Quantitative analysis of Sudan Black B staining. Symbols represent individual subjects; bars show the mean ± SEM. **E**, Representative transmission electron microscopy images showing an accumulation of lipofuscins in the SMG from an IgG4-RS patient. Right panels (bars = 500 nm) show higher-magnification views of the boxed areas in the left panels (bars = 2 μm). **F**, Senescence-associated (SA) β-gal staining in SMGs from controls and IgG4-RS patients (n = 4 per group). Bars = 100 μm. **G**, Western blot (top) and quantification (bottom) of β-gal expression in SMGs from controls and IgG4-RS patients (n = 6 per group). Symbols represent individual subjects; bars show the mean ± SEM. * = $P < 0.05$; ** = $P < 0.01$.

proteins were identified (ratio of fold change ≥1.3 or ≤0.77; $P < 0.05$), of which 578 were up-regulated and 316 were down-regulated in IgG4-RS (Figure 1A). KEGG pathway enrichment analysis revealed that the differentially expressed proteins were enriched in 84 pathways. The top 50 pathways followed a pattern similar to the aging process and included metabolic pathways, oxidative phosphorylation, and regulation of actin cytoskeleton, as well as pathways related to inflammatory processes (Figure 1B). Accordingly, we further analyzed the term "Aging" in Gene Ontology (GO)–enriched categories. Several aging-related proteins, such as β-gal, histone H2AX, and CDK inhibitor 1B were abnormally expressed in the SMGs of IgG4-RS patients (Figure 1C). These results implied that aging might be involved in the pathogenesis of IgG4-RS.

Epithelial cell senescence in the SMGs of patients with IgG4-RS. Sudan Black B and SA β-gal staining are 2 frequently used methods to evaluate cellular senescence. SA β-gal staining measures the activity of the lysosomal enzyme β-gal, a well-known marker of cellular senescence, whereas Sudan Black B staining directly detects the cellular aging process via the waste product lipofuscin, a hallmark of senescent cells (25,26). We observed more Sudan Black B–stained granules in the ductal cells in SMGs from IgG4-RS patients than in those from controls (Figure 1D). The accumulation of lipofuscins in the ductal cells in SMGs from IgG4-RS patients was further confirmed using electron microscopy (Figure 1E). SA β-gal staining indicated a significant increase in SA β-gal activity in SMGs from IgG4-RS patients compared with those from controls (Figure 1F). The increased β-gal protein expression was further validated by Western blotting (Figure 1G).

The expression of multiple senescence markers, such as $p14^{ARF}$, p53, and $p16^{INK4A}$, and SASP factors, such as IL-6 and TGFβ1, was higher in SMGs from IgG4-RS patients than in those from controls. In contrast, the levels of messenger RNA (mRNA) for p21 were unchanged (Figure 2A). The p53 and $p16^{INK4A}$ protein levels were significantly elevated in SMGs from IgG4-RS patients; however, only a slight, although significant, increase in the expression of p21 protein was detected (Figure 2B). Furthermore, increased intensities of p53 and $p16^{INK4A}$ were seen in the residual acinar and ductal cells of SMGs from IgG4-RS patients. Additionally, sporadic expression of p21 was observed (Figure 2C).

Since p21 signal was not activated, we did not further examine the expression and localization of its upstream molecule $p14^{ARF}$. However, there was no significant increase in lipofuscin or $p16^{INK4A}$ expression in SMGs from patients with chronic sialadenitis, a nonspecific inflammatory and fibrotic disease (Supplementary Figures 1A and B, available on the *Arthritis & Rheumatology* website at http://onlinelibrary.wiley.com/doi/10.1002/art.42052), indicating that cellular senescence might be specific to IgG4-RS. Both the proportion of apoptotic cells and the expression of cleaved caspase 3 were unchanged among IgG4-RS patients and controls (Supplementary Figures 2A and B, available on the *Arthritis & Rheumatology* website at http://onlinelibrary.wiley.com/doi/10.1002/art.42052), suggesting that apoptosis might not be the major pathologic process in IgG4-RS. These results indicate that both acinar and ductal epithelial cells undergo cellular senescence in IgG4-RS.

Elevated IL-4 expression in the SMGs of patients with IgG4-RS. The infiltration of lymphocytes plays a crucial role in the progression of IgG4-RS (27,28). CD20+ B cells were primarily located within the germinal centers, whereas CD3+ T lymphocytes were organized around germinal centers. Among CD3+ T lymphocytes, CD4+ T cells were the dominant population in SMGs from IgG4-RS patients (Figure 2D). The levels of CD4+ T cell–associated cytokines, such as IL-2, interferon-γ (IFNγ), IL-4, IL-13, and IL-10, were significantly higher in IgG4-RS patients than in controls. IL-4 in particular was one of the proinflammatory cytokines that was most up-regulated (Figure 2E). The increase in IL-4 protein expression, together with the increase in IL-4 receptor (IL-4R) mRNA, in SMGs from IgG4-RS patients was further validated by Western blotting and real-time polymerase chain reaction, respectively (Figures 2F and G).

We then costained SMGs with IL-4 and zonula occludens 1, a tight junction molecule expressed in epithelial cells. Expression of IL-4 was not found in controls and was slightly detected in SMGs from patients with chronic sialadenitis (Supplementary Figure 3A, available on the *Arthritis & Rheumatology* website at http://onlinelibrary.wiley.com/doi/10.1002/art.42052). In contrast, strong IL-4 staining was detectable in the inflammatory infiltration foci of SMGs from IgG4-RS patients (Figure 2H). Notably, IL-4 was partially colocalized with or accumulated surrounding CD4+ lymphocytes in SMGs from IgG4-RS patients, whereas IL-4 and CD4 staining was hardly observed in controls (Supplementary Figure 3B, available on the *Arthritis & Rheumatology* website at http://onlinelibrary.wiley.com/doi/10.1002/art.42052), indicating that a portion of IL-4 was produced or secreted from Th2 cells. Furthermore, a cytokine antibody array was performed to determine the cytokine profiles in the serum of IgG4-RS patients and controls. The levels of multiple cytokines, such as granulocyte-macrophage colony stimulating factor, IL-23, TGFβ, and tumor necrosis factor α, were higher among IgG4-RS patients (Supplementary Figure 4, available on the *Arthritis & Rheumatology* website at http://onlinelibrary.wiley.com/doi/10.1002/art.42052). In contrast, serum IL-4 levels were unchanged, suggesting that local IL-4 might play an important role in IgG4-RS.

To further study the relationship between IL-4 and cellular senescence, correlation analysis was performed. IL-4 mRNA expression positively correlated with the senescence marker $p16^{INK4A}$, but not with p53 or p21, in SMGs from IgG4-RS patients (Figure 2I). These results suggest that an association

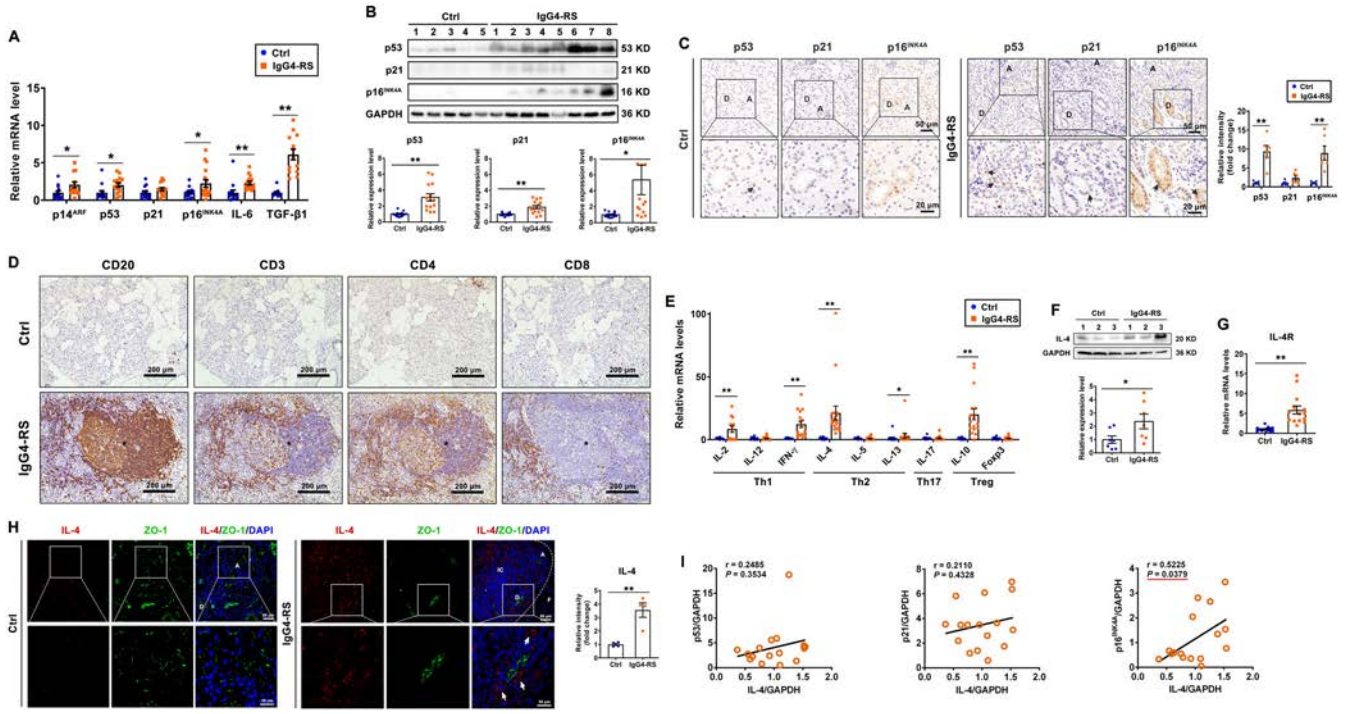

Figure 2. Relationship between elevated interleukin-4 (IL-4) expression and senescence in submandibular glands (SMGs) from patients with IgG4-related sialadenitis (IgG4-RS). **A**, Expression of mRNA for $p14^{ARF}$, p53, p21, $p16^{INK4A}$, IL-6, and transforming growth factor β1 (TGFβ1) in SMGs from controls (n = 11–14) and IgG4-RS patients (n = 13–16). **B**, Western blot (top) and quantification (bottom) of p53, p21, and $p16^{INK4A}$ protein expression in SMGs from controls (n = 12) and IgG4-RS patients (n = 14). **C**, Left, Immunostaining for p53, p21, and $p16^{INK4A}$ in SMGs from a control and an IgG4-RS patient. Bottom panels (bars = 20 μm) show higher-magnification views of the boxed areas in the top panels (bars = 50 μm). **Arrows** indicate positive staining. Right, Relative staining intensity in SMGs from controls (n = 5) and IgG4-RS patients (n = 6). **D**, Immunostaining for CD20, CD3, CD4, and CD8 in SMGs from a control and an IgG4-RS patient. **Asterisks** indicate lymphoid follicles. Bars = 200 μm. **E**, Levels of mRNA for IL-2, IL-12, interferon-γ (IFNγ), IL-4, IL-5, IL-13, IL-17, IL-10, and FoxP3 in SMGs from controls (n = 8–14) and IgG4-RS patients (n = 12–18). **F**, Western blot (top) and quantification (bottom) of IL-4 protein levels in SMGs from controls and IgG4-RS patients (n = 7 per group). **G**, Levels of mRNA for IL-4 receptor (IL-4R) in SMGs from controls and IgG4-RS patients (n = 14 per group). **H**, Left, Immunostaining for IL-4 and zonula occludens 1 (ZO-1) in SMGs from a control and an IgG4-RS patient. Bottom panels (bars = 25 μm) show higher-magnification views of the boxed areas in the top panels (bars = 50 μm). Right, Relative staining intensity in SMGs from controls and IgG4-RS patients (n = 4 per group). **I**, Correlations between the levels of IL-4 mRNA and senescence markers in SMGs from IgG4-RS patients (n = 16), determined by Spearman's test. In **A**–**C** and **E**–**H**, symbols represent individual subjects; bars show the mean ± SEM. * = $P < 0.05$; ** = $P < 0.01$. **A** = acini; **D** = ductal cells; **IC** = inflammatory cells; **F** = fibrosis. Color figure can be viewed in the online issue, which is available at http://onlinelibrary.wiley.com/doi/10.1002/art.42052/abstract.

exists between augmented IL-4 and cellular senescence in SMG lesions in IgG4-RS patients.

IL-4–induced cellular senescence in SMG-C6 cells. Considering that there is not a commonly accepted salivary gland ductal cell line, we chose to use SMG-C6 cells, a rat submandibular epithelial cell line with characteristics of acinar cells, for the in vitro studies. First, high-throughput RNA sequencing was performed in SMG-C6 cells with or without recombinant IL-4 stimulation. A total of 654 genes with significant differential expression were identified (ratios of fold change ≥2 or ≤0.5; $P < 0.05$), of which 434 were up-regulated and 220 were down-regulated (Figure 3A). The 20 most enriched biologic processes for significantly down-regulated and up-regulated genes are shown in Figure 3B and Supplementary Figure 5, available on the *Arthritis & Rheumatology* website at http://onlinelibrary.wiley.com/doi/10.1002/art.42052, respectively. Notably, the down-regulated genes related to the regulation of cell proliferation were screened, while the up-regulated genes were enriched in positive regulation of cell migration and localization.

Since low proliferation is one of the characteristics of senescent cells, we speculated that IL-4 could induce salivary gland cell senescence. Treating SMG-C6 cells with IL-4 for 48 hours led to inhibition of the proliferative capacity (Figures 3C and D). Cells exposed to IL-4 were arrested in the S phase (Figure 3E). Furthermore, IL-4 treatment significantly increased the activity of SA β-gal and caused a flattening and enlargement of cell morphology (Figure 3F). However, IL-4 neutralizing antibody significantly eliminated the IL-4–induced increase in SA β-gal activity and growth inhibition (Supplementary Figures 6A and B, available on the *Arthritis & Rheumatology* website at http://onlinelibrary.wiley.com/doi/10.1002/art.42052), again suggesting a direct relationship between IL-4 and senescence.

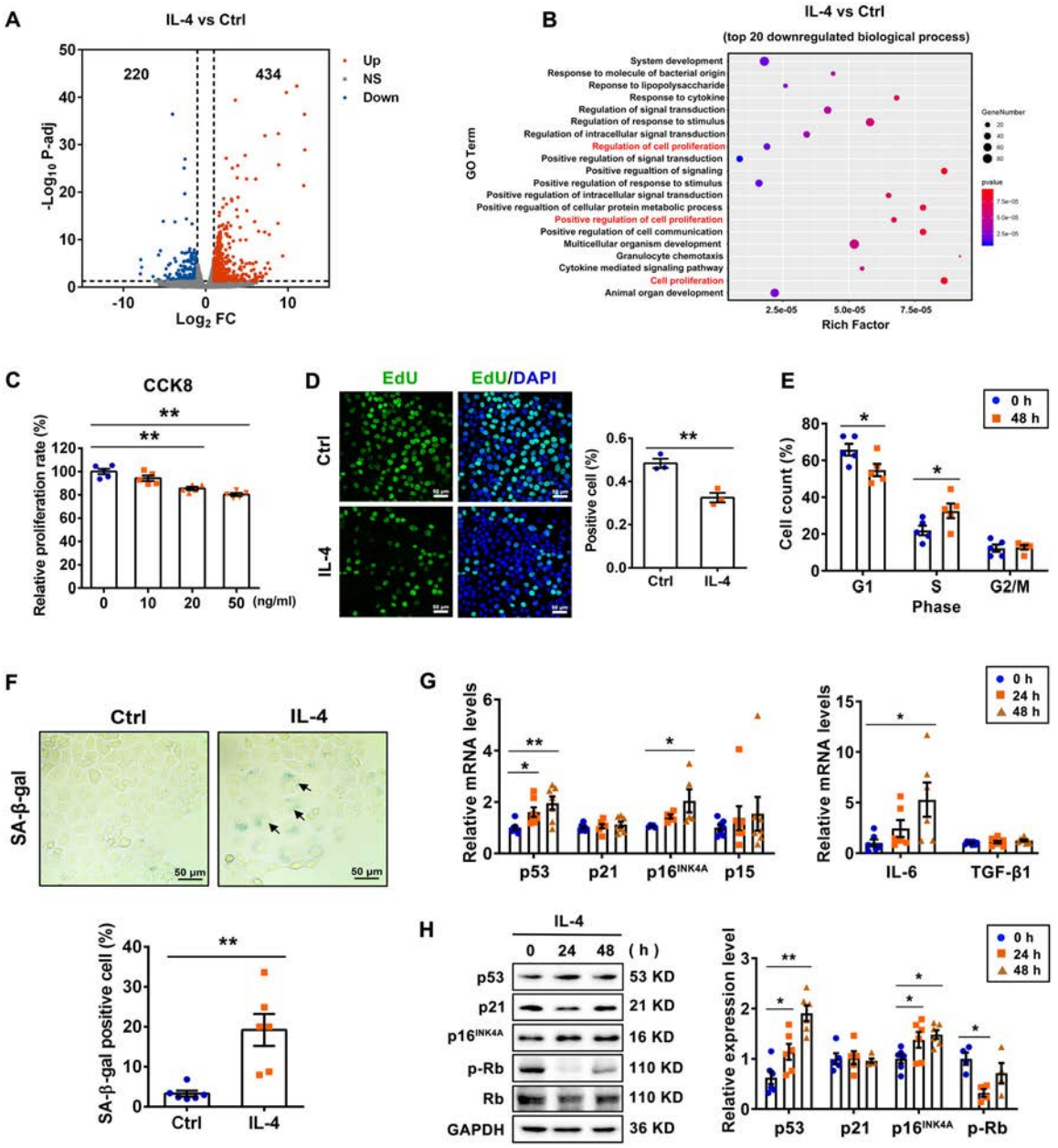

Figure 3. Direct induction of cellular senescence by interleukin-4 (IL-4). **A**, Volcano plot of RNA sequencing in SMG-C6 cells treated with IL-4 (20 ng/ml) for 48 hours (n = 3). Up-regulated genes (ratio of fold change [FC] ≥2) are shown in orange; down-regulated genes (ratio of fold change ≤0.5) are shown in blue. NS = not significant. **B**, The 20 most significantly enriched Gene Ontology (GO) terms for the down-regulated genes. **C**, Changes in proliferative capacity of SMG-C6 cells exposed to different concentrations of IL-4 for 48 hours, quantitated with Cell Counting Kit 8 (CCK8) (n = 5). **D**, Fluorescence images (left) and quantification of positive cells (right) showing changes in proliferative capacity of SMG-C6 cells exposed to IL-4, measured by 5-ethynyl-2′-deoxyuridine (EdU) assay (n = 3). Proliferative nuclei are green; cell nuclei were stained with DAPI. Bars = 50 μm. **E**, Cell cycle analysis for SMG-C6 cells treated with IL-4 (n = 5). **F**, Staining for (top) and quantification of (bottom) senescence-associated (SA) β-galactosidase (β-gal) in SMG-C6 cells treated with IL-4 (n = 6). **Arrows** indicate positive staining. Bars = 50 μm. **G**, Levels of mRNA for p53, p21, p16^{INK4A}, p15, IL-6, and transforming growth factor β1 (TGFβ1) in SMG-C6 cells treated with IL-4 (n = 5–8). **H**, Western blot (left) and quantification (right) of p53, p21, p16^{INK4A}, p-retinoblastoma (p-Rb), and Rb protein expression in SMG-C6 cells (n = 4–6). In **C**–**H**, symbols represent individual samples; bars show the mean ± SEM. * = $P < 0.05$; ** = $P < 0.01$. Color figure can be viewed in the online issue, which is available at http://onlinelibrary.wiley.com/doi/10.1002/art.42052/abstract.

IL-4 had no effect on LDH activity, the proportion of apoptotic cells, or the ratio of Bax to Bcl-2 proteins (Supplementary Figures 7A–C, available on the *Arthritis & Rheumatology* website at http://onlinelibrary.wiley.com/doi/10.1002/art.42052). The senescence markers p53/p21 and p16^{INK4A} are the 2 major mediators that modulate the cell cycle by inhibiting the activity of CDK, which phosphorylates and inactivates the retinoblastoma (Rb) protein. There was an

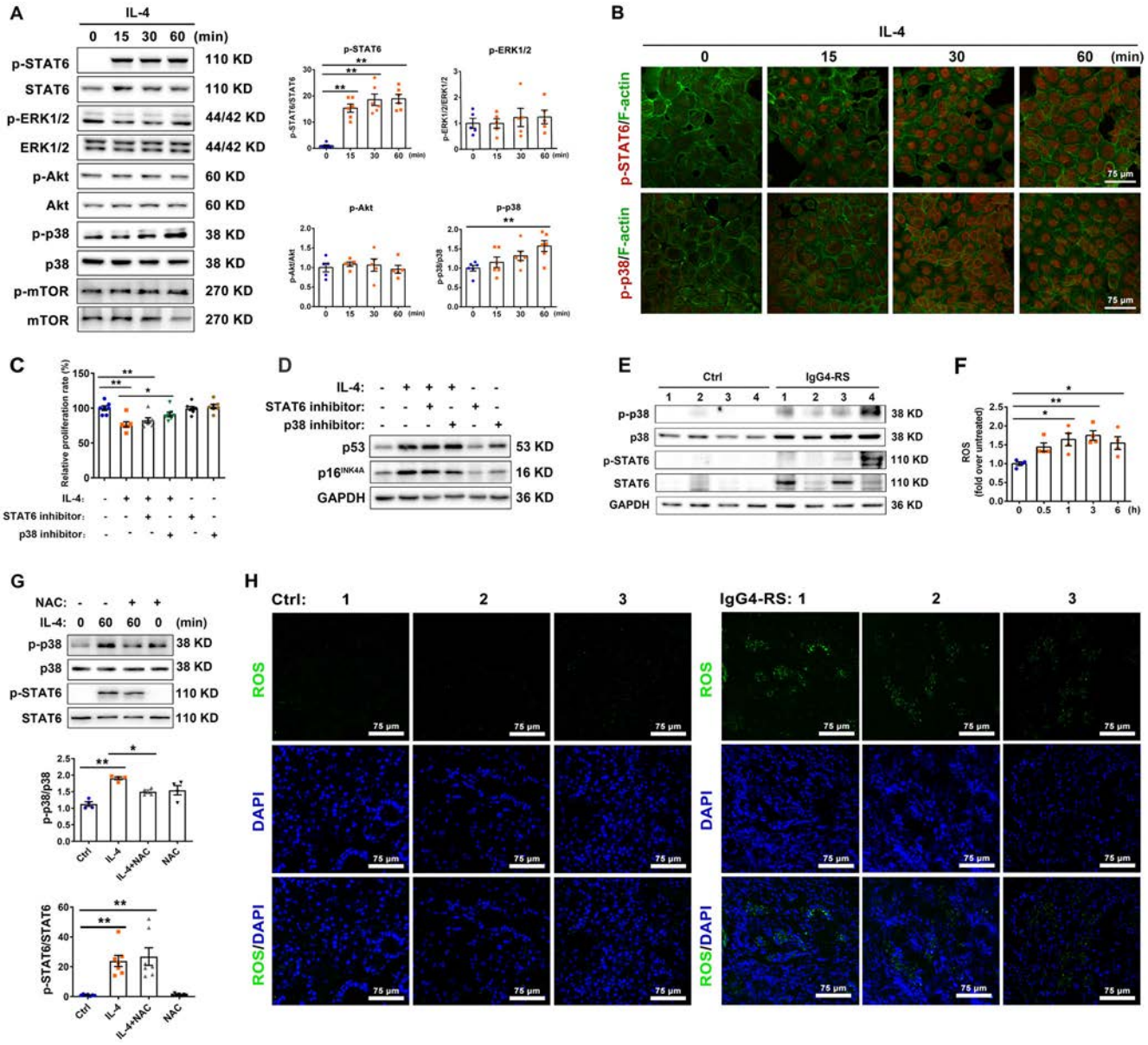

Figure 4. Mediation of interleukin-4 (IL-4)–induced cellular senescence by reactive oxygen species (ROS)/p38 MAPK (p38). **A**, Western blot (left) and quantification (right) of changes in the phosphorylation of STAT6, ERK1/2, protein kinase B (Akt), p38, and mechanistic target of rapamycin (mTOR) after treatment with IL-4 (20 ng/ml) for the indicated time periods (n = 3–6). **B**, Immunostaining for p-STAT6 and p-p38 in SMG-C6 cells stimulated with IL-4. F-actin was stained to show cell outlines. Bars = 75 μm. **C** and **D**, Changes in the proliferative capacity of SMG-C6 cells (**C**) and p53 and $p16^{INK4A}$ protein expression (**D**) in SMG-C6 cells left untreated or pretreated with the STAT6 inhibitor AS1517499 or the p38 MAPK inhibitor SB203580, before IL-4 treatment (n = 7). **E**, Phosphorylation of p38 and STAT6 in submandibular glands (SMGs) from controls and patients with IgG4-related sialadenitis (IgG4-RS). **F**, Changes in intracellular ROS levels in SMG-C6 cells treated with IL-4 for the indicated time periods, determined by flow cytometry (n = 5). **G**, Western blot (top) and quantification (bottom) of the phosphorylation of p38 and STAT6 in SMG-C6 cells pretreated with *N*-acetyl-L-cysteine (NAC; 5 m*M*) before IL-4 treatment (n = 4–7). **H**, ROS staining in SMGs from controls and IgG4-RS patients. Bars = 75 μm. In **A** and **C**, **F**, and **G**, symbols represent individual samples; bars show the mean ± SEM. * = $P < 0.05$; ** = $P < 0.01$. Color figure can be viewed in the online issue, which is available at http://onlinelibrary.wiley.com/doi/10.1002/art.42052/abstract.

increase in the expression of mRNA for p53 and $p16^{INK4A}$ and the SASP factor IL-6, but not p21 (Figure 3G). Western blotting also confirmed that treatment with IL-4 led to an increase in p53 and $p16^{INK4A}$ expression and a decrease in the phosphorylation levels of Rb (Figure 3H). In contrast, stimulation with IFNγ, a characteristic cytokine secreted by Th1 lymphocytes, caused a reduction in the expression of p53 and p21 mRNA (Supplementary Figure 7D). These results suggest that IL-4 could directly induce senescence and lead to growth inhibition in SMG-C6 cells.

Mediation of IL-4–induced cellular senescence by the ROS/p38 MAPK pathway. There are at least 2 distinct signaling pathways triggered by IL-4 that involve STAT6 and the insulin receptor substrate 1/2 (29,30). To investigate the mechanism underlying IL-4–induced cellular senescence, we next examined potential intracellular kinases, including STAT6, ERK1/2, and protein kinase B (Akt), and the potential signals that are thought to induce cellular senescence according to recent studies, such as p38 MAPK and mechanistic target of rapamycin (mTOR) (31). IL-4 stimulation caused up-regulation of p-STAT6, whereas the levels of p-ERK1/2 or p-Akt were unaffected (Figure 4A). Moreover, treatment with IL-4 led to a significant increase in the levels of p-p38 MAPK, but not p-mTOR (Figure 4A and Supplementary Figure 8A, available on the *Arthritis & Rheumatology* website at http://onlinelibrary.wiley.com/doi/10.1002/art.42052). Immunofluorescence staining further showed an increase in the intranuclear expression of both p-STAT6 and p-p38 MAPK after stimulation with IL-4 (Figure 4B). Preincubation with the p38

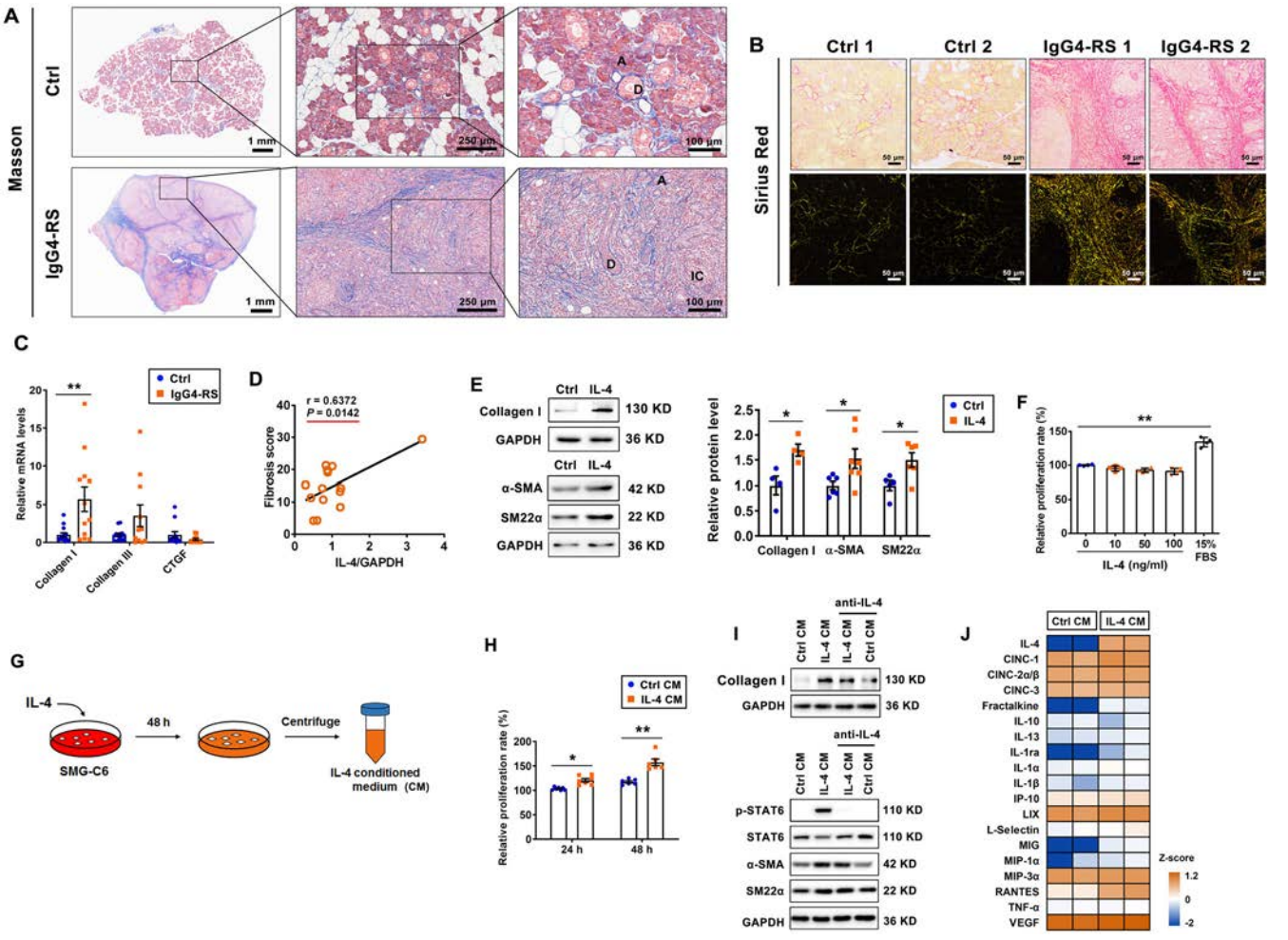

Figure 5. Promotion of fibrosis by interleukin-4 (IL-4)–induced epithelial cell senescence. **A**, Masson's trichrome staining of submandibular gland (SMG) samples from a control and a patient with IgG4-related sialadenitis (IgG4-RS). Middle panels (bars = 250 μm) show higher-magnification views of the boxed areas in the left panels (bars = 1 mm); right panels (bars = 100 μm) show higher-magnification views of the boxed areas in the middle panels. **A** = acini; **D** = ductal cells; **IC** = inflammatory cells. **B**, Light microscopy (top) and polarized microscopy (bottom) images of sirius red staining in SMG samples from controls and IgG4-RS patients. Bars = 50 μm. **C**, Levels of mRNA for type I collagen, type III collagen, and connective tissue growth factor (CTGF) in controls (n = 12–14) and IgG4-RS patients (n = 11–12). **D**, Correlation between IL-4 mRNA level and fibrosis score in SMGs from IgG4-RS patients (n = 14). **E**, Western blot (left) and quantification (right) of type I collagen, α-smooth muscle actin (α-SMA), and SM22α protein expression in rat fibroblasts after IL-4 stimulation (n = 4–7). **F**, Proliferative capacity of rat fibroblasts treated with IL-4 (n = 4). FBS = fetal bovine serum. **G**, Illustration of the procedure for collecting IL-4 conditioned medium. **H**, Proliferative capacity of rat fibroblasts treated with control or IL-4 conditioned medium, measured by Cell Counting Kit 8 (n = 6). **I**, Type I collagen, p-STAT6, α-SMA, and SM22α protein expression in rat fibroblasts incubated in control or IL-4 conditioned medium with or without IL-4 neutralizing antibody (n = 7–8). **J**, Relative expression of cytokines in control and IL-4 conditioned medium. In **C**, **E**, **F**, and **H**, symbols represent individual samples; bars show the mean ± SEM. * = $P < 0.05$, ** = $P < 0.01$. CINC-1 = cytokine-induced neutrophil chemoattractant 1; IL-1Ra = IL-1 receptor antagonist; IP-10 = interferon-γ–inducible 10-kd protein; LIX = lipopolysaccharide-induced CXC chemokine; MIG = monokine induced by interferon-γ; MIP-1α = macrophage inflammatory protein 1α; TNF = tumor necrosis factor; VEGF = vascular endothelial growth factor. Color figure can be viewed in the online issue, which is available at http://onlinelibrary.wiley.com/doi/10.1002/art.42052/abstract.

MAPK inhibitor, SB203580, but not the STAT6 inhibitor, AS1517499, abolished IL-4–induced growth inhibition as well as $p16^{INK4A}$ protein up-regulation (Figure 4C and D). However, the IL-4–induced up-regulation of p53 was unchanged. Consistent with the in vitro studies, there was a significant increase in total and p-p38 MAPK levels, but not STAT6 levels, in SMG lesions from IgG4-RS patients (Figure 4E). These findings suggest that p38 MAPK is an important mediator of IL-4–induced salivary gland epithelial cell senescence.

Oxidative stresses, such as ROS, are thought to cause many age-related chronic diseases (13). In SMG-C6 cells, IL-4 treatment significantly increased intracellular ROS levels (Figure 4F). Preincubation with *N*-acetyl-L-cysteine, a ROS scavenger, inhibited the IL-4–induced phosphorylation of p38 MAPK, whereas the phosphorylation of STAT6 was unaffected (Figure 4G). To determine if intracellular ROS were involved in the progression of IgG4-RS, we detected the level and localization of ROS and found only a few sporadic ROS-positive foci in the SMGs from controls, whereas excessive accumulation of ROS was observed in the cytoplasm of residual epithelial cells in SMG lesions from IgG4-RS patients (Figure 4H and Supplementary Figure 8B). These results indicate that IL-4 induced cellular senescence through the generation of ROS and by subsequently activating the p38 MAPK signal.

IL-4-induced epithelial cell senescence promotes fibrosis by activating fibroblasts both directly and indirectly. Storiform fibrosis is a characteristic feature of the salivary glands in IgG4-RS patients. We observed dense collagen deposition, which mainly consisted of type I collagen and appeared as yellow/orange birefringence under polarized light microscopy, inside the interlobular areas and around the residual epithelial cells in SMGs from IgG4-RS patients (Figures 5A and B). The expression of mRNA for type I collagen, but not type III collagen or connective tissue growth factor, was significantly higher in SMGs from IgG4-RS patients than in SMGs from controls (Figure 5C). We also observed a positive correlation between IL-4 and fibrosis score (Figure 5D).

To further understand the effect of IL-4 on SMG fibrosis, primary rat SMG fibroblasts were isolated and identified by vimentin staining (Supplementary Figure 8C). Stimulation with IL-4 increased the expression of type I collagen, and the myofibroblast markers α-smooth muscle actin (α-SMA) and smooth muscle 22α (SM22α), but had no effect on the proliferative or migration capacity of SMG fibroblasts (Figures 5E and F and Supplementary Figures 8D and E). Additionally, we investigated whether IL-4–induced senescent cells could influence the characteristics of fibroblasts. We collected supernatants from IL-4–treated SMG-C6 cells as conditioned medium (Figure 5G), and then incubated fibroblasts with IL-4 conditioned medium in the presence or absence of IL-4 neutralizing antibodies to eliminate the effect of exogenous IL-4. Incubation with IL-4 conditioned medium significantly enhanced the proliferation of fibroblasts and increased the expression of type I collagen, p-STAT6, α-SMA, and SM22α (Figures 5H and I and Supplementary Figures 9A–C, available on the *Arthritis & Rheumatology* website at http://onlinelibrary.wiley.com/doi/10.1002/art.42052). However, IL-4 conditioned medium did not affect the migration capacity (Supplementary Figures 10A and B, available on the *Arthritis & Rheumatology* website at http://onlinelibrary.wiley.com/doi/10.1002/art.42052). Moreover, the elimination of IL-4 by neutralizing antibody did not affect the IL-4 conditioned medium–induced up-regulation of type I collagen, α-SMA, and SM22α, whereas IL-4–dependent p-STAT6 activation was abolished (Figure 5I). These data suggest that the senescent epithelial cells that were induced by IL-4 could promote the proliferation and phenotype transition of fibroblasts by secreting SASP factors.

To identify potential inducers in the supernatants of IL-4–induced senescent epithelial cells, a cytokine array was performed in IL-4 conditioned medium. The results showed elevated levels of various inflammatory and profibrotic factors, such as IL-1α and IL-1β, as well as chemokines, such as macrophage inflammatory protein 3α and fractalkine (Figure 5J). These findings indicate that IL-4 is an important driver of fibrogenesis that affects fibroblasts both directly and indirectly via the interaction between senescent epithelial cells and fibroblasts in the SMGs of IgG4-RS patients.

IL-4–induced SMG fibrosis and cellular senescence in a mouse model. To further confirm the role of IL-4 in salivary gland epithelial cell senescence and fibrosis, we established a mouse model by injection of murine IL-4 into SMG tissues at multiple sites (Figure 6A). Administering IL-4 did not cause a significant change in body weight, SMG weight, or stimulated salivary flow rate (Figure 6B). Notably, the IL-4–treated glands showed significant atrophy of acinar and ductal cells and collagen deposition with thickened basement lumen compared with the controls (Figure 6C). Masson's trichrome staining revealed that the exogenous IL-4 led to fibrotic lesions in SMGs (Figure 6D). In addition to the fibrotic markers type I collagen and α-SMA, exogenous IL-4 also promoted the expression of $p16^{INK4A}$, but not that of p53. A p38 MAPK activation signal was detected in the IL-4 injection group (Figure 6E). These in vivo studies provide additional evidence regarding the profibrotic effect of IL-4, which may be closely related to the induction of epithelial cell senescence.

DISCUSSION

Fibrosis is the main pathologic feature of IgG4-RS; however, its pathogenic mechanism is unclear. In the present study, we demonstrated that both acinar and ductal cells in the SMGs of IgG4-RS patients exhibit many phenotypic features of senescence. Elevated IL-4 levels in SMG lesions activated the ROS/p38 MAPK-$p16^{INK4A}$ signaling pathway and led to the accumulation of senescent cells. We further showed that IL-4 induces SMG

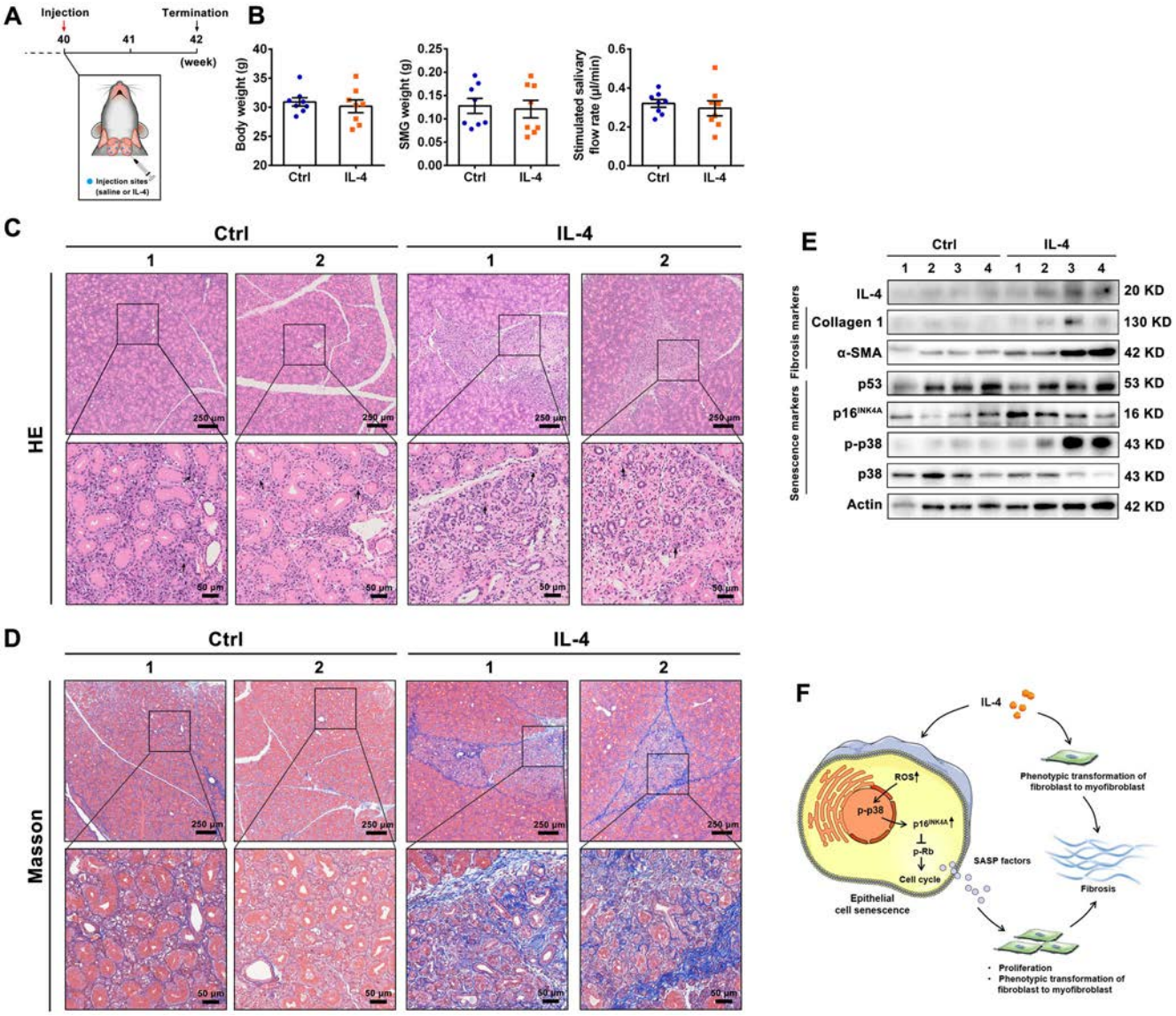

Figure 6. Effects of interleukin-4 (IL-4) on fibrosis and cellular senescence in vivo. **A**, Experimental design of an IL-4–injected mouse model. IL-4 or saline (control) was injected into the submandibular gland (SMG) tissues. **B**, Body weight, SMG weight, and stimulated salivary flow rate in mice injected with saline or IL-4 (n = 8 per group). Symbols indicate individual mice; bars show the mean ± SEM. **C** and **D**, Hematoxylin and eosin (H&E)–stained (**C**) and Masson's trichrome–stained (**D**) sections of SMGs from mice injected with saline or IL-4. Bottom panels (bars = 50 μm) show higher-magnification views of the boxed areas in the top panels (bars = 250 μm). **Arrows** indicate atrophic acini. **E**, Protein expression of the fibrotic markers type I collagen and α-smooth muscle actin (α-SMA), and the senescence markers p53, $p16^{INK4A}$, and p-p38 MAPK (p38), in SMGs from mice injected with saline or IL-4 (n = 4 per group). **F**, Schematic model of the role of IL-4 in the fibrogenesis of IgG4-related sialadenitis (IgG4-RS). The elevation of IL-4 in the SMGs of IgG4-RS patients is an important driver of fibrogenesis through both direct and indirect mechanisms, including 1) production of collagenous proteins by promoting fibroblast differentiation directly, and 2) induction of salivary gland epithelial cell senescence through the reactive oxygen species (ROS)/p38 MAPK-$p16^{INK4A}$ pathway, thereby producing senescence-associated secretory phenotype (SASP) factors to promote fibroblast proliferation and differentiation. p-Rb = p-retinoblastoma. Color figure can be viewed in the online issue, which is available at http://onlinelibrary.wiley.com/doi/10.1002/art.42052/abstract.

fibrosis directly by promoting myofibroblast differentiation and indirectly by inducing senescent epithelial cells that produce SASP factors to activate fibroblasts (Figure 6F).

Storiform fibrosis is a prominent feature of IgG4-RS that leads to the enlargement and dysfunction of salivary glands. Recent studies have demonstrated an accumulation of senescent cells in a number of fibrotic diseases. The lung alveolar epithelium exhibits increased $p16^{INK4A}$ and p21 expression and greater SA β-gal activity in idiopathic pulmonary fibrosis patients and in a mouse model of bleomycin-induced lung injury (32,33). In models of acute kidney injury, G2/M-arrested proximal tubular cell numbers increase and activate c-Jun NH2-terminal kinase signaling, which causes fibrosis by up-regulating profibrotic cytokine production (34). Epidemiologic studies revealed that the incidence

and mortality of fibrotic diseases increases with an aging population, reinforcing the notion that the accumulation of senescent cells might contribute to the onset of organ fibrosis (35,36). However, some studies have shown contrasting results. Senescent hepatic stellate cells reduce the levels of extracellular matrix proteins, enhance the secretion of degrading enzymes, and restrict liver fibrosis (17,37).

To date, it is still unknown whether senescence is present and involved in the fibrosis of IgG4-RS. Through liquid chromatography mass spectrometry/mass spectrometry screening, multiple molecules related to aging were found to be aberrantly expressed in the SMGs of patients with IgG4-RS. In addition, we observed increased lipofuscin accumulation, SA β-gal activity, SASP levels, and enhanced expression of senescence markers (p53 and $p16^{INK4A}$) in IgG4-RS. These findings indicate that salivary acinar and ductal cells undergo senescence during IgG4-RS. Anti-aging compounds or senolytics, which selectively eliminate senescent cells by targeting $p16^{INK4A}$, antiapoptotic proteins, or SASP factors without affecting their normal counterparts, have been shown to efficiently attenuate several age-dependent disorders including fibrosis (14). Although a combination of glucocorticoids and steroid-sparing agents are widely used to treat IgG4-RS, relapses and complications in some patients remain major challenges (38). The present study suggests that targeting cellular senescence might be a potential effective approach for treating IgG4-RS.

The Th2-derived cytokine IL-4 is pleiotropic and may be involved in differentiation, proliferation, or apoptosis depending on the cell type (39,40). A recent study showed that IL-4 induces senescence in human renal carcinoma cell lines by up-regulating p21 through STAT6 and p38 MAPK signals (41). IL-4 serves as a marker of inflammation in cardiac aging, as evidenced by its elevated level in the left ventricle of senescent mice (42). In the present study, we found higher IL-4 expression in local SMG tissues from patients with IgG4-RS, whereas serum IL-4 levels were unchanged, suggesting that IL-4 primarily originates from the infiltrated Th2 lymphocytes and contributes to the local lesions. Moreover, the levels of IL-4 positively correlated with those of $p16^{INK4A}$ and with the degree of fibrosis in IgG4-RS SMG lesions. In vitro, RNA sequencing analysis showed that most of the down-regulated and up-regulated genes were closely related to the regulation of cell proliferation and cell migration, respectively. Since low proliferation is a characteristic of senescent cells, we focused more attention on the down-regulated genes, which indicated that IL-4 might induce senescence in salivary gland epithelial cells.

IL-4 significantly up-regulated SA β-gal activity, changed the morphology of the cells into a senescence phenotype, induced cycle arrest and growth inhibition, caused resistance to apoptosis, and further increased the expression of senescence markers and SASP factors in SMG-C6 cells. In particular, IL-4 induced cellular senescence mainly through $p16^{INK4A}$ and subsequent Rb signal, and not via p53 or p21. The profibrotic role of IL-4 was further proven by the appearance of SMG fibrosis and increased senescence marker expression in mice injected with IL-4, a pathologic phenomenon similar to IgG4-RS. These data demonstrate a causal and direct role of increased IL-4 levels in local lesions in generating salivary gland epithelial cell senescence and fibrosis.

We then explored signal transduction pathways that potentially mediated IL-4–induced epithelial cell senescence. Although STAT6 was significantly activated by IL-4, the inhibition of STAT6 did not affect IL-4–induced senescence. A member of the MAPK family, p38 MAPK mediates numerous cellular processes, such as cellular senescence (31). Partial inactivation of p38 MAPK in p38AF/+ mice, which have mutations in the phosphorylation sites required for activation, led to the attenuation of age-induced up-regulation in the expression of $p16^{INK4A}$, p19, p15, and p21 in multiple tissues. Furthermore, it enhanced the proliferation and regeneration of islets, supporting the notion of an important role of p38 MAPK in the regulation of the cell cycle and senescence (43). In the present study, we found that IL-4 significantly activated p38 MAPK but not ERK1/2, and inhibiting p38 MAPK signaling prevented the IL-4–induced up-regulation of $p16^{INK4A}$ and growth arrest.

We further explored the molecule that linked IL-4 to p38 MAPK. ROS are regarded as the hallmarks of senescence (13). Intracellular ROS generation can serve as a secondary messenger and is responsible for the activation of p38 MAPK in response to cytokines (44). We found that intracellular ROS levels rapidly increased after IL-4 exposure, while treatment with antioxidants abrogated IL-4–induced p38 MAPK activation, suggesting that ROS act as sensors of IL-4 that activate p38 MAPK during the senescence process. In addition, this signaling pathway was detectable in the SMGs from IgG4-RS patients and in the mouse model, thereby supporting the notion of involvement of ROS/p38 MAPK in the development of IgG4-RS.

The transition into SASP makes senescent cells exert beneficial or detrimental effects on the microenvironment by inducing the secretion of cytokines, chemokines, proteases, and growth factors. These SASP factors play important roles in both tissue repair and fibrotic diseases (45). It is well known that fibroblasts are the key effectors that proliferate and differentiate into myofibroblasts in response to injury or inflammation, and lead to the excessive accumulation of extracellular matrix proteins and fibrosis (46). Thus, we investigated both the direct and indirect effects of IL-4 on SMG fibroblasts. IL-4 alone increased collagen synthesis and myofibroblast differentiation but had no effect on proliferation, suggesting that direct IL-4 stimulation only partially activated the fibroblasts. In contrast to this finding, the supernatants collected from IL-4–induced senescent SMG-C6 cells facilitated proliferation, collagen synthesis, and myofibroblast differentiation. Moreover, IL-4 neutralizing antibodies did not eliminate the fibroblast activation induced by IL-4 conditioned medium, which indicated that these effects did not depend on IL-4 but instead on the SASP factors that were secreted by senescent epithelial cells. The secretome of the IL-4–induced senescent cells includes

cytokines and chemokines, which might be important mediators of fibrosis and chronic inflammation in IgG4-RS. The above data show that IL-4 can have a direct and a novel indirect effect, through the interaction between senescent epithelial cells and fibroblasts, in driving the fibrogenesis of IgG4-RS.

In summary, we demonstrate that senescence in salivary epithelial cells is a novel mechanism of fibrogenesis in IgG4-RS. The elevated levels of IL-4 in lesions were responsible for the induction of senescence through the ROS/p38 MAPK-$p16^{INK4A}$ signaling pathway. Moreover, both local IL-4 and the SASP factors derived from IL-4–induced senescent epithelial cells contributed to fibroblast activation, resulting in fibrosis. These findings not only expand our understanding of the pathogenesis of IgG4-RS, but also present a potential intervention strategy for treating IgG4-RS by targeting senescent cells.

ACKNOWLEDGMENT

We thank Professor Guo-He Zhang (National Institute of Dental and Craniofacial Research, NIH, Bethesda, MD) for providing thoughtful suggestions.

AUTHOR CONTRIBUTIONS

All authors were involved in drafting the article or revising it critically for important intellectual content, and all authors approved the final version to be published. Dr. Cong had full access to all of the data in the study and takes responsibility for the integrity of the data and the accuracy of the data analysis.

Study conception and design. Min, Wu, Yu, Cong.
Acquisition of data. Min, Zhu, Mao, Li, Wei, Mei, Cong.
Analysis and interpretation of data. Min, Zhu, Mao, Li, Wei, Mei, Zhang, Wu, Yu, Cong.

REFERENCES

1. Stone JH, Zen Y, Deshpande V. IgG4-related disease. N Engl J Med 2012;366:539–51.
2. Geyer JT, Ferry JA, Harris NL, Stone JH, Zukerberg LR, Lauwers GY, et al. Chronic sclerosing sialadenitis (Küttner tumor) is an IgG4-associated disease. Am J Surg Pathol 2010;34:202–10.
3. Brito-Zerón P, Ramos-Casals M, Bosch X, Stone JH. The clinical spectrum of IgG4-related disease. Autoimmun Rev 2014;13:1203–10.
4. Liu Y, Xue M, Wang Z, Zeng Q, Ren L, Zhang Y, et al. Salivary gland involvement disparities in clinical characteristics of IgG4-related disease: a retrospective study of 428 patients. Rheumatology 2020;59:634–40.
5. Li W, Chen Y, Sun ZP, Cai ZG, Li TT, Zhang L, et al. Clinicopathological characteristics of immunoglobulin G4-related sialadenitis. Arthritis Res Ther 2015;17:186.
6. Inoue D, Yoshida K, Yoneda N, Ozaki K, Matsubara T, Nagai K, et al. IgG4-related disease: dataset of 235 consecutive patients. Medicine (Baltimore) 2015;94:e680.
7. Yamamoto M, Takahashi H, Tanaka H. Differences in clinical features of immunoglobulin G4-related disease between older and younger patients. Geriatr Gerontol Int 2019;19:564–5.
8. Yamamoto M, Takahashi H, Takano K, Shimizu Y, Sakurai N, Suzuki C, et al. Efficacy of abatacept for IgG4-related disease over 8 months. Ann Rheum Dis 2016;75:1576–8.
9. Yamamoto M, Takano K, Kamekura R, Suzuki C, Ichimiya S, Himi T, et al. Stage classification of IgG4-related dacryoadenitis and sialadenitis by the serum cytokine environment. Mod Rheumatol 2018;28:1004–8.
10. Shimatani K, Nakashima Y, Hattori M, Hamazaki Y, Minato N. PD-1^+ memory phenotype $CD4^+$ T cells expressing C/EBPα underlie T cell immunodepression in senescence and leukemia. Proc Natl Acad Sci U S A 2009;106:15807–12.
11. Muñoz-Espín D, Serrano M. Cellular senescence: from physiology to pathology. Nat Rev Mol Cell Biol 2014;15:482–96.
12. Lu L, Guo J, Hua Y, Huang K, Magaye R, Cornell J, et al. Cardiac fibrosis in the ageing heart: contributors and mechanisms. Clin Exp Pharmacol Physiol 2017;44 Suppl:55–63.
13. Hernandez-Segura A, Nehme J, Demaria M. Hallmarks of cellular senescence. Trends Cell Biol 2018;28:436–53.
14. Schafer MJ, Haak AJ, Tschumperlin DJ, LeBrasseur NK. Targeting senescent cells in fibrosis: pathology, paradox, and practical considerations. Curr Rheumatol Rep 2018;20:3.
15. Zhang LM, Zhang J, Zhang Y, Fei C, Wang L, Yi ZW, et al. Interleukin-18 promotes fibroblast senescence in pulmonary fibrosis through down-regulating Klotho expression. Biomed Pharmacother 2019;113:108756.
16. Tominaga K, Suzuki HI. TGF-β signaling in cellular senescence and aging-related pathology. Int J Mol Sci 2019;20:5002.
17. Kong X, Feng D, Wang H, Hong F, Bertola A, Wang FS, et al. Interleukin-22 induces hepatic stellate cell senescence and restricts liver fibrosis in mice. Hepatology 2012;56:1150–9.
18. Marmary Y, Adar R, Gaska S, Wygoda A, Maly A, Cohen J, et al. Radiation-induced loss of salivary gland function is driven by cellular senescence and prevented by IL6 modulation. Cancer Res 2016;76:1170–80.
19. Peng X, Wu Y, Brouwer U, van Vliet T, Wang B, Demaria M, et al. Cellular senescence contributes to radiation-induced hyposalivation by affecting the stem/progenitor cell niche. Cell Death Dis 2020;11:854.
20. Wang X, Bootsma H, Terpstra J, Vissink A, van der Vegt B, Spijkervet FK, et al. Progenitor cell niche senescence reflects pathology of the parotid salivary gland in primary Sjögren's syndrome. Rheumatology (Oxford) 2020;59:3003–13.
21. Pringle S, Wang X, Verstappen GM, Terpstra JH, Zhang CK, He A, et al. Salivary gland stem cells age prematurely in primary Sjögren's syndrome. Arthritis Rheumatol 2019;71:133–42.
22. Kobayashi S, Kamino Y, Hiratsuka K, Kiyama-Kishikawa M, Abiko Y. Age-related changes in IGF-1 expression in submandibular glands of senescence-accelerated mice. J Oral Sci 2004;46:119–25.
23. Kilkenny C, Browne W, Cuthill IC, Emerson M, Altman DG. Animal research: reporting in vivo experiments: the ARRIVE guidelines. Br J Pharmacol 2010;160:1577–9.
24. Umehara H, Okazaki K, Masaki Y, Kawano M, Yamamoto M, Saeki T, et al. Comprehensive diagnostic criteria for IgG4-related disease (IgG4-RD), 2011. Mod Rheumatol 2012;22:21–30.
25. Debacq-Chainiaux F, Erusalimsky JD, Campisi J, Toussaint O. Protocols to detect senescence-associated beta-galactosidase (SA-βgal) activity, a biomarker of senescent cells in culture and *in vivo*. Nat Protoc 2009;4:1798–806.
26. Evangelou K, Gorgoulis VG. Sudan Black B, the specific histochemical stain for lipofuscin: a novel method to detect senescent cells. Methods Mol Biol 2017;1534:111–9.
27. Akiyama M, Suzuki K, Yamaoka K, Yasuoka H, Takeshita M, Kaneko Y, et al. Number of circulating follicular helper 2 T cells correlates with IgG4 and interleukin-4 levels and plasmablast numbers in IgG4-related disease. Arthritis Rheumatol 2015;67:2476–81.
28. Della-Torre E, Bozzalla-Cassione E, Sciorati C, Ruggiero E, Lanzillotta M, Bonfiglio S, et al. A $CD8\alpha^-$ subset of $CD4^+SLAMF7^+$ cytotoxic T cells is expanded in patients with IgG4-related disease

and decreases following glucocorticoid treatment. Arthritis Rheumatol 2018;70:1133–43.

29. Hou J, Schindler U, Henzel WJ, Ho TC, Brasseur M, McKnight SL. An interleukin-4-induced transcription factor: IL-4 Stat. Science 1994; 265:1701–6.
30. Pernis A, Witthuhn B, Keegan AD, Nelms K, Garfein E, Ihle JN, et al. Interleukin 4 signals through two related pathways. Proc Natl Acad Sci U S A 1995;92:7971–5.
31. Xu Y, Li N, Xiang R, Sun P. Emerging roles of the p38 MAPK and PI3K/AKT/mTOR pathways in oncogene-induced senescence. Trends Biochem Sci 2014;39:268–76.
32. Lehmann M, Korfei M, Mutze K, Klee S, Skronska-Wasek W, Alsafadi HN, et al. Senolytic drugs target alveolar epithelial cell function and attenuate experimental lung fibrosis *ex vivo*. Eur Respir J 2017; 50:1602367.
33. Schafer MJ, White TA, Iijima K, Haak AJ, Ligresti G, Atkinson EJ, et al. Cellular senescence mediates fibrotic pulmonary disease. Nat Commun 2017;8:14532.
34. Yang L, Besschetnova TY, Brooks CR, Shah JV, Bonventre JV. Epithelial cell cycle arrest in G2/M mediates kidney fibrosis after injury. Nat Med 2010;16:535–43.
35. Dzeshka MS, Shahid F, Shantsila A, Lip GY. Hypertension and atrial fibrillation: an intimate association of epidemiology, pathophysiology, and outcomes. Am J Hypertens 2017;30:733–55.
36. Ley B, Collard HR. Epidemiology of idiopathic pulmonary fibrosis. Clin Epidemiol 2013;5:483–92.
37. Jin H, Lian N, Zhang F, Chen L, Chen Q, Lu C, et al. Activation of PPARγ/P53 signaling is required for curcumin to induce hepatic stellate cell senescence. Cell Death Dis 2016;7:e2189.
38. Hong X, Zhang YY, Li W, Liu YY, Wang Z, Chen Y, et al. Treatment of immunoglobulin G4-related sialadenitis: outcomes of glucocorticoid therapy combined with steroid-sparing agents. Arthritis Res Ther 2018;20:12.
39. Nelms K, Keegan AD, Zamorano J, Ryan JJ, Paul WE. The IL-4 receptor: signaling mechanisms and biologic functions. Annu Rev Immunol 1999;17:701–38.
40. Horvath CM. STAT proteins and transcriptional responses to extracellular signals. Trends Biochem Sci 2000;25:496–502.
41. Kim HD, Yu SJ, Kim HS, Kim YJ, Choe JM, Park YG, et al. Interleukin-4 induces senescence in human renal carcinoma cell lines through STAT6 and p38 MAPK. J Biol Chem 2013;288: 28743–54.
42. Ma Y, Chiao YA, Clark R, Flynn ER, Yabluchanskiy A, Ghasemi O, et al. Deriving a cardiac ageing signature to reveal MMP-9-dependent inflammatory signalling in senescence. Cardiovasc Res 2015;106: 421–31.
43. Wong ES, Le Guezennec X, Demidov ON, Marshall NT, Wang ST, Krishnamurthy J, et al. p38MAPK controls expression of multiple cell cycle inhibitors and islet proliferation with advancing age. Dev Cell 2009;17:142–9.
44. Tormos AM, Taléns-Visconti R, Nebreda AR, Sastre J. p38 MAPK: a dual role in hepatocyte proliferation through reactive oxygen species. Free Radic Res 2013;47:905–16.
45. Freund A, Orjalo AV, Desprez PY, Campisi J. Inflammatory networks during cellular senescence: causes and consequences. Trends Mol Med 2010;16:238–46.
46. Rockey DC, Bell PD, Hill JA. Fibrosis—a common pathway to organ injury and failure. N Engl J Med 2015;372:1138–49.

Arthritis & Rheumatology
Vol. 74, No. 6, June 2022, pp 1083–1090
DOI 10.1002/art.42070

AMERICAN COLLEGE of RHEUMATOLOGY
Empowering Rheumatology Professionals

BRIEF REPORT

Haploinsufficiency of PSMD12 Causes Proteasome Dysfunction and Subclinical Autoinflammation

Kai Yan,[1] Jiahui Zhang,[1] Pui Y. Lee,[2] Panfeng Tao,[3] Jun Wang,[1] Shihao Wang,[1] Qing Zhou,[1] and Minyue Dong[1]

Objective. Proteasome-associated autoinflammatory syndrome (PRAAS) is caused by mutations affecting components of the proteasome and activation of the type I interferon (IFN) pathway. This study was undertaken to investigate the pathogenic mechanisms of a newly recognized type of PRAAS caused by PSMD12 haploinsufficiency.

Methods. Whole-exome sequencing was performed in members of a family with skin rash, congenital uveitis, and developmental delay. We performed functional studies to assess proteasome dysfunction and inflammatory signatures in patients, and single-cell RNA sequencing to further explore the spectrum of immune cell activation.

Results. A novel truncated variant in *PSMD12* (c.865C>T, p.Arg289*) was identified in 2 family members. The impairment of proteasome function was found in peripheral blood mononuclear cells (PBMCs), as well as in PSMD12-knockdown HEK 293T cell lines. Moreover, we defined the inflammatory signatures in patient PBMCs and found elevated IFN signals, especially in monocytes, by single-cell RNA sequencing.

Conclusion. These findings indicate that PSMD12 haploinsufficiency causes a set of inflammation signatures in addition to neurodevelopmental disorders. Our work expands the genotype and phenotype spectrum of PRAAS and suggests a bridge between the almost exclusively inflammatory phenotypes in the majority of PRAAS patients and the almost exclusively neurodevelopmental phenotypes in the previously reported Stankiewicz-Isidor syndrome.

INTRODUCTION

Autoinflammatory diseases are characterized by spontaneous activation of inflammatory pathways primarily driven by innate immune cells (1). Understanding of autoinflammation has expanded drastically with rapid advances in recent decades.

Defects in the constitutive proteasome or immunoproteasome result in proteasome-associated autoinflammatory syndrome (PRAAS), also known as CANDLE/NNS/JMP/JASL (chronic atypical neutrophilic dermatosis with lipodystrophy and elevated temperature/Nakajo-Nishimura syndrome/joint contractures, muscle atrophy, microcytic anemia, and panniculitis-induced lipodystrophy syndrome/Japanese autoinflammatory syndrome with lipodystrophy) (2). PRAAS is clinically characterized by recurrent fever, neutrophilic dermatosis, lipodystrophy, joint contractures, and failure to thrive (2). Several genes encoding immunoproteasome or proteasome 20S subunits, such as *PSMB8*, *PBMB9*, *PSMB10*, *PSMB4*, *PSMA3*, and the chaperones essential for proteasome assembly, such as *POMP* and *PSMG2*, have been identified as causative genes in PRAAS (2–7). Biallelic mutations in the proteasome subunits can cause defective proteasome function by disrupting proteasome assembly and/or catalytic activity, ultimately leading to the accumulation of ubiquitin protein conjugates as a consequence of impaired capacity to remove damaged proteins,

Mr. Yan's work was supported by the Zhejiang Provincial Natural Science Foundation of China (grant LQ19H040016). Dr. Zhou's work was supported by the National Key Research and Development Program of China (grant 2018YFC1004903), the National Natural Science Foundation of China (grants 31771548 and 81971528), and the Zhejiang Provincial Natural Science Foundation of China (grant LR19H100001). Dr. Dong's work was supported by the Key Research and Development Program of Zhejiang Province (grant 2019C03025).

[1]Kai Yan, MSc, Jiahui Zhang, BS, Jun Wang, BS, Shihao Wang, PhD, Qing Zhou, PhD, Minyue Dong, MD: Zhejiang University, Hangzhou, China; [2]Pui Y. Lee, MD, PhD: Harvard Medical School, Boston, Massachusetts; [3]Panfeng Tao, PhD: Zhejiang University and Zhejiang University Medical Center, Hangzhou, China.

Mr. Yan and Ms. Zhang contributed equally to this work. Drs. Zhou and Dong contributed equally to this work.

Author disclosures are available at https://onlinelibrary.wiley.com/action/downloadSupplement?doi=10.1002%2Fart.42070&file=art42070-sup-0001-Disclosureform.pdf.

Address correspondence to Qing Zhou, PhD, The MOE Key Laboratory of Biosystems Homeostasis and Protection, Life Sciences Institute, Zhejiang University, Hangzhou 310058, China (email: zhouq2@zju.edu.cn); or to Minyue Dong, MD, Women's Hospital, School of Medicine, Zhejiang University, Hangzhou 310005, China (email: dongmy@zju.edu.cn).

Submitted for publication February 16, 2021; accepted in revised form January 18, 2022.

while deficiency of other proteasome-associated genes, such as *PSMC3* and *PSMB1*, may cause only neurodevelopmental disorders (8,9).

Rpn5, a 52.9-kd protein in the 19S regulatory subunit of the proteasome encoded by *PSMD12*, facilitates deubiquitination of captured substrates. Previous studies have demonstrated the association between loss-of-function variants in *PSMD12* and a syndromic neurodevelopmental disorder named Stankiewicz-Isidor syndrome (OMIM no. 604450). Its symptoms include brain abnormalities, dysmorphic features, ophthalmologic abnormalities, genital anomalies, and skeletal defects (10–13), without typical autoinflammatory features. In the current study, we investigated a novel PSMD12 nonsense mutation found in 2 generations of family members who presented with skin rash and congenital uveitis in addition to developmental delay. Mechanistic studies revealed that individuals carrying the PSMD12 truncated variant exhibit a variety of inflammatory signatures similar to those found in patients with PRAAS.

PATIENTS AND METHODS

Ethical considerations. The study was approved by the Institutional Review Board of Women's Hospital, Zhejiang University, where the patients were evaluated. The patients and control subjects (or their legal guardians if minors) provided written informed consent.

Cell collection, culture, and stimulation. Peripheral blood mononuclear cells (PBMCs) were separated from peripheral blood using lymphocyte separation medium and SepMate tubes (StemCell Technologies). PBMCs and HEK 293T cells were cultured in RPMI 1640 or Dulbecco's modified Eagle's medium (Gibco) with 10% fetal bovine serum (ExCell Bio) and 10% penicillin/streptomycin (HyClone). Lipopolysaccharide (LPS) (1 μg/ml; Sigma) poly(I-C) (50 μg/ml; Invitrogen), interferon-β (IFNβ) (10 ng/ml; PeproTech), and baricitinib (0.5 μ*M*; Selleck) were used to treat PBMCs for 6 hours (LPS and poly[I-C]) or 4 hours (IFNβ and baricitinib).

Whole-exome sequencing. Peripheral blood DNA was sequenced using a Roche SeqCap EZ MedExome Enrichment Kit and the Illumina HiSeq X Ten platform. A set of 150-bp paired-end reads was mapped to hg38 reference genome using BWA, version 0.7.17 and the bam files were sorted and indexed using Picard followed by calling variants with GATK, version 4.1.4.1.

RNA sequencing. Total RNA was extracted from PBMCs with an RNeasy Mini kit (Qiagen). Libraries were generated from 1 μg RNA with a NEBNext UltraTM RNA Library Prep Kit for Illumina (NEB) followed by sequencing on Illumina HiSeq X Ten.

Single-cell RNA sequencing. A total of 8,000–10,000 single cells for each sample were captured and barcoded with a 10X Genomics Chromium console. The barcoded complementary DNA (cDNA) was amplified and sequenced using Illumina Novaseq. Data were processed with CellRange, version 6.0.1 (10x; Genomics) and the Seurat R package, version 3.2.0. Hallmark gene set in MsigDB, version7.1 (https://www.gsea-msigdb.org/gsea/msigdb/index.jsp) was used for gene set enrichment analysis.

Real-time polymerase chain reaction (PCR). Total RNA was extracted with an RNeasy Mini kit, followed by cDNA amplification and quantitative PCR (qPCR) analysis with TB Gree Premix Ex Ta II (Takara). Relative messenger RNA expression was normalized to the expression of *ACTB* and analyzed by the $\Delta\Delta C_t$ method.

Antibodies and expression plasmids. Antibodies used and their commercial sources were as follows: β-actin, STAT2, phosphorylated STAT2, IFN regulatory factor 3 (IRF3), phosphorylated IRF3, STAT1, phosphorylated STAT1, myeloma differentiation–associated protein 5 (MDA5), retinoic acid–inducible gene 1 (RIG-1), and K48 polyubiquitin (all from Cell Signaling Technology); PSMA7, PSMB4, PSMC5, PSMD1, PSMD2, PSMD3, PSMD12 polyclonal antibody, PSMD13, and PSME2 (all from ABclonal Technology); PSMD12 monoclonal antibody (Santa Cruz Biotechnology); PSMC6 and IFN-induced protein with tetratricopeptide repeats 3 (Abcam); and Flag (Sigma).

Wild-type human *PSMD12* was cloned from healthy control cDNA and cloned into pXN (Dbf4-dependent kinase tagged) vector constructed in-house. Mutant plasmid was constructed by site-directed mutagenesis.

Western blot analysis. Cells were resuspended for 15 minutes in ice-cold cell lysis buffer (20 m*M* Tris HCl [pH 7.4], 150 m*M* NaCl, 0.5% Nonidet P40, 10% glycerol with protease and phosphatase inhibitors) (ThermoFisher) and centrifuged (13,000*g* at 4°C for 15 minutes). The supernatants were collected and subjected to sodium dodecyl sulfate–polyacrylamide gel electrophoresis (PAGE). Immunoblotting with specific antibodies was performed.

Proteasome activity assay. Proteasome activity was measured with Proteasome-Glo Chymotrypsin-Like, Trypsin-Like, and Caspase-Like Cell-Based Assays (Promega). Proteasome inhibition with 5 μ*M* epoxomicin was performed for 2 hours at 37°C. All experiments were conducted on 384-well plates with 4 technical replicates. Data were collected with a multimode plate reader (BioTek).

Construction of PSMD12 knockdown cell lines. Four different short hairpin RNA (shRNA) sequences (sh*PSMD12*-1 [CCGGCCTAGCTGTGAAGGATTACATCTCGAGATGTAATCCT

TCACAGCTAGGTTTTTG], sh*PSMD12*-2 [CCGGCCGAATAAGTGGTGACAAGAACTCGAGTTCTTGTCACCACTTATTCGGTTTTTG], sh*PSMD12*-3 [CCGGCCTTCCTATCAAACTTCGATTCTCGAGAATCGAAGTTTGATAGGAAGGTTTTTG], and sh*PSMD12*-4 [CCGGGCCAAGTATTATACTCGGATACTCGAGTATCCGAGTATAATACTTGGCTTTTTG]) were constructed into pLKO.1 plasmid and transfected into wild-type HEK 293T cells, followed by treatment with 1.5 μg/ml puromycin for 5–7 days. Clones were separated and verified by qPCR and Western blot analysis.

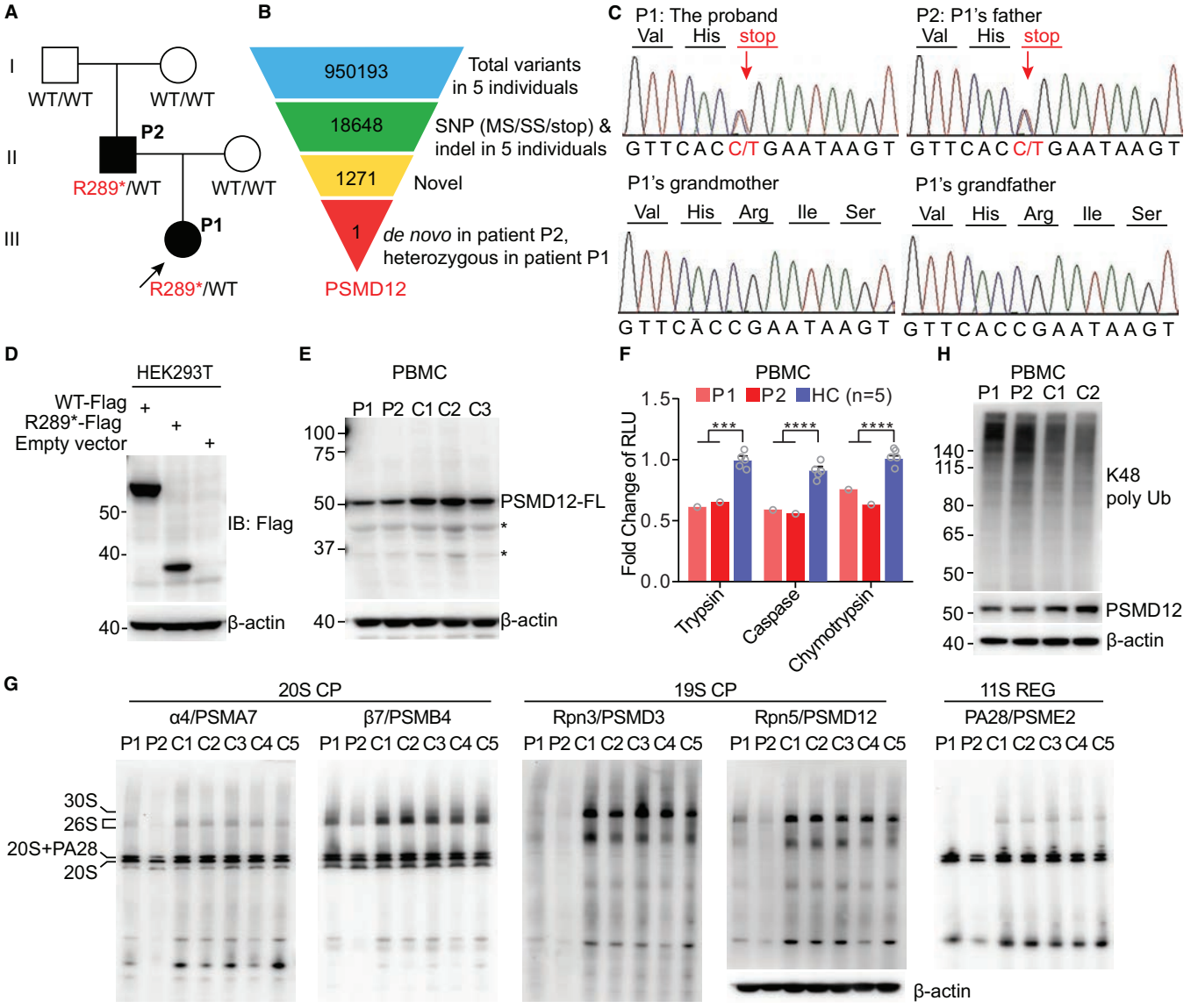

Figure 1. Identification of the *PSMD12* variant and proteasome dysfunction in patients with the variant. **A**, Pedigree of the family carrying the heterozygous novel *PSMD12* truncated variant p.R289*. Family members with the variant are patient 1 (P1) (proband [**arrow**]), an 8-year-old girl with urticarial skin rashes, severe intellectual disability, and developmental delay, and her father, patient 2 (P2), with congenital uveitis and mild intellectual disability. **B**, Schematic representation of the whole-exome sequencing analysis and variant filtering approach used to identify the pathogenic variant in *PSMD12*. Single-nucleotide polymorphism (SNP) includes missense (MS), splice site (SS), and stop codon variants and indel, frameshift, and non-frameshift insertions and deletions. **C**, Confirmation of the nonsense variant by Sanger sequencing. **D** and **E**, Wild-type (WT) and truncated PSMD12 expression in transfected HEK 293T cells (**D**) and in patient and control (C) peripheral blood mononuclear cells (PBMCs) (**E**). Experiments were performed at least 3 times for each sample. **F**, Significant differences in 3 types of proteasome proteolytic activity between patient and healthy control (HC) PBMCs. Symbols represent individual samples; for healthy controls, bars show the mean ± SEM. *** = $P < 0.001$; **** = $P < 0.0001$. **G**, Native gel analysis of the proteasome assembly in PBMCs from patients and controls. The assembly of different parts of the proteasome was illustrated using antibodies to the corresponding subunits. The loading amount of each sample is presented relative to the level of β-actin determined by sodium dodecyl sulfate–polyacrylamide gel electrophoresis. **H**, K48 ubiquitin (Ub) levels in PBMCs from the patients and 2 controls. FL = full-length; RLU = relative luminescence units; CP = core particle; REG = regulatory particle.

Native PAGE. Cells were lysed in TSDG buffer (10 m*M* Tris HCl, 10 m*M* NaCl, 1.1 m*M* $MgCl_2$, 0.1 m*M* EDTA, 1 m*M* dithiothreitol, 2 m*M* ATP, 10% glycerol [pH 7.2]) by freeze-thawing 15–20 times and suspended in loading buffer (5 m*M* Tris HCl, 5% glycerol, 0.01% bromphenol blue) followed by electrophoresis on NativePAGE 3–12% Bis-Tris gels (ThermoFisher). The proteasome subunits were analyzed by immunoblotting with antibodies.

Enzyme-linked immunosorbent assay (ELISA), cytometric bead array system, and IFN response gene score. Interleukin-6 (IL-6), tumor necrosis factor (TNF), and IL-1β in the supernatants of unstimulated PBMCs were quantified by ELISA (R&D Systems). Serum samples were tested with a BDFlex set of human cytokines/chemokines, which includes IL-8, IL-1β, IFNγ-inducible protein 10 (IP-10), and IFNγ, with buffer kit and normalization beads (BD). The IFN response gene score was calculated as previously described (14).

Statistical analysis. Cell-based experiments were performed in triplicate. Results were compared by Student's *t*-test (unpaired and 2-tailed). *P* values less than 0.05 were considered significant.

RESULTS

Patients with the heterozygous *PSMD12* nonsense variant. The proband (patient 1) was an 8-year-old girl with urticarial skin rashes, severe intellectual disability, and developmental delay. Her father (patient 2) exhibited congenital uveitis and mild intellectual disability. Both subjects displayed mild facial dysmorphic features including frontal bossing, hypertelorism, and nasal bridge depression. Lymphocyte phenotyping revealed increased numbers of CD4+ naive T cells in patient 1 and CD8+ T cells in patient 2. (Supplementary Tables 1 and 2, on the *Arthritis & Rheumatology* website at https://onlinelibrary.wiley.com/doi/10.1002/art.42070). Genomic analysis of patients and their family members by whole-exome sequencing revealed a novel heterozygous nonsense variant in *PSMD12*: c.865C>T, p.Arg289*, which was de novo in the father and inherited by his daughter (Figures 1A–C). The probability of loss-of-function intolerance of *PSMD12* is 1.0, which strongly supports the notion that this loss-of-function nonsense variant is pathogenic.

To determine how the mutation affected protein expression, wild-type and mutant *PSMD12* were transfected into HEK 293T cells, and a truncated PSMD12 containing amino acid residues 1–288 was observed (Figure 1D). Additionally, the expression of PSMD12–full-length was reduced and the truncated form was not detected in patient PBMCs (Figure 1E), suggesting the possibility of spontaneous degradation of the truncated protein in vivo. Therefore, the novel loss-of-function variant resulted in haploinsufficiency of PSMD12.

Proteasome defects associated with PSMD12 haploinsufficiency. Patient PBMCs exhibited significantly reduced proteolytic capacity (Figure 1F), confirming their impaired proteasome functions. Native gel electrophoresis was performed to analyze the assembly of proteasome complex in patient PBMCs. Immunoblotting with antibodies to 19S and 20S proteasome subunits showed markedly decreased levels of 19S and slightly decreased levels of 20S in PBMCs from patients compared to control PBMCs (Figure 1G).

PSMD12-knockdown HEK 293T cell lines were constructed to evaluate the effect of PSMD12 haploinsufficiency in vitro (Supplementary Figures 1A and B, https://onlinelibrary.wiley.com/doi/10.1002/art.42070). The 3 types of proteasome activities in the knockdown cells were also decreased (Supplementary Figure 1C). Native gel electrophoresis with PSMD12-knockdown cells demonstrated defective 26S proteasome assembly compared to cells treated with scrambled shRNA (Supplementary Figure 1D). Interactions of the truncated PSMD12 with a set of 19S subunits, including ATPase and non-ATPase subunits, were all reduced (Supplementary Figure 1E). Impaired proteasome functions led to an accumulation of polyubiquitinated proteins. Both patients showed an accumulation of K48 ubiquitin–modified proteins compared to healthy controls (Figure 1H). Taken together, these data revealed profound disruptions of proteasome dysfunction associated with PSMD12 haploinsufficiency.

Elevated inflammatory signals in patient PBMCs. Proteasome defects are accompanied by ineffective removal of unfolded protein and ubiquitin–protein aggregates, which promotes a type I IFN response. Therefore, disruption of proteasome function can lead to enhanced production of type I IFN (2). To test whether PSMD12 haploinsufficiency is associated with dysregulated IFN production, PBMCs from the 2 patients and 4 control subjects were stimulated with poly(I-C), and phosphorylation of downstream targets and expression of IFN-stimulated genes (ISGs) were investigated. Patient 1 displayed enhanced phosphorylation of STAT1, STAT2, and IRF3 and increased expression of MDA5 and RIG-1, indicating augmented activation of the IFN signaling pathway by poly(I-C). Patient 2 exhibited enhanced phosphorylation of STAT2 and IRF3 (Figure 2A).

We next examined the production of proinflammatory cytokines in the supernatants of PBMCs from patient 2, by ELISA. Basal production of IL-6, TNF, and IL-1β was significantly higher in this patient compared to PBMCs from controls (Figure 2B). Correspondingly, transcription levels of ISGs, including *ISG15*, *IFNB1*, and *OAS1*, were elevated in PBMCs from patient 2, with or without LPS stimulation (Figure 2C). In addition, PBMCs from patient 2 were hyperresponsive to IFNβ stimulation, with increased levels of ISG expression (Figure 2D). Cytometric bead array analysis in serum from patients and controls showed that levels of proinflammatory cytokines such as IL-8, IFNγ, and IL-1β, as well as the chemokine IP-10, were consistently

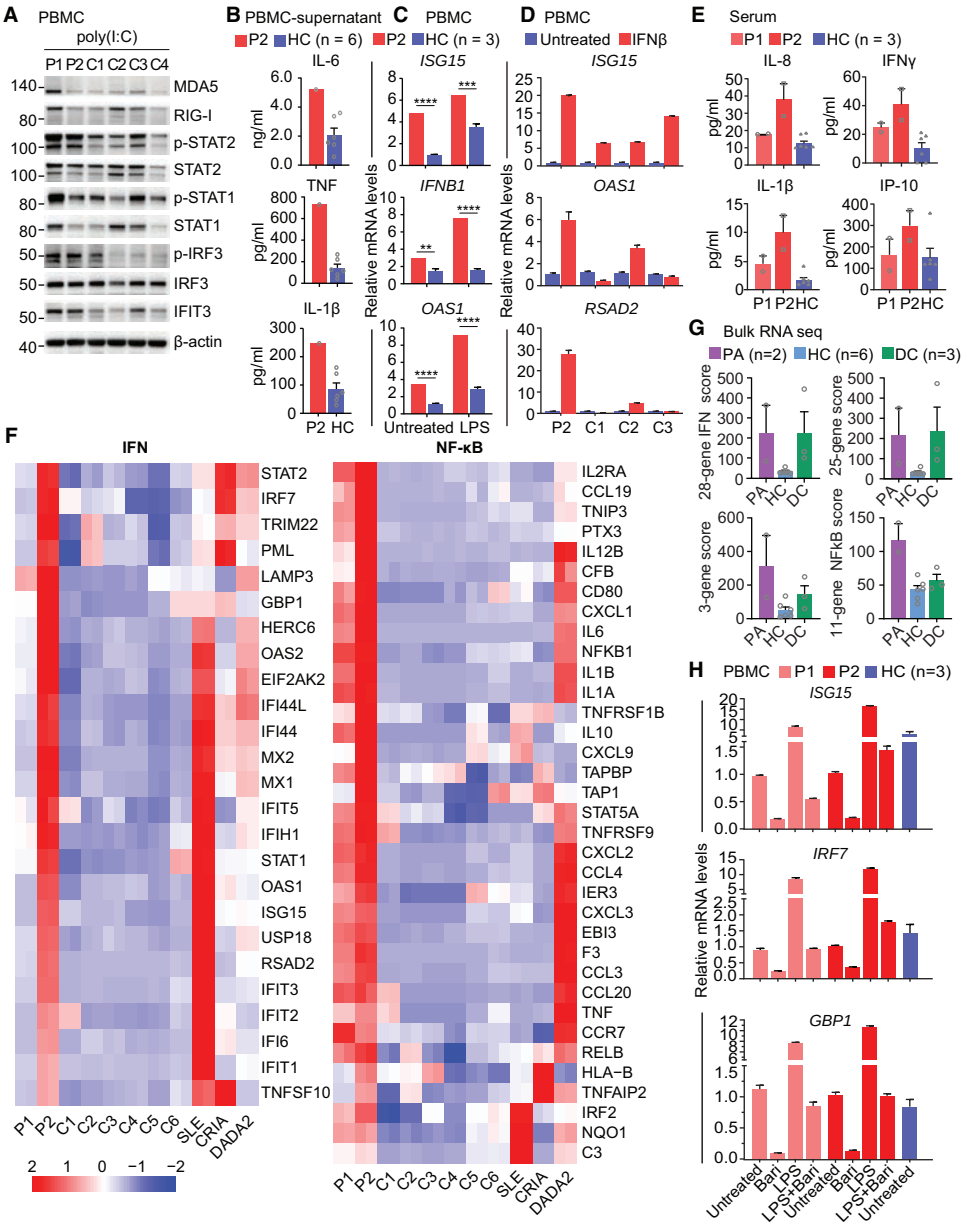

Figure 2. Elevated inflammatory signals in PBMCs from patients with the *PSMD12* variant. **A**, Western blots of interferon (IFN) signaling pathway–involved proteins in poly(I-C)–stimulated PBMCs from patients 1 and 2 and control subjects. Results shown are representative of 2 independent experiments. **B**, Levels of the cytokines interleukin-6 (IL-6), tumor necrosis factor (TNF), and IL-1β in cultured supernatants of PBMCs from patient 2 and 6 control subjects, measured by enzyme-linked immunosorbent assay. **C** and **D**, Expression levels of IFN-stimulated genes in PBMCs from patient 2 and 3 control subjects. PBMCs were treated with lipopolysaccharide (LPS) (**C**) or IFNβ (**D**) or were left untreated. ** = $P < 0.01$; *** = $P < 0.001$; **** = $P < 0.0001$. **E**, Concentrations of the proinflammatory cytokines IL-8, IFNγ, and IL-1β and the chemokine IFNγ-inducible protein 10 (IP-10) in serum from patients 1 and 2 and from control subjects, determined by cytometric bead array analysis. Two samples from each subject, obtained at different times, were assessed. **F**, Expression patterns of genes involved in the IFN and NF-κB signaling pathways in PBMCs from patients 1 and 2, healthy control subjects, and disease controls, determined by RNA sequencing. **G**, IFN response gene scores (28-gene, 25-gene, and 3-gene) and NF-κB score (11-gene) in the 2 patients (PA), healthy controls, and disease controls (DC), determined using bulk RNA sequencing data. **H**, Expression levels of IFN pathway genes in LPS-stimulated PBMCs from patients 1 and 2 and healthy controls, with and without baricitinib (Bari) treatment. In **B–E**, **G**, and **H**, symbols represent individual samples; for healthy controls (and for studies in which >1 sample from each of the 2 patients was assessed), bars show the mean ± SEM. MDA5 = myeloma differentiation–associated protein 5; RIG-I = retinoic acid–inducible gene I; IRF3 = IFN regulatory factor 3; IFIT3 = IFN-induced protein with tetratricopeptide repeats 3; SLE = systemic lupus erythematosus; CRIA = cleavage-resistant receptor-interacting protein kinase 1–induced autoinflammatory; DADA2 = deficiency of adenosine deaminase 2; (see Figure 1 for other definitions).

increased in the 2 patients, especially in patient 2 (Figure 2E). The heterogeneity of inflammatory signatures between patient 1 and patient 2 was probably due to different disease activity and inflammatory conditions during sample collection.

Bulk RNA sequencing of PBMCs demonstrated that both patients had elevated basal expression of genes in the IFN signaling pathway (Figure 2F) compared to 6 healthy controls, and the top 20 genes that were differentially expressed between patient 2 and healthy controls included some ISGs (Supplementary Table 3, on the *Arthritis & Rheumatology* website at https://onlinelibrary.wiley.com/doi/10.1002/art.42070). These findings were further confirmed by the higher IFN response gene score in the 2 patients (Figure 2G). The IFN signature in patient 2 was as strong as that in a patient with active systemic lupus erythematosus and higher than that in patients with other autoinflammatory diseases (disease controls) such as CRIA (cleavage-resistant receptor-interacting protein kinase 1–induced autoinflammatory) (15) and DADA2 (deficiency of adenosine deaminase 2) (16) (Figure 2F). NF-κB signaling was also elevated in both patients compared to healthy controls, and the signaling was higher than that observed in a CRIA patient during a febrile episode (Figure 2F). These results demonstrated systemic inflammation with activation of IFN and NF-κB signaling in the setting of PSMD12 haploinsufficiency.

We further found that type I IFN signaling in PBMCs from the 2 patients could be suppressed by treatment with the JAK inhibitor baricitinib in vitro (Figure 2H). These data suggest that JAK inhibition may be a potential strategy to control the inflammatory response in patients with PSMD12 deficiency, in accordance with the utility of this class of medication for the treatment of PRAAS and other interferonopathies.

Single-cell RNA sequencing was performed in both patients and in 2 age- and sex-matched controls, and identified a total of 13 different cell clusters (Figure 3A). Patient 1 expressed increased levels of ISGs, such as *STAT1*, *ISG15*, and *OAS1*, in different cell types, especially in CD14+ classic monocytes and CD16+ nonclassic monocytes (Figure 3B). Genes that mediate proinflammatory responses were prominently expressed in patient monocytes, with markedly greater expression of genes in the type I IFN pathway compared to that in controls (Figure 3C and Supplementary Figure 1F [https://onlinelibrary.wiley.com/doi/10.1002/art.42070]).

We next sought to identify gene expression patterns in monocytes and their relationship to the elevated inflammatory response in the patients. Of note, we observed a significant enrichment of inflammatory response and IFN response gene sets in CD14+ monocytes identified by single-cell RNA sequencing using gene set enrichment analysis (Figures 3D and E). Additionally, CD14+ classic monocytes and CD16+ nonclassic monocytes from the patients exhibited elevated expression of genes in the type I IFN pathway (Figure 3F). These results suggest that monocytes may have a prominent role in propagating the inflammatory response in PSMD12 haploinsufficiency.

DISCUSSION

The proteasome is a protease complex and an important cellular machinery that regulates protein turnover; the integrity of each of its subunits is of great importance to the overall function of this sophisticated complex. Biallelic pathogenic mutations in genes encoding proteasome subunits can cause PRAAS due to excess type I IFN signaling. However, the mechanism by which disrupted proteasome function translates into type I IFN production remains unclear. The potential contributions of oxidative stress and endoplasmic reticulum stress to IFN production have been considered as possible explanations (3).

Unlike most other forms of PRAAS that require biallelic mutations, haploinsufficiency of PSMD12 is sufficient to cause type I IFN up-regulation and autoinflammation. Previous studies have focused on the association of *PSMD12* variants, including microdeletions and point mutations, with neurodevelopmental disorders, and autoinflammation has frequently not been addressed in such neurology-based investigations. This is the first study to identify strong IFN and NF-κB signaling, as found in typical autoinflammatory diseases and systemic lupus erythematosus, in patients with PSMD12, establishing a correlation between PSMD12 haploinsufficiency and PRAAS. Importantly, our results demonstrate that defective proteasome subunits, in addition to *PSMB4*, *PSMB8*, *PSMB9*, *PSMB10*, *PSMA3*, *PSMG2*, and *POMP* (17), are linked to interferonopathy. With the identification of additional patients with *PSMD12* loss-of-function mutations in the future, more systemic autoinflammation phenotypes may be reported. Our results also implicate the likelihood of latent or subclinical autoinflammation in patients with Stankiewicz-Isidor syndrome and those with predominantly neurodevelopmental disorders who have proteasome defects due to deficiency of PSMB1 and PSMC3. It is possible that such inflammation may be a pathogenic factor in these neurodevelopmental disorders.

In addition, reduced penetrance in patients with the *PSMD12* mutation needs to be taken into consideration, and may explain the variable disease expressivity and severity among individuals with mutations in the same gene. Reduced penetrance has been reported in some type I interferonopathies, including Aicardi Goutières syndrome (due to dominantly inherited mutations in *IFIH1*) and STING-associated vasculitis with onset in infancy (caused by gain-of-function mutations in *TMEM173*) (18–20).

This study had some limitations. Skin biopsy specimens or histologic images from the patients were unavailable as the skin features appeared very early in the clinical course and were not assessed histologically. We were also unable to acquire sufficient blood samples from the patients during disease flares, for more comprehensive exploration of disease mechanisms. With the small number of patients, it was also difficult to explore the

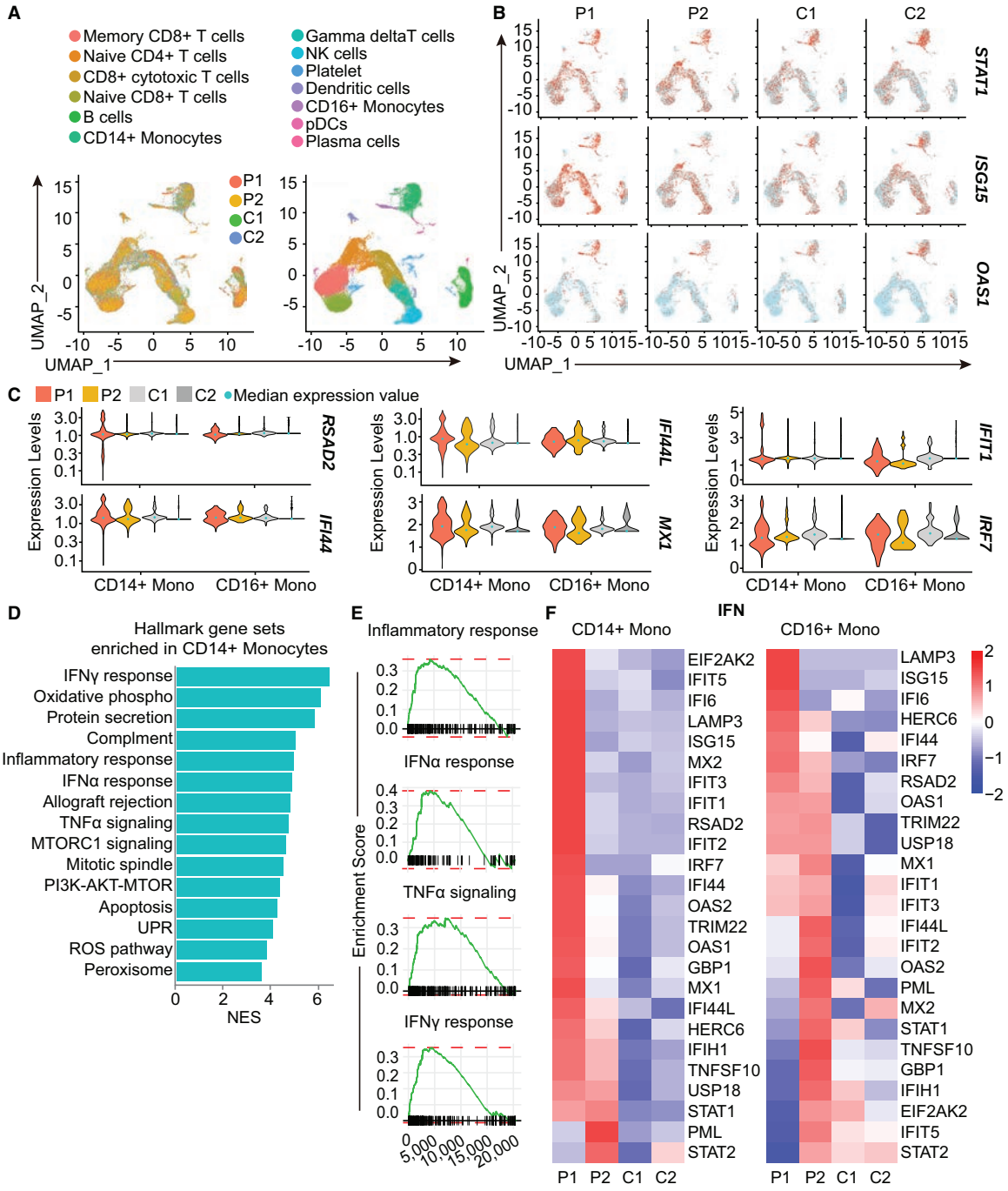

Figure 3. Enrichment of inflammatory pathways in monocytes from patients with the *PSMD12* variant. **A**, Single-cell RNA sequencing analysis of cell type distributions in PBMCs from the 2 patients and 2 healthy controls (left), and different cell clusters in the patients and controls (right). Control 1 was age- and sex-matched to patient 1, and control 2 was age- and sex-matched to patient 2. **B**, FeaturePlots of interferon (IFN)–related genes, created using single-cell RNA sequencing data. Colored dots indicate single cells in the UMAP plot; red color indicates a higher level of gene expression. **C**, Violin plots showing the expression of IFN-stimulated genes in CD14+ and CD16+ monocytes (Mono) from the 2 patients and 2 healthy control subjects. Light blue dots show the median expression level of all cells. **D**, Enriched hallmark gene set pathways of pathways in CD14+ monocytes analyzed by gene set enrichment analysis (GSEA). **E**, GSEA plot of inflammatory response, as well as IFNα, tumor necrosis factor (TNF), and IFNγ responses in CD14+ monocytes from the patients and controls. **F**, Comparison of type I IFN signaling pathways in CD14+ and CD16+ monocyte subsets from patients and controls, determined by single-cell RNA sequencing. NK = natural killer; pDCs = plasmacytoid dendritic cells; mTORC1 = mechanistic target of rapamycin complex 1; PI3K = phosphatidylinositol 3-kinase; UPR = unfolded protein response; ROS = reactive oxygen species; NES = normalized enrichment score (see Figure 1 for other definitions).

heterogeneity of inflammatory features among patients. Therefore, further studies are needed to investigate the relationship of proteasome dysfunction and elevated type I IFN signatures.

In conclusion, we have identified a novel *PSMD12* truncating variant that impairs proteasome subunit assembly and reduces proteasome catalytic activity. We have described autoinflammatory features of PSMD12 haploinsufficiency and defined, for the first time, the inflammatory signals at the single-cell level. Taken together, our findings provide further insights into the biology of proteasomes and the pathologic basis of PRAAS.

ACKNOWLEDGMENTS

We thank the patients and control subjects for their support during the study.

AUTHOR CONTRIBUTIONS

All authors were involved in drafting the article or revising it critically for important intellectual content, and all authors approved the final version to be published. Drs. Zhou and Dong had full access to all of the data in the study and takes responsibility for the integrity of the data and the accuracy of the data analysis.

Study conception and design. Yan, Zhang, Tao, Zhou.

Acquisition of data. Yan, Zhang, Zhou, Dong.

Analysis and interpretation of data. Yan, Zhang, Lee, Tao, J. Wang, S. Wang, Zhou.

REFERENCES

1. Manthiram K, Zhou Q, Aksentijevich I, Kastner DL. The monogenic autoinflammatory diseases define new pathways in human innate immunity and inflammation. Nat Immunol 2017;18:832–42.
2. Brehm A, Liu Y, Sheikh A, Marrero B, Omoyinmi E, Zhou Q, et al. Additive loss-of-function proteasome subunit mutations in CANDLE/PRAAS patients promote type I IFN production. J Clin Invest 2015;125:4196–211.
3. Poli MC, Ebstein F, Nicholas SK, de Guzman MM, Forbes LR, Chinn IK, et al. Heterozygous truncating variants in POMP escape nonsense-mediated decay and cause a unique immune dysregulatory syndrome. Am J Hum Genet 2018;102:1126–42.
4. De Jesus AA, Brehm A, vanTries R, Pillet P, Parentelli AS, Sanchez GA, et al. Novel proteasome assembly chaperone mutations in PSMG2/PAC2 cause the autoinflammatory interferonopathy CANDLE/PRAAS4. J Allergy Clin Immunol 2019;143:1939–43.
5. Sarrabay G, Mechin D, Salhi A, Boursier G, Rittore C, Crow Y, et al. PSMB10, the last immunoproteasome gene missing for PRAAS. J Allergy Clin Immunol 2020;145:1015–7.
6. Çetin G, Klafack S, Studencka-Turski M, Kruger E, Ebstein F. The ubiquitin-proteasome system in immune cells. Biomolecules 2021;11:60.
7. Kanazawa N, Hemmi H, Kinjo N, Ohnishi H, Hamazaki J, Mishima H, et al. Heterozygous missense variant of the proteasome subunit β-type 9 causes neonatal-onset autoinflammation and immunodeficiency. Nat Commun 2021;12:6819.
8. Kroll-Hermi A, Ebstein F, Stoetzel C, Geoffroy V, Schaefer E, Scheidecker S, et al. Proteasome subunit PSMC3 variants cause neurosensory syndrome combining deafness and cataract due to proteotoxic stress. EMBO Mol Med 2020;12:e11861.
9. Ansar M, Ebstein F, Ozkoc H, Paracha SA, Iwaszkiewicz J, Gesemann M, et al. Biallelic variants in PSMB1 encoding the proteasome subunit β6 cause impairment of proteasome function, microcephaly, intellectual disability, developmental delay and short stature. Hum Mol Genet 2020;29:1132–43.
10. Kury S, Besnard T, Ebstein F, Khan TN, Gambin T, Douglas J, et al. De novo disruption of the proteasome regulatory subunit PSMD12 causes a syndromic neurodevelopmental disorder. Am J Hum Genet 2017;100:689.
11. Naud ME, Tosca L, Martinovic J, Saada J, Metay C, Drevillon L, et al. Prenatal diagnosis of a 2.5 Mb de novo 17q24.1q24.2 deletion encompassing KPNA2 and PSMD12 genes in a fetus with craniofacial dysmorphism, equinovarus feet, and syndactyly. Case Rep Genet 2017;2017:7803136.
12. Khalil R, Kenny C, Hill RS, Mochida GH, Nasir R, Partlow JN, et al. PSMD12 haploinsufficiency in a neurodevelopmental disorder with autistic features. Am J Med Genet B Neuropsychiatr Genet 2018;177:736–45.
13. Palumbo P, Palumbo O, Di Muro E, Leone MP, Castellana S, Biagini T, et al. Expanding the clinical and molecular spectrum of PSMD12-related neurodevelopmental syndrome: an additional patient and review. Arch Clin Med Case Rep 2019;03.
14. De Jesus AA, Hou Y, Brooks S, Malle L, Biancotto A, Huang Y, et al. Distinct interferon signatures and cytokine patterns define additional systemic autoinflammatory diseases. J Clin Invest 2020;130:1669–82.
15. Tao P, Sun J, Wu Z, Wang S, Wang J, Li W, et al. A dominant autoinflammatory disease caused by non-cleavable variants of RIPK1. Nature 2020;577:109–14.
16. Zhou Q, Yang D, Ombrello AK, Zavialov AV, Toro C, Zavialov AV, et al. Early-onset stroke and vasculopathy associated with mutations in ADA2. N Engl J Med 2014;370:911–20.
17. Crow YJ, Stetson DB. The type I interferonopathies: 10 years on. Nat Rev Immunol 2021.
18. Rice GI, Duany YD, Jenkinson EM, Forte GM, Anderson BH, Ariaudo G, et al. Gain-of-function mutations in IFIH1 cause a spectrum of human disease phenotypes associated with upregulated type I interferon signaling. Nat Genet 2014;46:503–9.
19. Zheng S, Lee PY, Wang J, Wang S, Huang Q, Huang Y, et al. Interstitial lung disease and psoriasis in a child with Aicardi-Goutieres syndrome. Front Immunol 2020;11:985.
20. Jeremiah N, Neven B, Gentili M, Callebaut I, Maschalidi S, Stolzenberg MC, et al. Inherited STING-activating mutation underlies a familial inflammatory syndrome with lupus-like manifestations. J Clin Invest 2014;124:5516–20.

Arthritis & Rheumatology
Vol. 74, No. 6, June 2022, pp 1091–1097

American College of Rheumatology
Empowering Rheumatology Professionals

LETTERS

DOI 10.1002/art.42067

COVID-19 vaccine uptake and vaccine hesitancy in rheumatic disease patients receiving immunomodulatory therapies in community practice settings

To the Editor:

Patients with autoimmune and inflammatory rheumatic diseases (AIIRDs) may be more likely to contract SARS–CoV-2 and have greater morbidity and mortality resulting from COVID-19. Recognizing these risks, the American College of Rheumatology (ACR) recently released the second version of its guidance for COVID-19 vaccination in patients with rheumatic and musculoskeletal diseases, recommending vaccination and supplemental (booster) dosing (1). However, patients with AIIRDs may exhibit vaccine hesitancy for a variety of reasons, including fear of side effects (e.g., disease flare, new-onset autoimmune manifestations) (2,3) or uncertainty regarding the benefits of vaccination, given the attenuating effects of immunomodulatory therapy on vaccine response. As part of a research agenda, the ACR Task Force recommended that future studies of COVID-19 vaccination should include approaches to address vaccine hesitancy in high-risk AIIRD patients, with particular attention to vulnerable populations (1).

Given the uncertainties regarding the scale of vaccine hesitancy in rheumatic disease patients, we analyzed data collected for ascertaining SARS–CoV-2 vaccine uptake in a large community practice–based rheumatology research network (Bendcare). The tablet-based, electronic survey was conducted at 101 rheumatology providers' offices from June 2021 to September 2021 and collected information on patients' self-reported vaccination status and, for those not vaccinated, their intent to be vaccinated in the future. The uncompensated survey consisted of ~3 items (depending on responses and branching logic) and was implemented as part of routine care. The survey had a 98% completion rate (the number of patients who finished the survey divided by the number of patients who started the survey) and was linked back to electronic health record data in the network's data repository (Columbus). We used descriptive statistics to evaluate vaccination status by AIIRD condition and multivariable logistic regression to model the association between having an AIIRD condition and vaccine receipt, controlling for age, sex, and race/ethnicity.

In all, 58,529 patients provided complete data, and 20,987 of those patients had an AIIRD and were receiving targeted therapies, including biologics or JAK inhibitors, at the time of data collection. As of September 9, 2021, 77.0% of the patients had been vaccinated (n = 43,675), 16.9% were not vaccinated and did not plan to be, and 6.1% were not vaccinated but still planned to be.

AIIRD patients were significantly less likely to have been vaccinated than patients with osteoarthritis or osteoporosis who had not received treatment with disease-modifying antirheumatic drugs (76.9% versus 87.0%; $P < 0.0001$) (Figure 1). After controlling for age, sex, and race/ethnicity, it was found that individuals with AIIRDs were less likely to be vaccinated (odds ratio [OR] 0.84 [95% confidence interval (95% CI) 0.77–0.92], $P < 0.001$)

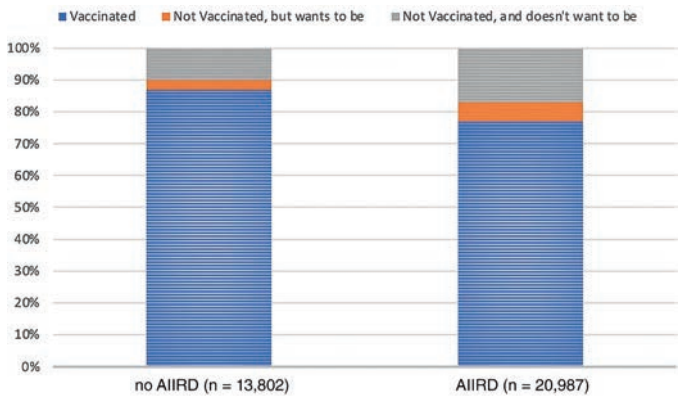

Figure 1. Vaccination status stratified by the presence of an autoimmune and inflammatory rheumatic disease (AIIRD) (patients with rheumatoid arthritis, systemic lupus erythematosus, or spondyloarthritis who were also receiving treatment with a biologic agent or disease-modifying antirheumatic drug [DMARD]) or the absence of an AIIRD (patients with a non-AIIRD condition [e.g., osteoarthritis or osteoporosis] who were also not receiving treatment with a DMARD).

compared to patients without an AIIRD. We also found that older patients and Asian patients were more likely to be vaccinated (OR per 10 years 1.49 [95% CI 1.448–1.530] and 2.42 [95% CI 1.77–3.33], respectively) and Black and Hispanic patients had slightly (but nonsignificantly) lower rates of vaccination (OR 0.92 [95% CI 0.8–1.04] and 0.95 [95% CI 0.85–1.06], respectively).

As anticipated by the ACR Task Force, these findings indicate that vaccine hesitancy remains an important and persistent problem despite the wide availability of the COVID-19 vaccine. Fortunately, increasing data suggest that recommendations from health care professionals may increase patient willingness and intention to receive the vaccine (3). Particularly for at-risk immunocompromised AIIRD patients, health care providers should make specific efforts to both ascertain vaccination status and recommend vaccination and supplemental dosing in the absence of contraindications.

Author disclosures are available at https://onlinelibrary.wiley.com/action/downloadSupplement?doi=10.1002%2Fart.42067&file=art42067-sup-0001-Disclosureform.pdf.

Stephanie S. Ledbetter, MS
Fenglong Xie, PhD
Gary Cutter, PhD
Kenneth G. Saag, MD, MSc
Lesley Jackson, MD
Maria I. Danila, MD, MSc, MSPH
University of Alabama at Birmingham
Patrick Stewart, BS
Bendcare
Boca Raton, FL
Michael George, MD, MSCE
University of Pennsylvania Medical Center
Philadelphia, PA
William Benjamin Nowell, PhD
Global Healthy Living Foundation
Nyack, NY
Ted Mikuls, MD, MSPH
University of Nebraska Medical Center and VA Nebraska–Western Iowa Health Care System
Omaha, NE
Kevin Winthrop, MD, MPH, MD
Oregon Health & Science University
Portland, OR
Jeffrey R. Curtis, MD, MS, MPH
University of Alabama at Birmingham

1. Curtis JR, Johnson SR, Anthony DD, Arasaratnam RJ, Baden LR, Bass AR, et al. American College of Rheumatology guidance for COVID-19 vaccination in patients with rheumatic and musculoskeletal diseases: version 2. Arthritis Rheumatol 2021;73:e30–45.
2. Gaur P, Agrawat H, Shukla A. COVID-19 vaccine hesitancy in patients with systemic autoimmune rheumatic disease: an interview-based survey. Rheumatol Int 2021;41:1601–5.
3. Felten R, Dubois M, Ugarte-Gil MF, Chaudier A, Kawka L, Bergier H, et al. Vaccination against COVID-19: expectations and concerns of patients with autoimmune and rheumatic diseases. Lancet Rheumatol 2021;3:e243–5.

DOI 10.1002/art.42095

A clinician's perspective on why the trial did not work: comment on the editorial by Merrill

To the Editor:

Optimization of the signal-to-noise ratio is key to a successful outcome of clinical trials of new treatments for systemic lupus erythematosus (SLE), and this is addressed nicely in the editorial by Dr. Merrill (1). In distinguishing the response to active treatment from the response to placebo, the ratio of signal to noise may be augmented by high disease activity and the use of objective measures of disease activity; for example, a focus on higher swollen joint counts as well as on swollen joints over tender joints may be appropriate as enrollment criteria. However, Merrill's editorial raises several concerns.

First, with the recent availability of several new drugs that are effective against SLE, the rationale for enrolling patients with high disease activity in placebo-controlled trials is problematic. If low disease activity is an exclusion criterion and administration of placebo to patients with high disease activity raises ethical issues, there will be few patients left to enroll. Comparative efficacy studies, which are rare for treatments targeting rheumatic diseases but common for other treatments (2), may need to become the norm. Moreover, head-to-head data are needed by clinicians when considering whether to prescribe a new medication, rather than available alternative drugs, for a particular rheumatic disease. Second, the emphasis on swollen joints ignores patient-centric goals. If a trial demonstrates nothing about whether a patient's tender but not objectively swollen joints will improve, then the incentive for using the trial intervention is diminished in patients for whom joint pain is their primary concern. Third, if available trial data only reflect the 30% of patients with the highest SLE activity, those data will not be applicable to most lupus patients. Fourth, the push to get the perfect subject population makes it increasingly difficult to know if clinical trial data apply to one of my patients. For example, a recent large, multicenter phase IIb trial includes the following inclusion criterion: "Arthritis (at least 3 tender and swollen joints) must involve joints in the hands or wrists for the hSLEDAI scoring" (3). This criterion is not an accurate reflection of hybrid SLE Disease Activity Index (hSLEDAI) scoring; rather, it is a further modification that narrows the hSLEDAI's applicability, and this nuance will not be apparent to most clinicians who use these data.

Author disclosures are available at https://onlinelibrary.wiley.com/action/downloadSupplement?doi=10.1002%2Fart.42095&file=art42095-sup-0001-Disclosureform.pdf.

Michael R. Bubb, MD
Malcom Randall Department of Veterans Affairs Medical Center and University of Florida College of Medicine
Gainesville, FL

1. Merrill JT. What did not work: the drug or the trial [editorial]? Arthritis Rheumatol 2021;73:1773–5.
2. Goldberg NH, Schneeweiss S, Kowal MK, Gagne JJ. Availability of comparative efficacy data at the time of drug approval in the United States. JAMA 2011;305:1786–9.
3. Amgen, sponsor. A phase 2b dose ranging study to evaluate the efficacy and safety of rozibafusp alfa (AMG 570) in subjects with active systemic lupus erythematosus (SLE) with inadequate response to standard of care (SOC) therapy. ClinicalTrials.gov identifier: NCT04058028; 2019.

DOI 10.1002/art.42096

Reply

To the Editor:

The clinical trialist would agree with Dr. Bubb that comparative efficacy studies of treatments for SLE would be helpful to clinicians who are treating SLE patients. Unfortunately, head-to-head trials require demonstration that the efficacy of the study drug is superior or equivalent to those of proven treatments. Since no single drug has been proven to be effective against lupus, a head-to-head trial comparing single agents is not possible. Comparative trials would require comparing an approved treatment plus standard of care to a new investigational drug plus standard of care, which increases the risk of polypharmacy effects that can narrow the gap between effective treatments and placebo.

A clumsy polypharmacy design such as this might allow an equivalency end point, and more drugs might be approved, but at what cost? How can the clinician interpret data for their patients in the presence of so much noise from various combined treatments? Suppose that a treatment is effective for fewer patients than an approved agent but that these patients are from a different biologic subset of the lupus population. The treatment would fail in the comparative trial, and its true value would be missed.

Dr. Bubb states that if low disease activity is a study exclusion criterion and the administration of placebo to patients with high disease activity raises ethical issues, there will be few patients left to enroll in studies of new lupus drugs. However, there are effective trial designs for patients without severe disease that limit the use of background medications (1,2). Patients with more severe disease can also participate in trials with interpretable outcomes, although they require more background treatment. Optimally, we will learn to use more uniform background treatments that complement the investigational drug and are less likely to interfere with or reduplicate its effects. Gradual tapering of background medications has also improved the interpretability of trial data, including those from studies involving patients with various levels of illness severity (3–5).

Dr. Bubb proposes that available trial data only reflect the 30% of patients with the greatest disease severity. This is not correct; these vulnerable patients are usually excluded. Most trials require some objectively swollen joints at entry, and Dr. Bubb thinks this makes it difficult to evaluate a treatment for people whose primary concern is pain. However, tender joint counts are ubiquitous among outcome measures for trials of new lupus drugs, as are patient-reported end points, which allow insight into patients' concerns. Furthermore, the majority of patients with no joint-specific symptoms other than pain for >6 months are likely experiencing the effects of joint damage, rather than lupus activity, and are unlikely to benefit from immune modulation. This is confirmed by data from trials in which individuals who did not satisfy screening criteria tended to be older and were more likely to have inactive disease based on serologic disease activity measures, with potentially confounding comorbid conditions. These people deserve consideration but might be more appropriate candidates for trials of chronic pain treatment, general physical conditioning interventions, and rehabilitation techniques.

Finally, Dr. Bubb raises the concern that "the push to get the perfect subject population makes it increasingly difficult to know if clinical trial data apply to my patient." On the contrary, perfect patients are not being sought; rather, trialists are seeking better trial designs and a better understanding of heterogeneous patient subsets that may help improve treatment selection and guide optimal dosing for individual patients.

Author disclosures are available at https://onlinelibrary.wiley.com/action/downloadSupplement?doi=10.1002%2Fart.42096&file=art42096-sup-0001-Disclosureform.pdf.

Joan T. Merrill, MD
University of Oklahoma Health Sciences Center
Oklahoma City, OK

1. Merrill JT, Immermann F, Whitley M, Zhou T, Hill A, O'Toole M, et al. The Biomarkers of Lupus Disease study: a bold approach may mitigate interference of background immunosuppressants in clinical trials. Arthritis Rheumatol 2017;69:1257–66.
2. Merrill JT, Guthridge J, Zack D, Foster P, Burington B, Tran L, et al. SAT0187 discrimination of systemic lupus (SLE) patients with clinical response to obexelimab (XMAB®5871) based on a pattern of immunologic markers [poster]. Ann Rheum Dis 2020;79:1035–6.
3. Furie R, Khamashta M, Merrill JT, Werth VP, Kalunian K, Brohawn P, et al. Anifrolumab, an anti–interferon-α receptor monoclonal antibody, in moderate-to-severe systemic lupus erythematosus. Arthritis Rheumatol 2016;69:376–86.
4. Furie RA, Rovin BH, Houssiau F, Malvar A, Teng YK, Contreras G, et al. Two-year, randomized, controlled trial of belimumab in lupus nephritis. N Engl J Med 2020;383:1117–28.
5. Rovin BH, Teng YK, Ginzler EM, Arriens C, Caster DJ, Romero-Diaz J, et al. Efficacy and safety of voclosporin versus placebo for lupus nephritis (AURORA 1): a double-blind, randomised, multicentre, placebo-controlled, phase 3 trial. Lancet 2021;397:2070–89.

DOI 10.1002/art.42084

Absent in melanoma 2 protein in systemic lupus erythematosus: friend or foe? Comment on the article by Lu et al

To the Editor:

Systemic lupus erythematosus (SLE) is a systemic autoimmune disease that can be complicated with severe

manifestations, such as lupus nephritis (1). To date, a clear pathogenesis of SLE has not been fully elucidated. Therefore, searching for the mechanisms involved in the development of SLE and targeting potential mechanisms for treatment remain topics of investigation.

Absent in Melanoma 2 (AIM2) is a member of the pyrin and hematopoietic interferon (IFN)–inducible nuclear domain proteins. This protein has wide-ranging, propyroptotic properties. Regarding innate immunity, AIM2 serves as a cytoplasmic double-stranded DNA (dsDNA) sensor, regulating the initiation of innate immune responses (2). The recognition of dsDNA by AIM2 results in the assembly of a large multiprotein oligomeric complex known as the inflammasome, which regulates interleukin-1β (IL-1β) and IL-18 generation and induces cell death. In the cytosol, sensing of dsDNA by AIM2 is important for protection against invading pathogens, such as bacteria, viruses, and fungi. Conversely, the response of AIM2 to dsDNA released by damaged host cells may lead to the production of different cytokines that are involved in the pathogenesis of sterile inflammatory diseases, such as skin and kidney diseases. AIM2 contributes to lung tumorigenesis through the inflammasome-dependent release of IL-1β and the regulation of mitochondrial dynamics. The AIM2 inflammasome becomes activated in the presence of atherosclerotic plaque, abdominal wall aortic aneurysm, and injured myocardium.

To date, the findings of studies on AIM2 in the setting of lupus have been inconsistent. In a recent study by Dr. Lu and colleagues (1), it was found that *Aim2* gene–deficient mice developed lupus, demonstrated by high histologic scores and high serum levels of dsDNA, myeloperoxidase, proteinase 3, albumin, and urea nitrogen, after pristane treatment. Increased infiltration of dendritic cells, macrophages, neutrophils, B cells, and T cells as well as high type I IFN signatures were also found in the kidneys of *Aim2* gene–deficient mice treated with pristane. *Aim2* deficiency resulted in elevated expression of type I IFN–induced genes in the kidneys, suggesting that AIM2 inhibits the development of lupus (1).

Similarly, Panchanathan et al predicted that *Aim2* deficiency contributed to increased susceptibility to lupus (2). In their study, *Aim2* gene–deficient mice had high expression of p202 protein, which correlated with increased expression of IFNβ, STAT1, and IFN-inducible genes (2). In contrast, Huang et al evaluated *Aim2* expression in lupus nephritis patients and found that *Aim2* was highly expressed in the glomerular cells of patients with lupus nephritis class II (3).

Yang et al found that in SLE patients, *Aim2* expression was increased in germinal center B cells and plasma cells from peripheral blood, and in tonsil memory and skin lesions (4). Proportions of CD19+ cells were down-regulated in the lymph nodes and spleens of mice with lupus and *Aim2* gene-deficient B cells. *Aim2* deficiency in B cells attenuated the development of lupus, as shown by reduced glomerulonephritis, lower proportions of germinal center B cells, T follicular helper cells, and plasma cells, up-regulated secretion of B lymphocyte–induced maturation protein 1 (BLIMP-1), and reduced expression of Bcl-6 (4). Interestingly, knockout of the genes for BLIMP-1 and Bcl-6 did not affect *Aim2* expression. These findings suggest that AIM2 promotes lupus pathogenesis by regulating BLIMP-1/Bcl-6 axis–mediated B cell differentiation.

Additionally, Zhang et al found that *Aim2* expression was related to severity of disease in SLE patients and mice with lupus (5). *Aim2* expression was elevated in apoptotic DNA–induced macrophages and was related to macrophage activation. Knockout of *Aim2* blunted apoptotic DNA–induced macrophage activation and suppressed lupus development by impeding macrophage activation and reducing inflammatory responses (5).

Based on the findings reviewed above, it is uncertain whether AIM2 is able to inhibit lupus development or promote SLE pathogenesis. Therefore, more studies with *Aim2* gene deficiency or conditional knockout are needed to further clarify the role of AIM2 in lupus.

Supported by grants from the National Natural Science Foundation of China (81701606). Author disclosures are available at https://onlinelibrary.wiley.com/action/downloadSupplement?doi=10.1002%2Fart.42084&file=art42084-sup-0001-Disclosureform.pdf.

Wang-Dong Xu, MD
Southwest Medical University
An-Fang Huang, MM
Affiliated Hospital of Southwest Medical University
Luzhou, China

1. Lu A, Wu S, Niu J, Cui M, Chen M, Clapp WL, et al. Aim2 couples with Ube2i for sumoylation-mediated repression of interferon signatures in systemic lupus erythematosus. Arthritis Rheumatol 2021;73:1467–77.
2. Panchanathan R, Duan X, Shen H, Rathinam VA, Erickson LD, Fitzgerald KA, et al. Aim2 deficiency stimulates the expression of IFN-inducible Ifi202, a lupus susceptibility murine gene within the Nba2 autoimmune susceptibility locus. J Immunol 2010;185:7385–93.
3. Huang T, Yin H, Ning W, Wang X, Chen C, Lin W, et al. Expression of inflammasomes NLRP1, NLRP3 and AIM2 in different pathologic classification of lupus nephritis. Clin Exp Rheumatol 2020;38:680–90.
4. Yang M, Long D, Hu L, Zhao Z, Li Q, Guo Y, et al. AIM2 deficiency in B cells ameliorates systemic lupus erythematosus by regulating Blimp-1-Bcl-6 axis-mediated B-cell differentiation. Signal Transduct Target Ther 2021;6:341.
5. Zhang W, Cai Y, Xu W, Yin Z, Gao X, Xiong S. AIM2 facilitates the apoptotic DNA-induced systemic lupus erythematosus via arbitrating macrophage functional maturation. J Clin Immunol 2013;33:925–37.

DOI 10.1002/art.42083

Reply

To the Editor:

We thank Drs. Xu and Huang for their interest in our recently published article. As we mentioned in our report, *Aim2* deficiency

leads to elevated type I IFN generation and SLE-like nephritis, which has been implied in previous publications (1,2). The finding of elevated type I IFN signatures in both resting and pristane-treated *Aim2*$^{-/-}$ mice provides direct evidence that AIM2 inhibits type I IFN production, not only upon DNA transfection in cultured cells (3,4), but also in the SLE mouse model in vivo. Of note, *Aim2* deficiency results in not only elevated type I IFN production, but also an enhanced response to IFNβ stimulation (2). Importantly, our work revealed the mechanism through which AIM2 represses type I IFN: sumoylation-mediated inhibition of type I IFN transcription requires ubiquitin-conjugating enzyme 2i (Ube2i) (5), and Aim2 partners with Ube2i for its optimal function. In the absence of AIM2, the activity of Ube2i is compromised, which leads to decreased cellular sumoylation; thus, a stronger type I IFN signal appears and more severe lupus nephritis develops.

With regard to another autoimmune disease model (multiple sclerosis), 2 recent studies demonstrated that *Aim2* deficiency in Treg cells or microglia exacerbates the development of experimental autoimmune encephalomyelitis (EAE) (6,7). In both Treg cells and microglia, *Aim2* deficiency resulted in stronger expression of type I IFN–stimulated genes (ISGs) including *Irf7* and *Ddx58*, as well as Stat1 phosphorylation (6,7). Therefore, although the *Aim2*$^{-/-}$ mice we used were on a mixed (129 × B6) genetic background, *Aim2*$^{-/-}$ mice on the C57BL/6 background also exhibited elevated type I IFN signatures and enhanced autoimmune disease activity, demonstrating that, at least in macrophages, Treg cells, and microglia, AIM2 inhibits type I IFN signaling (6,7). Conditional knockout of *Aim2* in macrophages has not been achieved, but *Aim2* is mainly expressed in innate immune cells. Therefore, the findings with universal *Aim2* deletion should be largely attributed to innate immune cells including macrophages.

Additionally, in our study *Aim2*$^{-/-}$*Rag1*$^{-/-}$ mice clearly exhibited improvement in disease activity, implying that adaptive immune cells are involved in the nephritis of *Aim2*$^{-/-}$ mice, despite deficiency of *Aim2* in the B cells and T cells of these mice. In light of findings reported by Yang et al (8), it would be interesting to compare *Aim2* deficiency in different types of cells among animals in the same facility with SLE development upon pristane injection, because lupus induction is a long process and microbiota may affect disease development.

With regard to the elevated *Aim2* expression in SLE patients and apoptotic DNA–treated BALB/c mice (8,9), it should be noted that the *Aim2* gene itself is an ISG whose expression can be induced by IFN. Moreover, as demonstrated in the study by Yang et al, IL-10 can also induce the expression of *Aim2* (8). Therefore, the elevated expression of *Aim2* is likely a result of SLE development rather than a driving factor of the disease. It would be interesting to generate a line of *Aim2*-overexpressing mice to investigate whether enforced expression of this gene leads to enhancement or alleviation of autoimmune diseases, including SLE and EAE.

Supported by grants from the National Key Basic Research Program (2018YFA0507300), the Natural Science Foundation of China (81830049), and the Shanghai Research Leader Program (20XD1403900).

Ailing Lu, PhD
Guangxun Meng, PhD
The Center for Microbes, Development and Health
CAS Key Laboratory of Molecular Virology and Immunology
Institut Pasteur of Shanghai
Chinese Academy of Sciences
and the University of Chinese Academy of Sciences
Shanghai, China

1. Choubey D, Panchanathan R. Absent in melanoma 2 proteins in SLE [review]. Clin Immunol 2017;176:42–8.
2. Panchanathan R, Duan X, Shen H, Rathinam VA, Erickson LD, Fitzgerald KA, et al. Aim2 deficiency stimulates the expression of IFN-inducible Ifi202, a lupus susceptibility murine gene within the Nba2 autoimmune susceptibility locus. J Immunol 2010;185:7385–93.
3. Wang Y, Ning X, Gao P, Wu S, Sha M, Lv M, et al. Inflammasome activation triggers caspase-1-mediated cleavage of cGAS to regulate responses to DNA virus infection. Immunity 2017;46:393–404.
4. Yan S, Shen H, Lian Q, Jin W, Zhang R, Lin X, et al. Deficiency of the AIM2-ASC signal uncovers the STING-driven overreactive response of type I IFN and reciprocal depression of protective IFN-γ immunity in mycobacterial infection. J Immunol 2018;200:1016–26.
5. Crowl JT, Stetson DB. SUMO2 and SUMO3 redundantly prevent a noncanonical type I interferon response. Proc Natl Acad Sci U S A 2018;115:6798–803.
6. Chou WC, Guo Z, Guo H, Chen L, Zhang G, Liang K, et al. AIM2 in regulatory T cells restrains autoimmune diseases. Nature 2021;591:300–5.
7. Ma C, Li S, Hu Y, Ma Y, Wu Y, Wu C, et al. AIM2 controls microglial inflammation to prevent experimental autoimmune encephalomyelitis. J Exp Med 2021;218:e20201796.
8. Yang M, Long D, Hu L, Zhao Z, Li Q, Guo Y, et al. AIM2 deficiency in B cells ameliorates systemic lupus erythematosus by regulating Blimp-1-Bcl-6 axis-mediated B-cell differentiation. Signal Transduct Target Ther 2021;6:341.
9. Zhang W, Cai Y, Xu W, Yin Z, Gao X, Xiong S. AIM2 facilitates the apoptotic DNA-induced systemic lupus erythematosus via arbitrating macrophage functional maturation. J Clin Immunol 2013;33:925–37.

DOI 10.1002/art.42088

Airway obstruction as a pulmonary manifestation of rheumatoid arthritis: comment on the article by Prisco et al

To the Editor:

We read with great interest the report by Dr. Prisco et al (1), describing their study which demonstrated much greater odds of both restrictive and obstructive pulmonary patterns among rheumatoid arthritis (RA) cases, compared with controls, in an analysis of data from the UK Biobank. However, some concerns are worth addressing.

In discussions about pulmonary function abnormalities, a crucial variable is the presence of chronic respiratory disease.

The authors addressed this by using self-reported patient data, which could undermine the validity of the diagnosis and lead to information bias. We believe that inaccurate measurement of the prevalence of 2 key chronic respiratory diseases, bronchiectasis and chronic obstructive pulmonary disease (COPD), is especially relevant here.

First, previous studies showed a bronchiectasis prevalence of ~30% among RA patients (2). However, the current study, which relied on self-reported bronchiectasis, revealed a prevalence of only 0.9%. This vast discrepancy implies that, in many patients with RA-associated bronchiectasis, the disease is clinically silent and unrecognized yet can be readily detected by pulmonary function tests.

Second, COPD is notoriously prone to evading clinical detection; one study showed that it was undiagnosed in ~70% of COPD patients worldwide (3). In the current study, mean pack-years of smoking and the percentages of participants who were current or past smokers were all higher among RA cases than among controls. These differences suggest that the rate of undiagnosed COPD might have been higher in the RA group and could have contributed in part to the increased odds of obstructive patterns among these patients. Moreover, quitting smoking requires strong personal motivation, and we wonder whether RA patients had a greater prevalence of more severe smoking-related airway symptoms and disease and, in turn, a higher rate of smoking cessation.

We understand that image correlation is difficult in databank analysis. However, chest images (if available) from these participants would be very informative for assessing the scale of information bias, if present.

Finally, the prevalence of rheumatoid factor (RF) positivity in the RA group (86%) was much higher than typically reported (4). In a small study, we found that 42% of COPD patients tested positive for RF (5). Therefore, we wonder whether the excess RF positivity reported by Prisco et al (1) could have been attributable to undiagnosed COPD among RA cases, since RF positivity was common in this group.

We appreciate the robust work done by the authors and look forward to their reply.

Author disclosures are available at https://onlinelibrary.wiley.com/action/downloadSupplement?doi=10.1002%2Fart.42088&file=art42088-sup-0001-Disclosureform.pdf.

Sheng-Yuan Wang, MD
National Cheng Kung University Hospital and National Cheng Kung University
Tainan, Taiwan
Chih-Wei Chen, FRGS, MPhil
Chung Shan Medical University
James Cheng-Chung Wei, MD, PhD
Chung Shan Medical University Hospital Chung Shan Medical University and China Medical University
Taichung, Taiwan

1. Prisco L, Moll M, Wang J, Hobbs BD, Huang W, Martin LW, et al. Relationship between rheumatoid arthritis and pulmonary function measures on spirometry in the UK Biobank. Arthritis Rheumatol 2021; 73:1994–2002.
2. Kadura S, Raghu G. Rheumatoid arthritis–interstitial lung disease: manifestations and current concepts in pathogenesis and management. Eur Respir Rev 2021;30:210011.
3. Diab N, Gershon AS, Sin DD, Tan WC, Bourbeau J, Boulet LP, et al. Underdiagnosis and overdiagnosis of chronic obstructive pulmonary disease. Am J Respir Crit Care Med 2018;198:1130–9.
4. Yang DH, Huang JY, Chiou JY, Wei JC. Analysis of socioeconomic status in the patients with rheumatoid arthritis. Int J Environ Res Public Health 2018;15:1194.
5. Yang DH, Tu CC, Wang SC, Wei CC, Cheng YW. Circulating anti–cyclic citrullinated peptide antibody in patients with rheumatoid arthritis and chronic obstructive pulmonary disease. Rheumatol Int 2014;34:971–7.

DOI 10.1002/art.42086

Reply

To the Editor:

We thank Dr. Wang and colleagues for allowing us to expound on how we identified chronic respiratory diseases and analyzed smoking history in our study. Clinicians typically diagnose chronic respiratory diseases through patient self-report, physical examination, and physiologic analyses (such as spirometry) and chest imaging usually prompted by symptoms, signs, or clinical events. The UK Biobank is renowned for the depth and breadth of the measurements included in its research protocol, but chest imaging data were unavailable for our study. Thus, we relied on patient self-report to identify whether chronic respiratory diseases were present.

In total, 18.0% of RA patients reported a chronic respiratory disease as compared to 13.2% of control participants. We agree that some chronic respiratory diseases that we considered, such as bronchiectasis (reported by 0.9% of RA patients) and interstitial lung disease (ILD) (reported by 0.3%), may have been underreported. In our recent systematic review of bronchiectasis in RA, the pooled prevalence of bronchiectasis was 18.7% (1). However, this observation was mostly driven by bronchiectasis prospectively detected by high-resolution computed tomography (CT) of the chest (prevalence 24.1%) (1). When only considering bronchiectasis identified through clinical care, the prevalence was 3.8% (1). Similarly, the prevalence of ILD among RA patients varies widely, based on whether it was identified clinically during care or subclinically by high-resolution CT of the chest (2,3).

Spirometry is the cornerstone to the diagnosis of COPD and was used to detect an obstructive pattern, a coprimary outcome of our study. We used self-report to determine the presence of COPD (characterized as "known" in our study), but this may have been an inaccurate measure (4). The analysis among never smokers lowered the possibility that underreported COPD contributed to our findings. Ascertainment of asthma had similar limitations. Some individuals with chronic respiratory disease report several conditions concurrently.

Many respiratory conditions overlap, as in asthma–COPD overlap syndrome (5) and a spectrum of endotypes (6). Therefore, we used a composite variable, history of chronic respiratory disease (present or absent), as an adjustment variable and in stratified analyses. Thus, while we acknowledge some loss in granularity in specific diagnoses by using self-reported data, the association of RA with obstructive lung disease is supported by objective measurements.

One strength of our study was the use of granular data on smoking history, an established RA risk factor (7). All analyses were adjusted for smoking status and pack-years. Since chronic respiratory disease would be expected to lead to spirometric abnormalities, history of chronic respiratory disease was adjusted for in models. All findings persisted in subgroups of never smokers and those without self-reported chronic respiratory disease. Therefore, potential inaccuracies of diagnoses due to self-reported chronic respiratory disease and smoking history are unlikely to explain our findings.

Our study emphasizes that many patients with RA may have either subclinical or unrecognized chronic respiratory disease that is not explained by smoking status and pack-years. These findings add to the growing literature implicating the importance of airways and emphysema in RA pathogenesis and outcomes (3,8,9) and suggest that obstructive lung disease may be an extraarticular RA manifestation in addition to restrictive lung diseases, such as ILD. Future longitudinal studies are needed to integrate accurate clinical diagnoses, patient-reported symptoms, chest imaging findings, and pulmonary function test results to better define the respiratory burden of RA throughout the disease course.

The contents of this letter are solely the responsibility of the authors and do not necessarily represent the official views of Harvard University and its affiliated academic health care centers or those of the National Institutes of Health. Dr. Sparks' work was supported by the National Institute of Arthritis and Musculoskeletal and Skin Diseases (grants R01-AR-077607, K23-AR-069688, R03-AR-075886, L30-AR-066953, P30-AR-070253, and P30-AR-072577), the Rheumatology Research Foundation (R Bridge Award), and the R. Bruce and Joan M. Mickey Research Scholar Fund. Dr. Doyle's work was supported by the National Heart, Lung, and Blood Institute (grants K23-HL-119558 and R03-HL-148484). Ms. Prisco and Dr. Moll contributed equally to this work.

Lauren Prisco, BA
Brigham and Women's Hospital
Matthew Moll, MD, MPH
Tracey J. Doyle, MD, MPH
Michael H. Cho, MD, MPH
Jeffrey A. Sparks, MD, MMSc
Harvard Medical School and Brigham and Women's Hospital
Boston, MA

1. Martin LW, Prisco LC, Huang W, McDermott G, Shadick NA, Doyle TJ, et al. Prevalence and risk factors of bronchiectasis in rheumatoid arthritis: a systematic review and meta-analysis. Semin Arthritis Rheum 2021;51:1067–80.
2. Huang S, Kronzer VL, Dellaripa PF, Deane KD, Bolster MB, Nagaraja V, et al. Rheumatoid arthritis–associated interstitial lung disease: current update on prevalence, risk factors, and pharmacologic treatment. Curr Treatm Opt Rheumatol 2020;6:337–53.
3. Esposito AJ, Sparks JA, Gill RR, Hatabu H, Schmidlin EJ, Hota PV, et al. Screening for preclinical parenchymal lung disease in rheumatoid arthritis. Rheumatology (Oxford). doi: 10.1093/rheumatology/keob891 2021. E-pub ahead of print.
4. Barr RG, Herbstman J, Speizer FE, Camargo CA Jr. Validation of self-reported chronic obstructive pulmonary disease in a cohort study of nurses. Am J Epidemiol 2002;155:965–71.
5. Mart MF, Peebles RS Jr. Asthma–chronic obstructive pulmonary disease overlap syndrome. Curr Opin Immunol 2020;66:161–6.
6. Chupp GL, Kaur R, Mainardi A. New therapies for emerging endotypes of asthma. Annu Rev Med 2020;71:289–302.
7. Sparks JA, Karlson EW. The roles of cigarette smoking and the lung in the transitions between phases of preclinical rheumatoid arthritis. Curr Rheumatol Rep 2016;18:15.
8. Demoruelle MK, Weisman MH, Simonian PL, Lynch DA, Sachs PB, Pedraza IF, et al. Airways abnormalities and rheumatoid arthritis–related autoantibodies in subjects without arthritis: early injury or initiating site of autoimmunity? Arthritis Rheum 2012;64:1756–61.
9. Sparks JA, Lin TC, Camargo CA Jr, Barbhaiya M, Tedeschi SK, Costenbader KH, et al. Rheumatoid arthritis and risk of chronic obstructive pulmonary disease or asthma among women: a marginal structural model analysis in the Nurses' Health Study. Semin Arthritis Rheum 2018;47:639–48.